

6th Iranian Fuel Cell Seminar

2013
March 12 & 13

6th Iranian Fuel Cell Seminar

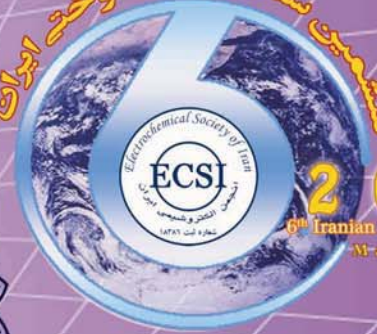
مجموعه مقالات کامل

ششمین سمینار

پیل سوختی ایران

۲۲ و ۲۳ اسفند ماه سال ۱۳۹۱

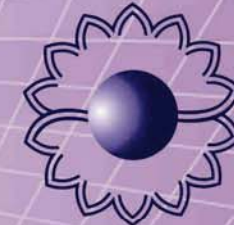
ششمین سمینار پیل سوختی ایران



2013
6th Iranian Fuel Cell Seminar
March 12 & 13



سازمان توسعه منابع انرژی



سازمان توسعه منابع انرژی



دانشگاه تربیت مدرس



FUEL CELL RESEARCH LABORATORY



پژوهشکده انرژی‌های نو (انستیتو پد دانشگاه امیرکبیر)

Full Papers
6th Iranian Fuel Cell Seminar

www.iranecs.ir

fuelcell@iranecs.ir



بِسْمِ اللَّهِ الرَّحْمَنِ الرَّحِيمِ



Full Papers

6th Iranian Fuel Cell Seminar

Shahid Rajaei Teacher Training University

Faculty of Science

Tehran – Iran

March 12&13 , 2013

6th Iranian Fuel Cell Seminar

Held in Shahid Rajaei Teacher Training University, Tehran, Islamic Republic of Iran, 12-13 March 2013.

Conference Chairman: Dr Rasol Abdullah Mirzaie

© Copyright 2013, Electrochemical Society of Iran

Faculty of Science, Department of Chemistry, 3rd floor, Tarbiat Modares University, Tehran, Islamic Republic of Iran

P.O. Box: 14115-111

Phone: +98-21-82884713

Fax: +98-21-82884713

Email: info@iranecs.ir

Website: www.iranecs.ir

Full papers proceedings of 6th Iranian Fuel Cell Seminar, 12-13 March 2013, Electrochemical Society of Iran.
Event jointly organized by Development energy resources organization.

All rights reserved. No part of this may be reproduced, stored in a retrieval system, or transmitted, in any form or by any means, without the prior written permission of the Electrochemical Society of Iran.

Electrochemical Society of Iran is not responsible for the use which might be made of the information contained in this book.

Organizers



Welcome to 6th Iranian fuel cell seminar

Dear colleague,

On behalf of all members of scientific and organizing committees, it is my great honor to welcome you to the 6th Iranian fuel cell seminar. This seminar is hosted by the Electrochemical Society of Iran, Development energy resources organization and Shahid Rajaei Teacher Training University from 12 to 13 March 2013. The aim of this seminar is to get together and present the latest scientific findings and to share information in the field of fuel cell systems for professionals within academia, research and industry.

Fuel cell is the best way for clean energy production in Hydrogen economy. It can help for producing electricity with low noise and good efficiency. As fuel cells generate electricity through a chemical reaction, rather than combustion, they do not produce harmful emissions. Currently, technologists are developing and adapting fuel cell technology for practical use in exhaust-free automobiles and in electricity-generating plants.

Participants at this seminar celebrate 62 paper presentations, posters as well as workshop sessions. Professor Hossein Gharibi as an invited speaker provided insightful ideas and questions for many seminar participants by tackling issues in the innovation in fuel cell systems especially about materials of MEA. In this seminar, energy education workshop for children is provided interactive environment in order to learning energy concepts.

This seminar would not be possible without your participation and support. We would like to thank you for your participation and also all those involved in the organization of this conference. We hope that you have had a fruitful and memorable seminar and a delightful stay in Tehran at Shahid Rajaei Teacher Training University.

Dr Rasol Abdullah Mirzaie

Scientific Chairman

Hojat Aliloo

Executive chairman

Organizing Committee



Director of Electrochemical Society of Iran : Prof. JahanBakhshRaof
University of Mazandaran



Scientific Chairman: Dr. Rasol Abdullah Mirzaie
Shahid Rajaei Teacher Training University
Fuel cell Research Laboratory



Executive Chairman: Hojat Aliloo
Development of energy resources organization



Prof. Majid Jafarian
K. N. Toosi University of Technology



Prof. Hossein Gharibi
Tarbiat Modares University

Scientific Committee:



Prof. Majid Jafarian , K. N. Toosi University of technology



Prof. Hossein Gharibi , Tarbiat Modares University



Prof. Jahan Bakhsh Raouf , University of Mazandaran



Prof. Reza ojani , University of Mazandaran



Dr Niloufar Bahrami Panah , Payame Noor University



Dr Soosan Rowshanzamir , Iran University of science of Technology



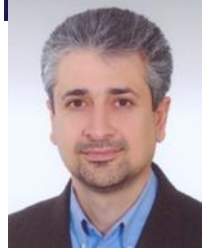
Dr Mohsen Shakeri , Noshirvani University of Technology



Dr Seyed Majid Hashemianzadeh, Iran University of science and technology



Dr Mohammad J. Kermani , Amirkabir University of Technology



Dr Amir Maghsoudipour , Materials and Energy Research Centre



Dr Mohammad Zhiani , Isfahan University of Technology



Dr Mehdi Kheirmand , Yasouj University



Dr Mohammad Safi Rahmanifar , Shahed university



Dr Mehran Javanbakht, Amirkabir University of Technology



Dr Saeed Olyae , Shahid Rajae Teacher Training University



Dr Mahmoud Ziarati , Malek Ashtar University of Technology



Dr Soheila Javadian Farzaneh , Tarbiat Modares University



Dr Mostafa Dehghani Mobarake , Research Institute of Petroleum Industry (RIPI)



Dr Javad Beheshtian , Shahid Rajae Teacher Training university



Dr Pejman Kazempoor , Tarbiat Modares University



Dr Rasol Abdullah Mirzaie , Shahid Rajae Teacher Training university

Dr Ahmad Nozad Goli-Kand, Material School, NSTRI

Executive Committee:

Hojat aliloo, Executive Secretary

Arash Abdullah Mirzaie , The seminar secretariat

Aida khajeh , Staff of Electrochemical Society of Iran

Dr. Hamid Mesgarani , Deputy of Shahid Rajae Teacher Training University

Dr. Ayoub Esmailpour , Head of Faculty of Basic science, Shahid Rajae Teacher Training University

Dr. Mehdi Saadat , Deputy of Faculty of Basic science, Shahid Rajae Teacher Training University

Dr. Ali Zaeembashi tajAbadi of Faculty of Basic science, Shahid Rajae Teacher Training University

Shahla manouchehrian

Zohreh babaei

Fatemeh shakeri

Mojtaba safari

Ali Zali

Mohammad Reza Jafarpanah

Mahmood Darvishi

Arezo Vaez

Arezo Asfa

Behjat Ghasemi

Shirin Shakeri

Post Graduate students

Yekta Majidifard

Ilqar Abdollahi

Neda Zerafat Doost

Farmand Farzin

Ehsan Mahnani

Samane Sajediniya

Kumarse Shamkhali

Fatemeh Hamedi

Nasrin Farshadi

Elena Yashmi

Behnam Moeini

Maryam Azamiyan

Narges Mohammadkhani

Key Speaker



Professor Hossein Gharibi

“How is our approach for materials of MEA”

Department of Chemistry
Faculty of Science
Tarbiat Modares University
Tehran, Iran

Biography

Gust Editor of International Journal of Hydrogen Energy (International Association of Hydrogen Energy, USA 2009 up to now)

Chairman of Electrochemical society of Iran 2004 –Jan 2012

Visiting Professor, Dept of Material Sci. & Eng. , University of UTAH 2012, USA

Chairman of Department of Chemistry 4 years

Director of IRANDOC, [www. Irandoc.ac.ir](http://www.Irandoc.ac.ir) (1992-2008)

Organizer of too many scientific conferences

B.Sc. 1985 from Shiraz University (IRAN)

M.Sc .1987 from Salford University (UK)

PhD 1990 from Salford University (UK)



Contents	Page
Modeling Local Structure and Dynamics of Aromatic Sulfonated poly(2,6-Dimethyl-1,4-Phenylene Oxide) Fuel Cell Membranes	1
Mathematical modeling of plate solid oxide fuel cell	9
Electrosynthesis of Pt-Co alloy catalyst on the carbon-ceramic electrode for methanol oxidation	25
Comparison conductivity between Yb and Dy co-doped CeO ₂ -Gd ₂ O ₃ systems for IT-SOFCs	34
Electricity Generation and Sulfide Removal by dual chamber Microbial fuel cell simultaneously	46
Economical comparison of power generation in microbial fuel cell by Nafion 117 and SPEEK as proton exchange membranes	53
A technical assessment of the CO ₂ capture modeling for GT/SOFC/CHP hybrid cycles	67
Comparative Study of Platinum and Non-Platinum Cathode Nanocatalysts in Direct Borohydride Fuel Cell	77
Electrochemical oxidation of hydrazine on the surface of silver particles/polymer modified carbon paste electrode in alkaline media	85
Experimental Study on the effect of Bipolar Plates Substance on the Performance of Poroton Exchange Membrane Fuel Cells	91
Membraneless Mixed Reactant Direct Methanol Fuel Cell	98
Manufacturing of yttria stabilized Zirconia based solid electrolyte thin films by Combined tape casting/Impregnation method	105
An analytic and numerical modeling of a membrane humidifier for PEM fuel cell	111
Synthesis of nanocatalysts of graphene oxide/TiO ₂ /Pt and study of its characterization	120
Polybenzimidazole/MnTiO ₃ nanocomposite membranes for polymer electrolyte membrane fuel cells	127
Corrosion Behavior and Interfacial Contact Resistance of TiN Coated Type 316L Stainless Steel as Bipolar Plate for Proton Exchange Membrane Fuel Cell	137



Electrooxidation of Sodium Borohydride on Porous Nano Structured Ni/PtNi electrode in basic media	151
Investigation the Stability and Methanol Oxidation Activity of Alloy Nanoparticles	160
Electrocatalytic oxidation of methanol on semiconducting polymer nanocomposite in alkaline media	167
Electrophoretic deposition of NiFe ₂ O ₄ spinel on SOFC interconnect	175
Hybrid Genetic Algorithm-Neural Network for Membrane RI Measurement Error Modeling in PEM Fuel Cells	181
Study of ORR kinetic on Pt/C at the presence of super paramagnetic of Fe ₃ O ₄ nanoparticles in PEMFC	192
Modification of Nafion Membranes with Different Clays for Direct Methanol Fuel Cell Applications	200
Electrocatalytic activity of graphene- carbon nanotube supported Pt ₃ Co as an electrocatalyst for oxygen reduction reaction in PEM fuel cell gas diffusion electrodes	210
Study of adsorption of oxygen molecule on the structures of Ptn/Graphene as an electrode in the PEM Fuel Cell	215
Parametric study and optimization of the cathode catalyst layer in PEM fuel cells	220
Characterization and preparation of single wall nanotubes materials for hydrogen storage	230
Study of synergism effect in platinum – Gold alloy electrocatalyst for glucose oxidation in direct glucose alkaline fuel cell	246
Lactose Electrooxidation on the Nickel Oxide Nanoparticles Electrocatalyst Prepared on the Multi-walled Carbon Nanotubes Modified Electrode	253
Hydrogen Evolution Reaction on Graphene Supported Pt Hollow Nanospheres	263
Designing H4KIDS software for hydrogen energy teaching to children	272
Theoretical Study of Hydrogen Bonding in Blend Membranes Based on Sulfonated poly(ether ether ketone)-Sulfonated poly(ether sulfone)	284
Organically Modified Nanoclays and Chitosan–Phosphotungstic Acid Complex Nanocomposites as Polyelectrolytes for Fuel Cells Applications	292



Using the electrode based on various core- shell electrocatalyst in polymer electrolyte fuel cells	302
Investigation of Electrolyte Conductivity on Performances of Sediment Microbial Fuel Cell	315
Synthesis and characterization of PVA/sulfonated graphene oxide nanocomposite membranes for used in PEMFC	323
Dynamic Response Analysis of Two Conventional Types of SOFCs to the Inlet Air Mass Flow Rate Variation	333
Problems, components and methods for making polymer fuel cell electrodes and applying nanotechnology to solve their problems	343
Electrochemical characterization of binary carbon supported Pd ₃ Co nanocatalyst for oxygen electroreduction reaction in direct methanol fuel cells	356
Hydrogen storage: A DFT investigation of adsorption hydrogen Molecule on born nitride nanofullerens like structure	365
Proton exchange membrane fuel cell modeling based on harmony search algorithm	371
Study design and construction techniques and types of bipolar plates used in fuel cell stack	381
Numerical Simulation of a PEM fuel cell with partially blocked channel	387
Hydrogen storage: A DFT investigation of adsorption of hydrogen Molecule on Si ₁₆ C ₁₆ and Si ₂₄ C ₂₄ nanofulleren like structures : A comparison with adsorption of hydrogen molecule on Si ₁₆ C ₁₆ @Li ⁺ and Si ₁₆ C ₁₆ @K	397
Electrochemical impedance study on methyl orange and methyl red as power enhancing electron mediators in glucose fed microbial fuel cell	401
Electrochemical Study of the Energy Generation Performance of Glucose, Lactose, Sucrose and Starch as Substrates in a Mixed Culture Microbial Fuel Cell	411
Design and constructing DC-DC convertor with Ripple-mitigating for fuel cell system	421
Studies of DFT modeling of methanol oxidation in fuel cell	430
Fabrication of MEA based on sulfonic acid functionalized carbon supported platinum nanoparticles for oxygen reduction reaction in PEMFCs	437



Fabrication and modification of graphene Supports for Platinum Electro catalyst using in Proton Exchange Membrane Fuel Cells	447
Pt-Sn-SnO ₂ /C Electrocatalysts for Ethanol Oxidation in Acidic Media	450
Study of some construction parameters on the Air electrode performance of Zinc-Air semi fuel cell	455
Study of catalyst layer degradation mechanism in proton exchange membrane fuel cell	463
Chemical and Oxidative Stability of Self-humidifying Membranes Based on SPEEK for Proton Exchange Membrane Fuel Cell Applications	473
Highly Active Ni-Pt /carbon paper electrode for Methanol Electro oxidation for DMFC applications	481
Study of Graphite addition on electrochemical activity of platinum on zinc oxide electrocatalyst for oxygen reduction reaction in PEM fuel cell	486
Cetyltrimethyl Ammonium Bromide Effect on Improved Hydrogen Evolution onto Pt Modified Glassy Carbon Electrode	492
Ni/PMT(TX-100)/MCPE as Anode Catalyst for Direct Ethanol Fuel Cells	500
Analysis of coolant flow and temperature distribution within PEM fuel cell stack	507
MODELING AND SIMULATION OF FUEL-CELL/BATTERY HYBRID VEHICLE AND POWER MANAGEMENT CONTROLLER DESIGN	525
Oxygen reduction reaction on Pt/C at the presence of super paramagnetic of Fe ₃ O ₄ nanoparticles in PEMFC	535
The study of synergism effect in physical mixture of Cobalt and platinum electro catalyst for oxygen reduction reaction in PEM fuel cell	543
Novel organic-inorganic nanocomposite membranes for PEM fuel cells	548



Modeling Local Structure and Dynamics of Aromatic Sulfonated poly(2,6-Dimethyl-1,4-Phenylene Oxide) Fuel Cell Membranes

Ghasem Bahlakeh^{1,*}, Manouchehr Nikazar², Ahmad Lashgar³, Hajar Falahati⁴, Seyed Emadodin Shakeri⁵, Mahdi Tohidian⁶,

*Department of chemical engineering, Amirkabir university of technology
ghasem.bahlakeh@gmail.com*

Abstract

MD simulations were used to analyze the structure and dynamics of the solvated sulfonated poly(2,6-dimethyl-1,4-phenylene oxide) membranes with hydration level of $\lambda = 6$ at varied temperatures. Obtained simulation results based on the RDF analyses revealed that the backbone of SPPO membranes behaves as hydrophobic at all temperatures. In addition, RDFs of sulfonic acid groups in terms of sulfur and oxygen atoms showed that correlation of sulfonic acid groups remains unchanged with a change in temperature. Finally, it was understood that diffusion coefficients of sulfonic acid groups, hydronium ions and water molecules are enhanced as the operating temperature is increased which can lead to improvement in fuel cell performance of hydrated membrane.

Keywords: Fuel cell, Polymer electrolyte membrane, Sulfonated poly(2,6-dimethyl-1,4-phenylene oxide) (SPPO), Modeling

1 Introduction

Because of their potential for use in polymer electrolyte membrane fuel cells (PEMFCs) and direct methanol fuel cells (DMFCs), polymer electrolyte membranes (PEMs) have been significantly studied during recent years [1]. It has been understood that physicochemical properties of these membranes is a factor that highly impacts their performance. Perfluorosulfonic Nafion with a poly(tetrafluoroethylene) backbone is the first used PEM in both PEMFCs and DMFCs due to high conductivity at optimum membrane hydrations and good chemical and mechanical stability [2]. Despite these advantages, a number of problems including high methanol permeability, high production cost as well as reduced conductivity at higher temperatures limited Nafion applications and motivated development of hydrocarbon-type membranes like sulfonated poly(ether ether ketone) (SPEEK), sulfonated poly(2,6-dimethyl-1,4-phenylene oxide) (SPPO), and so forth [3-4].

Various types of SPPO based PEMs have been recently synthesized as a candidate for PEMFCs and DMFCs usages since they have proved acceptable mechanical and thermal properties and possess simple structure which makes easier their modification [5-6]. Guan et al. [7] found larger ionic domains within SPPO materials with higher degrees of sulfonation which were

¹ -PhD student

² -Professor, Department of chemical engineering, Amirkabir university of technology, Nikazar@aut.ac.ir

³ -MSc, Computer engineering department, University of Tehran, ahmad.lashgar@gmail.com

⁴ -PhD student, Department of computer engineering, Sharif university of technology, hfalahati@ce.sharif.edu

⁵ -MSc student, Polymer engineering and color technology, Amirkabir university of technology, emzh.1368@gmail.com

⁶ -MSc student, Polymer engineering and color technology, Amirkabir university of technology, m.tohidian68@gmail.com

ascribed to increased water uptakes of membrane. Yang et al. [8] concluded that high conductivity of SPPO membrane at higher sulfonation levels is mainly because of continuous aqueous channels formed under higher water uptake conditions. In another study, Hasani-Sadrabadi et al. [9] reported that the methanol permeability of nanocomposite PEMs made of SPPO and organically modified montmorillonite clay was decreased as compared to Nafion. In contrast to experimental works concerned with fuel cell characteristics of SPPO materials, theoretical works for these types of membranes were not addressed in past investigations. Theoretical techniques such as molecular dynamics (MD) simulations are helpful tools that enable us to obtain deeper knowledge of membrane behaviors which is not possible using experiments [10-11]. Therefore, we perform MD simulations over pure SPPO based PEMs. As an extension to our previous work [10], influences of temperature on membrane properties of hydrated SPPO materials is investigated in this research work.

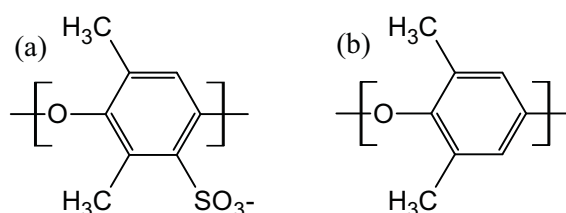


Figure 1: Chemical structure of (a) ionized sulfonated and (b) non-sulfonated PPO monomer used during MD simulations.

2 Details of simulation

2.1 Molecular models and amorphous cell construction

To investigate the influences of temperature on properties of hydrated SPPO membranes, MD simulations were carried out at three temperatures of 353, 333 and 313 K. The number of water molecules for SPPO membrane was specified using hydration level of $\lambda = 6$ (λ is the ratio of the number of water molecules to the number of sulfonic acid groups). Three-dimensional amorphous cell which consist of SPPO polymeric chains, hydronium ions (H_3O^+) and water molecules was constructed to do simulations. 20 SPPO chains with degree of polymerization of 20 and degree of sulfonation of 25% were used. Degree of sulfonation of SPPO polymers is defined as the ratio of number of sulfonated PPO monomers to the total number of sulfonated and non-sulfonated PPO monomers shown in Figure 1. Using 25% degree of sulfonation, each SPPO chain contains 5 sulfonated and 15 non-sulfonated monomers. These monomer units were randomly arranged within the SPPO chains. All sulfonic acid groups attached to PPO backbone were supposed to completely dissociate, as displayed in part (a) of Figure 1. Therefore, to maintain the charge neutrality of the simulation cells, the same number of hydronium ions as the total number of sulfonic acid groups was employed. Using the number of different molecules listed in Table, initial cell was created at initial density of 0.005 g/cm^3 by using amorphous cell module of the Materials Studio software [12].

Table 1: Composition of SPPO membranes used for MD simulations and equilibrated densities and cell sizes for hydration levels of $\lambda = 6$.

No. of SPPO chains	20
No. of H ₂ O	600
No. of H ₃ O ⁺	100
Total No. of atoms	9340

2.2 Force field parameters and MD simulation

DREIDING [13] and flexible 3-centered (F3C) [14] force fields were employed for SPPO chains and water molecules, respectively, which have been used in our previous study. Partial charges for SPPO were assigned using charge equilibration procedure [15]. Potential parameters and charges for hydronium ions were from Jang et al. [16].

After construction, amorphous simulation cell was minimized using conjugate gradient algorithm. Optimized cell was then equilibrated using shrinking box method at maximum temperature of 353 K, as discussed in our previous studies [10-11]. In this method, NPT MD simulations were first performed at 353 K for 10 ps during which operating pressure was increased from 1 to 100 atm. Next, the simulation cells were further compressed from 100 to 150 atm for 1 ns using NPT runs. In these simulations, only the bonded and repulsive non-bonded Lennard-Jones (LJ) interactions were included. Afterwards, NPT simulations were continued at 150 atm for 10 ps with inclusion of both repulsive and attractive parts of LJ interactions, which was followed by another NPT MD run at 150 atm for 50 ps where columbic interactions were also turned on. Subsequently, MD cell was equilibrated for time period of 10 ns in NPT ensemble at 353 K and 1 atm. This equilibration phase of MD simulations was used to quickly equilibrate SPPO structure. Equilibrated structure was used as input for production NVT simulations performed for 2 ns at 353 K, where trajectories were saved every 1 ps for subsequent analyses. For the lower temperatures, the final structure obtained at the end of production run of higher temperature was further equilibrated for 1 ns NPT MD simulation at 1 atm, which was followed by production run of 2 ns.

Simulations were performed by using LAMMPS (large-scale atomic/molecular massively parallel simulator) open-source classical MD code [17]. Non-bonded interactions were truncated at 12 Å cutoff distance and the long-range electrostatic interactions were computed using particle-particle particle-mesh (PPPM) method [18]. Newton's equation of motion was solved with velocity Verlet integrator using a time step of 0.5 fs [19]. During simulations, temperature and pressure were controlled via Nose-Hoover algorithm as thermostat and barostat [20-22]. Periodic boundary conditions were imposed in all directions of simulation cells.

3 Results and discussion

3.1 Amorphous cell equilibrium

Since attainment of cell equilibrium in MD simulation is important, we have checked it before analyzing results of simulation. For this purpose equilibrated density of simulation cells at all temperatures were monitored. The densities were calculated as 1.0320, 1.0310 and 1.0163 g/cm³ for simulation temperatures of 313, 333 and 353 K, respectively. It is seen that the computed densities for SPPO cell with water content of $\lambda = 6$ decreases with an increase in temperature. In literature, there has been no experimental density reported for hydrated SPPO, and so it is not possible to make a direct comparison. However, Kruczek et al. [23] reported experimental density of 1.19 g/cm³ for dry SPPO materials containing

25.2% sulfonation level. It is known that acidic PEMs like SPPO swell upon the uptake of water molecules, and thus it can be concluded that the obtained densities in our simulation are satisfactory. Consequently, the simulated density for water solvated SPPO membranes indicates that the MD cells have reached equilibrium condition.

3.2 Structural property

The radial distribution function (RDF) $g_{A-B}(r)$ was used to investigate the local structure of hydrated membrane as a function of operating temperature. RDF shows the probability distribution of B atoms around reference A atoms, and is defined as equation (1):

$$g_{A-B}(r) = \frac{\left(\frac{n_B}{4\pi r^2 \Delta r} \right)}{\left(\frac{N_B}{V} \right)} \quad (1)$$

where n_B is the number of B atoms located around A atoms inside a spherical shell of thickness Δr , N_B is the total number of B atoms employed when constructing simulation cell and V is the equilibrated cell volume.

To analyze the intermolecular interactions of water molecules with backbone of SPPO chains as a function of operating temperature, RDFs of oxygen atoms in water (Ow) with respect to carbon atoms in SPPO backbone (C) was analyzed, as displayed in Figure 2. It is observed that with increasing the temperature from 313 to 353 K, the behavior of C-Ow RDFs do not change, and as a result, the interaction of water molecules regards to polymer backbone is independent of fuel cell operating temperature. It is also observed that at all temperatures, the C-Ow RDFs first increase in height, reaches unity and finally become unchanged, which imply that aromatic backbone in SPPO materials is hydrophobic.

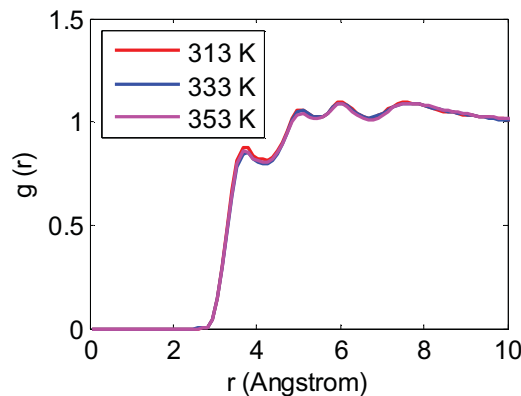


Figure 2: RDFs of carbon (SPPO)-oxygen (water) pairs for temperatures of 313, 333 and 353 K.

Since anionic sulfonic acid groups in acid-based PEMs like hydrated SPPO play very important role in proton conductivity process among polymeric membrane, it is better to investigate sulfonic acid group properties as a function of applied temperature. Figure 3 (a) and (b) illustrates this property in terms of RDFs of sulfur (S) and oxygen (Os) atoms in sulfonic acid group. In the case of S-S RDFs, a first high is occurred at around 5.94 Å for all temperatures, an observation which suggests the clustering trend in neighboring sulfonic acid groups. Also, the peak height show very slight variation against temperature. The same behavior is seen for Os-Os RDFs. Therefore, from these RDF analyses, it is inferred that structural property of

correlation of sulfonic acid groups with each other inside the solvated SPPO membranes remains unaltered.

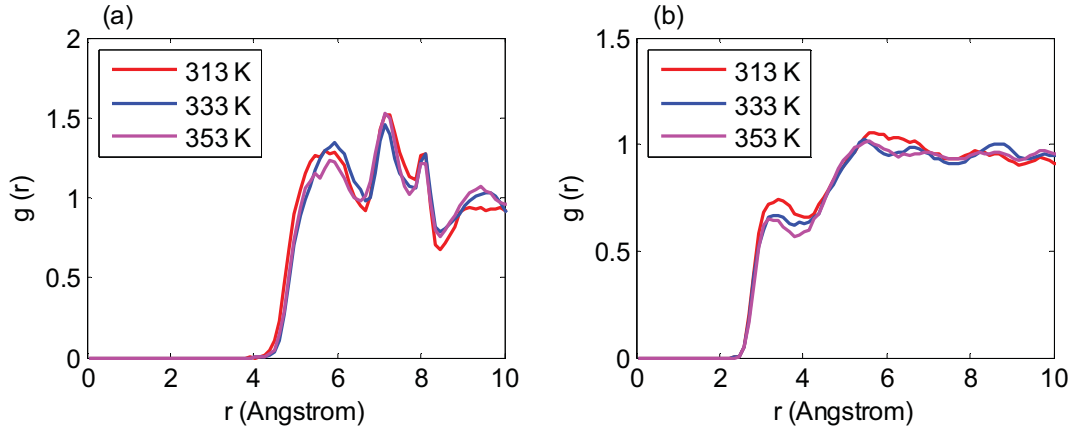


Figure 3: RDFs of (a) sulfur-sulfur and (b) oxygen-oxygen atomic pairs of sulfonic acid group for temperatures of 313, 333 and 353 K.

3.3 Dynamic property

Dynamic property of hydrated SPPO membranes under varied operating temperatures was explored by means of the diffusion coefficients (D) for sulfonic acid groups, water molecules and hydronium ions inside the hydrated membrane. Diffusivity was calculated using the slope of mean squared displacement (MSD) or Einstein relation according to the following equation:

$$D = \frac{1}{6} \lim_{t \rightarrow \infty} \frac{dMSD(t)}{dt} = \frac{1}{6N} \lim_{t \rightarrow \infty} \frac{d}{dt} \sum_{j=1}^N [(r_j(t) - r_j(0))^2] \quad (2)$$

where N is the total number of j atoms (here, sulfur atoms for sulfonic acid groups, oxygen atoms for water molecules or hydronium ions), $r_j(t)$ and $r_j(0)$ are the positions for j atoms at time t and at the beginning of production MD simulations, respectively. It should be noted the diffusivity for water and hydronium ion was computed using both hydrogen and oxygen atoms and the results were the same.

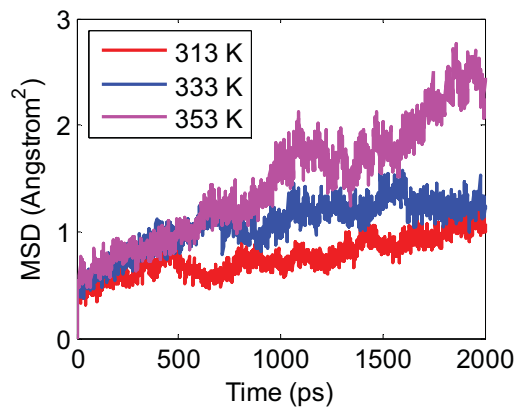


Figure 4: Mean squared displacement of sulfonic acid groups for temperatures of 313, 333 and 353 K.

Figure 4 indicates the mobility of sulfonic acid groups in terms of MSD of sulfur atoms for all temperatures. It is found that sulfonic acid groups demonstrate increased dynamics at higher temperatures which is attributed to increased kinetic energy of such groups at increased temperatures. Furthermore, as displayed in parts (a) and (b) in Figure 5, MSD of both hydronium ions and water molecules enhances as the temperature is increased. Therefore, increasing the temperature enables hydronium ions and water molecules to migrate more quickly within the solvated morphology of aromatic SPPO based PEMs.

The MD simulated diffusion coefficients via equation (2) for sulfonic acid groups, hydronium ions and water molecules were listed in Table 2. It is simply observed that all calculated diffusivities exhibit an increasing trend against temperature. Sulfonic acid groups have the least diffusion coefficient values due to the fact that unlike the hydronium ions and water molecules they are attached to SPPO backbone. Additionally, it can be seen that the hydronium ion diffusion coefficient is lower than that of water molecules since the calculation of diffusivity of hydronium ion via equation (2) only includes the vehicular diffusion mechanism for hydronium ions while transport of hydronium ions inside the membrane happens by two well known mechanisms of vehicular and hopping. The enhanced hydronium ion diffusion coefficient at higher temperatures implies that with increasing the temperature, the transport property of proton conductivity among SPPO membranes is increased and thereby the performance of the hydrated membrane for fuel cell applications is improved.

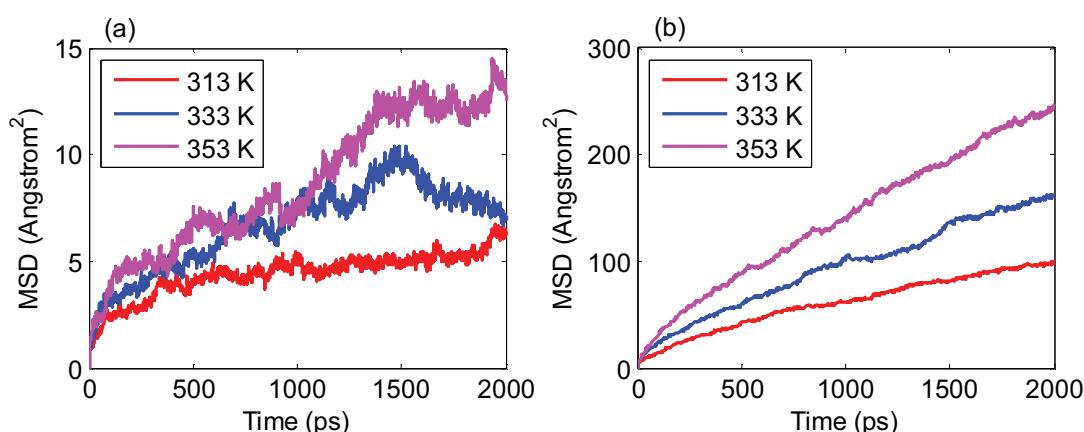


Figure 5: Mean squared displacement of (a) hydronium ions and (b) water molecules for temperatures of 313, 333 and 353 K.

Table 2: Diffusion coefficients of sulfonic acid groups, hydronium ions and water molecules for temperatures of 313, 333 and 353 K.

Temperature (K)	D ($\times 10^{-4}$, cm ² /s)		
	SO ₃ H	H ₃ O ⁺	H ₂ O
313	0.000045	0.00027	0.0073
333	0.000056	0.0005	0.0122
353	0.000152	0.0009	0.0183

Acknowledgement

The authors gratefully acknowledge the use of High Performance Computing Research Center (HPCRC) of Amirkabir University of Technology, and School of Computer Science, Institute for Research in Fundamental Science (IPM).



References

- [1] L. Carrette, K.A. Friedrich, U. Stimming, Fuel Cells – fundamentals and applications, Fuel Cells, (2001), 1, 5-39.
- [2] K.A. Mauritz, R.B. Moore, State of understanding of Nafion, Chem. Rev., (2004), 104, 4535-4586.
- [3] M. Rikukawa, K. Sanui, Proton-conducting polymer electrolyte membranes based on hydrocarbon polymers, Prog. Polym. Sci., (2000), 25, 1463-1502.
- [4] H. Ahmad, S.K. Kamarudin, U.A. Hasran, W.R.W. Daud, Overview of hybrid membranes for direct-methanol fuel-cell applications, Int. J. Hydrogen Energy, (2010), 35, 2160-2175.
- [5] T. Xu, D. Wu, L. Wu, Poly (2, 6-dimethyl-1, 4-phenylene oxide)(PPO)--A versatile starting polymer for proton conductive membranes (PCMs), Prog. Polym. Sci., (2008), 33, 894-915.
- [6] B. Vishnupriya, K. Ramya, K. Dhathathreyan, Synthesis and characterization of sulfonated poly (phenylene oxides) as membranes for polymer electrolyte membrane fuel cells, J. Appl. Polym. Sci., (2002), 83, 1792-1798.
- [7] R. Guan, C. Gong, D. Lu, H. Zou, W. Lu, Development and characterization of homogeneous membranes prepared from sulfonated poly(phenylene oxide), J. Appl. Polym. Sci., (2005), 98, 1244-1250.
- [8] S. Yang, C. Gong, R. Guan, H. Zou, H. Dai, Sulfonated poly (phenylene oxide) membranes as promising materials for new proton exchange membranes, Polymers for Advanced Technologies, (2006), 17, 360-365.
- [9] M.M. Hasani-Sadrabadi, S.H. Emami, H. Moaddel, Preparation and characterization of nanocomposite membranes made of poly (2, 6-dimethyl-1, 4-phenylene oxide) and montmorillonite for direct methanol fuel cells, J. Power Sources, (2008), 183, 551-556.
- [10] G. Bahlakeh, M. Nikazar, Molecular dynamics simulation analysis of hydration effects on microstructure and transport dynamics in sulfonated poly(2,6-dimethyl-1,4-phenylene oxide) fuel cell membranes, Int. J. Hydrogen Energy, (2012), 37, 12714-12724.
- [11] G. Bahlakeh, M. Nikazar, M. Mahdi Hasani-Sadrabadi, Understanding structure and transport characteristics in hydrated sulfonated poly(ether ether ketone)-sulfonated poly(ether sulfone) blend membranes using molecular dynamics simulations, J. Membr. Sci., (2013), 429, 384-395.
- [12] Accelrys Software Inc. SD, 2009.
- [13] S.L. Mayo, B.D. Olafson, W.A. Goddard, DREIDING: a generic force field for molecular simulations, J. Phys. Chem., (1990), 94, 8897-8909.
- [14] M. Levitt, M. Hirshberg, R. Sharon, K.E. Laidig, V. Daggett, Calibration and testing of a water model for simulation of the molecular dynamics of proteins and nucleic acids in solution, J. Phys. Chem. B, (1997), 101, 5051-5061.
- [15] A.K. Rappe, W.A. Goddard, Charge equilibration for molecular dynamics simulations, J. Phys. Chem., (1991), 95, 3358-3363.
- [16] S.S. Jang, V. Molinero, T. Cagin, W.A. Goddard, Nanophase-segregation and transport in Nafion 117 from molecular dynamics simulations: effect of monomeric sequence, J. Phys. Chem. B, (2004), 108, 3149-3157.
- [17] S.J. Plimpton, Fast parallel algorithms for short-range molecular dynamics, J. Comput. Phys., (1995), 117, 1-19.
- [18] R.W. Hockney, J.W. Eastwood, Computer simulation using particles, McGraw-Hill, New York, 1981.
- [19] W.C. Swope, H.C. Andersen, P.H. Berens, K.R. Wilson, A computer simulation method for the calculation of equilibrium constants for the formation of physical clusters of molecules: Application to small water clusters, J. Chem. Phys., (1982), 76, 637-649.



6th Iranian Fuel Cell Seminar
March 12 & 13 , 2013
Shahid Rajaei Teacher training University
Tehran - Iran



- [20] S. Nose, A unified formulation of the constant temperature molecular dynamics methods, J. Chem. Phys., (1984), 81, 511-519.
- [21] S. Nose, A molecular dynamics method for simulations in the canonical ensemble, Mol. Phys., (1984), 52, 255-268.
- [22] S. Nose, An extension of the canonical ensemble molecular dynamics method, Mol. Phys., (1986), 57, 187-191.
- [23] B. Kruczek, T. Matsuura, Effect of metal substitution of high molecular weight sulfonated polyphenylene oxide membranes on their gas separation performance, J. Membr. Sci., (2000), 167, 203-216.



Mathematical modeling of plate solid oxide fuel cell

Mansour. Kalbasi, Amin. Ahmadpour*

National Iranian Petrochemical Company, Bandar Imam Petrochemical Company, Mahshahr, Iran

**aminnimaamin2000@yahoo.com*

Abstract

In this research, three-dimensional model for a planar solid oxide fuel cell was developed, which includes the flow channels, electrodes, current collectors, and electrolyte. The proposed model includes mass and momentum transport in the flow channels and electrodes, electrochemical reaction in electrodes, and charge transfer in all parts of fuel cell.

The most important characteristic of this model is consideration of all electrodes' thickness as triple phase boundaries, thin layers in the vicinity of the electrolyte, where the electrochemical reactions take place and produce electrons, oxide ions and water vapor.

It was observed that the concentration profile of hydrogen and oxygen decreases with increasing the voltage of cell along the fuel channels and electrodes. Furthermore, our results showed that the concentration of gases, as well as the rate of reaction and current density, increases by rising the temperature. The performance of SOFC is also validated with measured data found in the literatures and good agreement is found between the results of this model and experimental data.

Keywords: solid oxide fuel cell, triple phase boundary, finite element method, mathematical modeling.

Introduction

Currently, due to concerns about the future of fossil fuels and harmful and irreparable effects of their combustion gases on the environment, researches have led toward the use of alternative energy sources. Fuel cell is a device that can be



used for future energy production. Lack of environmental problems and high efficiency, has led to extensive uses of fuel cell. Several types of fuel cell are available and they are distinguishing with their electrolytes foundations difference which are as follows:

Phosphoric Acid Fuel Cell (PAFC)

Polymer Electrolyte Membrane Fuel Cell (PEMFC)

Direct Methanol Fuel Cell (DMFC)

Alkaline Fuel Cell (AFC)

Molten Carbonate Fuel Cell (MCFC)

Solid Oxide Fuel Cell (SOFC)

The most famous electrolyte component in SOFC is Yttria- Stabilized Zirconia (YSZ) which is oxygen ion conductor (instead of empty oxygen). SOFC operating temperature is usually between 1000-600 ° c. High operating temperatures also has drawbacks and benefits. Stuck issue includes hardware, sealant and joints. High temperatures cause problems with the selection of materials, mechanical and thermal expansion. Benefits of this approach are including high performance and fuel flexibility. SOFC electrical efficiency is about 60-50% and the total thermal efficiency can reach to 90%. SOFC with average temperature (400-700c °) can remove many disadvantages of high temperature SOFC. These kinds of SOFC required much cheaper sealant and cheaper stuck metals (compared to ceramics). This SOFC also provide appropriate fuel efficiency and flexibility to. However, fundamental problems must be resolved.

Mathematical modeling:

The assumptions used in the fuel cell modeling are:

- 1 - Solid oxide fuel cell operates in very high temperature that gas mixture within the flow channels and electrodes always are far from critical conditions in all the modeling so ideal gas law assumed for the gas mixture [1].
- 2 - Within the flow channels, gases have speed much less than the speed of sound. In such circumstances (low Mach numbers) gas mixture density changes were very minor which is related to changes in mass caused by electrochemical

reactions. For all fuel cell modeling for gas mixtures laminar flow and incompressible flow has been considered [1, 2].

3 - All presented models in the field of solid oxide fuel cell are steady state because of changes in cell parameters are too short and rapidly ended [3].

4 - In many models is assumed that ohm losses in the collector is negligible because of high electrical conductivity coefficient of collectors than electrodes.

5 - Temperature has a major role in solid oxide fuel cells, because a significant effects of cell temperature on the electrical properties such as cell voltage and current density distribution affects [4, 5]. Many models have been performed in isothermal conditions, because the temperature is always constant and controlled by incoming gases through the cell or electric furnaces [6, 7].

6 - Three phase boundaries are considered as dimensionless boundary. Electrochemical reaction is confined to the cell electrode and electrolyte interface that is the result of high electrical conductivity cell ratio compared to the Ion conductivity coefficient.

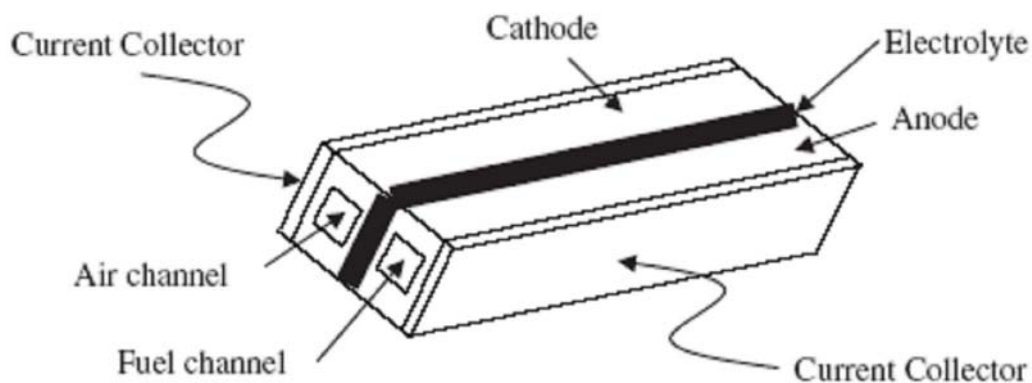


Figure (1): Geometry used in fuel cell modeling

Geometry has four regions. These areas include: current collector, flow channels, electrodes and electrolyte. Just inside the electrolyte ion conduction process is done and in collectors, electron conduction process is done but in the electrodes, both processes are happened.

The relevant equations of cell components are:

Flow channels: mass and momentum balance.

Electrodes: mass balance, load balance (ions and electrons), momentum balance.

Electrolytes: load balance (ion).

Collector current: load balance (electrons).

Stefan - Maxwell equation is expressed for mass balance equation. Navier – Stoke equation for momentum balance and Ohm's law for load balancing.

A-Mass transfer:

Fick's law is valid for binary mixtures penetration and indicated interaction between them. Stefan – Maxwell equation is used for multi-component gas mixtures with low-density. Therefore in this simulation, Stefan - Maxwell equation is expressed for cathode mass transport components (oxygen, nitrogen and water) and anode components (hydrogen and water) [8.9]:

$$\nabla \cdot \left(\omega_i \rho u - \rho \omega_i \sum_{j=1}^k D_{ij} \left(\frac{M}{M_j} \left(\nabla \omega_j + \omega_j \frac{\nabla M}{M} \right) + (x_j - \omega_j) \frac{\nabla P}{P} \right) \right) = R_i$$

Where ω_i is mass fraction of component i , ρ density of gas mixture, u flow rate, D_{ij} diffusion, M gas mixture molecular weight, M_j molecular weight of component i , x_j component mole fraction, P pressure and R_i is heterogeneity term (production or consumption of a component) caused by the electrochemical reaction as expressed below:

$$R_i = \nu_i \frac{J M_i}{n_i F}$$

In this equation, ν_i is stoichiometry coefficient, F Faraday constant, n_i the number of moles of electrons in half-reaction transition and J is current density. Stefan - Maxwell equation is used flow for channels and electrodes when heterogeneity term is zero.

B - Momentum transfer

Navier - Stoke equation has been used for momentum transfer in channel flow [9]:

$$\rho(u \cdot \nabla)u = \nabla \cdot \left[-PI + \mu((\nabla u + (\nabla u)^T) - \frac{2}{3}(\nabla \cdot u)I) \right]$$

$$\nabla \cdot (\rho u) = 0$$

The second equation of the above equation is the continuity equation. Brinkman equation is used for gases flow within electrodes:

$$\left(\frac{\mu}{\kappa} + Q\right)u = \nabla \cdot \left[-PI + \mu((\nabla u + (\nabla u)^T) - \frac{2}{3}(\nabla \cdot u)I) \right]$$

$$\nabla \cdot (\rho u) = Q$$

$$Q = \sum S \frac{J M_i}{n_i F}$$

In this equation κ is the permeability of the electrodes, S electrodes active area and Q is heterogeneity term caused by the reaction.

C. – Load transfer

Ohm's law was used for the transfer time in different parts of cell [1, 9, and 10]. Inside the collector current balance is charged that is written below as equation:

$$\nabla \cdot (-k_e \nabla \phi_e) = 0$$

That k_e is electrical conductivity coefficient of current collector and ϕ_e is electric potential. For ion electrolyte balance load following relationship is used:

$$\nabla \cdot (-k_i \nabla \phi_i) = 0$$

That k_i is coefficient of ion conductivity electrolyte and ϕ_i is ion potential of electrolyte.

Inside the electrodes, due to electrochemical reactions, ionic balance and electrical load balance are charged by the following relations:

$$\nabla \cdot (-k_e \nabla \phi_e) = S J$$

$$\nabla \cdot (-k_i \nabla \phi_i) = S J$$

That k_e is electrical conductivity coefficient, k_i is ion conduction coefficient, ϕ_e is electric potential and ϕ_i is Ion potential of electrodes.

Results

Figure (2) shows voltage - flow curve which has good agreement with experimental data [11.12].

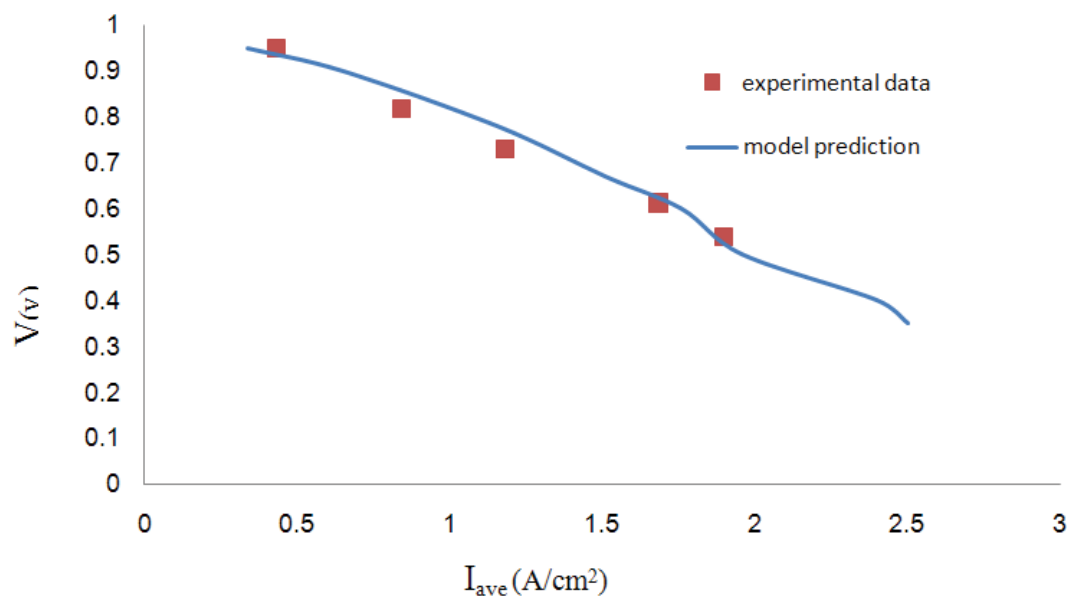


Figure (2): voltage – current curve

Reactant concentration in electrodes and flow channels and also their distribution are an important factor in determining the amount of cell reactions speed, rate of cell production and distribution of electric current. Uniform distribution and high concentration of reactant causes increase in reaction rate and finally increasing in cell electric current production. Therefore, concentration of reactants had to be checked. First, the concentration of oxygen and hydrogen outlines. Figures (3) and (4) show distribution of oxygen concentration in the flow channel and cathode electrodes and distribution of hydrogen concentration in the anode fuel flow channels for the operating voltage 0.8 ($V_{cell} = 0.8$).

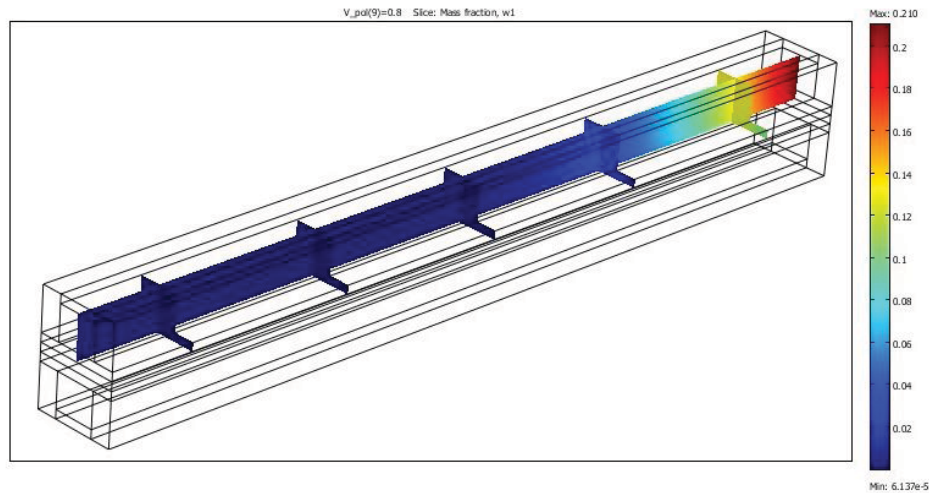


Figure (3): Distribution of oxygen concentration in the flow channels and cathode electrode

As the figure (3) implies, distribution of oxygen concentration is non-uniform and immediately decreases in the flow channels and cathode that causes reduces of passing oxygen ions in the electrolyte and thus reduces of hydrogen half rate oxidation reaction. In Figure (4) concentration of hydrogen in the fuel flow inside the channel and the anode electrode is a non-uniform distribution, but its concentration does not suffer rapid decline due to hydrogen high penetration.

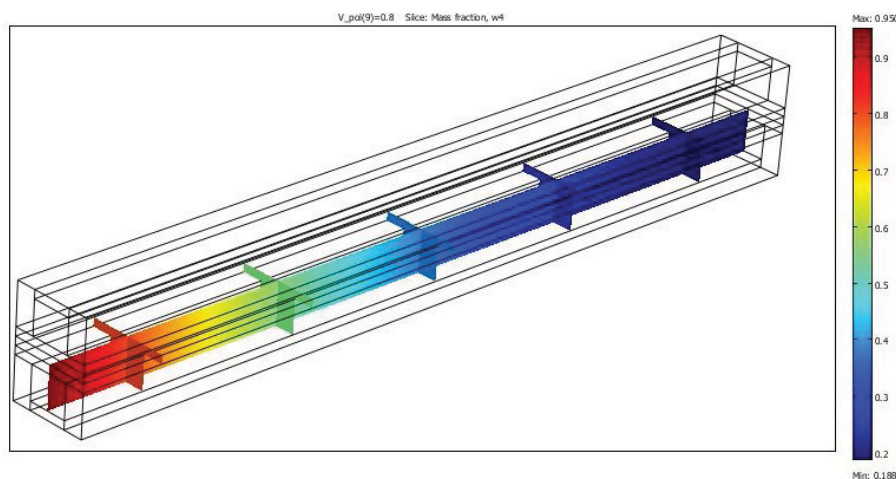


Figure (4): distribution of hydrogen concentration in the fuel flow channel and the anode electrode

Figures (5) and (6) show electrical current density distribution in the electrodes and electrolyte interface points.

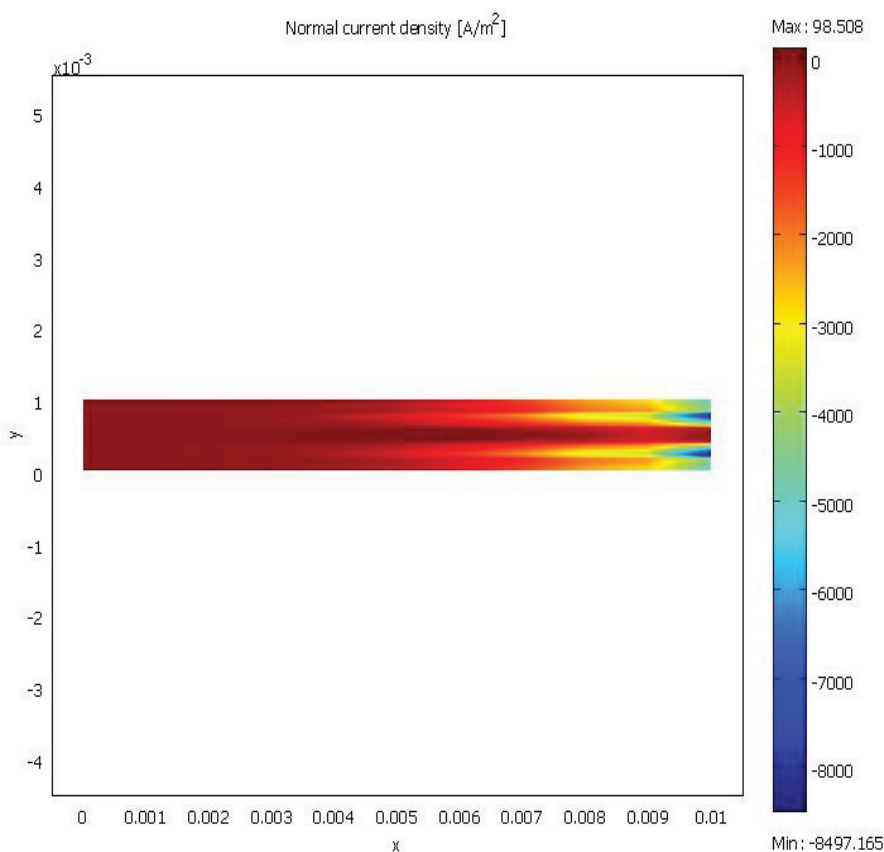


Figure (5): Distribution of current density in electrolyte- cathode interface

In Figure (5), electric current density in electrolyte -cathode interface is a non-uniform distribution due to non-uniform distribution of oxygen concentration. The highest current density is in the entrance of cathode flow channel because the electric current density and reaction rate have a direct relationship with reactant concentration and oxygen concentration is high at the flow channel entrance. In Figure (6) the highest current density is in the output of flow channel because the highest concentration of oxygen is in the output of anode flow channel therefore the highest current density is on the output of flow channel.

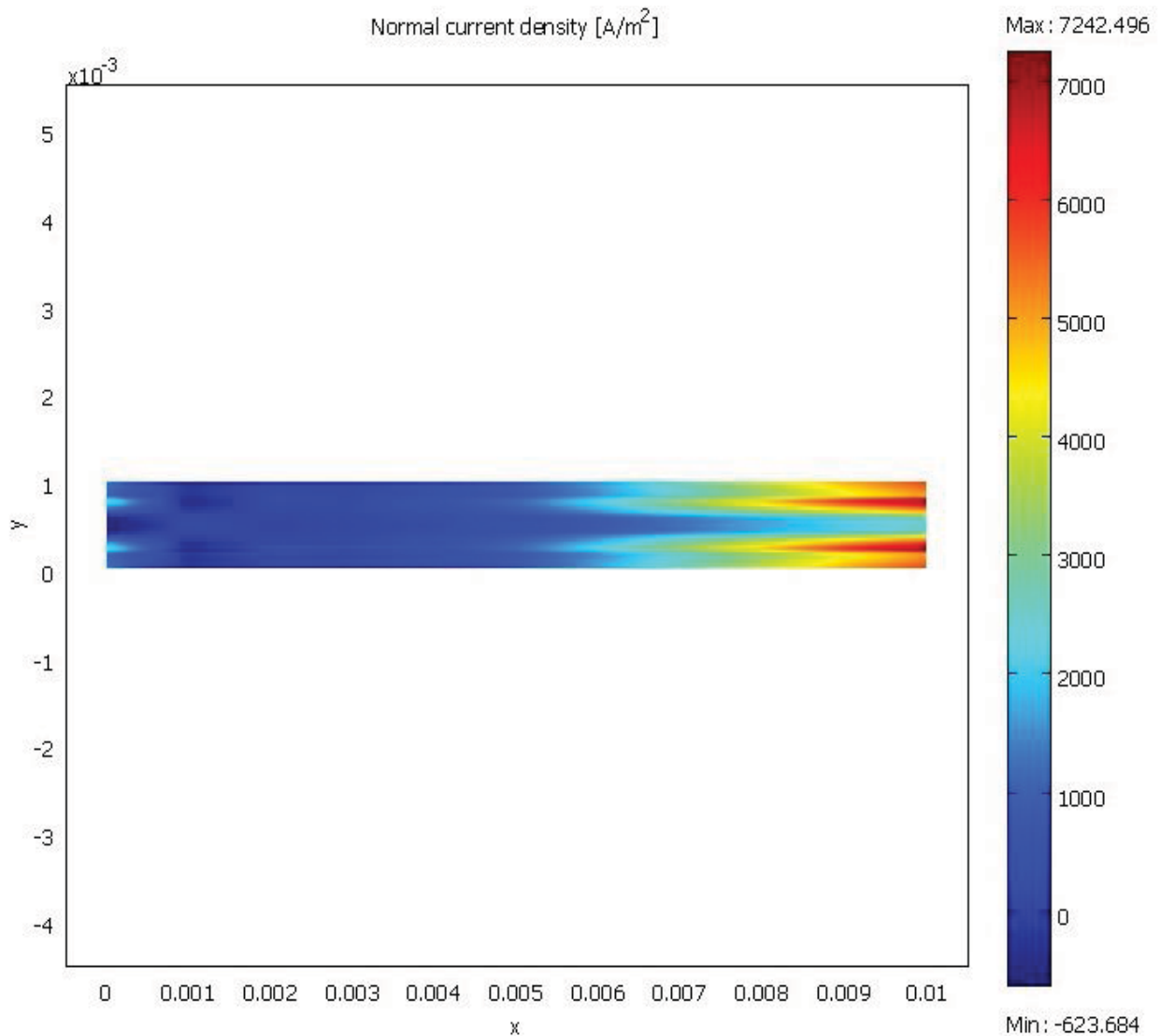


Figure (6): Distribution of current density in electrolyte - anodes interface

Figure (7) shows current density distribution in the anode- flow channels interface and anode- current collector. In the central part, current density distribution is uniform, but in other parts, anode- current collector interface, is non-uniform because at the central part or anode- current collector interface, hydrogen concentration is nearly uniform.

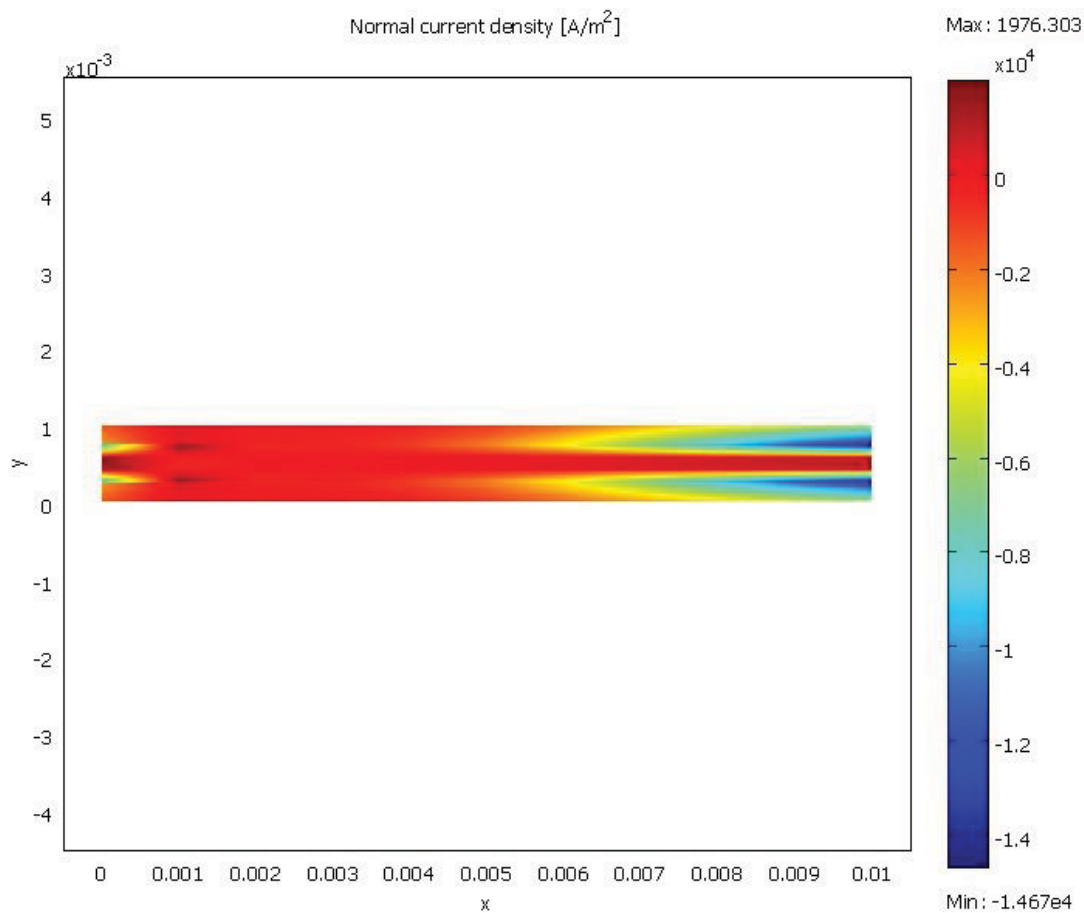


Figure (7): current density distribution in the anode- flow channels interface and anode- current collector

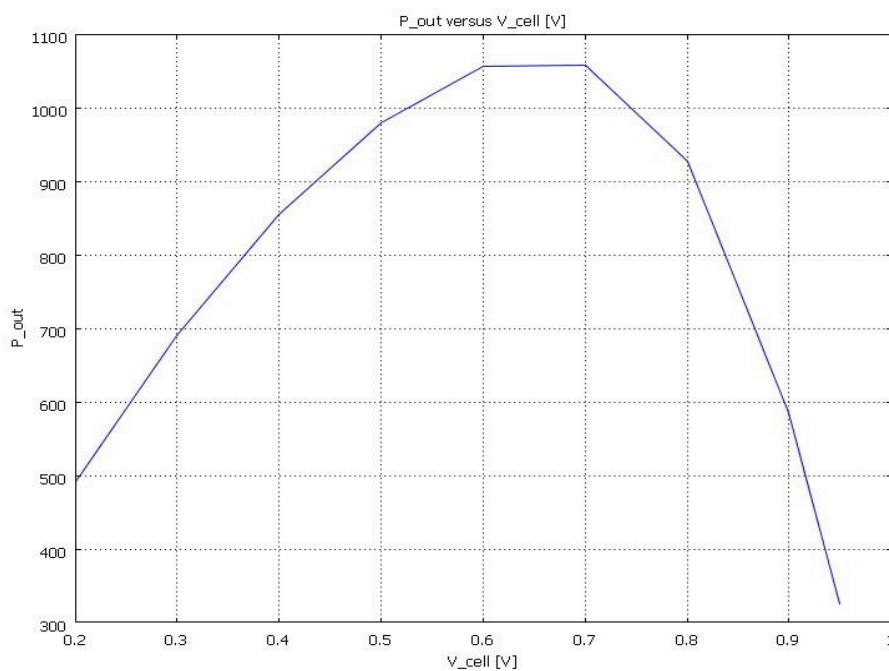


Figure (8): cell output power as a function of cell operating voltage

Figure (8) shows cell output power. All figures presented in the previous section are given for the cell operating voltage equal to 0.8. In figures (9) and (10) oxygen concentration profiles are shown along the flow channel and cathode electrodes for operating voltage levels 0.2, 0.4 and 0.6.

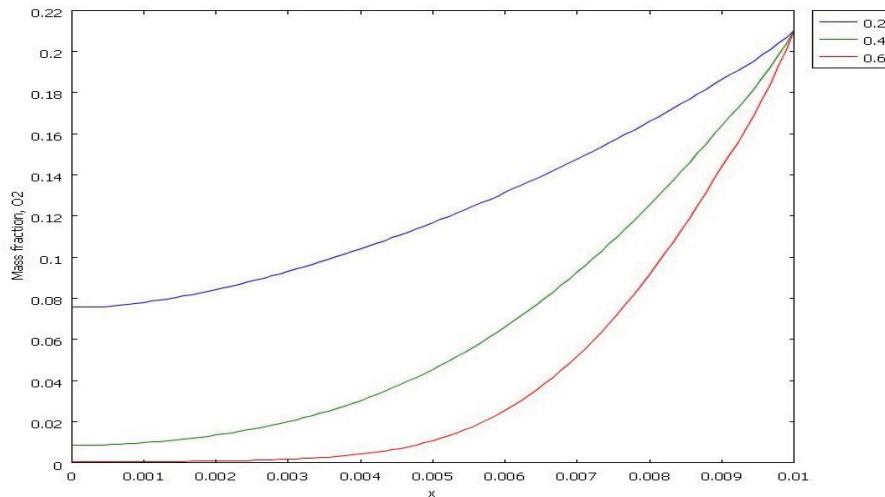


Figure (9): Oxygen concentration profiles along the channel flow

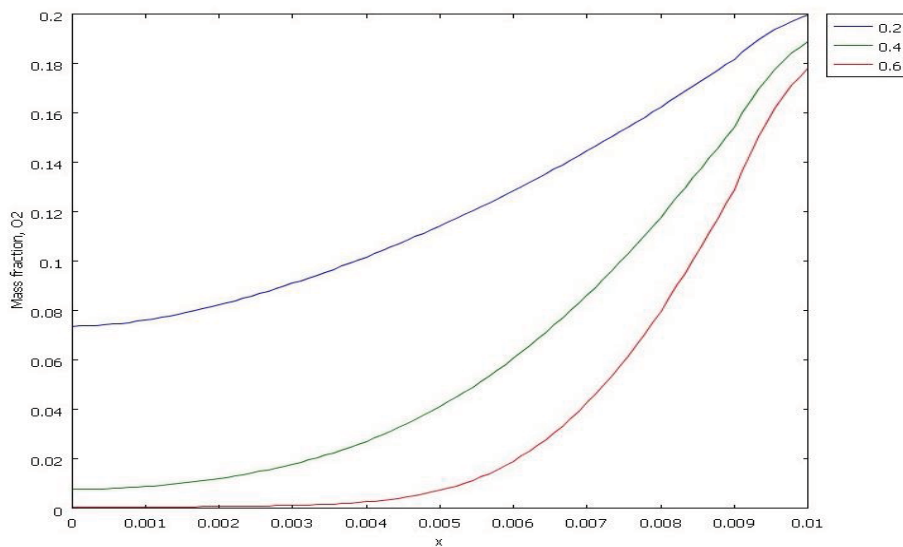


Figure (10): Oxygen concentration profiles along the cathode

From figures (9) and (10) observed that in the channel and electrode, oxygen concentration has decreased with increasing cell operating voltage in gas flow. With increasing cell electric current voltage production decreases according to voltage- current curves and because of direct effect of current density on reaction rate, the reaction rate decreases and consequently concentration decreases.

Proceeding of concentration reduction with increasing of hydrogen cell operating voltage also can be observed. Figures (11) and (12) show the hydrogen concentration profile during flow channel and anode electrodes.

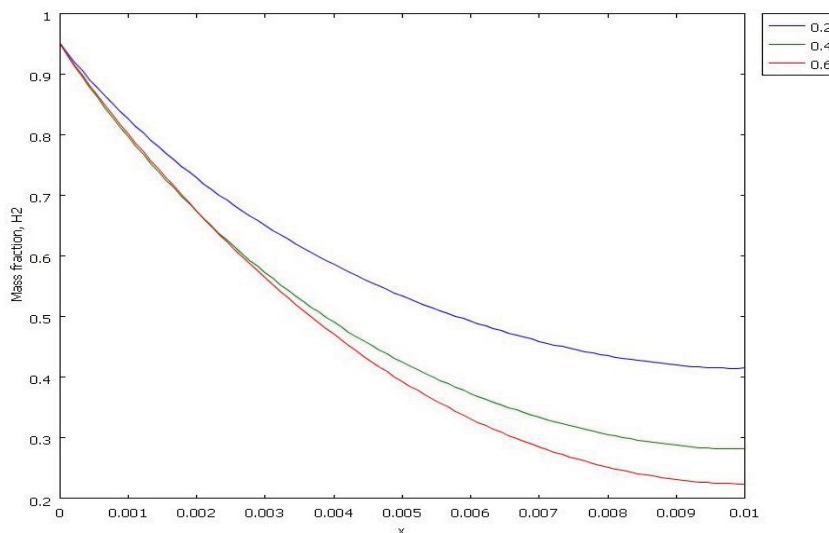


Figure (11): hydrogen concentration profile during channel flow

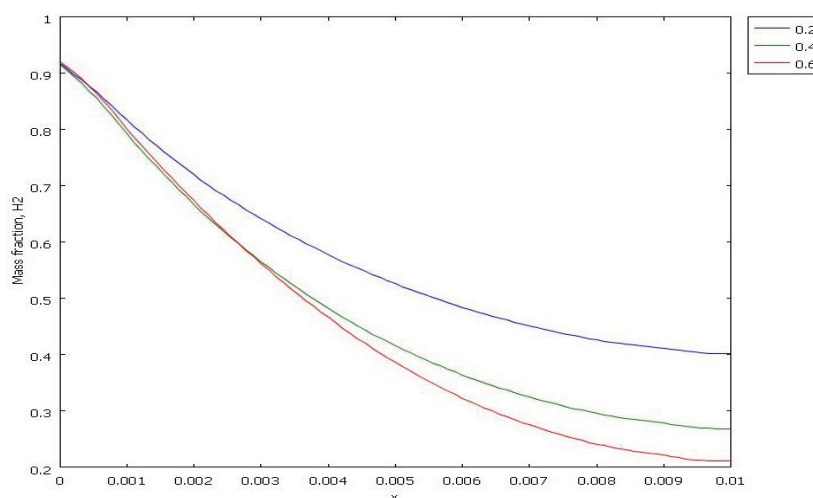


Figure (12): hydrogen concentration profile during cathode

All previous figures were in temperature 800 ° C. For evaluate the effect of temperature on reaction rate and current density, hydrogen and oxygen concentration profile are compared. Figures (13) and (14) show Hydrogen concentration profiles in the anode, respectively 800 and 900 ° C temperature for the operating voltage of 0.8. It can be observed that with increasing temperature, hydrogen concentration has increased over the anode. Because increasing

temperature, the total concentration increases. Therefore, the temperature rises due to high hydrogen concentration, reaction rate and current density increase.

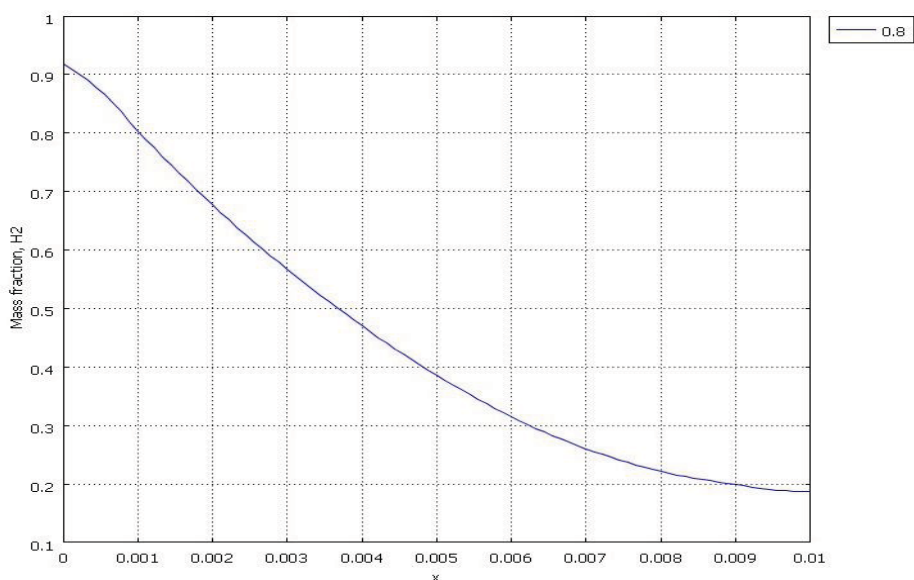


Figure (13): hydrogen concentration profile during the anode at a temperature 800 ° C

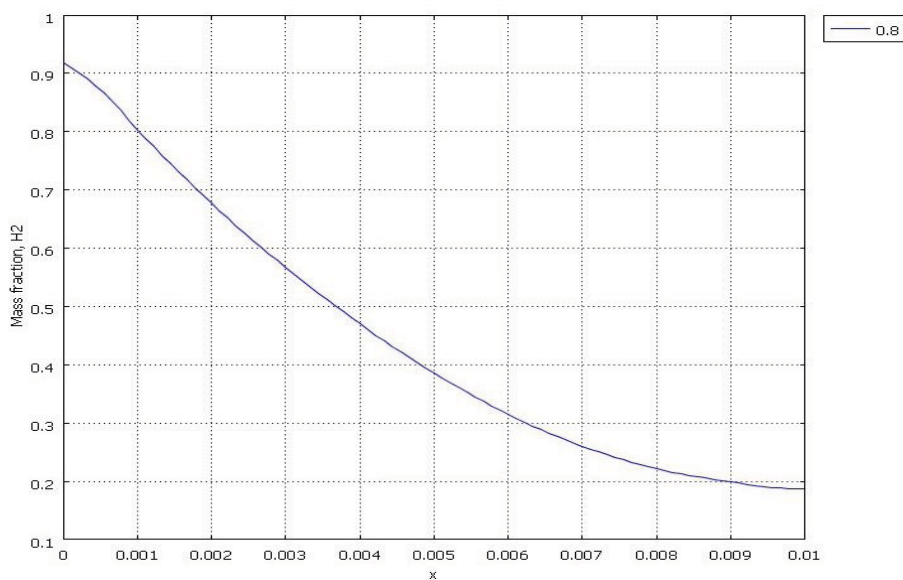


Figure (14): hydrogen concentration profile during the anode at a temperature 900 ° C

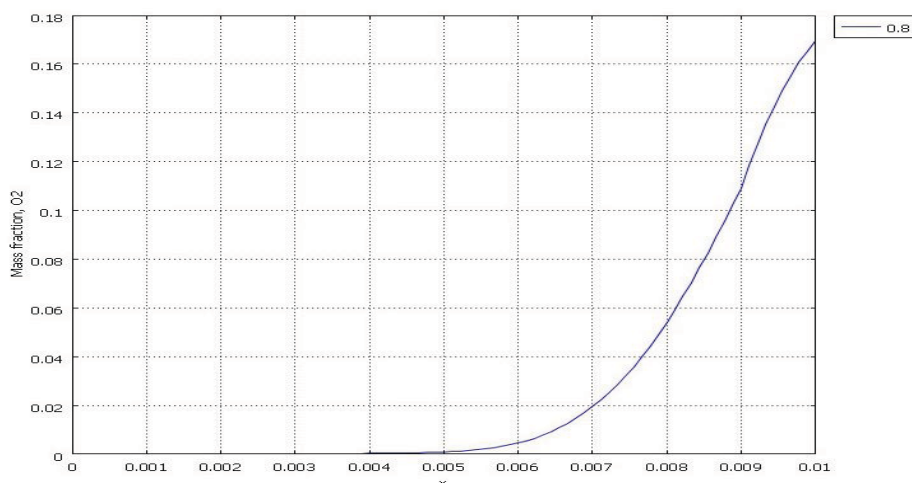


Figure (15): Oxygen concentration profile during the anode at a temperature 800 °C

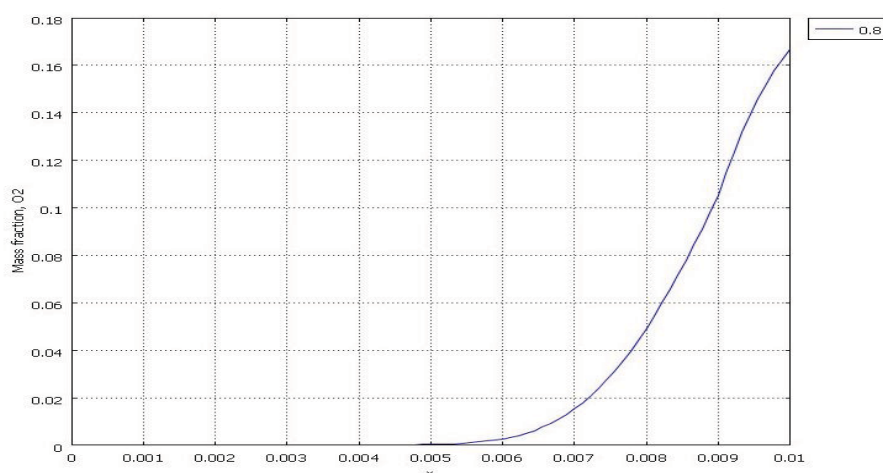


Figure (16): hydrogen concentration profile during the cathode at a temperature 900 °C

With increasing temperature, the oxygen concentration as the concentration of hydrogen in accordance with figure (16) has increased over the cathode.

Conclusion

In solid oxide fuel cells modeling two three phase boundaries are available which are: dimensionless border (boundary condition) or a certain thickness of the border. So in this model instead of the above two cases, the entire thickness of the cell electrodes is considered as three phase boundary. Cell modeling results showed circumstances consistent with the laboratory results. Therefore we can say that in solid oxide fuel cell three phase boundaries or reaction locations can be total thickness of the electrode and electrochemical reactions should be done



during the whole cell electrode. The reactant concentrations in the flow channels and electrodes according to obtained curves have significant effect on reaction rate and current density.

References:

- [1] Bove R, Ubertini S. modeling solid oxide fuel cell operation: approaches, techniques and results. *J Power Sources* 2006; 159(1): 543-59.
- [2] Khaleel MMA, Lin Z, Singh P, Surdoval W, Collin D. a finite element analysis modeling tool for solid oxide fuel cell development: coupled electrochemistry, thermal and flow analysis in MARC. *J Power Sources* 2004; 130:136-48.
- [3] Qi Y, Huang B, Chuang K. dynamic modeling of solid oxide fuel cell: the effect of diffusion and inherent impedance. *J Power Sources* 2005; 150:32-47.
- [4] Aguiar P, Adjiman C.S, Brandon N.P. *J Power Sources* 2005; 147:136-47.
- [5] Stiller C, Thorud B, Bolland O, Kandepu R, Imsland L. *J Power Sources* 2006; 158: 303-315.
- [6] Bhattacharyya D, Rengaswamy R, Finnerty C. isothermal models for anode-supported tubular solid oxide fuel cells. *J Chemical Engineering Science* 2007; 62: 4250-67.
- [7] Andreassi L, Rubeo G, Ubertini S, Lunghi P, Bove R. experimental and numerical analysis of a radial flow solid oxide fuel cell. *International Journal of Hydrogen Energy* 2007; 32: 4559-74.
- [8] Liu S, Song C, Lin Z. the effects of the interconnect rib contact resistance on the performance of planar solid oxide fuel cell stack and the rib design optimization. *J Power Sources* 2008; 183:214- 225.
- [9] Chaisantikulwat A, Diaz-Goano C, Meadows E.S. dynamic modeling and control of planar anode- supported solid oxide fuel cell. *J Computers and Chemical Engineering* 2008; 32: 2365- 2381.equ
- [10] Chan SH, Khor KA, Xia ZT. A complete polarization model of a solid oxide fuel cell and its sensitivity to the change of cell component thickness. *J Power Sources* 2001; 93:130-140.



[11] Hussain M.M, Li X, Dincer I. mathematical modeling of planar solid oxide fuel cells. J Power Sources 2006; 161:1012-1022.

[12] Rogers W.A, Gemmen R.S, Johnson C, Prinkey M, Shahnam M. validation and application of a CFD- based model for solid oxide fuel cells and stacks. FuelCell Sci. Eng. Technol. ASME 2003:517-520



Electrosynthesis of Pt-Co alloy catalyst on the carbon-ceramic electrode for methanol oxidation

Biuck habibi and Kaveh Rahmani

*Electroanalytical Chemistry Laboratory, Department of Chemistry, Faculty of Sciences,
Azarbaijan Shahid Madani University, Tabriz, Iran
E-mail: B.Habibi@Azaruniv.edu*

Abstract

The electrooxidation of methanol was investigated in acidic media on the platinum-cobalt alloy carbon-ceramic modified electrode (Pt-Co/CCE) via cyclic voltammetric analysis in the mixed 0.5 M methanol and 0.1 M H₂SO₄ solutions. The Pt-Co/CCE catalyst, which has excellent electrocatalytic activity for methanol oxidation than the Pt nanoparticles carbon-ceramic modified electrode (Pt/CCE) and smooth Pt electrode, shows great potential as less expensive electrocatalyst for these fuels oxidation. These results showed that the presence of Co in the structure of catalyst and application of CCE as a substrate greatly enhance the electrocatalytic activity of Pt towards the oxidation of methanol. Moreover, the presence of Co contributes to reduce the amount of Pt in the anodic material of direct methanol fuel cells, which remains one of the challenges to make the technology of direct methanol fuel cells possible. On the other hand, the Pt-Co/CCE catalyst has satisfactory stability and reproducibility for electrooxidation of methanol when stored in ambient conditions or continues cycling making it more attractive for fuel cell applications.

Keywords: Electrosynthesis, Pt-Co alloy, Methanol oxidation, Carbon-ceramic electrode

1. Introduction

Among the all metals, Pt is a single component catalyst that shows a significant activity for methanol oxidation [1]. However, the obtained results have been shown that the Pt metal may be easily poisoned by CO in the methanol oxidation and the high cost limits its application as electrocatalyst in commercial field of the fuel cells [2]. Therefore, to overcome these problems, synthesis and preparation of the new and less expensive Pt based materials as anodes for methanol oxidation have been the topic of current interest [3-6]. The development of bimetallic Pt alloy catalysts is one of the ways that enhance the catalytic activity, prevent the poisoning problems and reduced the cost of anodic materials in the fuel cell applications [7] and now some works have been carried out to design and synthesize Pt-based alloy electrocatalysts resulting in a lowered Pt content and a better electrocatalytic performance [8-10]. Binary alloy catalysts with various transition metals such as Co, Fe, Cr, and Ni were employed to increase the catalytic activity and to reduce the cost [11, 12].

There is now a consensus that the Pt-Co alloys offer an intrinsic enhancement of electrocatalytic oxygen reduction reaction activity on a Pt mass and surface-area basis [13] and also it has been found that Pt-Co alloys have high activity and excellent tolerance to CO poisoning in comparison with pure Pt catalysts [14], therefore Pt-Co alloys have been used in a few works as an electrocatalyst for methanol oxidation [15-18]. Pt-Co alloys have been prepared by various methods. The obtained results have been shown that the Pt-Co electrocatalysts which were synthesized by nonelectrochemical methods always have some problems such as inactive catalyst sites that are not available for fuel cell reaction [13]. In order to overcome these limitations, the electrochemical method should be applied for preparation of

Pt-Co electrocatalysts. The electrochemical method offers not only enhanced catalyst utilization but also simplification of preparation [19].

In this paper, the Pt-Co alloy nanoparticles are co-deposited by a simple electrochemical procedure on the carbon-ceramic electrode (CCE) to produce carbon-ceramic supported Pt-Co catalyst (Pt-Co/CCE), aiming to have a less expensive electrocatalyst in the direct methanol fuel cell. The electrochemical properties and electrochemical activities of the Pt-Co alloy for methanol oxidation are investigated. It was found that Pt-Co/CCE is catalytically more active than Pt nanoparticles (alone) supported on the CCE and smooth Pt.

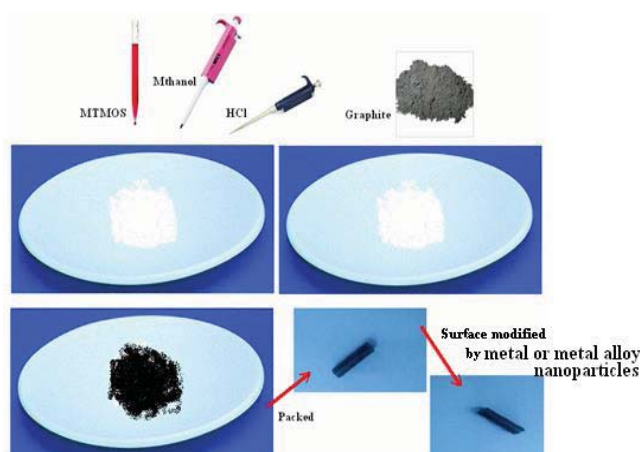
2. Experimental

2.1. Chemicals

Methyltrimethoxysilane, methanol, $\text{H}_2\text{PtCl}_6 \cdot 5\text{H}_2\text{O}$, CoCl_2 , HCl , H_2SO_4 and graphite powder of high purity were obtained from Merck or Fluka. All solutions were prepared with double distilled water.

2.2. Procedure of Pt-Co/CCE preparation

The sol-gel processing method was used for fabricating CCE according to our previously work [7] (scheme 1).



Scheme 1: Sol-gel processing for fabricating CCE

The Pt-Co alloy catalyst on the CCE was electrodeposited (Potentiostatically) from an aqueous solution of 0.1M Na_2SO_4 (pH=4) comprising 2:1 ratio of $\text{H}_2\text{PtCl}_6 \cdot 6\text{H}_2\text{O}$ and CoCl_2 (total concentration of two salts equal to 1 mM) at 25 °C. Before deposition, the CCE was polished and subjected to electrodeposition at a fixed potential of -0.2V versus a saturated calomel electrode (SCE) for a certain time. The charge resulting from the complete reduction of the precursor salts at the given time is 1367 mC cm^{-2} . This value corresponds to an equivalent amount of platinum of $691 \mu\text{g cm}^{-2}$ when platinum is considered as the only metal deposited [20]. After electrodeposition, the obtained modified electrode was washed thoroughly with double distilled water and dried before further investigation.

2.3. Instrumentation

The electrochemical experiments were carried out using an AUTOLABPGSTAT-30 (potentiostat/galvanostat) equipped with a USB electrochemical interface and a driven GEPS soft ware was used for electrochemical experiments. A conventional three electrode cell was used at room temperature. The smooth (Pt or CCE) or the modified electrode (Pt/CCE or Pt-

Co/CCE) (3 mm diameter) was used as a working electrode. A SCE and a platinum wire were used as the reference and auxiliary electrodes, respectively. JULABO thermostat was used to control cell temperature at 25 °C.

3. Results and discussion

3.1. Electrochemical characteristics of Pt-Co/CCE in acidic media

To understand the electrochemical behavior of the Pt-Co/CCE and comparison study, the cyclic voltammograms (CVs) of the Pt-Co/CCE, Pt/CCE, smooth Pt and CC electrodes were recorded at a scan rate of 50 mV s⁻¹ in supporting electrolyte (0.1 M H₂SO₄ solution). Fig. 1 shows the CVs of the Pt-Co/CCE (curve 1), Pt/CCE (curve 2), smooth Pt and CCE (inset, curves 1 and 2, respectively). Although the typical Pt-peaks for the hydrogen under-potential deposition (H_{upd}), the oxidation of hydrogen (H_{oh}), formation of Pt oxides (PtO_{for}), and its reduction (PtO_{red}) are present on the Pt-Co/CCE, they become ill-shaped compared to the smooth Pt (inset, curve 1) and even to the unalloyed Pt nanoparticles modified CCE (Pt/CCE) (Fig. 1, curve 2). On the other hand, compared with the Pt/CCE, both peaks for hydrogen adsorption and desorption of Pt-Co/CCE decrease. In fact decreasing of hydrogen peaks was linear with the increasing of amount of Co in the Pt-Co/CCE due to the decreasing of Pt amount. So the contribution of the Co atoms (θ_{Co}) deposited together with Pt atoms on the CCE surface was calculated by the following equation [21]:

$$\theta_{Co} = Q_{(Pt)H} - Q_{(Pt-Co)H} / Q_{(Pt)H} \quad (1)$$

$Q_{(Pt-Co)H}$ is the electric charge of Pt-Co/CCE evaluated from the CV in the hydrogen region charge between -0.30 and +0.10 V in Fig. 1 (curve 1). $Q_{(Pt)H}$ is the electric charge measured from Pt/CCE in the same region on the CV profile (Fig. 1, curve 2). In calculating the adsorption charge, i.e. the integrated area under the peaks, we assume that the double layer capacitance is constant across the entire potential range. Under the deposition conditions [Pt-Co (2:1)], a stable Co contribution (0.33) can be easily got.

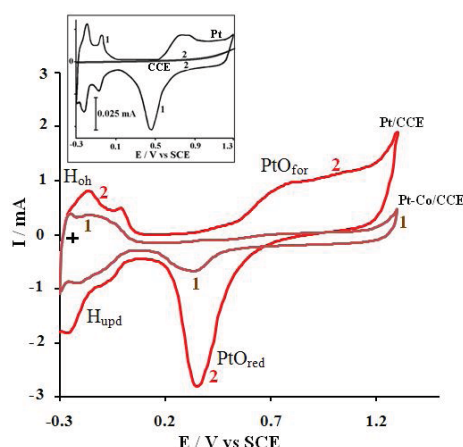


Figure 1. CVs of Pt-Co/CCE (curve 1) and Pt/CCE (curve 2) in 0.1M H₂SO₄ at a scan rate of 50 mV s⁻¹. The inset is CVs of smooth Pt (curve 1) and bare CCE (curve 2) in the same conditions.

The high surface area and porosity are required for better performance as electrode materials for direct methanol fuel cell application. In the Pt-based electrocatalysts the measurement of hydrogen adsorption is widely used in determining of the real active surface area [22]. The actual active surface area of the Pt-Co/CCE is equivalent to the number of Pt sites available for hydrogen adsorption/desorption. The Pt-Co/CCE produced $Q_{(Pt-Co)H}$ of 0.958

mC. Accordingly, the actual active surface area (A_r) can be obtained from charge for hydrogen adsorption as: $A_r = Q_{(Pt-Co)H} / Q_0$ (Q_0 has been commonly taken as $210 \mu\text{C}/\text{real cm}^2$) = 4.82 cm^2 . The hydrogen adsorption charge of smooth Pt was calculated at 0.021 mC. These results show that the actual active surface area of the Pt-Co/CCE is about 45 times larger than that of smooth Pt. Curve 2 in inset of Fig. 1 shows the CV of bare CCE in 0.1M H_2SO_4 solution. No adsorption/desorption peaks of hydrogen appeared at the bare CCE.

3.2. Electrocatalytic activity of the Pt-Co/CCE towards methanol oxidation

The electrocatalytic activity of the Pt-Co/CCE towards to the oxidation of methanol was evaluated by using CV. Fig. 2 shows the CV of the Pt-Co/CCE (curve 1) in a 0.5 M methanol of 0.1M H_2SO_4 solution. It was recorded at a scan rate of 20 mV s^{-1} in the potential range from -0.3 to +1.7 V (SCE). For comparison, the CV of Pt/CCE catalyst is scanned in same solution (curve 2). It can be observed from the CV of methanol on the Pt-Co/CCE (curve 1), that in the forward scan there aren't any adsorption/desorption peaks of hydrogen on the potentials regain between -0.3 V to 0 V due to the presence of methanol which implying that methanol is adsorbed preferentially on the electrode surface at those potentials [5, 7]. Of course, it should be noted that, for low concentration of methanol (not shown here), the hydrogen adsorption/desorption peaks are still visible showing that methanol does not prevent completely the hydrogen adsorption on the surface of electrode in low concentrations. In potential after these regain a main anodic peak (A_1) at 0.81 V and a small another anodic peak (A_2) at about 1.20 V were observed. In the backward scan a small cathodic peak (C_1) at 0.40 V and a sharp anodic peak (A_3) at about 0.30 V were observed [5]. Comparison of the CVs in Fig. 2 (curve 1) and CV of methanol on the Pt/CCE (curve 2) shows that the CV of the methanol oxidation on the Pt-Co/CCE and Pt/CCE electrocatalysts has same profiles and both of them have the usual characteristics of the smooth Pt except that the oxidation current of main peak in the forward scan on the Pt-Co/CCE (4.1 mA) is much higher than that on the smooth Pt, and moreover, it is higher than that on the Pt/CCE (0.95 mA) [$I_{pA1}(\text{Pt-Co/CCE}) \gg I_{pA1}(\text{Pt/CCE})$]. Therefore, Pt-Co/CCE exhibits the high electrocatalysis performance in methanol oxidation with respect to Pt/CCE.

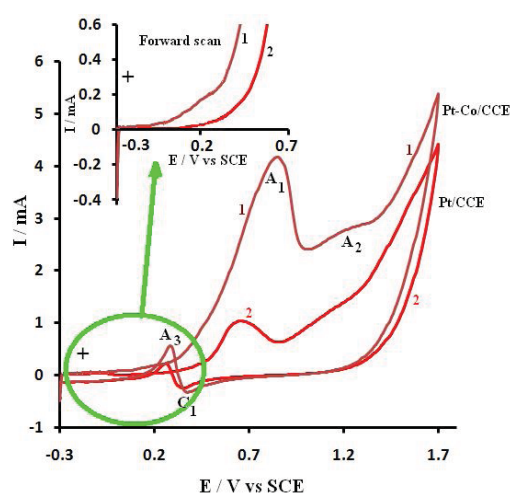


Figure 2. CVs of 0.5M methanol on the Pt-Co/CCE (curve 1) and Pt/CCE (curve 2) in 0.1M H_2SO_4 at a scan rate of 20 mV s^{-1} . Inset is the magnification of CVs in the onset potential region at forward scan.

Inset of Fig. 2 shows the magnification of CVs of the methanol oxidation in the onset potential region on the Pt-Co/CCE (curve 1) and Pt/CCE (curve 2) at forward scan. As can be seen, the Pt-Co/CCE exhibits the high electrocatalytic activity in the methanol oxidation with respect to Pt/CCE, because it is generally recognized that the onset potential can be an indicator in determining the electrochemical activity for methanol oxidation. Another noticeable difference between the CV of methanol oxidation on the Pt-Co/CCE and Pt/CCE is the ratio of anodic current in the forward scan and backward scan (I_{A1}/I_{A3}). The ratio of I_{A1}/I_{A3} for Pt-Co/CCE in methanol oxidation is 13.6 which is more than 1.43 multiple higher than that of the Pt/CCE (9.5). Such a high value for Pt-Co/CCE electrocatalyst indicates that most of the intermediate carbonaceous species were oxidized to CO_2 in the forward scan, suggesting that the interaction of Pt and Co leads to the less poisoning of Pt by the CO-like intermediates formed during methanol activation [23]. This improvement at Pt-Co/CCE electrocatalyst may be explained by the fact that alloying Co together with Pt lowers the electronic binding energy to enhance the C-H cleavage reaction at a lower potential value. Additionally, CO_{ads} oxidation reaction is facilitated by the presence of cobalt atoms [14].

It should be noted that, in addition to the presence of Co, the final potential in the cyclic voltammetric method can also affect the ratio of I_{A1}/I_{A3} in the electrooxidation of methanol on the Pt-Co/CCE (Fig. 3). With an increase in the final potential, the I_{A1} remains almost constant while I_{A3} decrease and consequently the ratio of I_{A1}/I_{A3} increase. In fact, increasing of the final potential accelerates the formation of Pt oxide. Acceleration of PtO formation cases the acceleration of the dehydration pathway and decreasing of CO_{ads} and consequently decreasing of the I_{pb} . This phenomenon again shows that the ratio of I_{A1}/I_{A3} is a sign of electrocatalytic and promoter activity of catalyst towards the poisonous intermediate CO_{ads} oxidation. In other words by increasing the final potential the conversion of metal to metal oxides is accelerated and as a result, an increase in reduction current peak of Pt oxide to Pt happens. In case of potential of peaks, it can be seen that the potential of methanol oxidation peak in the forward scan remains invariable, while the potential of oxidation peak in backward scan shifts positively and consequently difference between $E_{A1}-E_{A3}$ increases by increasing of final potential. In fact, the presence of high clean metal particles surface improves poisonous intermediate CO_{ads} oxidation reaction thermodynamically and the lowers potential peak of their oxidation in backward scan.

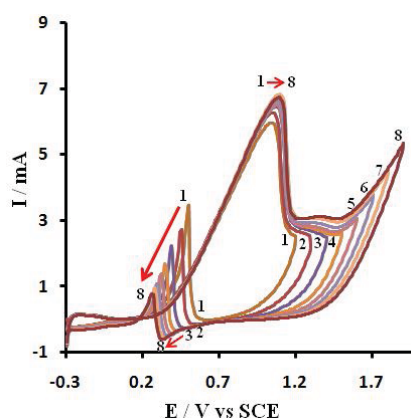


Figure 3. Effect of upper limit of potential scanning region in the electrooxidation of 0.5M methanol on the Pt-Co/CCE in 0.1M H_2SO_4 . (1) -0.3–1.2 V, (2) -0.3–1.3 V, (3) -0.3–1.4 V, (4) -0.3–1.5 V, (5) -0.3–1.6 V, (6) -0.3–1.7 V, (7) -0.3–1.8, and (8) -0.3–1.9 V. Scan rate 50 mV s^{-1} .

For investigation of the transport characteristics of the methanol on the Pt-Co/CCE, the influence of the scan rate (ν) in the oxidation of methanol on the Pt-Co/CCE was investigated (Fig. 4). The anodic peak currents are linearly proportional to $\nu^{1/2}$ [inset (up) of Fig. 4] which suggests that the electrocatalytic oxidation of the methanol on the Pt-Co/CCE is a diffusion-controlled process. While the anodic peak currents are nonlinear with respect to ν [inset (down) of Fig. 4] which is another sign for diffusion-control process.

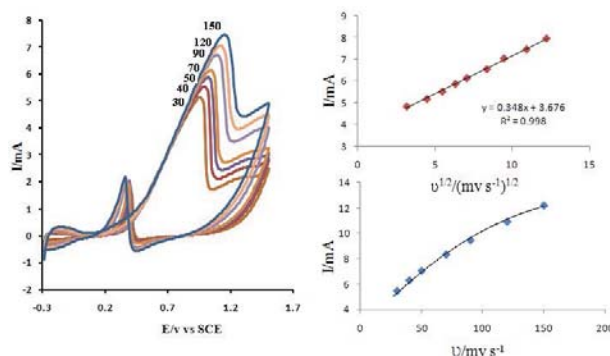


Figure 4. Effect of scan rate on 0.5M methanol oxidation on the Pt-Co/CCE in 0.1M H₂SO₄. Scan rates are shown on CVs. The insets show the dependence of the forward anodic peak currents on the square root of scan rates ($\nu^{1/2}$) and scan rates (ν), respectively.

In order to obtain some kinetic parameters in the oxidation of methanol, a set of experiments was made to study the effect of methanol concentration. For this purpose the CVs of the Pt-Co/CCE were recorded in presence of various concentrations of methanol (0.5 to 3.5 M) (Fig. 5). Inset (up) of Fig. 5 represents the dependence of the peak current of methanol oxidation on the bulk concentration of methanol. It was found that both the methanol oxidation peak current linearly increase with increasing methanol concentration up to 2 M after which the anodic peak current decrease with increasing of methanol concentration. On the other hand, the same deviation which is in the relation between methanol concentration and the oxidation peak potential may be attributed to the IR drop due to high oxidation current at high concentrations. The logarithmic plot [inset (down) of Fig. 5] of the peak current of methanol oxidation with its concentration up to a value of 0.5M produces a straight line of a slope equal to the order of the reaction with respect to methanol concentration according to the relation:

$$\text{rate} \propto I = k C^n \quad (2)$$

$$\log I = \log k + n \log C \quad (3)$$

where I is the peak current, k the reaction rate constant, C the bulk concentration and n is the reaction order. A value of 0.35 was calculated for the reaction order in agreement with the values obtained by other authors [24, 25].

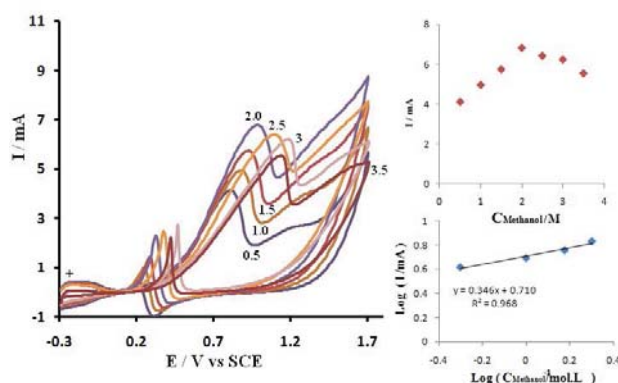


Figure 5. CVs of the methanol oxidation on the Pt-Co/CCE in 0.1M H_2SO_4 at various concentration of methanol. Scan rate 20 mVs^{-1} . Concentrations are shown on CVs. The insets show the dependence of the forward anodic peak currents (Up) and it's Log on the concentrations and its Log (down), respectively.

And finally, the long-term stability of Pt-Co/CCE was examined in 0.1 M H_2SO_4 solution containing 0.5M methanol. The obtained results show that the anodic current decreases with an increase in the scan number at the initial stage. i.e. the anodic current starts to decrease until to 40 cycles and remains constant afterwards. The peak current of the 200th cycles is about 91% than that of the first scan. In general, the loss of the catalytic activity after successive number of scans may result from the consumption of methanol during the CV scan. It may also be due to poisoning and the structure change of the Pt-Co catalyst as a result of the perturbation of the potentials during the scanning in aqueous solutions, especially in presence of the organic compound. The diffusion process occurring between the surface of the electrode and the bulk solution might be another factor. After the long-term CV experiments, the Pt-Co/CCE was stored in water for a week and then the methanol oxidation was carried out again by the CV. This process revealed that the excellent electrocatalytic activity the methanol oxidation was still observable. In order to further evaluate the stability of the electrocatalytic activity of the Pt-Co/CCE towards methanol oxidation, chronoamperometric measurement was performed. Fig. 6 shows the chronoamperometric curves of 0.5M methanol + 0.1M H_2SO_4 solution on the Pt-Co/CCE and smooth Pt electrode at 0.9V for 1000s, respectively. It was found that the currents observed from chronoamperograms were in good agreement with the currents observed from cyclic voltammetry.

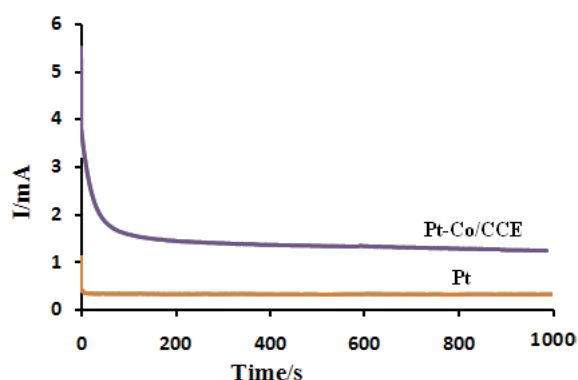


Figure 6. chronoamperometric curves of the electrooxidation of 0.5M methanol on the Pt-Co/CCE and smooth Pt electrode.



4. Conclusion

Platinum and cobalt can be co-deposited on CCE using a simple electrochemical process to form stable bimetallic particles. Methanol oxidation at the obtained catalyst (Pt-Co/CCE) was studied. It was found that the catalytic activity of the synthesized catalyst exceeds that of Pt nanoparticles (alone) on CCE and smooth Pt electrode. The prepared catalyst exhibits satisfactory stability and reproducibility when stored in ambient conditions or continues cycling, which makes it attractive as anode in direct methanol fuel cells and applications.

Acknowledgment

The authors gratefully acknowledge the research council of Azarbaijan Shahid Madani University for financial support.

References:

- [1] H.J. Huang, D.P. Sun, X.Wang "PtCo alloy nanoparticles supported on graphene nanosheets with high performance for methanol oxidation". *Chin. Sci. Bull.*, (2012), 57, 3071-3079.
- [2] Y.J. Gu, W.T. Wong "Nanostructure PtRu/MWNTs as anode catalysts prepared in a vacuum for direct methanol oxidation", *Langmuir*, (2006), 22, 11447-11452.
- [3] S. Basri, S.K. Kamarudin, W.R.W. Daud, and Z. Yaakub "Nanocatalyst for direct methanol fuel cell (DMFC)", *Int. J. Hydrogen Energy*, (2010) 35, 7957-7970.
- [4] C.H.Wang, H.Y. Dub, Y.T. Tsai, C.-P. Chen, C.-J. Huang, L.C. Chen, K.H. Chen, and H.C. Shih "High performance of low electrocatalysts loading on CNT directly grown on carbon cloth for DMFC". *J. Power Sources*, 2007, 171, 55-62.
- [5] M.H. Pournaghi-Azar and B. Habibi "Preparation of a platinum layer-modified aluminum electrode by electrochemical and electroless cementations and its use for the electrooxidation of methanol", *J. Electroanal. Chem.* (2005), 580, 23-34.
- [6] B. Habibi and M.H. Pournaghi-Azar "Methanol oxidation on the polymer coated and polymer-stabilized Pt nano-particles: A comparative study of permeability and catalyst particle distribution ability of the PANI and its derivatives", *Int. J. Hydrogen Energy* (2010), 25, 9318-9328.
- [7] B. Habibi and E. Dadashpour "Carbon-ceramic supported bimetallic Pt–Ni nanoparticles as an electrocatalyst for electrooxidation of methanol and ethanol in acidic media", *Int. J. Hydrogen Energy*. In Press, Corrected Proof. Available online 21 July 2012.
- [8] Q. Jiang, L. Jiang, H. Hou, J. Qi, S. Wang, and G. Sun "Promoting effect of Ni in PtNi bimetallic electrocatalysts for the methanol oxidation reaction in alkaline media: Experimental and density functional theory studies", *J. Phys. Chem. C* (2010), 114, 19714-19722.
- [9] R. Ahmadi, M.K. Amini, and J.C. Bennett "Pt–Co alloy nanoparticles synthesized on sulfur-modified carbon nanotubes as electrocatalysts for methanol electrooxidation reaction", *J. Catal.* (2012), 292, 81-89.
- [10] J. Zhang, J. Ma, Y. Wan, J. Jiang, and X.S. Zhao "Dendritic Pt–Cu bimetallic nanocrystals with a high electrocatalytic activity toward methanol oxidation" *Mater. Chem. Phys.* (2012), 132, 244-247.
- [11] C.T. Hsieh, and J.Y. Lin "Fabrication of bimetallic Pt–M (M= Fe, Co, and Ni) nanoparticle/carbon nanotubes electrocatalysts for direct methanol fuel cells", *J. Power Sources* (2009), 188, 347-352.
- [12] L. Xiong, A.M. Kannan, and A. Manthiram "Pt–M (M=Fe, Co, Ni and Cu) electrocatalysts synthesized by an aqueous route for proton exchange membrane fuel cells", *Electrochem. Commun.* (2002), 4, 898-903.



- [13] S. Wooa, I. Kimb, J.K. Leec, S. Bonga, J. Lee, and H. Kim "Preparation of cost-effective Pt–Co electrodes by pulse electrodeposition for PEMFC electrocatalysts", *Electrochim. Acta* (2011), 56, 3036-3041.
- [14] E. Antolini, J.R.C. Salgado, and E.R. Gonzalez "The methanol oxidation reaction on platinum alloys with the first row transition metals-the case of Pt-Co and -Ni alloy electrocatalysts for DMFCs: A short review", *Appl. Catal. B: Environ.* (2006), 63, 137-149.
- [15] J.H. Zeng, and J.Y. Lee "Effects of preparation conditions on performance of carbon-supported nanosize Pt-Co catalysts for methanol electrooxidation under acidic conditions", *J. Power Sources* (2005), 140, 268-273.
- [16] J. Qiana, W.Weia, X. Huang, Y. Tao, K. Chen, and X. Tang "A study of different polyphosphazene-coated carbon nanotubes as a Pt–Co catalyst support for methanol oxidation fuel cell", *J. Power Sources* (2012), 210, 345-349.
- [17] C.T. Hsieh, J.L. Wei, J.Y. Lin, and B.H. Yang "Preparation of Pt–Co nanocatalysts on carbon nanotube electrodes for direct methanol fuel cells", *Diam. Related Mater.* (2011), 20, 1065-1071.
- [18] H. Zhao, J. Yang, L. Li, H. Li, J. Wang, and Y. Zhang "Effect of over-oxidation treatment of Pt–Co/polypyrrole-carbon nanotube catalysts on methanol oxidation", *Int. J. Hydrogen Energy* (2009), 34, 3908-3914.
- [19] H. Kim, N.P. Subramanian, and B.N. Popov "Preparation of PEM fuel cell electrodes using pulse electrodeposition", *J. Power Sources* (2004), 138, 14-24.
- [20] B.Habibi, M.H. Pournaghi-Azar, H. Abdolmohammad-Zadeh, and H. Razmi "Electrocatalytic oxidation of methanol on mono and bimetallic composite films: Pt and Pt–M (M = Ru, Ir and Sn) nano-particles in poly(o-aminophenol) International" *Int. J. Hydrogen Energy* (2009), 34, 2880-2892.
- [21] E. Lamy-Pitara, and J. Barvier "Platinum modified by electrochemical deposition of adatoms", *Appl. Catal. A* (1997), 149, 49-87.
- [22] D. Chen, Q. Tao, L.W. Liao, S.X. Liu, Y.X. Chen, and S. Ye "Determining the Active Surface Area for Various Platinum Electrodes", *Electrocatal* (2011), 2, 207-219.
- [23] E. Antolini, J.R.C. Salgado, and E.R. Gonzalez "Carbon supported Pt₇₅M₂₅ (M=Co, Ni) alloys as anode and cathode electrocatalysts for direct methanol fuel cells", *J. Electroanal. Chem.* (2005), 580, 145-154.
- [24] B. Beden, F. Kadirgan, C. Lamy, J. M. Leger "Oxidation of methanol on a platinum electrode in alkaline medium: Effect of metal ad-atoms on the electrocatalytic activity", *J. Electroanal. Chem.* (1982), 142, 171-190.
- [25] A. V. Tripković, K. Dj. Popović, J. D. Mončilović, D. M. Dražić "Kinetic and mechanistic study of methanol oxidation on a Pt(100) surface in alkaline media", *J. Electroanal. Chem.* (1998), 448, 173-181.



Comparison conductivity between Yb and Dy co-doped CeO₂-Gd₂O₃ systems for IT-SOFCs

Zahra Khakpour*, Amir Ali Yuzbashi, Amir Maghsoudipour, M. Javaheri

Ceramic Department, Materials and Energy Research Center, Alborz, Iran

*z-khakpour@merc.ac.ir, Zahra_khakpour@yahoo.com (Corresponding author)

Tel: +982616204131

Abstract

The effect of co-doping with Dy and Yb elements on electrical properties of grain and grain boundary in Gd_{0.15}Dy_{0.05}Ce_{0.8}O_{1.9} and Gd_{0.15}Yb_{0.05}Ce_{0.8}O_{1.9} solid electrolytes was studied. In order to investigate the electrical properties of the series of ceria co-doped with Gd³⁺ and Dy³⁺ (Yb³⁺), the effects of co-doping and sintering conditions on grain and grain boundary conductivity are discussed in detail. The phase identification, ionic conductivity and microstructures of samples were studied by X-ray diffraction (XRD), AC impedance spectroscopy (IS) and scanning electron microscopy (SEM). Impedance spectroscopy measurements indicated that GDC doped by Dy and Yb electrolytes have higher grain conductivity in air at 400-700 °C compared with those of GDC. The addition of Dy and grain size together are influenced on grain boundary conductivity, however, the segregation amount of Yb³⁺ to the grain boundaries lead to increase grain boundary activation energy and higher schottky barrier in Gd_{0.15}Yb_{0.05}Ce_{0.8}O_{1.9} sample. It is verified that Dy and Gd co-doped CeO₂ show acceptable conductivities especially in the intermediate temperature region compared with singly doped CeO₂ ceramics.

Keywords: Co-doped ceria, Solid electrolyte, Impedance spectroscopy

1. Introduction

Solid oxide fuel cells (SOFCs) are of considerable interest as efficient and clean energy converters [1-2]. The performance of the oxide-ion electrolyte of the SOFC is critical to the development of a low or intermediate-temperature system. Although yttria-stabilized zirconia (YSZ) electrolyte has been used in SOFC under commercial development, their operating temperature are too high (800–1000 °C), which leads to high costs of interconnector and other construction materials, as well as short lifetimes of the devices [3-4]. Then there are efforts for investigating and finding ways to decrease the operating temperature. In order to develop fuel cells having low inner resistance at intermediate temperature, three research routes have been adopted: (1) reducing the thickness of the electrolyte (especially YSZ) film [5-6]; (2) developing new electrolyte materials of higher ionic conductivity for operation at IT [3,4,7,8]; and (3) improving the electrodes and catalysts to reduce the over potentials [9]. One such alternative electrolyte with a higher ionic conductivity than YSZ in air is rare earth doped ceria



and common dopants which enhance the ionic conductivity of the ceria electrolyte are La_2O_3 , Y_2O_3 , Sm_2O_3 and Gd_2O_3 [3-5,7-8,10]. The main drawback of ceria-based electrolytes, complicating their commercial application is the increase in electronic conductivity under low oxygen partial pressure (below 10–10 atm) at 800 °C that is accompanied by a reduction of Ce^{4+} to Ce^{3+} [11]. It has been reported that a reduction of ceria can be neglected at lower temperature around 600–700 °C [8]. However, such low temperatures are not suitable for singly doped ceria as an electrolyte in a SOFC or other devices, due to high electrical resistance. Structural modification of ceria-based solid solutions by co-doping is one possible way to improve their electrical conductivity at this temperature range [12]. A mechanism for an improvement of the electrical conductivity in co-doped ceria was proposed to be connected with the lowering of an association enthalpy of oxygen vacancy and the dopant ions [13]. Other factors which may play a role in co-doping effect are: rise of configurational entropy, modification of an elastic strain in the crystal lattice and changes of the grain boundary composition [14-15]. Some co-doped ceria-based electrolytes have been investigated, such as $(\text{Ce}_{(1-x-y)}\text{La}_x\text{M}_y)\text{O}_{2-\delta}$ ($\text{M} = \text{Ca}, \text{Sr}$) [16,17], $(\text{La}_{0.75}\text{Sr}_{0.2}\text{Ba}_{0.05})_{0.175}\text{Ce}_{0.825}\text{O}_{1.891}$ [18], $\text{Ce}_{1-x-y}\text{Sm}_x\text{Ca}_y\text{O}_{2-z}$ [19], $\text{Ce}_{0.8+x}\text{Y}_{0.2-2x}\text{Ca}_x\text{O}_{1.9}$ [20], $\text{Ce}_{1-a}\text{Gd}_{a-y}\text{Sm}_y\text{O}_{2-0.5a}$ [21], $\text{Ce}_{1-x-y}\text{Gd}_x\text{Pr}_y\text{O}_{2-z}$ [22], $\text{Ce}_{0.85}\text{Gd}_{0.1}\text{Mg}_{0.05}\text{O}_{1.9}$ [23], $\text{Ce}_{0.8}\text{Sm}_{0.2-x}\text{Y}(\text{La})_x\text{O}_{1.9}$ [12], $\text{Ce}_{0.8}\text{La}_{0.2-x}\text{Y}_x\text{O}_{1.9}$ [24], $\text{Ce}_{1-x}(\text{Sm}_{0.5}\text{Nd}_{0.5})_x\text{O}_\delta$ [25] and so on. However, there is no studies reported on Dy^{3+} and Yb^{3+} doped GDC, in which the ionic radii of the Dy^{3+} (1.027 Å) and Yb^{3+} (0.98 Å) is smaller than Gd^{3+} (1.053 Å) and more than Ce^{4+} (0.97 Å). It is expected that in our suggesting system, the elastic strain due to larger dopant cation (Gd) that leads to some distortion in fluorite lattice may be decreased if some present Gd will replace by lower dopant these cations. Moreover, the microstructure of sintered electrolytes, which is affected by chemical composition and preparation, has strong influence on the ionic conductivity. Enhance grain boundary conductivity by utilizing additives and changing microstructure by sintering regime [26-27] to scavenge the impurity phase in the grain boundaries is still debatable.

The present work summarizes a study on the preparation of co-doped ceria solid solutions in the $\text{CeO}_2\text{-Gd}_2\text{O}_3\text{-Dy}_2\text{O}_3$ and $\text{CeO}_2\text{-Dy}_2\text{O}_3\text{-Yb}_2\text{O}_3$ system. Their conductivity was compared with singly doped GDC electrolyte and the effects of co-doping and sintering conditions on grain and grain boundary conductivity have been investigated in detail.

2. Experimental

The material sources for the powder synthesis were CeO_2 , Gd_2O_3 , Dy_2O_3 and Yb_2O_3 from Alfa Aesar with 99.99% purity. They were inserted into a planetary ball mill according to the given composition of $\text{Gd}_{0.2}\text{Ce}_{0.8}\text{O}_{1.9}$ (20GDC), $\text{Gd}_{0.15}\text{Dy}_{0.05}\text{Ce}_{0.8}\text{O}_{1.9}$ and $\text{Gd}_{0.15}\text{Yb}_{0.05}\text{Ce}_{0.8}\text{O}_{1.9}$. The powder mixtures were processed with a rotary speed of 270 rpm, a ball to powder weight ratio of 10:1, using zirconia vial (60 ml) and balls (10 and 20 mm diameters). The mechanical alloying was carried out for up to 30 hours. More detailed were explained in previous paper [28]. For the phase identification, X-ray diffraction profile was equipped with a Philips $\text{Cu K}\alpha$ radiation ($\lambda = 1.54 \text{ \AA}$). All XRD experiments were performed with step size of 0.02° and a step time of 2 s. The crystallite size was estimated from the resultant spectra using the Williamson–Hall method [29]. The lattice parameter (a) was determined by fitting the observed reflection with a least squares refinement program. After the synthesizes powder, green samples were prepared. TSS was conducted on the green compact pellets (13 mm in diameter and 1-2 mm in thickness) pressed at 500 MPa with a relative density of about 64%. In the first step, the pellets in static air were heated up to the higher temperature of $T_1 = 1450^\circ\text{C}$, with a heating rate of $10^\circ\text{C}/\text{min}$, after which they were cooled down to the lower temperature of $T_2 = 1300^\circ\text{C}$ with a cooling rate of $50^\circ\text{C}/\text{min}$ and held there for 20 h. For comparing TSS and CS methods in a



complementary process, compact bodies were sintered in static air, heated at 2 °C/min to the desired temperature (1500 °C), and held isothermally for 5 h (CS). The bulk density of sintered pellets was determined using Archimedes method. The relative density of sintered pellets was calculated from the ratio between bulk density and the density calculated from X-ray diffraction data. The average grain size of the sintered bodies was calculated using linear intercept method measuring from at least 100 randomly selected grains recorded by SEM. To prepare SEM specimens, the surfaces of the samples were polished and thermally etched at 50-100 °C lower than the sintering temperature prior to SEM observation.

For the electrical conductivity measurement, platinum electrodes were applied to both sides of the sintered bodies by removing the surface layer, applying a coating of Pt paste, drying and heat treatment at 600 °C for 1 h. The conducting properties of the sintered bodies were measured by ac two-probe impedance spectroscopy (IS) at a temperature between 400-700 °C, and 1-10⁶ Hz frequency range.

3. Results and Discussion

X-ray diffraction pattern of 30 h milled mixture powder with supposed composition of Gd_{0.15}Dy_{0.05}Ce_{0.8} O_{1.9}, Gd_{0.15}Yb_{0.05}Ce_{0.8} O_{1.9} and Gd_{0.2}Ce_{0.8} O_{1.9} (20GDC) is shown in Fig. 1. The XRD patterns confirmed that these samples were single phase with CeO₂ cubic fluorite phase corresponding to the same Gd-doped ceria solid solution. The ionic radius of Yb³⁺ and Dy³⁺ respectively 0.98 Å and 1.027 Å that are smaller than the ionic radius of Gd³⁺ (1.053 Å) and the critical radius defined for element substitution in CeO₂ (1.038Å) too [10, 30]. So it was expected with replacing 0.05 mol % Dy³⁺ or Yb³⁺ in 2GDC instead of Gd³⁺, the amount of lattice strain caused by adding Gd₂O₃ was reduced that lead to decrease the lattice parameter. The lattice parameter was calculated and results were shown in Table 1. It can be seen that the lattice parameter of Gd_{0.15}Dy_{0.05}Ce_{0.8} O_{1.9} and Gd_{0.15}Yb_{0.05}Ce_{0.8} O_{1.9} are lower than 2GDC.

Table1: Some physical properties of the samarium doped ceria (SDC) solid solution, a is the lattice parameter and D_{XRD} is the crystallite size obtained by XRD analysis

milled powders after heat treatment	a (Å)
2GDC	5.419
Gd _{0.15} Dy _{0.05} Ce _{0.8} O _{1.9}	5.417
Gd _{0.15} Yb _{0.05} Ce _{0.8} O _{1.9}	5.415

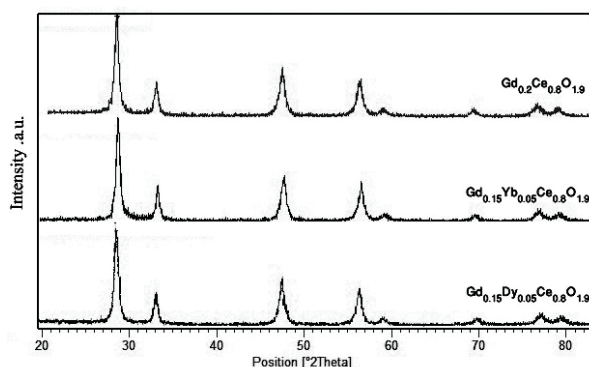


Fig. 1. XRD patterns of the 30 h milled mixture powder with supposed composition of: $Gd_{0.2}Ce_{0.8}O_{1.9}$ (20GDC) (a) $Gd_{0.15}Dy_{0.05}Ce_{0.8}O_{1.9}$ (b) and $Gd_{0.15}Yb_{0.05}Ce_{0.8}O_{1.9}$ (c).

In researches have been done in relation to the system consists of more than one add-rare-earth elements so far, the issue of sintering less explored. Yushida et. al [31] with the addition of gallium (Ga) compounds based on ceria containing Gd, Sm, Y, Nd, and La has reported improving the sintering by increase the relative density and grain growth. Improved the sintering has been indicated in CaO-GDC system as well [32]. Fig. 2 shows SEM micrographs of polished and thermally etched surfaces of normally (CS) and TSS sintered of GdYbCe, GdDyCe. As it can be seen, samples have high relative density and the porosity in the samples is almost never seen. However, a somewhat undesirable grain growth can also be observed. This phenomenon, especially in CS-sample containing additives ytterbium (Yb) was evident, as the non-uniform distribution of grain sizes is seen as well.

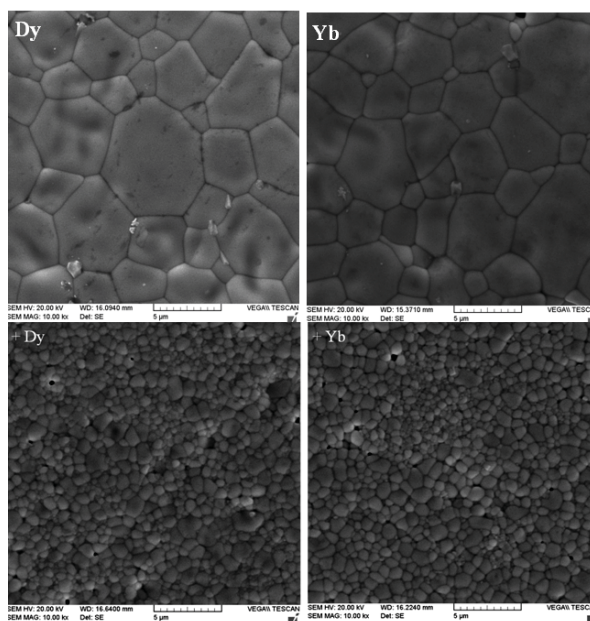


Fig. 2. Microstructures of polished and thermally-etched surface of conventional sintering (CS)(top) and TSS (down) $Gd_{0.15}Dy_{0.05}Ce_{0.8}O_{1.9}$ (Dy) and $Gd_{0.15}Yb_{0.05}Ce_{0.8}O_{1.9}$ (Yb) ceramics.

The average grain size of the conventionally sintered $Gd_{0.15}Dy_{0.05}Ce_{0.8}O_{1.9}$, $Gd_{0.15}Yb_{0.05}Ce_{0.8}O_{1.9}$ samples are respectively 3.1 and 3.8 μm with the relative density of about 98.5 % of theoretical density that are reach higher densities compared to singly doped 2GDC [33]. This

behavior can be related to that the co-doping approach lead to improved the grain boundary diffusion during sintering [31,34]. By employing the TSS technique, the resultant grain size is relatively low and relative density increases. The relative density for TSS $Gd_{0.15}Dy_{0.05}Ce_{0.8}O_{1.9}$ and $Gd_{0.15}Yb_{0.05}Ce_{0.8}O_{1.9}$ samples are about 99 % and average grain size are respectively 600 and 500 nm. Finer grain sizes that obtained in $GdYbCe$ samples maybe due to more immigration and segregation of Yb into grain boundaries area.

The ac impedance method was applied to determine the electrical properties of co-doped samples obtained by conventional and TSS method. The typical impedance spectra and equivalent circuit model of $Gd_{0.15}Dy_{0.05}Ce_{0.8}O_{1.9}$ and $Gd_{0.15}Yb_{0.05}Ce_{0.8}O_{1.9}$ which conventionally (CS) and TSS sintered electrolytes at 600 °C are shown in Fig. 3. For better comparison, the ac spectra of 2GDC (singly doped sample) has been shown too. The frequency increased from the right to left across the plots, the frequency change of $Gd_{0.15}Yb_{0.05}Ce_{0.8}O_{1.9}$ has been seen in plot. Two arcs are observed in the spectra of these samples. Three parts contributions can be distinguishes from each other with the aid of the equivalent circuit model shown in Fig. 3. These various contributions can be ascribed the various conduction processes occurring in the grain or bulk (high frequency), grain boundaries (intermediate frequency), and electrode interfaces (low frequency) and are based on different resistances R and capacitances C in the equivalent parallel RC circuits. R_b is bulk resistance, R_{gb} the grain boundary resistance, R_{ct} the electrode interface resistance, CPE_{gb} grain boundary capacitance, and CPE_{ct} is electrode interface capacitance. The calculated values of the geometrical capacitances at 500 °C for different composition are in the range of 10^{-9} to 10^{-11} F for high frequency contribution and 10^{-7} to 10^{-8} F for the intermediate frequency term. Therefore, the resistance data for each specimen at different temperatures can be obtained and then the grain (bulk) conductivity (σ_b), grain boundary conductivity (σ_{gb}), and total conductivity can be calculated [35]. It can be seen from Fig. 3, co-doped samples sintered normally or TSS exhibited more grain conductivity than single doped 2GDC sample. Adding Yb^{3+} lead to increase the grain boundary conductivity and different sintering regime has not effect on grain boundary conductivity in these samples. The lowest and highest grain boundary conductivity at 600 °C is belonged to Dy^{3+} and Gd^{3+} co-doped samples that sintered conventionally at 1500 °C (CS) and TSS respectively.

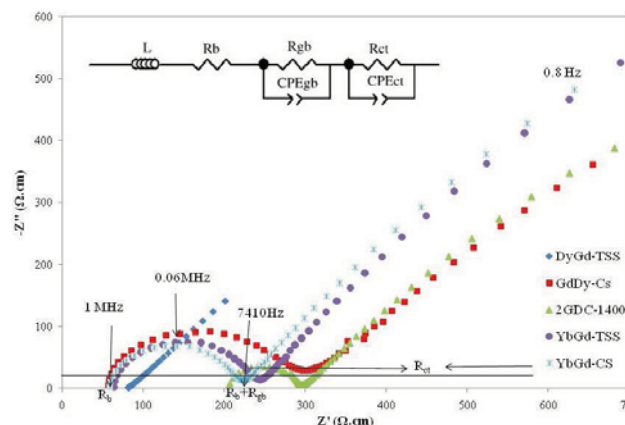


Fig. 3. Complex impedance spectra and equivalent circuit model of CS and TSS sintered $Gd_{0.2}Ce_{0.8}O_{1.9}$ (20GDC), $Gd_{0.15}Dy_{0.05}Ce_{0.8}O_{1.9}$ and $Gd_{0.15}Yb_{0.05}Ce_{0.8}O_{1.9}$ electrolytes at 600 °C.

Fig. 4 gives the Arrhenius plots of grain (bulk) conductivity of TSS and CS co-doped and singly GDC doped samples as a function of testing temperature. It can be seen that the bulk conductivity of the co-doped samples at the test temperatures comparing to the single doped

sample (2GDC) with the same amount of dopant concentrations (20% mol) have been increased. The differences between the bulk conductivity of co-doped samples, especially at temperatures higher than 500 °C are not very and following this trend: DyGdCe-TSS > DyGdCe-CS > YbGdCe-CS > YbGdCe-TSS. The change of sintering regime and average grain size has not a significant influence on the bulk conductivity of the DyGdCe and YbGdCe ceramics at $T \geq 500$ °C. The bulk conduction activation energy values were calculated using the slope of the curves is presented at the Fig. 4 too. As it can be seen, the bulk conductivity of the co-doped samples was decreased and the lowest values are belonged to DyGdCe-TSS sample. Fig. 5 gives the Arrhenius plots of grain boundary conductivity of TSS and CS co-doped and singly GDC doped samples as a function of testing temperature.

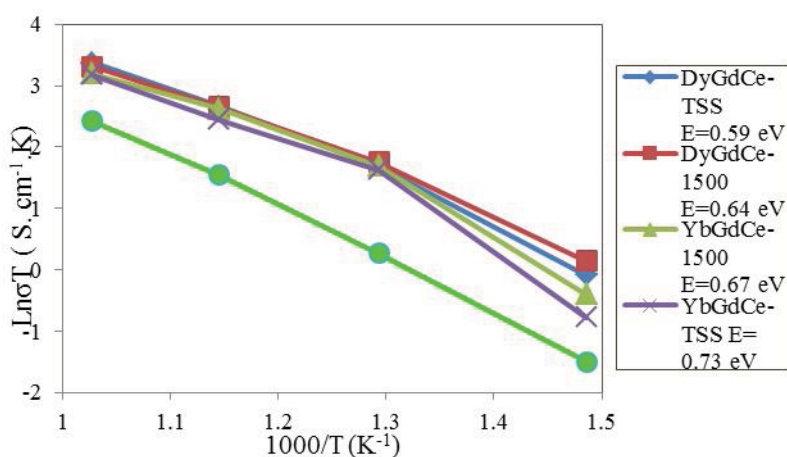


Fig. 4. Arrhenius type plots of bulk conductivity for CS and TSS sintered $Gd_{0.2}Ce_{0.8}O_{1.9}$ (20GDC), $Gd_{0.15}Dy_{0.05}Ce_{0.8}O_{1.9}$ and $Gd_{0.15}Yb_{0.05}Ce_{0.8}O_{1.9}$ electrolytes. The values of bulk conduction activation energy are illustrated too.

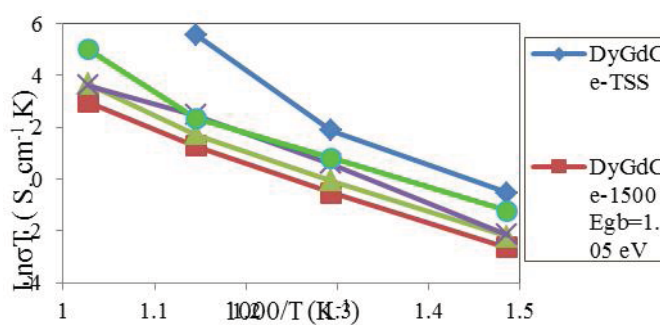


Fig. 5. Arrhenius type plots of grain boundary conductivity for CS and TSS sintered $Gd_{0.2}Ce_{0.8}O_{1.9}$ (20GDC), $Gd_{0.15}Dy_{0.05}Ce_{0.8}O_{1.9}$ and $Gd_{0.15}Yb_{0.05}Ce_{0.8}O_{1.9}$ electrolytes. The values of grain boundary conduction activation energy are illustrated too.

Table 2. Ionic conductivity at 500 and 700°C, activation energies, pre-exponential terms and effective index of

Sample	Average		$\sigma_{500(t)}$ (S.cm ⁻¹)	E (e.V)	σ_0 (S.cm ⁻¹ .K)	ΔE_0 at 500 °C (V)	Effective index
	grain size (μm)	$\sigma_{700(t)}$ (S.cm ⁻¹)					
DyGdCe-CS	3.8	0.011	0.0007	0.96	8.7×10^5	0.37	0.81
DyGdCe-TSS	0.6	0.03	0.0032	0.82	7.5×10^5	0.22	0.81
YbGdCe-CS	3.1	0.015	0.0011	0.93	1.01×10^6	0.35	0.78
YbGdCe-TSS	0.55	0.02	0.0011	0.94	2.6×10^6	0.36	0.78
2GDC	1.7	0.011	0.0009	0.96	5.1×10^5	0.30	-

the co-doped electrolyte ceramics.

The grain boundary conduction activation energy values were calculated using the slope of the curves is shown at the Fig. 5 too. The DyGdCe-TSS electrolyte exhibited the highest grain boundary conductivity at test temperatures. The obtained results indicated that TSS regime could improve the grain boundary conductivity of DyGdCe-TSS electrolyte but had not significant influence on Yb and Gd co-doped electrolyte. The change in electrical behavior of the grain boundary depends upon two main factors: 1) the segregation of dopant cations that cause space charge effect and (2) the grain boundary impurity or glassy phase that blocks the ionic motion across the grain boundaries area [36]. In order to better investigate the role of microstructure and composition on grain boundary conductivity of co-doped samples, the Schottky barrier height (ΔE_0) was calculated. The total activation energy for conduction, pre-exponential factor (σ_0) and ΔE_0 at 500°C in co-doped and singly doped 2GDC ceramics are summarized in Table 2. The proposed formal in a Matt-Schottky grain boundary model describes a relation between the space charge potential in the interface core/space charge layer (ΔE_0) and bulk to specific grain boundary ratio [36,37]

$$\frac{\sigma_b}{\sigma_{gb}^{sp}} = \frac{\exp(2e\Delta\phi_0 / KT)}{4e\Delta\phi_0 / KT} \quad (1)$$

Where σ_b is the bulk conductivity, σ_{gb}^{sp} is the specific grain boundary conductivity and ΔE_0 is Schottky barrier height. Comparison of the calculated values of $\Delta\phi_0$ reveal that co-dopin of Dy and Gd reduce Schottky barrier height in TSS regime and lead to increasing the conductivity at low temperatures (500 °C). So it can conclude that replacing the Gd by Dy in combination the decreasing sintering temperature (or average grain size) lead to change the structure of grain boundaries by lowering the electrical potential at the grain boundaries area (cations and vacancies accumulation). In contrast, the behavior of ytterbium as a second dopant is so different. The Schottky barrier height in Yb and Gd co-doped samples sintered by the

conventional method or TSS increased. It shows different behavior of Dy and Yb as a second dopant. It has been found that ionic conductivity of doped ceria is related to the concentrations and distribution of oxygen vacancy (configurational entropy) and lattice strain (activation enthalpy). According to Kim [38], the reduction of lattice deviation of doped ceria ceramics would lead to the reduction of the lattice strain of doped ceria. Morie et al [39] introduces the concept of effective index to explain the co-doping effect. The effective index for a fast oxide ionic conduction in doped CeO₂ electrolytes was defined using ionic radii and the amount of oxygen vacancies that are produced by dopant substitution on the idealized graphic sites. The effective index was defined in Eq. (2):

$$\text{Effective index} = (\text{ave. } r_c / \text{eff. } r_o) \times (r_d / r_h) \quad (2)$$

Where avg. r_c , r_d and r_h are the average ionic radius of the cations, the average radius of the dopant ions and the ionic radius of the host cation (Ce⁴⁺), respectively. The eff. r_o is the effective oxygen ionic radius, which can be given by:

$$\text{eff. } r_o = 1.4 \times \{(2-\delta)/2\} \quad (3)$$

where δ is the level of expected oxygen vacancy, and 1.4 is the commonly used ionic radius of oxygen in oxides. The effective index of the samples is summarized in Table 2. It could be seen the effective index increase by adding Dy dopant, unlike replacing Yb lead to reduce the effective index. These results confirm the decreasing the bulk activation energy in Dy and Gd co-doped sample comparing with the Yb and Gd co-doped and singly doped samples. Comparing the calculated pre-exponential values (Table 2) indicated that the co-doping increased the configurational entropy of doped ceramics leads to increase the bulk conductivity in Dy-Gd and Yb-Gd co-doped electrolytes too. So there would be smaller micro domains in the co-doped electrolyte [39], which enhanced the bulk conductivity. The amount of configuration entropy in Yb and Gd co-doped ceramics are more but the total electrical conductivity is lower than others. It seems, the microstructure and grain boundary influence was dominant, so the microstructure of grain boundary was investigated by EDS analysis. Fig. 6 shows the EDS analysis of CS- YbGdCe sample.

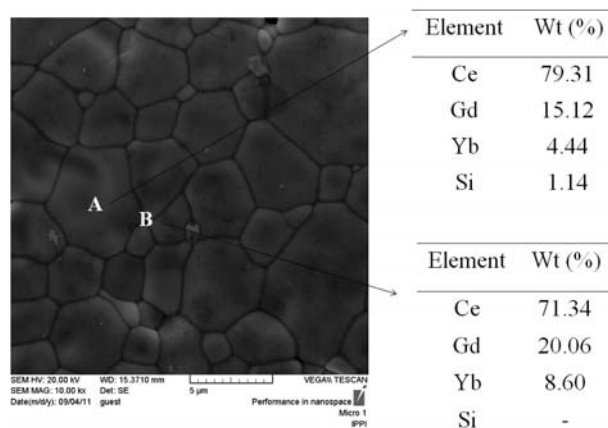
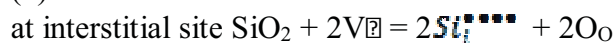


Fig. 6. Scanning electron microscopy image for microstructure of CS-Gd_{0.15}Yb_{0.05}Ce_{0.8}O_{1.9} electrolyte. The corresponding elemental analyzes (EDS) for the distribution amount of Yb, Gd and Ce in grain and grain boundaries are presented

The first noticeable is the presence of high concentrations of additives especially Gd (about 20%) in the grain boundaries. In addition, the presence of trace Si impurities (about 1.4%) was detected in the grain (that was not detected in Dy and Gd co-doped samples). It seems that the



presence of Si impurity inside the grains was due to dissolution of the SiO₂ in the CeO₂ lattice. According to J. Ma [40], at a higher sintering temperature, a small quantity of SiO₂ can be dissolved into GDC ceramic at either substitutional sites or interstitial sites, i.e.,



Although the dissolution of SiO₂ substitutional sites produces no charge carriers as described in Eq. (4), a large lattice distortion usually leads to accumulation and segregation of dopant (Gd) at the grain boundary. It seems this phenomena cause to increasing the Schottky barrier height and increasing the grain boundary conductivity in the Yb and Gd co-doped ceramic. However, the interstitial dissolution of SiO₂ filling some oxygen vacancies is as described in Eq. (5). This results in a decrease in the concentration of oxygen vacancies, and thus reduces the bulk conductivity. A various effect of co-doping on the bulk and grain boundary conductivities is related both structure and composition. The grain boundary conductivity of TSS (Yb& Gd) co-doped electrolyte not very changed by changing sintering regime. It seems that according to above mentioned, the composition is more influence on grain boundary microstructure in that composition ceramic. TSS regime led to improvement of the grain boundary conductivity in Dy and Gd co-doped electrolyte due to the minor concentration of the segregated dopant in grain boundaries regions. So co-doping and sintering regime must have changed the grain boundary microstructure of Dy and Gd co-doped ceria.

4. Conclusions

Co-doped ceria electrolyte with nominal composition of Gd_{0.15}Dy_{0.05}Ce_{0.8}O_{1.9} and Gd_{0.15}Yb_{0.05}Ce_{0.8}O_{1.9} were prepared and studied. The effect of co-doping with Dy³⁺ and Yb³⁺ and sintering condition (conventionally and TSS) on grain and grain boundary conductivity were investigated and comparison to singly doped ceria (2GDC). Co-doping led to decreased sintering temperature (50 °C) in CS samples and grain sizes in TSS and CS samples. Impedance spectroscopy measurement indicated that bulk conductivity increased by co-doping that means decreasing the local ordering of oxygen vacancies (configurational entropy) and lattice strain. High grain boundary conductivity which was higher than that of singly doped 2GDC enhanced by co-doping Dy³⁺ and TSS regime. The Gd_{0.15}Dy_{0.05}Ce_{0.8}O_{1.9} co-doped samples maybe the better electrolyte of intermediate-temperature solid oxide fuel cells.

References:

- [1] N. Q. Minh, **Ceramic** fuel cells, J. Am. Ceram. Soc. 1993; 76 (3): 563-588.
- [2] S. M. Haile, "Fuel cell materials and components", Acta Materialia 51(2003) 5981-6000.
- [3] T. Mori, R. Buchanan, D. R. Ou, F. Ye, T. Kobayashi, J. Deok Kim, J. Zou, J. Drennan, "Design of nanostructured ceria-based solid electrolytes for development of IT-SOFC", J. Solid State Electrochem, 12 (7-8) (2008) 841-849.
- [4] H. Yashiro, K. Eguchi and H. Arai, Electrical properties and reducibilities of Ceria-rare earth oxide and their application to solid oxide fuel cell, Solid State Ionics, 1989; 36: 71-75.



- [5] F. L. Chen, M. L. Liu, Preparation of yttria-stabilized zirconia (YSZ) films on $\text{La}_{0.85}\text{Sr}_{0.15}\text{MnO}_3$ (LSM) and LSM–YSZ substrates using an electrophoretic deposition (EPD) process, *J. Eur. Ceram. Soc.* 21 (2001) 127-134.
- [6] L. Jia, Z. Lu, X. Huang, Z. Liu, K. Chen, X. Sha, G. Li, W. Su, Preparation of YSZ film by EPD and its application in SOFCs, *J. Alloys Compd.* 424 (2006) 299-303.
- [7] B. C. H. Steele, Appraisal of $\text{Ce}_{1-y}\text{Gd}_y\text{O}_{2-y/2}$ electrolytes for IT-SOFC operation at 500°C, *Solid State Ionics* 2000; 129: 95-110.
- [8] K. Eguchi, T. Setoguchi, T. Inoue and H. Arai, Electrical properties of ceria-based oxides and their application to solid oxide fuel cell, *Solid State Ionics* 1992; 83: 165-172.
- [10] H. Inaba, H. Tagawa, Ceria-based solid electrolytes, *Solid State Ionics* 1996; 83: 1-16.
- [11] H. L. Tuller and A. S. Nowick, "Small polaron electron-transport in reduced CeO_2 single-crystals", *J. Phys. Chem. Solids*, 38 [8] (1977) 859-867.
- [12] M. Dudek, W. Bogusz, L. Zych, B. Trybalska, "Electrical and mechanical properties of CeO_2 -based electrolytes in the CeO_2 – Sm_2O_3 – M_2O_3 (M= La, Y) system", *Solid State Ionics*, 179 (2008) 164–167.
- [13] J.A. Kilner, R.J. Brook, □ A study on oxygen ion conductivity in doped non-stoichiometric oxides □, *Solid State Ionics* 6 (1982) 237-252.
- [14] J. Kim and D. Lee, "The effect of multiple doping on electrical conductivity of Gadolinia-Doped Ceria electrolyte", *Korean J. Chem Eng.*, 19(3) 421-424(2002).
- [15] S. Omar, E.D. Wachsman, J.C. Nino, □ A co-doping approach towards enhanced ionic conductivity in fluorite-based electrolytes □, *Solid State Ionics* 177 (2006) 3199–3208.
- [16] Y. Zheng, Y. Shi, H. Gu, L. Gao, H. Chen, L. Guo, □ La and Ca co-doped ceria-based electrolyte materials for IT-SOFCs □, *Materials and Research Bulletin*, 44 (2009) 1717-1721.
- [17] N. Jaiswal, S. Upadhyay, D. Kumar, O. Parkash, □ Ionic conductivity investigation in lanthanum (La) and strontium (Sr) co-doped ceria system □, *J. Power Sources* 222 (2013) 230-236.
- [18] E. Yu. Pikalova, V. I. Maragou, A. N. Demina, A. K. D.emin, P.E. Tsiakaras, □ The effect of co-dopant addition on the properties of $\text{Ln}_{0.2}\text{Ce}_{0.8}\text{O}_{2-\delta}$ (Ln = Gd, Sm, La) solid-state electrolyte □, *J. Power Sources* 181 (2008) 199-206.
- [19] T. Mori, H. Yamamura, □Preparation of Alkali-Elements or alkali-earth-element- doped CeO_2 - Sm_2O_3 system and its operation properties as the electrolyte in planar solid oxide fuel cells □, *J. Mater. Synth. Process.* 6 (1998) 175-179.
- [20] X. Homgemi, Y. Hongge, C. Zhenhua, □ Preparation and properties of Y^{3+} and Ca^{2+} co-doped ceria electrolyte materials for ITSOFC □, *Solid State Sciences* 10 (2008) 1179-1184.



- [21] F. Y. Wang, S. Chen, S. Cheng, □ Gd³⁺ and Sm³⁺ co-doped ceria based electrolytes for intermediate temperature solid oxide fuel cells □, *Electrochemistry Communications*, 6 (2004) 743-756.
- [22] S. Lubke, H. D. Wiemhofer, □ Electronic conductivity of Gd-doped ceria with additional Pr-doping □, *Solid State Ionics* 117 (1999) 229-243.
- [23] F. Wang, S. Y. Chen, Q. Wang, S. Yu, S. Cheng, □ Study on Gd and Mg co-doped ceria electrolyte for intermediate temperature solid oxide fuel cell □, *Cata. Today* 97 (2004) 189-194.
- [24] H. Yoshida, H. Deguchi, K. Miura, M. Horiuchi, T. Inagak, □ Investigation of the relationship between the ionic conductivity and the local structures of singly and doubly doped ceria compounds using EXAFS measurement □, *Solid State Ionics* 140 (2001) 191-199.
- [25] B. Li, Y. Liu, X. Wei, W. Pan, □ Electrical properties of ceria Co-doped with Sm³⁺ and Nd³⁺ □, *J. Power Sources*, 195 (2010) 969-976.
- [26] S. M. Haile, D. L. West, J. Campbell, "The role of the microstructure and processing on the proton conducting properties of gadolinium-doped barium cerate ", *J. Mater. Res.* 13 (1998) 1576-1595.
- [27] D. Suk Kim, P. Seok Cho, J. Heun Lee, D. Yeon Kim, S. Bo Lee, 'Improvement of grain-boundary conduction in gadolinia-doped ceria via post-sintering heat treatment, *Solid State Ionics*, 177 (2006) 2125-2128.
- [28] Z. Khakpour, A. A. Youzbashi, A. Maghsoudipour, K. Ahmadi, Synthesis of nano sized Gadolinium Doped Ceria solid solution by high energy ball milling, *Powder Technology*, 214 (2011) 117-121.
- [29] G.K. Williamson, W.H. Hall, X-ray line broadening from filed aluminium and wolfram *Acta Metall.* 1 (1953) 22-31.
- [30] L. Minervini, M. O. Zacate, R. W. Grimes, "Defect cluster formation in M₂O₃-doped CeO₂ *Solid State Ionics*", 116 (1999) 339-349.
- [31] H. Yushida, K. Miura, T. Fukui, S. Ohara, T. Inagaki, "Sintering behavior of Ln-doped ceria compounds containing Gallia", *J. Power Sources*, 106 (2002) 136-141.
- [32] P. S. Cho, S. B. Lee, D. S. Kim, J. H. Lee, D. Y. Kim, H. M. Park, "Improvement of grain-boundary conduction in gadolinia-doped ceria by the addition of CaO", *Electrochemical and Solid State Letters*, 9(9) A399-A402 (2006).
- [33] Z. Khakpour, A. A. Youzbashi, A. Maghsoudipour, K. Ahmadi, Electrical behavior of Gd-doped CeO₂ electrolyte ceramics sintered from nano powders prepared by mechanical alloying process, *J. Mater. Sci: Mater Electron* 23 (2012) 786-794.
- [34] J. X. Zhu, D. F. Zhou, S. R. Guo, J. F. Ye, X. F. Hao, X. Q. Cao, J. Meng, " Grain boundary conductivity of high purity neodymium-doped ceria nanosystem with and without the doping of molybdenum oxide", *J. Power Sources*, 174 (2007) 114-123.



- [35] S. P. Jiang, J. G. Love, S. P. S. Badwal, □ Electrochemical techniques in studies of solid ionic conductors □, Key Engineering Materials, 125-126 (1997) 81-132.
- [36] X. Guo, R. Waser, "Electrical properties of the grain boundaries of oxygen ion conductors: Acceptor-doped Zirconia and Ceria", Progress in Materials Science, 51 (2006)151-210.
- [37] D. Perez-Coll, P. Nunez, J. C. Ruiz-Morales, J. Pena-Martines, J. R. Frade, "Re-examination of bulk and grain boundary conductivities of $Ce_{1-x}Gd_xO_{2-\delta}$ ceramics", Electrochimica Acta, 2007; 52: 2001-2008.
- [38] D. J. Kim, □Lattice Parameters, Ionic Conductivities, and Solubility Limits in Fluorite-Structure MO_2 Oxide [M = Hf^{4+} , Zr^{4+} , Ce^{4+} , Th^{4+} , U^{4+}] Solid Solutions □, J. Am. Ceram. Soc., 72 [8] (1989) 1415-1421.
- [39] T. Mori, J. Drennan, J. H. Lee, J. Guang Li, T. Ikegami, "Oxide ionic conductivity and microstructures of Sm- or La-doped CeO_2 -based systems", Solid Oxide Ionics, 154-155 (2002) 461-466.
- [40] J. Ma, T. S. Zhang, L. B. Kong, P. Hing, S.H. Chan, " $Ce_{0.8}Gd_{0.2}O_{2-\delta}$ ceramics derived from commercial submicron-sized CeO_2 and Gd_2O_3 powders for use as electrolytes in solid oxide fuel cells", J. Power Sources, 132 (2004) 71-76.



Electricity Generation and Sulfide Removal by dual chamber Microbial fuel cell simultaneously

Paniz Izadi¹, Mostafa rahimnejad^{*2}, Ali Ghoreyshi³, Ghasem Najafpour⁴, Karim Hassaninejad⁵, Zahra Najafgoli⁶

¹Biotechnology Research Lab., Faculty of Chemical Engineering, Noshirvani University, Babol, Iran

paniz_izadi@yahoo.com

Abstract

Microbial fuel cells (MFCs) have been used to alter different sources of substrates to bioelectricity recently. It can also be used for wastewater treatment and electricity generation simultaneously. Sulfur compounds such as sulfides are commonly exist in wastewater and organic waste. In this study a dual chamber MFC was constructed for power production. Sulfide was used as electron donor in anaerobic anode compartment. Mixed culture of microorganisms was used as active biocatalyst to convert substrate toward electricity. The obtained experimental results expose that this MFC can successfully alter sulfide to elementary sulfur and power generation. Maximum generated power and current density with out aeration were 364 mW.m⁻² and 1335 mA.m⁻², respectively. The influence of the oxygen was examined in the cathode chamber and during aeration the cell voltage gradually increased and reached to 480 mV after 1200 s. Hexacyanoferrate was added to cathodic solution in different concentrations and its affect was investigated. Maximum generated voltage , power and current density were 988.9145 mV ,346.22 mW.m⁻² ,1257.51 mA.m⁻² , respectively and they were obtained in peresence of 1.2 g l⁻¹ mediator.

Keywords: bioelectricity, power density, sulfide, Hexacyanoferrate, dual chamber.

1 Introduction

Since the use of fossil fuels has created serious problems for human being, such as global warming and environment pollution, renewable bioenergy is viewed as one of the ways to decrease the current crisis[1]. Microbial fuel cell (MFC) is a biological system which alter biodegradable organic substance to electricity using bacteria as biocatalyst [2]. A MFC generate electricity from bio-convertible substrate. Bacteria switch from the natural electron acceptor,

¹ MS. student

² Assistant professor of chemical engineering, Babol Noshirvani university, rahimnejad@nit.ac.ir

³ Assosiated professor of chemical engineering, Babol Noshirvani university,, aa_ghoreyshi@yahoo.com

⁴ professor of chemical engineering, Babol Noshirvani university, Naafpour@nit.ac.ir

⁵ Assistant professor of chemistery, Babol Noshirvani university,Skariminejad@nit.ac.ir

⁶ MS student of chemical engineering, Babol Noshirvani university,, rahimnejad@nit.ac.ir



such as oxygen to an insoluble acceptor, such as the MFC anode [3]. Advantages of this technology such as non-pollution, high energy efficiency, mild operating conditions, strong biocompatibility and great application potential in various areas are the reason that it has received so many attention from scientists [4].

MFCs are capable to produce clean energy, apart from effective treatment of waste material such as wastewater. The active microorganisms in the anaerobic anode compartment have capabilities to use organic matter exist in the wastewater as energy source and generate protons and electrons, through which electricity can be recovered [5]. Sulfide is commonly found in wastewaters by the action of anaerobic bacteria on organic substance. High levels of sulfide ions in waters are perilous to living beings so it should be treated from wastewater before released into environment [6]. Besides, exploring new energy sources is an important measure to achieve sustainable development and circulation economy [7]. Microbial communities in MFC for power generation and sulfide alteration have been investigated [6] Table 1 shows a list of MFCs was examined for elimination of different pollutant and electricity generation.

Table 1. Different elimination of substrate via MFC.

Elimination of	Cathode Material	Anode Material	Maximum power	Removal at	Removal efficiency (%)	Reference
Carbon	Granular graphite	Granular graphite	34.6 W.m ⁻³	Anode chamber	100	[8]
COD	Graphite felt	Graphite felt	7.6 mW	Anode chamber	90	[9]
Dye	Graphite plate	Graphite plate	15.73 mW.m ⁻²	Anode chamber	93.15	[10]
Nitrogen	Granular graphite	Granular graphite	34.6 W.m ⁻³	Cathode chamber	67	[8]
Copper	Graphite plate	Graphite plate	339 mW.m ⁻³	Cathode chamber	96	[11]

At the cathode compartment, oxygen as the final electron acceptor commonly was used[12]. Consumption of electrons and protons that are combined with oxygen, forms water at last, and end this transfer cycle. Oxidized mediators, can also accelerate reaction of forming water in cathode chamber. Substrate as nutrient source of the cell played an important biological role besides other factors such as mediator, microorganism and nutrients affected the bioelectricity production pattern[13].

In this study, A two chamber MFC was designed and fabricated for power production and sulfide removal . Mixed culture of microorganisms was used for this aim. The influences of concentration of oxidizer agent and aeration on power generation, voltage and sulfide removal efficiency of MFC were investigated.

2 Materials and methods

2.1 MFC construction

The used MFC in this paper was constructed of two 750 ml cubic plexiglass chambers as anode and cathode compartment (figure 1). Two chambers were separated by a PEM (3.0cm× 3.0 cm, Nafion-117, SigmaeAldrich, USA) and assembled using stainless steel studding, nuts and washers. Graphite plate was used as anode(area, 21cm²) and cathode(area, 18 cm²). The electrodes are connected with copper wire to provide the connections for the external circuit. The voltage is measured by data logger (fabricated analog digital data acquisition to record data point) and recorded by a personal computer. The MFC was operated in fed-batch mode and at room temperature varying between 16 °C and 22 °C. The cathode solution was 500 ml deionized water. Activated sludge was used as inoculums. Wastewater containing 4.28 g l⁻¹ sulfide was used as the anode solution and the total liquid volume was 600 ml. The anode chamber was purged with nitrogen gas for 10 min to remove dissolved oxygen so as to maintain anaerobic conditions.

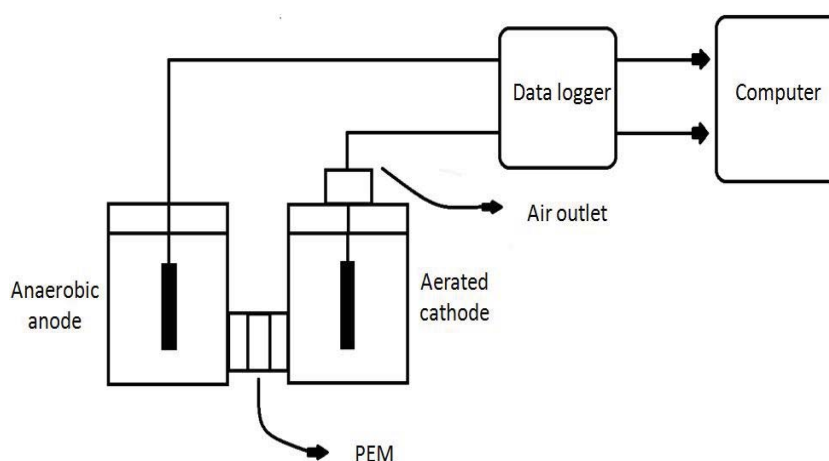


Figure 1. Schematic diagram of the dual chamber MFC for bioelectricity production.

2.2 Chemical and analysis

All chemicals and reagents used for the experiments were analytical grades and supplied by Merck (Darmstadt, Germany). Sulfide concentration was analyzed by electrochemically method. Voltage was measured by data logger and polarization curves were obtained using an adjustable external resistance when the voltage was kept constant. Sulfide concentration was determined by electrochemical method. Power and current were calculated based on following equations:

$$P = IR \quad (1)$$

$$P = (E/R) \quad (2)$$

Where P is produced power and E measured cell voltage; R is external resistance and I indicates produced current. The current and power generation density were normalized to the geometric area of membrane (9 cm²).

2 Results and discussion

Microbial fuel cell (MFC) is a new technology that can produce electricity and wastewater treatment concurrently. After inoculation of 4.28 g.l⁻¹ sulfide in anode chamber with *active mixed culture* as electrically active bacteria, data logger was set to obtain data in form of open circuit voltage until getting steady state condition. The fabricated MFC was operated in batch mode at room temperature. Then, performance of the microbial fuel cell was evaluated by the polarization curve. The steady-state conditions are achieved after 72 hours of operation time. At the steady-state conditions, the maximum produced power and current density were 9.76 mW.m⁻² and 134.49 mA.m⁻², respectively. Maximum power and current density of MFC in these 3 days are shown in table 2.

Table 2. Maximum power and current density generated in 3 days after incubation of MFC by active microorganisms.

Day	Maximum power (mW.m ⁻²)	Maximum current (mA.m ⁻²)
1	7.867	108.890
2	8.134	121.191
3	9.758	134.487

power density and polarization curves of used MFC at steady state condition are presented in Figure 2. The maximum current density and power density obtained with out aeration and optimization were 9.758 mA.m⁻² and 9.758mW.m⁻², respectively (see Figure. 2).

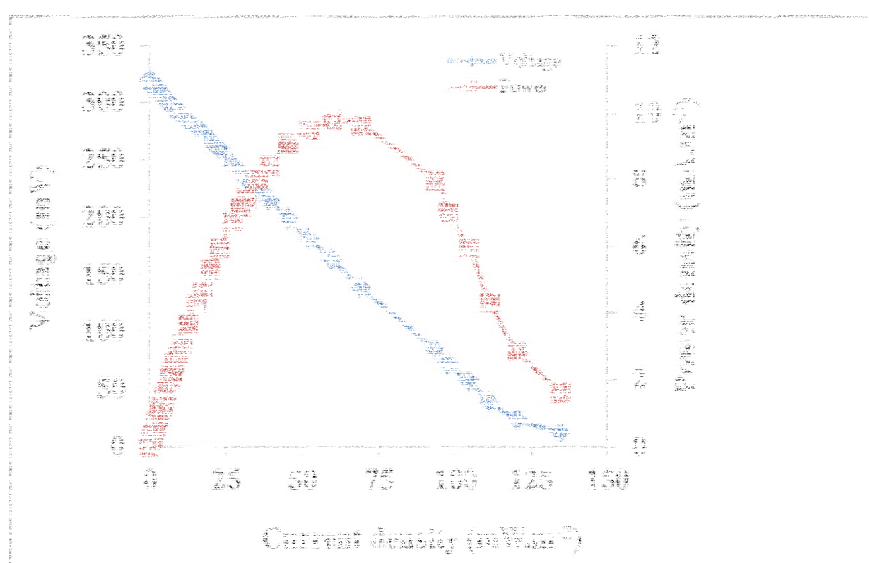


Figure 2. Polarization curve of MFC in batch mode (after 3 days of MFC operation).

In steady-state condition the influence of the oxygen in cathode chamber on OCV and generated bioelectricity has been examined. While OCV results showed the stable value, the air supply

was started to aerate in cathode chamber. Figure 3 shows MFC performance in terms of OCV improvement with respect to time in the present and absent of aeration at the cathode compartment. It can be observed that during aeration, the cell voltage rapidly increased and reached to 480 mV. The maximum generated power and current density in the presences of aeration at the cathode chamber were 23.78 mW.m^{-2} and 212.77 mA.m^{-2} , respectively.

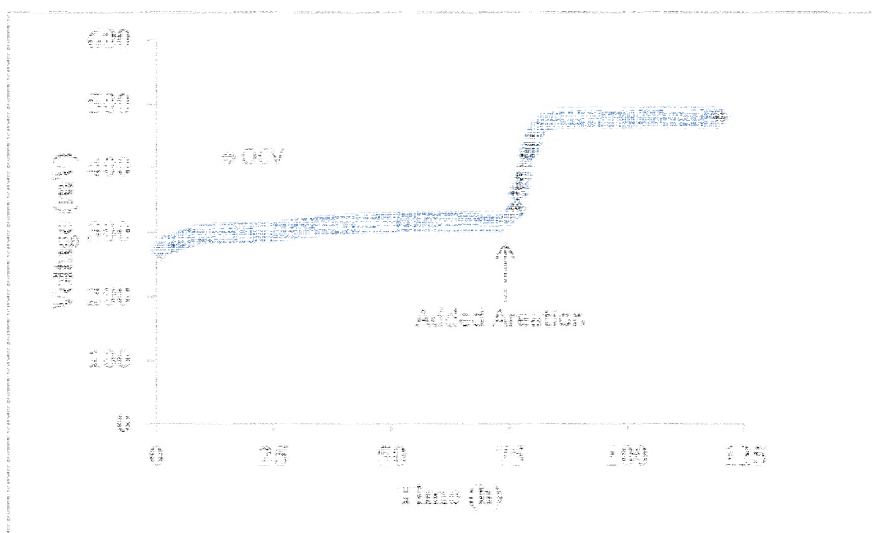


Figure 3: Open circuit voltage produced in MFC at steady-state condition after 72 h and 48 h after aeration.

In each power supply, the main parameter is to enhance power and then to acquire the highest current density under this situation of the maximum power density. Affect of mediators in cathode compartment on MFC performances were investigated. Hexacyanoferrate was used as a mediator in cathode chamber. Effect of aeration and oxidizer agent on MFC performances are shown at figure4. When 0.2 g l^{-1} hexacyanoferrate was added to cathode solution, the [roduced power density increased up to 38.773 mW.m^{-2} .

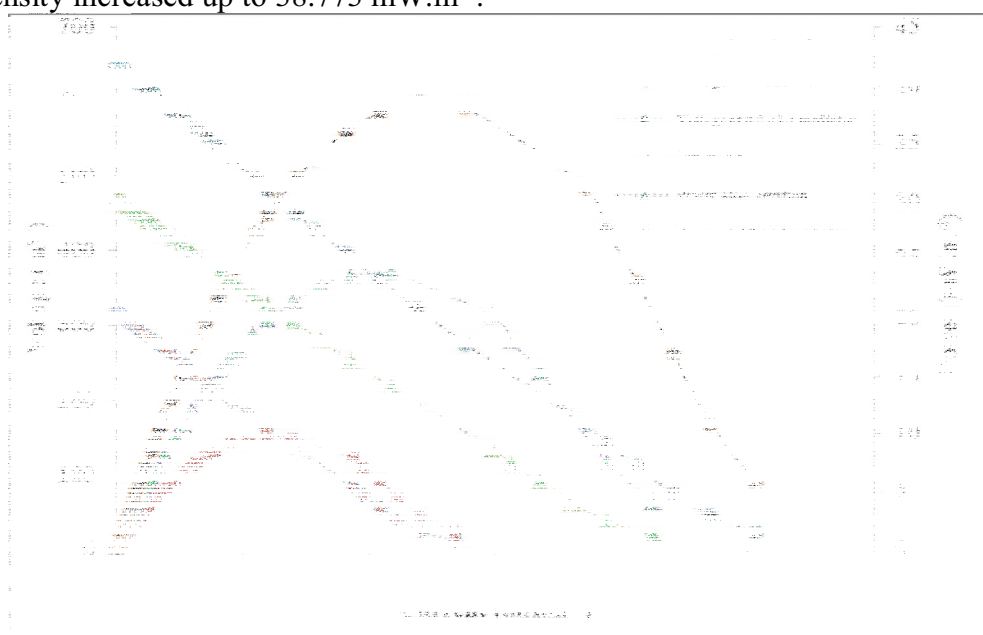


Figure 4: Variation of polarization curves in batch mode, after aeration and while using 0.2 g l^{-1} hexacyanoferrate as mediator in cathode chamber.



Different concentration of hexacyanoferrate was examined in cathode solution. At each concentration polarization data was obtained when the voltage output became stable (after 2 h). Maximum power densities and open circuit voltages are shown in table 3. At any concentration of oxidizer agent greater than 1.2 g.l⁻¹ there was no positive impact for additional current and power (See Table 3).

Table 3. Maximum power and current density and OCV of MFC in different concentration of hexacyanoferrate in cathode chamber as mediator.

Hexacyanoferrate concentration in cathode chamber (g l ⁻¹)	OCV (mV)	Maximum power (mW.m ⁻²)	Maximum current (mA.m ⁻²)
0	480.3073	9.752	99.392
0.2	648.1525	38.773	253.268
0.4	814.0657	88.727	442.238
0.6	836.7671	124.732	588.015
0.8	929.2631	221.841	855.273
1	968.9145	291.127	1063.141
1.2	988.9145	346.220	1257.51
1.4	988.9145	346.746	1258.798

the initial concentration of sulfide in wastewater was determined. 4.23 g l⁻¹. sulfide was consumed by microorganisms and produce bioelectricity. The highest sulfide removal was 98% and it was obtained after 6 days operation time. Zhao and coworkers used sulfur compounds as substrates in MFC [14] also Ryckelynck et al. produced electricity in sedimentary MFCs by sulfide oxidation [15].

4 Conclusion

In this study a fabricated MFC has been successfully operated to treat sulfide in wastewater and generate electricity simultaneously. The system used sulfide as a substrate at concentration of 4.28 g l⁻¹ and it was nearly completely removed from the wastewater during the MFC operation and oxidized to elemental sulfur. The effect of aeration in cathode chamber has been investigated. Hexacyanoferrate was used with several concentration as oxidizing agent in cathode chamber to enhance the performances of MFC. The maximum obtained power and current density were 364.746 mW.m⁻² and 1335.79 mA.m⁻², respectively.



Acknowledgments

The authors wish to acknowledge Biotechnology Research Center, Babol Noshirvani University of Technology, Babol, Iran for the facilities provided to accomplish this research.

References

- [1] Rahimnejad, M., et al., "A novel microbial fuel cell stack for continuous production of clean energy". *International Journal of Hydrogen Energy*, (2012). 37(7): p. 5992-6000.
- [2] Katuri, K.P. and K. Scott, "On the dynamic response of the anode in microbial fuel cells". *Enzyme and Microbial Technology*, (2011). 48(4–5): p. 351-358.
- [3] Rabaey, K. and W. Verstraete, "Microbial fuel cells: novel biotechnology for energy generation". *TRENDS in Biotechnology*, (2005). 23(6): p. 291-298.
- [4] Girguis, P.R., M.E. Nielsen, and C.E. Reimers, "Fundamentals of benthic microbial fuel cells: theory, development and application". *Bioelectrochemical Systems: From Extracellular Electron Transfer to Biotechnological Application*. Edited by Rabaey K, Angenent LT, Schröder U, Keller J. IWA Publishing, (2010): p. 327-346.
- [5] Reddy, L.V., S.P. Kumar, and Y.J. Wee, "Microbial fuel cells (MFCs)—a novel source of energy for new millennium in", (2010), *Current Research, Technology and Education Toipcs in Applied Microbiology and Microbial Biotechnology*.
- [6] Sun, M., et al., "Microbial communities involved in electricity generation from sulfide oxidation in a microbial fuel cell". *Biosensors and Bioelectronics*, (2010). 26(2): p. 470-476.
- [7] Zhang, P.-Y. and Z.-L. Liu, "Experimental study of the microbial fuel cell internal resistance". *Journal of Power Sources*, (2010). 195(24): p. 8013-8018.
- [8] Viridis, B., et al., "Microbial fuel cells for simultaneous carbon and nitrogen removal". *Water research*, (2008). 42(12): p. 3013-3024.
- [9] Moon, H., et al., "Residence time distribution in microbial fuel cell and its influence on COD removal with electricity generation". *Biochemical engineering journal*, (2005). 27(1): p. 59-65.
- [10] Yadav, A.K., et al., "Performance assessment of innovative constructed wetland-microbial fuel cell for electricity production and dye removal". *Ecological Engineering*, (2012). 47: p. 126-131.
- [11] Tao, H.C., et al., "Removal of copper from aqueous solution by electrodeposition in cathode chamber of microbial fuel cell". *Journal of Hazardous Materials*, (2011). 189(1): p. 186-192.
- [12] Rahimnejad, M., et al., Synthesis, characterization and application studies of self-made Fe₃O/PES nanocomposite membranes in microbial fuel cell₄ ". *Electrochimical Acta* (2012). 85, pp 700– 706.
- [13] Najafpour, G., M. Rahimnejad, and A. Ghosheshi, The Enhancement of a Microbial Fuel Cell for Electrical Output Using Mediators and Oxidizing Agents. *Energy Sources, Part A: Recovery, Utilization, and Environmental Effects*, 2011. 33(24): p. 2239-2248.
- [14] Zhao, F., et al., "Factors affecting the performance of microbial fuel cells for sulfur pollutants removal". *Biosensors and Bioelectronics*, (2009). 24(7): p. 1931-1936.
- [15] Rabaey, K., et al., "Microbial fuel cells for sulfide removal". *Environmental science & technology*, (2006). 40(17): p. 5218-5224.



Economical comparison of power generation in microbial fuel cell by Nafion 117 and SPEEK as proton exchange membranes

Mostafa Ghasemi^{1,2*}, Mostafa Rahimnejad³, Wan Ramli Wan Daud^{1,2}, Ahmad Fauzi Ismail⁴, Yaghoob Jafari⁵, Alireza Mayahi^{4,6} and Jamal Othman⁵

¹ Fuel Cell Institute, University Kebangsaan Malaysia, 43600 UKM Bangi, Selangor, Malaysia

² Department of Chemical and Process Engineering, Faculty of Engineering and Built Environment, University Kebangsaan Malaysia, 43600 UKM Bangi, Selangor, Malaysia

³ Biotechnology Research Lab., Faculty of Chemical Engineering, Noshirvani University, Babol, Iran

⁴ Advanced Membrane Technology Research Centre (AMTEC), Universiti Teknologi Malaysia, 81310 Johor Bahru, Johor, Malaysia

⁵ Faculty of Economics and Management, University Kebangsaan Malaysia, 43600 UKM Bangi, Selangor, Malaysia

⁶ Department of Chemical Engineering, Universiti Teknologi Malaysia, 81310 Johor Bahru, Johor, Malaysia

mostafag@eng.ukm.my (Mostafa Ghasemi)

Abstract

Microbial Fuel Cell (MFC) is a new device for simultaneous electricity production and wastewater treatment. The major concern of this technique is the high operational cost that is caused by Nafion 117 used as a Proton Exchange Membrane (PEM) and Pt as a cathode catalyst for oxygen reduction. Sulfonated Poly Ether Ether Ketone (SPEEK) was used as a PEM in MFC for this study. The results indicate that even though the power production of MFC with SPEEK (77.3 mW.m^{-2}) was lower than Nafion 117 (106.7 mW.m^{-2}), it is more cost effective, because of its lower price. Our economic evaluation suggests that the use of SPEEK in power production is almost two times more cost effective than that of Nafion 117. Furthermore, its Chemical Oxygen Demand (COD) removal (88%) is higher than Nafion 117 (76%); and thus, SPEEK is a promising PEM in MFCs at an industrial scale.

Keywords: Cost Efficiency Analysis, PEM, Nafion 117, SPEEK, Power production

1. Introduction

Because of the high energy requirements of conventional wastewater treatment systems, the demand for alternative cost effective and commercialized treatment technologies is increasing[1]. Moreover, due to a lack of worldwide energy, there is an emergent high interest in finding new sources of clean and sustainable sources of energy, with zero hydrocarbon content. Microbial fuel cell is a new device that converts the chemical energy of substrates into electrical energy using microorganisms[2]. Microbes in the anode part of the device oxidize the substrates to generate electrons and protons. Electrons are transferred to the cathode compartment through the external circuit, while the protons pass through the membrane[3]. MFCs are simultaneously used for wastewater treatment and the production of clean energy. Thus, this use of MFCs has a great potential in broad applications, such as home electrical generators, self-feeding robots, etc.[4]. However, applications have become limited, due to low power output, short stability, and non-economic reasons[5]. Generally, MFCs consist of two



chambers (i.e., anode and cathode), which are separated by a Proton Exchange Membrane (PEM). Several factors affect the performance of MFCs, including types of microorganisms, substrates, electrodes, and membranes. Of these, membranes have the very important role of separating the anode from the cathode. The membrane should be able to allow the protons to pass from the anode to cathode, whilst preventing the passing of oxygen and substrates[6-7].

The high cost of MFCs depends mostly on the expensive price of cathode catalyst, which is usually Pt, and the Nafion 117 PEM, which is commonly used as the separator in MFCs. Together, they cover 90% of the total cost of MFCs. Therefore, the development of an economical catalyst and PEM has attracted wide attention from scientists. In 2011, Rahimnejad et al., [8] used a Poly Ether Sulfone (PES)/Fe₃O₄ nanocomposite membrane as an alternative for Nafion 117 PEM. They concluded that it could produce higher amounts of energy compared to Nafion 117. However, the problem with the nanocomposites membranes, was their porous structure, which made long-term operation impossible. In another study by our group, Ghasemi et al., [9] used Nafion/Activated Carbon Nanofiber (ACNF) as a PEM. The power generated by this novel carbon nanocomposite membrane was 30% higher than Nafion 117. However, because the membrane was still a nafionic membrane, the capital cost of the MFC was still commercially viable, and the membranes used were still porous.

Sulfonated Poly Ether Ether Ketone (SPEEK) can be a good alternative to Nafion 117, due to its good hydrophilic properties and proton conductivity. It has some negative fixed charge ions (SO₃⁻) that allow cations to pass through, whilst it rejects the passing of anions[10-11]. Furthermore, from previous use as a PEM in Direct Methanol Fuel Cell (DMFC), it produced good results. Due to the expensive price of Nafion 117[12], which makes MFC non-commercial, and the properties of SPEEK as a good PEM, the objective of this study is to compare the power generation performance of two types of membrane in microbial fuel cell and their cost effectiveness.

2. Experimental methods

2.1. Synthesis of SPEEK and the determination of the Degree of Sulfonation (DS)

For the preparation of SPEEK, 20g of PEEK powder (Goodfellow Cambridge Limited, UK) was dissolved slowly in 500mL of 95-98% concentrated sulphuric acid (R & M Chemicals, Essex, UK).

This solution was stirred vigorously until the entire PEEK was dissolved completely. Next, the homogenous solution was continuously and thoroughly stirred at a controlled temperature of 80°C for 30 hours (in this study), in order to obtain 52% DS. The SPEEK solution was then poured into a large excess of ice water, in order to precipitate the SPEEK. The solid was then collected by filtering the solution through a Whatman filter paper. Finally, the SPEEK was dried at 70°C to removing any remaining water before use.

2.2. Determination of DS

The degree of sulfonation was measured by ¹H Nuclear Magnetic Resonance (FT-NMR ADVANCE 111 600 MHz with Cryoprobe) spectroscopic analysis (Bruker, Karlsruhe, Germany). Before measurement, the SPEEK was dissolved in dimethyl sulfoxide (DMSO-d₆). The DS can be calculated by the following equation

$$\frac{DS}{5-2DS} = \frac{A1}{A2} \quad (0 \leq DS \leq 1) \quad (1)$$



where S is the total number of hydrogen atoms in the repeat unit of the polymer before sulfonation which is 12 for PEEK, $A_1(H_{13})$ is the peak area of the distinct signal and A_2 is the integrated peak area of the signals corresponding to all other aromatic hydrogen [Please reference our paper in Separation here if it is possible]. To calculate DS in percent (DS %), the answer for DS has to be multiplied by 100.

2.3. MFC configuration

Two cubicshaped chambers were constructed from Plexiglas, with a height of 10cm, width of 6cm, and length of 10cm (giving a working volume of 420ml). They were separated by a Nafion 117 Proton Exchange Membrane (PEM). Oxygen was continuously fed into the cathode by an air pump at a rate of 80ml/min. Both the cathode and the anode projected surface areas of 12cm^2 . The cathode was carbon paper, coated with 0.5 mg/cm^2 Pt and the anode (as described above) was plain carbon paper [8, 13].

2.4. Enrichment

Palm Oil Mill Effluent (POME, Indah Water Konsortium) anaerobic sludge was used for the inoculation of MFCs. The media contained 5g of glucose, 0.07g of yeast extract, 0.2g of KCl, 1g of $\text{NaH}_2\text{PO}_4 \cdot 4\text{H}_2\text{O}$, 2g of NH_4Cl , 3.5g of NaHCO_3 (all from the Merck company), 10ml of Wolfe's mineral solution and 10ml of Wolfe's vitamin solution (added per litre). All experiments were conducted in an incubator at 30°C . Furthermore, the cathode chamber contained a phosphate buffer solution, which consisted of 2.76g/l of NaH_2PO_4 , 4.26g/l of Na_2HPO_4 , 0.31g/l of NH_4Cl , and 0.13g/l of KCl (all from the Merck company)[14].

2.5. Analysis and calculation

Nicolet 5700 FTIR (Thermo Electron, USA) was performed to identify the functional group of the membranes before pre-treatment, after pre-treatment, and after fouling. Scanning Electron Microscopy (SEM, Supra 55vp-Zeiss, Germany) was implemented to observe the attachment of microorganisms onto the surface of the anode electrode. Moisture had to be removed from the biological samples (POME mix culture sludge) by critical drying. They were then coated with a conductive material (such as gold or carbon), with a thickness of approximately 20e50 nm, in order to make them conductive for the SEM analysis.

To measure the COD, samples were first diluted 10 times and mixed with 2ml of diluted samples with a digestion solution of a high-range COD reagent, then heated at 150°C for 2 hours in a thermoreactor (DRB200), which was read with a spectrophotometer (DR 2800). The voltage was measured using a multimeter (Fluke 8846A), and the power density curve was obtained by applying different loads to the system and calculating the power at different loads.

The current was measured using the:

$$I = \frac{V}{R} \quad (2)$$

Where, I is the current (amps), V is the voltage (volt), and R is the applied external resistance (ohm).

The power density was calculated using the following equation:

$$P = R \times I^2 \quad (3)$$

Where, R is the applied external resistance (ohm) and I is the current (amps) (calculated using Equation 1)



The Coulombic Efficiency (CE) was calculated as the current over time; until the maximum theoretical current was achieved. The evaluated CE over time was calculated using the following equation:

$$CE = \frac{M \int_0^t I dt}{F b V_{an} \Delta COD} \quad (4)$$

Where, M is the molecular weight of oxygen (32), F is Faraday's constant, b=4 indicates the number of electrons exchanged per mole of oxygen, V_{an} is the volume of liquid in the anode compartment, and ΔCOD is the change in Chemical Oxygen Demand (COD) over time, 't'.

2.6. Pre-treatment of PEMs

Nafion 117 should be pre-treated before use in MFC system. The pre-treatment procedure is boiling in distilled water, 3% hydrogen peroxide, or 0.5 M sulphuric acid for 1 h each one and then stored in water until applying in the system. Also SPEEK should be kept in the water after fabrication till use.

3 Results and discussion

3.1 FTIR analysis of SPEEK and the degree of sulfonation

Fig. 1a. shows the FTIR analysis of SPEEK and pre-treated Nafion 117. As shown, there are two clear bands in both of PEMs; one in the range $1020-1250\text{cm}^{-1}$ and the other (big peak) at $3200-3500\text{cm}^{-1}$. The first band revealed the SO_3^- group of the membrane that was introduced by the pre-treatment Nafion 117 and the sulfonation to SPEEK, which by its negative charge, makes the membrane a promising choice for the passing of protons. Meanwhile, the second band is the O-H group that increases the hydrophilicity of the membrane, which directly increases the conductivity of the membranes. This is an important factor of PEMs[15].

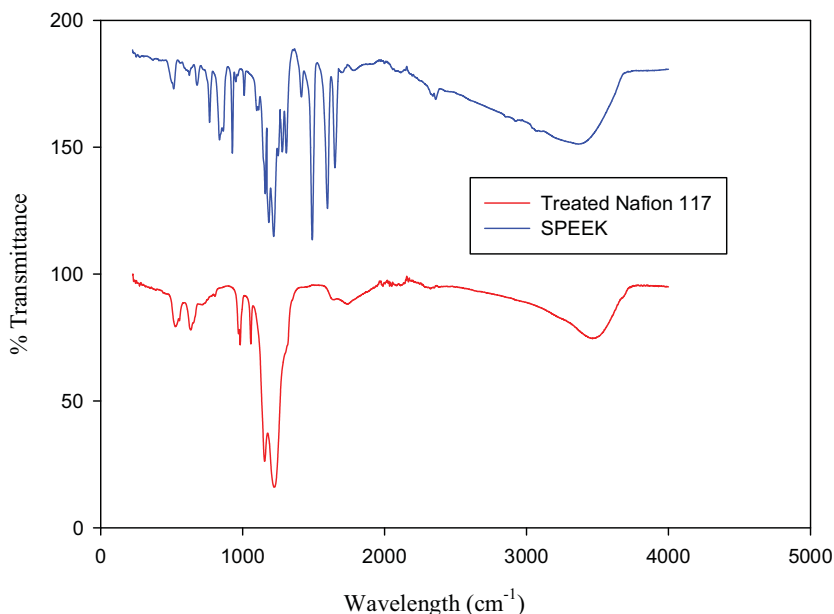


Fig. 1a. FTIR analysis of SPEEK and pre-treated Nafion 117

Also, NMR analysis of the SPEEK is shown in Fig. 1b. The reason for producing SPEEK in the range of 50% DS (52%) was because, as the DS increases to 60-70%, proton conductivity enhances. However, this reduces the mechanical and thermal stabilities of the polymer[16]. So, SPEEK with 52% DS was used in this study, based on the better results achieved from the MFC, as reported in pervious study; and from the better mechanical and thermal strengths of PEEK at about a 52% degree of sulfonation[17].

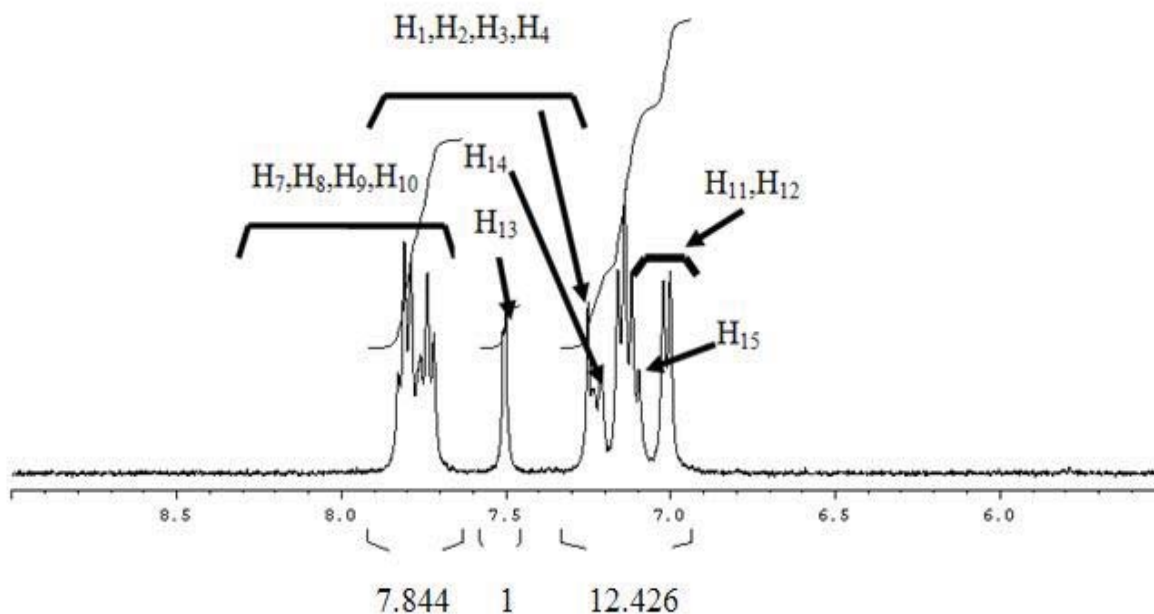


Fig. 1b. ¹H NMR spectra of sulfonation

3.2 Bacteria attachment

Fig. 2. shows the biofilm attached to the electrode in the anode chamber, when the MFC was in a stable condition. As shown, different types of bacteria (which play the role of a biocatalyst in transferring electrons to the electrode) were attached to the electrode[18].

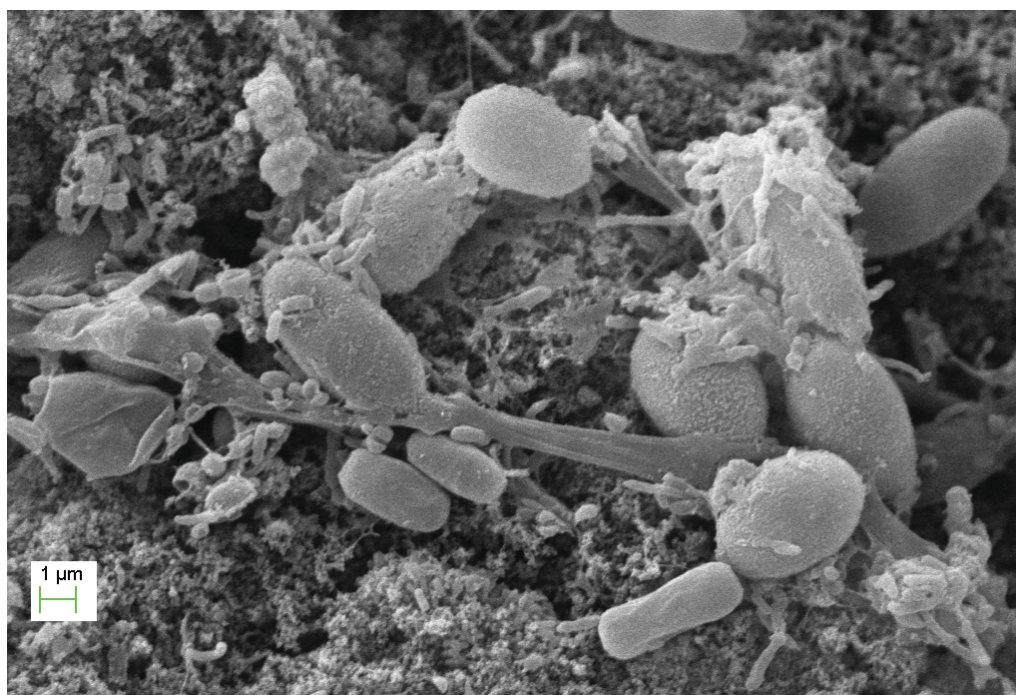


Fig. 2. Picture of attached biofilm to the electrode in the anode chamber

In order to see the catalytic activity of the biocatalysts, the developed mix culture biofilm (which formed on the electrode's surface) was analysed by CV under the same conditions of the MFC experiment. As shown in Fig. 3. there was no oxidation and reduction peaks, before inoculation of the anode chamber, with the mix culture microorganisms. However, after inoculation, a clear oxidation peak can be seen. The oxidation peak shows that POME is an active biocatalyst for oxidation in the anode compartment. The maximum oxidation peak is at around 0.01mA and 200mV (0.2 V), which is provided by POME sludge microorganism[19].

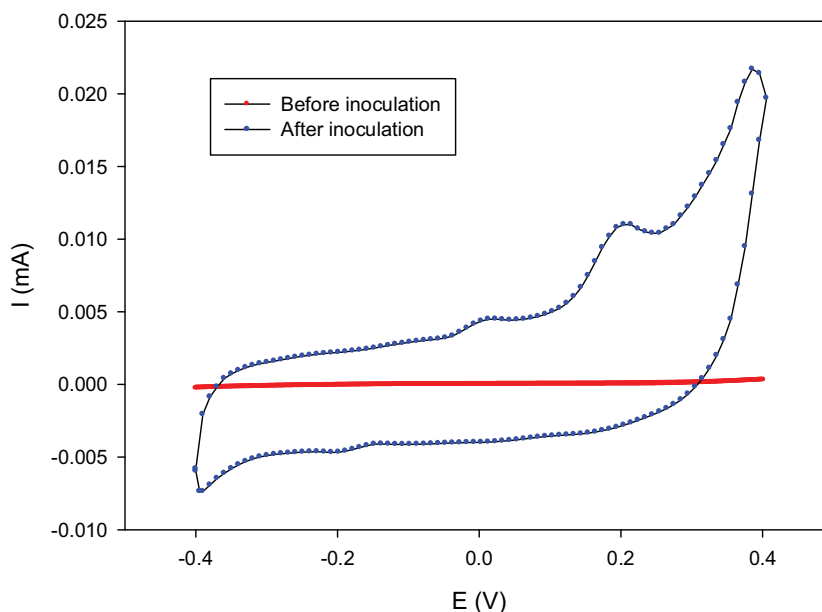


Fig. 3. Catalytic activity of the biocatalysts

3.3 Power density and polarization curve

Fig. 4. shows the power density graph of the microbial fuel cells working with Nafion 117 and SPEEK PEM, whilst the other factors were constant. As shown, both power density graphs go up and reach a maximum value before starting to fall back down[20]. The maximum power generated by the MFC working with SPEEK as the PEM was $77.3\text{mW}\cdot\text{m}^{-2}$, whilst $106.7\text{mW}\cdot\text{m}^{-2}$ was obtained from the MFC working with Nafion 117 as the PEM. This means that the system working with Nafion 117 as the PEM can produce 27.5% more power than the system working with SPEEK.

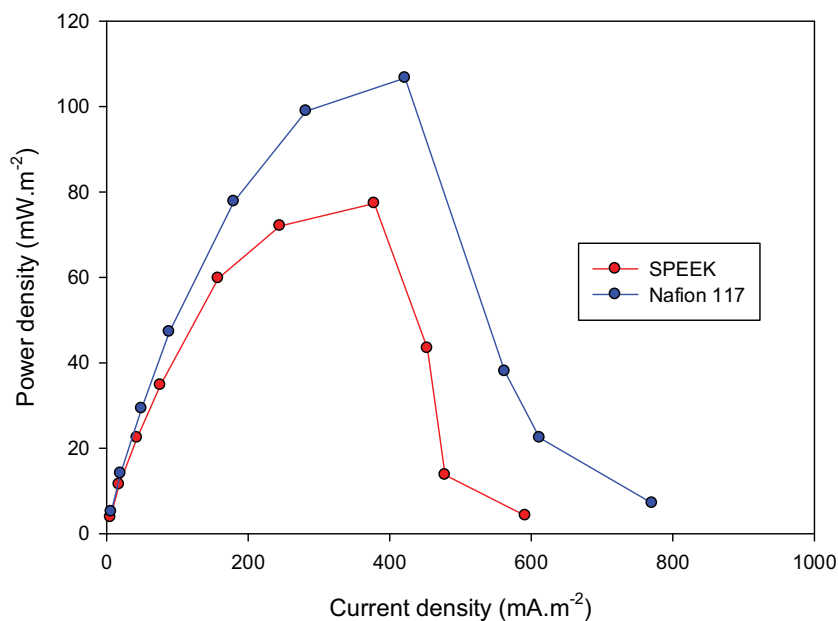


Fig. 4. Power density of the Nafion 117 and SPEEK membranes in microbial fuel cell

The MFC's polarization curve is shown in Fig. 5. The internal resistance of the MFC is the slope of the V-I curve, or in other words, the slope of the current versus the voltage is the internal resistance. Based on that, the internal resistance of the MFC working with Nafion 117 is about 727 Ω . However, for the MFC working with SPEEK, it was higher at about 811 Ω . This could have been due to a higher conductivity and lower activation loss in the MFC working with Nafion 117.

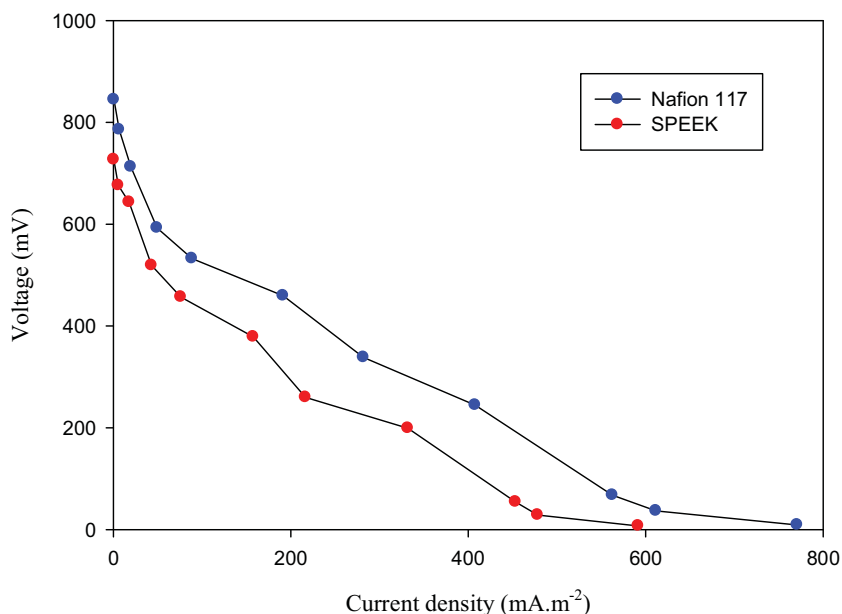


Fig. 5. Polarization curve for SPEEK and Nafion 117 membranes

Table1 shows a summary of the data taken from the MFC systems working with Nafion 117 and SPEEK as PEMs.

Table 1

Summary of the collected SPEEK and Nafion 117 membranes MFC system data

Types of Membrane	$P_{max}(mW.m^{-2})$	$I_{max}(mA.m^{-2})$	OCV in a stable condition (mV)	Internal resistance (Ω)
Nafion 117	106.7	421.7	645	727
SPEEK	77.3	378.3	813	811

3.4 COD removal and coulombic efficiency

Fig. 6. shows the coulombic efficiency and COD removal of the MFC systems working with Nafion 117 and SPEEK as PEMs. As shown, both systems have a high COD removal of more than 70%. The MFC working with Nafion 117 had 76% COD removal whilst the system working with SPEEK had 88% removal. However, the CE percentage of the system working with Nafion 117 was 61% more than the system working with SPEEK. This shows that the COD removal of the SPEEK membrane was higher, but the energy generation of Nafion 117

was better. This could have been due to the higher internal resistance of the SPEEK membrane when the other system conditions were the same[20-21].

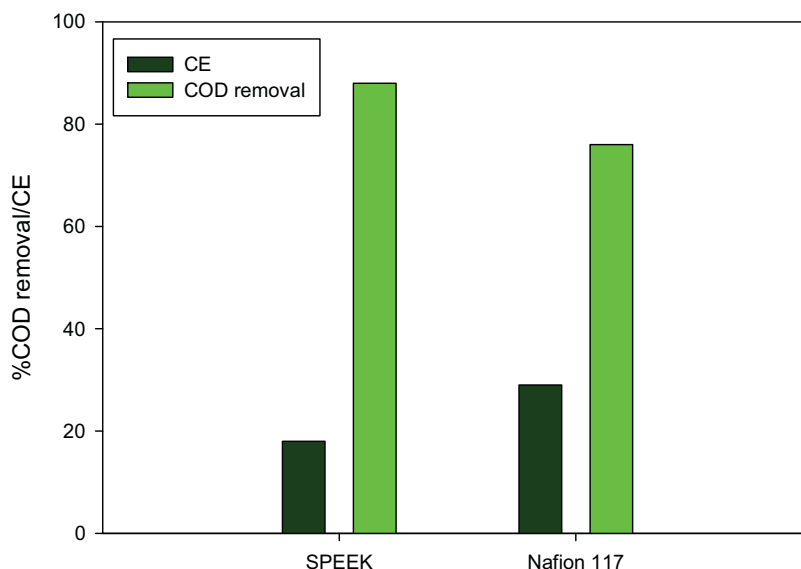


Fig. 6. Columbic efficiency and COPD removal of the Nafion 117 and SPEEK membranes in MFC system

3.5 Economic Analysis

This section attempts to compare the performances of two types of membranes in microbial fuel cell; namely Nafion 117 and SPEEK, for power generation from an economical point of view. Whilst Nafion 117 membranes demonstrated a higher level of electricity generation compared to SPEEK, their cost is significantly higher. As shown in Table 2, the electricity generation from 12cm² of Nafion 117 and SPEEK were 106.7 and 77.3mw.m⁻², respectively. Meanwhile, the cost of 12cm² of Nafion is almost three times higher than that of SPEEK[22]. Therefore, it is imperative to investigate the costs associated with each type of membrane simultaneously, using a cost efficiency measurement (revenue-cost ratio); to show how much cost is associated with a given level of revenue. Such a policy analysis tool provides decision-makers with useful information to compare the costs and benefits of using alternative membranes, and assists them in understanding which type of membrane is more cost efficient and perhaps more economically viable to use.

Table 2 shows the costs and revenues associated with the use of 12cm² of Nafion 117 and SPEEK. The feedstock for both types of membranes is Palm Oil Mill Effluent (POME). A huge amount of POME is generated every year in Malaysia. It can be used with no purchasing cost, and in this study, we assumed no costs for the use of membranes, except prices. Revenues were calculated based on multiplying the units of electricity generated per 12cm² of membrane and the electricity tariff rate. The commercial electricity tariff rate in Peninsular Malaysia was obtained from the Ministry of Energy, Green Technology, and Water (2011). Since the tariff rate is reported in Malaysian Ringgit (RM), we converted the rate into an international currency (USD), using the current market exchange rate of 1 RM= 0.33 USD. In this study, the electricity tariff was assumed to be 10 US cents (or 30.22Malaysian Sen) per kw/h. This rate is also assumed as an average world electricity tariff, as Malaysia is a mean income country, where



subsidies on electricity consumption have been removed. The potential revenue associated with 1mW generation of electricity is shown in Table 2. Consequently, a cost-to-revenue ratio (i.e., the cost associated with the use of each membrane as a proportion of the revenue generated from that membrane) was used to identify which membrane was relatively more cost efficient; where the higher the ratio, the lower the cost efficiency of that membrane. Detailed economic calculations can be found in Table 2. The results clearly show that even though the amount of electricity generated from Nafion 117 was higher than that of SPEEK, the low costs associated with the use of SPEEK suggest that the use of this membrane is more economical. It should be noted that this study did not consider the lifespan of these two alternative membranes, but rather it considered the use of these two membranes in their maximum power generation. Future studies are encouraged to investigate this area further, in order to find out whether or not the use of these two alternatives is economical. However, our results indicate that the use of SPEEK is two times more cost efficient than that of Nafion 117.

Table 2

Economic Analysis of SPEEK and Nafion 117 in the maximum power generation of MFCs

		<i>Nafion 117</i>	<i>SPEEK</i>	<i>Source</i>
<i>A</i>	<i>Price per 12cm² (USD)</i>	120	45	Neburchilov et al., (2007)
<i>B</i>	<i>Electricity Generated (mW)</i>	106.7	77.3	<i>Estimated</i>
<i>C</i>	<i>Electricity tariff (mW)(USD)</i>	0.10×10^{-6}	0.10×10^{-6}	<i>Ministry of Energy, Green Technology and Water(2011)*</i>
$D=A \times C$	<i>Revenue from electricity generation per 12cm² (USD)</i>	0.10679	0.07730	<i>Estimated</i>
$E= A/D$	<i>Cost/ Revenue ratio</i>	1124	582	<i>Estimated</i>

*Ministry of Energy, Green Technology, and Water (2011). (Available at <http://talkenergy.files.wordpress.com/2011/02/asean-electricity-tariff-2011.pdf>)

4 Conclusion

This study compares the cost efficiency use of SPEEK compared to Nafion 117 in an MFC system. Our results have shown that SPEEK is a better choice, as the system cost of operating with SPEEK is 50% less than a system working with Nafion 117. This study shows a new horizon in the industrialization of MFC; especially in Malaysia, which has a vast amount of POME from wastewater. Furthermore, it opens up the way to find new types of membranes and



catalysts, which can produce as much power as conventional ones, but which are actually economically viable for real systems.

References

- [1] S.E. Oh, B.E. Logan, Proton exchange membrane and electrode surface areas as factors that affect power generation in microbial fuel cells, *Applied microbiology and biotechnology*, 70 (2006) 162-169.
- [2] M. Ghasemi, M. Ismail, S.K. Kamarudin, K. Saeedfar, W.R.W. Daud, S.H.A. Hassan, L.Y. Heng, J. Alam, S.E. Oh, Carbon nanotube as an alternative cathode support and catalyst for microbial fuel cells, *Applied Energy*, (2012).
- [3] S.E. Oh, S. Van Ginkel, B.E. Logan, The relative effectiveness of pH control and heat treatment for enhancing biohydrogen gas production, *Environmental science & technology*, 37 (2003) 5186-5190.
- [4] J.R. Kim, S. Cheng, S.E. Oh, B.E. Logan, Power generation using different cation, anion, and ultrafiltration membranes in microbial fuel cells, *Environmental science & technology*, 41 (2007) 1004-1009.
- [5] K. Rabaey, W. Ossieur, M. Verhaege, W. Verstraete, Continuous microbial fuel cells convert carbohydrates to electricity, *Water Science & Technology*, 52 (2005) 515-523.
- [6] I.S. Chang, J.K. Jang, G.C. Gil, M. Kim, H.J. Kim, B.W. Cho, B.H. Kim, Continuous determination of biochemical oxygen demand using microbial fuel cell type biosensor, *Biosensors and Bioelectronics*, 19 (2004) 607-613.
- [7] J.K. Jang, I.S. Chang, K.H. Kang, H. Moon, K.S. Cho, B.H. Kim, Construction and operation of a novel mediator-and membrane-less microbial fuel cell, *Process Biochemistry*, 39 (2004) 1007-1012.
- [8] M. Rahimnejad, M. Ghasemi, G.D. Najafpour, M. Ismail, A.W. Mohammad, A.A. Ghoreyshi, S.H.A. Hassan, Synthesis, characterization and application studies of self-made Fe₃O₄/PES nanocomposite membranes in microbial fuel cell, *Electrochimica Acta*, 85 (2012) 700-706.
- [9] M. Ghasemi, S. Shahgaldi, M. Ismail, Z. Yaakob, W.R.W. Daud, New generation of carbon nanocomposite proton exchange membranes in microbial fuel cell systems, *Chemical Engineering Journal*, (2012).
- [10] C. Zhao, X. Li, Z. Wang, Z. Dou, S. Zhong, H. Na, Synthesis of the block sulfonated poly (ether ether ketone) s (S-PEEKs) materials for proton exchange membrane, *Journal of membrane science*, 280 (2006) 643-650.
- [11] S. Zhong, X. Cui, H. Cai, T. Fu, C. Zhao, H. Na, Crosslinked sulfonated poly (ether ether ketone) proton exchange membranes for direct methanol fuel cell applications, *Journal of Power Sources*, 164 (2007) 65-72.
- [12] E. Peled, T. Duvdevani, A. Aharon, A. Melman, A Direct Methanol Fuel Cell Based on a Novel Low-Cost Nanoporous Proton-Conducting Membrane, *Electrochemical and Solid-State Letters*, 3 (2000) 525-528.
- [13] M. Ghasemi, S. Shahgaldi, M. Ismail, B.H. Kim, Z. Yaakob, W.R. Wan Daud, Activated carbon nanofibers as an alternative cathode catalyst to platinum in a two-chamber microbial fuel cell, *International Journal of Hydrogen Energy*, 36 (2011) 13746-13752.
- [14] M. Ghasemi, W.R.W. Daud, N. Mokhtarian, A. Mayahi, M. Ismail, F. Anisi, M. Sedighi, J. Alam, The effect of nitric acid, ethylenediamine, and diethanolamine modified polyaniline nanoparticles anode electrode in a microbial fuel cell, *International Journal of Hydrogen Energy*, (2012).
- [15] M. Ghasemi, W.R. Wan Daud, M. Ismail, M. Rahimnejad, A.F. Ismail, J.X. Leong, M. Miskan, K. Ben Liew, Effect of pre-treatment and biofouling of proton exchange membrane on microbial fuel cell performance, *International Journal of Hydrogen Energy*, (2012).
- [16] Y. Paik, S. Chae, O.H. Han, S.Y. Hwang, H.Y. Ha, Influence of water and degree of sulfonation on the structure and dynamics of SPEEK studied by solid-state¹³C and¹H NMR, *Polymer*, 50 (2009) 2664-2673.
- [17] S.S. Lim, W.R.W. Daud, J. Md Jahim, M. Ghasemi, P.S. Chong, M. Ismail, Sulfonated poly (ether ether ketone)/poly (ether sulfone) composite membranes as an alternative proton exchange membrane in microbial fuel cells, *International Journal of Hydrogen Energy*, (2012).



6th Iranian Fuel Cell Seminar
March 12 & 13 , 2013
Shahid Rajaei Teacher training University
Tehran - Iran



- [18] O. Schaetzle, F. Barrière, K. Baronian, Bacteria and yeasts as catalysts in microbial fuel cells: electron transfer from micro-organisms to electrodes for green electricity, *Energy Environ. Sci.*, 1 (2008) 607-620.
- [19] M. Rahimnejad, A.A. Ghoreyshi, G. Najafpour, T. Jafary, Power generation from organic substrate in batch and continuous flow microbial fuel cell operations, *Applied Energy*, 88 (2011) 3999-4004.
- [20] K. Fricke, F. Harnisch, U. Schröder, On the use of cyclic voltammetry for the study of anodic electron transfer in microbial fuel cells, *Energy & Environmental Science*, 1 (2008) 144-147.
- [21] F. Zhao, F. Harnisch, U. Schröder, F. Scholz, P. Bogdanoff, I. Herrmann, Challenges and constraints of using oxygen cathodes in microbial fuel cells, *Environmental science & technology*, 40 (2006) 5193-5199.
- [22] V. Neburchilov, J. Martin, H. Wang, J. Zhang, A review of polymer electrolyte membranes for direct methanol fuel cells, *Journal of Power Sources*, 169 (2007) 221-238.



A technical assessment of the CO₂ capture modeling for GT/SOFC/CHP hybrid cycles

Gh.Arab^{1*}, H.Ghadamian²

^{1*} *Department of Energy and Environment, Sciences & Research Branch, Islamic Azad university, Tehran, Iran
Email: gh_arab@srbiau.ac.ir*

² *Material and Energy Reserch Center (MERC), P.O.Box: 14155-4777, Tehran, Iran
Email: h.ghadamian@merc.ac.ir*

** Corresponding author, Ph.D. Course, Tel: +98 9122541353, Mailing Address: Energy Engineering Department, Azad University Campus (Hesarak), Pounak Square, Ashrafi-Isfahani Highway, Tehran, IRAN, Postal Code: 1477893855.*

Abstract

In GT/SOFC/CHP hybrid systems, to achieve green production, CO₂ capturing pattern is essential. The use of CO₂ capture system reduces emissions, but it reduces the total efficiency as a disadvantage. The aim of this study is to select the best technology as a goal for maximizing CO₂ capturing with the minimum achievable energy penalty. In this research, by using an analytical approach, a novel categorization of CO₂ capture technologies in GT/SOFC/CHP systems is presented. Six categories of various technologies are described by using Strength-Weakness (S-W) analysis. Then, with a comparative approach, an assessment in some selected cycles is conducted. By this mean, their modelling targets, type of CO₂ capture systems, and technical and performance specifications are evaluated. By using this analysis, current areas of research, international research orientation and potential future research areas are identified. The results show that oxy-anode combustion technology is the best CO₂ capture technology for GT/SOFC/CHP systems with respect to all research factors and the current feasibilities.

Key words

SOFC/GT/CHP; CO₂ Capture; S-W analysis; Modelling.



1- Introduction

Power generation and its environmental issues are an important world challenges. Nowadays, more than 67% of the world electricity use is generated using conventional fossil fuels [1]. Combustion of these fossil fuels emits environmental emissions such as CO₂, CO, CH₄, NO_x and SO_x that subsequently results in regional and global warming. So, developing clean power generation technologies is vital to prevent disastrous environmental losses. Solid Oxide Fuel Cell (SOFC) as a source of power generation in distributed generation can be used for small and large stations [2]. In order to overcome some problems of Gas Turbine (GT), such as low power generation efficiency, combined SOFC and GT technology has been developed. This hybrid cycle results in more power generation using synergy advantage [2]. In the recent decade, many studies have been done on the modelling, simulation, design and optimization of these systems. A description of the different hybrid configurations has been studied before [3]. Overall system efficiency of 63% has been achieved at 32/68 GT/SOFC power ratio [4]. The high temperature of this hybrid system provides the possibility of recovering waste heat to generate more power in the steam turbine cycle, space heating or process heating (CHP) [5]. As this hybrid system, couples a clean power generation source and a conventional technology (GT), it is expected that in the same power generation amount, the emission level will be more than SOFC system and lower than GT system. Results in [6] show that the use of SOFC in the CO₂ market is an attractive option from the economic point of view. In [7], different CO₂ capture cycles for GT systems have been compared and results show that the GT/SOFC system has the highest total efficiency (67.3%). Due to the SOFC nature that produces CO₂; different CO₂ capture technologies can be proposed. One of this categorization has been presented by JW dijkstra & D.Jansen [8] which is based on the SOFC technologies. Bredesen [9] has proposed another categorization that focuses on ITM which works at high temperatures (800-900 °C). In [10], in order to develop clean power generation technologies, by using sorption-enhanced steam methane reforming process (SE-SMR) and Zero Emission Gas power concept (ZEG), efficiency of 77% as well as 100% CO₂ capture have been achieved.

In this research, based on following terms, specific papers are selected:

- Specified within SOFC/GT/CHP cycles including CO₂ capturing systems,
- Including quantitative and qualitative information contributed to cycle performance specification.

Hence, other cycles in connection with CO₂ capture in SOFC, GT or other similar combined cycles have not been considered. In the following sections, important parameters in system modelling are studied and literature papers are categorized too. Based on this kind of analyses, a new categorization of CO₂ capture technologies in hybrid GT/SOFC/CHP systems is presented.

2- Categorizing the CO₂ capture technologies

Selecting the type of CO₂ capture technology depends on various factors such as partial pressure of CO₂ in the stream, amount of CO₂ to be recovered, sensitivity to impurities, required purity with regard to CO₂ content, and capital and operational costs [11]. As a classic categorization, the CO₂ capture systems can be categorized by the type of capturing process as shown in Figure 1 [12].

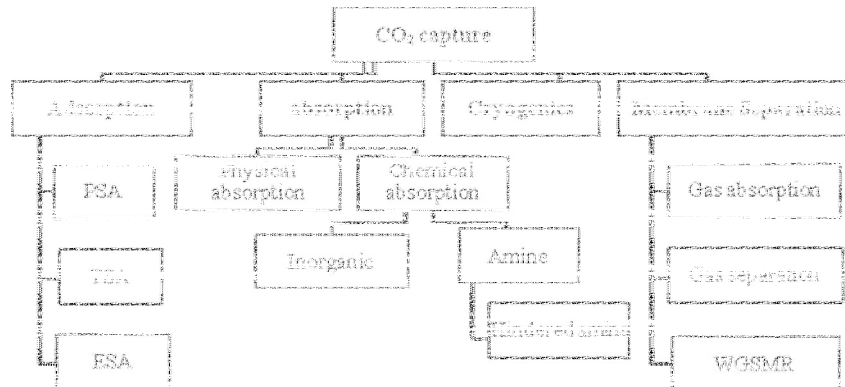


Figure 1. Categorizing by CO₂ capture process [12]

Completion of the classic categorization of CO₂ capture technologies and SOFC systems has resulted in a novel categorization of CO₂ capture technologies in SOFC/GT/CHP cycles in six main groups which have been shown in Figure 2. These categories are described below:

2-1- Post combustion

This technology is based on the CO₂ separation from combustion products using various chemical or physical adsorption methods. Applying this technology is applicable in common combined cycle power plants or in modification of power generation processes. In basic design of the new systems such a combined cycle power plants, applying this technology is not attractive because of the low purity of the absorbed CO₂, high capital and energy costs and high energy penalties. So, in SOFC/GT systems, this technology has been paid less attention.

2-2- Pre-combustion

This technology is based on fuel separation before entering the combustion process. Natural gas or coal, as the input fuel, enters an internal or external reformer and after reforming and shifting processes it converts to H₂ and CO₂. Subsequently, they are separated and only H₂ participates in the combustion process. Combustion products do not contain CO₂ and are discharged into the atmosphere. This technology seems to be suitable for SOFC, especially coal-fuelled ones which reforming operations are necessary before fuel charge activity. However, in the case that use internal reformer, separation of CO₂ from H₂ is difficult. Therefore, in the case of fuels such as coal, this technology is considered much.

2-3- Oxy-fuel combustion

This technology is based on the decomposing air into oxygen and nitrogen, and subsequently, use of pure oxygen in the combustion process. In this case, the exhaust gas is composed of CO₂ and H₂O that are separable easily using condensing process. In conventional cycles, the oxygen is produced in Air Separation Unit (ASU). Based on new improvements in developing pure oxygen production systems, use of this technology in systems has been paid more attention. In this method, due to the large amount of the required oxygen, the increasing is expected for energy and capital costs of this systems.

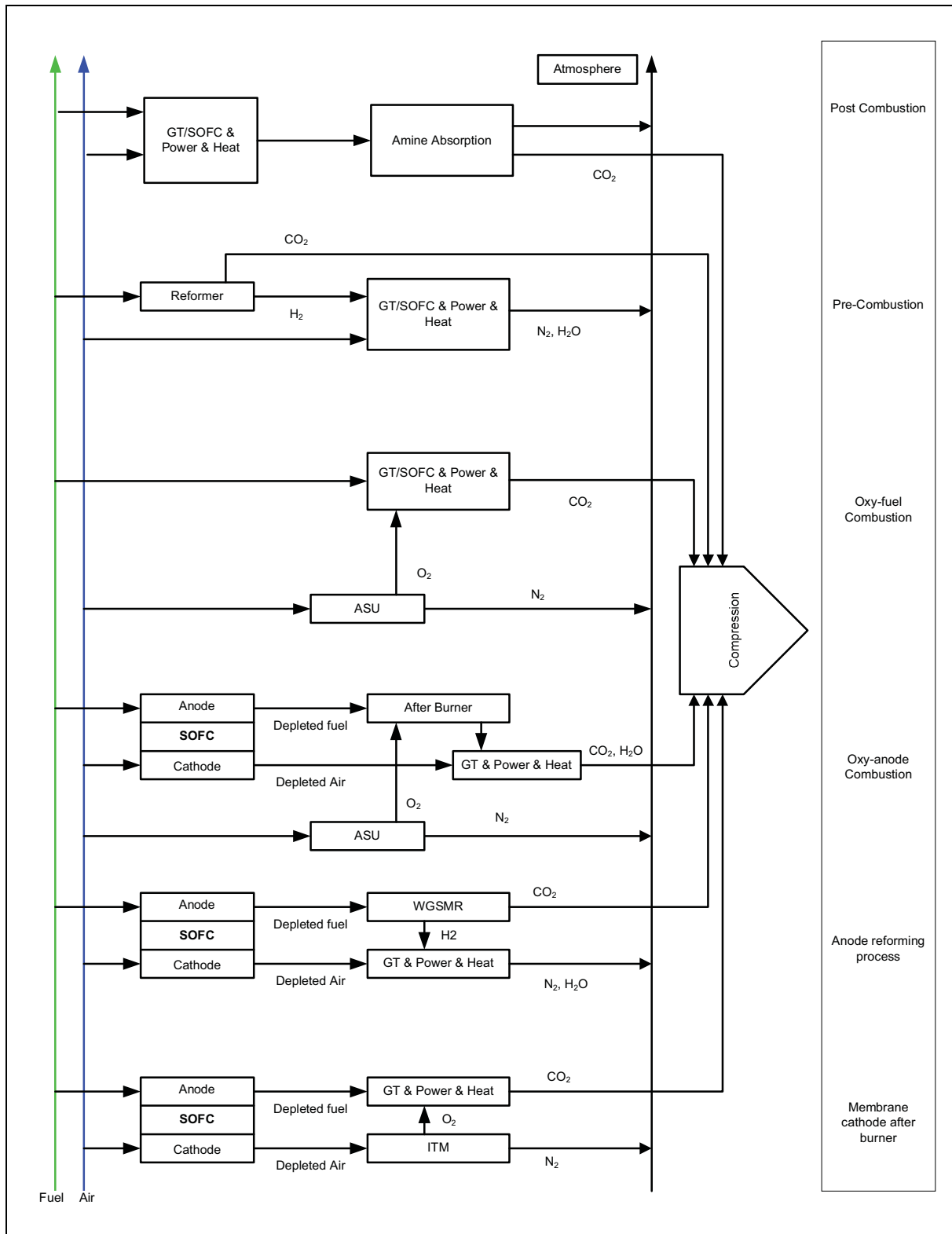


Figure 2. The novel proposed categorizations (by authors)

2-4- Oxy-anode combustion

Oxy-combustion systems are very efficient but due to the huge amount of the required oxygen, as well as complexities and maintenance cost of large scale oxygen production systems; use of this technology

is not applicable in general cases. In SOFC systems, based on increasing the contact area of oxygen and cathode, use of pure oxygen in the cathode of the cell is recommended, but oppose that, for the carbon capture technology, use of the pure oxygen in the combustion of the exhaust gases in anode side is paid attention. In this method, unburned fuel from anode, which contains H_2 and CO_2 , enters a combustion chamber, burns with pure oxygen, and produces water and CO_2 . Then it condenses and CO_2 is separated, compressed and stored. High temperature combustion products can be used in a gas turbine to generate electricity, or they can be used to provide hot water or process steam, instead.

2-5- Reforming anode after burner

In this technology, exhaust gas from SOFC's anode enters a WGSMR, and through a shifting process, hydrogen is produced. This hydrogen is burnt with exhaust gas from cathode, and produces power and heat. Exhaust products from WGSMR are water and CO_2 , then they are separated through condensing and CO_2 is collected, compressed and stored as shown in Figure 3. This is an emerging technology.

2-6- Membrane cathode after burner

Exhaust air from SOFC cathode contains a lot of oxygen. By using an Ion transport membrane (ITM), this oxygen is separated and then it burns with the exhaust gases from anode in a combustion chamber to generate heat and power as shown in Figure 4. This is an emerging technology which is in the research phase.

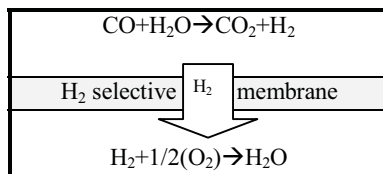


Figure 3. WGSMR concept

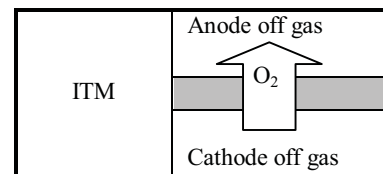


Figure 4. ITM concept

S-W analysis for these technologies with the aim of applying them in SOFC/GT hybrid cycles is presented in Table 1.

3- Modelling assessment of SOFC/GT system with CO_2 capture technology

A comprehensive assessment has been done on the literature papers and key factors in SOFC/GT systems modelling are suggested as following:

3-1- Purpose of paper

Purpose of the paper can be categorized into the following categories or combinations of them:

3-1-1- Parametric analysis

Evaluation the effect of various parameters on the overall efficiency of a system is an important objective of each simulation. Therefore, in each system modelling, the most effective parameters are identified and used as limitations or optimizers.

3-1-2- Configuration analysis

Prediction of the overall efficiency of the system in different configurations is an important objective of a simulation. There are many different structures in the simulation of SOFC/GT systems with CO_2 capture system, which they apply various equipment in their configurations like compressor, heat exchangers, reformers, mixers, HRSG, combustion chamber, air separation unit and etc. In this point

of view, the effects and layout of the elements has been considered in order to achieve the maximum overall efficiency of the site.

Table 1. S-W analysis for CO₂ capture technologies in SOFC/GT hybrid cycles

	Strength	Weakness
Post-combustion	<ul style="list-style-type: none"> • Mature technology, • Possibility of waste heat recovery after the turbine and suitable for CHP systems. 	<ul style="list-style-type: none"> • Cost of equipment, • Low purity of CO₂ and problems to pass strict environmental regulations, • Complex processes of absorption and desorption, • High energy penalty for CO₂ capturing.
Pre-combustion	<ul style="list-style-type: none"> • Use of high purity hydrogen, • CO₂ separation through condensing, • Possibility of using higher U_F, • Possibility of using various fuels, especially solid fuels, • Possibility of waste heat recovery after the turbine and suitable for CHP systems. 	<ul style="list-style-type: none"> • additional equipment requires to decompose the fuel, • Energy intensive, • Low total efficiency, • High energy penalty for CO₂ capturing.
Oxy-fuel combustion	<ul style="list-style-type: none"> • Mature technology, • High efficiency combustion, • CO₂ separation through condensing, • Low energy penalty for CO₂ capturing. 	<ul style="list-style-type: none"> • High cost of oxygen production in ASU, • High energy use of the oxygen production unit that reduces the net electrical efficiency.
Oxy-anode combustion	<ul style="list-style-type: none"> • Mature technology, • Low required oxygen, • High efficiency of combustion, • CO₂ separation through condensing, • Low energy penalty for CO₂ capturing. 	<ul style="list-style-type: none"> • Energy use of the oxygen production unit that reduces the net electrical efficiency.
Reforming anode process	<ul style="list-style-type: none"> • Combustion of the anode exhausts gas to produce additional heat or power, • Possibility of WHR after the turbine, • State-of-art within technology, • Suitable for decreasing CO₂ capture costs in the future. 	<ul style="list-style-type: none"> • High capital cost and • Non commercial.
Membrane cathode after burner	<ul style="list-style-type: none"> • Possibility of waste heat recovery after the turbine and suitable for CHP systems, • State-of-art within technology, • Suitable for decreasing CO₂ capture costs. 	<ul style="list-style-type: none"> • High capital cost, • Non commercial, • High R&D costs.

3-1-3- Optimization

Development of an optimized hybrid power generation system depends on different parameters. Due to the large number of involved parameters, as well as dependant nature of them, selection of the optimization method is very critical. Usually, in order to optimize a normal hybrid cycle, 10 to 15 or more independent variables must be considered simultaneously. In the case of systems within CO₂ capture system, there are more including variables. Optimization is based on the maximizing thermodynamic efficiencies or minimizing power generation cost. Generally, optimization of these systems is done by using genetic algorithm or non-linear mathematical programming.

3-1-4- Economic analysis

The most important goal of engineering efforts is to decrease costs of emerging technologies and to increase their competitiveness. Economic analyses play an important role in development of the hybrid systems market.

3-2- Modelling approach

Theoretical or semi-experimental, Siemens Westinghouse company has successfully examined a pressurized 220 kW SOFC/ GT hybrid system [13]. Some modelling results are validated by using the results of this pilot system if they confirm. Other modelling purposed are in following.

3-3- Heat recovery (equipment and applications)

In hybrid cycles, some equipment, such as recuperator, economizer and HRSG, are used for different purposes such as generating more power in the steam cycle, district heating, process heat and hot water supply. All papers have considered the use of gas-to-gas heat exchanger to maximize the utilization of waste heat from the system and increase the total efficiency of the site.

3-4- Other noticeable points in modelling

Other noticeable points in modelling include the modelling mode (steady state or transient), models dimensions (zero dimensional to three dimensional), codes developing, fuel type considerations, validation by using experimental results, reformer type, fuel recycling and CO₂ purity in applications.

4- Results

Important details and results of the papers have been summarized in Tables 2 & 3.

Table 2. Summary of design parameters in the studied papers

Ref.	[14]	[15]	[16] Case 1A/1B	[16] Case 2A/2B	[16] Case 2C	[17] Case 2	[17] Case 3	[18]
Total output power	1.1 MW	490.4 MW	479.97 MW	618.81	539.70	1.5 MW	1.5 MW	1058.2 kW
SOFC power	N.A.	305.9 MW	151.91	290.43	238.36	N.A.	N.A.	868.9 kW
GT power	N.A.	82.77 MW	284.8	303.04	177.65	N.A.	N.A.	87.47 kW
SOFC/GT ratio	N.A.	3.7	0.5	0.9	1.3	N.A.	N.A.	9.9
ST power	-	193.9 MW	155.14	159.53	194.27	-	-	101.8 kW
ASU power	-	-36.18 MW	-65.07	-36.41	-54.99	-	0.6 % penalty	0
CO ₂ compression power	-	- 21.79 MW	-30.35	-36.41	-54.99	N.A.	N.A.	-64 kW
Net efficiency	63 %	51.6	37.48	40.25	46.59	44.7	58.2	69.2
CO ₂ capture penalty	N.A.	2.67	N.A.	N.A.	N.A.	0.7 %	2.1 %	6.1 %
CO ₂ emission	N.A.	30.9 g/kWh	N.A.	N.A.	N.A.	0.057 kg/s	.001 kg/s	0
Percentage of captured carbon	67 %	95.3 %	N.A.	N.A.	N.A.	N.A.	N.A.	100 %
U _F	.79	74 %	.7	.7	.7	.85	.85	.7
Oxygen purity	N.A.	95 %	95 %	95 %	95 %	N.A.	N.A.	N.A.
CO ₂ pressure compression	N.A.	N.A.	150 bar	150 bar	150 bar	90 bar	90 bar	150 bar
Fuel cell temperature/ pressure	1049.4	800/34.15 bar	900/19 bar	900/19 bar	900/19 bar	934.3/4.12 bar	1026/4.1 bar	900 / 8 bar
Steam to carbon ratio	2	N.A.	N.A.	N.A.	N.A.	2	2	3
GT TIT	1049.4	1419.5 °C	1500	1500	1500	940	800	946

Table 3. Specifications of the modelling systems

		[14]	[15]	[16] Case 1A/1B	[16] Case 2A/2B	[16] Case 2C	[17] Case 2	[17] Case 3	[18]
Purpose of paper	Parameter analysis		✓						✓
	Configuration analysis		✓	✓	✓	✓	✓	✓	✓
	Optimization	✓					✓	✓	
	Economical analysis						✓	✓	
Fuel type	Hydrogen								
	Methane/ NG	✓					✓	✓	✓
	Coal		✓	✓	✓	✓			
	Biogas/Others								
FC type (temperature)	LT								
	IT		✓						
	HT	✓		✓	✓	✓	✓	✓	✓
Reforming type	Internal	✓					✓	✓	✓
	External		✓	✓	✓	✓			
Anode recirculation	Yes/No	Y	N	Y	Y	Y	Y	Y	Y
Model dimension	0-D	✓	✓	✓	✓	✓	✓	✓	✓
	>0-D								
Dependency to time	Steady-state	✓	✓	✓	✓	✓	✓	✓	✓
	Transient								
Validation with experiments	Yes/No	N	N	N	N	N	N	N	N
Simulation software		IPSEPRO	Aspen	-	-	-	WTEMP	WTEMP	Aspen
Heat recovery	HRSG		✓	✓	✓	✓			
	economizer								
	Recuperator	✓					✓	✓	✓
Heat recovery uses	Power Generation		✓	✓	✓	✓			
	District heating								
	Process heating	✓					✓	✓	✓
	Other								
CO ₂ capture category	Pre combustion		✓	✓	✓		✓		
	Post combustion	✓							
	Oxy anode combustion					✓		✓	✓

5- Conclusion

The main findings of this study may be summarized as the following items:

- 1- In all cases, SOFC/GT hybrid cycles are pressurized cycles and GT is in downstream position as bottoming cycle.
- 2- In coal-fuelled cases, external reformers are used because the syn-gas from gasification must be entered the fuel cell.
- 3- If gaseous fuels with high sulphur content are used, use of a de-sulphurizer is necessary.
- 4- In most studies, high temperature fuel cells have been studied. Although global development of fuel cells is toward low and intermediate temperature ones, but the low temperature decreases heat recovery potential in downstream; however, it has considerable effects on reducing production and maintenance costs.
- 5- Partial recycling of the exhausted fuel from the anode has been paid much attention in all cycles as a proven solution in order to increase overall efficiency.
- 6- Most developed models emphasize mass and energy flow analysis, and simulations are based on the steady state mode.



- 7- Most models are developed in order to compare different configurations from overall efficiency point of view.
- 8- Cycles modelling from the second law of thermodynamics point of view need more researches and studies. Furthermore, more economic studies are required.
- 9- In large steam turbine power plants, use of waste heat in order to generate more electricity was paid attention. Regarding power plants up to 1.5 MW, waste heat is utilized to supply process heat, and maximize use of flows heat is paid more attention.
- 10- Due to the disadvantages of post combustion systems, in these hybrid cycles, they have not been paid much attention; moreover, with respect to researches trends, they are not recommended.
- 11- Global researches about CO₂ capture technologies are moving toward oxy-anode combustion. Many researches are in progress to develop economic and efficient methods of oxygen production.
- 12- Many researches are in progress regarding the use of state-of-the-art systems, such as ITM and WGSMR. All these new systems focus on post fuel cell area and mainly emphasize simulation and construction of these exchangers.
- 13- Oxy-anode combustion, as an efficient method to fully CO₂ capture with high efficiency, is the best method for these hybrid cycles, at present time.

6- Recommendations and future attitudes

Considering development of technologies related to construction of gas turbines and fuel cells, as well as the results of the studied papers, the following research areas are suggested:

- 1- More studies regarding economic calculations, parametric analyses and thermodynamic optimization mainly based on exergy concept.
- 2- Developing new models based on bio fuels, especially biomass.
- 3- Application of low and intermediate temperature fuel cells.
- 4- In the researches, the types of fuel cells (planar or tubular) have not been paid much attention. Considering global researches trends which are toward planar fuel cells, application of this type in simulations is more reasonable and appropriate.
- 5- In the researches, ASPEN software has been used which considering its capabilities and features, it is an appropriate simulation tool for this purpose.
- 6- To develop researches regarding state-of-the-art technologies such as ITM and WGSMR.
- 7- Use of the waste heat for district heating.

Acronyms			
ASU	Air Separation Unit	SOFC	Solid Oxide Fuel Cell
CHP	Combined Heat & Power	S-W	Strength- Weakness
ESA	Electric Swing Adsorption	TIT	Turbine Inlet Temperature, K
GT	Gas Turbine	TSA	Temperature Swing Adsorption
HRSG	Heat Recovery Steam Generator	U _f	Fuel utilization factor
ITM	Ion Transport Membrane	WGSMR	Water Gas Shifting Membrane Reactor
PSA	Pressure Swing Adsorption	WHR	Waste Heat Recovery



References

- [1]- Key World Energy Statistics, International Energy Agency (IEA); 2010.
- [2]- Sung Ku Park, Tong Seop Kim, Jeong L. Sohn, Young Duk Lee. An integrated power generation system combining solid oxide fuel cell and oxy-fuel combustion for high performance and CO₂ capture. *J. Applied Energy* 88 (2011) 1187–1196
- [3]- G j Williams, A Siddle, K Pointon. Design Optimisation of a hybrid Solid Oxide Fuel cell & Gas turbine power generation system. Alstom Power Technology centre; 2001.
- [4]- Eric Grol. Technical Assessment of an Integrated Gasification Fuel Cell Combined Cycle with Carbon Capture. *J. Energy Procedia* 1 (2009) 4307–4313.
- [5]- Ali Volkan Akkaya, Bahri Sahin, Hasan Huseyin Erdem. An analysis of SOFC/GT CHP system based on exergetic performance criteria. *International journal of hydrogen energy* 33 (2008) 2566 – 2577.
- [6]- Takeshi Kuramochi, Hao Wu, Andrea Ramirez, Andre Faaij and Wim Turkenburg. Techno-economic prospects for CO₂ capture from a Solid Oxide Fuel Cell – Combined Heat and Power plant. Preliminary results. *J. Energy Procedia* 1 (2009) 3843–3850.
- [7]- Hanne M. Kvamsdal, Kristin Jordal, Olav Bolland. A quantitative comparison of gas turbine cycles with CO₂ capture. *J. Energy* 32 (2007) 10–24.
- [8]- J.W.Dijkstra, D.Jansen. Novel Concepts for CO₂ capture with SOFC. GHGT-6. Japan; 2002.
- [9]- Rune Bredesen, Kristin Jordal, Olav Bolland. High-temperature membranes in power generation with CO₂ capture. *Chemical Engineering and Processing* 43 (2004) 1129–1158.
- [10]- Julien Meyer, Johann Mastin, Tor-K. Bjørnebole, Tomas Ryberg, Nils Eldrup. Techno-economical study of the Zero Emission Gas power concept. *J. Energy Procedia* 4 (2011) 1949–1956.
- [11]- Murlidhar Gupta, Irene coyle, Kelly Thambimuthu. CO₂ capture technologies and Opportunities in Canada. CANMENT energy technology centre. Canada; 2003.
- [12]- Gardiner Hill. Progress of the CO₂ Capture Project (CCP) and Technology Development. Second Annual Conference on Carbon Sequestration; 2003
- [13]- Farshid Zabihian, Alan Fung. A Review on Modeling of Hybrid Solid Oxide Fuel Cell Systems. *International Journal of Engineering (IJE)*, Volume (3): Issue (2).
- [14]- B. Fredriksson Möller, J. Arriagada, M. Assadi, I. Potts. Optimisation of an SOFC/GT system with CO₂-capture. *Journal of Power Sources* 131 (2004) 320–326.
- [15]- Matteo C. Romano, Vincenzo Spallina, Stefano Campanari. Integrating IT-SOFC and gasification combined cycle with methanation reactor and hydrogen firing for near zero-emission power generation from coal. *J. Energy Procedia* 4 (2011) 1168–1175.
- [16]- Sung Ku Park, Ji-Ho Ahn, Tong Seop Kim. Performance evaluation of integrated gasification solid oxide fuel cell/gas turbine systems including carbon dioxide capture. *J. Applied Energy* 88 (2011) 2976–2987.
- [17]- A. Franzoni, L. Magistri, A. Traverso, A.F. Massardo. Thermo economic analysis of pressurized hybrid SOFC systems with CO₂ separation. *J. Energy* 33 (2008) 311–320.
- [18]- Sung Ku Park, Tong Seop Kim, Jeong L. Sohn, Young Duk Lee. An integrated power generation system combining solid oxide fuel cell and oxy-fuel combustion for high performance and CO₂ capture. *J. Applied Energy* 88 (2011) 1187–1196.



Comparative Study of Platinum and Non-Platinum Cathode Nanocatalysts in Direct Borohydride Fuel Cell

M.Zhiani^{*1}, N.Salehi¹, M.Mohammadi²

1-Department of Chemistry, Isfahan University of Technology, Isfahan 84156-83111, Iran.

m_zhiani@hc.iut.ac.ir

2-Asian Hydrogen New Science Co., Technology Commercialization Complex, Isfahan Science and Technology Town, Isfahan, Iran

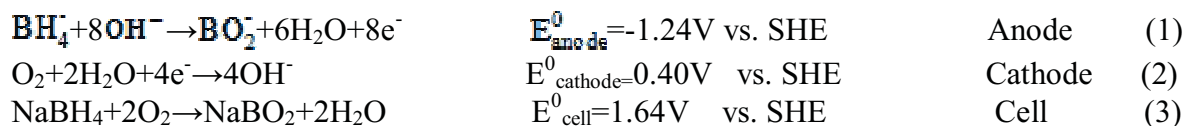
Abstract

In the recent years, extensive research work is being carried out and reported on improving the performance of nanocatalysts for both anode and cathode of polymer electrolyte membrane fuel cell. The single cell performance of carbon supported non-platinum electrocatalyst (HypermecTMK₁₄) as cathode material was used in alkaline electrolyte borohydride fuel cells and compared to that of 10% Pt/C (commercial). The structural and electrochemical aspects of the HypermecTM K₁₄ and 10% Pt/C (commercial) electrocatalysts were further investigated. X-ray diffraction (XRD) indicates the Pt and K₁₄ particles average size. Their morphology was analyzed by SEM. The HypermecTMK₁₄ cathode showed superior performance to that observed using the 10% Pt/C cathode, e.g. power density of K₁₄ is up to 138 mWcm⁻². Cyclic voltammetry data exhibit the better borohydride tolerance for K₁₄. So the difference in performance can be attributed to variations in activity towards oxygen reduction reaction and in borohydride tolerance among the cathodes.

Keywords: non-platinum electrocatalyst, alkaline electrolyte borohydride fuel cells, single cell performance, borohydride tolerance.

1- Introduction

The direct borohydride fuel cell (DBFC) has attracted renewed interest as a potential source of high electrical power recently. The following reactions occur in the DBFC:



The theoretical open circuit voltage of 1.64 V is about 0.43 V higher than that of the direct methanol fuel cell.

Research into catalysts for the anode of the DBFC has been well documented, but the cathode has rarely been addressed. Recent work has identified the challenge from the cathode, particularly the negative effect of borohydride crossover on Pt cathodes, which were widely used and was expensive [1, ii]. Alternative non-platinum cathode catalysts, e.g. Ag, MnO₂ and FeTMPP [iii, iv, v, vi], were explored but Ag and MnO₂ are not borohydride tolerant [2, 5] and Kinetic parameters for oxygen reduction reaction (ORR) on FeTMPP was not good [6]. A further study is required to understand activity, borohydride tolerance and stability of the tested catalysts; to find more economic and robust cathode materials for the DBFC. Hence, in this



study non-platinum cathode catalyst, HypermecTMK₁₄ (Acta), was used. The catalyst was analyzed for their electrochemical performance in the DBFC.

HypermecTMK₁₄ determined and were compared to platinum cathode. The performance was explained based on borohydride tolerance. Their activity towards ORR are the same for platinum and K₁₄ as cathode catalysts which has been discussed by M. Zhiani^[vii].

To the authors' best knowledge, this is the first investigation using HypermecTMK₁₄ as a cathode catalyst for the direct borohydride–oxygen fuel cell, although the HypermecTMK₁₄ has been studied as a cathode catalyst for direct alcohol fuel cells and also for H₂/O₂ fuel cells.

2- Experimental

Electrochemical tests were performed on a single cell with an active electrode area of 5cm².

2-1- Materials and Chemicals

The following materials and chemicals were used as received: NaBH₄ (99%, Merck), NaOH (99.99%, Merck), Nafion solution (5 wt.%, Aldrich), carbon powder (Vulcan XC-72R, Cabot), carbon paper (E-TEK), Pt/C10%(electrochem), anion-exchange membrane A-006 (OH-form, Tokuyama).

2-2- Electrodes fabrication for ADBFC

2-2-1-Anode electrodes preparation

The anode electrode were prepared by coating a paste made of commercial anode catalyst (HypermecTMK₁₄, provided by Acta), 5 wt% of PTFE (on dry weight basis) and water directly on Ni foam support. The electrodes were dried at 60⁰C for 30 min in the oven. The anode catalyst loading was 10 mg/cm².

2-2-2-Cathode electrodes preparation

The cathode electrodes were prepared by painting the cathode ink on carbon cloth as diffusion medium. The cathode catalyst ink was prepared by mixing HypermecTMK₁₄ with 10 wt% PTFE (on dry weight basis) and water. The electrodes were dried at 60⁰C for 30 min in the oven. The cathode catalyst loading was at 1.7 mg/cm². Another cathode containing 10 wt% Pt/C and 10 wt% PTFE with loading of 1.7 mg/cm² of the catalyst was prepared as comparative sample in the same way. The geometrical surface area of both electrodes used in this study was 5 cm².

2-2-3-Membrane electrode assemblies

An Anion-exchange membrane was used as solid electrolyte in ADBFC. The electrodes and membrane were sandwiched at room temperature in the cell hardware without using hot press. The cell has been assembled according to T.S Zhao et al.

2-3- Electrochemical characterization

2-3-1-Physical characterization

XRD analysis was carried out with 'X'Pert-PRO analytical powder X-ray diffractometer using crystal monochromatized CuK α 1 radiation of 40 kV and 30 mA. Step scans were



conducted between 10° and 80° (2θ) using a 0.05° step size and a 10.1s scan step time. The morphology of the surfaces of the HypermecTMK₁₄, and 10% Pt/C commercial catalysts were investigated with a JEOL-JSM-6360 scanning electron microscope (SEM) at an accelerating potential of 25 kV.

2-3-2-Single cell performance test

The DBFC assemblies were tested using alkaline fuel containing 5 wt% NaBH₄ at the anode side and air at the cathode side. All tests were conducted on Scribner test station (model 850 e) at ambient temperatures and pressures obtaining polarization curves by measuring the cell voltage at different currents after reaching steady state. Passive fuel was fed at the anode side and air fed at the cathode side.

2-3-3-Cyclic voltammetry

Three-electrode cell assemblies consisting of Pt or K14 base electrode were used as working electrode, palladium base electrode was used as counter electrode and reference electrode. The voltammetry experiments were performed in 5 wt% NaBH₄ (alkali solution) at room temperature. Nitrogen gas was purged into the electrolyte. Stable voltammogram curves were recorded after scanning for 6 cycles in the potential range from 0 to 1000 mV at a scan rate of 20 mV s⁻¹.

3- Results and discussion

3-1- Physical characterization

Fig. 2 shows the XRD patterns of HypermecTMK₁₄ and 10wt% Pt/C. All the XRD patterns displayed for HypermecTMK₁₄ (211), (200), (110) reflection characteristic of platinum body-centered cubic (bcc) crystal structure and patterns for 10wt% Pt/C (111), (200), (220) reflection characteristic of platinum face-centered cubic (fcc) crystal structure. The particle size (d) of the catalysts were evaluated from the X-ray diffraction peaks (at 110 for K₁₄ and was not observed a sharp peak for 10wt% Pt/C) using the following Debye–Scherrer formula:

$$d(\text{nm}) = \frac{k\lambda}{\beta_{1/2} \cos \theta_{\max}}$$

where 'd' is the average particle size (nm), λ the wavelength of X-ray (0.15406 nm), θ is the angle (110) at which the peak maximum occurs, β_{1/2} is the width (in radian) of the diffraction peak at a half height and 'k' is the coefficient 0.89–1.39 (here 0.9). The values of particle size are tabulated in Table 1.

Table 2. Particle size of cathode catalysts obtained from its XRD pattern.

Catalyst	2θ(°)	Particle size (nm)
10wt% Pt/C	-	<10
Hypermec TM K ₁₄	43.48	23

K₁₄ and Pt/C catalysts showed nano size particles produced on carbon substrate material.

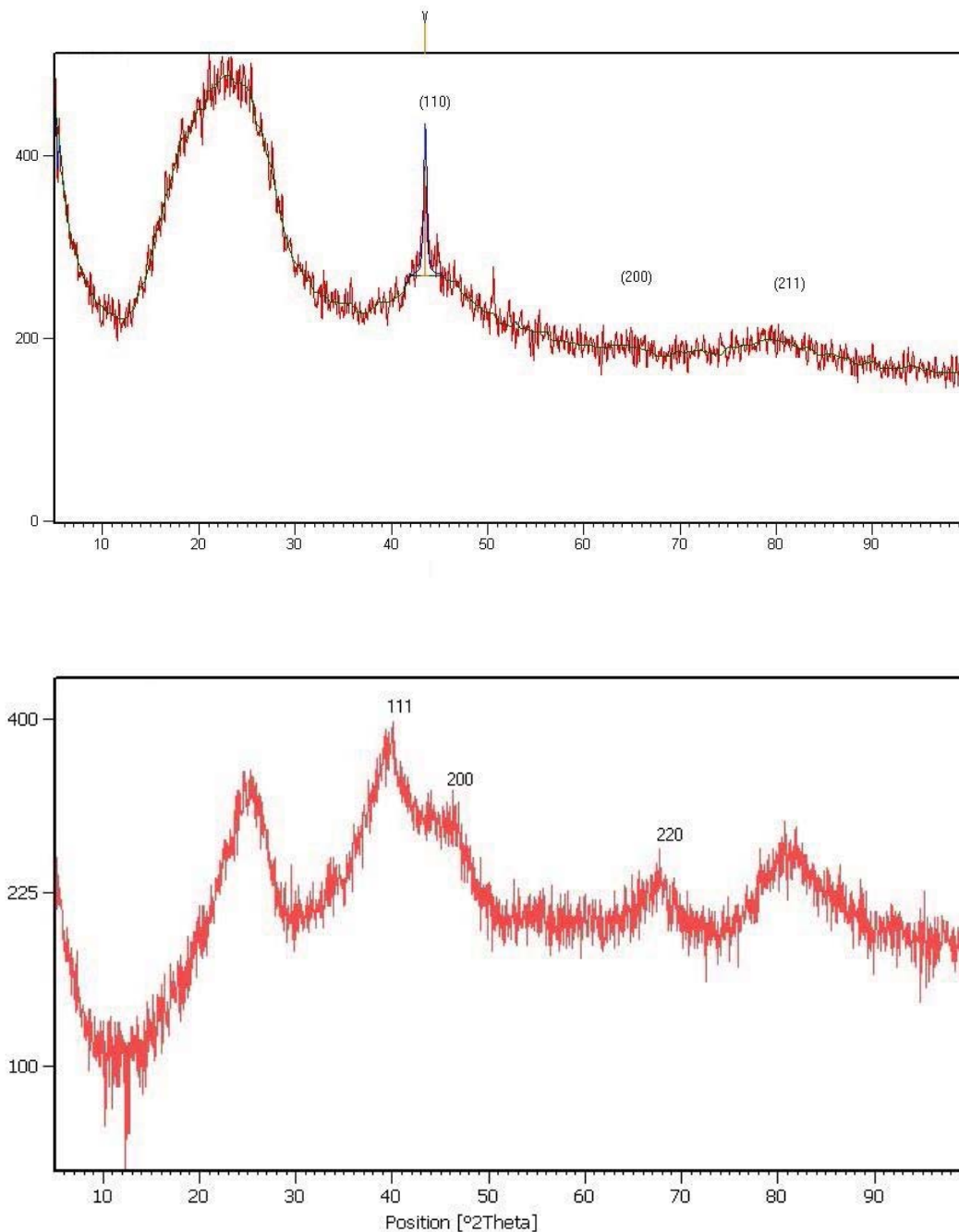


Fig. 2. X-ray diffraction patterns of catalysts. (A) HypermecTMK₁₄ (B) 10% Pt/C.

Microstructures of catalyst particles shown in Fig. 3 and 4 that are typical scanning electron microscopy (SEM) images of HypermecTMK₁₄ and 10% Pt/C.

The Pt and K₁₄ particles were distributed homogeneously across the substrate matrix, typically as a granular dense microstructure, although macro pores or defects and cauliflower-like clusters were present on the surface.

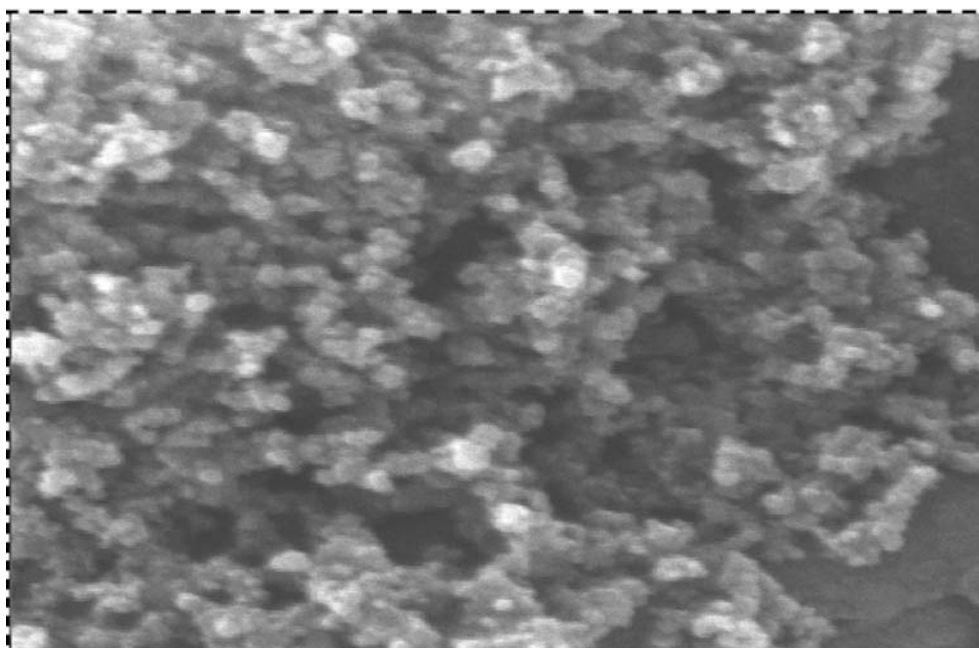


Fig. 3. Scanning electron micrograph of the carbon-supported Pt material($\times 4,000$)^{viii}.

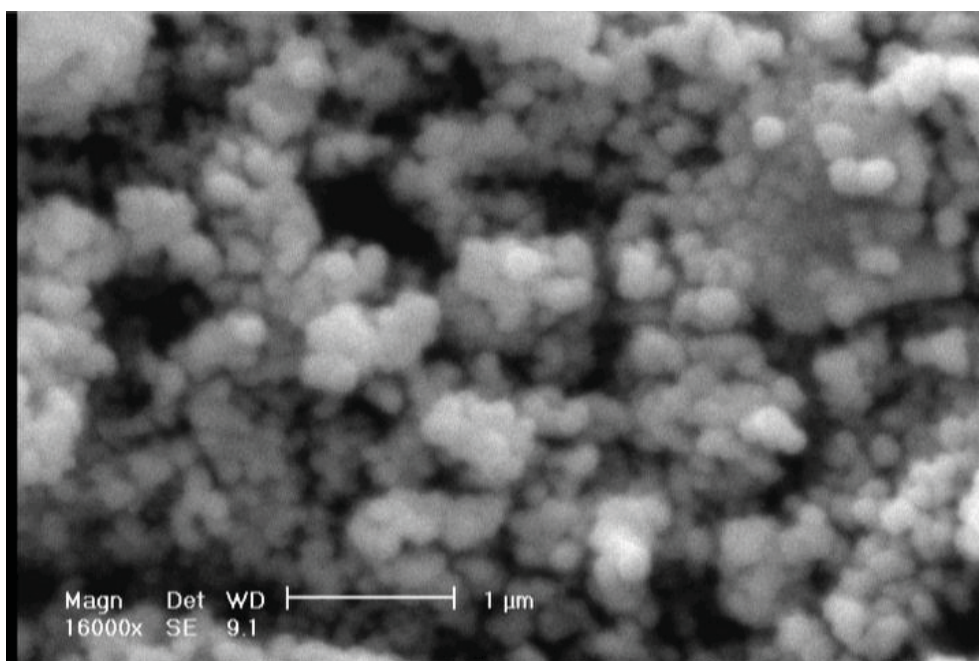


Fig.4. Scanning electron micrograph of the carbon-supported HypermecTMK₁₄ ($\times 16000$).

3-2- Electrochemical characterization

3-2-1-Single cell performance

Figs.5 shows the MEA performances and table 1 indicates the performance of both cells at ambient condition. The results demonstrate that the cell made by K₁₄ cathode catalyst produces higher performance in terms of power density and OCV. This is attributed to the higher activity of transition metal-based cathode catalyst in alkaline media as it demonstrated by Zhiani et al[7].

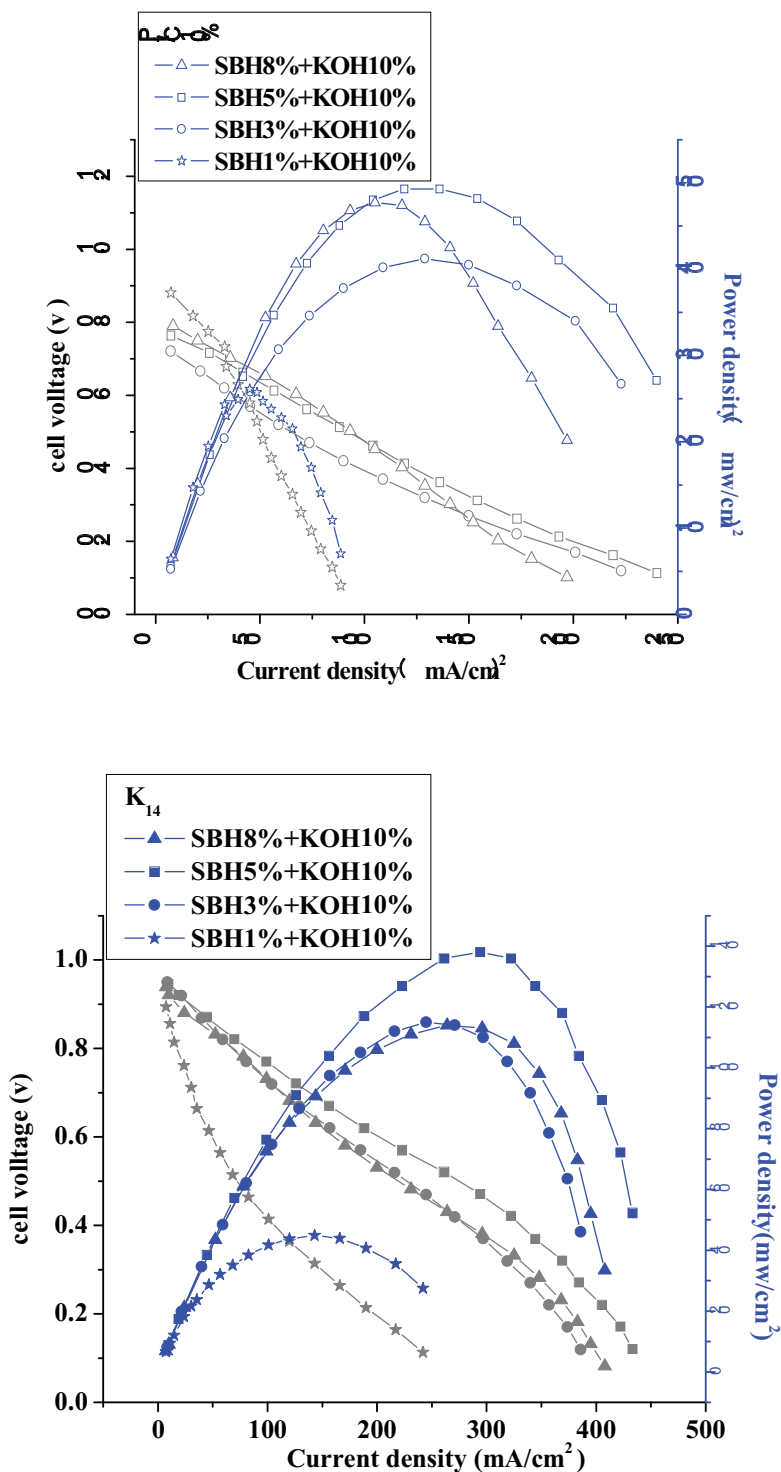


Fig.5. Cell polarization curves of 10 wt% Pt/C, K₁₄, with air at ambient temperatures and pressures.

Table 2. ADBFCs performance with two different cathodes with air at ambient temperatures and pressures

Cathode nanocatalyst	OCV mV	MPD mW/cm ²
Hypermec TM K ₁₄	970	138
Pt/C 10%	752	50

3-2-2-Cyclic voltammetry

Fig. 6 indicates the BH_4^- -crossover current density measurement using driven-cell mode. As it can be seen in the Fig. 3 the BH_4^- -crossover current density on the surface of HypermecTMK₁₄ is almost zero; it means that HypermecTMK₁₄ is not sensitive toward the BH_4^- oxidation. In fact, it shows a remarkable selectivity to oxygen reduction and inertness to borohydride oxidation BH_4^- -crossover. Current density on the surface of 10 wt% Pt/C increases up to 70 mA/cm² by increasing cell potential, leading to a cathode potential drop, which lowers the operating cell voltage.

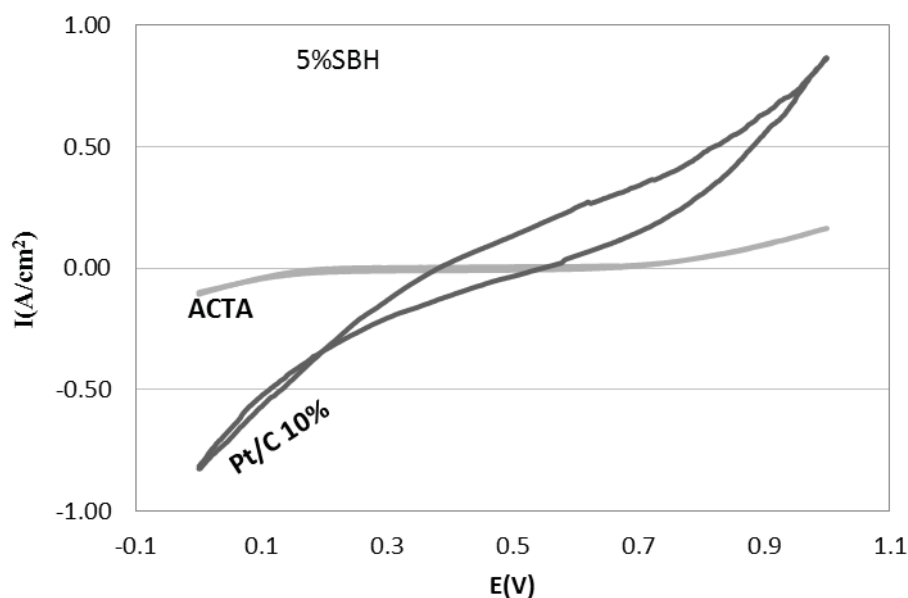


Fig. 6. Cyclic voltammograms on the carbon-supported K₁₄ and Pt electrodes in the alkali solutions saturated with N₂. Cell: undivided cell



4- Conclusions

In this study we compared the performance of commercial non-noble metal cathode catalyst (K_{14}) and conventional cathode electrode containing 10 wt% Pt/C, in the alkaline direct borohydride fuel cell (ADBFC). X-ray diffraction characterization is carried out to determine the crystalline size that average size for K_{14} is about 23 nm and for 10wt%Pt/C is lesser than 10 nm. Scanning electron microscopy (SEM) shows the spherical shape of Pt and K_{14} particles and distributed homogeneously across the substrate matrix. Electrochemical experiments including cyclic voltammetry are also conducted to determine the borohydride tolerance among the cathodes. Comparative cathode polarization results demonstrate higher performance and OCV for K_{14} as a cathode catalyst in alkaline media. The activity enhancement of K_{14} compared to pure 10wt%Pt/C was explained on the basis of properties of high surface transition metals, their remarkable activity and selectivity for oxygen reduction in alkaline solution, high borohydride tolerance (low activity for borohydride oxidation) and acceptable stability in alkaline media. Hence, HypermecTM K_{14} is a promising cathode catalyst for the direct borohydride fuel cell.

[ⁱ] Li Z.P., Liu B.H., Arai K., Suda S., “A Fuel Cell Development for Using Borohydrides as the Fuel”, *J. Electrochem. Soc.*, Vol. 150, pp. A868-A872, 2003.

[ⁱⁱ] Cheng H, Scott K. “Influence of operation conditions on direct borohydride fuel cell performance”. *J Power Sources*, Vol. 160, pp. 407–412, 2006.

[ⁱⁱⁱ] Li ZP, Liu BH, Arai K, Asaba K, Suda S. “Evaluation of alkaline borohydride solutions as the fuel for fuel cell”. *J Power Sources*, Vol. 126, pp. 28–33, 2004.

[^{iv}] Verma A, Jha AK, Basu S. “Manganese dioxide as a cathode catalyst for a direct alcohol or sodium borohydride fuel cell with a flowing alkaline electrolyte”. *J Power Sources*; Vol.141, pp. 30–34, 2005.

[^v] Feng RX, Dong H, Wang YD, Ai XP, Cao YL, Yang HX. “A simple and high efficient direct borohydride fuel cell with MnO₂-catalyzed cathode”. *Electrochem Commun*; Vol. 7, pp. 449–452, 2005.

[^{vi}] Cheng H, Scott K. “Investigation of non-platinum cathode catalysts for direct borohydride fuel cells”. *J Electroanal Chem*, Vol. 596, pp. 117–123, 2006.

[^{vii}] Zhiani. M, Hubert A. Gasteiger, Michele Piana, Stefano Catanorchi. “Comparative study between platinum supported on carbon and non-noble metal cathode catalyst in alkaline direct ethanol fuel cell (ADEFC)”, *international journal of hydrogen energy*, Vol. 36, pp. 5110-5116, 2011.

[^{viii}]Nagarajan Muthuraman, Paruthimal Kalaignan Guruvaiah, Pathanjali Gnanabaskara Agneeswara. “High performance carbon supported Pt–WO₃ nanocomposite electrocatalysts for polymer electrolyte membrane fuel cell”. *Materials Chemistry and Physics*, Vol. 133, pp. 924– 931, 2012.



Electrochemical oxidation of hydrazine on the surface of silver particles/polymer modified carbon paste electrode in alkaline media

Reza Ojani^{*}, Ali Alinejad, Mohammad Ja'far Aghajani, Saeid Safshekan

Electroanalytical Chemistry Research Laboratory, Faculty of Chemistry, University of Mazandaran, Babolsar, Iran (fer-o @umz.ac.ir)

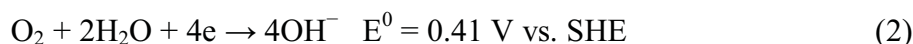
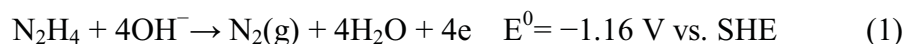
Abstract

Silver particles were deposited on the surface of poly ortho-toluidine modified carbon paste electrode (Ag/POT/MCPE) by the electrochemical method. The electrocatalytic activity of the prepared modified electrode towards the hydrazine oxidation in alkaline solutions was evaluated using cyclic voltammetry (CV) and chronoamperometry (CHA) methods. The CV experiment in the range of -0.4 V to 0.1 V vs. SCE show that the Ag/POT/MCPE electrode is electrochemically active towards the hydrazine oxidation. The onset potential for the hydrazine oxidation moreover a sharp increment in the current of hydrazine oxidation with the increase of the hydrazine concentration was observed. CHA results show stable steady-state current densities (i_{ss}) for the hydrazine oxidation. A linear dependence of the i_{ss} upon the hydrazine concentration was found in the range of $2.5 - 40$ μ M hydrazine. Results imply that the Ag/POT/MCPE presents stable and significantly high electroactivity for the hydrazine oxidation.

Keywords: Electrocatalysis, Fuel cell, Hydrazine oxidation

1. Introduction

Considerable attention has been given to direct liquid fuel cells, such as the methanol, formic acid, hydrazine and borohydride systems because of their high energy capacity compared to advanced batteries [1]. For the direct hydrazine fuel cell, its most attractive feature may be the high theoretical cell voltage of 1.57 V according to the anode reaction (1) and cathode reaction (2) in alkaline solutions:



Thus, there have been increasing reports for the investigation of hydrazine oxidation by various electrocatalysts [2–12]. Hydrazine oxidation on single-crystal platinum surfaces (1 1 1) and (3 2 2) were studied by Alvarez-Ruiz [13,14]. The onset potential of hydrazine oxidation on polyoriented Pt disc electrode in alkaline solutions is 0.1 V vs. SHE (or -0.141 V vs. SCE) [15] showing that the electrochemical oxidation of hydrazine at Pt electrode requires a higher over-potential. O'Mullane et al. have prepared polyaniline (PANI) thin films modified with platinum nanoparticles and investigated their electroactivity for hydrazine oxidation [16]. The electrochemical oxidation of hydrazine at a silver electrode was studied by Korinek [17].



Electro-oxidation of hydrazine at gold [17,18], nickel [25] and mercury [17,19] electrodes has also been reported. Razmi-Nerbin prepared the nickel pentacyanonitrosylferrate film modified aluminum electrode and evaluated its electroactivity for hydrazine oxidation [21]. Because of a large overpotential for hydrazine oxidation at ordinary carbon electrodes, electrocatalytic modified electrodes based on a variety of catalysts including metals, polymer films and metal complexes were used to minimize the overpotential effects [20]. Cobalt(II) and cobalt(III) complexes have been applied as mediators to modify carbon paste electrodes in order to obtain a catalytic activity for hydrazine oxidation [22–24]. A modified carbon paste electrode prepared by using tetracyanoquinodimethanide adsorbed on silica modified with titanium oxide showed an excellent catalytic activity and stability for hydrazine oxidation.

In the present study, we have fabricated a silver supported poly ortho-toluidine modified carbon paste electrode using an electrochemical process to obtain a high electrocatalytic effect for hydrazine oxidation. Our work showed that silver is a stable catalyst at the surface of polymer. The electrochemical activity of the prepared Ag/POT/MCPE for hydrazine oxidation was assessed using voltammetric techniques and chronoamperometric measurements.

2. Experimental

2.1. Chemicals:

Sodium hydroxide (from Merck), hydrazine hydrate (80%), silver nitrate, Ortho-toluidine (OT) (Arak Chemical Eng. Co.). Water used in this work was firstly treated by ion exchange resins and then doubly distilled.

2.2. Instrumentation:

The electrochemical experiments were performed using potentiostat/galvanostat (BHP 2061-C-Electrochemical Analysis System, Behpajooh, Iran) coupled with a Pentium IV personal computer. The utilized three-electrode system was composed of Ag/AgCl/KCl (sat'd) as reference electrode, a platinum wire as auxiliary electrode, unmodified carbon paste electrode and Ag/POT/MCPE as working electrode substrate.

2.3. Synthesis and characterization of the Ag/POT/MCPE:

The electrochemical deposition of Poly Ortho-toluidine (POT) films was carried out by cyclic voltammetry from 0.0 to 2.0 V vs. SCE at 50 mV s^{-1} in an aqueous solution containing 2.0 mM OT and 0.5 M H_2SO_4 up to reach 20 complete cycles.

Freshly prepared POT films were washed with distilled water and a monomer-free electrolyte solution. After that, they were dipped into a 5 mM silver nitrate solution at room temperature for 40 minutes. This procedure allowed us to physically adsorption silver ions into the POT film. The electrode then transferred in 0.1 M NaOH solution and 10 successive potential cyclings were performed.

3. Results and discussion

3.1. Cyclic voltammetric (CV) experiments of Ag/POT/MCPE:

Fig. 1 shows successive scanning CV profiles of the Ag/POT/MCPE in 0.1 M NaOH solution. It

is found from Fig. 1 that the Ag/POT/MCPE presents similar CV profiles to silver electrode moreover that the Ag/POT/MCPE exhibits much high anodic and cathodic currents, showing a large surface area of the modified electrode. Overlapped CV curves were observed to be increase with cycling numbers and then stable after 10 cycles which shows the stabilization of catalytic particles on the POT/MCPE surface.

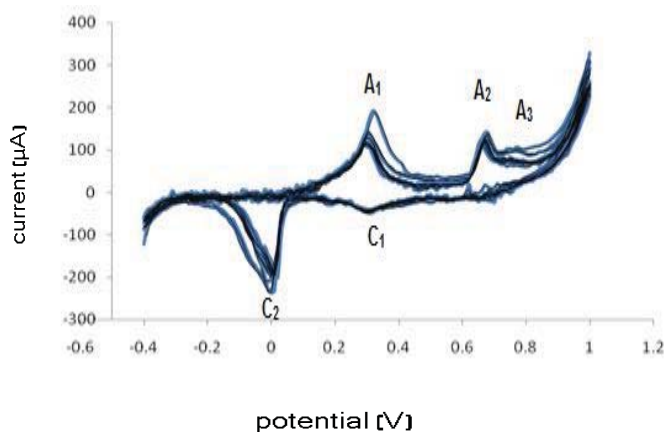
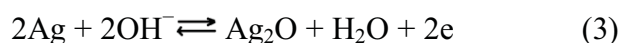


Figure 1. 10 continuously sweeping cyclic voltammograms of Ag/POT/MCPE at a scan rate of 100 mVs^{-1} in the 0.1 M NaOH solution.

In the anodic oxidation range of silver two anodic peaks A_1 at 0.30 V and A_2 at 0.68 V were obtained as shown in Fig. 1. The peaks A_1 and A_2 could be ascribed to the formation of Ag_2O and AgO respectively. Among them, the peak A_1 is attributed to the production of Ag_2O and peak A_2 showed the production of AgO . The peaks A_1 is caused by the following reaction:



The further forward potential sweep leads to the arising of the peak A_2 at $0.43\text{--}0.55 \text{ V}$ which is attributed to the formation of highvalence silver oxide (AgO):



The variation in the potential of the peak A_3 with the cyclic scan number could be related to the unstability of the high-valence AgO . In the reverse scan two reduction peaks C_1 and C_2 were delivered at 0.32 and 0.02 V , which correspond to the reduction of AgO and Ag_2O , respectively. The high reduction current in Fig. 1 indicates the presence of large active sites on the surface of the Ag/POT/MCPE electrode.

3.2. Electrochemically Oxidation of hydrazine:

Cyclic voltammetric responses of the Ag/POT/MCPE in 0.1 M NaOH solution containing different hydrazine concentrations are presented in Fig. 2. It can be seen, upon the addition of hydrazine, an enhancement in the anodic current was observed.

From the CV profile in the absence of hydrazine (Fig. 2 (a)) and those in the presence of hydrazine (b-f), it is found that an enhancement in the anodic current commences at the potential of -0.28 V , showing the high capability of Ag particles for oxidation of hydrazine in alkaline solution as shown in reaction (1).

With the increase of hydrazine concentration, the current for the hydrazine oxidation increases. These results show that the prepared Ag/POT/MCPE presents high electroactivity towards the hydrazine oxidation. It is further observed from Fig. 2 that with the addition of hydrazine, there was an increase in the anodic peak current.

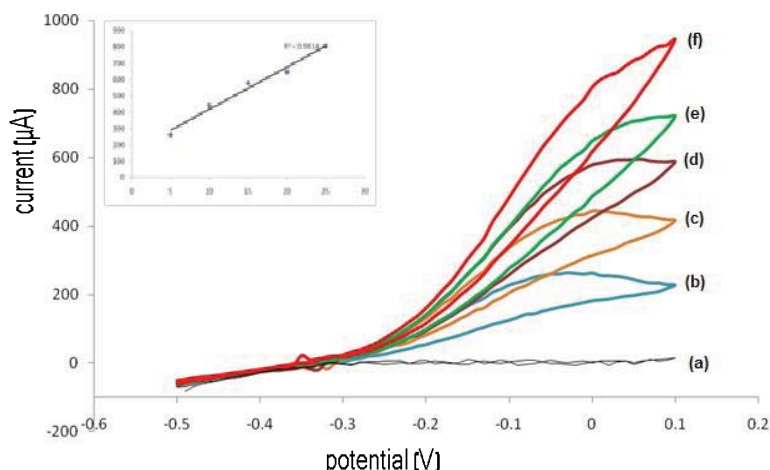
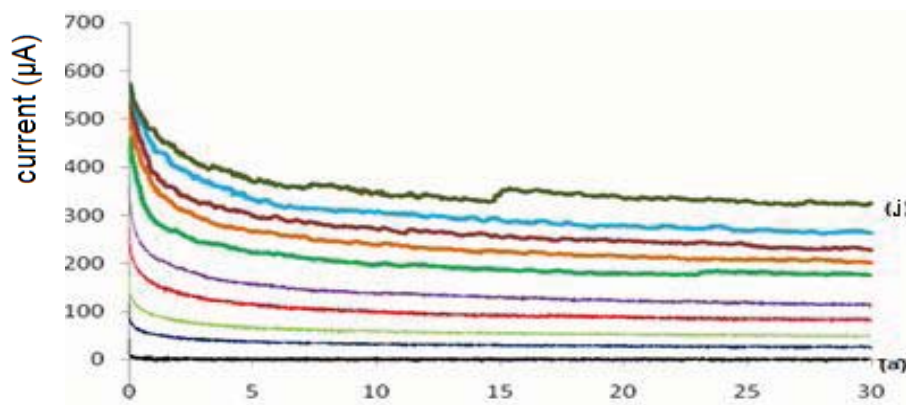


Figure 2. Electrochemical responses of Ag/POT/MCPE in 0.1 M NaOH in the (a) absence and presence of (b) 10 μ M (c) 20 μ M (d) 30 μ M (e) 40 μ M (f) 50 μ M hydrazine

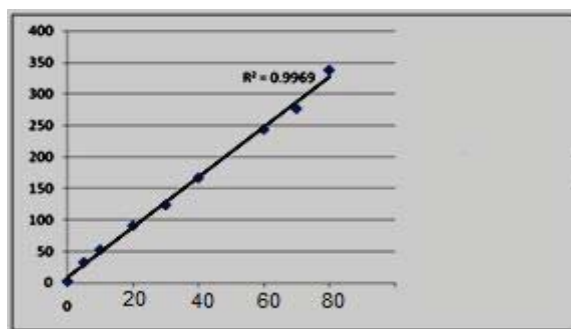
Plot of the anodic peak current (i_p) vs. added hydrazine concentrations are shown in inset of Fig. 2 where a well linear relationship ($R^2 = 0.9861$) appears from 10 to 50 μ M, showing sensitive hydrazine detection at the Ag/POT/MCPE.

3.4. Chronoamperometric study of hydrazine oxidation on the Ag/POT/MCPE:

Chronoamperometry was used for the detection of hydrazine at a fixed potential of 0.05 V vs SCE. Effect of the hydrazine concentration on chronoamperograms for the Ag/POT/MCPE at a potential step of 0.05 V is shown in Fig. 3. At this potential in the absence of hydrazine no anodic or cathodic current observed which makes Ag/POT/MCPE as a suitable electrode for detection of hydrazine. With the addition of hydrazine, there is an increase in the anodic current. An increase in the concentration of N_2H_4 from 5.0 to 80 μ M caused a linear increase in the steady-state current. The oxidation reaction of hydrazine results in the visible evolution of N_2 gas on the surface of the Ag/POT/MCPE. Therefore, the current oscillation at 80 μ M hydrazine could be ascribed to the bubbling of N_2 gas through the reaction (1). The linear relationship of i_{ss} with $C(N_2H_4)$ reveals that the prepared Ag/POT/MCPE would be a promising sensor for the detection of hydrazine.



(A)



(B)

Figure 3. (A) Chronoamperogram plots of different N_2H_4 concentrations: (a) 0.0, (b) 5.0, (c) 10, (d) 15, (e) 20, (f) 30, (g) 40, (h) 50, (i) 60 and (j) 80 μM (at potential step of 0.05 V , $t = 30$ s) (B) Plot of currents ($t = 20$ s) versus N_2H_4 concentrations ($R^2 = 0.9969$).

3.5. Long-term stability of the Ag/POT/MCPE:

The long-term stability of Ag/POT/MCPE was examined by using CHA technique. Fig. 4 presents current–time plots for hydrazine oxidation at the Ag/POT/MCPE in 0.1 M NaOH in the presence of 25 μM N_2H_4 . For evaluate the activity and stability of the Ag/POT/MCPE, chronoamperogram was recorded for a large time window in the presence of N_2H_4 . It is obvious that the Ag/POT/MCPE exhibits a good stability toward N_2H_4 oxidation.



Figure 4. Chronoamperometric responses for the Ag/POT/MCPE in the 0.1 M NaOH + 20 μM N_2H_4 solution at potential step of 0.05 ($t = 600$ s)



4. Conclusions

Silver particles were deposited on the surface of modified carbon paste electrode using the electrochemical method kept highly stability in alkaline solutions. This electrode presented large current and low onset potential for the hydrazine oxidation. Stable and high steady state currents were observed from chronoamperometric measurements at the potential step of 0.05 V and hydrazine concentrations. The high electroactivity of the Ag/POT/MCPE could be related to its large surface area. Results show that the prepared modified electrode could be applied to direct hydrazine fuel cells as a potential anodic electrode.

References:

- [1] M.H. Atwan, D.O. Northwood, E.L. Gyenge, *Int. J. Hydrogen Energy* 32 (2007) 3116–3125.
- [2] A. Salimi, L. Miranzadeh, R. Hallaj, *Talanta* 75 (2008) 147–156.
- [3] J.B. Zheng, Q.L. Sheng, L. Li, Y. Shen, *J. Electroanal. Chem.* 611 (2007) 155–161.
- [4] K. Yamada, K. Yasuda, H. Tanaka, Y. Miyazaki, T. Kobayashi, *J. Power Sources* 122 (2003) 132–137.
- [5] J. Li, X.Q. Lin, *Sens. Actuator B* 126 (2007) 527–535.
- [6] W.C. Ye, B. Yang, G.Y. Cao, L.Y. Duan, C.M. Wang, *Thin Solid Films* 516 (2008) 2957–2961.
- [7] H.R. Zare, N. Nasirizadeh, *Electrochim. Acta* 52 (2007) 4153–4160.
- [8] K. Yamada, K. Asazawa, K. Yasuda, T. Ioroi, H. Tanaka, Y. Miyazaki, T. Kobayashi, *J. Power Sources* 115 (2003) 236–242.
- [9] A. Salimi, R. Hallaj, *Electroanalysis* 16 (2004) 1964–1971.
- [10] A. Salimi, K. Abdi, *Talanta* 63 (2004) 475–483.
- [11] J.S. Pinter, K.L. Brown, P.A. DeYoung, G.F. Peaslee, *Talanta* 71 (2007) 1219–1225.
- [12] C. Batchelor-McAuley, C.E. Banks, A.O. Simm, T.G.J. Jones, R.G. Compton, *Analyst* 131 (2006) 106–110.
- [13] B. Alvarez-Ruiz, R. Gomez, J.M. Orts, J.M. Feliu, *J. Electrochem. Soc.* 149 (2002) D35–D45.
- [14] C. Nishihara, I.A. Raspini, H. Kondoh, H. Shindo, M. Kaise, H. Nozoye, *J. Electroanal. Chem.* 338 (1992) 299–315.
- [15] V. Rosca, M.T.M. Koper, *Electrochim. Acta* 53 (2008) 5199–5205.
- [16] A.P. O'Mullane, S.E. Dale, T.M. Day, N.R. Wilson, J.V. Macpherson, P.R. Unwin, *J. Solid State Electrochem.* 10 (2006) 792–807.
- [17] K. Korinek, J. Korita, M. Nusiloua, *J. Electroanal. Chem.* 21 (1969) 421–427.
- [18] S.M. Golabi, F. Noor-Mohammadi, *J. Solid State Electrochem.* 2 (1998) 30–37.
- [19] M. Felischmann, K. Korinek, D. Plrtcher, *J. Electroanal. Chem.* 34 (1972) 499–506.
- [20] U. Eissner, E. Gileadi, *J. Electroanal. Chem.* 28 (1970) 81–88.
- [21] H. Razmi-Nerbin, M.H. Pournaghi-Azar, *J. Solid State Electrochem.* 6 (2002) 126–133.
- [22] G. Cepriaa, J.R. Castillo, *J. Appl. Electrochem.* 28 (1998) 65–70.
- [23] J.J. Zhang, W.J. Pietro, A.B.P. Lever, *J. Electroanal. Chem.* 403 (1996) 93–100.
- [24] D.W. Pang, H.B. Deng, Z.L. Wang, *Electrochim. Acta* 39 (1994) 847–854.
- [25] G.W. Yang, G.Y. Gao, C. Wang, C.L. Xu, H.L. Li, *Carbon* 46 (2008) 747–752.



Experimental Study on the effect of Bipolar Plates Substance on the Performance of Proton Exchange Membrane Fuel Cells

Mohammad Dehsara¹, Farshad Kimiaghalam², Bahram Ghorbani³, Majid Amidpour⁴

¹*Energy Conversion Research Laboratory, and The New Technologies Research Center, Department of Mechanical Engineering, Amirkabir University of Technology (Tehran Polytechnic), 424 Hafez Avenue, P.O. Box, 15875-4413, Tehran, Iran, E-mail: bm_dehsara@aut.ac.ir*

²*Energy Integration Institute Department of Energy System Engineering, K.N. Toosi University of Technology, P.O. Box, 19395-1999, Tehran, Iran, E-mail: fkimia66@gmail.com*

³*Energy Integration Institute Department of Energy System Engineering, K.N. Toosi University of Technology, P.O. Box, 19395-1999, Tehran, Iran, E-mail: bahram330ghorbani@gmail.com*

⁴*Energy Integration Institute Department of Energy System Engineering, K.N. Toosi University of Technology, P.O. Box, 19395-1999, Tehran, Iran, E-mail: Amidpour@kntu.ac.ir*

Abstract

Bipolar plate is a vital component of PEM fuel cells (PEMFCs), which supplies fuel and oxidant to reactive sites, removes reaction products, collects produced current and provides mechanical support for the cells in the stack. The design of the bipolar plates should minimize plate thickness for low volume and mass. The flow fields should provide for efficient heat and mass transport processes with reduced pressure drops. The weight, volume and cost of the fuel cell stack can be reduced significantly by improving layout configuration of flow field and use of lightweight materials. In this paper, four PEMFCs have been made to fabricate bipolar plates (BPPs) from substances graphite, stainless steel (SS316), aluminum and titanium. The present results demonstrated that the PEMFC made by SS316 has more weight, stiffness and cell performance than other PEMFCs. Also, the PEMFC made by aluminum has the lowest expense. In addition, from the view of fabricating BPPs, SS316 BPPs are made easier than other BPPs.

Keywords: Bipolar Plate, PEMFC

1 Introduction

Among several types of fuel cells, the applications of Proton Exchange Membrane Fuel Cell (PEMFC) and its counterparts are from small cell-phones to interesting applications in vehicles. It is expected that the PEM fuel cells will play a significant role in new generation energy



systems. The advantages of PEMFCs are low operating temperature, high energy efficiency, and low pollution level. In recent years much advance has happened in PEMFCs, but researchers are continuously working on new cell designs for higher performance and lower prices.

The PEM fuel cell is composed of bipolar plates, gas diffusion layers (GDLs), catalyst layers (CLs), and membrane. Each part plays an important role in the fuel cell behaviour and performance. The bipolar plates are one of the most significant components of fuel cells and their performance in cell has direct effect on the system efficiency and output. The main duties of the bipolar plates can be briefly expressed as follows: uniform distribution of reactive gases inside fuel cell, collecting and directing the electric current generated inside fuel cell, management and transport of the heat generated inside fuel cell to the environment, making a suitable contact surface with gas diffusion layer in order to reduce the surface electric resistance, and effectively managing and directing the water generated within cathode to outside of fuel cell.

One of the main duties of the bipolar plates is the uniform distribution of reactive gases inside fuel cell. This work is done by making gas passing slides (gas transport channels) on these plates. The configuration of channels may be different in anode and cathode. The selection and optimization of flow distribution channels' configuration has a considerable effect on the fuel cell performance particularly in affairs such as water management and gas distribution on the catalyst layer.

Different combinations of materials, flow-field layouts and fabrication techniques have been developed for bipolar plates to achieve aforementioned functions efficiently, with the aim of obtaining high performance and economic advantages. For this goal many flow fields on the bipolar plates have been designed with different channel patterns, such as: parallel, serpentine, interdigitated or other combinations [1-8].

Kumar and Reddy [9] investigated the effect of gas flow-field design in the bipolar/end plates on the steady and transient state performance of the polymer electrolyte membrane fuel cell (PEMFC). Simulations were performed with different flow field designs: (1) serpentine; (2) parallel; (3) multi-parallel; and (4) discontinuous. Results showed that the transient response for the parallel type of design was highest. However, the steady-state voltage for parallel flow-field is comparatively lower than the other three designs.

Kumar and Reddy [10] studied on the improvement in the performance of the polymer electrolyte membrane fuel cell (PEMFC) through optimization of the channel dimensions and shape in the flow field of bipolar/end plates. Single-path serpentine flow field design was used for studying the effect of channel dimensions on the hydrogen consumption at the anode. It was found that for high fuel consumption (~80%), which is more close to a practical case, the optimum channel width, land width and channel depth were close to values of 1.5, 0.5 and 1.5 mm, respectively. Also, Studies on the effect of channel shapes showed that triangular and hemispherical shaped cross-section resulted in increase in hydrogen consumption by around 9% at the anode.

Boddu and et al. [11] analyzed bipolar plates with different serpentine flow channel configurations using computational fluid dynamics modeling. Flow characteristics including variation of pressure in the flow channel across the bipolar plate are presented. Pressure drop



characteristics for different flow channel designs are compared. Results show that with increased number of parallel channels and smaller sizes, a more effective contact surface area along with decreased pressure drop can be achieved.

Yan and his co-workers [12] proposed a novel style of straight flow channel tapered in height or width to improve the efficiency of fuel utilization for PEM fuel cells. Fuel channels of various height and width taper ratios are numerically analyzed to understand their effects on fuel transport characteristics and cell performance. The present results demonstrated that, with the tapered channel designs, the flow area contraction along the flow channel leads to increase in fuel velocity and thus enhances the fuel transport through porous layers, fuel utilization, and the capability of the liquid water removal. The results also reveal that the cell performance can be improved by either decreasing height taper ratio or increasing width taper ratio.

Wang and et al. [13] used three-dimensional numerical model to investigate the local transport phenomena and cell performance of PEM fuel cells with parallel and interdigitated flow field designs. Their study emphasized on the effects of the flow channel aspect ratio and flow channel cross-sectional area. They found that the interdigitated design has superior cell performance over the parallel design for all the conditions considered. With the baffle blockages, the reactant transport in the interdigitated design to the gas diffusion layer and the catalyst layer is mainly driven by forced convection, which enhances the liquid water removal and forces more oxygen into the porous layers. Therefore, the oxygen utilization efficiency is increased and the cell performance improves.

Shimpalee et al. [14] compared four different serpentine channels with 3, 6, 13 and 26 ways, and channel cross section of 1×1 mm². The active area used by them were 200 cm² and they showed that 13 ways flow field pattern has the best performance but 26 ways serpentine give better durability and uniformity of pressure distribution. Finally they proposed the use of 26 ways serpentine.

Despite the configuration of gas transport channels in bipolar plates, the substance of plates is also an important factor in PEM fuel cell efficiency and fabrication. Many factors should be taken into account when selecting bipolar plates' substance, some of which are cheap and simple method of fabrication, low electric resistance, high thermal conductance, appropriate resistance against corrosion and performance conditions of PEM fuel cell, low price, low density and high mechanical resistance.

In the present paper, the effect of bipolar plates' substance is investigated on the performance of PEM fuel cell. To achieve this, four PEM fuel cells with the same gas transport channels' configuration but with different bipolar plates' substances, i.e. graphite, stainless steel (SS316), aluminium and titanium are fabricated. The single-way helix configuration of flow field for anode side and parallel configuration of flow field for cathode side are used. It is observed that the PEM fuel cells fabricated by stainless steel, graphite, titanium and aluminium have the highest to the lowest amount of output power density respectively.

2 Materials and Flow Field Design of fuel cells

The PEM fuel cell anode and cathode bipolar plates fabricated by graphite, stainless steel, aluminum and titanium are shown in Figs. 1(a) to (d). As it can be seen, these plates have two

different configurations. The anode side bipolar plates are designed and fabricated with single-way helix flow field configuration and the cathode side bipolar plates are designed and fabricated with parallel flow field configuration. The gas transport channels' geometry is designed by software Solidwork. Table 1 shows the fuel cell dimensions and operating conditions.



Fig. 1 The bipolar plates of PEM fuel cells are fabricated by: (a) Graphite, (b) Stainless Steel (SS316), (c) Aluminum, and (d) Titanium.

3 Operating conditions

Fig. 2 shows the PEM fuel cell in the fuel cell set. All the experiments were performed Engineering Research Center (IERC). It is assumed that the cell operates under a fixed condition of 80°C, 2 atm. The hydrogen enters to the anode side with 95% relative humidity while the oxygen enters to the cathode side with 95% relative humidity. The inlet flow rate of anode side is 5×10^{-6} [m³/s] and inlet flow rate of cathode side is 5.83×10^{-6} [m³/s]. Also, the reaction area of the cell is 5cm × 5cm.

4 Results and discussion

In the present paper, the effect of bipolar plates' substance on the PEM fuel cell performance is investigated. To do this, four bipolar plates are fabricated by graphite, stainless steel (SS316), aluminum and titanium. The results of this experimental study are as follows:

- 1) Figure 3 shows the polarization and output power density for the fabricated PEM fuel cells. As it can be seen, the fuel cells fabricated by stainless steel and aluminum generate respectively the highest and the lowest output power density on the same operating conditions.
- 2) The fuel cell fabricated by the stainless steel: the bipolar plates fabricated by the stainless steel have higher strength compared to the other fabricated bipolar plates. The fabrication by stainless steel is difficult due to its hardness, and as it can be observed in Fig. 3, the PEM fuel

cell fabricated by SS316 has the highest output power density among the fabricated PEM fuel cells.

3) The fuel cell fabricated by the titanium: the physical properties of titanium bipolar plates are similar to those of stainless steel. However, the difference is that the maximum obtained output power of the PEM fuel cell fabricated by titanium is relatively low.

4) The fuel cell fabricated by the aluminum: the aluminum bipolar plates are soft but the high softness and flexibility of this substance causes it to deform under low pressures, and this makes it hard to work with. The density of power generated by the PEM fuel cell fabricated by aluminum has the lowest value compared to the other cells which is due to the low electric conductivity of aluminum.

5) The fuel cell fabricated by the graphite: the graphite bipolar plates are the most used type of bipolar plates. The reason is the simple fabrication and appropriate electric conductivity of graphite. Its total price is higher compared to other fabricated fuel cells, but the PEM fuel cell fabricated by graphite has an acceptable power generation.

It can be concluded that the fabricated fuel cells can be classified from the highest to the lowest due to the following factors as: (1) due to total price: graphite, titanium, stainless steel and aluminum, (2) due to strength of bipolar plates substances: stainless steel, titanium, aluminum and graphite, (3) due to the fuel cell weight: stainless steel, titanium, aluminum and graphite, (4) due to the simplicity of fabrication: aluminum, graphite, titanium and stainless steel, and (5) due to the output power density of fuel cell: stainless steel, graphite, titanium and aluminum. Noting the factors investigated in the present study, it can be said that the PEM fuel cell fabricated by the graphite bipolar plates is the most appropriate type of PEM fuel cell, although it has the highest price.



Fig. 2 The fuel cell test station.

Table1. Fuel cell dimensions and operating conditions.

Quantity	Value
Channel height	1 [mm]
Channel width	1 [mm]
Rib width	1 [mm]
Reaction area	5×5 [cm ²]
Pressure inlet	2 [atm]
Anode inlet flow rate	5×10^{-6} [m ³ /s]
Cathode inlet flow rate	5.83×10^{-6} [m ³ /s]
Operating temperature	80 °C
Relative humidity	95%

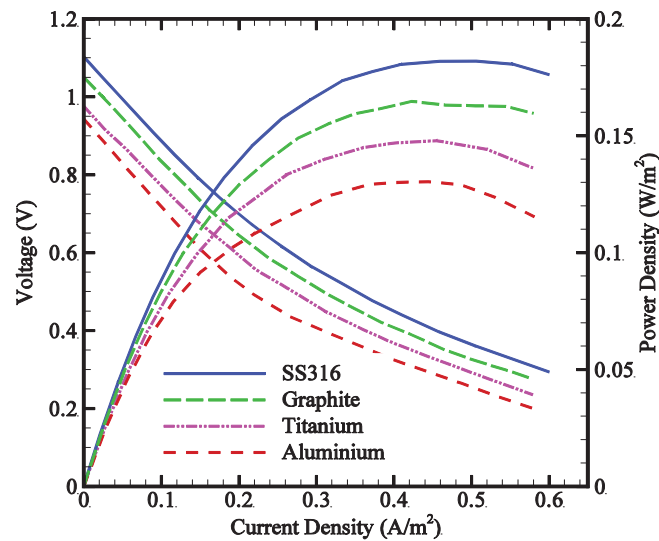


Fig. 3 Polarization and power density curves for four PEM fuel cells with various bipolar plates substances; stainless steel (SS316), graphite, titanium and aluminum.

References

- [1] Thitakamol V.; Therdthianwong A.; Therdthianwong S. 2011. Mid-baffle interdigitated flow fields for proton exchange membrane fuel cells, Int J Hydrogen Energy, 36(5), 3614-22.



- [2] Li X.; Sabir I. 2005. Review of bipolar plates in PEM fuel cells: Flow-field designs, *Int J Hydrogen Energy* 30(4), 359-71.
- [3] Yan W.M.; Wang X.D.; Lee D.J.; Zhang X.X.; Guo Y.F.; Su A. 2011. Experimental study of commercial size proton exchange membrane fuel cell performance, *Applied Energy*, 88, 392–6.
- [4] Nguyen T.V. 1996. A gas distributor design for proton exchange membrane fuel cells, *J Electrochem Soc*, 143(5), L103–L105.
- [5] Liu H.C.; Yan W.M.; Soong C.Y.; Chen F. 2005. Effects of baffle-blocked flow channel on reactant transport and cell performance of a proton exchange membrane fuel cell, *J Power Sources*, 142(1-2), 125-33.
- [6] Chow C.Y.; Wozniczka B.; Chan J.K.K. 1999. Integrated reactant and coolant fluid flow field layer for a fuel cell with membrane electrode assembly. Canadian Patent No. 2,274,974.
- [7] Kazim A.; Liu H.T.; Forges P. 1999. Modelling of performance of PEM fuel cell with conventional and interdigitated flow fields, *J Appl Electrochem* 29, 1409–16.
- [8] Wood D.L.; Yi J.S.; Nguyen T.V. 1998. Effect of direct liquid water injection and interdigitated flow field on the performance of proton exchange membrane fuel cells, *Electrochim Acta* 43(24), 3795–809.
- [9] Kumar A.; and Reddy R.G. 2006. Effect of gas flow-field design in the bipolar/end plates on the steady and transient state performance of polymer electrolyte membrane fuel cells, *J. Power sources*, 155(2), 264-271.
- [10] Kumar A.; and Reddy R.G. 2003. Effect of channel dimensions and shape in the flow-field distributor on the performance of polymer electrolyte membrane fuel cells, *J. Power sources*, 113(1), 11-18.
- [11] Boddu R.; Marupakula U.K.; Summers B.; and Majumdar P. 2009. Development of bipolar plates with different flow channel configurations for fuel cells, *J. Power sources*, 189(2), 1083-1092.
- [12] Yan W.M.; Liu H.C.; Soong C.Y.; Chen F.; and Cheng C.H. 2006. Numerical study on cell performance and local transport phenomena of PEM fuel cells with novel flow field designs, *J. Power sources*, 161(2), 907-919.
- [13] Wang X.D.; Duan Y.Y.; Yan W.M.; and Peng X.F. 2008. Effects of flow channel geometry on cell performance for PEM fuel cells with parallel and interdigitated flow fields, *J. Electrochimica acta*, 53(16), 5334-5343.
- [14] Shimpalee S.; Greenway S.; Van Zee J.W. 2006. The impact of channel path length on PEMFC flow-field design, *J. Power Sources*, 160(1), 398-406.



Membraneless Mixed Reactant Direct Methanol Fuel Cell

Mohsen Khosravi babadi¹, Mojtaba Masoudi²

Nanotechnology Department, University of Isfahan, Hezar-jareeb st., Isfahan 81746-73441,
I.R.Iran

m.khosravi@ast.ui.ac.ir

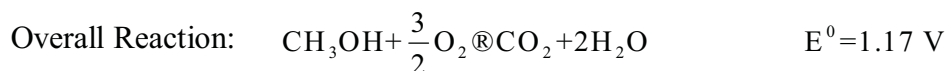
Abstract

A conventional direct methanol fuel cell (DMFC) consists of a polymer electrolyte membrane (PEM) pressed between an anode and a cathode electrode. This architecture is limited by parameters such as: overall size and cost, fuel crossover, membrane degradation and structures complexity. Here, we report a membraneless mixed reactant DMFC in which, using a selective cathode electrocatalyst. There is no membrane for separation anode and cathode compartments. The maximum power densities obtained from polarization curves were 4 and 2.8 mW/cm² for operational temperatures 35 and 20 °C, respectively.

Keywords: Membraneless fuel cell, Mixed reactant fuel cell, Membraneless mixed reactant DMFC, Selective electrocatalyst

Introduction

DMFCs are the most advanced amongst direct liquid fuel cell. DMFC operates with an aqueous methanol fuel and an oxygen oxidant typically derived from the air or pure oxygen.[1] The electrochemical reactions for this type of fuel cell at ambient temperature and pressure (25 °C, 1atm) are as follows:



The membrane electrode assembly (MEA) is the major component in a conventional DMFC [2] and consists of three separate components, the polymer electrolyte membrane, an anode

¹ Associate Professor of Analytical chemistry

² Nanotechnology Department, University of Isfahan, Hezar-jareeb st., Isfahan 81746-73441, I.R.Iran.

M. Sc. Students of Nanochemistry.(m.masoudi1364@ yahoo.com).

electrode and a cathode electrode, that hot-pressed or compressed together at certain pressure and temperature as shown in Figure 1.

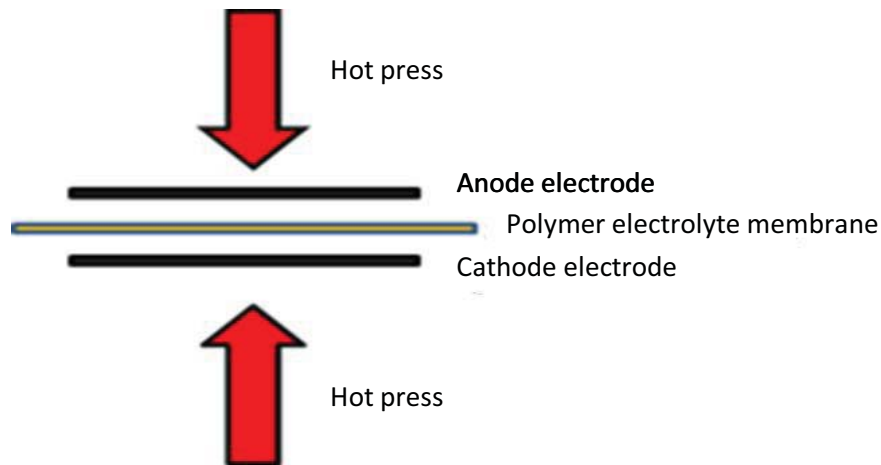


Figure 1: Hot press process for fabrication of MEA

Limitations and wide development barriers of the DMFC with the conventional design due to using MEA include: high overall cost and size, structure complexity, fuel crossover, need to water and temperature management and membrane degradation[3,4,5]. Elimination of polymer electrolyte membrane (PEM) and using selective electrocatalysts are two strategies for simplification of the conventional design, resulting in new structures that are called membraneless [6] and mixed reactant [4] fuel cells, respectively. In membraneless fuel cells, there is not a physical barrier to separate the anode and cathode compartments. The most common configuration is microfluidic fuel cell which utilizes two laminar flows in the same channel (Figure 2). In this structure, which was fabricated by Ferrigno et al. in 2002[6], the microfluidic flow at low Reynolds numbers should be used to delay the convective mixing of fuel and oxidant. Two aqueous streams, one containing fuel (anolyte) and one containing oxidant (catholyte), are allowed to flow in parallel in a single microfluidic channel that the electrodes are integrated on its walls. Mixing of the two streams occurs by transverse diffusion only, and is limited to an interfacial area at the center of the channel. The position and orientation of the electrodes, channel dimensions, and flow rate influence on mixing quantity and fuel cell performance [7].

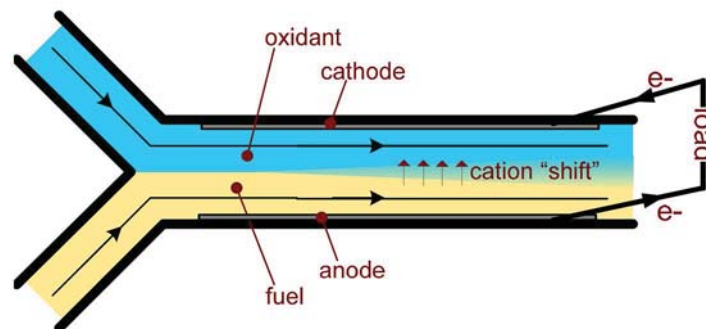


Figure 2: Membraneless fuel cell (Microfluidic fuel cell based laminar flow) architecture[6].

In mixed reactant structure, electrocatalysts are chosen in such a way that maximizes selectivity towards electrodes reactions. this feature minimizes adverse effect of methanol crossover compared to such non selective electrocatalysts as Pt [8,9]. Since Pt is very active both for methanol oxidation and oxygen reduction, it cannot be used as a cathode electrocatalyst in mixed reactant DMFCs. Pt-free precious metal chalcogenides have been suggested as alternatives as they have successfully demonstrated comparable oxygen reduction activity in the presence of methanol [10-16]. Some instances include cluster-like materials such as in Ru_xSe_y , Ru_xS_y , or $Mo_xRu_ySe_z$ nanoparticle chalcogenides.[17-25] that have been reported to exhibit catalytic activity even higher than Pt nanoparticles during the oxygen reduction reaction in the presence of methanol.

In this work carbon supported RuSe and PtRu were synthesized using microwave assisted polyol method and were integrated as a membraneless DMFC.

Experimental

$H_2PtCl_6 \cdot 6H_2O$, $RuCl_3$ (38%), $Na_2SeO_3 \cdot 5H_2O$, Etylene Glycole, KOH and Carbon black were used for preparation of carbon supported RuSe and PtRu. The catalysts nanoparticles were synthesized by microwave assisted polyol method [26-28]. catalyst inks were prepared by dissolving catalyst powders in ethanol, deionized water and nafion solution (5%). The catalyst inks were homogenized in ultrasonic bath for 60 min. the fuel cell electrodes were prepared by spraying catalyst inks on carbon cloth. a Single cell of membraneless mixed reactant DMFS was fabricated as follow: anode and cathode electrodes were sandwiched with Plexiglas end plates. and separated by two specially designed Plexiglas spacers. Titanium mesh and silicon sheet were used as current collector and sealing layer, respectively. Plexiglas end plates have appropriate inlets, outlets and flow fields (Figure 3).



Figure 3: Membraneless and mixed reactant direct methanol fuel cell

Physical characterization

The crystalline phase and structure of the electrocatalysts were demonstrated by XRD as shown in Figure 4. Pt and PtRu XRD patterns contain four characteristic peaks corresponding to (111), (200), (220) and (311) plane of fcc Pt crystalline[29]. The diffraction peaks for the PtRu catalyst

(Figure 4(a)) are shifted slightly to the higher 2θ values compared with the peak position of pure Pt. These shifts indicate that Ru has entered into the Pt lattice and PtRu alloy was formed [29-32]. In the Ru and RuSe XRD pattern there observed one major peak corresponding to overlapped peaks of (100), (002) and (101) planes of hcp Ru crystalline [26]. The diffraction peak of RuSe is shifted to a smaller angles (about 1 degree) compared with the peak of pure Ru as shown in Figure 4(b). This shift is related to formation of RuSe alloy [22,33]. Moreover, particle size of PtRu and RuSe was 5.5 and 6.5 nm, respectively, as calculated by Scherrer equation.

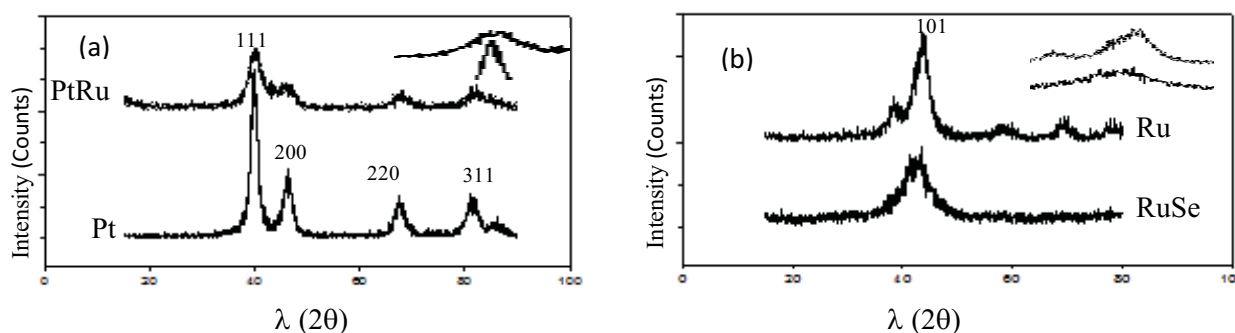


Figure 4: XRD pattern of RuSe, Ru 4(a) and PtRu, Pt 4(b).

Electrochemical characterization

Performance characteristics of the cell were investigated by plotting the polarization curve at certain condition. Figure 5 shows polarization curves of the cell at two temperatures. The open circuit potential was 560-570 mV and the maximum power densities were achieved to about 2.8 and 4 $\text{mW} \cdot \text{cm}^{-2}$, for temperatures of 20 and 35 $^{\circ}\text{C}$ respectively.

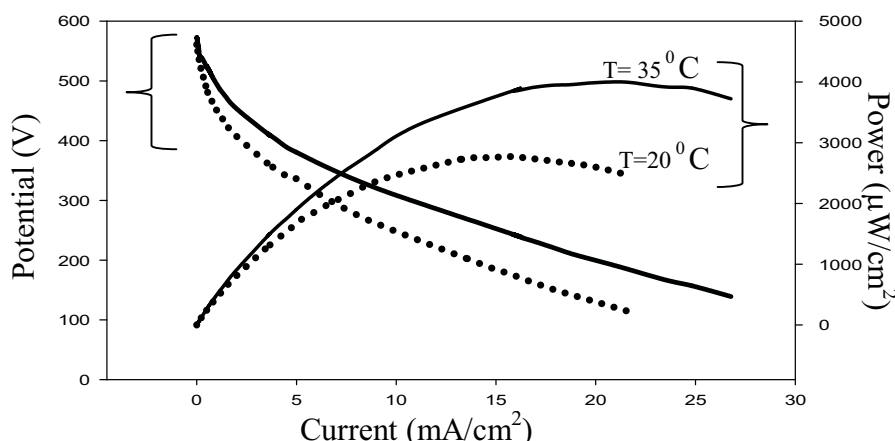


Figure 5: Polarization curve of membraneless direct methanol fuel cell.

Conclusion

Carbon supported PtRu and RuSe electrocatalyst powders were synthesized and characterized. Using the synthesized electrocatalysts, a single cell membraneless mixed reactant DMFC was



fabricated. Obtained polarization curves of the cell it is revealed that temperature has effective role on the cell performance. showed good open circuit potential as well as acceptable power peaks.

References

- [1] C. Lamy, A. Lima, V. Lerhun, F. Delime, C. Coutanceau, J. Leger “Recent advances in the development of direct alcohol fuel cells (DAFC)”, *J. of Power Sources*, (2002). 105, 283-296
- [2] A. Roy, M. Hickner, O. Lane, J. McGrath “Investigation of membrane electrode assembly (MEA) processing parameters on performance for wholly aromatic hydrocarbon-based proton exchange membranes”, *J. of Power Sources*, (2009). 191, 550-554
- [3] V. Neburchilov, J. Martin, H. Wang, J. Zhang “A review of polymer electrolyte membranes for direct methanol fuel cells”, *J. of Power Sources*, (2007). 169, 221-238
- [4] A. Shulka, R. Raman, K. Scott “Advances in mixed reactant fuel cells” *J. of Fuel cells*, (2005). 5, 436-447
- [5] F. Chen, M. Chang, M. Lin “Analysis of membraneless formic acid microfuel cell using a planar microchannel”, *J. of Electrochimica Acta*, (2007). 52, 2506-2514
- [6] R. Ferrigno, A. D. Stroock, T. D. Clark, M. Mayer, G. M. Whitesides “Membraneless Vanadium Redox Fuel Cell Using Laminar Flow”, *J. of American Chemical Society*, (2002). 124(44), 12930-12931
- [7] R.F. Ismagilov, A.D. Stroock, P. J. A. Kenis, G. Whitesides, H. A. Stone, “Experimental and theoretical scaling laws for transverse diffusive broadening in two-phase laminar flows in microchannels”, *J. of Applied Physics Letters*, (2000). 76(17), 2376-2378
- [8] M. Priestnall, V.P. Kotzeva, D.J. Fish, E. M. Nilsson “Compact mixed-reactant fuel cells” *J. of Power Sources*, (2002). 106(1-2), 21-30
- [9] D. Papageorgopoulos “Compact Mixed-Reactant (CMR) DMFCs: a commercial application for Methanol-tolerant ORR Catalysts”, www.CMR.com
- [10] A. S. Arico, S. Srinivasan, V. Antonucci “DMFCs: From Fundamental Aspects to Technology Development”, *J. of Fuel Cells*, (2001). 1(2), 133-161
- [11] M. Winter, R. J. Brodd “What Are Batteries, Fuel Cells, and Supercapacitors?”, *J. of Chem. Rev.*, (2004). 104(10), 4245-4270
- [12] M. S. Dresselhaus and I. L. Thomas, “Alternative energy technologies”, *J. of Nature*, (2001). 414, 332-337
- [13] S. Wasmus, A. Kuver “Methanol oxidation and direct methanol fuel cells: a selective review”, *J. of Electroanal. Chem.*, (1999). 461(1-2), 14-31



- [14] P. H. C. Camargo, Z. Peng, X. Lu, H. Yangb, Y. Xia “Synthesis and application of RuSe_{2+d} nanotubes as a methanol tolerant electrocatalyst for the oxygen reduction reaction”, J. of Materials Chemistry, (2009). 19, 1024-1030
- [15] N. Alonso-Vante, H. Tributsch “**Energy conversion catalysis using semiconducting transition metal cluster compounds**”, J. of Nature, (1986). 323, 431-432
- [16] D. C. Papageorgopoulos, F. Liu, O. Conrad “A study of Rh_xSy/C and RuSex/C as methanol-tolerant oxygen reduction catalysts for mixed-reactant fuel cell applications”, J. of Electrochimica Acta, (2007). 53(2), 1037-1041
- [17]. N. Alonso-Vante, P. Bogdanoff, H. Tributsch “On the Origin of the Selectivity of Oxygen Reduction of Ruthenium-Containing Electrocatalysts in Methanol-Containing Electrolyte”, J. of Catalysis (2000). 190(2), 240-246
- [18]. P. J. Sebastian, F. J. Rodriguez, O. Solorza, R. Rivera “Development of PEM (Proton Exchange Membrane) fuel cell using carbon supported Mo-Ru-Se electrodes”, J. of New Materials Electrochemical Systems, (1999). 2, 115-119
- [19] H. Tributsch, M. Bron, M. Hilgendorff, H. Schulenburg, I. Dorbandt, V. Eyert, P. Bogdanoff, S. Fiechter “Methanol-resistant cathodic oxygen reduction catalysts for methanol fuel cells”, J. of Appl Electrochem, (2001). 31(7), 739-748
- [20] Cao D, Wieckowski A, Inukai J, Alonso-Vante N “Oxygen Reduction Reaction on Ruthenium and Rhodium Nanoparticles Modified with Selenium and Sulfur Batteries”, Fuel Cells, and Energy Conversion (2006) J Electrochem Soc, (2006). 153, 869-874
- [21] P. J. Kulesza, K. Miecznikowski, B. Baranowska, M. Skutnik, S. Fiechter, P. Bogdanoff, I. Dorbandt “Tungsten oxide as active matrix for dispersed carbon-supported RuSe_x nanoparticles: Enhancement of the electrocatalytic oxygen reduction”, J. Of Electrochem Commun,(2006). 8(5), 904-908
- [22] V. I. Zaikovskii, K. S. Nagabhushana, V. V. Kriventsov, K. N. Loponov, S. V. Cherepanova, R. I. Kvon, H. BoInnemann, D. I. Kochubey and E. R. Savinova “Synthesis and Structural Characterization of Se-Modified Carbon-Supported Ru Nanoparticles for the Oxygen Reduction Reaction”, J. of Phys. Chem. B, (2006). 110(13), 6881-6890
- [23]. L. Colmenares, Z. Jusys and R. J. Behmm “Electrochemical Surface Characterization and O₂ Reduction Kinetics of Se Surface-Modified Ru Nanoparticle-Based RuSe_y/C Catalysts”, Langmuir, (2006). 22(25), 10437-10445
- [24].L. Colmenares, Z. Jusys and R. J. Behm “Activity, Selectivity, and Methanol Tolerance of Se-Modified Ru/C Cathode Catalysts”, J. Phys. Chem. C, (2007). 111(3), 1273-1283
- [25] S. Fiechter, I. Dorbandt, P. Bogdanoff, G. Zehl, H. Schulenburg, H. Tributsch, M. Bron, J. Radnik, M. F. Erdmann “Surface Modified Ruthenium Nanoparticles: □ Structural Investigation



and Surface Analysis of a Novel Catalyst for Oxygen Reduction”, J. of Phys. Chem. C, (2007). 111(1), 477-487

[26] P. Nekooi, M. K. Amini “Effect of support type and synthesis conditions on the oxygen reduction activity of RuSe catalyst prepared by the microwave polyol method”, J. of Electrochimica Acta, (2010). 55, 3286-3294

[27] Q. Zheng, X. Cheng, T. Jao, F. Weng, A. Su, Y. Chiang “Microwave assisted synthesis of high performance Ru₈₅Se₁₅/MWCNTs cathode catalysts for PEM fuel cell Applications”, J. of Hydrogen energy, (2011). 36, 14599-14607

[28] S. Harish, S. Baranton, C. Coutanceau, J. Joseph “Microwave assisted polyol method for the preparation of Pt/C, Ru/C and PtRu/C nanoparticles and its application in electrooxidation of methanol”, J. of Power Sources, (2012). 214, 33-39

[29] F. Ye, X. Cao, L. Yu, S. Chen, W. Lin “Synthesis and Catalytic Performance of PtRuMo Nanoparticles Supported on Graphene-Carbon Nanotubes Nanocomposites for Methanol Electro-Oxidation”, Int. J. of Electrochem. Sci., (2012). 7, 1251-1265

[30] Y. Chen, Y. Tang, C. Liu, W. Xing, T. Lu “Room temperature preparation of carbon supported Pt-Ru catalysts”, J. of Power Sources, (2006). 161(1), 470-473

[31] L. Zhang, J. Kim, H. M. Chen, F. Nan, K. Dudeck, R. Liu, G. A. Botton, J. Zhang “A novel CO-tolerant PtRu core-shell structured electrocatalyst with Ru rich in core and Pt rich in shell for hydrogen oxidation reaction and its implication in proton exchange membrane fuel cell”, J. of Power Sources, (2011). 196(22), 9117-9123

[32] Y. Gu, G. Wu, X. F. Hu, D. A. Chen, T. Hansen, H. Loye, H. J. Ploehn “PAMAM-stabilized Pt-Ru nanoparticles for methanol electro-oxidation”, J. of Power Sources, (2010). 195 (2), 425-434

[33] G. Liu, H. Zhang, J. Hu “Novel synthesis of a highly active carbon-supported Ru₈₅Se₁₅ chalcogenide catalyst for the oxygen reduction reaction”, J. of Electrochemistry Communications. (2007). 9 (11), 2643-2648



Manufacturing of yttria stabilized Zirconia based solid electrolyte thin films by Combined tape casting/Impregnation method

Mojtaba Ghatee¹, Hasan Salehi²

*Mechanical Engineering Department, Shahrood University of Technology,
Shahrood, Iran
mghatee@yahoo.com*

Abstract

In this paper, tetragonal/cubic Zirconia composite thin film electrolytes were prepared by combined Tape casting-Polymer impregnation method. In order to prepare composite thin films, at first, porous thin 3 mol yttria stabilized zirconia (3YSZ) was prepared by tape casting method. The porous thin films were then impregnated by yttria solution to prepare composite electrolytes. The samples were sintered at 1450 °C. Microstructure and phases of samples were investigated by SEM and XRD analysis. Hardness and toughness of samples were measured by Vickers micro hardness method. It was found composite thin film with thickness of 140 μm and hardness and toughness up to 13 GPa and 4.3 MPa√m respectively, can be obtained.

Keywords: Zirconia, Fuel cells, thin films, Tape casting, Impregnation.

Introduction

Solid oxide fuel cells (SOFCs) are electrochemical devices for producing electricity[1]. They have received a lot of attention due to their high conversion efficiency and low pollutant emissions.

In solid oxide fuel cells the electrolytes are subjected to varying physical and chemical environments during operation[1]. In addition to exhibiting resistance to these environments the electrolyte material has to possess high ionic conductivity and low electronic conductivity at the operating temperatures of SOFCs. Since the cell resistance is dependent on the electrolyte thickness the electrolyte should be as thin as possible.

yttria doped Zirconia (YSZ) is the most frequently used material in SOFC electrolytes. Zirconia doped with 8% mol of yttria (8YSZ) with the cubic crystal structure has the highest ionic conductivity[2,3]. Unfortunately, the mechanical properties of 8YSZ are poor preventing its use in the electrolyte-supported SOFC configuration[4]. In contrast, the tetragonal structure associated with low dopant concentrations, such as 3% mol of yttria, exhibits good mechanical properties[2,5–6]. This explains the wide use of 3YSZ as raw material for self-supported electrolyte SOFC configuration despite its lower ionic conductivity[2,3]. Various methods have been used to improve mechanical properties of Zirconia based thin films. It has been shown that 3YSZ/8YSZ composite electrolytes have an improved combination of electrical and mechanical properties[7].

¹- Assistant Professor.

²- MSc Student, Shahrood University of Technology, salehi650@yahoo.com.

One of the most important challenges of high temperature solid electrolytes is the reduction of their working temperature which would be accomplished by improving conductivity of electrolyte's material or reduction of their thickness by preparing thin films.

There are many techniques for preparing ceramics thin films including Sol-Gel, Electrophoretic deposition, Sputtering, Screen Printing, Tape casting and etc. Tape casting is one of the most commercial methods for preparing ceramic thin films[8,9].

Tape-casting is a method for obtaining large-area thin ceramic films[10]. The tape-casting process consists of preparing a slurry containing the ceramic particles of interest and casting this slurry with the help of a doctor blade on a moving carrier material. The obtained wet cast goes through a drying chamber where the solvent is evaporated resulting in a dried green ceramic tape.

Typically, organic solvents are favored in the tape casting process due to their fast evaporation rate. However, the use of organic solvents raises some environmental and health concerns.

In recent years, water-based tape-casting for obtaining SOFC components has been reported in the literature. Water-based tape casting has been used to fabricate anodes [11,12], electrolytes [6,10–13], and interconnects [14].

The aim of the present research is the preparation of 3YSZ/8YSZ composite thin film electrolytes by combination of Tape casting and Polymer Impregnation methods. In addition, mechanical properties of these thin films are investigated

Experimental

Slurry for tape casting prepared in several stages (see the flow chart in Figure 1).



Figure 1: Sequence of process

Appropriate amount of 3YSZ powder (TOSOH, Japan) was added to distilled water to obtain 78 wt.% suspension. In order to prepare a well dispersed slip, 0.5 wt.% (based on powder weight) Dollapix CE64 (Schimmer & Schwartz) was added to suspension. The suspension was then milled using Polyethylene container and Zirconia grinding media for 24hr at the rate of 30rpm. Ammonia was used to adjust pH at 9. After preparing stable suspension, various amount of glycerin as a plasticizer (Merck) was added and milled again for 24hr at the rate of 5rpm. At last, 7 wt.% (based on powder weight) Polyvinyl alcohol was added as a binder and milled again for 24hr.

De airing of the slip was performed under vacuum followed by rotating the slip without balls at the rate of 2rpm. The slip was cast by laboratory-scale tape-caster (shown in Figure 2) on glass substrate. The thickness of the tapes was adjusted by the distance between blade and glass surface.

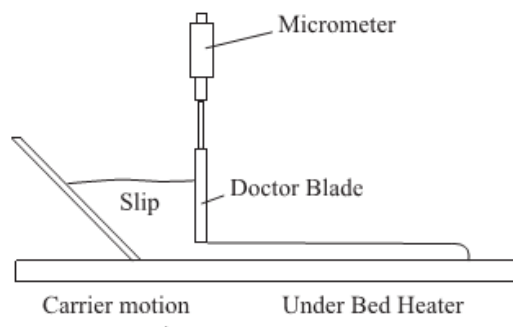


Figure 2: sheme of tape cast set up

The sample were then heated to the temperature of 650°C by heating rate of 100°C/hr and held at that temperature for 2h to remove binder and other organic additives. The resulted porous thin films were then immersed in solution of yttrium nitrate for 10 minutes and after drying under atmospheric condition, the impregnated samples were heated to 450 °C to decompose yttrium nitrate to oxide. The samples were then sintered at 1450 °C for 2h. Density of the samples was measured by Archimedes method.

Microstructure and phase assemblage of samples were investigated by SEM and XRD respectively. The hardness and toughness of the thin composite films were measured by Vickers microhardness method. The fracture toughness of the samples was calculated by Anstis formula[15].

Result and discussion

The final goal of tape casting is to prepare uniform and defect free thin tapes which is controlled by various processing variables including powder characteristics, additives content and casting parameters which are of course interrelated. In this study we found that the optimum amount of glycerin as a plasticizer and polyvinyl alcohol as a binder were respectively 11 and 7 wt.% (based on powder weight). Any deviation from this compositions caused wrapping (Figure 3a), central cracks (Figure 3b) wrinkling (Figure 3c) and sticking of the tape to the substrate. It was found that increasing binder content reduce crack formation which is due to increased strength of green tapes.

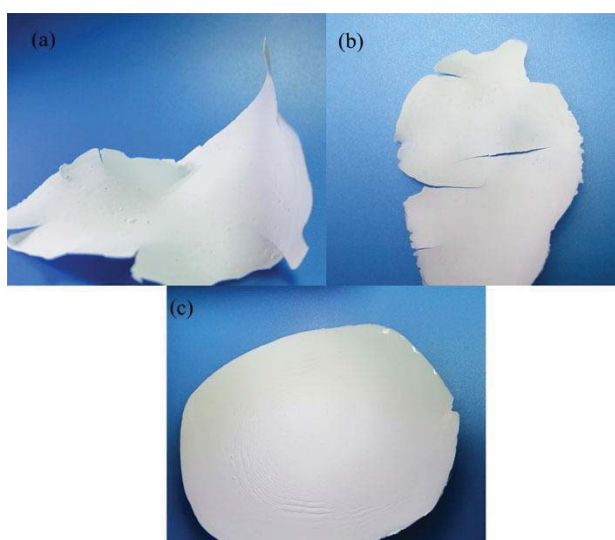


Figure 3: Various defect of tape casting including wrappe(a), central crack (b) and wrinkling(c)

Increasing glycerin increase plasticity of the green tapes which releases stress during drying and increase formability of the tapes. The density and thickness of the tapes after sintering are presented in Table 1. The SEM image of the cross section and surface of the sample is presented in Figure 4. As can be seen high density crack free samples with uniform grain size has been obtained. The result of XRD analysis is shown in Figure 5. The impregnated sample consists of both cubic and tetragonal phases (Figure 5a). Increasing the amount of yttria by increasing the impregnation cycles can create samples with only cubic phases (Figure 5b). According to XRD analysis, by controlling the impregnation process the phase composition of the samples can be controlled. The phase content of the sample controls the electrical and mechanical properties of the samples, both of which are critical for proper performance of thin solid electrolytes.

Table 1

Sample	Thickness (μm)	Density (gr/cm^3)
Composite 3YSZ/8YSZ	140~340	5.9

The mechanical properties of the composite samples are presented in Table 2. The mechanical properties of pure 3YSZ are also presented for sake of comparison. The composite sample which is composed of cubic and tetragonal phases has lower toughness which is due to presence of cubic phase. The toughness of composite sample is higher than the reported fracture toughness of pure cubic zirconia.

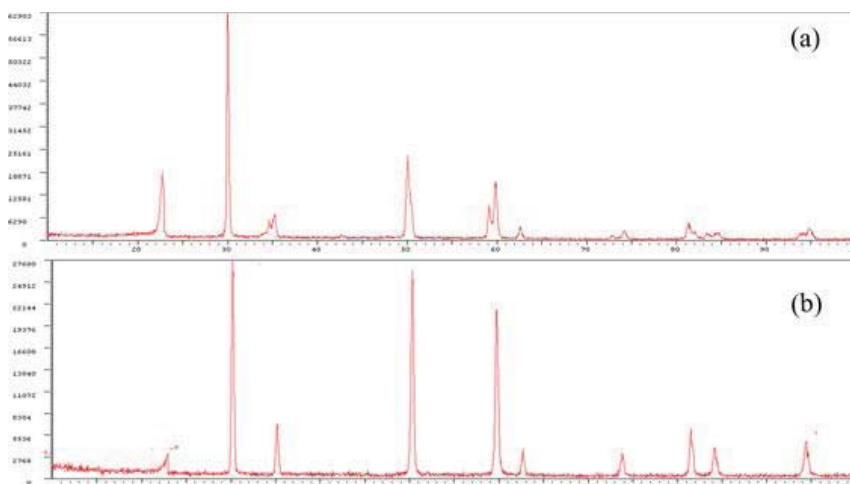


Figure 5: XRD result of composite samples with single(a) and multi impregnation(b)

Table 2

Sample	Hardness(GPa)	Fracture toughness($\text{MPa m}^{1/2}$)
Composite 3YSZ/8YSZ	13	5.8
Pure 3YSZ	13	2.4



Conclusions

It was found that the proper amount of the plasticizer and binder for preparation of defect free thin tape of yttria stabilized zirconia was 11 and 7 wt.% (based on powder weight) respectively. In addition the amount of the tetragonal and cubic phases can be controlled by the number of yttria impregnation process. Increasing amount of yttria increase the amount of the cubic phases which cause reduction of fracture toughness.

References

- [1] S.C. Singhal, K. Kendall, High Temperature Solid Oxide Fuel Cells: Fundamentals, Design and Applications, first edition, Elsevier Ltd., 2003.
- [2] S.P.S. Badwal, Zirconia-based solid electrolytes – microstructure, “stability and ionic-conductivity”, Solid State Ionics, (1992), 52, 23.
- [3] Y. Arachi, H. Sakai, O. Yamamoto, Y. Takeda, N. Imanishai, “Electrical conductivity of the ZrO₂-Ln (2) O (3) (Ln = lanthanides) system, Solid State Ionics, (1999), 121, 133–139.
- [4] A.J. Feighery, J.T.S. Irvine, “Effect of alumina addition upon electrical properties of 8mol.% yttria-stabilised zirconia”, Solid State Ionics, (1999), 121, 209.
- [5] J. Kondoh, H. Shiota, K. Kawachi, T. Nakatani, “yttria concentration dependence of tensile strength in yttria-stabilized zirconia”, Journal of Alloys and Compounds, (2004), 365, 253–258.
- [6] P. Timakul, S. Jinawath, P. Aungkavattana, “Fabrication of electrolyte materials for solid oxide fuel cells by tape-casting”, Ceramics International, (2008), 34, 867–871.
- [7] M. Ghatee, M.H. Shariat, J.T.S. Irvine, “Investigation of electrical and mechanical properties of 3YSZ/8YSZ composite electrolytes”, Solid State Ionics, (2009), 180, 57–62.
- [8] S.C. Singhal, “Solid oxide fuel cells for stationary, mobile, and military applications”, Solid State Ionics, (2002), 152, 405-410.
- [9] W. Weppner, “Tetragonal zirconia polycrystals - a high performance solid oxygen ion conductor”, Solid State Ionics, (1992), 52, 15-21.
- [10] R.E. Mistler, E.R. Twiname, Tape Casting - Theory and Practice, first edition, The American Ceramic Society, (2000), Ohio, US.
- [11] N. Hashimoto, S. Nijjima, J.-I. Inagaki, “Fabrication of 80 mm diameter-sized solid oxide fuel cells using a water-based NiO-YSZ slurry”, Journal of the European Ceramic Society, (2009), 29, 3039–3043.
- [12] M. Cologna, A.R. Contino, D. Montinaro, V.M. Sglavo, “Effect of Al and Ce doping on the deformation upon sintering in sequential tape cast layers for solid oxide fuel cells”, Journal of Power Sources, (2009), 193, 80–85.



- [13] F. Snijkers, A. de Wilde, S. Mullens, J. Luyten, “Aqueous tape casting of yttria stabilised zirconia using natural product binder”, *Journal of the European Ceramic Society*, (2004), 24, 1107–1110.
- [14] L.F.G. Setz, I. Santacruz, M.T. Colomer, S.R.H. Mello-Castanho, R. Moreno, “Fabrication of Sr- and Co-doped lanthanum chromite interconnectors for SOFC”, *Materials Research Bulletin*, (2011), 46(7), 983–986.
- [15] G.R. Anstis, P. Chantikul, B.R. Lawn, D.B. Marshall, “A Critical Evaluation of Indentation Techniques for Measuring Fracture Toughness: I, Direct Crack Measurements”, *J. Am. Ceram. Soc.*, (1981), 64, 533-538.



An analytic and numerical modeling of a membrane humidifier for PEM fuel cell

Nasser Baharlou Houreh^{1*}, Ebrahim Afshari^{2*}

**Department of Mechanical Engineering, Faculty of Engineering, University of Isfahan, Isfahan, Iran*

1- E-mail address: Nasser.baharloo@yahoo.com

2- E-mail address: e.afshari@eng.ui.ac.ir (E. Afshari)

Abstract

The performance of a proton exchange membrane fuel cell (PEMFC) is intensively depends on the proper humidification. A membrane humidifier is mainly applied to the external humidification of PEM fuel cell. In the present study, an analytical (thermodynamic) and numerical (two-dimensional CFD) steady state model developed for a plate-and-frame membrane humidifier for PEM fuel cell. The results show that the water transfer rate increases with an increase in the inlet flow rate at wet side, and an increase in the average temperature of system. The value of RH decreases noticeably as gas flow channel height increases. By employing these models many parameters can be studied such as all geometric parameters, membrane properties (porosity, permeability and thickness) and operation conditions.

Keywords: membrane humidifier, water transport, thermodynamic model, CFD

1 Introduction

Water management is extremely important for balancing the operation of PEM fuel cells [1]. One critical requirement for operated PEM fuel cell is to provide high water content in the electrolyte to ensure high ionic conductivity [2]. To avoid flooding while maintaining proper membrane hydration to achieve the best possible performance an appropriate water balance in the cell is essential [3]. To date, a variety of methods have been developed to make the membrane well humidified, and they are mainly categorized into external humidification and internal humidification [4]. The internal humidification include: Stack-Integrated Humidifiers [5], Steam or Liquid Water Injection [6], Alternate Membrane Chemistry [7] and Passive water distribution [8]. The external humidification contains: bubble humidifiers [9], direct water vapor injection in to the reactant gases, enthalpy wheel exchanger [10] and membrane humidification [11-16]. In the membrane humidifier, dry gas, which flows through one channel, is humidified and heated by the gas or liquid going through another channel. The membrane humidifier is mainly used for gas humidification [11]. Kang et al. [12] and. Park et al. [13] developed models for a shell-and-tube membrane humidifier. They investigated the effect of operating conditions and geometric parameters on the humidifier performance. An experimental study and thermodynamic modeling for a membrane humidifier for PEM fuel cell were performed by Chen et al. [14&15]. Their modeling was performed to identify the minimum number of units essential for a target fuel cell stack. Yu et al. [16] proposed a static model for a planar membrane humidifier. They investigated the effect of the humidity of the wet gas, membrane thickness and channel length on humidifier performance. Bhatia et al [17]

employed an analytical method to do sensitivity analysis. The results show that neglecting the effect of mass transfer on heat transfer would result in a wrong prediction of humidity and temperature.

2 Analytic Modeling of Membrane Humidifier

Humidifier is a thermodynamic system. Based on the first law of thermodynamics, as indicated in figure 1 the governing equation for control volumes 1 and 2:

$$\dot{m}_{1,v,out} + \dot{m}_{1,v,in} + \dot{m}_{1,v,mem} = \dot{m}_{1,v,out} + \dot{m}_{1,v,in} + \dot{m}_{1,v,mem} + \dot{m}_{1,v,mem} \quad (1)$$

$$\dot{m}_{2,v,out} + \dot{m}_{2,v,in} + \dot{m}_{2,v,mem} = \dot{m}_{2,v,out} + \dot{m}_{2,v,in} + \dot{m}_{2,v,mem} + \dot{m}_{2,v,mem} \quad (2)$$

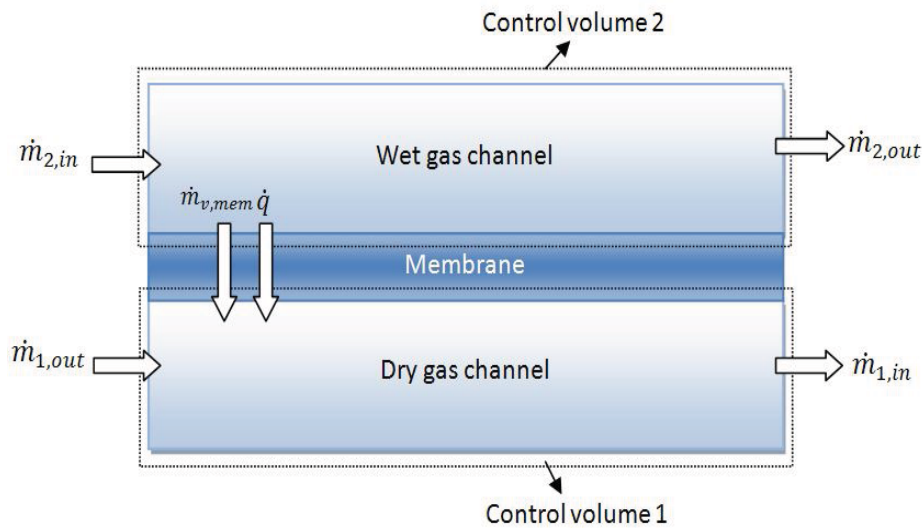


Figure1: A schematic of a membrane humidifier

In previewed equations $\dot{m}_{1,v,out}$, $\dot{m}_{1,v,in}$, $\dot{m}_{1,v,mem}$, $\dot{m}_{1,v,mem}$, are air and vapor mass flow rate entering and leaving control volume 1 and $\dot{m}_{2,v,out}$, $\dot{m}_{2,v,in}$, $\dot{m}_{2,v,mem}$, $\dot{m}_{2,v,mem}$ are air and vapor mass flow rate entering and leaving control volume 2 obtained by equations 3 to 8.

$$\dot{m}_{1,air,in} = \frac{1}{1+\omega_{1,in}} \dot{m}_{1,in} \quad (3)$$

$$\dot{m}_{2,air,in} = \frac{1}{1+\omega_{2,in}} \dot{m}_{2,in} \quad (4)$$

where $\omega_{1,in}$ and $\omega_{2,in}$ are humidity ratio of CV1 and CV2.

Mass conservation resulted in:

$$\dot{m}_{1,air,in} = \dot{m}_{1,air,out}, \quad \dot{m}_{1,v,in} + \dot{m}_{v,mem} = \dot{m}_{1,v,out} \quad (5) \text{ and } (6)$$

for CV1, and

$$\dot{m}_{2,air,in} = \dot{m}_{2,air,out}, \dot{m}_{2,v,in} - \dot{m}_{v,mem} = \dot{m}_{2,v,out} \quad (7) \text{ and } (8)$$

for CV2.

$\dot{m}_{v,mem}$ is the vapor mass flow rate transferred from CV2 to CV1 throw membrane. \dot{q} is the heat transferred from CV2 to CV1.

The parameter h shows the enthalpy and h_{mem} can be expressed as:

$$h_{mem} = C_{p,v} \cdot T_{mem} \quad (9)$$

where $C_{p,v}$ is vapor specific heat and is determined by following equation:

$$C_{p,v} = 1.79 + 0.107\left(\frac{T}{1000}\right) + 0.506\left(\frac{T}{1000}\right)^2 - 0.2\left(\frac{T}{1000}\right)^3 \quad (10)$$

where T is in term of Kelvin. T_{mem} is membrane temperature and approximated as:

$$T_{mem} = \frac{T_{1,out} + T_{2,out}}{2} \quad (11)$$

2.1 Vapor mass transfer

By assuming that the amount of transferred vapor mass is equal to the membrane vapor diffusion rate, it can be determined as follow:

$$\dot{m}_{v,mem} = D_w \frac{C_2 - C_1}{t_m} M_v A \quad (12)$$

M_v is vapor molar mass, A is the membrane cross section area, C1 and C2 represent water concentrations in CV1 and CV2, respectively. D_w is determined by the following empirical equation

$$D_w = D_\lambda e^{2416 \left(\frac{1}{298} - \frac{1}{T_{mem}} \right)} \quad (13)$$

The coefficient D_λ is determined empirically as follow:

$$D_\lambda = \begin{cases} 10^{-6} & \lambda_m < 2 \\ 10^{-6}(1 + 2(\lambda_m - 2)) & 2 \leq \lambda_m \leq 3 \\ 10^{-6}(1 - 1.67(\lambda_m - 3)) & 3 < \lambda_m < 4.5 \\ 1.25 \times 10^{-6} & \lambda_m \geq 4.5 \end{cases} \quad (14)$$

where λ_m is the membrane water content, and is obtained as:

$$\lambda_m = 0.043 + 17.81a_m - 39.85a_m^2 + 36.0a_m^3 \quad (15)$$

where a_m is the membrane relative humidity(RH) and assumed to be:

$$a_m = \frac{\phi_1 + \phi_2}{2} \quad (16)$$

where ϕ_1 and ϕ_2 are the RH of CV1 and CV2 and are determined as:

$$\phi_1 = \phi_{1,out} = \frac{P_{2,out}\omega_{2,out}}{P_{2,sat}(\omega_{2,out} + \beta)}, \quad \phi_2 = \phi_{2,out} = \frac{P_{2,out}\omega_{2,out}}{P_{2,sat}(\omega_{2,out} + \beta)} \quad (17) \text{ and } (18)$$

where $\beta = \frac{M_v}{M_{air}}$

The water concentrations in CV1 and CV2 are obtained as:

$$C_1 = \frac{\rho_{m,dry}}{W_{m,dry}} \lambda_1, \quad C_2 = \frac{\rho_{m,dry}}{W_{m,dry}} \lambda_2 \quad (19) \text{ and } (20)$$

where $\rho_{m,dry}$ is the membrane dry density, $W_{m,dry}$ is the membrane dry equivalent weight. λ_1 and λ_2 represent water content of CV1 and CV2 and can be written as:

$$\lambda_1 = 0.043 + 17.81\phi_1 - 39.85\phi_1^2 + 36.0\phi_1^3 \quad (21)$$

$$\lambda_2 = 0.043 + 17.81\phi_2 - 39.85\phi_2^2 + 36.0\phi_2^3 \quad (22)$$

2.2 Heat transfer

The heat transfer rate is determined as:

$$\dot{q} = UA\Delta T, \quad \Delta T = \frac{(T_{2,in} - T_{1,in}) - (T_{2,out} - T_{1,out})}{\ln((T_{2,in} - T_{1,in}) / (T_{2,out} - T_{1,out}))} \quad (23) \text{ and } (24)$$

where ΔT is the log mean temperature difference between the two control volumes and determined as:

U is the total heat transfer coefficient defined as:

$$U = \frac{\bar{h}}{2}, \quad \bar{h} = \frac{kNu}{D_h} \quad (25) \text{ and } (26)$$

where k is the thermal conductivity, Nu is the Nusselt number, and D_h is the channel hydraulic diameter.

3 Mathematical modeling

The two-dimensional single-phase model domain consists of the following subregions: the dry gas channel, the wet gas channel and membrane as shown in Fig. 1.

3.1 Governing equations

In contrast to the usual approach which employs a separate differential for different subregions, here a unified single-domain approach with a single set of governing equations is applied to all sub-regions. In the developed single-domain method, one set of conservation equations is considered for different regions of humidifier [1]. Thus, under the above mentioned assumption, the model has a set of coupled non-linear partial differential equations. The relevant equations are presented in Table 1. In these equations, \vec{u} , ρ , p and μ are mixture velocity, density, pressure and gas mixture viscosity, respectively. ϵ is volume fraction of membrane. In channels this parameters value is equal to 1. C is the total concentration of water vapor transferred throw membrane and D_w is the diffusivity of water in membrane that was defined in eq(13).

3.2 Boundary conditions

Equations of conservations of mass, momentum, heat and species, form a complete set of governing equations for five unknowns: u, v, p and T. Solving these equations needs to

specify the suitable boundary conditions. No-flux condition is applied to the equations for flow and transport at all boundaries except inlet and outlet channel. Fully developed flow with a given back pressure is assumed to take place at the outlet.

3.3 Numerical procedures

The geometry is given in Fig. 1 with the specifications listed in Table 2. The governing equations were discretized using a finite-volume method and solved using a computational fluid dynamic code. In this code, the pressure and velocity fields are treated with the SIMPLE pressure correction algorithm, where a single-domain model is used. Stringent numerical tests were carried out to ensure that the solution was independent of grid size. 100 grids along the channel and 50 grids along the thickness of each channel width and membrane were used. The coupled set of equations was solved iteratively, and the solution was checked to be convergent when the relative error in each field between the two consecutive iterations was less than 10^{-6} .

Table1. Governing equations for a two-dimensional model.

	Conservation equation	Number of equation
Mass	$\nabla \cdot (\varepsilon \rho \vec{u}) = 0$	(27)
Momentum	$\frac{1}{\varepsilon^2} \nabla \cdot (\rho \vec{u} \vec{u}) = -\nabla p + \nabla \cdot (\mu \nabla \vec{u}) + S_u$ $S_u = -\frac{\mu}{K} \vec{u}$	(28)
heat	$\nabla \cdot (\rho \vec{u} C_p T) = \nabla \cdot (K \nabla T)$	(29)
Species	$\nabla \cdot (\vec{u} C) = \nabla \cdot (D_w \nabla C)$	(30)

4 Results and discussion

In this study, the performance of a membrane humidifier was investigated in terms of, mass flow rate, relative humidity and temperature. The parameters of the humidifier system are listed in Table 2.

The following assumptions are made in implementing the models, (i) steady-state flow, (ii) ideal gas mixtures, (iii) laminar and incompressible flow with low Reynolds numbers and pressure gradients, (iv) constant viscosity of gas mixture is calculated for the inlet condition, (v) isotropic and homogeneous membrane characterized by effective porosities and permeabilities, (vi) well insulated from its surroundings, (vii) neglected the kinetic and potential energies of the gas molecules, (viii) No external work, (ix) constant specific heats, (x) constant total convection heat transfer coefficient and (xi) ignored diffusion of air across the membrane.

As shown in figure 2 when the gas flow rate at dry side inlet increases, relative humidity at dry side outlet for a carrier gas declines intensely. As shown in figure 3 increasing in wet gas flow rate resulted in higher vapor transfer rate and the High temperature for membrane resulted in high vapor transfer rate. When the membrane temperature increases the effect of wet inlet gas flow rate on vapor transfer rate throw membrane increases. It should be considered that high temperature and high wet flow rate can cause danger for durability of membrane, therefore these parameters value should be optimized.

Table2. Dimensional parameters and transport properties.

Description	Unit	Value
Dimensional parameters		
Channel length	mm	70
Flow channel height	mm	1
Flow channel width	mm	1
Membrane thickness	μm	25
Operating conditions		
Dry side inlet temperature, T	K	305
Wet side inlet temperature, T	K	345
Pressure, P	kPa	101.325
Relative humidity at dry side inlet	%	0
Relative humidity at wet side inlet	%	100.
Transport parameters		
Air specific heat, C_p	kJ/kg.k	1.007
Vapor specific heat, C_v	kJ/kg.k	1.88
Gas viscosity, μ	Pa.s	1.88×10^{-5}
Air thermal conductivity, K	W/m.K	0.028
Nusselt number	-	5.4
Material properties		
Membrane porosity, ε		0.6
Membrane permeability, K	m^2	10^{-9}
Membrane dry density, $\rho_{m,dry}$	kg/cm^3	0.001
Membrane dry equivalent weight, $W_{m,dry}$	kg/mol	1.0

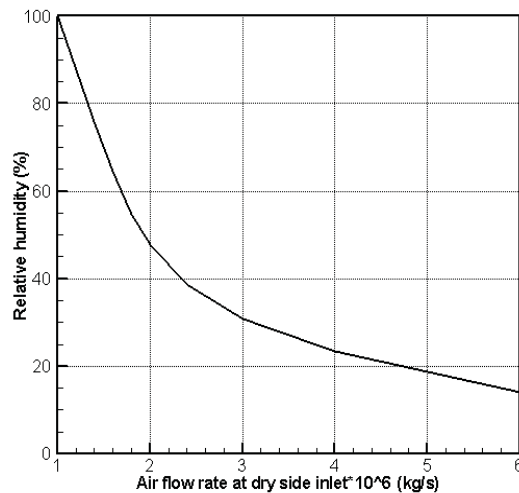


Figure 2: effect of air flow inlet rate on the RH of outlet air

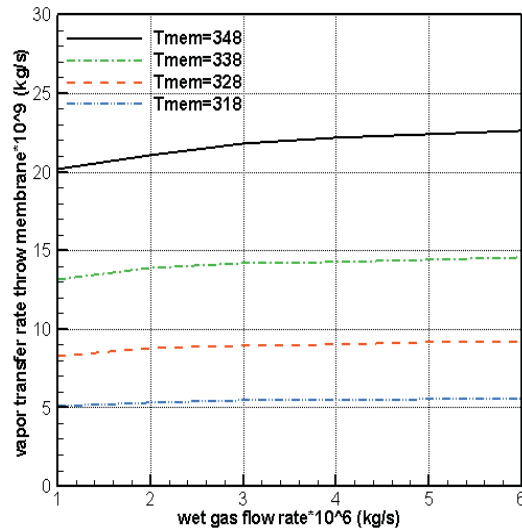


Figure 3: effect of wet gas flow inlet rate on the vapor transfer rate at various membrane temperatures

Fig. 4 indicates the values of RH at dry side outlet with different gas flow channel height. The value of RH decreases noticeably as gas flow channel height increases. By the increasing air flow rate at dry side inlet RH decreases intensively. Figure 5 exhibits the distribution of water concentration in whole 2-dimensional model. In this figure and figure 6 can be seen obviously that the concentration of water at wet side decreases along channel. The water transferred from wet side to dry side causes an increase in water concentration at dry side, thus at the outlet, gases leave dry and wet channel at the same water molar fraction.

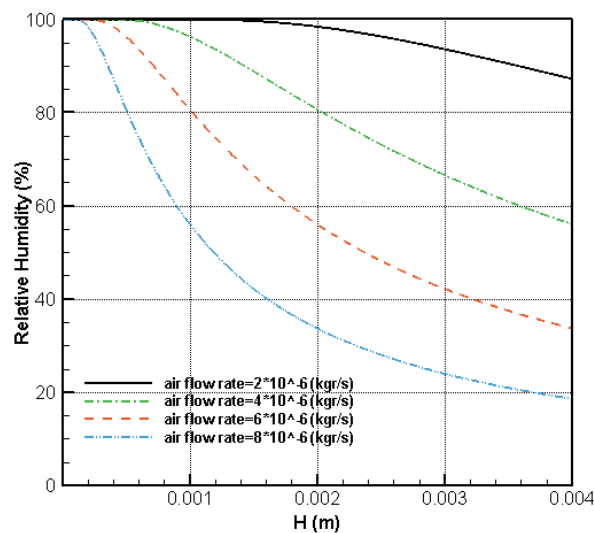


Figure 4: effect of gas flow channel height on RH at dry side outlet at various air flow rates

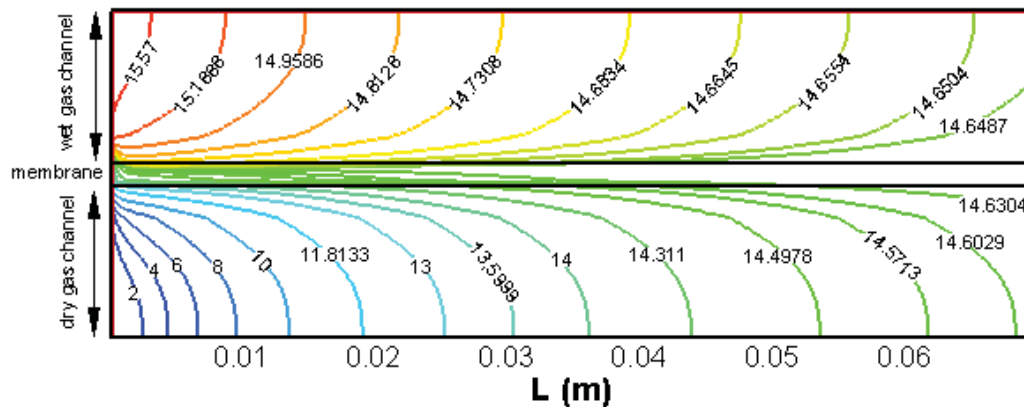


Figure 5: water vapor molar concentration in terms of mol/m³

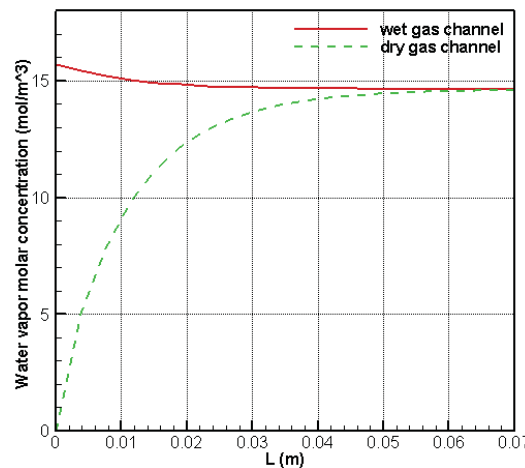


Figure 6: water concentration distribution along wet and dry channels

5- Conclusion

An analytic modeling and two-dimensional mathematical model (CFD) is performed for a plate-and-frame membrane humidifier for PEM fuel cell. . By employing these models many parameters can be studied such as all geometric parameters, membrane properties (porosity, permeability and thickness) and operation conditions. The water transferred from wet side to dry side resulted in an increase in water concentration at dry side. It is shown that the water transfer rate increases with an increase in the inlet flow rate at wet side, and an increase in the average temperature of system (membrane temperature). The value of RH decreases noticeably as gas flow channel height increases. Also by the increasing air flow rate at dry side inlet RH decreases intensively. By employing these models many parametric studies can be performed and models can be utilized to proper design of membrane humidifier for PEM fuel cells.

Acknowledgments

The authors are grateful for the financial support of the Renewable Energy Organization of Iran [SUNA].

References

1- E. Afshari and S.A. Jazayeri, “Analyses of heat and water transport interactions in a proton exchange membrane fuel cell, J. of Power Sources, (2006) 194, 423–432.



- 2- Z.M. Wan , J.H. Wan, J. Liu, Z.K. Tu, M. Pan, Z.C. Liu and W. Liuc, “Water recovery and air humidification by condensing the moisture in the outlet gas of a proton exchange membrane fuel cell stack”, Applied Thermal Engineering (2012). 42, 173-178.
- 3- B.J. Kim and M.S. Kim, “Studies on the cathode humidification by exhaust gas recirculation for PEM fuel cell”, Int. J. of hydrogen energy, (2012). 37, 4290e4299.
- 4- T. Kitahara, H. Nakajima and M. Morishita, “Water vapor exchange system using a hydrophilic microporous layer coated gas diffusion layer to enhance performance of polymer electrolyte fuel cells without cathode humidification”, J. of Power Sources, (2012). 214, 100-106.
- 5- M. Santis, D. Schmid, M. Ruge, S. Freunberger, and F. Büchi, “Modular Stack-Internal Air Humidification Concept-Verification in a 1 kW Stack”, Fuel Cells,(2004). 4(3), 214-218.
- 6- D.L. Wood, J.S. Yi, and T.V. Nguyen, “Effect of direct liquid water injection and interdigitated flow field on the performance of proton exchange membrane fuel cells”, Electrochimica Acta, (1998). 43(24), 3795-3809.
- 7- M. Han, S. Chan, and S. Jiang, “Investigation of self-humidifying anode in polymer electrolyte fuel cells”, Int. J. of hydrogen energy, (2007), 32(3), 385-391.
- 8- S. Ge, X. Li, and I. Hsing, “Internally humidified polymer electrolyte fuel cells using water absorbing sponge,” Electrochimica Acta, (2005). 50(9), 1909-1916.
- 9- G. Vasu, A.K. Tangrila, B. Viswanathan and K.S. Dhathathreyan, “Continuous bubble humidification and control of relative humidity of H₂ for a PEMFC system”, Int. J. of Hydrogen Energy, (2008). 33, 4640-4648.
- 10- A. Casalegno, S.D. Antonellis, L. Colombo and F. Rinaldi, “Design of an innovative enthalpy wheel based humidification system for polymer electrolyte fuel cell”, Int. J. of Hydrogen Energy, (2011). 36, 5000-5009.
- 11- S. Kang, K. Min and S. Yu, “Dynamic modeling of a proton exchange membrane fuel cell system with a shell-and-tube gas-to-gas membrane humidifier”, Int. J. of Hydrogen Energy, (2012). 37, 5866-5875.
- 12- S. Kang, K. Min and S. Yu, “Two dimensional dynamic modeling of a shell-and-tube water-to-gas membrane humidifier for proton exchange membrane fuel cell”, Int. J. of Hydrogen Energy, (2010). 35, 1727–1741.
- 13- S.Y. Park, S.Y. Choe and S.H. Choi, “Dynamic modeling and analysis of a shell-and-tube type gas-to-gas membrane humidifier for PEM fuel cell applications”, Int. J. of Hydrogen Energy, (2008). 33, 2273–2282.
- 14- D. Chen, W. Li and H. Peng, “A thermodynamic model of membrane humidifiers for PEM fuel cell humidification control”, J. Power Sources, (2008). 180, 461–467.
- 15- D. Chen and H. Peng, “A Thermodynamic Model of Membrane Humidifiers for PEM Fuel Cell Humidification Control”, J. of Dynamic Systems, Measurement, and Control, (2005). 127, 424-432.
- 16- S. Yu, S. Im, S. Kim, J. Hwang, Y. Lee, S. Kang and K. Ahn, “A parametric study of the performance of a planar membrane humidifier with a heat and mass exchanger model for design optimization”, Int. J. Heat Mass Transfer, (2011). 54, 1344–1351.
- 17- D. Bhatia, M. Sabharwal and C. Duell, “Analytical model of a membrane humidifier for polymer electrolyte membrane fuel cell systems”, Int. J. of Heat and Mass Transfer, (2013). 58, 702–717.



Synthesis of nanocatalysts of graphene oxide/TiO₂/Pt and study of its characterization

Parvin Alizadeh Eslami^{1*}, Parisa Mohammad Jafarieh¹, Maliheh Amirzehni¹

1. Applied Chemistry Department, Tabriz Branch, Islamic Azad University, Tabriz, Iran

Abstract

Polymer Electrolyte Fuel Cell (PEMFCs) convert directly the chemical energy of hydrogen into electrical energy. Graphene is a layer of carbon atoms, connected in a hexagonal 2-D crystalline lattice. Graphene sheets have excellent mechanical, electrical, thermal and optical properties. Graphene oxide (GO) is easy to functionalize. In this project, the GO nanosheet was synthesized using the simplified Hummers method. The FT-IR results confirmed the existence of oxygen-containing groups on the GO nanosheets. Titanium oxosulfate (TiOSO₄), and hexachloroplatinic acid (H₂PtCl₆), were used as the source of titanium and platinum, respectively. TiO₂/Graphene oxide catalysts have been successfully prepared with graphene oxide and TiOSO₄ in an initial reaction, titanium induced by the hydrolysis of TiOSO₄ diffused into the graphene oxide interlayer using the hydrothermal method and ultrasonic. Pt nanoparticles were added to TiO₂/GO to study for an increase in efficiency on the performance of a proton exchange membrane fuel cell. The structure and composition of the nanocatalyst have been characterized by X-ray diffraction, and FT-IR.

Keywords: Proton exchange membrane fuel cell, Graphene oxide, GO/TiO₂/Pt nanocatalyst

1. Introduction

Proton exchange membrane fuel cells (PEMFCs) have attracted great attention as alternative clean energy technologies for transportation vehicles, small-scale portable electronics and stationary power supplies [1]. Low operating temperature and zero/low emissions have made PEM fuel cells the most promising fuel cell technology for the future as a potential alternative power source [2, 3]. During the last decade, carbon-based nanomaterials such as carbon nanotube (CNT), fullerene and graphene have gained considerable interest because of their potential use as multifunctional materials and wide range of applications in different kinds of devices [4]. The goal is to utilize these carbon nanostructures as highly conductive carbon scaffolds to attain large surface areas on which to disperse platinum nanoparticles. Other nanostructured materials with large surface areas and high conductivity have also been tested as supports for dispersing electrocatalysts [5-7]. Graphene, a monolayer of carbon atoms in a crystal lattice, has received attention as a substrate or a nanocomposite with metallic particles for various applications [8]. Recently, graphene has been studied as a catalyst support in PEM fuel cells due to its basal plane structure with high surface area and high conductivity [9, 10] and minimizing the use of precious metals, typically Pt. Such support materials not only maximize the availability of nanosized electrocatalyst surface area for electron transfer but also provide better mass transport of reactants to the electrocatalyst. Graphene is a single sheet of sp² hybridized carbon that can be exfoliated from bulk graphite using mechanical cleavage, thermal exfoliation, and chemical functionalization. Though the chemical oxidation method is convenient to exfoliate graphene sheets via



solution based processes, it introduces functional groups such as carboxyl and epoxides. The presence of these functional groups makes the individual graphene oxide sheets suspend able in both polar and nonpolar solvents but drastically decreases the conductivity as a result of a loss in the conjugated sp^2 network. Hydrazine has been widely used by restoring the sp^2 hybridized network. Other reductants such as NaBH_4 and hydroquinone have also been found useful [11]. Recently the deposition of TiO_2 nanoparticles assisted in dispersing graphene oxide sheets in solution. More recently support materials like non-stoichiometric mixture of several titanium oxide phases, TiO_2 , Ti_4O_7 and Ti_5O_9 know Magnnelli phases [12, 13] are available for catalyst supports. In particular, titania has proven to be the most suitable photocatalyst, due largely to its high catalytic activity, long-term stability and low cost. On the other hand, unfortunately, photocatalytic reactions on TiO_2 are normally insufficiently selective: in most cases organic pollutants can be mineralized into CO_2 and H_2O [14]. In recent years, great efforts have been made to develop carbon nanotubes (CNTs)/ TiO_2 or C_{60} / TiO_2 nanocomposite [15]. The coupling of TiO_2 with CNTs or C_{60} has been shown to provide a synergistic effect which can enhance the overall efficiency of a photocatalytic process. Chen et al. [16] studied the method oxidation by Pt-Ru-Ti/C catalysts and reported that the role of Ti is to avoid the agglomeration of catalyst particles Pt and Ru, effectively disperse and control the nanostructure of catalyst. The ability of graphene sheets to support nanoparticles opens new ways to develop electrocatalysts for fuel cell. We now report here the deposition of TiO_2 and Pt nanoparticles on reduced graphene oxide sheets and their utilization in proton exchange membrane. In this work, TiO_2 /Graphene oxide catalysts has been successfully prepared with graphene oxide and TiOSO_4 in initial reaction, titanium induced by the hydrolysis of TiOSO_4 diffused into graphene oxide interlayer with used hydrothermal method and ultrasonic. Pt nanoparticles doped in to TiO_2 /GO to study for increase efficiency on the performance proton exchange membrane fuel cell.

2. Experimental

2.1 Material

Graphene powder, hexachloroplatinic acid (H_2PtCl_6) and titanium oxosulphate (TiOSO_4) were obtained from Sigma-Aldrich. Sulphuric acid of 98% concentration (98% H_2SO_4), Hydrogen peroxide of 30% concentration (30% H_2O_2), Potassium permanganate (KMnO_4), DI water, Sodium nitrate (NaNO_3), sodium borohydride (NaBH_4), Ethylene glycol, Methanol, Ammonia were obtained from Merck.

2.2 Preparation of GO nanosheets

GO nanosheets were prepared by a modified Hummers method [17]. Typically, 100 g graphene powder and 0.05 g sodium nitrate were mixed with 2.3 ml sulfuric acid in a 250 ml flask place in an ice bath. The obtained solution was stirred and slowly added 0.3 g potassium permanganate, the stirring was continued for 2 h. The mixture solution was transferred to a 35 °C water bath and stirred for 30 min. After that, 46 ml of deionized (DI) water was slowly added into the solution and the solution temperature monitored was about 98 °C. The mixture solution was maintained at this temperature by heating for 30 min. Then, 14 ml deionized water and 1 ml of hydrogen peroxide was added sequentially to the mixture solution to terminate the reaction. The observed color of mixture was dark



yellow. The resulting product centrifugation and was filtered by distilled water for several times. Graphene oxide suspension as shown in figer 1.a. The graphene oxide powder was obtained after drying in vacuum at 60°C for 12 h. Finally brown GO powder was obtained.

2.3 Synthesis of GO/TiO₂ nanocatalysts

Firstly, 100 mg GO was dispersed in 200 ml of distilled water under ultrasonic for 2 hours to obtain a well-dispersed GO suspension with a concentration of 0.5 g L⁻¹. Meanwhile, a dilute H₂SO₄ solution (1M) was prepared from concentrated H₂SO₄ and distilled water, and titanium oxosulfate (TiOSO₄) was dissolved in this solution to give a TiOSO₄ concentration of 0.5 M. Secondly, a specific amount of the GO suspension was introduced into 50 ml TiOSO₄ solution with a designed mass ratio of GO to titania (0, 0.1, 0.5, 1 and 2 wt%), and the corresponding final products are denoted as GO_x/TiO₂, where x is (0, 0.1, 0.5, 1 and 2 wt%) respectively. After stirring for another 30 min, the mixed suspension was transferred to a 200 ml Teflon-lined autoclave. This autoclave was sealed and maintained at 180 C° for 6 h. The obtained white or black-white precipitates were collected and washed thoroughly with distilled water and absolute methanol for several cycles, and then dried in vacuum at 80 C° for 12 h to get the GO_x/TiO₂ nanocatalyst. GO_x/TiO₂ nanocatalyst was shown in figure 1.b.

2.4 Synthesis of GO/TiO₂/Pt nanocatalysts

For the synthesis of GO_x/TiO₂-supported Pt amount of GO_x/TiO₂ when X is is 0, 0.1, 0.5, 1 and 2 wt%, was dispersed in ethylene glycol and sonicated for 30 min. then specific amount of hexachloroplatinic acid solution was added into the GO_x/TiO₂ solution and stirred with ultrasonic for 30 min. The pH value of this mixture was adjusted to 10 using ammonia, which could partly protect carboxylic acid groups and then stirred by ultrasonic for 1h. Excessive NaBH₄ aqueous solution with a concentration 2.5 mg ml⁻¹ was slowly added and stirred until to obtain pH value of this mixture was adjusted to 12 this mixture was stirred by ultrasonic for 2h under room temperature. In these cases the suspension was not acidified and the reduction was carried out under the natural pH of the solution. The solution centrifugation at 4500 rpm and washed several time with methanol and DI water, and dried in an oven at 80C° for 12 h. GO_x/TiO₂/Pt nanocatalysts as shown in figure 1.c.

2.5 Characterization

Chemical bonding was analyzed using a Fourier Transformed Infrared (FT-IR) spectrum measured with Bruker Almane FTIR spectrometer in the range of 500 to 4000.

Power X-Ray diffraction (XRD) patterns were obtained with Simens diffractometer D500. The voltage and the applied current were 40Kv and 30 mA., and the 2 theta angular from 2° to 90°.

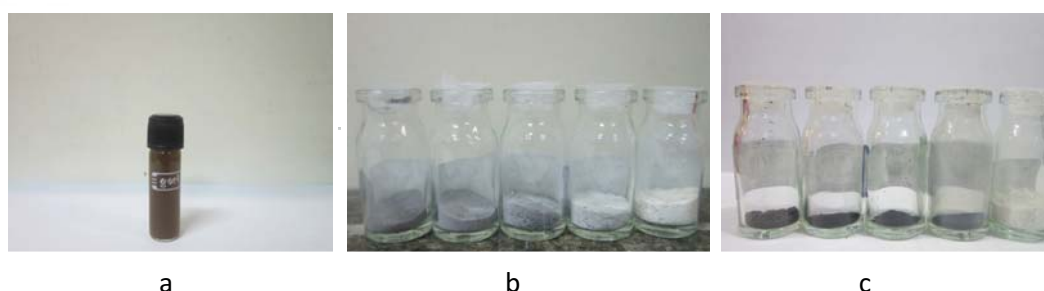


Figure 1: (a) graphene oxide powder, (b) GO_x/TiO_2 nanocatalysts, and (c) $\text{GO}_x/\text{TiO}_2/\text{Pt}$ nanocatalysts

3. Results and Discussion

The characterization FTIR spectrum of graphene and GO nanosheets are depicted figure 2(a,b). It is seen with oxygen containing groups in which the main absorption band at 3424 cm^{-1} is assigned to the O-H group stretching vibrations. The absorption peak at 1725 cm^{-1} and 1623 cm^{-1} can be assigned to C=O stretching of carboxylic and/or carbonyl moiety functional groups. The two absorption peaks at about 1222 cm^{-1} and 1034 cm^{-1} are assigned to the C-O stretching vibration. This supports the fact that GO is a highly absorptive material, as verified by its ability to become a gel-like solution.

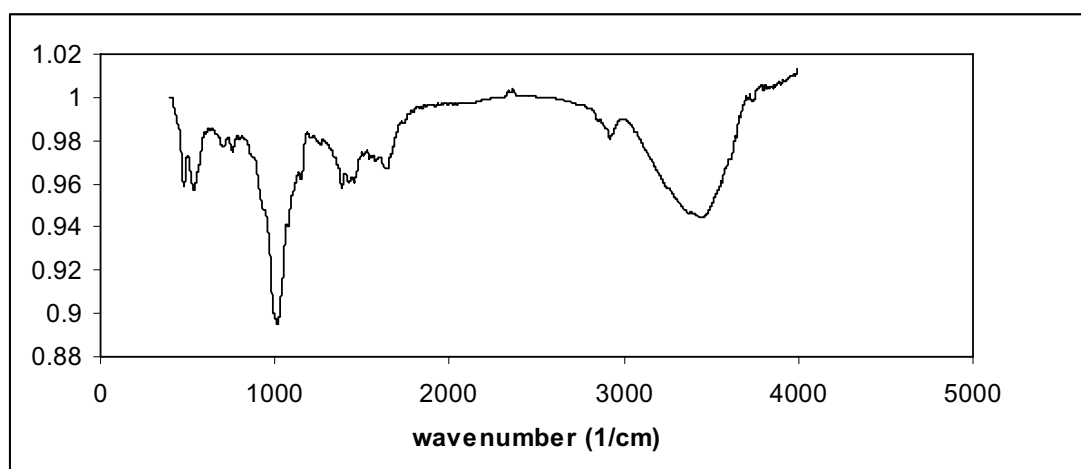


Figure 2a. FTIR spectra analysis of graphene

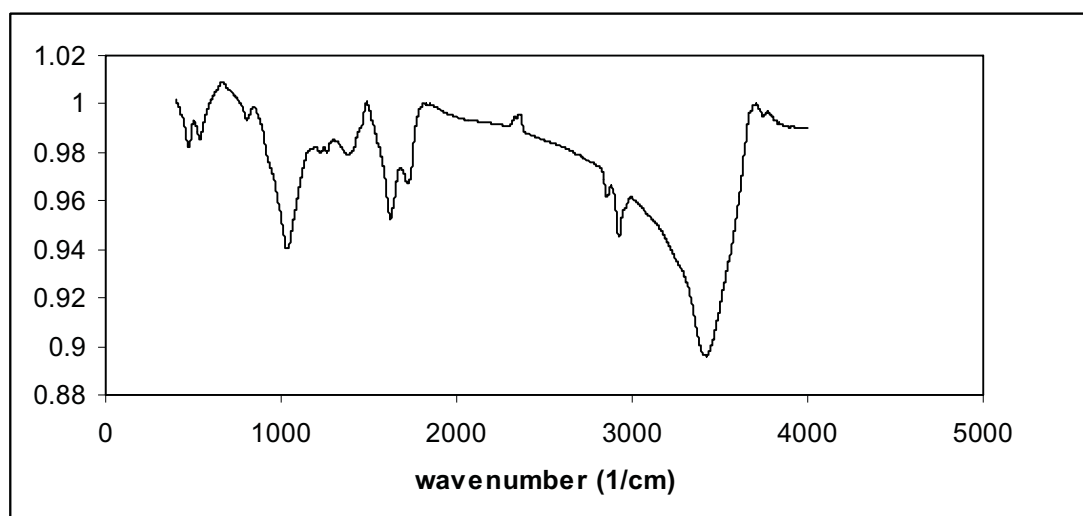


Figure 2b. FTIR spectra analysis of graphene oxide

Figure 3 shows the XRD patterns for GO/TiO₂/Pt nanocatalysts synthesized with different contents of graphene compared to the pure TiO₂. The present peak at 25.3°, 37.8°, 48.1°, 54.0°, and 55.1° clearly represent the formation anatase crystallites. The diffraction peaks at 39.8°, 46.3°, and 67.5° corresponding to Pt in the GO/TiO₂/Pt nanocatalysts. In the Scherrer equation, $\tau = K\lambda/\beta\cos\theta$ where K is the shape factor, λ is the X-ray wavelength, β is the line broadening at half the maximum intensity (FWHM) in radians, and θ is the Bragg angle; τ is the mean size of the ordered (crystalline) domains, which may be smaller or equal to the grain size.

Table1. Grain Size of GO_x/TiO₂/Pt nanocatalysts

sample	TiO ₂	GO _{0.1} /TiO ₂ /Pt	GO _{0.5} /TiO ₂ /Pt	GO ₁ /TiO ₂ /Pt	GO ₂ /TiO ₂ /Pt
Graphene Content (wt %)	0	0.1	0.5	1	2
Average Crystalline size of TiO ₂ / nm	3.82	3.08	2.7	2.9	2.9
Average Crystalline size of Pt/ nm	0	3.3	2.4	2.8	2.3

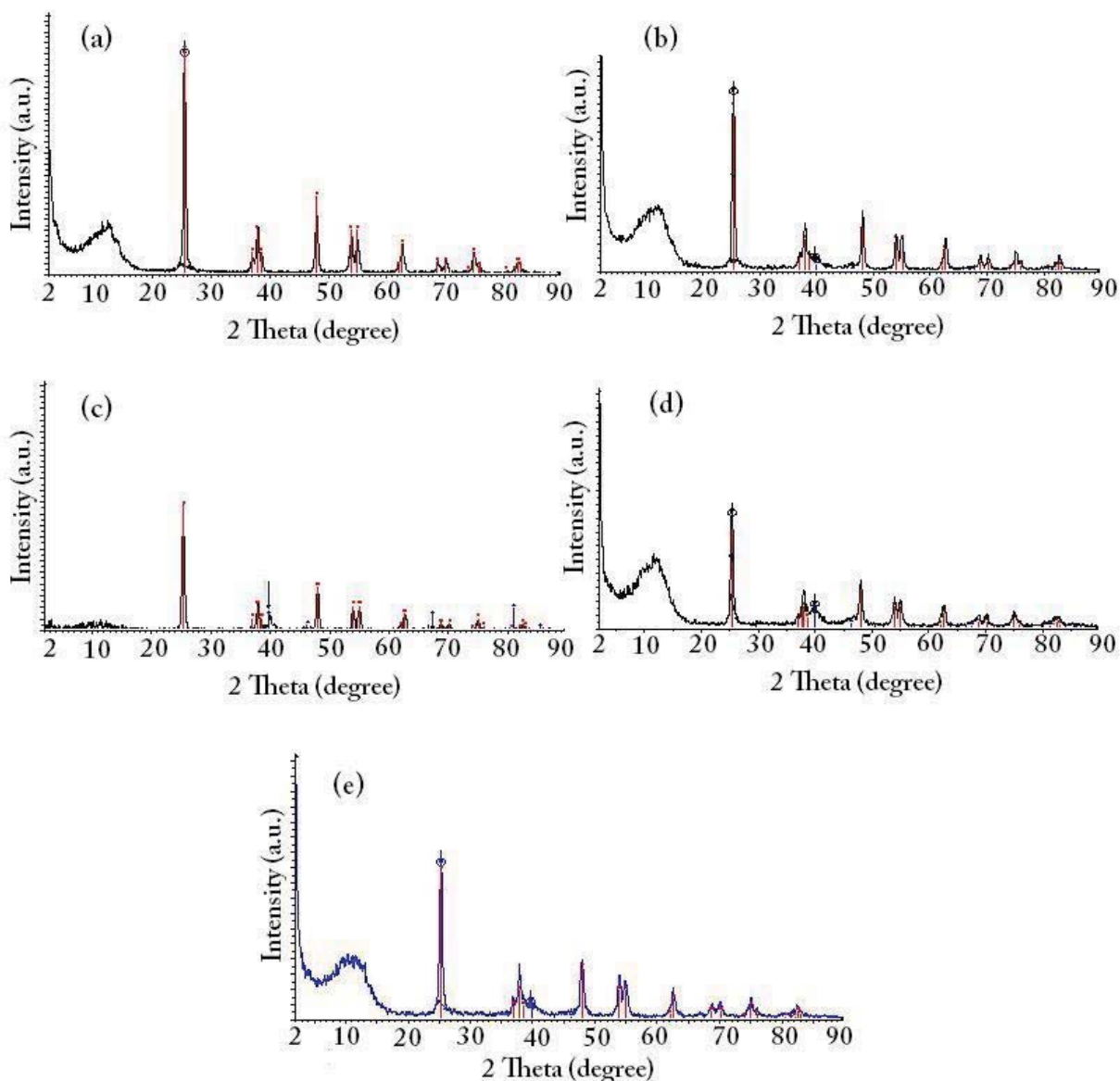


Figure3. XRD patterns of (a) TiO_2 , (b) $\text{GOx/TiO}_2/\text{Pt}$, $x=0.1$, (c) $\text{GOx/TiO}_2/\text{Pt}$, $x=0.5$, (d) $\text{GOx/TiO}_2/\text{Pt}$, $x=1$, (e) $\text{GOx/TiO}_2/\text{Pt}$, $x=2$

Table 1 shows the Crystallite size for nanoparticles of TiO_2 and Pt doped in GO is 2.3- 4nm. Therefore it suggests a very good distribution of nanoparticles on the GO substrate for Fuel cell applications.



References

- [1] B.C.H. Steele, A. Heinzl, Nature, (2001). 414, 345.
- [2] J. Larminie, A. Dicks " Fuel cell explained " , John Wiley & Sons, (2000)
- [3] YM. Ferng, YC. Tzang, BS. Pei, CC. Sun, A. Su. " Analytical and experimental investigation of a proton exchange membrane fuel cell " , Int J Hydrogen Energ., (2004). 29, 381-91.
- [4] S. Stankovich, DA. Dikin, GHB. Dommett, KM. Kohlhaas, EJ. Zimney, EA Stach. Graphene-based composite materials". Nature (2006). 442, 282-286. "
- [5] G. Girishkumar, M Rettker, R. Underhile, D. Bize, K. Vindogopal, P. McGinn, P. Kamat, "Single-wall carbon nanotube-based proton exchange membrane assembly for hydrogen fuel cell". Langmuir., (2005). 21, 8487-8494.
- [6] R.S. Lee, H.J. Kim, J.E. Fischer, A. Thess, R.E Smalley,. "Conductivity enhancement in single-walled carbon nanotube bundles doped with K and Br. Nature" , (1997). 388, 255-257.
- [7] B. Seger, K. Vinodgopal, P.V. Kamat, "Platinum Dispersed on Silica Nanoparticles for PEM Fuel Cells. J. Electroana"l. Chem. (2008). 19, 8-204.
- [8] C.Xu, X. Wang, J. Zhu, Phys. Chem. (2008), 112, 19841.
- [9] Y. Li, L. Tang, J. Li, Electrochem. Commun. (2009), 11, 846.
- [10] B. Segar, P.V. Kamat, J. Phys. Chem C Lett. (2009), 113, 7990.
- [11] Y. Si, E.T. Samulski, "Synthesis of water Soluble Graphene". Nano Lett, (2008). 8, 1679-1682.
- [12] V. Jalan, EJ. Taylor, "Importance of interatomic spacing in Catalytic Reduction of Oxygen in Phosphoric Acid". J. Electrochem. Soc, (1983). 130, 2299-302.
- [13] He, L., Franzen, HF., Vitt, JE., Johnson, DC. "Synthesis and characterization of Pt-Ti4O7 microelectrode arrays". J. Appl. Electrochem, (1996). 26, 758.
- [14] Y. Shiraishi and T. Hirai, J. Photochem. Photobiol., C, (2008). 9, 157, (b) P. Madhusudan, J. Ran, J. Zhang, J. Yu and G. Liu, Appl. Catal., B,(2011), 110, 286.
- [15] Y. Gao, H.T. Liu, M.J. Ma, "Preparation and photocatalytic behavior of TiO 2-carbon nanotube hybrid catalyst for acridine dye decomposition". React Kinet Catal Lett, (2007). 90, 11–18.
- [16] JM. Chen, S. Sarma, CH. Chen, MY. Cheng, SC. Shih, GR. Wang, "Mutli-scale dispersion in fuel cell anode catalysts: Role of TiO2 Towards achieving nanostructured materials", J of power sources, (2006). 159, 29-33.
- [17] WS. Hummers, PE. Offeman, "preparation of graphtic oxide", J Am Chem Soc, (1958). 80, 1339.



Polybenzimidazole/MnTiO₃ nanocomposite membranes for polymer electrolyte membrane fuel cells

Khadijeh Hooshyari^{1,*}, **Mehran Javanbakht**², **Morteza Enhessari**³

Department of Chemistry, Amirkabir University of Technology, Tehran, Iran

khadijeh_hooshyari@yahoo.com

Abstract

PBI (polybenzimidazole)-MnTiO₃ (PMT) nanocomposite membranes have been prepared with solutions casting method. The nanocomposite membranes were characterized by using AC impedance spectroscopy (IS), Fourier transform infrared spectroscopy (FT-IR), scanning electron microscopy (SEM) coupled with energy dispersive x-ray (EDX) and thermogravimetric analysis (TGA). The results showed that the water uptake and proton conductivity of the PMT nanocomposite membranes were higher than that of PBI based membrane because of hydrophilic nature of MnTiO₃ nanoparticles. When the prepared membranes doped with phosphoric acid (PA), due to proton transfer from PA, PA-PMT nanocomposite membranes displayed higher proton conductivity than PMT nanocomposite membranes. Incorporation of nanoparticles in nanocomposite membranes increased the thermal stability of PA-PMT nanocomposite membranes compared with PA-PBI membranes.

Keywords: PEMFC, Polybenzimidazole, Nanocomposite, Proton exchange membrane, Proton conductivity.

1. Introduction

Proton exchange membrane fuel cells (PEMFCs) display the highest power densities compared to the other type of fuel cell [1]. Polyperfluorosulfonic acid (PFSA) membranes, such as Nafion, are the most common type of polymeric membranes used for PEMFC due to their excellent chemical, mechanical, thermal stability and high proton conductivity in their hydrated state [2]. PEMFC based on Nafion membranes have two main limitations. The first one is their high cost. The second is their dehydration at temperatures above 80°C, causing a dramatic decrease in their proton conductivity and mechanical stability [3]. This also limits the working temperature below 80 °C, since the membrane dehydrates and the conductivity decays sharply above this temperature. The development of high-temperature PEM fuel cells (working at 150–200 °C) is pursued worldwide in order to solve the problems of current cells based on Nafion [4].

Commercially available polybenzimidazole (PBI) has been the most extensively studied and used for this application in membranes doped with all sorts of strong inorganic acids [4]. The

¹- Department of Chemistry, Amirkabir University of Technology, Tehran, Iran.

²- Renewable Energy Research Center, Amirkabir University of Technology, Tehran, Iran, mehranjavanbakht@Gmail.com.

³- Department of Chemistry, Naragh Branch, Islamic Azad University, Naragh, Iran, Enhessari@gmail.com



proton conductivity of pure PBI is low. However, its proton conductivity can be improved by adding different acids such as sulfuric acid, PA, perchloric acid, nitric acid, or hydrochloric acid. Among these acids, phosphoric acid is the most widely used. PA has a high boiling point, high thermal stability, and high proton conductivity even in its anhydrous form. The proton conductivities of PA-doped PBI membranes have been extensively investigated [5]. Recently, we introduced new proton conducting hybrid membranes based on poly vinyl alcohol, PVA, and nanoporous silica containing phenyl sulfonic acid[6] and poly (sulfonic acid)-grafted silica nanoparticles[7] for PEM fuel cells.

2. Experimental

2.1. Materials

Polybenzimidazole was obtained from fume tech. Phosphoric acid and N,N-dimethylacetamide (DMAc) were purchased from Merck. Distilled deionised water (DI) was used through all experiments. MnTiO₃ nanoparticles respectively with a particle size range of 22-30 nm, were kindly provided by *Enhessari* research group [8].

2.2. Preparation of membranes

The PBI nanocomposite membranes were prepared by a solution-casting method. In this method, the nanocomposite membranes were fabricated using DMAc as a casting solvent. At room temperature, different weight percentages of nanoparticles were dispersed in DMAc. Then appropriate amounts of commercial PBI powder were added to this homogeneous solution under stirring. The obtained brown solution was cast onto a glass plate and the solvent was evaporated slowly at 120 °C for 5 h. The glass plates were then soaked in a deionized water bath. The membranes were slowly removed from the glass plates. Table 1 gives the names and the detailed process information for the PBI nanocomposite membranes. In this table, UD-PMT and PA-PMT stands for the un-doped PBI-MnTiO₃ and PA-doped PBI-MnTiO₃, nanocomposite membranes respectively.

2.3. Water uptake and acid-doping

The membrane was equilibrated in de-ionized water at room temperature for 24 h. The saturated membrane was removed and the remaining water on the surface was dried by tissue papers, finally weighed instantly. For dried weight, the membrane was dried in oven at 80 °C for 24 h, and then weighed immediately. This process was reiterated for several times until reaching a stable result. The water uptake was calculated by the following equation:

$$\text{water uptake\%} = \frac{W_{\text{wet}} - W_{\text{dry}}}{W_{\text{dry}}} \times 100 \quad (1)$$

Where, W_{wet} and W_{dry} are weights of wet and dry membrane, respectively. Acid-doping level was obtained by a similar manner.

2.4. FT-IR ATR spectra

The FT-IR ATR spectra (600-4000 cm⁻¹, resolution 4 cm⁻¹) were recorded with a Bruker Equinox 55 using an attenuated total reflectance (ATR, single reflection) accessory purged with ultra dry compressed air.

2.5. Proton conductivity measurements



The proton conductivity of membranes was calculated by the AC impedance spectroscopy with PGSTAT303N potentiostat/galvanostat (Ecochemie). The resistance of the membrane was obtained from the high-frequency intercept of the impedance. The conductivity values were calculated by using the equation ($\sigma = L/RS$), where, σ , L, R, S respectively refer to, proton conductivity ($S\text{ cm}^{-1}$), thickness (cm), resistance from the impedance data (Ω) and cross-sectional area (cm^2) of the membranes.

2.6. SEM and EDX measurements

The morphology of nanocomposite membranes were investigated by using a Scanning electron microscopy (SEM), (JSM-5600, Jeol Co.), coupled with energy dispersive x-ray (EDX) spectroscopy. The samples were freeze-fractured in liquid N_2 and coated with gold plate before SEM observations were carried out.

2.7. Thermal properties

Thermogravimetry analysis (TGA) of the nanocomposite membranes were carried out by using a TGA TA Instruments 2050 system, at the heating rate of $20\text{ }^\circ\text{C}/\text{min}$ in nitrogen atmosphere from 25 to $600\text{ }^\circ\text{C}$.

3. Results and Discussion

3.1. FT-IR ATR spectra

The PA-doped PBI (PA-PBI) membranes were characterized by FT-IR spectroscopy. The infrared spectrum of nanocomposite membranes is shown in Figure. 1.

The bands at $500\text{--}1300\text{ cm}^{-1}$ were attributed to the vibration of HPO_4^{2-} and PA groups. Three characteristic absorptions of the HPO_4^{2-} , P-OH, and H_2PO_4^- groups for PA-PBI membranes appear at 1090 , 1008 , 970 cm^{-1} , respectively [9]. The peak around 1445 cm^{-1} suggests the deformation of benzimidazole “Breathing” mode of imidazole rings. The peak at 1600 cm^{-1} was assigned to the C=C and C=N stretching groups. The bands at $2250\text{--}2500\text{ cm}^{-1}$ and $2500\text{--}300\text{ cm}^{-1}$ were attributed to the O–H stretching and $\text{N}^+\text{--H}$ stretching in present of PA receptivity [10]. The peak at 2900 cm^{-1} was assigned to the stretching vibration of aromatic C–H groups. The bands at 3195 cm^{-1} and 3390 cm^{-1} were attributed to the hydrogen bonded N–H groups and non-hydrogen bonded N–H stretching groups receptivity. The peak around 3615 cm^{-1} suggests the O–H stretching due to absorbed water [10].

3.2. Water uptake and proton conductivity of un-doped membranes

The results of water uptake and proton conductivity of un-doped PBI (UD-PBI) nanocomposite membranes demonstrated in Figure. 2. It is well known that PBI has a high affinity for moisture and is hydrophilic. By immersing UD-PBI membranes in distilled water at room temperature, it was found that 15 % of water absorbed.

UD-PMT nanocomposite membranes displayed a high water uptake and proton conductivity compared with UD-PBI membranes. This improvement was attributed to the hydrophilic nature of MnTiO_3 nanoparticles within the UD-PBI matrix. It is believed that the proton transfer takes place on the surface of these nanoparticles and their high surface area improves the proton transfers, probably by creating an easier path for proton transport, and the result increase the proton conductivity [11]. It seems plausible that the hydroxyl groups introduced by MnTiO_3 nanoparticles form hydrogen bonds with the PBI chains. The hydrogen bonding may offer paths for more efficient proton transport. As MnTiO_3 content increases, more and more hydrogen bonds are formed, so proton transport becomes easier. The UD-PMT₄ nanocomposite



membranes displayed a higher water uptake and proton conductivity compared with other UD-PMT nanocomposite membranes.

Figure. 3 (a) displayed a Nyquist plot of UD-PMT nanocomposite membranes (2-4 wt %) at fully hydrated state. The UD-PMT₄ nanocomposite membranes demonstrated a lower resistance (higher proton conductivity) than that of the other UD-PMT nanocomposite membranes.

Bode Modulus plots of UD-PMT nanocomposite membranes (2-4 wt %) (Figure. 3(b)) confirm a result, obtained from Nyquist plots, which showed lower resistance for UD-PMT₄ nanocomposite membrane corresponds to the Nyquist plots. Bode Modulus plots also show that the lowest resistance is observed at the highest frequency. Hence according to the equation ($\sigma = L/RS$), a resistance at low frequencies in the Nyquist plot was used to achieve high proton conductivity.

3.3. Acid uptake and proton conductivity of PA-doped membranes

The acid uptake and proton conductivity of PA-doped PBI (PA-PBI) membranes was obtained 20 % and 1.4×10^{-3} S/cm respectively. The enhanced proton conductivity of PA-PBI membranes compared with UD-PBI membranes were attributed to the PA-doped effect of membranes. The reported proton conductivity value for UD-PBI was 10^{-12} S/cm. Thus, un-doped PBI is not a proton conducting polymer, and cannot be used as solid electrolyte. PBI is one of the most prominent membranes doped with PA, in which PA acts as protons conducting carrier and no water is needed for protons conduction in the membranes.

The results of acid uptake and proton conductivity of PA-PBI nanocomposite membranes demonstrated in Figure. 4. The added MnTiO₃ nanoparticles in the nanocomposite membranes enhanced the ability to trap PA, which improved the proton conductivity of the nanocomposite membranes. Hence PA-PMT nanocomposite membranes displayed a high acid uptake and proton conductivity compared with PA-PBI membranes.

PA-PMT nanocomposite membranes due to PA-doped effect displayed a higher proton conductivity compared with UD-PMT nanocomposite membranes. Thus, after doping with PA, nanocomposites membranes could have better proton conductivity than the UD-PBI membranes. This results shows that doping membranes with PA is very important parameter in increasing proton conductivity. The acid uptake of nanocomposite membranes increases a little with increasing MnTiO₃ content. Figure. 4 demonstrated that PA-PMT₄ nanocomposite membranes show the highest acid uptake and proton conductivity compared with other nanocomposite membranes respectively.

Figure. 5 displayed a Nyquist and bode modulus plots of PA-PBI nanocomposite membranes (2-4 wt %) at fully hydrated state. Figure. 5(a) shows that PA-PMT₄ nanocomposite membranes show the lowest resistance (highest proton conductivity) compared with other nanocomposite membranes. Bode Modulus plots (Figure. 5(b)) confirm a result, obtained from Nyquist plots, which showed lower resistance for PA-PMT₄ nanocomposite membrane corresponds to the Nyquist plots.

3.4. SEM and EDX measurements

SEM images of PA-PBI (a) and PA-PMT₄ (b) membranes were shown in Figure. 6 (a) and Figure. 6 (b) respectively. The SEM image showed in Figure. 6 (a), demonstrated that the PA-PBI membrane has a homogenous structure. From SEM images in Figure. 6 (b) the MnTiO₃ nanoparticles in the cross-section of PA-PMT₄ nanocomposite respectively can be clearly seen. EDX distribution of nanoparticles in the cross-section of PA-PMT₄ nanocomposite membranes

were displayed in Figure. 7. A homogenous distribution of Mn and Ti nanoparticles in the cross-section of PA-PMT₄ nanocomposite membranes were observed.

3.5. Thermal properties

The thermal stability of PBI based membranes have been extensively studied by thermogravimetric analysis (TGA). From the Figure. 8, the decomposition onset temperatures of PA-PMT₄ nanocomposites membranes were higher than PA-PBI membranes and they shift towards the higher temperature range. The MnTiO₃ nanoparticles have proved to be an effective way to improve the stability of the PA-PMT nanocomposite membranes. Incorporation of MnTiO₃ nanoparticles in PBI polymer matrix leads to increase the decomposition temperature of nanocomposite membranes compared with PA-PBI membranes. It was found that these thermal stability and conductivity were influenced by PA-doped. The high stability and conductivity for PA-PBI complexes result from strong interaction between PBI and PA. The PA-PMT₄ membranes, exhibits excellent thermal stability. It also exhibits high proton conductivity even at anhydrous state and are available to work at high temperatures and low humidity environment.

Conclusion

Advanced nanocomposite membranes based of PBI-MnTiO₃ were prepared by solution casting method. The results showed that the water uptake and proton conductivity of the nanocomposite membranes were higher than that of PBI based membrane because of hydrophilic nature of nanoparticles. When the nanocomposite membranes doped with PA, due to hydrogen bonding from PA demonstrated higher proton conductivity compared with un-doped membranes. The results of SEM-EDX analysis have provided detailed information about the homogenous distribution of nanoparticles in the nanocomposite membranes. The strong surface interactions of nanoparticles and great interfacial interactions of PA increase the mechanical properties of nanocomposite membranes. FT-IR ATR spectra confirmed characteristic peaks of HPO₄²⁻, P-OH, H₂PO₄⁻, C=C, C=N, O-H, N⁺-H and N-H groups at nanocomposite membranes.

Table 1- Names and the detailed process information for PBI nanocomposite membranes

Membrane		Nanoparticles (wt %)	Nanoparticles
Un-doped	PA-doped		
UD-PMT ₂	PA-PMT ₂	2	
UD-PMT _{2.5}	PA-PMT _{2.5}	2.5	MnTiO ₃
UD-PMT ₃	PA-PMT ₃	3	
UD-PMT ₃	PA-PMT _{3.5}	3.5	
UD-PMT ₄	PA-PMT ₄	4	

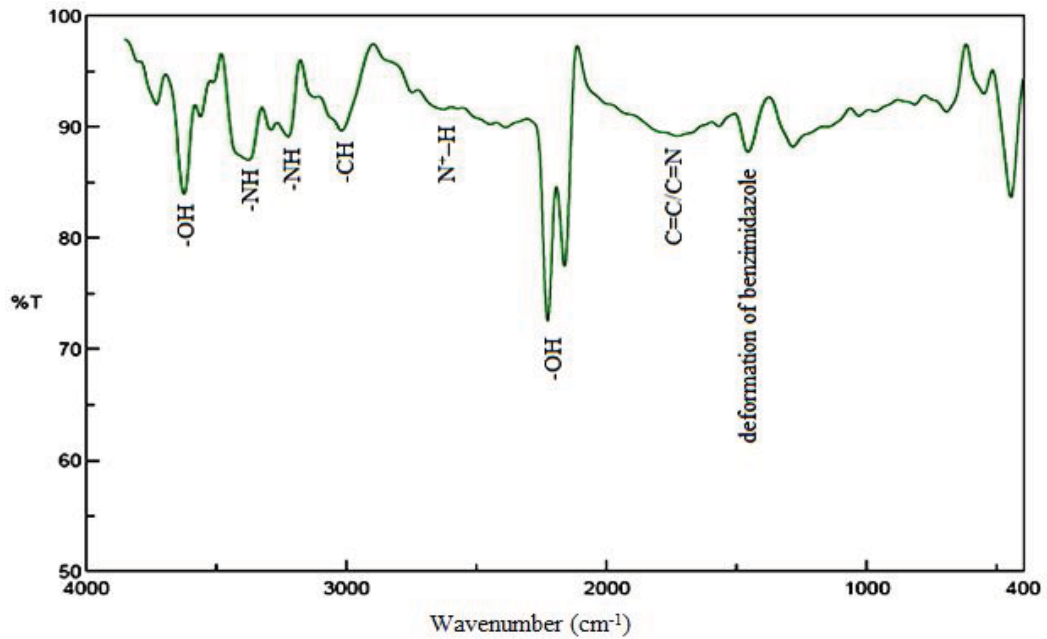


Figure. 1. FT-IR spectra of PA-PBI nanocomposite membranes.

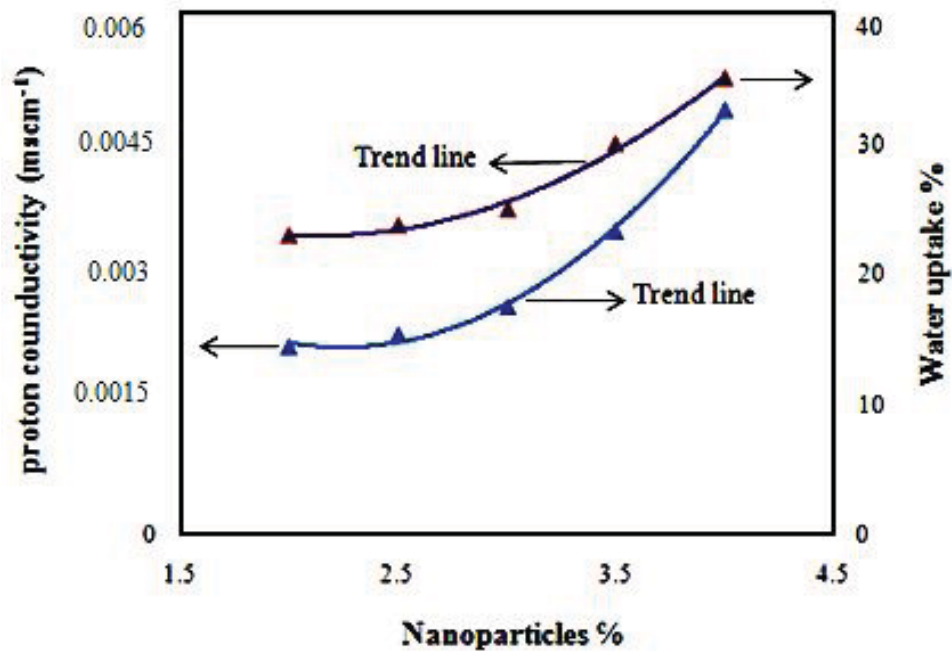


Figure. 2. Water uptake and proton conductivity plots of UD-PMT nanocomposite membranes.

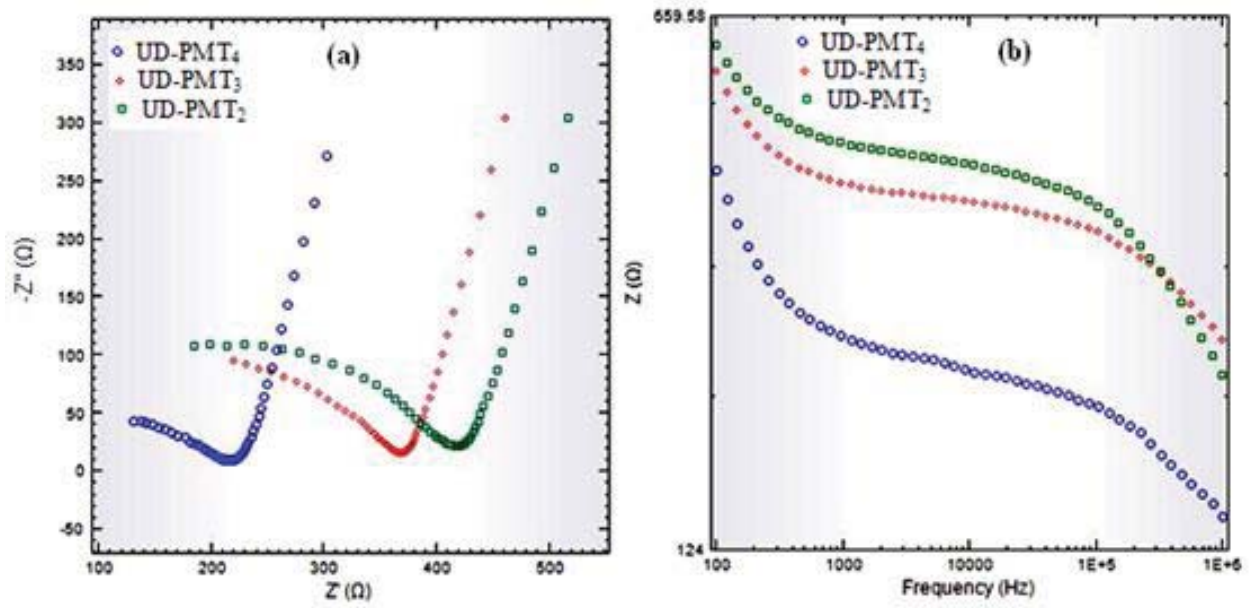


Figure. 3. Nyquist (a) and bode modulus (b) plot of UD-PMT nanocomposite membranes at fully hydrated state.

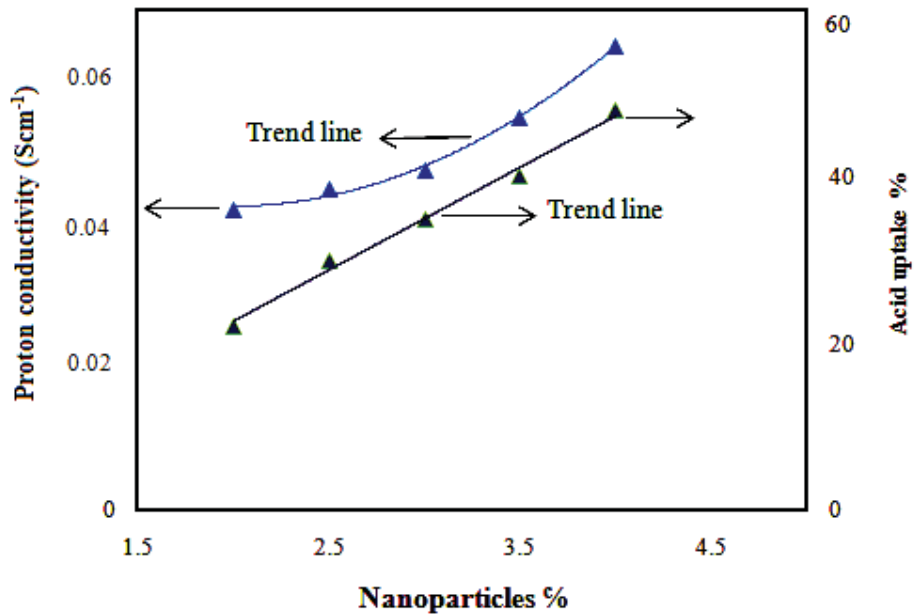


Figure. 4. Acid uptake and proton conductivity plots of PA-PMT nanocomposite membranes.

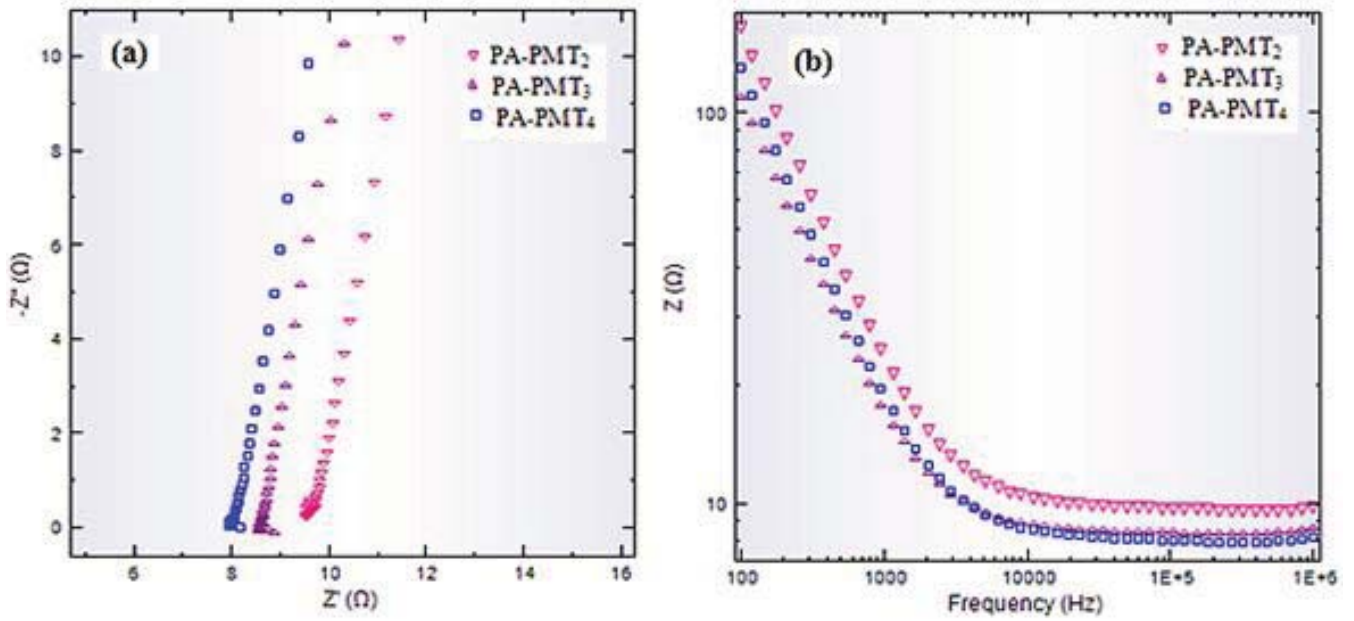


Figure. 5. Nyquist (a) and bode phase (b) plots of PA-PMT nanocomposite membranes at fully hydrated state.

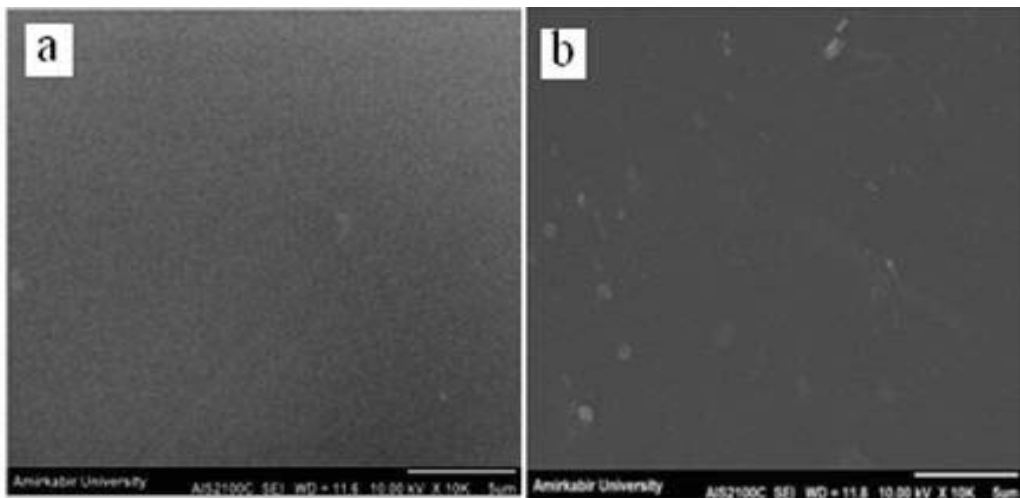


Figure. 6. The SEM images of the cross-section of PA-PBI (a) and PA-PMT₄ (b).

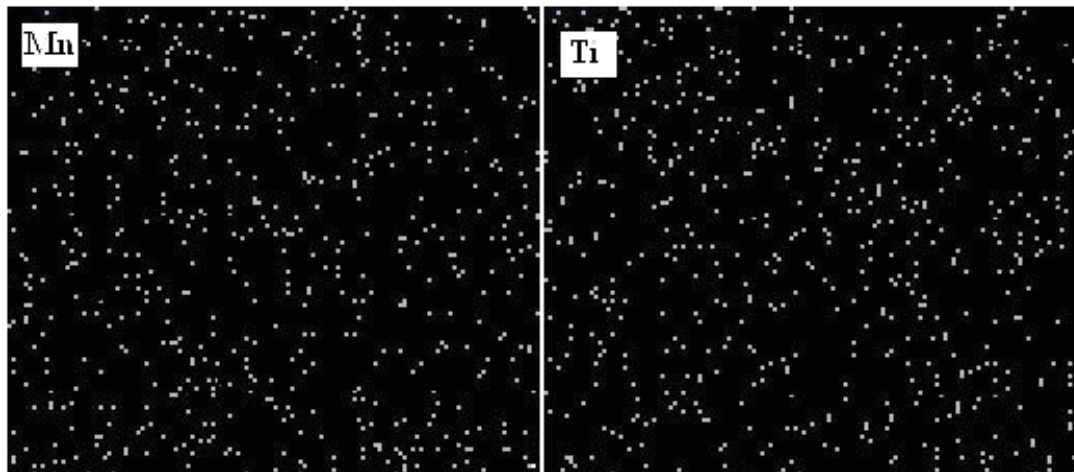


Figure. 7. EDX distribution of Mn and Ti nanoparticles in the cross-section of PA-PMT₄ nanocomposite membranes.

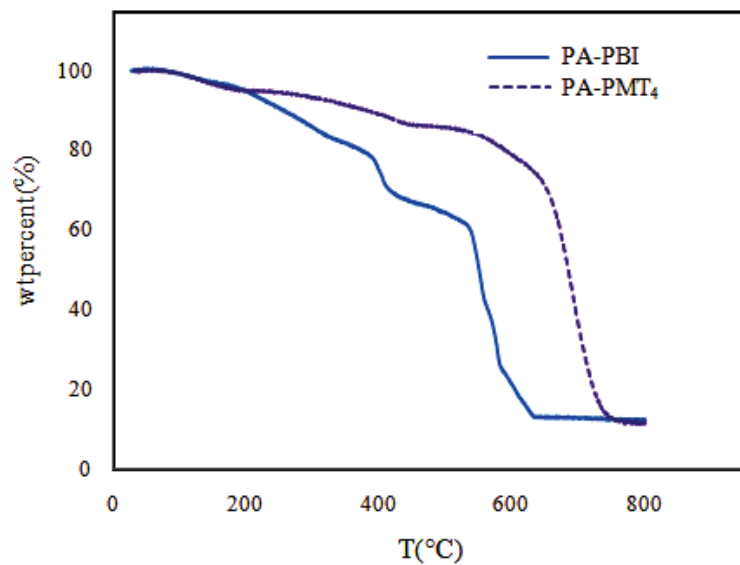


Figure. 8. TGA plot of PA-PBI and PBI-PMT₄ membranes.

References

- [1] J.M. Andujar, F. Segura "Fuel cells: History and updating. A walk along two centuries", J. Renewable Sustainable Energy, (2009). 13, 2309-2322.
- [2] H. Tang, S. Peikang, S.P. Jiang, F. Wang, M. Pan "A degradation study of Nafion proton exchange membrane of PEM fuel cells", J. Power Sources, (2007). 170, 85-92.



- [3] C.Y. Chen, J.I. Garnica, M.C. Duke, R.F. Dalla, A.L. Dicks, J.C. Diniz “Nafion/polyaniline/silica composite membranes for direct methanol fuel cell application”, *J. Power Sources*, (2007). 166, 324-330.
- [4] J. Antonio, M. Eduardo, S. nchezab, P. mez-Romero “Proton-conducting membranes based on benzimidazole polymers for high-temperature PEM fuel cells. A chemical quest”, *Chem. Soc. Rev*, (2010). 39. 3210–3239.
- [5] J.S. Wainright, J.-T. Wang, D. Weng, R.F. Savinell, M. Litt “Acid Doped Polybenzimidazoles: A New Polymer Electrolyte”, *J. Electrochem. Soc*, (1995). 142, 121.
- [6] H. Beydagh, M. Javanbakht, H. SalarAmoli, A. Badii, Y. Khaniani, M.R. Ganjali, P. Norouzi, M Abdouss “Synthesis and characterization of new proton conducting hybrid membranes for PEM fuel cells based on poly(vinyl alcohol) and nanoporous silica containing phenyl sulfonic acid”, *Int J Hydrogen Energy*, (2011). 36, 13310-13316.
- [7] P. Salarizadeh, M. Javanbakht, M. Abdollahi, L. Naji “Preparation, characterization and properties of proton exchange nanocomposite membranes based on poly(vinyl alcohol) and poly(sulfonic acid)-grafted silica nanoparticles”, *Int J Hydrogen Energy*, (2012).
- [8] M. Enhessaria, A. Parviza, E. Karamalib and K. Ozaee “Synthesis, characterisation and optical properties of MnTiO₃ nanopowders”, *Journal of Experimental Nanoscience*, (2011). 1–9.
- [9] R. Tanaka, H. Yamamoto, S. Kawamura, T. Iwase “Proton conducting behavior of poly(ethylenimine)-H₃PO₄ systems”, *Electrochim. Acta*, (1995). 40, 2421-2424.
- [10] J. Lobato, P. Canizares, M.A. Rodrigo, J.J. Linares, G “Synthesis and characterisation of poly [2, 2-(*m*-phenylene)-5, 5-benzimidazole] as polymer electrolyte membrane for high temperature PEMFCs”, *J. Membr. Sci*, (2006). 280, 351–362.
- [11] R.K. Nagarale, W. Shin, P.K. Singh “Progress in ionic organic-inorganic composite membranes for fuel cell applications”, *Polym. Chem*, (2010). 1, 388–408.



Corrosion Behavior and Interfacial Contact Resistance of TiN Coated Type 316L Stainless Steel as Bipolar Plate for Proton Exchange Membrane Fuel Cell

Ali Hedayati¹, Saeed Asghari² and Amirhosein Alinoori³

Engineering Research Institute, 7th kilometer of Imam Khomeini, Isfahan
a.hedayati@fuelcell.ir

Abstract

AISI 316L stainless steel (SS) due to its superior features such as availability, low material and production costs and good corrosion resistance, strength, and weldability can be a suitable choice for bipolar plate material in proton exchange membrane fuel cells (PEMFCs). However, there are two important problems with using this type of steel as a bipolar plate: low corrosion resistance and high interfacial contact resistance (ICR) in PEMFC conditions. For solving these problems, investigations and development of different coatings and/or surface treatments are inevitable. In this paper, corrosion behavior and ICR of 1 mm-thick 316L metallic bipolar plates coated with TiN at three different thicknesses (1, 2, and 3 μm) using a physical vapor deposition (PVD) technique are investigated. The potentiodynamic polarization and electrochemical impedance tests are conducted at 80 °C in pH3 H₂SO₄+2 ppm HF solution purged with either O₂ or H₂, and the potentiostatic corrosion tests are performed under both simulated cathode and anode conditions. The TiN coated 316L plates exhibit improved corrosion resistance and retard the corrosion. The promising results in about all electrochemical tests is related to 3 μm -TiN coated specimens. The TiN coated 316L SS exhibits much lower ICR than uncoated 316L SS.

Keywords: Proton Exchange Membrane Fuel Cell, Stainless Steel Bipolar Plate, Titanium Nitride Coating, Corrosion Properties, Electrochemical Impedance Spectroscopy, Interfacial Contact Resistance

1. Introduction

In the polymer electrolyte membrane fuel cells (PEMFCs), the bipolar plates carry out many functions, such as separating and distributing fuel and oxidant, and carrying away reaction products and heat from each cell. Therefore, identifying and selecting a right material to perform these functions well is very important. This material as a bipolar plate should have high thermal and electrical conductivity, good mechanical and surface properties, adequate corrosion resistance, and low ICR and gas permeability [1-6]. According to the bipolar plate functions mentioned above, United State Department of Energy (DoE) has determined the quantitative requirements for bipolar plates of fuel cells, as shown in table 1 [7]. Conventional materials used as bipolar plate material in PEMFCs are graphite or graphite composite. These materials have excellent chemical stability and corrosion properties, high conductivity, and low interfacial contact resistance (ICR). However, the high cost and poor mechanical properties of these materials are the main technical barriers. One of the best strategies to solve these problems is to replace these materials with metallic materials. Metals are good candidates for bipolar plates because of having excellent mechanical strength, very

¹ Research Scientist, Fuel Cell Department, Engineering Research Institute

² Assistant Professor, Fuel Cell Department, Engineering Research Institute, asghari@fuelcell.ir

³ Research Scientist, Fuel Cell Department, Engineering Research Institute, ah.alinoori@grad.kashanu.ac.ir

high electrical and thermal conductivity, recyclable capability, low gas permeability, and relatively low material and manufacturing cost. However, the majority of metals do not have sufficient corrosion resistance for using as bipolar plate material in PEMFCs. The majority of candidate metals such as titanium, niobium, and gold are too expensive. Stainless steels are the most promising materials [8]. It is well known that the austenitic stainless steels have better corrosion resistance than the other types of stainless steel such as the ferritic or martensitic [2, 9-11]. AISI 316 stainless steel is one of the most corrosion resistant austenitic stainless steels due to its higher Ni content (~10-14 wt%) and the presence of Mo. The 316L grade has very low carbon content (<0.03 wt%) which is suitable for increasing the weldability and corrosion resistance [9, 12]. However, corrosion resistance of this type of steel is not at desired levels for working in acidic, humid and warm environment of the PEMFC. Hence, applications of different coating types on 316L SS have been studied to improve the corrosion resistance. One of the most promising coatings is TiN due to have excellent corrosion resistance, high conductivity, similar water contact angle of graphite, wide industrial feasibility and cost consideration, and also wide research. One of the most widely used methods for TiN coating is Physical Vapor Deposition (PVD).

Table 1: DoE technical targets for bipolar plate [7].

Characteristic	Units	2011 Status	2017	2020
Cost	\$ / kW	5-10	3	3
Plate H ₂ coefficient	Std cm ³ (sec cm ² Pa) @ 80°C, 3 atm 100% RH	N/A	<1.3 × 10 ⁻¹⁴	<1.3 × 10 ⁻¹⁴
Corrosion, anode ^a	μA/cm ²	<1	<1	<1
Corrosion, cathode ^b	μA/cm ²	<1	<1	<1
Electrical conductivity	S/cm	>100	>100	>100
Areal specific resistance ^c	Ohm.cm ²	0.03	0.02	0.01
Flexural Strength	MPa	>34 (carbon plate)	>25	>25
Forming elongation ^d	%	20-40	40	40

^a pH 3 0.1ppm HF, 80°C, peak active current <1×10⁻⁶ A/cm² (potentiodynamic test at 0.1 mV/s, -0.4V to +0.6V (Ag/AgCl)), de-aerated with Ar purge.

^b pH 3 0.1ppm HF, 80°C, passive current <5×10⁻⁸ A/cm² (potentiostatic test at +0.6V (Ag/AgCl) for >24h, aerated solution).

^c Includes interfacial contact resistance (on as received and after potentiostatic test) measured both sides per Wang, et al. J. Power Sources 115 (2003) 243-251 at 200 psi (138 N/cm²).

Ma et al. [13] showed that the corrosion behavior of a commercially available TiN coating on 316L SS was only suitable in short-term tests, but this coating was mostly dissolved after approximately 1 hour of the electrolysis test. They stated that the TiN coating had poor quality. Li et al. [14] illustrated that TiN coated 316 SS under both simulated anode and cathode conditions have much better corrosion resistance and electrical conductivity than the bare 316 SS. They stated that improving the coating quality and investigating long-term electrochemical stability of TiN coatings are necessary for applying it as coating of SS in PEMFCs. Cho et al. [15] indicated that electrical contact resistance and water contact angle of graphite and TiN-coated 316 SS were nearly the same. They also reported that corrosion-protective TiN layer on 316 SS significantly improved lifetime. Their manufactured 1kW short stack using TiN-coated bipolar plates operated well for 1028 h. Wang et al. [2, 16, 17] observed the corrosion behavior of PVD TiN-coated 316L SS and 410 SS, 15 μm thick, in simulated PEMFC cathode environments. They found that the corrosion of PVD TiN-coated SSs was related to the presence of pinholes on the TiN coating surface. Kumagai et al. [18] found that the nanosized TiN as coating on 310 SS bipolar plates can reduce ICR and therefore it can improve fuel cell performance. TiN nanoparticles were not dissolved after 300 h cell operation. Wang et al. [19]



showed that EBPVD TiN-coated 316L has a higher corrosion resistance in the anodic environment than in the cathodic environment. Based on the potentiodynamic polarization corrosion tests, corrosion resistance of TiN-coated 316L was higher in H₂ bubbled environment and lower in O₂ bubbled environment than that of the bare 316L SS. Based on the potentiostatic corrosion tests, initially TiN coating in the simulated anode conditions had a lower corrosion current density than the bare 316L SS but with increasing test time, this coating had higher corrosion current density because of occurring corrosion at pinholes existed on the coatings. In the cathode test conditions, TiN coating has a higher corrosion current density than bare 316L SS. ICR of TiN coating was lower than bare 316L SS. Zhang et al. [20] deposited TiN on 304 SS by means of two surface coating techniques: pulsed bias arc ion plating (PBAIP) and magnetron sputtering (MS). Based on the potentiostatic corrosion tests, TiN-coated 304 SS corroded in the simulated cathode conditions because of increasing of current density with time. TiN coating provides lower ICR than the bare 304 SS. The author stated that the corrosion behavior of TiN-coated 304 depends strongly on microstructures. Dur et al. [21] reported that some of the PVD TiN-coated 316L sample in corrosion tests had lower corrosion resistance than the bare 316L SS. Some of these inconsistent results in the literature may be related to the electrolyte composition, pH and temperature, specimen surface finishing, differences on the material composition and the coating methods [22]. Such diverse and sometimes conflicting results on the performance and durability of this type of coating applied on stainless steels are needed further research. In this Paper, the performance and durability of 1 mm-thick 316L metallic bipolar plates coated with TiN at three different thicknesses (1, 2, and 3 μm) using a physical vapor deposition (PVD) technology are investigated in a simulated PEMFC environment by measuring corrosion resistance and ICR. The bare 316L stainless steel (316L SS) was used as a reference material.

2. Materials and Methods

2.1. Test Specimen Preparation

In this study, substrate material selected from a commercial hot rolled 316L SS strip with a thickness of 1 mm. The chemical composition of this strip is given in the Table 2. The strip was cut into 25 mm \times 25 mm specimens. In order to prepare these specimens for coating process, they were polished by using SiC polishing paper and alumina particles. TiN coating at three different thicknesses (1, 2, and 3 μm) were deposited on 316L SS substrates by physical vapor deposition method (PVD).

Table 2 Chemical composition of the 316L SS used in this study

C	Si	Mn	P	S	Cr	Mo	Ni	Cu	Fe
0.027	0.34	1.86	0.026	0.004	17.5	2.0	9.8	0.4	Bal.

2.2. Corrosion Properties

Three different corrosion test methods (potentiodynamic, PD, potentiostatic, PS, and electrochemical impedance spectroscopy, EIS) were used for investigating corrosion behavior of both uncoated and coated specimens. In order to simulate the working condition of PEMFC, the temperature, pH, and the composition of electrolyte were selected as 80 °C, 3, H₂SO₄ + 2 ppm HF, respectively. In order to simulate the cathode and anode conditions, electrolyte was purged with O₂ and H₂, respectively. A conventional three-electrode system test with a platinum counter electrode, a saturated calomel electrode (SCE) bridged with a luggin capillary as the reference electrode and the test specimen as the working electrode was used to conduct the electrochemical experiments using a 2273 Potentiostat (Princeton Applied Research Instruments) controlled by a computer.

2.2.1. Potentiodynamic (PD) Polarization

PD polarization tests were used to measure and to compare corrosion resistances of the uncoated and the coated 316L SS. The specimens were stabilized for 1 h at the open-circuit potential (OCP). In PD test, the potential was changed from -1 V vs. SCE to 1 V vs. SCE at a scan rate of 1 mVs⁻¹.

2.2.2. Potentiostatic (PS) Polarization

PS polarization test was used to investigate the suitability of uncoated and coated 316L SS as the anodes and cathodes in a PEMFC. PS tests were conducted for 7 h at the simulated cathode condition and for 4 h at the simulated anode conditions. The simulated cathode and anode conditions were -0.1 V vs. SCE purged with H₂ and 0.6 V vs. SCE purged with O₂, respectively.

2.2.3. Electrochemical Impedance Spectroscopy (EIS)

The EIS measurements were performed at steady-state in the frequency range of 2 MHz to 0.01 Hz. The AC amplitude was set to 5 mV. The Potentiostat/Galvanostat and Frequency Response Analyzer PARSTAT 2273 were used for EIS measurements. EIS spectra were interpreted using the ZView[®] software and modified complex nonlinear least square (CNLS) fitting method [23]. A CPE model was enough to explain the EIS data [24-26]. The E_{corr} and EIS data were recorded at usual intervals from 3 h up to 100 h for cathodic simulations and up to 72 h for anodic simulations.

2.3. Interfacial Contact Resistance (ICR)

In this study, Wang's method [27] used to measure ICR of uncoated and TiN coated 316L SS specimens and a graphite specimen for comparison purposes. As shown in Fig. 1(a), the specimens were sandwiched between two pieces of GDL and two Au coated copper plates. In order to calculate the total resistance of this setup by Ohm law ($R=VI^{-1}$), an electrical current range (1 A) was applied via the two Au coated copper plates and then the total voltage drop through this setup was measured as a function of the gradually increasing compaction force. The total resistance of this setup (R_{T1}) consists of bulk resistance of two Au coated copper plates (R_{CP}), two ICR between Au coated copper plate and GDL ($2R_{CP/GDL}$), two bulk resistances of GDL (R_{GDL}), two interfacial contact resistances between GDL and specimen ($R_{GDL/S}$), and the bulk resistance of the specimen (R_S) (stainless steel substrate (R_{ss}) with/without PVD coatings (R_{film})), $R_S = R_{ss} + (2R_{film})$. The R_{T1} can be expressed as:

$$R_{T1} = 2R_{CP} + 2R_{CP/GDL} + 2R_{GDL} + 2R_{GDL/S} + R_S \quad (1)$$

$R_{CP/GDL}$ can be calculated by using an arrangement shown in Fig. 1(b).

This configuration consists of the bulk resistance of two Au coated copper plates (R_{CP}) and two interfacial contact resistances between Au coated copper plate and GDL ($2R_{CP/GDL}$), and the bulk resistance of the GDL (R_{GDL}). Therefore, R_{T2} can be expressed as:

$$R_{T2} = 2R_{CP} + 2R_{CP/GDL} + R_{GDL} \quad (2)$$

ICR between the specimen and the GDL can be calculated by using (1) and (2) equations as following:

$$R_{GDL/S} = (R_{T1} - R_{T2} - R_{GDL} - R_S) / 2 \quad (3)$$

Bulk resistance values of the GDL and the specimen are very small (compared with the other

resistances) and therefore negligible [19, 28, 29]. Therefore, ICR between the GDL and the specimen can be expressed as follows:

$$R_{GDL/S} \approx (R_{T1} - R_{T2}) / 2 \quad (4)$$

The compaction pressure was applied in the range of 25 to 310 Ncm⁻² using a compressive test machine (SMT 20, SANTAM co.) on both sides of the specimens with the contact area of 2.25 cm². Before measurement, bare 316L SS specimen polished with #800 grit SiC abrasive paper. Then, uncoated and TiN coated specimens were cleaned with acetone and dried with nitrogen. For each measurement test, GDL was only used once.

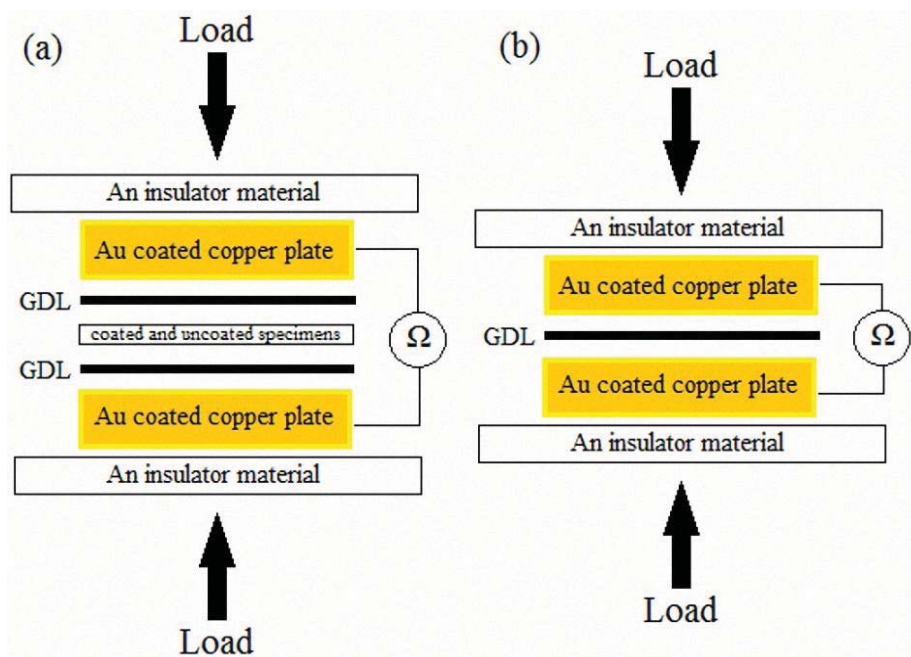


Figure 1: Schematic of the interfacial contact resistance measurement setup.

3. Results and Discussions

3.1. Potentiodynamic (PD) Corrosion Test

From potentiodynamic (PD) polarization curve, corrosion potential and current can be obtained. They indicate the corrosion resistance of the materials. A lower corrosion current and higher corrosion potential generally show a higher corrosion resistance. Fig. 2 shows PD curves of bare 316L SS and TiN coated 316L SS at three different thicknesses (1, 2, and 3 μm) in both simulated cathode (purged with O₂, Fig. 2(a)) and anode conditions (purged with H₂, Fig. 2(b)). Table 3 shows the corrosion potential (E_{corr}), current density (i_{corr}) and polarization resistance (R_p) obtained by the Tafel calculations for the uncoated and the coated SS316L. In the simulated cathode conditions, the corrosion potential of the bare 316L SS is lower than those of the coated specimens. Thus, applied TiN coating on 316L SS substrate retards the corrosion. From Fig. 2(a) and table 3, we can see that the corrosion behaviors of the TiN coated specimens with three different thicknesses are the same. Current densities (i_{corr}) of all TiN coated specimens are below 1 μAcm⁻² and at the range of (0.35-0.51) μAcm⁻²; however current density (i_{corr}) of bare 316L SS is 1.12 μAcm⁻². Thus TiN coating in the simulated cathode condition increases the corrosion resistance. According to Figs 2(a), 2(b) and table 3, E_{corr} of 316L SS in an environment containing O₂ (-178 mV) is higher than that in an environment containing H₂ (-376 mV) and i_{corr} of 316L SS in an environment containing O₂ (1.1 μAcm⁻²) is approximately 6 times less than that in an environment containing H₂ (6.1



μAcm^{-2}). This is not unexpected because stainless steels in an environment containing O_2 can be passivated more easily and the passive layer is stable and thicker than that in an environment containing H_2 [9]. According to Fig. 2(b) and table 3 in the simulated anode conditions, i_{corr} of all TiN coated specimens are below $1 \mu\text{Acm}^{-2}$ and are located in the range of $(0.06-0.38) \mu\text{Acm}^{-2}$. Furthermore, i_{corr} of bare 316L SS is $6.1 \mu\text{Acm}^{-2}$. In both cathode and anode conditions, the coated specimens display much better corrosion resistance than bare 316L SS.

3.2. Potentiostatic (PS) Corrosion Test

Figs. 3(a) and 3(b) show that the potentiostatic polarization curves at $+0.6\text{V}$ vs. SCE electrode in an O_2 -purged solution and -0.1V vs. SCE electrode in a H_2 -purged solution. The stabilized current density for TiN coated specimens and bare specimen in simulated cathode and anode conditions took place after 7 and 4 hours, respectively. The value of stabilized current density of the TiN coated specimens with different thicknesses and the bare specimens in both simulated cathode and anode conditions are listed in table 4.

In the simulated anode conditions (Fig. 3(b) and table 4), the corrosion current density of the uncoated 316L SS stabilizes at about $0.2 \mu\text{Acm}^{-2}$ while this value was the lowest stabilization current density after 4 hours PS test. As seen from PD curves (Fig. 2), the TiN coated specimens have a more positive potential than the uncoated 316L SS. Therefore, H_2 formation from H^+ ions on the surface of the TiN coated specimens is easier. The corrosion current density of $2\mu\text{m}$ -thick-TiN coated specimen became negative immediately after 185 minutes. Therefore, it can be corroded in the simulated anode condition. This unusual behavior can be attributed to unsuitable preparation of $2\mu\text{m}$ -thick-TiN coated specimen. The corrosion current density of both the uncoated and TiN-coated specimens, except $2\mu\text{m}$ -thick-TiN coated specimen, is positive after 185 minutes in all cases. This positive current provides cathodic protection for both the uncoated and TiN-coated specimens. Therefore, the TiN coated specimens with thickness of 1 and 3 μm undergoes no corrosion in the anode conditions.

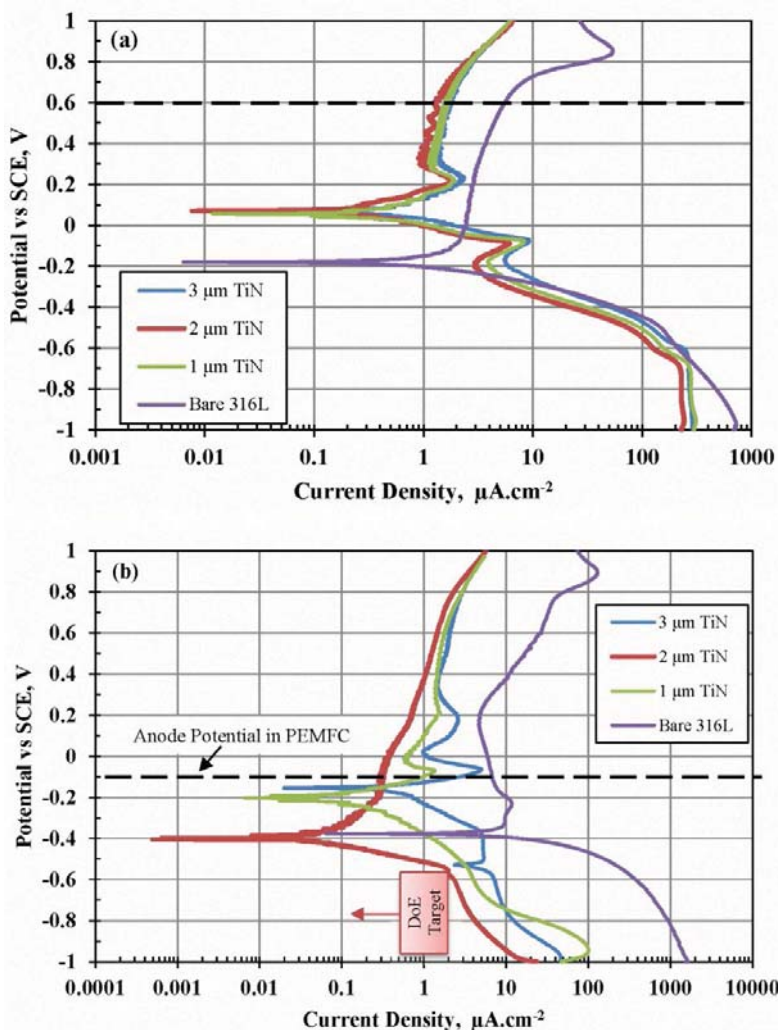


Fig. 2. Potentiodynamic polarization curves for uncoated and TiN-coated specimens in a pH3 H_2SO_4+2 ppm HF solution at 80 °C with (a) O_2 purging and (b) H_2 purging.

Table 3: Potentiodynamic polarization parameters of uncoated and TiN-coated stainless steel 316L specimens in a pH3 H_2SO_4+2 ppm HF solution at 80 °C with either H_2 or O_2 purging.

		β_a (mV)	β_c (mV)	E_{corr} (mV)	i_{corr} (μAcm^{-2})	R_p (Ωcm^2)
316L SS	H_2	218.021	57.935	-375.566	6.123	3.25
	O_2	344.540	112.091	-178.424	1.128	32.60
1 μm TiN	H_2	199.570	1222.357	-199.146	0.1379	239.15
	O_2	203.032	100.628	52.532	0.3542	82.59
2 μm TiN	H_2	322.111	99.964	-399.555	0.06913	479.81
	O_2	207.412	133.443	68.859	0.3505	100.73
3 μm TiN	H_2	71.879	179.471	-155.709	0.3832	58.23
	O_2	202.273	105.991	68.967	0.5105	59.23

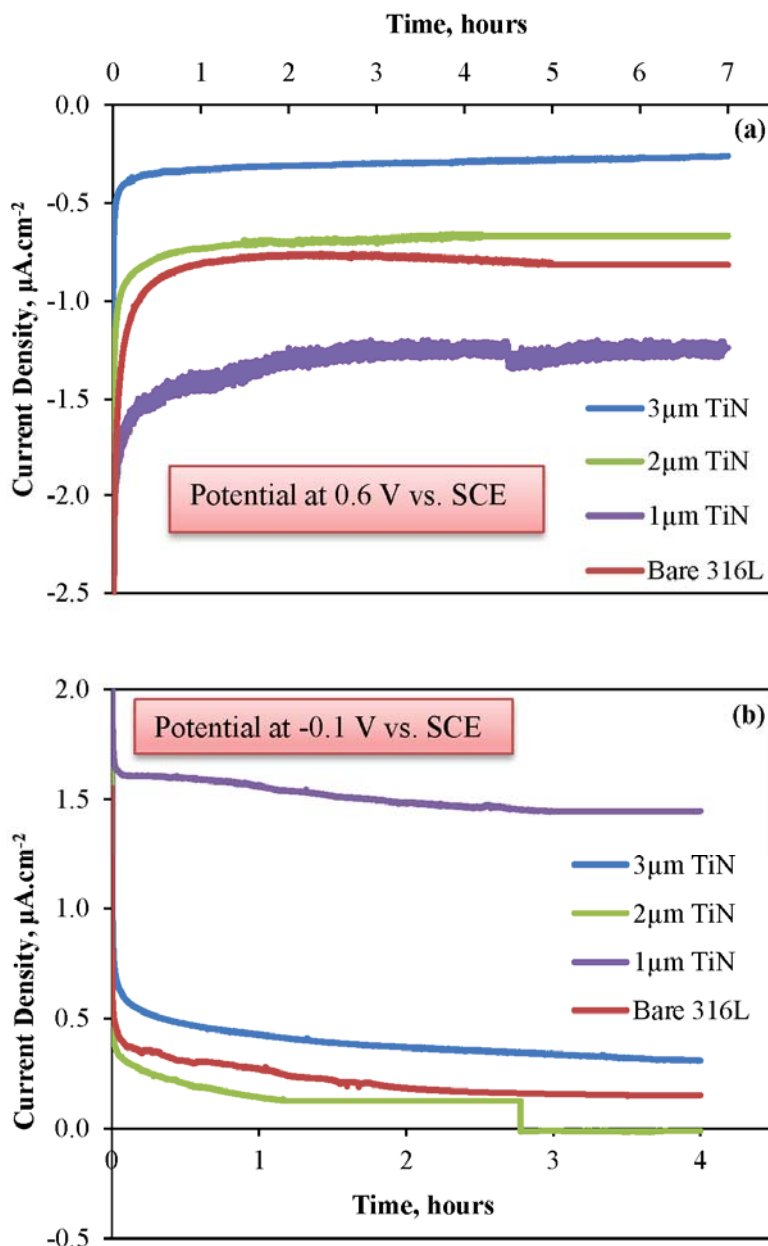


Figure 3: Potentiostatic polarization curves for uncoated and TiN-coated specimens in a pH3 H₂SO₄+2 ppm HF solution at 80 °C with (a) O₂ purging and (b) H₂ purging.

Table 4: The stabilized current density for TiN coated specimens and bare specimen in both simulated cathode and anode conditions

The stabilized current density value	Bare 316L (μAcm ⁻²)	1 μm TiN (μAcm ⁻²)	2 μm TiN (μAcm ⁻²)	3 μm TiN (μAcm ⁻²)
simulated cathode condition after 7 h	-0.82	-1.20	-0.64	-0.26
simulated anode condition after 4 h	0.20	1.45	-0.01	0.31

3.3. Electrochemical Impedance Spectroscopy (EIS)

Nyquist plots ($-Z''$ imaginary versus Z' real part of the impedance), measured at an over

potential of -100 mV and 600 mV in the simulated cathode and anode environments, are shown in Fig. 4(a) and Fig. 4(b), respectively. In general, two semi-circles with a depressed angle was found on all electrodes over the explored frequency range; thereby, indicating that the charge transfer process was the principal reaction on the electrodes [30]. The experimental data in the figures are presented as points and the continuous lines are obtained by curve fitting using the program of Complex Nonlinear Least-Squares Fitting Program (CNLS) provided by Macdonald et al.[31]. A depressed semi-circle in the complex-plane plots suggests that inhomogeneity exists on the electrode surface. This phenomenon can be theoretically modeled with a constant phase element (CPE), which replaces the capacitance of the double layer (C_{dl}) due to the roughness and inhomogeneity of the electrode surface [30-32]. An equivalent circuit (Fig. 5) was used for fitting the EIS data of the 316 SS substrate and the coatings [33]. The circuit as shown in Fig. 5 consists of the solution resistance (R_s), Pore resistance (R_p), faradic processes resistance or charge transfer resistance (R_{ct}) and two constant phase elements (CPE); constant phase elements of coatings (CPE_{coat}) and double layer (CPE_{dl}).

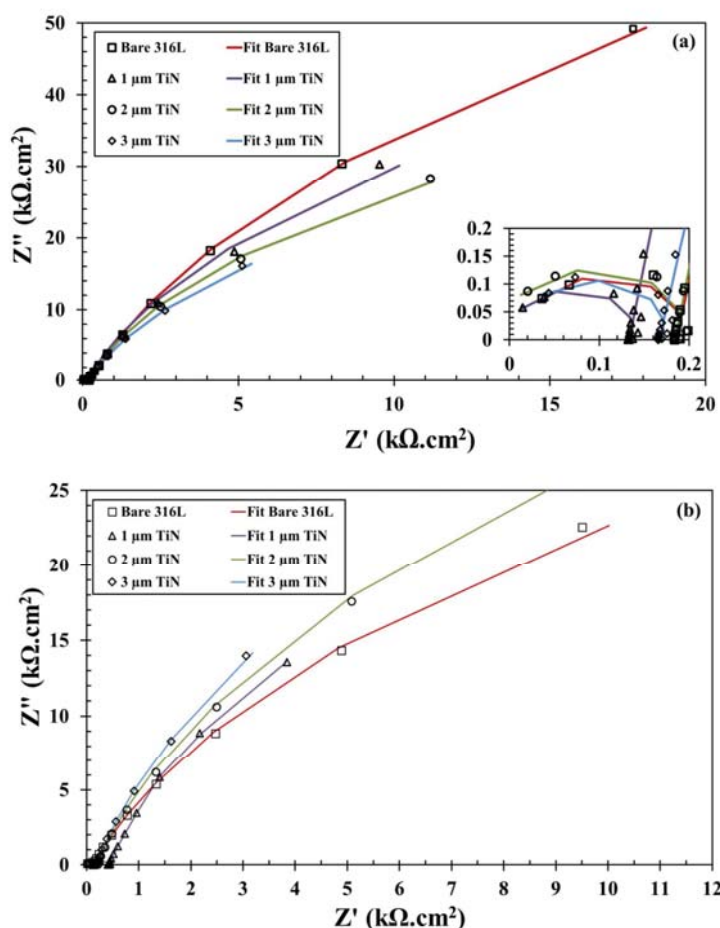


Figure 4: Nyquist plots of uncoated and TiN-coated specimens on steel (a) in the simulated cathode environments, and (b) in the simulated anode environments.

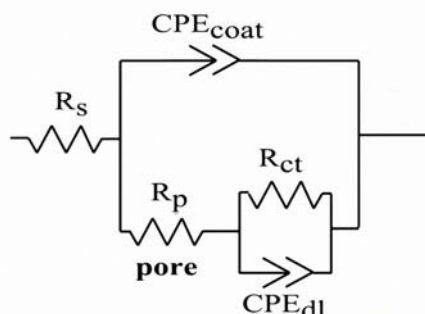


Figure 5: Electrochemical equivalent circuits used for fitting the experimental data of the uncoated and TiN-coated specimens; R_s : solution resistance, R_p : Pore resistance, R_{ct} : faradic processes resistance, CPE_{coat} : constant phase element of coatings, and CPE_{dl} : constant phase element of double layer.

The presence of the CPE causes a rotation of the complex–plane plot clockwise by a constant angle. The constant phase element impedance is described by:

$$Z_{CPE} = C^{-1}(j\omega)^{-(1-\alpha)} \quad (5)$$

where ω is the angular frequency of the AC voltage, $j = \sqrt{-1}$, α the frequency independent parameter related to the depression angle φ which is equal to $\alpha \times 90^\circ$ and C is a constant related to the double-layer capacitance of the electrodes, C_{dl} .

The pore resistance (R_p) and the resistance associated with faradic processes (R_{ct}) were added together in a term called the corrosion resistance (R_{corr}):

$$R_{corr} = R_p + R_{ct} \quad (6)$$

The corrosion resistance term R_{corr} was used as a measure of the barrier properties of the systems.

Roughness factor (R.F.) of an electrode vs. a smooth electrode can be obtained by dividing C_{dl} value of the electrode by $20 \mu F cm^{-2}$ (which equals to C_{dl} value of a smooth electrode). It has been established that the high values of R_{ct} and the low values of C_{dl} imply a better corrosion protective ability of coatings [34-38], while the C_{dl} value is also related to the porosity of the coating [39-41]. The R_{ct} and C_{dl} values of TiN coated specimens are shown in Tables 5 and 6. The R_{ct} and C_{dl} values increased with an increase in the thickness of TiN. The TiN coated specimens with the thickness of $3 \mu m$ have the highest values of R_{corr} ; implying the better anti-corrosion ability.

Table 5: Corrosion resistance, R_{corr} , double layer capacity, C_{dl} , φ , depression angle, and roughness factor R.F. values compared with $20 \mu F cm^{-2}$ for smooth electrode, in the simulated cathode environments.

Electrode	C_{dl} ($\mu F cm^{-2}$)	φ_{dl} ($^\circ$)	R.F.	R_{corr} (Ωcm^2)
316L SS	27.6	82.29	1.38	$3.39 \times 10^{+05}$
1 μm TiN	46.2	82.98	2.31	$3.67 \times 10^{+05}$
2 μm TiN	48.0	83.25	2.4	$5.18 \times 10^{+05}$
3 μm TiN	85.4	82.04	4.27	$8.53 \times 10^{+05}$

Table 6: Corrosion resistance, R_{corr} , double layer capacity, C_{dl} , depression angle ϕ ($^{\circ}$), and roughness factor R.F. values compared with $20 \mu F cm^{-2}$ for smooth electrode, in the simulated anode environments.

Electrode	C_{dl} ($\mu F cm^{-2}$)	ϕ_{dl} ($^{\circ}$)	R.F.	R_{corr} (Ωcm^2)
316L SS	56.9	80.81	2.85	$2.8 \times 10^{+05}$
1 μm TiN	69.1	81.94	3.1	$8.25 \times 10^{+05}$
2 μm TiN	93.7	82.32	4.65	$8.43 \times 10^{+05}$
2 μm TiN	117.2	83.65	5.85	$8.58 \times 10^{+05}$

So, it can be concluded that TiN coated specimens were in passive state in the simulated environments. TiN coated specimens with $3 \mu m$ thickness have the best R_{corr} values and anti-corrosion ability in the simulated environments. In addition, a comparison of C_{dl} values measured by impedance of specimens indicated that C_{dl} increased slightly by increasing TiN Coating thickness. It might be related to the increase of the porosity within coating process.

3.4. Interfacial Contact Resistance

Interfacial Contact Resistance (ICR) between GDL and specimens (graphite, Bare 316L SS, and $3 \mu m$ -thick-TiN coated 316L SS) at different compaction pressures was measured for both sides. The ICR of a typical graphite plate was measured only for comparison. The ICR results are presented in Fig. 6. The inset in Fig. 6 is an enlarged plot at compacting pressures in the range of 100 – $320 N cm^{-2}$. In general, the ICR decreases rapidly at low compaction pressure range and then decreases gradually at higher compaction pressures. In a specified compaction pressure, the resistance increases in the order of Graphite < TiN < 316L SS. For Instance, at the compaction pressure of $138 N cm^{-2}$, the ICR of graphite, Bare 316L SS, and $3 \mu m$ -thick-TiN coated 316L SS was 10.8 , 30.9 , and $199.2 m\Omega cm^2$, respectively. In the DOE's technical target for bipolar plate (Table 1), the ICR measured both sides of specimens at compaction pressure of $138 N cm^{-2}$ for 2011 status, 2017 target, and 2020 target is 30 , 20 , $10 m\Omega cm^2$, respectively. Therefore, ICR value of $3 \mu m$ -thick-TiN coated 316L SS is near to 2011 status and TiN coating do not meet the DOE's target for 2017 and 2020. The higher ICR of bare 316L SS than the TiN coated specimen may be related to the natural oxide passive layer formed on the stainless steel surface [19, 21].

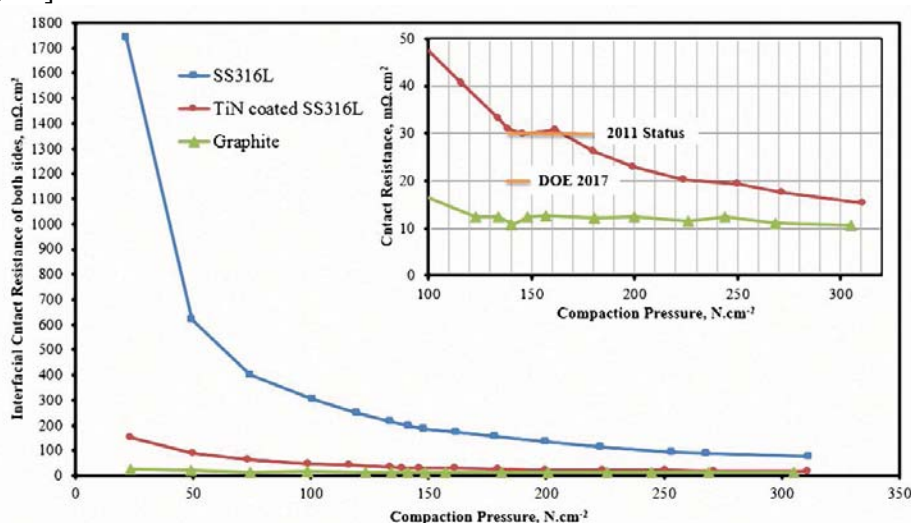


Figure 6: Interfacial Contact Resistance of graphite, bare 316L SS, and TiN coated specimens.



4. Conclusion

1. The results from potentiodynamic polarization curves in both simulated cathode and anode conditions showed that all of the TiN coated specimens have higher corrosion potential and lower corrosion current density than the uncoated specimen. Thus, applying TiN coating on the 316L SS surface can retard corrosion and increase the corrosion resistance.
2. In the simulated cathode conditions, potentiostatic test results showed that the TiN coated specimens with the thicknesses of 2 and 3 μm have lower stabilization current density values than the bare specimen. The 1 μm -thick-TiN coated specimen showed higher stabilization current density value than the uncoated specimen because of occurring pitting corrosion on the coated specimen.
3. In the simulated anode conditions, potentiostatic test results showed that the corrosion current density of the uncoated 316L SS was the lowest stabilization current density (about 0.2 μAcm^{-2}). The TiN coated specimens with the thicknesses of 1 and 3 μm undergo no corrosion in the simulated anode conditions of PEMFCs.
4. The EIS results indicated that the TiN coated specimen with 3 μm thickness showed best physical and electrochemical stability with high corrosion resistance as compared with 316L SS in the simulated cathode and anode environments.
5. The thickness of TiN coating must be at least 3 μm to provide suitable corrosion resistance.
6. At the compaction pressure of 138 Ncm^{-2} , the ICR of graphite, uncoated 316L SS, and 3 μm -thick-TiN coated 316L SS was 10.8, 30.9, and 199.2 $\text{m}\Omega\text{cm}^2$, respectively. However, ICR value of 3 μm -thick-TiN coated 316L SS is near to 2011 status of DOE but it does not meet the DOE's target for 2017 and 2020. ICR value of TiN coated 316L SS is much lower than uncoated 316L SS.
7. In general, the TiN coated 316L SS decrease ICR and improve corrosion resistance in simulated aggressive PEMFC environments.

Acknowledgement

The authors would like to thank the financial support of Renewable Energy Organization of Iran (SUNA).

References

- [1] Wilkinson DP. Proton exchange membrane fuel cells: materials properties and performance. 1st ed. Boca Raton, FL: CRC Press/Taylor & Francis; 2010.
- [2] Wang Y, Northwood DO. An investigation into TiN-coated 316L stainless steel as a bipolar plate material for PEM fuel cells. *J Power Sources* 2007;165:293-8.
- [3] Yoon W, Huang X, Fazzino P, Reifsnider KL, Akkaoui MA. Evaluation of coated metallic bipolar plates for polymer electrolyte membrane fuel cells. *J Power Sources* 2008;179:265-73.
- [4] Hermann A, Chaudhuri T, Spagnol P. Bipolar plates for PEM fuel cells: A review. *Int J Hydrogen Energy* 2005;30:1297-302.
- [5] Asghari S, Akhgar H, Imani BF. Design of thermal management subsystem for a 5kW polymer electrolyte membrane fuel cell system. *J Power Sources* 2011;196:3141-8.
- [6] Asghari S, Shahsamandi M, Ashraf Khorasani M. Design and manufacturing of end plates of a 5kW PEM fuel cell. *Int J Hydrogen Energy* 2010;35:9291-7.
- [7] DoE. Technical Plan - Fuel Cells. Multiyear research, development and demonstration plan 2011:Page 3.4 - 29.
- [8] Steele BCH, Heinzel A. Materials for fuel-cell technologies. *Nature* 2001;414:345-52.



- [9] Jones DA. Principles and prevention of corrosion. 2nd ed. New Jersey: Prentice Hall; 1996.
- [10] Hedayati A, Najafizadeh A, Kermanpur A, Forouzan F. The effect of cold rolling regime on microstructure and mechanical properties of AISI 304L stainless steel. *J Mater Process technol* 2010;210:1017-22.
- [11] Forouzan F, Najafizadeh A, Kermanpur A, Hedayati A, Surkialiabad R. Production of nano/submicron grained AISI 304L stainless steel through the martensite reversion process. *Mater Sci Eng A* 2010;527:7334-9.
- [12] Atkinson J, VanDroffelaar H, Corrosio ENAO. Corrosion and its Control: NACE; 1982.
- [13] Ma L, Warthesen S, Shores D. Evaluation of materials for bipolar plates in PEMFCs. *J New Mater Electrochem Syst* 2000;3:221-8.
- [14] Li M, Luo S, Zeng C, Shen J, Lin H, Cao C. Corrosion behavior of TiN coated type 316 stainless steel in simulated PEMFC environments. *Corros Sci* 2004;46:1369-80.
- [15] Cho E, Jeon US, Hong SA, Oh IH, Kang SG. Performance of a 1 kW-class PEMFC stack using TiN-coated 316 stainless steel bipolar plates. *J Power Sources* 2005;142:177-83.
- [16] Wang Y, Northwood DO. An investigation of the electrochemical properties of PVD TiN-coated SS410 in simulated PEM fuel cell environments. *Int J Hydrogen Energy* 2007;32:895-902.
- [17] Wang Y, Northwood DO. Effect of substrate material on the corrosion of TiN-coated stainless steels in simulated anode and cathode environments of proton exchange membrane fuel cells. *J Power Sources* 2009;191:483-8.
- [18] Kumagai M, Myung ST, Asaishi R, Sun YK, Yashiro H. Nanosized TiN-SBR hybrid coating of stainless steel as bipolar plates for polymer electrolyte membrane fuel cells. *Electrochim Acta* 2008;54:574-81.
- [19] Wang L, Northwood D, Nie X, Housden J, Spain E, Leyland A, et al. Corrosion properties and contact resistance of TiN, TiAlN and CrN coatings in simulated proton exchange membrane fuel cell environments. *J Power Sources* 2010;195:3814-21.
- [20] Zhang D, Duan L, Guo L, Tuan WH. Corrosion behavior of TiN-coated stainless steel as bipolar plate for proton exchange membrane fuel cell. *Int J Hydrogen Energy* 2010;35:3721-6.
- [21] Dur E, Cora ÖN, Koç M. Experimental investigations on the corrosion resistance characteristics of coated metallic bipolar plates for PEMFC. *Int J Hydrogen Energy* 2011.
- [22] Antunes RA, Oliveira MCL, Ett G, Ett V. Corrosion of metal bipolar plates for PEM fuel cells: A review. *Int J Hydrogen Energy* 2010;35:3632-47.
- [23] Li M, Luo S, Zeng C, Shen J, Lin H, Cao Cn. Corrosion behavior of TiN coated type 316 stainless steel in simulated PEMFC environments. *Corros Sci* 2004;46:1369-80.
- [24] Chen L, Lasia A. Ni-Al Powder Electrocatalyst for Hydrogen Evolution. *J Electrochem Soc* 1993;140:2464.
- [25] Los P, Lasia A, Ménard H, Brossard L. Impedance studies of porous lanthanum-phosphate-bonded nickel electrodes in concentrated sodium hydroxide solution. *J Electroanal Chem* 1993;360:101-18.
- [26] Jurczakowski R, Hitz C, Lasia A. Impedance of porous gold electrodes in the presence of electroactive species. *J Electroanal Chem* 2005;582:85-96.
- [27] Wang H, Sweikart MA, Turner JA. Stainless steel as bipolar plate material for polymer electrolyte membrane fuel cells. *J Power Sources* 2003;115:243-51.
- [28] André J, Antoni L, Petit J-P, De Vito E, Montani A. Electrical contact resistance between stainless steel bipolar plate and carbon felt in PEFC: A comprehensive study. *Int J Hydrogen Energy* 2009;34:3125-33.
- [29] Jayaraj J, Kim YC, Seok HK, Kim KB, Fleury E. Development of metallic glasses for bipolar plate application. *Mater Sci Eng A* 2007;449-451:30-3.



- [30] Ekdunge P, Jüttner K, Kreysa G, Kessler T, Ebert M, Lorenz W. Electrochemical impedance study on the kinetics of hydrogen evolution at amorphous metals in alkaline solution. *J Electrochem Soc* 1991;138:2660.
- [31] Macdonald JR, Johnson WB. *Fundamentals of Impedance Spectroscopy. Impedance Spectroscopy: John Wiley & Sons, Inc.; 2005. p. 1-26.*
- [32] Nyikos L, Pajkossy T. Fractal dimension and fractional power frequency-dependent impedance of blocking electrodes. *Electrochim Acta* 1985;30:1533-40.
- [33] Nam ND, Kim JG, Hwang WS. Effect of bias voltage on the electrochemical properties of TiN coating for polymer electrolyte membrane fuel cell. *Thin Solid Films* 2009;517:4772-6.
- [34] Brown R, Alias MN, Fontana R. Effect of composition and thickness on corrosion behavior of TiN and ZrN thin films. *Surf Coat Technol* 1993;62:467-73.
- [35] Huang J-H, Ouyang F-Y, Yu G-P. Effect of film thickness and Ti interlayer on the structure and properties of nanocrystalline TiN thin films on AISI D2 steel. *Surf Coat Technol* 2007;201:7043-53.
- [36] Yao Z, Jiang Z, Wang F. Study on corrosion resistance and roughness of micro-plasma oxidation ceramic coatings on Ti alloy by EIS technique. *Electrochim Acta* 2007;52:4539-46.
- [37] Gilbert JL. 1.103 - Electrochemical Behavior of Metals in the Biological Milieu. In: Editor-in-Chief: Paul D, editor. *Comprehensive Biomaterials*. Oxford: Elsevier; 2011. p. 21-48.
- [38] Chen Q, McEwen GD, Zaveri N, Karpagavalli R, Zhou A. Chapter 9 - Corrosion Resistance of Ti6Al4V with Nanostructured TiO₂ Coatings. *Emerging Nanotechnologies in Dentistry*. Boston: William Andrew Publishing; 2012. p. 137-50.
- [39] La Mantia F, Vetter J, Novák P. Impedance spectroscopy on porous materials: A general model and application to graphite electrodes of lithium-ion batteries. *Electrochim Acta* 2008;53:4109-21.
- [40] Liu X, Xiong J, Lv Y, Zuo Y. Study on corrosion electrochemical behavior of several different coating systems by EIS. *Prog Org Coat* 2009;64:497-503.
- [41] Jüttner K. Electrochemical impedance spectroscopy (EIS) of corrosion processes on inhomogeneous surfaces. *Electrochim Acta* 1990;35:1501-8.



Electrooxidation of Sodium Borohydride on Porous Nano Structured Ni/PtNi electrode in basic media

Mir Ghasem Hosseini¹, Mehdi Abdolmaleki^{2*}, Iraj Ahadzadeh³

Electrochemistry Research Laboratory, Department of Physical Chemistry, Chemistry Faculty, University of Tabriz, Tabriz, Iran

Corresponding author's email: mg-hosseini@tabrizu.ac.ir

Abstract

In this study, Ni/PtNi electrode prepared by electrodeposition process and galvanic replacement method was examined for electrocatalytic activities during the oxidation of sodium borohydride in alkaline solutions. The surface morphologies and compositions of coating before and after galvanic replacement were determined by energy dispersive X-ray (EDX) and scanning electron microscopy (SEM) techniques. It was found that the Ni/PtNi coating has a porous nano structure. The electrocatalytic activity of Ni/PtNi electrodes for electrooxidation of sodium borohydride in alkaline solutions was investigated by cyclic voltammetry. Borohydride electrooxidation on Ni/PtNi electrode was studied at various concentrations and potential scan rates. The anodic peak current density was found to be up to nine times higher on Ni/PtNi electrode for sodium borohydride compared to that for fat platinum. Therefore, the Ni/PtNi catalysts can be potential anode catalysts for the direct borohydride fuel cell.

Keywords: Electrooxidation of borohydride, Ni/PtNi electrode, Electrocatalysis, Galvanic replacement, Direct borohydride fuel cell

1. Introduction

In 2005, the world energy consumption was approximately 11000 million tones of oil equivalent, with 88% obtained from fossil fuels such as oil, gas and coal with the remaining 12% from nuclear, hydroelectric and other energy sources [1]. Electrical energy from fossil fuels burning is normally generated in robust and reliable large centralized power plants, able to satisfy the energy demands of domestic and industrial activities of most countries. However, the generation of electricity by burning these primary sources of energy is inefficient and generates pollution and green house gases. As the production rate of nomad electronics devices increases, the demand for high energy portable generator becomes stringent. The state of the art lithium-ion batteries cannot meet the size requirements due to

1 - Associate Professor in Physical Chemistry

2 - Ph. D student of physical chemistry. University of Tabriz, Tabriz, Iran, abdolmaleki11@gmail.com

3 - Ph. D of physical chemistry. University of Tabriz, Tabriz, Iran, irajahadzadeh@gmail.com



their energy density limitations (below 200 Wh kg⁻¹). In that context the chemical energy conversion into electrical energy through fuel cells is an attractive candidate for portable power generation. The present researches in this area are directing toward the development of an efficient and harmless to the environment way of energy generation. Direct liquid fuel cells, fed with borohydride, methanol [2] or ethylene glycol [3], represent possible alternatives [4, 5].

The direct borohydride fuel cell (DBFC) combines a high theoretical voltage (1.64 V) with the advantages of alkaline fuel cell: most reaction kinetics is faster in alkaline than in acid media and it is possible to use non-platinum electrocatalysts without detrimental performance and stability losses [6]. The fuel (borohydride salt), also presents several advantages: it is non toxic, easily stored and relatively stable in alkaline solution, while exhibits rather high energy density (9.3 Whg⁻¹ at 1.64V). However the borohydride oxidation reaction (BOR) occurring at the anode of DBFC is a complex eight-electron process [7, 8] (Eq. (1)):



The BOR kinetics and pathway depend on several variables, such as the catalysts material and solution composition or temperature [5, 9-11]. Recently, there is considerable interest in porous nanostructures because of their high specific surface, low density, and reduced cost [12].

The galvanic replacement reaction provides a very simple and effective method to prepare porous metal nanostructures having a lower standard electrode potential compared to that of the target material.

Here we demonstrate a protocol for synthesizing porous Ni/PtNi nanostructures via galvanic exchange reaction using Zn from Ni/ZnNi coating. NiZn coating was grown on Ni by electrodeposition technique and Ni/ZnNi electrode was obtained. Porous Ni/PtNi nanostructures were produced by exposing the Ni/ZnNi electrode to an alkaline aqueous solution of the corresponding platinum salt (0.001 mol L⁻¹ H₂PtCl₆+30 wt.% NaOH). These porous nanostructures formed are stable under ambient conditions and show a highly porous catalytic surface suitable for the electrooxidation of borohydride in alkaline solution.

2. Experimental

The copper electrodes were cut and coated with polyester except a surface area of 1 cm² for measurements. Electrical conductivity was provided by a copper wire. Before electrodeposition, the electrode surfaces were polished with emery paper (2500 grit size), then washed with distilled water, thoroughly degreased in a 30 wt.% NaOH solution for 5 min, washed again with distilled water, dipped into 10 wt.% H₂SO₄ solution for 1 min followed by a wash with distilled water and immersed in the bath solution. The electrochemical bath was prepared using analytical grade chemicals and double distilled water. The composition and conditions of plating baths were used for the different Ni coatings are presented in table 1. After deposition, the electrodes were rinsed with distilled water in order to remove residues of bath chemicals and unattached particles. The Pt deposition was performed simply by dipping the Ni/ZnNi electrode into a 30 wt.% NaOH solution of H₂PtCl₆ salt (Merck, 99.99%) with concentration of 0.001 mol L⁻¹ for 48 h at room temperature.

Table 1: Experimental conditions used in the electrodeposition of smooth Ni and Ni/ZnNi coatings

Composition and operating conditions	Type of coating	
	smooth Ni	Ni/ZnNi
NiSO ₄ ·6H ₂ O (g L ⁻¹)	330	330
NiCl ₂ ·6H ₂ O (g L ⁻¹)	45	45
H ₃ BO ₃ (g L ⁻¹)	37	37
ZnCl ₂	-	20
Current density (mA cm ⁻²)	50	50
Temperature (°C)	50	50
pH	4-4.5	4-4.5
Time (min)	40	30

The standard reduction potential of the PtCl₆⁻²/Pt pair (0.59 V vs. SHE) is higher than the reduction potential of the Zn⁺²/Zn pair (-0.762 V vs SHE), and it can be reduced by Zn as shown in the following equation:



The surface composition and morphology of electrodes before and after galvanic replacement were determined using scanning electron microscopy (SEM, Philips, and Model XL30) equipped with an energy dispersive X-ray spectrometer (EDX).

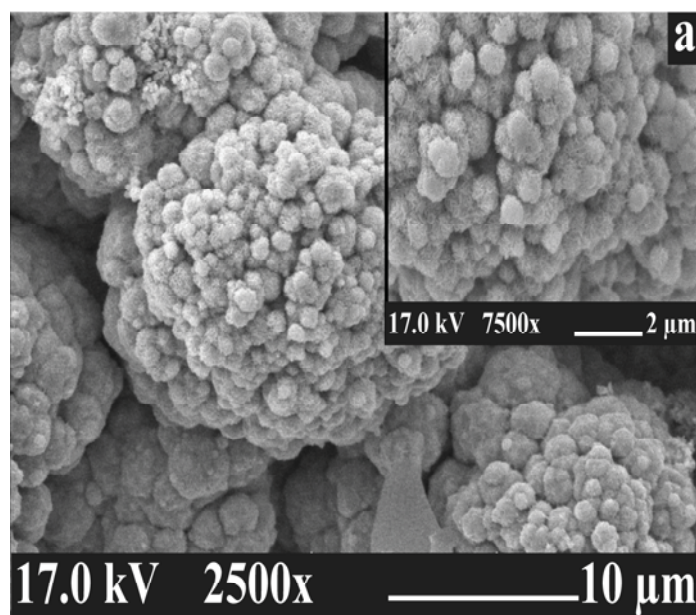
The electrochemical studies were carried out in a conventional electrochemical cell and all the solutions were purged with purified nitrogen for 10 min before the measurements. A standard three-electrode cell arrangement was used in all experiments. A platinum sheet of the geometric area of about 20 cm² was used as counter electrode, while all potentials were measured with respect to a commercial saturated calomel electrode (SCE). The catalytic activity of the electrodes was tested by cyclic voltammetry. Electrochemical experiments were carried out using a Princeton Applied Research, EG&G PARSTAT 2263 Advanced Electrochemical system run by PowerSuite software. For each experiment, a freshly prepared electrode and solution was used.

3. Results and discussion

3.1. Characterization of coatings

The SEM images of Ni/ZnNi electrode and Ni/PtNi electrode after are given in Figure 1. It can be seen from Figure 1a that the surface of Ni was fully covered by the NiZn layer. The Ni/NiZn coating is compact and has a porous structure. However, the morphology of surface changed significantly after leaching-galvanic replacement process of Zn from the deposit (Figure 1b). A great number of cracks and pores appeared leading a high surface area available for the borohydride oxidation reaction. Ni/PtNi deposits are nano-particulate and retain a high coverage of the substrate.

The chemical composition of surface before leaching-replacement was 16.87 at.% Ni and 83.13 at.% Zn. After alkaline leaching-galvanic replacement, the surface composition was changed as 59.47 at.% Ni, 28.28 at.% Zn and 12.25 at.% Pt. The results of chemical composition analysis revealed that the Zn content decreased considerably after selective dissolution, which leads to pore and crack formation, yielding a highly porous catalytic surface suitable for use in borohydride electrooxidation.



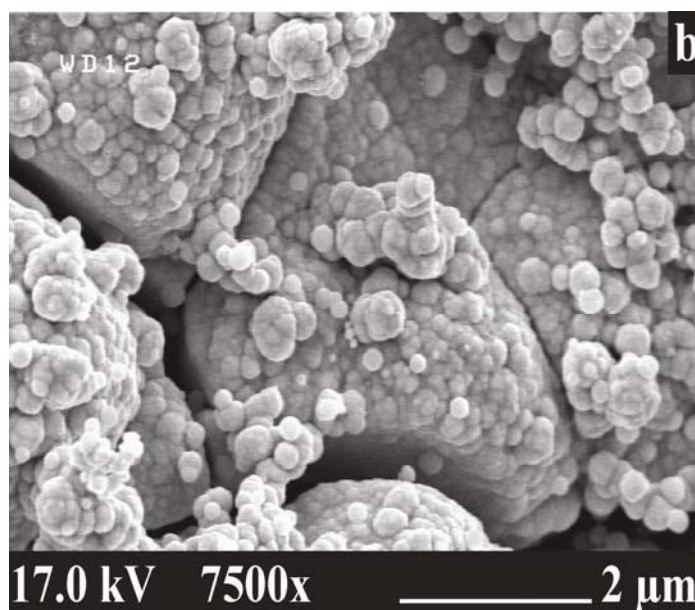


Figure 1: SEM images of Ni/ZnNi coating (a) and (b) Ni/PtNi after leaching-galvanic replacement process.

3.2. Cyclic voltammetry

Cyclic voltammograms in 2 M NaOH + 0.02 M NaBH₄ solution are shown in Figure 2, comparing the electrochemical behavior of the porous Ni/PtNi electrode to that of a flat Pt electrode with the same geometric area (1 cm²). In the potential range of -1.2 to +0.7V versus calomel, the electrochemical behavior of BH₄⁻ is fairly complex characterized by a number of oxidation peaks. It can be seen from Figure 2A, scanning in the positive direction, at a rate of 50 mV s⁻¹, the first oxidation peak occurs at -0.77 V (peak *a*₁), followed by two anodic peaks at about -0.38 V (peak *a*₂) and -0.048 V (peak *a*₃). On the return scan, interestingly, an additional oxidation peak has been observed with a peak potential of -0.487 V (peak *c*₁). Peak *a*₁ could be due to the oxidation of H₂ generated in the catalytic hydrolysis of NaBH₄. Then, a broad oxidation hump (that develops into a well-defined peak *a*₂) appears, which can be attributed to the oxidation of reaction intermediates on the partially oxidized platinum surface. Peak *a*₃ can be attributed to the direct, potentially eight-electron, oxidation of BH₄⁻ [11]. It is likely that peak *c*₁ in the reverse sweep is attributable to an adsorbed species such as BH₃OH⁻ or other borohydroxides formed as an intermediate during the oxidation of the borohydride ion [9]. The borohydride electro-oxidation on Ni/PtNi electrode was characterized by five well-defined current peaks on the forward and reverse scans (Figure 2B). An increment in the anodic peak current for previous peaks (*a*₁, *a*₃ and *c*₁) followed by the appearance of two new peaks (*a*₄ and *c*₂) at more positive potential are the main effects observed upon electro-oxidation of borohydride on the porous Ni/PtNi electrode. Also, the peak *a*₂ becomes ill-defined and is hard to distinguish. The appearance of the new peaks leads to the conclusion that borohydride oxidation takes place after the oxidation of Ni(OH)₂ to NiOOH [13, 14]. The Ni²⁺/Ni³⁺ redox couple acts as a catalyst for the oxidation of borohydride in basic solutions.

Figure 2 also shows that the current density of the Ni/PtNi electrode is much higher than flat Pt electrode (37 mA cm⁻² vs. 4 mA cm⁻²). It clearly illustrates the influence of the increased surface area of the Ni/PtNi electrode as a result of galvanic replacement.

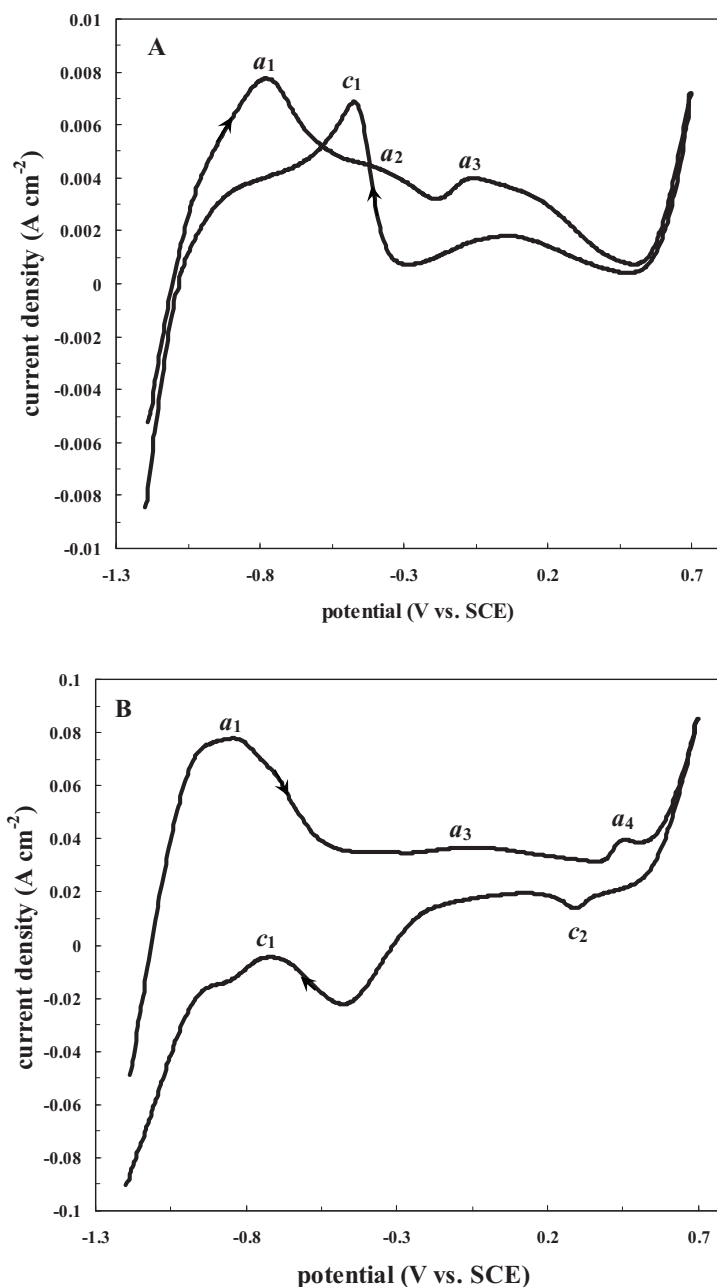


Figure 2: Cyclic Voltammograms recorded for 0.02 M sodium borohydride in 2 M NaOH solution on (a) flat Pd and (b) porous Ni/PtNi electrodes at 50 mV s⁻¹ scan rate. The influence of the scan rate on the cyclic voltammetry behaviour of porous Ni/PtNi electrode in 2 M NaOH/0.02 M borohydride is shown in Figure 3. The *a*₃ peak potential linearly changed with (scan rate)^{1/2} showing that an irreversible electrode reaction takes place on the Ni/PtNi electrode surface.

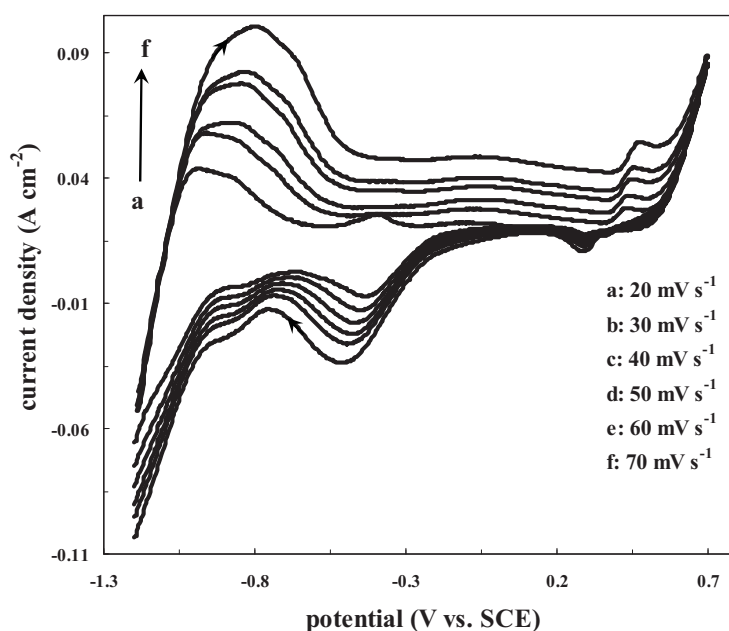


Figure 3: Cyclic Voltammograms recorded for 0.02 M NaBH₄ with different scan rate in 2 M NaOH solution at the porous Ni/PtNi electrode.

Figure 4 shows the typical CVs for Ni/PtNi electrode as a function of NaBH₄ concentration between 0.02 and 0.07 M. Looking at voltammograms with BH₄⁻, it is observed that the current density of those peaks increases with the concentration of BH₄⁻. Moreover, the first peak (*a*₁) is shifted to more positive potentials with the scan rate (Figure 3), and the ratio ($I_{p,a}/v^{1/2}$) form decreases. These results indicate a CE mechanism [15], i.e., the hydrolysis of BH₄⁻ followed by the hydrogen ionization. This is the same conclusion as has been arrived at by Gyenge [9].

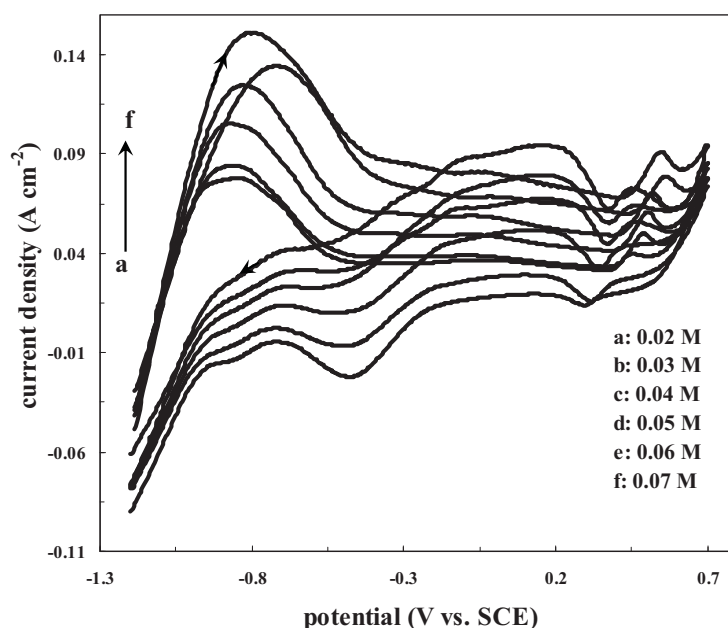


Figure 4: Cyclic voltammograms of the porous Ni/PtNi electrode from -1.2 to 0.7 V at the scan rate of 50 mV s⁻¹ with the various concentrations of borohydride.



4. Conclusions

The present study describes the successful synthesis of porous Ni/PtNi nanocatalyst by a simple galvanic replacement reaction of Ni/ZnNi in an alkaline platinum solution. The electrooxidation of BH_4^- on a Ni/PtNi electrode has been systematically studied by CV, as a function of the BH_4^- concentration and the potential scan rate. The results were compared with flat Pt electrode in 2 M NaOH solution. The SEM results showed that the Pt nano particles in Ni/PtNi catalyst were highly dispersed and the alkaline leaching-galvanic replacement process produces a highly porous catalytic surface suitable for use in electrooxidation of borohydride. The cyclic voltammetry experiment shows that current densities for borohydride oxidation on Ni/PtNi electrode (37 mA cm^{-2}) are greater than that observed for flat Au electrode (4 mA cm^{-2}) because the Ni/PtNi possesses smaller average size of the metal particles and improvement in the electronic properties of the catalyst. Therefore, the Ni/PtNi catalysts can be potential anode catalysts for the direct borohydride fuel cell.

Acknowledgment

The authors would like to acknowledge the financial support of Iranian Nanotechnology Society and the Office of Vice Chancellor in Charge of Research of University of Tabriz.

References

- [1] Energy Statistics Yearbook 2005. United Nations, Department of Economic and Social Affairs.
- [2] R. Feng, H. Dong, Y. Wang, X.P. Ai, Y.L. Cao, H.X. Yang "A simple and high efficient direct borohydride fuel cell with MnO_2 -catalyzed cathode", *Electrochem. Commun.* (2005). 7, 449-452
- [3] K. Matsuoka, Y. Iriyama, T. Abe, M. Matsuoka, Z. Oguma "Alkaline direct alcohol fuel cells using an anion exchange membrane", *J. Power Sources* (2005). 150, 27-31
- [4] M. Atwan, D.O. Northwood, E.L. Gyenge "Evaluation of colloidal Ag and Ag-alloys as anode electrocatalysts for direct borohydride fuel cells", *Int. J. Hydrogen Energy* (2007). 32, 3116-3125
- [5] M. Chatenet, F. Micoud, I. Roche, E. Chainet "Kinetics of sodium borohydride direct oxidation and oxygen reduction in sodium hydroxide electrolyte: Part I. BH_4^- electro-oxidation on Au and Ag catalysts", *Electrochim. Acta* (2006). 51, 5459-5467
- [6] W. Vielstich, A. Lamm, H.A. Gasteiger, in: W. Vielstich, A. Lamm, H.A. Gasteiger (Eds.), *Handbook of Fuel Cell*, vol 1-4, Wiley, Chichester, 2003.
- [7] J.H. Morris, H.J. Gysling, D. Reed, *Chem. Rev.* (1985). 85, 51-76
- [8] S. Amendola "A novel high power density borohydride-air cell", *J. Powers Sources* (1999). 84, 130-133
- [9] E. Gyenge "Electrooxidation of borohydride on platinum and gold electrodes: implications for direct borohydride fuel cell", *Electrochim. Acta* (2004). 49, 965-978



- [10] B.H. Liu, Z.P. Li, S. Suda “Electrocatalysts for the anodic oxidation of borohydrides”, *Electrochim. Acta* (2004). 49, 3097-3105
- [11] M.V. Mirkin, H. Yang, A.J. Bard, “Borohydride oxidation at a gold electrode”, *J. Electrochem. Soc.* (1992). 139, 2212-2217
- [12] M.G. Hosseini, M. Abdolmaleki “Synthesis and characterization of porous nanostructured Ni/PtNi electrode towards electrooxidation of borohydride”, *Int. J. Hydrogen Energy* (2012). in press.
- [13] M.G. Hosseini, M. Abdolmaleki, S. Ashrafpoor “Preparation, characterization, and application of alkaline leached Ni/Zn-Ni binary coatings for electro-oxidation of methanol in alkaline solution”, *J. Appl. Electrochem.* (2012). 42, 153-162
- [14] M.G. Hosseini, M.M. Momeni, M. Faraji “Highly Active Nickel Nanoparticles Supported on TiO₂ Nanotube Electrodes for Methanol Electrooxidation”, *Electroanalysis* (2010). 22, 2620-2625
- [15] R. Greef, R. Peat, L.M. Peter, D. Pletcher, J. Robinson, *Instrumental Methods in Electrochemistry*, Ellis Horwood, 1993, p. 187 (Chapter 6).



Investigation the Stability and Methanol Oxidation Activity of Alloy Nanoparticles

Mitra Amani¹, Hassan Pahlavanzadeh², Hussein Gharibi³, Mohammad Kazemeini⁴

^aDepartment of Chemical Engineering, Tarbiat Modares University, P.O. Box 14115-175, Tehran, Iran

*Corresponding Author's E-mail: mitra_amani@yahoo.com

Abstract

Polyaniline fibers (PANI) were synthesized by chemical interfacial method and doped with Para toluene sulfonic acid. The doped PANI was utilized for the fabrication of a Vulcan-Polyaniline composite (C-PANI). Pt and Sn particles were subsequently deposited by reduction onto the C-PANI composite to produce a PtSn(70:30)/C-PANI electrocatalyst. Catalytic activity of this electrocatalyst is compared with PtRu/C. Cyclic voltammetry studies in methanol oxidation reaction (MOR) show that the peak current density of PtSn(8:2)/C-20%PANI is about 40% more than PtRu/C and its onset potential is about 100 mV lesser. According to CO stripping test, PtSn(70:30)/C-20%PANI is more CO tolerant and it can be the main reason of its better catalytic activity in MOR. Also, durability in the MOR has been evaluated by accelerated durability test and it was shown that stability of PtSn(70:30)/C-PANI is considerably more than PtRu/C. Ultimately, the PtSn(70:30)/C-20%PANI electrocatalyst is a good substitution for PtRu/C in a direct methanol fuel cell.

Keywords: CO tolerance, polyaniline, methanol oxidation

Introduction

Direct methanol fuel cell (DMFC) has attracted extensive attention due to its many advantages, such as high energy density (6100Whkg^{-1} at $25\text{ }^{\circ}\text{C}$) and low operating temperature [1]. Electro oxidation of methanol is a complex process involving the adsorption of CH_3OH followed by successive dehydrogenation steps, exchange of six electrons and formation of numerous intermediates, especially linearly bonded CO which was believed to react with an adsorbed OH_{ads} intermediate at sufficiently anodic potentials. The reactions are slow and require active catalytic sites for adsorption and oxidation of methanol, as well as oxidation and desorption of the adsorbed intermediates. It is widely agreed that platinum is the only element to show a significant electrocatalytic activity for methanol oxidation but the catalytic activity of platinum is still too low and its loading is too high to consider the direct methanol fuel cells as a practical power source. The poor performance of pure platinum for methanol oxidation results from the strong adsorption of CO on the active Pt sites so that even parts per million levels of CO can cause serious poisoning and the fact that the formation of OH_{ads} on platinum takes place at potentials that are too high to be of practical interest. Also, platinum is a rare metal and is very expensive so it is necessary to reduce the cost-to-efficiency ratio. In order to enhance the CO tolerance and reduce the catalyst price, Pt-based bimetallic or multimetallic catalysts such as PtRu, PtSn, PtMo, PtSnRu have been widely

¹ PHD student of chemical engineering, Tarbiat modares university

² Prof. of chemical engineering, Department of Chemical Engineering, Tarbiat Modares University

³ Prof. of physical chemistry, Department of Chemistry, Faculty of Science, Tarbiat Modares University

⁴ Prof. of chemical engineering, Department of chemical engineering, Sharif University of Technology



studied, among which PtRu and PtSn are the most active catalysts of binary alloys [2]. The Pt-Ru alloy catalyst with a 50% Ru atomic composition is one of the most popular DMFC electrocatalysts known to date. However, poor CO tolerance of Pt-Ru for the higher CO concentrations expected at system start-up or during changes in load, Ru leaching from Pt-Ru anode electrocatalysts and crossing over to the cathode with a dramatic impact on the activity of Pt electrocatalyst in the cathode electrode and finally, the high value of Pt-Ru and the limited availability of Ru can limit its usage in DMFCs [3]. Compared with platinum, Sn can activate water at lower potentials so that some OH species is formed at low potentials on Sn sites and then the adsorbed CO reacts with adsorbed OH species to produce CO₂. On the other hand, a higher platinum dispersion on a suitable support should enable a decrease in the amount of platinum used in the DMFC active layer without performance loss and decrease the amount of adsorbed linear CO species. One way of getting a better distribution of the catalytic particles is to disperse the material within a convenient electron conducting matrix. Polyaniline with porous structure and high surface area is particularly attractive material as catalyst support in fuel cells but, its low conductivity compared with carbon and its stability during the catalyst workout however; limited its practical consumption in a fuel cell [4]. This paper explains that polyaniline is synthesized chemically by interfacial method and then PtSn nanoparticles are reduced on a composite of Vulcan and 20% polyaniline utilizing ethylene glycol. The catalytic activity and CO tolerance of the synthesized catalyst is compared by commercial PtRu/C (Electrochem).

Experimental section

Polyaniline nanofibers (PANI) were synthesized under ambient condition by interfacial polymerization. The oxidant solution consisted of APS in H₂SO₄ solution (1M) was carefully added to the organic phase consisted of aniline in chloroform. After 24hr, the aqueous layer was filled with dark green colored emeraldine salt of polyaniline that was washed repeatedly with distilled water and methanol. The sulfate-ion-doped PANI was converted into emeraldine base form (EB) by treatment with ammonium hydroxide and then PANI (EB) was redoped with PTSA for catalyst synthesis.

For electrocatalyst synthesis, the specified amounts of Vulcan (C) and PANI (20%wt) were mixed with 10 mL H₂O:IPA (1:1) ultrasonically for 30 min. The C-PANI composite was impregnated with Pt and Sn particles by the addition of H₂PtCl₆ salt in water and SnCl₂ followed by sonication of the suspension for 30 min and subsequently the mixture was magnet stirred for 2 h at room temperature. This suspension was mixed ultrasonically with excess of ethylene glycol then was stirred at 130 °C under Ar atmosphere for 16 h. Finally, the product (PtSn(70:30)/C-PANI) was washed with distilled water several times and dried at 80 °C. The Pt and Sn content were determined by ICP.

Results and discussion

The electrocatalytic activity of PtRu/C and PtSn(70:30)/C-20%PANI electrocatalysts toward methanol oxidation is compared in Fig.1. All electrodes show a typical methanol oxidation current peak in the forward scan and an oxidation peak in the backward scan corresponding to the removal of the residual carbon species formed in the forward scan. As can be seen the peak current density in PtSn(70:30)/C-20%PANI is about 40% more than PtRu/C and its onset potential is about 100 mV lesser.

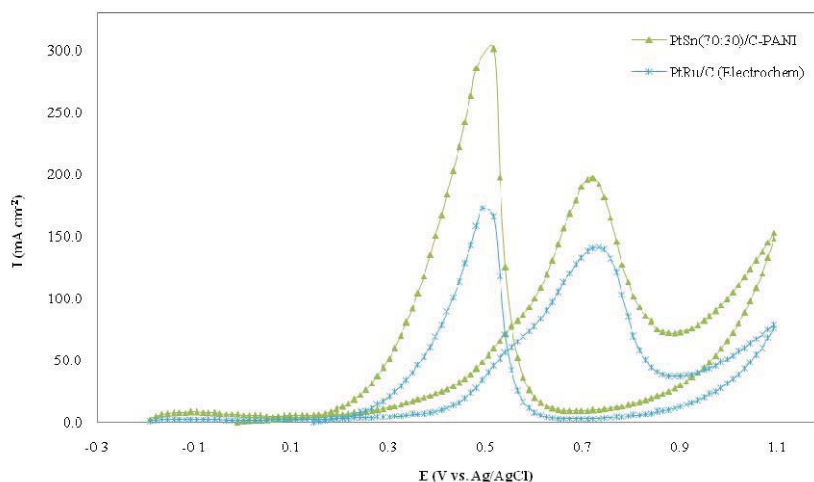


Fig1. Cyclic voltammograms of the PtRu/C and PtSn(8:2)/C-PANI electrodes in the potential range -0.2 to 1.2 V vs. Ag/ AgCl with a scan rate of $50 \text{ mV}\cdot\text{s}^{-1}$ in $1 \text{ M CH}_3\text{OH} + 0.5 \text{ M H}_2\text{SO}_4$ at 25°C

The mechanism of methanol oxidation on Sn modified electrocatalysts was complicated. It was suggested that the formation of tin oxygen containing species which was necessary for oxidation of formed poisoning intermediate in the oxidation of methanol, occurs at lower potential than Pt oxygen containing species. According to the theory of bi-functional catalysis mechanism, methanol dissociation occurs on the Pt sites and water dissociation occurs on the modified metal sites (Sn or Ru). It is well known that the formation of OH by water activation on Sn was much easier than that on Pt, which is a key step for the oxidative removal of adsorbed CO.

Since CO species are the main poisoning intermediate in methanol electro-oxidation reaction, a good catalyst should possess excellent CO electro-oxidizing ability. To analyze the enhanced electro-catalyzing activity of PtSn for methanol oxidation (as shown in Fig. 1), the CO eliminating ability of catalysts is studied by CO_{ad} stripping analysis. Briefly, CO is pre adsorbed at constant potential of -0.1V during 15 min and non-adsorbed CO was then bubbled out by flowing Ar for 30 min. The forward scan of CO_{ad} oxidation profiles recorded for the PtSn(8:2)/C-PANI and PtRu/C electrocatalysts are depicted in Fig.2 and the trend of their onset potential is shown in the inset of Fig.2.

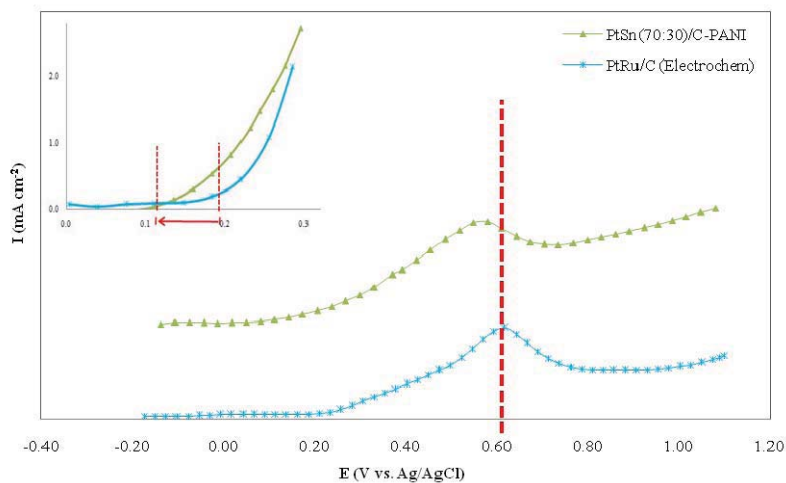
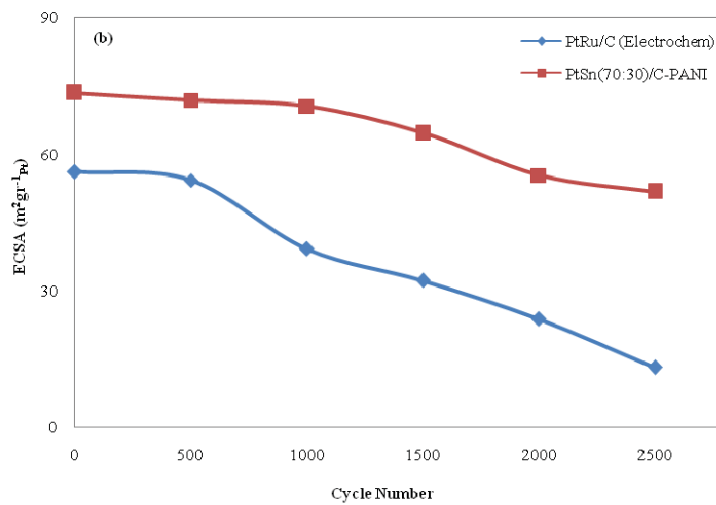
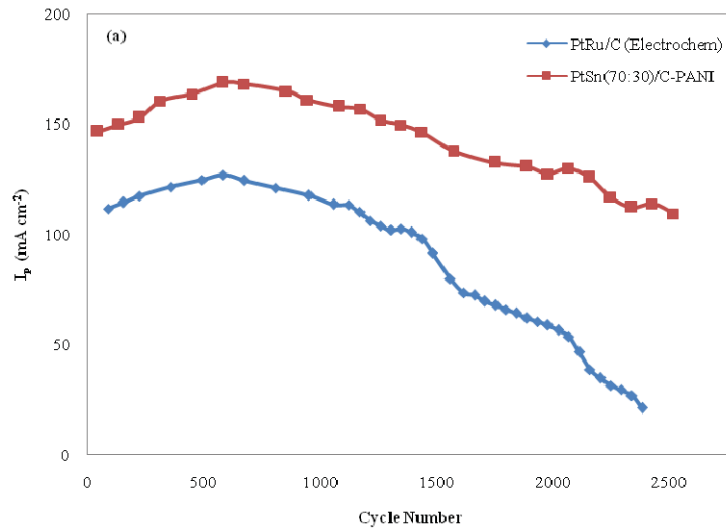


Fig 2. Forward scan of the CO stripping voltammograms of the PtRu/C and PtSn(8:2)/C-20%PANI catalysts in the potential range -0.2 to 1.2 V vs. Ag/ AgCl with a scan rate of 25 $\text{mV}\cdot\text{s}^{-1}$

As is clear in the inset of Fig.2, the onset potential of CO_{ads} oxidation on PtSn(8:2)/C-20%PANI is about 100 mV less than PtRu/C and its peak potential is about 40mV lesser, So the PtSn(8:2)/C-20%PANI is more CO tolerant.

Accelerated stability tests of the PtRu/C and PtSn(70:30)/C-PANI electro-catalysts were carried out by a consecutive sweep from -0.2 to 1.2 V for 2500 potential cycles in a H_2SO_4 (0.5M) + CH_3OH (1M) solution. The voltammograms of H_2 adsorption/desorption was used to determine the change of the Pt active surface area after each 500 cycles. Finally, CO stripping analysis was performed to survey the change of CO tolerance of electro-catalysts before and after 2500 potential cycles. The change of peak current density in MOR (I_p) and the variation of ECSA during the ADT are shown in Fig.3 (a) and (b). As can be seen in Fig.13 (a), methanol oxidation at both of electrodes show almost constant anodic current up to about 500th cycles. After that, the peak current decreased but with a lower rate on PtSn(70:30)/C-PANI. The I_p value of PtSn(70:30)/C-PANI decreases slowly with the number of CV cycles and reaches almost 75% of the initial current value at the 2500th scan. The I_p value of Pt-Ru/C drops much more rapidly with the number of CV cycles and reaches only around 20% of the initial value after the 2500 cycles. The loss of catalytic activity may have resulted either from the consumption of methanol during the potential scan or from the poisoning and structural changes of the electro-catalyst nanoparticles as a result of the applied potential during scanning in an aqueous solution, especially in the presence of an organic compound. As is clear in Fig.3 (b), ECSAs for both of electrodes are reduced of about 77% for PtRu/C and 30% for PtSn(70:30)/C-PANI, indicating a remarkable decrease of the Pt active surface area due to Pt sintering, the dissolution of Pt metal and the oxidation of the carbon support. This significant difference between these electro-catalysts may be due to positive effect of doped PANI in the electro-catalyst support. Fig.3 (c1) and (c2) shows the CO stripping voltammograms of these electro-catalysts before and after the ADT test. As can be seen, the location and pattern of CO stripping voltammograms of PtSn(70:30)/C-PANI do not change much; a minor shift of the onset potential is observed at the end of ADT but the location of the peak potential does not change. In contrast, a remarkable change in the CO stripping voltammograms of PtRu/C (Electrochem) is observed and the peak potential for CO_{ad} stripping is shifted from 0.618V to about 0.8V after the ADT. The positive shift of the

peak potential shows that this electro-catalyst loses its surface characteristic. The dissolution of Ru under an electrochemical condition is one of the major causes for the change in the electrochemical surface characteristics and the consequent performance deterioration. This finding shows that the PtSn(70:30)/C-PANI electro-catalyst has a better durability in the MOR in comparison with commercial PtRu/C due to the coexistence of PtSn alloy and doped PANI with PTSA in electro-catalyst structure.



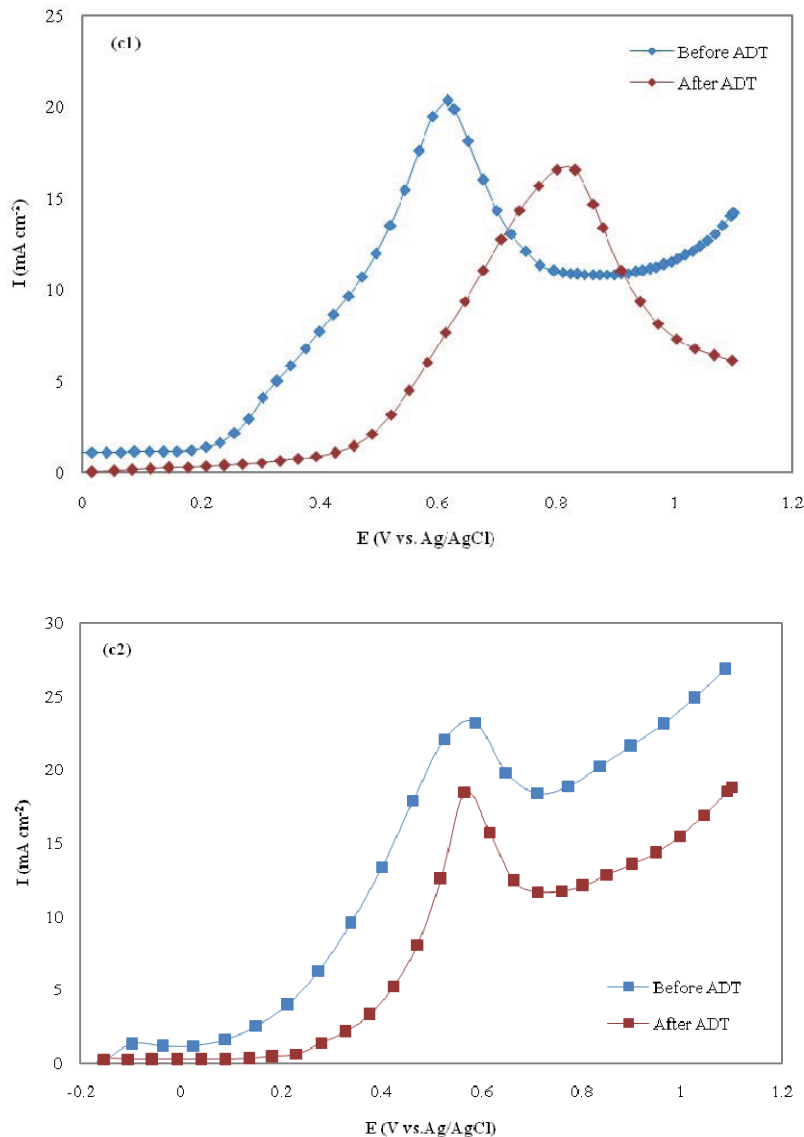


Fig.3. Obtained results of ADT on PtRu/C and PtSn(70:30)/C-PANI electrodes between -0.2 to 1.2V in H_2SO_4 (0.5M) + CH_3OH (1M): Variation the I_p in the MOR (a). Change in the ECSA (b). CO stripping voltammograms before and after the ADT on PtR/C (c1) and PtSn(70:30)/C-PANI (c2).

Conclusion

A new electrocatalyst ,PtSn(70:30)/C-PANI, is synthesized and its catalytic activity and CO tolerance is compared with commercial PtRu/C. The peak current density of PtSn(70:30)/C-20%PANI in MOR is about 40% more than PtRu/C and its onset potential is about 100 mV lesser. According to CO stripping voltammetry, The PtSn(70:30)/C-20%PANI is more CO tolerant and it's stability in MOR is significantly more than PtRu/C.

References

- [1] Wen Z, Wang Q, Zhang Q, Li J. *Hollow carbon spheres with wide size distribution as anode catalyst support for direct methanol fuel cells*. *Electrochem. Commun* 2007; 9:1867–72.
- [2] Zhang J. *PEM Fuel Cell Electrocatalysts and Catalyst Layers*. Canada: Springer; 2008



- [3] Yoo E, Okada T, Kizuka T, Nakamura J. *Effect of carbon substrate materials as a Pt–Ru catalyst support on the performance of direct methanol fuel cells*. J. Power Sources 2008; 180: 221–6.
- [4] Bleda-Martínez M.J, Morallon E, Cazorla-Amorós D. *Polyaniline/porous carbon electrodes by chemical polymerisation: Effect of carbon surface chemistry*. Electrochim. Acta 2007; 52 : 4962–8.
- [5] Bard A.J, Faulkner L.R. *Electrochemical methods, Fundamentals and Applications*. USA: Wiley; 2001.



Electrocatalytic oxidation of methanol on semiconducting polymer nanocomposite in alkaline media

A. Ehsani

Department of Chemistry, Faculty of science, University of Qom, Qom, Iran.

E-mail address: a.ehsani@qom.ac.ir

Abstract

Composites of multi-walled carbon nanotubes (MWCNT) and poly ortho aminophenol (POAP) semiconducting film with good uniformity for use as electrodes in catalytic oxidation were prepared by electropolymerization by using the ionic surfactant as electrolyte, for dispersing CNTs within conducting polymer/carbon nanotube composite films. The methods of cyclic voltammetry (CV) and electrochemical impedance spectroscopy (EIS) were employed for catalytic oxidation of methanol. A mechanism based on the electro-chemical generation of Ni (III) active sites and their subsequent consumptions by methanol have been discussed and the corresponding rate law under the control of charge transfer has been developed and kinetic parameters have been derived. In comparison with a Ni- POAP/ G, a Ni-MWCNT-POAP/G electrode shows a better catalytic performance for the electrocatalytic oxidation of methanol.

Keywords

Methanol, Impedance, Fuel cell, Nanocomposite, Electrocatalyst

Introduction

In recent years, electro-oxidation of small organic molecules has attracted much attention due to the development of direct liquid fuel cells, which require highly reactive fuels with high energy density. Methanol is one of the interesting future fuels for fuel cell application. Compared with other cells, the direct methanol fuel cell (DMFC) has several advantages such as high efficiency, very low polluting emissions, a potentially renewable fuel source, fast and convenient refueling, simple operation and ease of fuel storage and distribution. The low operation temperature of a DMFC (typically <95 °C) allows for easy start up and rapid response to changes in load or operating conditions. However, compared to the hydrogen based fuel cells, DMFC still remains to be further developed. One of the problems still unsolved is the slow kinetics of methanol oxidation on the fuel cell's anode. In the electrochemical oxidation of alcohol, the electrode material is clearly an important factor where a highly efficient electrocatalyst is needed. Ni has commonly been used as an electrocatalyst for both anodic and cathodic reactions in organic synthesis and water electrolysis. One of the very important uses of nickel as a catalyst is for the oxidation of alcohols. Several studies of the electro-oxidation of alcohols and methane on Ni have been reported [1-5].

The study of conducting polymer modified electrodes is motivated primarily from the anticipation of a synergistic electrocatalytic benefit from the very good conducting and



mechanical properties and their good adhesion to the electrode substrate. Due to their conductivity and stability, both in air and aqueous solution, polypyrrole, polyaniline, polyacetylene, polythiophene, polyindole, poly ortho aminophenol and polythionine has been extensively studied to application in sensor [6, 7] and catalysis [8-10]. Moreover, the possibility of dispersing metallic particles inside the polymers gives electrodes with higher surface areas, enhanced electrocatalytic activities and facilitates electron transfer due to semi conducting properties [11] and change in Fermi level toward the oxidation of organic molecules [12]. Organic-inorganic composite have attracted considerable attention as they can combine the advantages of both components and may offer special through reinforcing or modifying each other [13]. Electrodeposition is an effective way to make composite films with a large variety of tunable parameters and so has the advantage of convenient film control.

Carbon nanotubes (CNTs) exhibit excellent mechanical, electrical, and magnetic properties as well as nanometer scale diameter and high aspect ratio, which make them an ideal reinforcing agent for high strength polymer composites.

The purpose of the present work is to study the electrochemical oxidation of methanol on a POAP/MWCNT-nickel oxide composite film in a solution of 0.1 M NaOH aiming at the elucidation of the mechanism, derivation of the kinetic parameters of the process and the usefulness of the electrocatalytic process.

Experimental

The chemicals used in this work were of Merck origin and used without further purification. Typical MWCNT were uniform with outer diameters in the range of 5-20 nm and lengths up to several hundreds of nanometers were used. Their hollow Cores and multi-layer walls could be clearly seen by transmission electron microscopy (TEM) observation. All electrochemical measurements were carried out in a conventional three electrodes cell, powered by a potentiostat / galvanostat (EG&G273A) and a frequency response analyzer (EG&G, 1025). The system was run by a PC through M270 and M398 software using GPIB interface. The frequency ranges of 100 kHz to 100 mHz and modulation amplitude of 5 mV were employed for impedance studies. POAP films electrodeposited on a GC disk of 0.0314 cm² areas were employed as working electrode. Saturated calomel electrode (SCE) and a platinum wire were used as reference and counter electrodes respectively. POAP/MWCNT composites were prepared by NPV with 5 mV potential increment and plus width 0.005 s in a stirring solution containing 0.01 M monomer, 0.5 M HClO₄, 0.1 M LiCO₄, 5.0 × 10⁻³ M Sodium Dodecyl Sulfate (SDS) and 8% of MWCNT in suspension . SDS was used as an additive in order to suspend MWCNT particles and improve the stability and electroactivity of the resulting films. The coated electrode with POAP/MWCNT composite was thoroughly washed with distilled water and dried. In order to incorporate Ni (II) ions into the POAP composite film, the freshly electropolymerised POAP/G was placed at open circuit in a well stirred aqueous solution of 0.1M nickel sulfate.

Results and discussion

Fig. 1, show transmission electron microscopy (TEM) of POAP/MWCNT that obtained by NPV with potential scale of -0.2 to +0.9 V in an aqueous solution of 0.01 M monomer, 0.5 M HClO₄, 0.1 M LiCO₄, 5.0 × 10⁻³ M SDS and 8% of MWCNT in different magnification. These images confirm that the POAP has been wrapped on the surface of MWCNTs or MWCNTs have been dispersed in the polymer matrix.

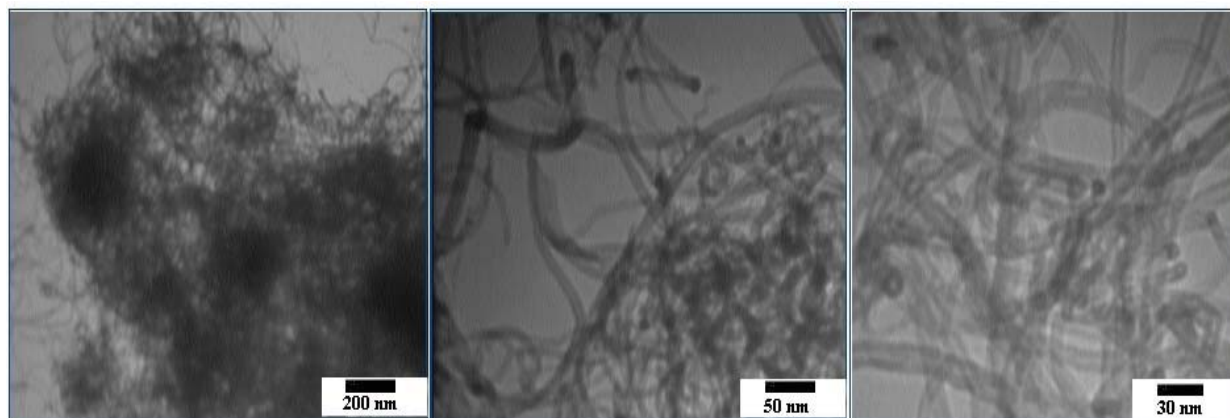


Fig.1: TEM images of POAP/MWCNT in different magnification.

Fig. 2 shows cyclic voltammograms of Ni-MWCNT-POAP/G electrode in 0.1 M NaOH solution in the presence of 0.1M methanol at a potential sweep rate of 10 mV s⁻¹. The larger methanol response at the Ni-MWCNT-POAP/G in respect to Ni-POAP/G electrode is proposed to be the Ni-MWCNT-POAP/G enhances the catalytic properties of nickel oxide through fine dispersion of the catalyst particles into the conductive polymer matrix to result in a drastic increase in surface area.

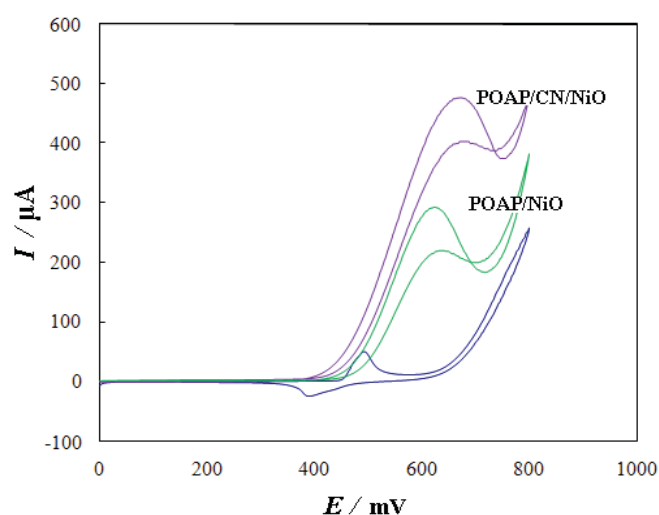


Fig.2: Cyclic voltammograms of Ni-MWNT-POAP/G (a) and Ni-OAP/G (b) electrode in 0.1 M NaOH solution in the presence of 3 mM methanol at a potential sweep rate of 10 mV s⁻¹.

Fig. 3 shows cyclic voltammograms of Ni-MWCNT-POAP/G electrode in 0.1 M NaOH solution in the presence of various concentrations of methanol at a potential sweep rate of 10 mV s^{-1} . At Ni-MWCNT-POAP/G electrode, oxidation of methanol appeared as a typical electrocatalytic response in alkaline media by $\text{Ni}(\text{OH})_2/\text{NiOOH}$. The anodic current in the positive sweep was proportional to the bulk concentration of methanol and any increase in the concentration of methanol caused an almost proportional linear enhancement of the anodic current. So, catalytic electrooxidation of methanol on Ni-MWCNT-OAP/G seems to be certain.

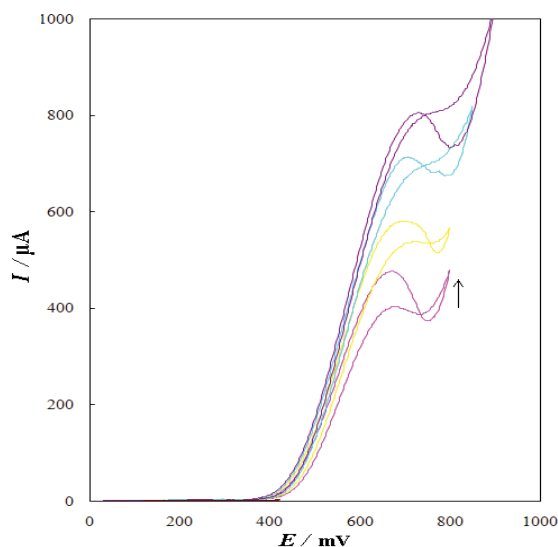


Fig. 3: Cyclic voltammograms of the Ni-MWNT-POAP/G electrode in 0.1M NaOH solution in the presence of (3-8) mM of methanol in the solution, Potential sweep rate was 10 mV s^{-1} .

Fig. 4 presents the Nyquist diagrams of POAP/MWCNT-NiO electrodes recorded at 650 mV/Ag , AgCl dc-offset both in the presence of methanol in 0.1 M NaOH solution. In the methanol's concentration range of 1-8 mM a steady decrease of the diameter of the semi-circle is witnessed. At further higher concentrations the Nyquist plot extended to the fourth quadrante in the low frequencies and an inductive loop appeared. The equivalent circuits compatible with the results are presented for both the low (inset a) and high (inset b) limits of methanol concentrations. In these circuits, R_s , CPE and R_{ct} represent solution resistance, a constant phase element corresponding to the double layer capacitance and the charge transfer resistance associated with the oxidation of methanol. R_L and L signify the characteristics of the inductive element representing the adsorption of the intermediates at higher methanol concentrations. However at potential higher than 650 mV/Ag-AgCl , the diagrams represented negative differential resistance and rolled over the real axis at low frequencies and went to the second quadrant. The diagram crossed the negative real axis at some finite frequencies indicating a dynamic instability of the stationary state. This negative impedance is characteristic of systems capable of exhibiting galvanostatic potential oscillation.

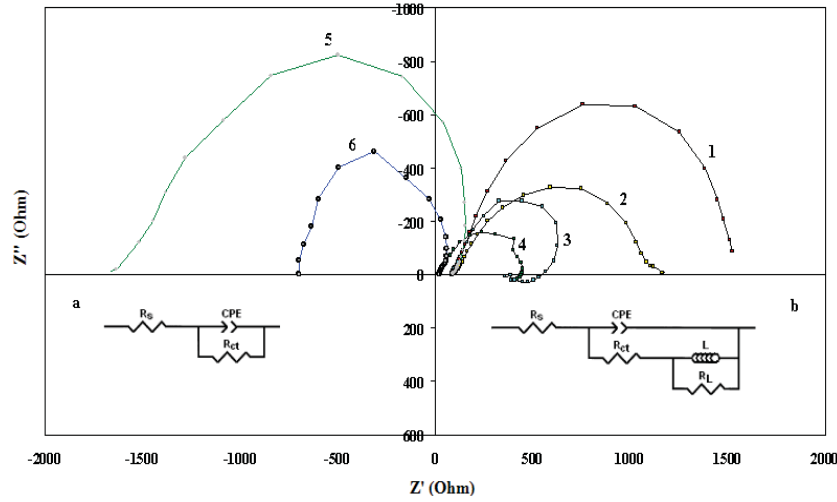


Fig. 4: Nyquist diagrams of Ni-MWNT-POAP/G electrode in the absence 1(1), 2 (2), 3 (3), 8 mM (4), methanol in 0.1 M NaOH solution and corresponding fitted curves. DC potential is 650 mV. (5) and (6) are Nyquist diagram in 700 mV/Ag,AgCl.

A number of mechanisms have been proposed for the electro-oxidation of alcohols on Ni in alkaline solutions. While Fleischmann et al. [14] assumed catalytic/intermediate role for NiOOH in the course of an anodic potential sweep.

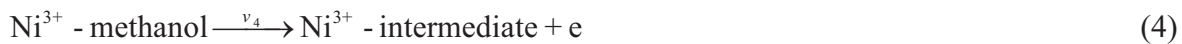
On the basis of the literature [15] the following mechanism is proposed for the mediated electro-oxidation of methanol on POAP/MWCNT-NiO and the corresponding kinetics is formulated. The redox transition of nickel species present in the film is



and methanol is oxidized on the modified surface via the following reaction



where Ni^{3+} sites are regenerated by the power source and on the Ni^{3+} oxide surface by direct electro-oxidation



Eqs. (2) and (3) are according to Fleischmann mechanism and in Eqs. (4) and (5), Ni^{3+} used as active surface for methanol oxidation. Observation of a new oxidation peak for methanol oxidation at a potential much more positive than that of the oxidation of Ni(OH)_2 potential is according to Eqs. (4) and (5). According to above equation the Faradic current density can be written as

$$I_F = (v_1 + v_4 + v_5)F \quad (6)$$



In the above sequence of reactions, (1) to (3), k_1 and k_{-1} are obviously potential dependent rate constants and are of the forms:

$$k_1(E) = k_1^{\circ} \exp\left[\frac{\alpha nF(E - E^{\circ})}{RT}\right] \quad (7)$$

$$k_{-1}(E) = k_{-1}^{\circ} \exp\left[\frac{(\alpha - 1)nF(E - E^{\circ})}{RT}\right] \quad (8)$$

where k° 's are the chemical rate constants measured at equilibrium potential, α being the anodic symmetry factor and other parameters have their usual meanings. The rate laws for the reactions (1) to (3) have the forms of:

$$v_1 = k_1 \Gamma \theta_{II} - k_{-1} \Gamma \theta_{III} \quad (9)$$

$$v_2 = k_2 \Gamma \theta_{III} C^* \quad (10)$$

Where Γ is the total number of adsorption sites per unit area of the electrode surface, θ 's represent the fractional coverage's of different nickel valence states and C^* is the bulk concentration of ethanol. With only the (II) and (III) valence states of nickel prevailing:

$$\theta_{II} + \theta_{III} = 1 \quad (11)$$

and the rates of changes of their coverage's as well as that of the intermediate compounds being:

$$\frac{d\theta_{II}}{dt} = -\frac{d\theta_{III}}{dt} = -k_1 \theta_{II} + k_{-1} \theta_{III} + k_2 \theta_{III} C^* + k_3 \theta_{III} C_i \quad (12)$$

$$\frac{dC_i}{dt} = k_2 \theta_{III} C^* - k_3 \theta_{III} C_i \quad (13)$$

where C_i is the concentration of intermediate.

Assuming that the steady state approximations dominating:

$$\frac{d\theta_{II}}{dt} = -\frac{d\theta_{III}}{dt} = 0 \quad (14)$$

$$\frac{dC_i}{dt} = 0 \quad (15)$$

one arrives at the values of the coverage's:

$$\theta_{II} = \frac{(k_{-1} + 2k_2 C^*)}{(k_1 + k_{-1} + 2k_2 C^*)} \quad (16)$$

$$\theta_{III} = \frac{k_1}{(k_1 + k_{-1} + 2k_2 C^*)} \quad (17)$$

On the basis of this rate equation the faradic current will be:

$$i_f = \frac{2FAk_1\Gamma k_2C^*}{(k_1 + k_{-1} + 2k_2C^*)} \quad (18)$$

where A being the surface area of the electrode and the corresponding charge transfer resistance is:

$$R_{ct} = \left(\frac{di_f}{dE} \right)^{-1} = \frac{(k_1 + k_{-1} + 2k_2C^*)^2}{2FA\Gamma k_2C^* k_1 \left(\frac{2\alpha Fk_2C^*}{RT} + \frac{k_{-1}F}{RT} \right)} \quad (19)$$

According to methanol concentrations dependency of R_{ct} where an initial sharp drop is terminated to a very slow change as the concentration of methanol is approaching 8 mM. The results are further fitted to Eq. (19) to estimate the values of the rate constants. From this equation the values of the rate constants as $k_1=3.3s^{-1}$, $k_{-1}=2.6 \times 10^{-2}s^{-1}$ and $k_2=8.35 \times 10^2 \text{ cm}^3 \text{ mol}^{-1} \text{ s}^{-1}$ have been calculated.

Conclusions

We have demonstrated a simple and general strategy, namely in situ electropolymerization by using the ionic surfactant as electrolyte, for dispersing disordered CNTs within conducting polymer/carbon nanotube composite films. Surfactant SDS has played a key role in the synthesis of CP/CNT composite films. The MWCNT has an obvious improvement effect, which makes the composites have more active sites for faradic reaction and larger specific capacitance than pure POAP. Also, it results in enhanced electric conductivity, lower the resistance, and facilitate the charge-transfer of the composites. In comparison with a Ni- POAP/G, a Ni-MWCNT-POAP/G electrode shows a better catalytic performance for the electrocatalytic oxidation of methanol. The modified electrodes showed electrocatalytic activity for the oxidation of methanol. A kinetic model was developed and the kinetic parameters were calculated using the methanol concentration dependency of charge transfer resistance derived from the impedance studies.

References

- [1] K. Scott, WM. Taama, P. Argyropoulos. Engineering aspects of the direct methanol fuel cell system. *J. Power Sources* 79 (1999) 43-59.
- [2] K. Kordesch, G. Simander. *Fuel Cells and their Application*, VCH Verlagsgesellschaft, Weinheim, 1996, p. 151.
- [3] R. Parsons, T. Vander Noot. The oxidation of small organic molecules : A survey of recent fuel cell related research. *J. Electroanal. Chem.* 257 (1988) 257.
- [4] HL. Pang, JP. Lu, JH. Chen, CT. Huang, B. Liu, XH. Zhang. *Electrochim. Acta*, 54 (2009) 2610-2615.



- [5] H. Razmi, Es. Habibi, H. Heidari. *Electrochim. Acta* 53 (2008) 8178-8185.
- [6] S. Cosnier. *Anal. Bioanal.Chem* 377 (2003) 507-520.
- [7] M. Gerard. *Biosens. Bioelectron* 17 (2002) 345-359.
- [8] A. Ehsani, M.G. Mahjani, M. Jafarian, A. Naeemy, *Prog. Org. Coat*, 69 (2010) 510-516.
- [9] A. Ehsani, M.G. Mahjani, M. Jafarian, *Synth. Met* 161 (2011) 1760-1765.
- [10] X-Y. Peng, X-X, Liu, P-J, Hua, D. *Diamond, K-T. Lau, J. Solid State. Electrochem*, 14 (2010) 1-7.
- [11] M.G. Mahjani, A. Ehsani, M. Jafarian, *Synth. Met* 160 (2010) 1252-1259.
- [12] S. Radhakrishnan, A. Adhikari, DK. Awasti. *Chem. Phys. Lett* 341(2001) 518-522.
- [13] S. Berchmans, H. Gomathi, GP. Rao. *J. Electroanal. Chem* 394 (1995) 267-270.
- [14] M. Fleischmann, K. Korinek, D. Pletcher. *J.Chem. Soc., Perkin Trans. 2*, 10 (1972) 1396-1402.
- [15] M. Jafarian, M.G. Mahjani, H. Heli, F. Gopal, H. Khajehsharifi, M.H. Hamed, *Electroch.Acta* 48 (2003) 3423-3429.



Electrophoretic deposition of NiFe₂O₄ spinel on SOFC interconnect

Reza Irankhah^{a,*}, Amir Maghsoudipour^a, Babak Raissi^a, Abdullah Irankhah^b

^a Department of Ceramic, Materials and Energy Research Center, Tehran, Iran

^b Hydrogen and Fuel Cell Research Lab., Chemical Engineering Department, University of Kashan, Kashan, Iran

Abstract

Ni-Fe spinel coating with a nominal composition of NiFe₂O₄ was synthesized by solid state reaction. Electrophoretic deposition method was used to insert NiFe₂O₄ spinel on a commercially available SUS 430 and the effect of different electric fields (100-300V) on surface morphology was investigated. The results indicated that the electric field of 100 V was an effective voltage to obtain crack-free coating.

Keywords: Electrophoretic Deposition, NiFe₂O₄ spinel, SOFC Interconnect, solid state reaction

Introduction

Interconnects in solid oxide fuel cells provide electrical connection between anode of one cell to the cathode of neighbor cell. It also acts to prevent of contact between the reducing and oxidizing atmosphere. Interconnects should have, excellent electrical conductivity and oxidation resistance, good thermal conductivity, thermal expansion coefficient (TEC) matching to those of electrodes and electrolyte [1 - 3]. At high temperatures (around 1000 °C) the interconnect is made of ceramic materials such as LaCrO₃. But ceramic interconnects have some problem such as low electrical conductivity and difficult to manufacture [1]. At lower operating temperatures (650 – 850 °C) metallic interconnects can be used as an replacement for ceramic ones [4,5]. Among the metallic alloys, ferritic stainless steels due to their appropriate thermal expansion, low cost and excellent formability are considered as a SOFC interconnect [6,7]. Under SOFC operating temperature, the use of ferritic stainless steel associated with Cr migration via Cr₂O₃ scale into the cathode and poisoning of the cathode is occurred [4, 8 – 10]. Numerous protective spinel coatings such as (Mn, Co)₃O₄ [11], (Cu,Mn)₃O₄ [11], Ni – Co [12] and Ni – Fe [13] spinels have been using to solve this problem. Different methods have been used to apply spinel coatings to the metallic interconnects [4]. For example Ni – Fe coatings can be



applied on ferritic stainless steel by a number of techniques such as electroplating [13, 14], screen printing [13] and magnetron sputtering [15]. In addition, the electrophoretic deposition (EPD) has recently attracted much attention for producing a thin and thick ceramic layer. In this process, dispersed ceramic particles in a liquid medium under a DC electric field migrate towards an opposite electrode and consequently deposit there [16]. Electrophoretic deposition (EPD) has advantages of short formation time, easy control of the thickness and morphology of a deposited film, needs simple apparatus [17]. In the present study EPD was used to deposit the NiFe₂O₄ spinel on SUS 430 as a SOFC interconnect. The main aim of this study is to investigate the deposition of NiFe₂O₄ spinel in acetone medium by EPD.

Experimental

NiFe₂O₄ spinel synthesis

NiO (Art No. 617130) and Fe₂O₃ (Art No. 3924) powders were used as precursors for synthesis of NiFe₂O₄ spinel by solid state reaction. NiO and Fe₂O₃ were mixed for 24 h in ethanol medium. The slurry was then dried at 100 °C followed by calcination at 1100 °C for 3 h.

SUS 430 treating

SUS 430 was used as the interconnect substrate. Its chemical composition, as determined by emission spectrometry, is listed in table 1. Substrate pieces with a dimension of 20×20×3 (mm×mm×mm) were prepared. Prior to deposition, the substrate surfaces were gritted with SiC abrasive paper of # 500 and cleaned in acetone.

Table 1. Chemical composition (Wt. %) of SUS 430.

	Wt. %		Wt. %		Wt. %
Fe	base	V	0.1	C	0.026
Cr	16.5	Si	0.31	W	<0.02
Mn	0.51	Mo	0.05	Ti	Trace
Ni	0.16	S	<0.003	Nb	<0.003
Cu	0.12	Al	Trace	Co	<0.002

Suspension preparation and EPD

1 gr/liter of NiFe_2O_4 homogeneous suspension was prepared in acetone by sonicating in an ultrasonic bath for 20 min. A DC high voltage power source, electric fields of 100 - 300 V/cm, was used for deposition of NiFe_2O_4 powder on SUS 430 electrodes for 1 min.

Result and discussion

Synthesis of NiFe_2O_4 spinel

Fig. 1 depicts the typical XRD analysis of NiFe_2O_4 spinel synthesized by solid state reaction. The XRD pattern was recorded (Philips PW3710, Amsterdam, the Netherlands) using a $\text{Cu K}\alpha$ mono chromatized radiation source. All of the peaks are consistent with a NiFe_2O_4 powder sample [reference code: 044 - 1485]. Particle size distribution analysis of NiFe_2O_4 spinel used for EPD is shown in Fig. 2. It is obvious that the average particles size of the spinel is less than 10 μm .

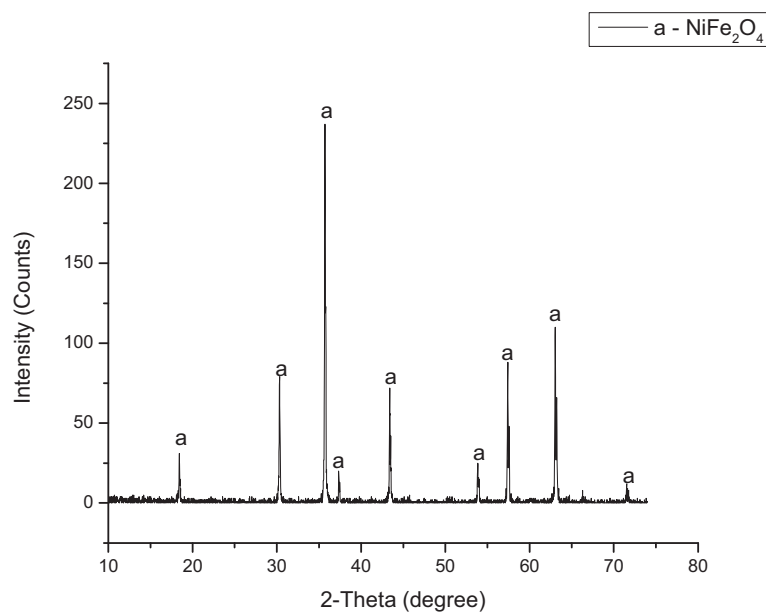


Fig 1. X-ray diffraction pattern of NiFe_2O_4 spinel powder.

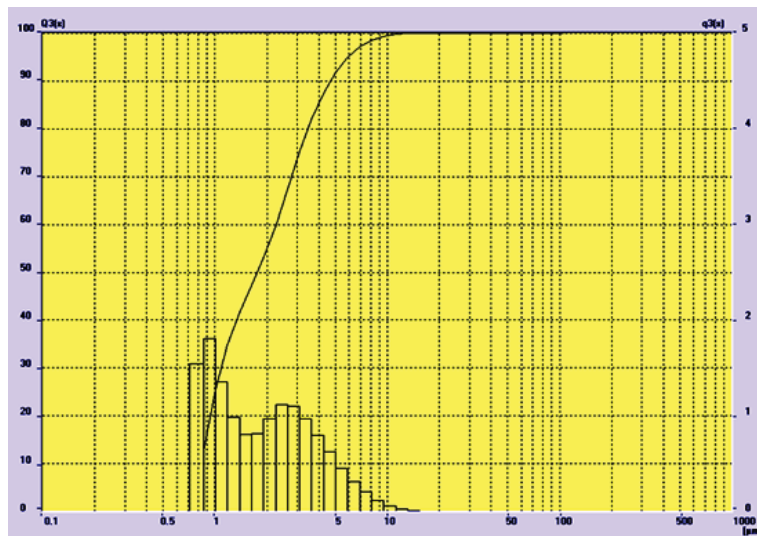


Fig 2. Particle size distribution of NiFe₂O₄ spinel.

Effect of Voltage on deposition weight

As it was mentioned above, different electric fields were used for EPD. Fig 3 shows the weight of deposited NiFe₂O₄ on SUS 430 substrate from an acetone based suspension at 100–300 V. The deposition weight is increased as a function of applied electric field because of higher deposition rate of particles. The results are accordance with the Hamaker Eq [17].

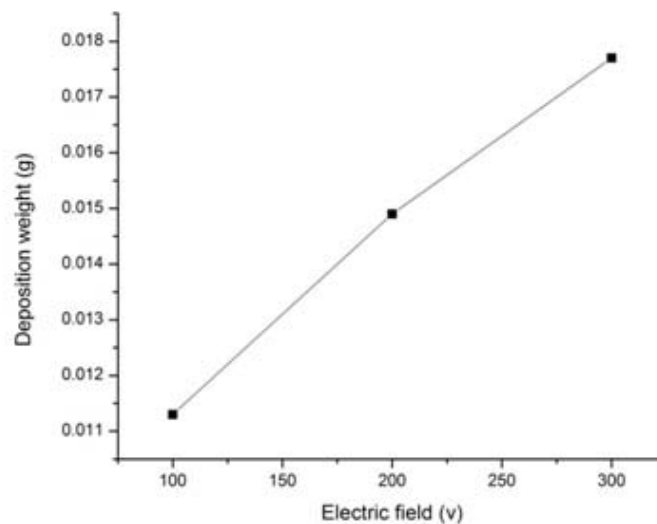


Fig. 3 - Deposition weight as a function of electric field for 1 min deposition duration.

Effect of Voltage on Surface Morphology

Fig. 4 shows the NiFe₂O₄ coating obtained by EPD from its suspension in acetone for 1min of deposition time at 300 V with and without dispersant. Deposition yields increased with poly ethylene imine additive and the coating adhered well to the substrate. But in deposition experiment performed without additive, the coating was prone to poor adhesion. It is obvious that the thickness of spinel layer for suspension with dispersant was more uniform than without one.

Fig. 5 (a & b) depicts the typical SEM images of as deposited NiFe₂O₄ spinel coatings precipitated by EPD at electric fields of 100 and 300 V in acetone suspension. As it shown in Fig. 5, the electrophoretically deposited layer in 300 V resulted in the formation of cracks on the surface but in 100 V Cracked free deposits was obtained that it could be attributed to the easily trapped acetone evaporation [18].

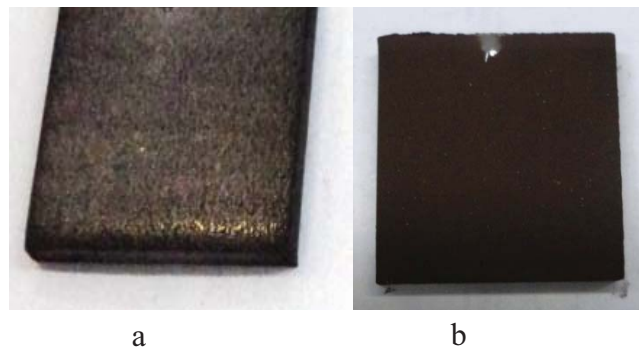


Fig. 4 . NiFe₂O₄ Coated SUS 430 at 300 V, Suspension without (a) and with additive (b).

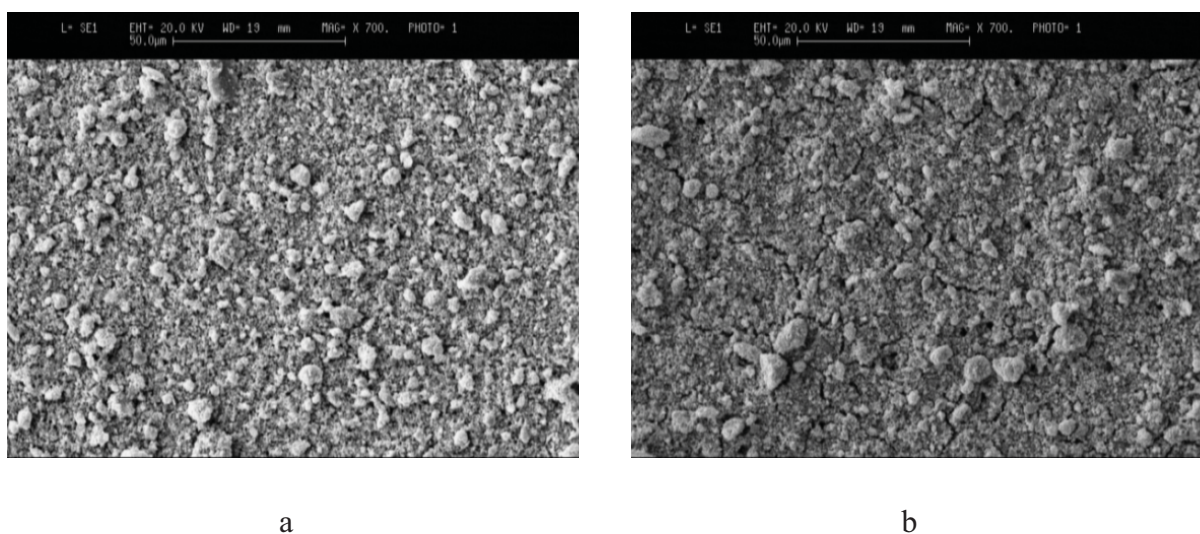


Fig 5.Surface morphologies of as-deposited NiFe₂O₄ coating, (a) 100 V and (b) 300 V.



Conclusion

The pure NiFe₂O₄ spinel with particle size of less than 10 μm was synthesized by solid state reaction and it was applied on SUS 430 ferritic stainless steel via EPD. Deposition of NiFe₂O₄ spinel in 100 and 300 V resulted in the formation of crack – free layer in 100 V.

Acknowledgments

This work was financially supported by Iran Renewable Energy Organization (SUNA).

References:

- [1] Fontana S, Amendola R, Chevalier S, Piccardo P, Caboche G, Viviani M, et al. Journal of Power Sources. **2007**, *171(2)*, 652 - 62.
- [2] W.Z. Zhu, S.C. Deevi, Mater. Res. Bull. **2003**, *38*, 957 – 972.
- [3] W.Z. Zhu, S.C. Deevi, Mater. Sci. Eng. **2003**, *A348*, 227 – 243.
- [4] Shaigan N, Qu W, Ivey DG, Chen W. **2010**, *195(6)*, 1529 - 42.
- [5] Ebrahimifar H, Zandrahimi M. Solid State Ionics. **2011**, *183(1)*, 71 - 9.
- [6] Z. Yang, K.S. Weil, D.M. Paxton, J.W. Stevenson, J. Electrochem. Soc. **2003**, *150*, 1188.
- [7] Bateni MR, Wei P, Deng X, Petric A. **2007**, *201(8)*, 4677 - 84.
- [8] Fergus JW. Materials science and engineering A. **2005**, *397(1-2)*, 271 - 83.
- [9] Simner SP, Anderson MD, Xia G-G, Yang Z, Pederson LR, Stevenson JW. J Electrochem Soc A. **2005**, *152(4)*, 740.
- [10] Yang Z, Xia G, Singh P, Stevenson JW J Power Sources. **2006**, 155 - 246.
- [11] A. Petric, H. Ling, Journal of the American Ceramic Society. **2007**, *90*, 1515 – 1520.
- [12] Hua B, Zhang W, Wu J, Pu J, Chi B, Jian L. Journal of Power Sources. **2010**, *195(21)*, 7375 - 9.
- [13] Liu Y, Chen DY. International Journal of Hydrogen Energy. **2009**, *34 (22)*, 9220 - 6.
- [14] Geng S, Qi S, Zhao Q, Zhu S, Wang F. International Journal of Hydrogen Energy. **2012**, *37(14)*, 10850 - 6.
- [15] Geng S, Wang Q, Wang W, Zhu S, Wang F. International Journal of Hydrogen Energy. **2012**, *37 (1)*, 916 - 20.
- [16] C. Kaya, F. Kaya, B. Su, B. Thomas, A.R. Boccaccini. Surf. Coat. Technol. **2005**, *19*, 1303 – 310.
- [17] L. Besra, M. Liu, Prog. Mater. Sci. **2007**, 521 – 61.
- [18] Chen C-C, Jwo C-S, Teng T-P. Particuology. **2011**, *9(5)*, 497 - 501.



Hybrid Genetic Algorithm-Neural Network for Membrane RI Measurement Error Modeling in PEM Fuel Cells

Saeed Olyae¹, Reza Ebrahimpour², Somayeh Esfandeh³

Nano-Photonics and Optoelectronics Research Laboratory (NORLab), Faculty of Electrical and Computer Engineering, Shahid Rajaei Teacher Training University (SRTTU), Lavizan, Tehran, Iran.

Email: s_olyae@srttu.edu

Abstract

In this paper, a method for determination of refractive index (RI) in membrane of fuel cell on basis of three-longitudinal-mod laser heterodyne interferometer is presented. The optical path difference between target and reference paths is fixed and phase shift is then calculated in terms of refractive index shift. The measurement accuracy of this system is limited by nonlinearity error. In this study, nonlinearity error is modeled by artificial neural network (ANN) and hybrid genetic algorithm–neural network (hybrid GA–ANN) methods. The real code version of genetic algorithm (GA) is used. Genetic operators and parameters are set and designed accurately to optimize the neural network. Results indicate that nonlinearity error can be effectively modeled by hybrid GA–ANN method and contains minimum mean square error (MSE) compared to neural network.

Keywords: Artificial neural network, Genetic algorithm, Heterodyne interferometer, Multi-layer perceptrons, Nonlinearity error.

1 Introduction

The use of fuel cell is one way for energy producing such as electricity and heat. Fuel cell is an electrochemical device for transmitting electrochemical energy to useful electrical energy [1]. We use fuel cell in order to produce electrical energy in power plants, portable devices, automobiles etc. Fuel cell is an important technology for producing clean energy with high efficiency. It consists of an anode, a cathode, and two current collectors, which are separated with a thin membrane [2]. Operation of fuel cell systems directly depends on amount of water content in membrane. High water content increases the efficiency of fuel cell but, if the water content is too high, then some problems occur such as swell, mechanical pressure, and destruction of fuel cell membrane [3]. Density and refractive index in membrane are commensurate together, thus estimating of refractive index cause measuring amount of water content in fuel cell membrane truly. There are many developed methods for imaging water content with magnetic resonance imaging, neutron imaging, and optical fluorescence spectroscopy [4,5]. All of these methods are expensive or have weak resolution and they are

¹ Assistant Professor in the Shahid Rajaei Teacher Training University, Faculty of Electrical and Computer Engineering, Tehran, Iran.

² Assistant Professor in the Shahid Rajaei Teacher Training University, Faculty of Electrical and Computer Engineering, Tehran, Iran, Rebrahimpour@srttu.edu

³ M.S. Student of electronic engineering in the Shahid Rajaei University, E-mail: Somayeh.Esfandeh@gmail.com



very complicate and time consuming. Therefore, interferometry methods are favorite and attractive for researchers to measuring refractive index recently. Mach-Zehnder and two-longitudinal-mode laser heterodyne interferometer used for recognizing variation water content percentage, duration penetrating process in fuel cell [6,7]. We use three-longitudinal-mode laser heterodyne interferometer to obtain more resolution capabilities rather than two-mode. Three-longitudinal-mode laser heterodyne interferometer has improved with high sensitive, which measures refractive index shift versus variation of water content in fuel cell membrane. Nonlinearity error in heterodyne interferometer limits measurement accuracy of refractive index. These errors are due to non-ideal laser polarization, optical devices, and electronically measurement system, thus modeling and analyzing of measurement errors are very important. Researchers have been worked for modeling, calculating and finally, compensation of nonlinearity by using complicated calculation analysis [8,9,10]. Nowadays, the neural network play an important role in modeling of nonlinearity error in laser interferometer [11,12]. Olyae *et al.* have modeled the nonlinearity of two-mode heterodyne interferometer by using MLPs and radial basis function, and Stacking method [13].

When nonlinearity error is modeled with MLPs neural network, using back propagation (BP) as their learning algorithm, cannot offer a good model. Gradient descent based techniques, usually tends to stick in local minimums and it depends on the shape of the error surface exactly. Thus, in order to obtain a better model of the nonlinearity error in interferometer, it is needed to optimize the BP algorithm by using an effective technique. Recently some studies successfully used the genetic algorithm for training neural networks to overcome the inherent limitations of BP. Genetic algorithm can be used in two different ways for training neural networks: 1- Weights optimization. 2- Structure and topology optimization [14]. Our methodology utilizes a hybrid genetic algorithm–neural network strategy. Genetic algorithm is used to train neural network. In learning process, weights and biases of neural network are optimized.

In this paper, nonlinearity error due to ellipticity and non-orthogonality of input polarized light of three-mode heterodyne is modeled. This modeling has been done in order to have more accurate system for measuring refractive index shift due to variation of water content in fuel cell. Modeling of nonlinear error has been implemented with the multi-layer perceptrons neural network using two different training methods: The classical BP training algorithm and its combination with a real coded GA strategy then performances were compared. Combining genetic-neural network method can avoid getting into the local minimum and approaches to the global convergence with searching all the problem space correctly and rapidly. Thus, this method expected to have better results.

2 Principles of refractive index determination

As the water content of a membrane changes, the refractive index and the thickness of the membrane will change correspondingly. Water index of refraction through the membrane can be measured using the setup shown in Fig. 1. The system includes a stabilized three-longitudinal-mode He-Ne laser, non-polarizing beam splitter (BS), two corner cube prism (CCPs), polarizing beam splitter (PBS), a quarter-wave plate (QWP), a compensator and two avalanche photodiodes (APDs). The fuel cell is inserted in front of the corner cube prism in the target path. As shown in Fig. 1, the laser beam emerging from a stabilized He-Ne laser at 632.8 nm wavelength is split off by a PBS into the target and reference paths. In the reference path, a quarter-wave plate with fast axis at 45 compared to the x-direction, and a compensator are used. Therefore, the orthogonal orientations are exchanged by quarter-wave plate. In the target path, the laser beam passes through the membrane of the fuel cell. The returned beams

form two paths and after passing through the beam splitter are interfered. This light is divided into two components in x- and y-directions using the PBS. The outputs of two avalanche photodiodes are led to the signal conditioner and digital signal processing circuits to detect the phase difference resulting from refractive index shift [15,16].

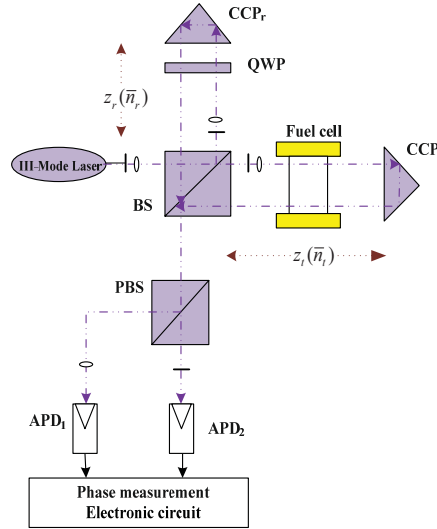


Figure 1: The schematic diagram of the three-longitudinal-mode laser heterodyne interferometer for refractive index determination in fuel cells.

The phase difference between the target and reference electrical fields is then given by:

$$\Delta\psi = \Psi_t - \Psi_r = 2\pi\nu\Delta t = (4\pi z / \lambda)\Delta n \quad (1)$$

where Ψ_t and Ψ_r the phase shift in the target and reference path respectively. ν is issued as optical reference frequency, $|\bar{n}_t - \bar{n}_r| = \Delta n$ is the refractive index difference resulting from changes of water content of membrane in fuel cell, λ is the wavelength, and z is the optical path. Two photocurrents from photodiode detectors are respectively given by:

$$I_{APD1} = k \cos(2\pi\nu_b + 2\Delta\psi) \quad (2)$$

$$I_{APD2} = k \cos(2\pi\nu_b - 2\Delta\psi + \Psi_{nl}) \quad (3)$$

where $\nu_b = \nu_{bH} - \nu_{bL}$, $\nu_{bH} = \nu_3 - \nu_2$ and $\nu_{bL} = \nu_2 - \nu_1$. ν_b is the inter mode beat frequency which is typically in order of several hundred MHz, Ψ_{nl} is the nonlinearity phase, and k is a constant value. The phase difference between two measured output signals $\Delta\Psi$ is then extracted as:

$$\Delta\Psi = 4\Delta\psi - \Psi_{nl} = (16\pi z / \lambda)\Delta n - \Psi_{nl} \quad (4)$$

The second term of this equation is none linear. The index of refraction shift is measured from measuring the phase shift:

$$\Delta n = \frac{\lambda}{16\pi z} (\Delta\Psi + \Psi_{nl}) \quad (5)$$

To measure the accurate refractive index, the nonlinearity phase should be cancelled. In the next section, we will analyze and model the nonlinearity via neural network and its combination with genetic algorithm.

3 Nonlinearity modeling

3.1 Multi-layer Perceptrons

Modeling of the nonlinearity error in the three-longitudinal-mode laser heterodyne interferometer by using artificial neural network is shown in Fig. 2. We use BP algorithm for training the MLPs. This MLPs Include an input layer, a hidden layer and an output layer.

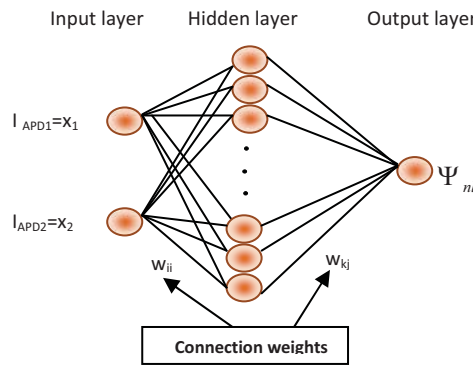


Figure 2: Structure of MLPs network for modeling of nonlinearity error

MLPs can have more than one hidden layer but it has been theoretically proved that only a hidden layer is sufficient for neural networks to estimate any complex nonlinear function [17]. The output currents of two avalanche photodiodes (APD₁, APD₂) as input and nonlinearity error heterodyne interferometer (Ψ_{nl}) as desired output for MLPs are considered.

Number of neurons in the hidden layer is obtained by trial and error. The structure of the neural network includes two neurons in input layer, 12 neurons in the hidden layer and one neuron in the output layer. The learning process finds the optimum value of connection weights and biases of the input-hidden layer and hidden-output layer. The output of each neuron is gained with summation over the multiplication of each input and its corresponding weight and finally, the result is passed through a nonlinear activation function (transfer function). The sigmoid tangent activation function $f(x)$ is used to transfer the values of input layer neurons to hidden layer neurons and linear activation function $p(x)$ is used to transfer the output of hidden layer neurons to the output layer. The neurons output of the hidden and last layers are calculated by Eqs. (6) and (7):

$$X_j = f\left(\sum_{i=1}^2 x_i w_{ji} + w_{j0}\right) \quad (6)$$

$$\hat{\Psi}_{nl} = p\left(\sum_{j=1}^{12} X_j w_{kj} + w_{k0}\right) \quad (7)$$

where x_i is a variable input and w_{ji} is connection weight between hidden and input neurons, w_{kj} is connection weight between output and hidden neurons and w_{j0} and w_{k0} are biases for

the j th and k th neuron respectively, i is a number of neurons for input and j is a number of neurons for the hidden layer, and k is the number of output neurons. Output of neural network, $\hat{\Psi}_{nl}$, is compared with the desired output, Ψ_{nl} , in the training phase, and the error in the form of mean square error (MSE) is calculated for all data. The MSE function is derived from the following equation:

$$MSE = \frac{1}{n} \sum_{P=1}^n [(\Psi_{nl})_P - (\hat{\Psi}_{nl})_P]^2 \quad (8)$$

Where n is the number of data in the training phase. The purpose is to reduce the amount of errors. The adjustment which applied to the synaptic weight is calculated as follows:

$$\Delta w_{ji} = -\eta \frac{\partial MSE}{\partial w_{ji}} \quad (9)$$

where, η is the learning rate, which is selected carefully. Through the training phase, the neural network learns and generalizes nonlinear relationship and maps the input to the output.

3.2 Genetic algorithm

GA is a member of large family of evolutionary algorithms that has grown rapidly in the field of artificial intelligence. For first time GA was introduced by John Holland in early 1970 [18]. This algorithm is a powerful optimization tool, inspired of natural genetic and Darwin's evolutionary theory. This algorithm operates under the genetic laws and natural selection. It is an effective search method for problems with complex space [19]. Three operators are described as follows:

3.2.1 Selection

In GA, selection of individuals for produce successive generations has a vital role. In this paper, we use stochastic universal sampling (SUS) method. SUS is a sampling method to implement selection proportionally to the fitness, Eq. (8) has been considered as the fitness function.

SUS is proposed to overcome some of the problems of roulette wheel sampling method. In roulette wheel selection method, the wheel turns N times that N is population size. In each time, each chromosome that its sector was faced against marker is selected for generation. In SUS method, the wheel runs only once and hence it is used to choice N parent from N marker that placed in same distance of each other. After the wheel stops, each chromosome is selected on basis of the number of markers that placed against it, then it transmit to marriage pool for participate to produce generations.

3.2.2 Crossover

Among of different crossover operator, the heuristic type is used in this work. In this operator using the fitness values of the two parent chromosomes, the direction of the search is determined. If X and Y are parent chromosomes and X', Y' are offspring then the offspring are made according to the following equation:

$$X' = X + r.(X - Y) \quad (10)$$

$$Y' = X \quad (11)$$

where, r is a random number between zero and one. If the chosen r causes one or more genes of chromosome to be outside from the allowable upper or lower bounds, then X' is not allowed. In this state, a new random number r is generated and a new offspring is created by Eq. (10).



3.2.3 Mutation

There are different types of mutation function, which is used in the GA; uniform mutation function is applied in this work. Firstly, according to the mutation probability, the number of variables in the population are selected randomly, then each variable according to type of mutation change and is replaced in the population. General structure of this operator for number with floating point is defined by the following equation:

$$X = (x_1, x_2, \dots, x_m) \xrightarrow{\text{Mutation}} X' = (x'_1, x'_2, \dots, x'_m) \quad x_i, x'_i \in [x_i^{lo}, x_i^{hi}] \text{ for } i = 1, 2, \dots, m \quad (12)$$

In this mutation, a variable that should be mutated is replaced with a random value in defined range, where r is a random number in the interval between zero and one, with a uniform distribution.

$$x'_i = x_i^{lo} + r.(x_i^{hi} - x_i^{lo}) \quad (13)$$

3.3 Methods and steps combining GA with BP

The learning process includes two steps for combining GA with neural network: first, searching for optimized weights and biases of the neural network by real form genetic algorithm and second, adjusting the final weights by the BP learning rule, Fig. 3 shows the flowchart of combining model GA-ANN that has been used in this study. The steps of optimization of this model are as follows: first, the phase of initialization values based on the structure of the neural network described in section 3.1, all connection weights and biases between the layers of the network are represented as each segment of chromosome. Therefore, each chromosome gives a set of weights. It should be noted that the initial population is selected randomly. Then the fitness of each member of the population (per chromosome) is calculated. The least mean square error (MSE) of the actual output and desired is considered as the fitness function. The evolutionary processes such as selection, crossover and mutation operators are used by genetic algorithms. At the end of each iteration of genetic algorithm, there are two generations of parents and offspring. Among of the two generations that includes $2N$ member, N number of members should be elected to continue the algorithm. Elitist selection method is also used in this work. Thus, most qualified chromosomes will be allowed to be transferred directly to the next generation. Algorithm stops when it reaches to its maximum number of iterations. Finally the best biases and connection weights which obtained by the best fitness function of GA is determined as the initial weight and bias of the neural network. Process are completed by applying the BP algorithm on the initial weights.

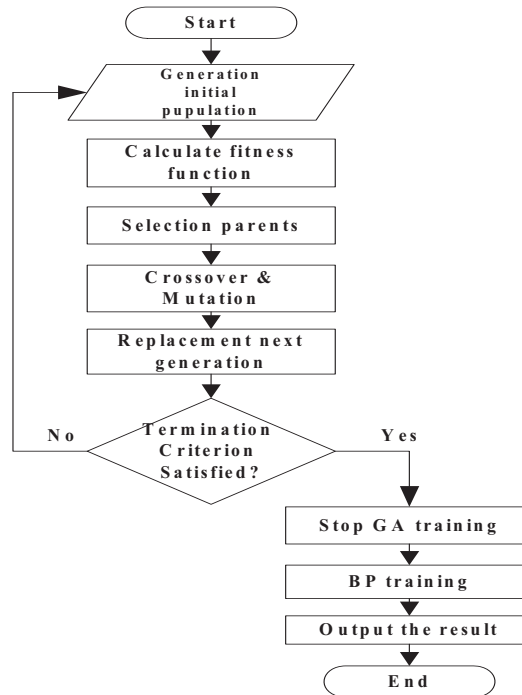


Figure 3: Framework of combining neural network and GA.

4 Simulation results

In this section, we investigate the performance of discussed algorithms for modeling nonlinearity of three mode heterodyne interferometer in measurement of refractive index shift in fuel cell. The input data for the neural network are two output currents of avalanche photodiodes. In the training phase, the training input vector $P = [I_{APD_1}, I_{APD_2}]$ is gained by putting the fixed parameters and nonlinear parameters in Eqs. (2) and (3). The target vector is generated by Eq. (4) $T = [\Psi_m]$. The structure of neural network is (2:12:1) and the training is done in 1000 epochs with the learning rate 0.01. Genetic algorithm is set for training the neural network with heuristic crossover probability 0.8, uniform mutation probability 0.01 and 150 chromosomes (population size). The algorithm is repeated for 100 generations and then it continues by the BP training algorithm here the learning rate is set to 0.01. The performances of genetic algorithm and back propagation algorithm in hybrid GA-ANN method are shown in Fig. 4. The nonlinearity error is simulated by using mathematical rules as reference. Figs. 5 and 6 show that the nonlinearity in testing phase with ANN and hybrid GA-ANN are modeling for parameters $|\alpha| = 0.02, |\beta| = 0.002, \varphi_\alpha = \varphi_\beta = 0.5rad$. According to Eq. (5) the value of nonlinearity error should decrease enough in order to a better modeling, and finally a better measurement of refractive index in membrane of fuel cell. Results show hybrid GA-ANN can model the nonlinearity much better than artificial neural network. The MSE values for various parameters of the nonlinearity error in testing phase, using each of aforementioned methods are shown in Table 1. As can be seen in ANN, MSE value is not decreased favorably; however, the network trains in a lot of epochs Whereas Combining the real form of genetic algorithm with BP algorithm for training neural network has better performance in nonlinearity error modeling.

Table 1: Results of adaptive filter algorithms to model none linearity for some parameters

$ \alpha $	$ \beta $	ϕ_α (rad)	ϕ_β (rad)	ANN	Hybrid GA-ANN
0.02	0.01	0.6	0.5	-44.74	-123.24
0.02	0.04	0.5	0.5	-46.34	-127.19
0.02	0.1	0.5	0.6	-35.61	-105.47
0.04	0.01	0.5	0.5	-37.52	-112.86
0.01	0.01	0.5	0.45	-45.43	-126.36
0.01	0.02	0.5	0.5	-40.84	-119.92
0.02	0.002	0.5	0.5	-42.08	-117.105

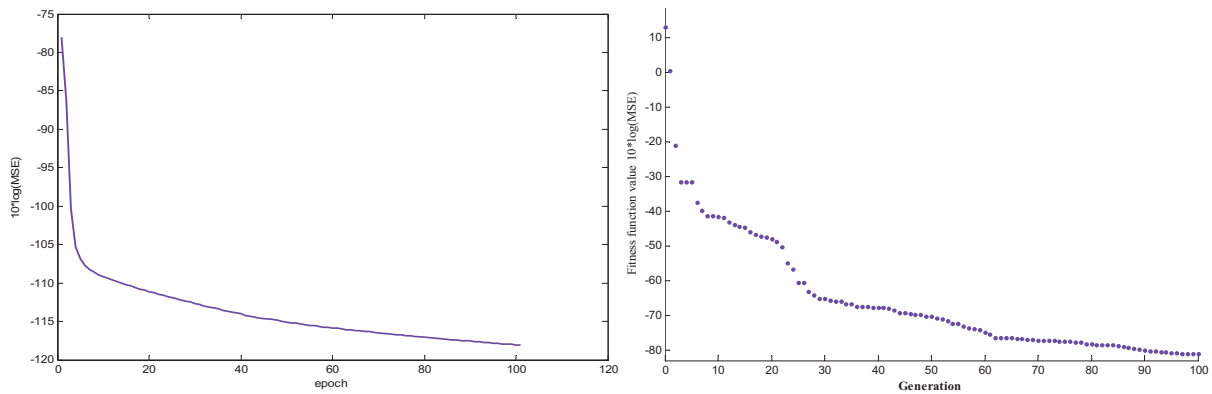


Figure 4: Training ANN with by hybrid GA-ANN method a) performance of genetic algorithm b) performances of back propagation algorithm.

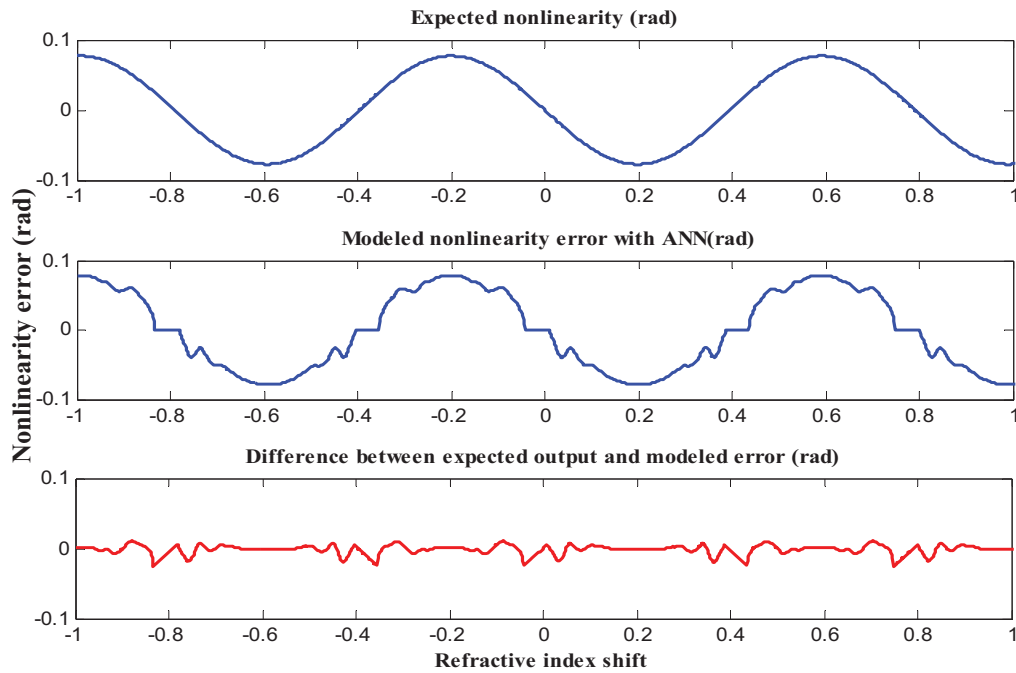


Figure 5: Modeling of nonlinearity error by ANN, (a) expected nonlinearity, (b) the modeled nonlinearity, and (c) the difference between expected and modeled nonlinearity

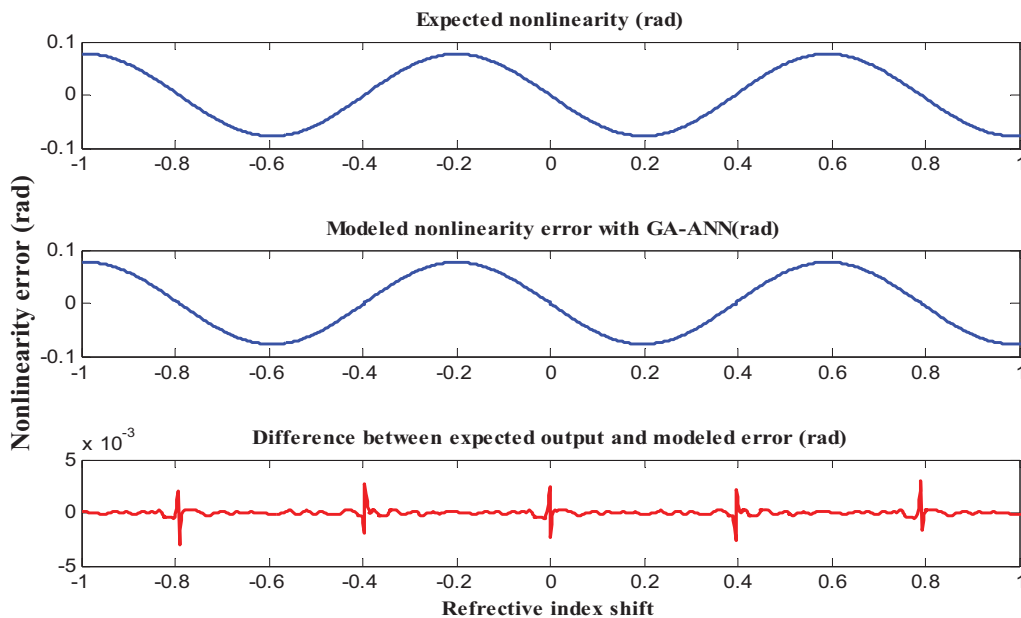


Figure 6: Modeling of nonlinearity error by hybrid GA-ANN, (a) expected nonlinearity, (b) the modeled nonlinearity, and (c) the difference between expected and modeled nonlinearity



5 Conclusion

In this paper, ANN and hybrid GA–ANN have been applied for modeling the nonlinearity error due to ellipticity polarization and non-orthogonality of input beam in three-longitudinal-mode laser heterodyne interferometer for determination refractive index of fuel cell. The genetic operators can find optimized weights and biases of the neural network much better than gradient descent method while they prevent from some problems like premature convergence and falling in local minimums. Performance of hybrid genetic algorithm with BP algorithm is better than BP alone because it has the global search capability of genetic algorithm with the local search ability of BP algorithm together. In a special case, the minimum MSE is equal to -127 dB.

References

- [1] Yazici MS. Hydrogen and fuel cell activities at UNIDO-ICHET. *International Journal of Hydrogen Energy* 2010; 35: 2754–2761.
- [2] Thomas s and Zalbowitz M. *Fuel Cells – Green Power Hand book*. U.S. Department of Energy. Office of Transportation Technologies.
- [3] Kirubakaran A and Jain RK. A review on fuel cell technologies and power electronic interface. *Renewable and Sustainable Energy Reviews* 2009; 13:2430–2440.
- [4] Motupally s and Becker AJ, Weidner JW. Diffusion of Water in Nafion 115 Membranes. *Journal of The Electrochemical Society* 2000; 147: 3171–3177
- [5] Tsushim S, Aotani K. Magnetic Resonance Imaging of A Polymer Electrolyte Membrane Under Water Meation. *Experimental Heat Transfer* 2009; 22: 1–11.
- [6] Waller L, Kim J, Shao-Horn Y, Barbastathis G. Interferometric tomography of fuel cells for monitoring membrane water content. *Opt Express* 2009;17:16806–16.
- [7] Olyae S and Abadi MSE, Hamedi S and Finizadeh F. efractive index determination and nonlinearity modeling in fuel cells using laser heterodyne interferometer. *International Journal of Hydrogen Energy*, 2011;36(20): 13255-13265.
- [8] Quenelle RC. Nonlinearity in interferometric measurements. *Hewlett-Parkard J* 1983;4310.
- [9] Sutton CM. Nonlinearity in the length measurement using hetrodyne laser Michelson interferometry. *J Phys E: Sci Instrum* 1987;20:1290–2.
- [10] Olyae S, Yoon TH, Hamedi S. Jones matrix analysis of frequency mixing error in three-longitudinal-mode laser heterodyne interferometer. *IET Optoelectron* 2009;3:215–24.
- [11] Li Z, Herrmann K, Pohlenz F. A neural network approach to correcting nonlinearity in optical interferometers. *Meas Sci Technol* 2003;14:376–81.
- [12] Heo G, Lee W, Choi S, Lee J, You K. Adaptive neural network approach for nonlinearity compensation in laser interferometer. Springer Press 2007; pp. 251–258.
- [13] Olyae S, Ebrahimpour R, Hamedi S. Modeling and compensation of periodic nonlinearity in two-mode interferometer using neural networks. *IETE Journal of Research* 2010; 56(2): 102–110
- [14] Whitfield D, Martin E. H. New directions in cryptography. *IEEE Transactions on Information Theory* 1986, 14(15), 644–654.
- [15] Olyae. S and Hamedi S, *A low-nonlinearity laser heterodyne interferometer with quadrupled resolution inthe displacement measurement*, *The Arabian Journal for Science and Engineering*, 2011;36: 279-286.



- [16] Hou. W, *Optical parts and the nonlinearity in heterodyne interferometers*, p. 337–346, Precision Engineering, 2006.
- [17] Hornik K, Stinchcombe M, White H. Multi-layer feed forward networks are universal approximators. *Neural Networks* 1989; 2(5), 359–366.
- [18] Fogel DB. An Introduction to Simulated Evolutionary Optimization. *J IEEE Trans* 1994;5(1):3–14.
- [19] Ganatra A, Kosta Y P, Panchal G, Gajjar C. Initial Classification Through Back Propagation In a Neural Network Following Optimization Through GA to Evaluate the Fitness of an Algorithm. *International Journal of Computer Science & Information Technology* (IJCSIT) 2011;3(1):98–116



Study of ORR kinetic on Pt/C at the presence of super paramagnetic of Fe₃O₄ nanoparticles in PEMFC

F. Rastegary-Fard^{*1}. M kheirmand²,

Department of chemistry, faculty of sciences, university of Yasouj, Yasouj, Iran

Corresponding Author E-mail: fereshteh_rastegary@yahoo.com

Abstract

Ion-exchange polymer membrane fuel cell (PEMFC) is as power source that fed by hydrogen gas and produce water. Electrochemical oxygen reduction reaction (ORR) is one of the most important reactions in the fuel cell energy conversion. ORR in acidic condition is four electron reaction of oxygen to water. Oxygen is a powerful oxidizing agent and is actually responsible for the extraction of energy from the fuel. But sluggish kinetic of ORR in Fuel cell is a problem. In this paper the role of super paramagnetic Iron oxide nanoparticles with different loadings, at the presence of commercial Pt/C was evaluated via conventional three electrode system and electrochemical tests such as Cyclic Voltammetry, Rotating disk electrode (RDE), Chronoamperometry.

Keywords: PEMFC, Oxygen reduction reaction, Rotating disk electrode

Introduction

Low temperature fuel cell technology has being considered as popular technology. Ion-exchange polymer membrane fuel cell (PEMFC) is as power source that fed by hydrogen gas and produce water. Through, has attracted much attention due to friendly environmental, high energy conversion efficiency, high power density, good temperature performance, No need to recharging and application in automobile. However, commercialization is the way it challenges, including the high price of platinum and limited sources. Although platinum widely still use as catalyst. So researchers are looking for alternatives to reduce the price of fuel that can be produced by two routes: (a) reducing the platinum loading in the catalyst (b) replacing the platinum catalyst with non- platinum catalyst [1]. The electrochemical reduction of oxygen is one of the most important reactions in electrochemistry due to its central role in fuel cells, metal-air batteries. Depending on the electrode material and the solution composition, the oxygen reduction reactions (ORR) precede as a direct four-electron process or a two-electron process. The production of water of four-electron reduction is favorite in

¹ M.Sc student of physical chemistry, Yasouj university ,Yasouj, Iran

² Assistance of prof. physical chemistry



PEMFC, while hydrogen peroxide is electrochemically generated by a two-electron reduction of oxygen. Carbon supported platinum catalyst shows a large surface area and increased catalytic activity for the ORR. Bimetallic catalysts were employed to increase the catalytic activity and to reduce the cost [2].

Some transition metal oxides, such as Oxides of Iron, Cobalt, Manganese and ruthenium can modify the electronic nature and is effective in reducing the platinum loading for instance Manganese Oxides have good activity for H₂O₂ decomposition. But the catalyst lifetime decreases by reducing Pt loading. Also Pt nanoparticles are placed onto carbon nanofibers such as carbon plate, graphen and carbon powder that is effective in oxygen reduction. Greater amount of Platinum used in fuel cell cathode to reduce oxygen because kinetic of oxygen reduction reaction (ORR) is slower than Hydrogen oxidation reaction (HOR). Overpotential of hydrogen oxidation and oxygen reduction is 25mv and 300mv respectively on pure platinum. Now the based platinum systems exhibit the best electrocatalytic activity. ORR reaction is reducing oxygen molecules to water molecules [3,4]:



Compared to other metal oxides Fe₃O₄ has the advantage of low cost and compatibility with the environment. Recently, extensive work has been done in this context. Lai and et al [5] put platinum nanoparticles on the surface of three-dimensional Fe₃O₄/C. and used for Methanol oxidation reaction (MOR) catalyst. The new nano-composites made of carbon and separate advantage of Fe₃O₄. The groups on surface of nano-composite three-dimensional Fe₃O₄/C as –NH₂ and –OH can keep platinum on surface firmly cause to increasing electrocatalytic activity that showed threefold current density Pt/C for MOR In this paper used of platinum nano clusters at the presence of super Paramagnetic Iron oxide nanoparticles to improve kinetic of ORR in PEMFC.

Experimental:

For electrochemical test, 80 mg of Pt/C (10 wt.%) In 20ml of a 1:1 ratio of water and 2 - propanole was dispersed for 30 minutes using the ultrasonic. Then put in the oven until the ink becomes thick, viscous substance on the surface of glass carbon electrode was distilled. Electrochemical system include three electrodes system, Ag/AgCl reference electrode and plate platinum as the auxiliary electrode(counter) and glass carbon electrode were as working electrode. 80 mg of Pt/C ratio of 1:1 and 1:2 and 1:3 away from the Pt/C: Fe₃O₄ were mixed in separate containers in a 1:1 solution of water and 2 - propanole was poured. Using ultrasonic disperses for 30 minutes then placed in the oven.

Cyclic Voltmetry:

Cyclic voltammetry tests were performed using an EG&G in conventional three-electrode system at room temperature. An Ag/AgCl used as reference electrode and platinum as counter electrode. The working electrode prepared by applying catalyst ink on glassy carbon surface then distilled a drop of nafion (5 wt. %) solution and dried. Voltamograms obtained in -0.3v

to 1.2v in solution of sulfuric acid (0.5M) that was bubbled by inert gas (N₂). The electrochemical specific surface areas (EAS) of electrocatalysts were calculated by integrating the areas under the peaks of hydrogen adsorption. To determine the EAS, the charge due to hydrogen adsorption (QH) was obtained by [6]:

$$EAS = \frac{Q_H}{[Pt] \times 0.21} \quad (1)$$

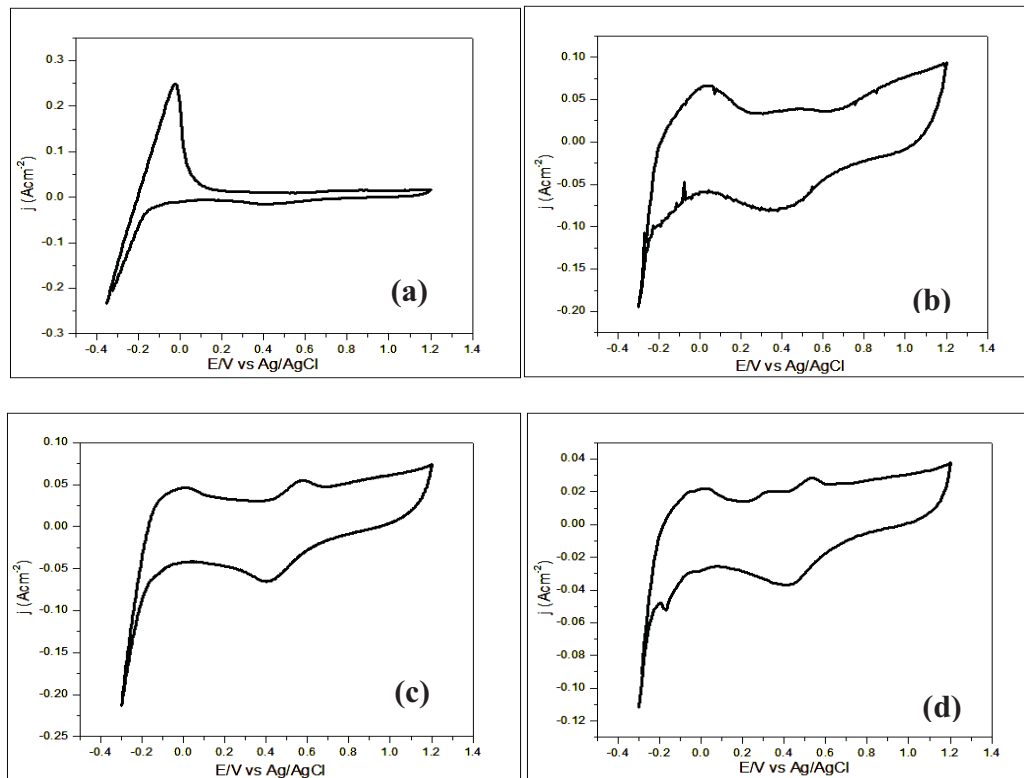


Figure 1: Cyclic Voltammetry of (a) Pt/C, (b) 1:1, (c) 1:2 and (d) for 1:3 ratio electrocatalysts of Pt/C: Fe₃O₄ in scan rate 50mvs⁻¹ and N₂ atmosphere and room temperature.

To investigate the effect of Iron oxide nanoparticles at the presence of Pt/C, cyclic voltammetry test was performed for methanol oxidation reaction. Sharp peak of MOR is seen for Pt/C electrocatalyst and for 1:1 ratio of Pt/C: Fe₃O₄ smaller peak for methanol oxidation reaction shows. Therefore Result is hope for selectivity of the electrocatalytic on oxygen reaction.

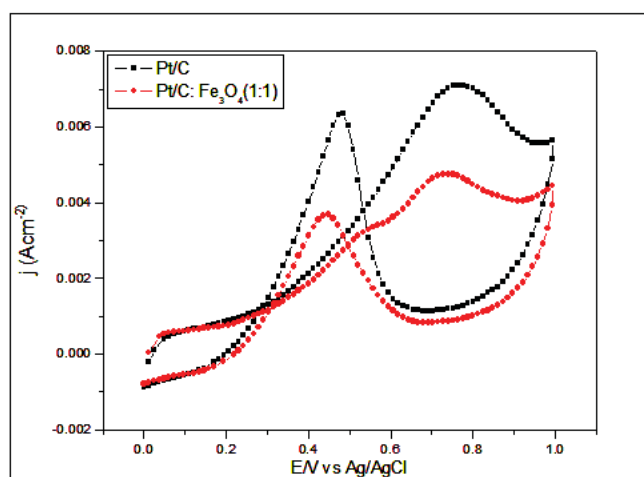


Figure 2. Comparison cyclic voltammograms of methanol oxidation reaction (MOR) in 0.5M of H_2SO_4 and 1M Methanol solution at the potential scan rate $50mvs^{-1}$ at room temperature.

Table 1. Electrochemical active surface area calculated for electrocatalysts.

electrocatalyst	EAS($cm^2 g^{-1}$)
Pt/C (10%wt)	124.90
Pt/C : $Fe_3O_4(1:1)$	106.11
Pt/C : $Fe_3O_4(1:2)$	61
Pt/C : $Fe_3O_4(1:3)$	33.36

Chronoamperometry:

Chronoamperometric technique is an effective method to evaluate the electrocatalytic stability of catalysts. Using this technique easily diffusivity, solubility and permeability, gas permeability of oxygen penetrating electrodes is obtained. These parameters depend on the extent of the time, according to the Cottrell equation is [7]:

$$i(t) = \frac{nFA D^{1/2} C_0}{(\pi t)^{1/2}} \quad (2)$$

n is the number of electrons exchanged for the overall electrode reaction. A , F , t and π are the area of electrode penetration and reagent concentration and Faraday's constant, the time, and the ratio of circumference to diameter, respectively. Slope for the Pt/C. Most of the time the reaction is Iron oxide. Penetration is calculated from the slope. Electrocatalytic slope was calculated by the results is shown in Table 2.

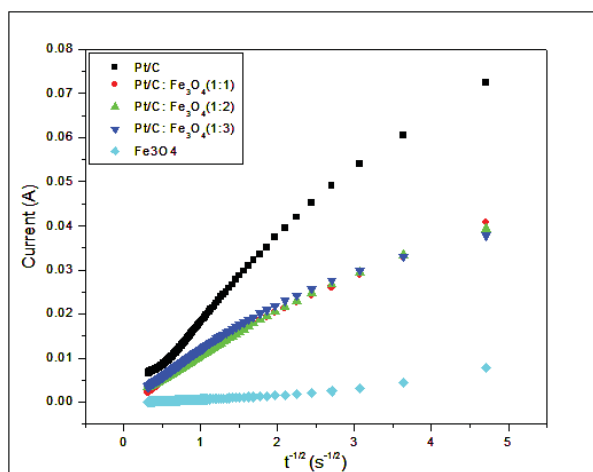


Figure 3: Chronoamperometry plots in O₂ saturated and room temperature.

Chronoamperometry results Pt/C electrocatalytic activity has more of the other electrocatalytic, But diffusion coefficient has been calculated on the electrocatalytic that Iron oxide is present close to diffusion coefficient of Pt/C electrocatalytic. Magnetic Iron oxide, which can absorb oxygen, then absorbed gas permeability of oxygen to provide to Pt/C catalyst.

Table 2. Diffusion Coefficient of Oxygen that calculated of Chronoamperometry slop.

electrocatalyst	D _{o2} (cm ² /s)
Pt/C (10%wt)	1.13 × 10 ⁻⁵
Pt/C : Fe ₃ O ₄ (1:1)	3.93 × 10 ⁻⁶
Pt/C : Fe ₃ O ₄ (1:2)	3.18 × 10 ⁻⁶
Pt/C : Fe ₃ O ₄ (1:3)	3.18 × 10 ⁻⁶

Iron oxide nanoparticles can be a barrier of Oxygen reduction reaction on Pt nanoparticles. Given that Iron oxide is also somewhat of a non-conductive insulation is in electrochemical systems. Presence of non-conductive in electrochemical system, electron transfer and ion transport can barrier against diffuse of oxygen molecules.

Rotating disk electrode (RDE)

The ORR activities of electrodes were investigated in O₂ saturated 0.1 M H₂SO₄ solution. Fig 4 shows the linear scan voltammetry plots of electrodes measured with a scan rate of 1mvs⁻¹ at room temperature. To obtain kinetic parameters for the oxygen

$$\frac{1}{f} = \frac{1}{j_k} + \frac{1}{j_d}$$

reduction reaction at fabricated electrodes followed [8]:

(3)

$$\frac{1}{j} = \frac{1}{nFk C_{O_2}^b} + \frac{1}{0.62nF D_{O_2}^{2/3} C_{O_2}^b \nu^{-1/6} \omega^{1/2}} \quad (4)$$

Spinning solution in electrochemical systems, will facilitate diffusion coefficient of oxygen to the electrode surface and the diffusion limitation of oxygen recovery takes so kinetic starting potential change in response to the higher values and lower overpotential. A RDE result of electron exchange reaction in ORR was 3/6 for Pt/C electrocatalyst. So it can be stated that the reaction mechanism of the four-electron pathway is gone. Electrocatalytic with the number of electrons in 1:1 ratio of Pt/C: Fe₃O₄ was 2/9 ≈ 3. Oxygen reduction reaction proceeds of both the electron and 2-electron 4 is gone in a direction that is parallel to both directions.

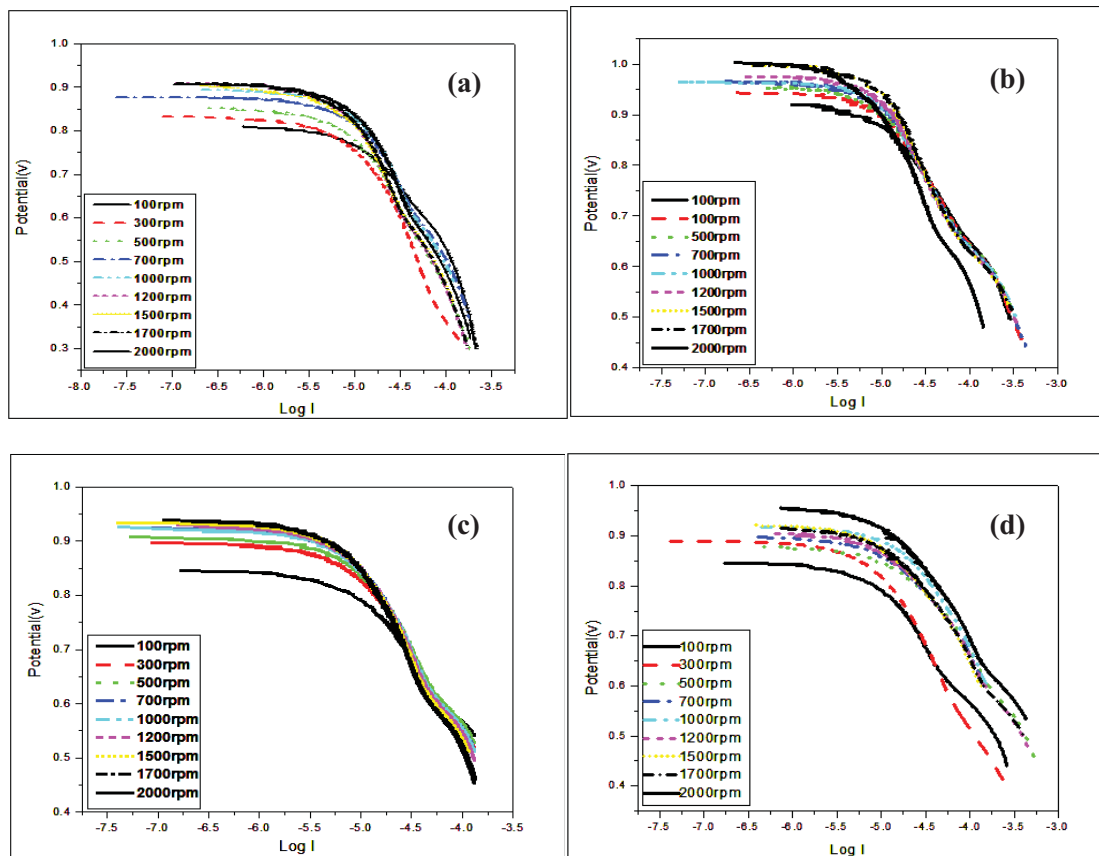


Figure 4. Linear sweep voltammetry on RDE for (a) Pt/C, (b) 1:1 ratio, (c) 1:2 ratio, (d) 1:3 ratio electrocatalyst in H₂SO₄ 0.5M and scan rate mvs⁻¹ in 100rpm to 2000rpm.

With the assumption that the transition metals are more likely to produce H_2O_2 , Number of electrons exchange is reduced in the reaction of oxygen of these metals. On the other hand, H_2O_2 catalyst to attract more smaller particles are then absorbed by hydrogen peroxide in the presence of Iron oxide nanoparticles can also be involved. Can reduce the number of exchanged electrons to Iron oxide insulator and block attributes. Considering that the oxygen reduction reaction, 4 electron reduction ideally, the electrocatalytic four-electron reduction of oxygen would figure more attention. In this test, a combination of the two and four-electron electrocatalytic ratio is 1:1. Therefore, more research on this than the Pt / C: Fe_3O_4 focus.

Reaction kinetic study and reaction to achieve the number of electrons exchanged the RDE results in charts $1/j$ by $\omega^{-1/2}$ were plotted [8]. The results are shown in the chart in Table 3.

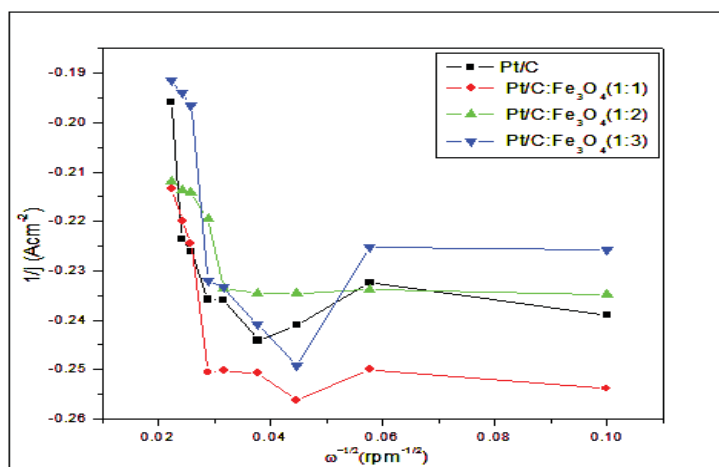


Figure 5. Koutechy–Levich reciprocal plot obtained using the data in 100rpm to 2000rpm.

Table 3. Number of electron that calculated by Koutechy–Levich data.

electrocatalyst	Number of electron
Pt/C (10. wt%)	3.6
Pt/C : Fe_3O_4 (1:1)	2.9
Pt/C : Fe_3O_4 (1:2)	2.4
Pt/C : Fe_3O_4 (1:3)	2.4



Conclusions

In this study the low loading of Pt (10%wt) was used as the cathode PEMFC for ORR with super paramagnetic of Fe₃O₄ nanoparticles. With regard to the different effects of the magnetic field on the molecule super paramagnetic particles of iron oxide can be used to increase the oxygen adsorption and increase its kinetic. These results were obtained from experiments conducted by the electrocatalytic Pt / C: Fe₃O₄ with a 1:1 ratio after Pt/C, for having more electrochemical active surface area for hydrogen adsorption and diffusion coefficient can be good electrocatalyst for Oxygen reduction reaction. However, due to the negative effects of iron oxide, including effects on carbon and platinum corrosion are waste reduction field and study of these effects is wide.

Reference

- [1] G. Liu, X. Li, P. Ganesan and B. Popov “Development of non-precious metal oxygen-reduction catalysts for PEM fuel cells based on N-doped ordered porous carbon”, J. of Applied Catalysis B: Environmental, (2009). 93, 156–165.
- [2] A. Ishihar, Y. Ohgi, K. Matsuzawa, S. Mitsushima and K. Ota Zhang “Progress in non-precious metal oxide-based cathode for polymer electrolyte fuel cells”, J. of Electrochimica Acta, (2010). 55, 8005–8012.
- [3] I. Kruusenberg, L. Matisen, Q. Shah, A.M. Kannan and K. Tammeveski “Non-platinum cathode catalysts for alkaline membrane fuel cell ”, J. of Hydrogen Energy, (2012). 37, 4406-4412.
- [4] X. Cheng, Zh. Shi, N. Glass, L. Zhang and J. Zhang “A review of PEM hydrogen fuel cell contamination: Impacts, mechanisms, and mitigation”, J. of Power Sources, (2007). 156, 739-756.
- [5] L. Lai, G. Huang, X. Wang and J. Weng “Preparation of Pt nanoparticle-loaded three-dimensional Fe₃O₄/carbon with high electro-oxidation activity”, J. of CARBON, (2011). 49, 1581-1587.
- [6] H. Sun, J. You, M. Yang and F. Qu “Synthesis of Pt/Fe₃O₄–CeO₂ catalyst with improved electrocatalytic activity for methanol oxidation”, J. of Power Sources, (2012). 205, 231-234.
- [7] J. Zeng, S. Liao, J. Y. Lee and Zh. Liang “Oxygen reduction reaction operated on magnetically-modified PtFe/C electrocatalyst”, J. of Hydrogen Energy, (2010). 35, 942-948.
- [8] A. Nozad Golikand , M. Asgari and E. Lohrasbi “Study of oxygen reduction reaction kinetics on multi-walled carbon nano-tubes supported Pt-Pd catalysts under various conditions”, J. of Hydrogen Energy, (2010). 1-8.



Modification of Nafion Membranes with Different Clays for Direct Methanol Fuel Cell Applications

M. Azimi¹, S. J. Peighambaroust^{*1}, M. G. Hosseini²

¹ *Department of Chemical Engineering, University of Tabriz, Tabriz, Iran*

² *Electrochemistry Research Laboratory, Physical Chemistry Department,
Chemistry Faculty, University of Tabriz, Tabriz, Iran
j.peighambaroust@tabrizu.ac.ir*

Abstract

Fuel cells due to their particular properties are on the verge of creating a vast revolutionary change in the field of electricity. Proton exchange membrane fuel cells (PEMFCs) have attracted tremendous attention because of their high efficiency compared to other types of fuel cells. Nafion is the most commonly used polymer for membranes used in PEMFCs. A large variety of nanoparticles of different natures and sizes can be blended with a Nafion matrix, generating a new class of nanostructured electrolyte membrane with interesting physical properties. In this article, we summarized some of the recent works done on modification of nafion membranes with different type of clays to increase the selectivity (the ratio of proton conductivity to methanol crossover) of nanocomposite membrane in the direct methanol fuel cells.

Keywords: Proton exchange membrane, Nafion, direct methanol fuel cell, methanol permeability and selectivity.

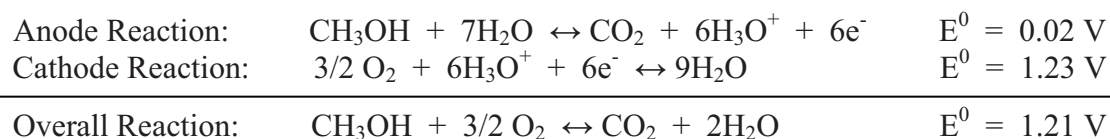
1- Introduction

A fuel cell is a device that converts the chemical energy from a fuel into electricity through a chemical reaction with oxygen or another oxidizing agent. Proton exchange membrane fuel cells (PEMFCs) are considered to be a promising technology for clean and efficient power generation in the twenty-first century. Direct methanol fuel cells (DMFCs) have great potential in generating electricity owing to their high efficiency and lightness. However, two major technical limitations restrict the commercialization of the DMFC. They are the slow oxidation kinetics of methanol and the high methanol crossover from the anode to the cathode [1]. Perfluorosulfonic acid (PFSA) group such as Nafion has been commercially used in hydrogen-oxygen fuel cell applications to serve as an electrolyte. Due to its good conductivity and good thermal stability, its use has been established in DMFC and PEMFC [2]. However, Nafion faces several drawbacks which limit its industrial applications. One of the disadvantages is the high production cost which is 700 USD\$/m² [3]. Furthermore, it has low conductivity at high temperatures because of fast dehydration and loss of fluorine ion in the exhaust gas due to OH radical attack [4]. Besides that, the key problem for Nafion use in DMFC is the high methanol crossover which allows methanol diffusivity of $1.0 \times 10^{-6} \text{ cm}^2 \cdot \text{s}^{-1}$ even at room temperature [5]. For the past 20 years, polymer-clay composites have attracted much attention both academically and industrially [6]. The large researches have been conducted by incorporating polymer with clay and the result showed that clay was a methanol barrier. This discovery was proven by the decrease in methanol permeability of the composite membranes as compared to pristine based polymer [7]. However, the addition of clay into polymer will reduce its proton conductivity which is not favorable in DMFC application [8]. Thus, several attempts have been made to reduce methanol permeability without sacrificing too much proton conductivity by using silane agent [9], grafting sulfonic group into silicate

layer [10,11] or by organically modifying the clay using quaternary ammonium salt [12-14], etc. In this article, we summarized some of the recent works done on modification of nafion membranes with different types of clays to increase the selectivity (the ratio of proton conductivity to methanol crossover) of nanocomposite membrane in the direct methanol fuel cells.

2- Direct methanol fuel cells (DMFCs)

Significant efforts in recent decades have been focused on the direct electrochemical oxidation of alcohol and hydrocarbon fuels. Among the liquid organic fuels, methanol has promising characteristics in terms of reactivity at low temperatures, storage and handling. Accordingly, a methanol-feed proton exchange membrane fuel cell (PEMFC) would help to alleviate some of the issues surrounding fuel storage and processing for fuel cells [15]. The direct methanol fuel cell (DMFC) is a promising transportable power source. In this type of fuel cell, an aqueous solution of methanol constitutes the fuel and is fed to a polymer electrolyte membrane based fuel cell. Briefly, with the direct methanol fuel cell system the complexity of processing the methanol into hydrogen is eliminated. The liquid feed operation also facilitates easy thermal management of the stack [16]. Methanol is cheap and can be distributed by using the present infrastructure for liquid fuels. It can be obtained from fossil fuels, such as natural gas or coal, as well as from sustainable sources through fermentation of agricultural products and from biomasses. Compared with ethanol, methanol has the significant advantage of high selectivity to CO₂ formation in the electrochemical oxidation process [17]. However, despite these practical system benefits, DMFCs are characterized by a significantly lower power density and lower efficiency than a PEMFC operating with hydrogen because of the slow oxidation kinetics of methanol and methanol crossover from the anode to the cathode [18]. The DMFC relies upon the oxidation of methanol on a catalyst layer to form carbon dioxide. Water is consumed at the anode and is produced at the cathode. Protons (H⁺) are transported across the proton exchange membrane - often made from Nafion - to the cathode where they react with oxygen to produce water. Electrons are transported through an external circuit from anode to cathode, providing power to connected devices. Reactions in a direct methanol fuel cell are:



At anode, the methanol is oxidized into carbon dioxide and six protons (as hydronium ions) plus six electrons. The six protons formed react at the cathode with oxygen to form water. The overall reaction looks like a combustion reaction and is thus sometimes referred to as cold combustion. Actually the cell is a mean to control this reaction and use it to produce current directly. The standard cell voltage for a DMFC at 25°C is 1.21V. However, this potential is never obtained in reality. The open circuit potential is usually about 0.6 to 0.8V in the best case [19].

3- Proton exchange membranes for DMFCs

Membranes have a great effect on DMFC performance, especially their behavior toward methanol crossover. A compromise needs to be found between membrane proton conductivity and methanol diffusion. Nanocomposite membranes have shown low methanol permeability but have also a higher resistance to protons transfer. Consequently, thinner membranes with lower electrical resistance may be used to minimize crossover [20]. The standard electrolyte membrane for DMFCs is usually a perfluorosulfonic acid membrane such as Nafion, which is also widely used in PEMFCs. Most of the electrolyte alternatives to Nafion, both the proton-



conducting and alkaline type, are cheaper than the classic perfluorosulfonic membranes used in PEMFCs; in some cases, they are also characterized by lower methanol crossover; however, life time characteristics similar to those shown by Nafion type membranes in fuel cells (60000 h of operation) have not been achieved yet with the alternative membranes [21]. Perfluorosulfonic polymer electrolyte membranes are currently used in H₂/air and methanol/air fuel cells because of their excellent conductivity and electrochemical stability [15]. Unfortunately, they suffer several drawbacks such as methanol crossover and membrane dehydration. The latter severely hinders fuel cell operation above 100°C, which is a prerequisite for high rate oxidation of small organic molecules involving the formation of strongly adsorbed reaction intermediates such as CO-like species. Since methanol is rapidly transported across per-fluorinated membranes and is chemically oxidized to CO₂ and H₂O at the cathode, there is a significant decrease in columbic efficiency for methanol consumption, as much as 20% under practical operating conditions [22]. Thus, it is very important to modify these membranes by, for example, developing composites or finding alternative proton conductors with the capability of inhibiting methanol transport. It is generally accepted that a solid-state proton conductor is preferable for liquid fuel fed DMFCs because it hinders corrosion and rejects carbon dioxide (produced during the methanol oxidation). However, there are some prerequisites that should be properly considered. The polymer electrolyte should have a high ionic conductivity ($5 \times 10^{-2} \text{ ohm}^{-1} \cdot \text{cm}^{-1}$) under working conditions and low permeability to methanol (less than $10^{-6} \text{ moles min}^{-1} \cdot \text{cm}^{-2}$). Furthermore, it must be chemically and electrochemically stable under operating conditions [23]. Concerning conductivity, only recently membrane alternatives to Nafion type have shown similar levels of performance. One critical aspect is related to the fact that the presence of water is a requirement of low temperature DMFCs for the occurrence of the electrochemical reactions and to promote ion conductivity. As methanol is highly soluble in water, the transport of water through the membrane is commonly associated with methanol permeation. This effect is more critical with protonic membranes because, besides methanol transport due to the concentration gradient (diffusion), there is an effect due to the electro-osmotic drag. High ionic conductivity is often associated with the presence of high levels of water uptake by the membrane whereas what is required is a low water uptake. These aspects are mainly related to polymer electrolyte membrane DMFCs [24].

4- Modification of membranes for DMFC applications

Methanol crossover occurs in PEMs of DMFCs due to the concentration gradient of water and methanol across the membrane. Since methanol is fed at the anode, the resulting concentration gradient drives mass transfer from the anode side to the cathode side. This leads to an electrode over-potential since methanol that has permeated to the cathode side will oxidize to liberate electrons at the electrode where reduction and absorption of electrons should occur instead. A lower potential drop between the electrodes reduces the attainable power density of the fuel cell. Reducing methanol crossover over the membrane involves reducing proton conductivity as well. This is because the mechanism of methanol crossover through the membrane is the same as the mechanism of proton transfer. It is very likely that due to the dipole-dipole attraction, the OH⁻ present in methanol is attracted to the H₃O⁺ and so methanol is transferred through the membrane to the cathode side along with protons (H⁺) and water molecules (H₂O). So modifications to the membrane material to reduce methanol crossover would reduce conductivity as well. A balance has to be found between the two when evaluating techniques for methanol crossover reduction [25]. Protons are transported through ionomer membranes such as Nafion by means of surface, vehicular, and Grotthuss diffusion. However, methanol only migrates through Nafion. Therefore, this research hypothesized that altering the structure and properties of ionic channels in Nafion would change the protonic conductivity and methanol permeability of the membrane to different extents. The following



points are important to impede proton transport (and hence methanol crossover) across Nafion membranes: a) Increasing thickness of membrane, b) Decreasing acidity of the membrane, c) Incorporating fillers and dopants into the membrane. In simplified terms, the flux of methanol across the membrane can be described as following equation:

$$J_{\text{MeOH}} = -D_{\text{MeOH}} \frac{\partial C}{\partial z}$$

Increasing the thickness of the membrane would reduce the concentration gradient of water and methanol and so fewer methanols would crossover to the cathode. Acid groups are negatively charged and therefore attract protons and encourage proton transport. Decreasing the acidity of the membrane would reduce the concentration of protons available for transport. Further it would reduce hydrophilicity of the membrane and hence water uptake. So reducing the number and strength of acid groups would impede proton conductivity and methanol crossover [26]. The term polymer nanocomposite (PNC) is generally defined as the combination of a polymer matrix and a filler that has at least one dimension in the nanometer range (<100 nm). The filler can be one-dimensional such as nanotubes and fibers; two dimensional such as layered silicate minerals like clay; and three-dimensional such as spherical nanoparticles. Over the past two decades, PNC technology has attracted great interest in both academia and industry because of its outstanding mechanical as well as the improved thermal properties with a very small amount (2–5 wt.-%) of filler incorporation [27]. In recent years, one of the most extensively used nanoparticles for the preparation of PNCs has been the layered silicate or clay. The presence of a high aspect ratio (length to width) filler is expected to decrease significantly the methanol (MeOH) crossover of the Nafion membrane as a result of a much longer pathway [28]. In 2003, Jung et al. first reported the preparation of Nafion/Montmorillonite (MMT) composite membranes for fuel cell applications. They used both pristine and organically modified MMT (OMMT) for the preparation of nanocomposite membranes. In a typical preparative method, a perfluoro-sulfonyl fluoride copolymer and MMT were first mechanically mixed by an internal mixer. The protonation of composite membranes were made by the lower methanol permeability. This improvement was, however, observed at the expense of the ionic conductivity, more likely as a result of the exchange of protons of Nafion with much less mobile ammonium cations of the nanoclay. The best performances were observed with Cloisite 30B type of MMT, with a content as low as 0.5 wt.% [29]. The Fig. 1 shows the methanol permeability weight of perfluoro-sulfonyl fluoride copolymer resin and MMT with various contents by GC, as function of time. The methanol permeability weight of the composite membrane decreased slightly with increasing the contents of MMT in the composite membrane, as shown in Fig. 1a. It was found that the methanol permeability weight decreased slightly with increasing the contents of m-MMT in the nanocomposite membrane. Thus, the methanol permeability weight of the composite membrane was lower than that of normal pure membrane as electrolyte. The ionic conductivities of these acid-form composite membranes were measured at various temperatures, and the data are plotted in Fig. 2a and b. Fig. 2 shows the proton conductivity of perfluoro-sulfonyl fluoride copolymer resin and MMT membrane. All the membrane exhibits a marked increase in conductivity with increasing temperature. This is due to temperature plays a main role in the kinetics of proton motion in the polymeric membrane and mobility of polymer chains. So it was found that the proton conductivity of perfluoro-sulfonyl fluoride copolymer resin and MMT, m-MMT membranes decreased slightly with increasing the contents of MMT and m-MMT in the composite membrane and lower than normal pure membrane. But it was considered that the composite membrane containing MMT and m-MMT could be used as electrolyte membrane for DMFCs. However, the addition of MMT particles, whether organically modified or not, results in decreased ionic conductivity in parallel to the lower methanol permeability [29].

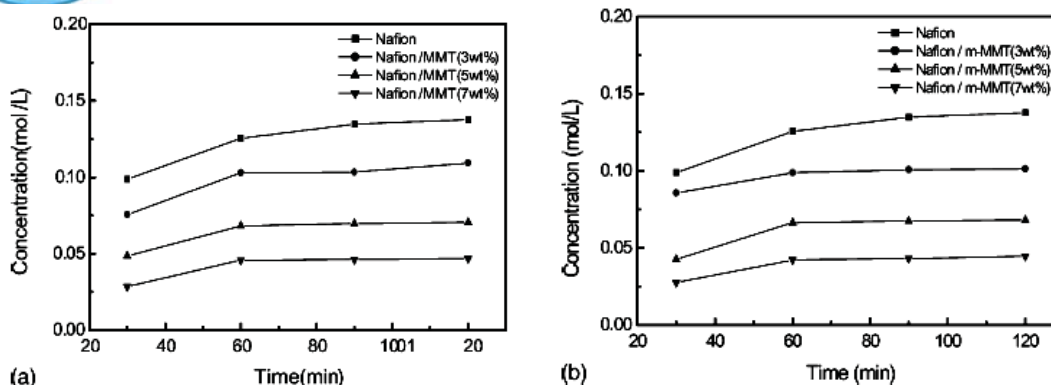


Fig1. Methanol concentration of a) MMT and b) m-MMT/Nafion composite membrane with various content of MMT as a function of time [29].

Rhee et al. have made claims on overcoming this drawback by grafting an organic sulfonic acid containing compound onto the surface of the aluminosilicates layers by silane condensation. But this did not yield significant improvement on the ionic conductivity of the composite membrane [30]. Silva et al. used the solvent casting method to prepare MMT containing Nafion membranes, and the results showed that the addition of a very small amount of MMT (≈ 1 wt. %) did not alter the ionic conductivity but rather produced a marked decrease of methanol permeability [31]. Kim .Y. et al. has been many attempts to reduce methanol permeability through polymer electrolyte membranes, namely: (i) treatment of the surface of the membranes to block the methanol transport; (ii) control of the size of the proton transport channels using different block copolymers and cross linkage; (iii) development of new types of electrolyte polymers; (iv) introduction of a winding pathway for a methanol by making a composite with inorganic fillers. On the other hand, they modified the surface of MMT with an organic sulfonic acid group and formed composite membranes with Nafion in order to minimize the loss of proton conductivity caused by adding the inorganic materials while reducing the methanol permeability. Indeed, MEA containing MMT functionalized with organic sulfonic acid groups demonstrated much improved performance of DMFCs compared with MEA containing the pristine Nafion membrane and the composite membranes made with unmodified MMT. In this work, they report a new type of sulfonated MMT ($\text{HSO}_3\text{-MMT}$) functionalized with perfluorinated sulfonic acid groups, which was employed to form composite electrolyte membranes with Nafion.

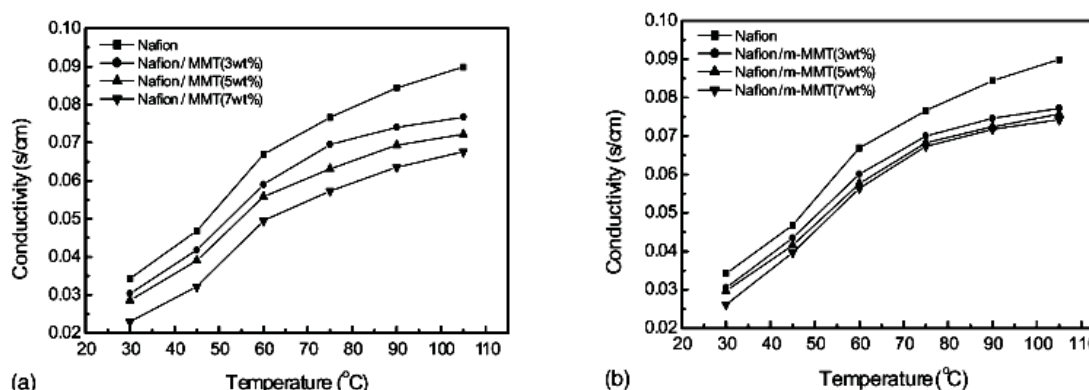


Fig.2 Proton conductivity as a function of temperature for a) normal membrane and Nafion resin/MMT and b) m-MMT (3, 5 and 7 wt.%) at completely humidified stage [29].

The terminal perfluorinated sulfonic acid functional groups containing the strongly-electron withdrawing fluorine atoms increase the acid strength of the terminal sulfonic acid groups

giving super-acidity, and thus increase the proton conductivity through the membrane. For comparison, composite membranes are prepared containing MMT fillers decorated with non-fluorine organic sulfonic acid groups. The characteristics of the membrane are studied in terms of methanol crossover, proton conductivity and spectroscopic properties, and the performance of the MEA fabricated from these membranes is evaluated for a DMFC. Fig. 3 shows the relative permeability and proton conductivities of a pristine Nafion membrane and the composite membranes. As shown, the proton conductivities of composite membranes are slightly lower than that of Nafion. The ionic conductivity values of the composite membrane containing 5 wt% HSO₃-MMT are higher than those of the other composite membranes and, in particular, the value is close to (98%) that of Nafion at 303K and 98% relative humidity.

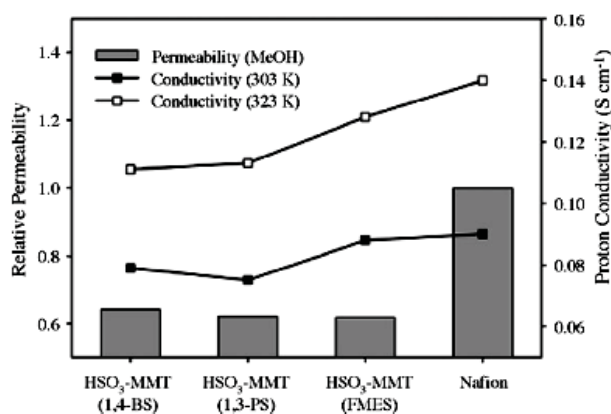


Fig. 3. Relative permeability and proton conductivity of recast Nafion and composite membranes fabricated with different HSO₃-MMTs. All composite membranes have the same membrane thickness of 150 μm and the same amounts of 5 wt% sulfonated MMTs [32].

The difference becomes more significant at 323 K [32]. Lin et al. prepared a novel functional organoclay using POP-backed quaternary ammonium salts that contained sulfonic acid (-SO₃H) to improve the performance of Nafion membranes used in direct methanol fuel cells. Modified layered silicate clays were cast with Nafion. To modify organoclay the adduct of amine/1,3-propane sultone was synthesized using poly(propylene oxide)-backboned diamines of MW 400 as the starting material and was abbreviated as POPD400. The preparation of diamine bearing one sulfonic acid (-SO₃H), abbreviated as POPD400-PS was carried out in a glass reactor equipped with a stirrer. Organoclay has been prepared by cation exchange between Na⁺ in clay galleries and poly(oxypropylene) (POP)-backboned diaminescations in aqueous solution. Fig. 4 presents the methanol permeability and proton conductivity of membranes fabricated with various proportions (0–6 wt%) of MMT-POPD400-PS in Nafion. The methanol permeability decreased rapidly as the amount of MMT-POPD400-PS added to Nafion increased. The methanol permeability of the composite membranes that contained 6 wt% MMT-POPD400-PS was $1.2 \times 10^6 \text{ cm}^2 \cdot \text{S}^{-1}$, 60% of that of pristine Nafion. The proton conductivity of the composite membranes increased with added MMT-POPD400-PS. The proton conductivity of the composite membranes generally declined from that of pristine Nafion membrane as the inorganic filler content increased. The Nafion/MMT-POPD400-PS composite membranes exhibit a higher selectivity than pristine Nafion, perhaps because of the increased proton conductivity and decreased methanol permeability of the composite membranes. The high selectivity reveals that the composite membrane is suited to DMFC applications [33]. Kim et al. made attempts to overcome the problem of methanol permeability while at the same time increase the ion conductivity of the composites membrane by preparing Nafion/sulfonated clay (SMMT) nanocomposite membranes via the film coating process. The results are given in Fig. 5, the proton conductivity decreased linearly from 0.096 to 0.077 $\text{S} \cdot \text{cm}^{-1}$ as the content of SMMT increased from 0 to 10 wt. %.

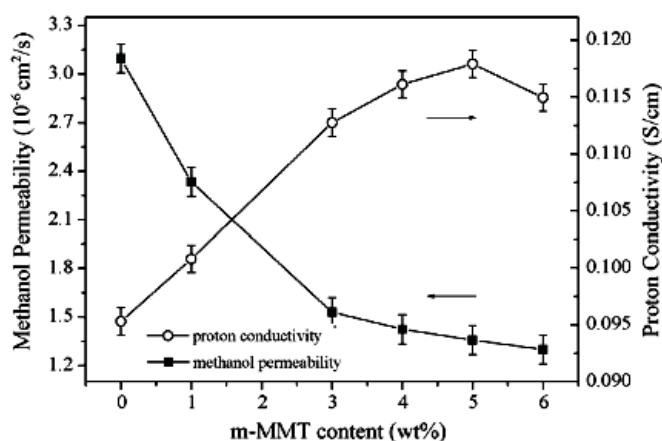


Fig.4. The proton conductivity and methanol permeability of the pristine Nafion and composite membranes fabricated with different amounts of MMT-POPD400-PS.

The composite membranes are expected to have proton conductivity values of 0.08 S.cm^{-1} or more at room temperature to reduce the current loss occurred by the ohmic resistance of SMMT in the cell performance test. Based on the proton conductivity and methanol permeability, the composite membrane prepared with 5 wt. % SMMT loading amount was selected for film coating process because the composite membrane had the lowest permeability value with an allowable conductivity value of 0.083 S.cm^{-1} . As shown in Table 1, the selectivity of the film coated composite membrane had a higher value by 37 % than that of Nafion 115. The high performances of the film coated composite membrane could be elucidated by the decrease of ohmic resistance in MEA part and methanol crossover from anodes to cathodes. The decrease of ohmic resistance of the MEA with the film coated composite membrane was attributed to a higher conductance (defined as conductivity/thickness) of thin composite membrane (dry thickness: $80 \mu\text{m}$) than that of the thick Nafion 115 (dry thickness: $124 \mu\text{m}$).

Table1. Properties of scaled-up Nafion S-MMT composite membrane compared to Nafion 115

Membranes	Proton conductivity (S.cm^{-1})	Permeability (cm^2s^{-1})	Selectivity
Film coated composite membrane (scale-up)	0.093	1.14×10^{-6}	8.2×10^4
Nafion115	0.093	1.55×10^{-6}	6.0×10^4

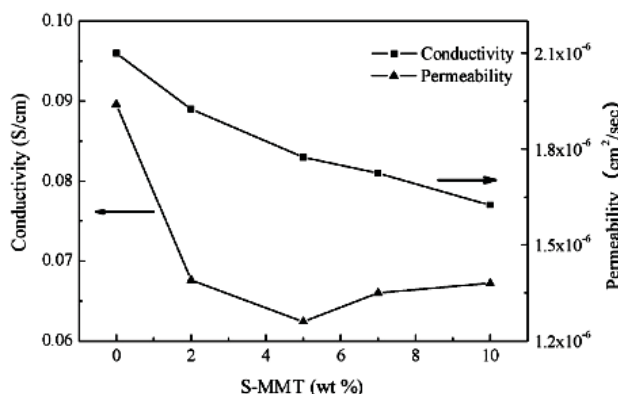


Fig .5. Effect of S-MMT amounts on proton conductivity and methanol permeability of cast Nafion S-MMT composite membranes.



Although their attempt was not successful, their results showed that many factors strongly affect methanol permeability as well as the conductivity of the membranes. Results also showed that the humidity should be considered and controlled during the synthesis and characterization of the membranes, especially for mechanical properties improvements [34]. In 2009, Hasani-Sadrabadi et al. fabricated polyelectrolyte membranes based on Nafion and bio-functionalized montmorillonite (BMMT) with chitosan biopolymer by solvent casting method. The proton conductivity behaviors of fabricated nanocomposites with different MMT and BMMT loading weights are compared. The proton conduction of both kinds of nanocomposite membranes is decreasing with increasing filler loading weight. On the other hand, in the presence of filler, SO_3^- groups in the polymer chains were decreased per unit volume. From the proton conductivity comparison of Nafion/MMT and Nafion/BMMT nanocomposite, the higher proton transporting ability of Nafion/BMMT could be understood. Polycationic chitosan chains were used as a macromolecular intercalating agent for functionalization of montmorillonite. Therefore, in present application, chitosan plays the role of a functional compatibilizer. Permeability results clearly demonstrate the methanol crossover has been decreased effectively thanks to the addition of BMMT. The reduction of permeability arises from the longer diffusive pathway in the presence of filler. Proton conductivity and methanol permeability are the two transport properties that determine DMFC performance. The presence of BMMT has a beneficial influence on methanol permeability and the opposite effect on proton conductivity. For identification of the optimum composition, the membrane selectivity parameter (ratio of proton conductivity to methanol permeability) of Nafion/BMMT nanohybrid membranes at various BMMT loadings was calculated. The higher selectivity value leads to a better membrane performance. As illustrated, the maximum selectivity appears at 2.0 wt. % of BMMT loading. It could be concluded that modification of MMT with positively charged polyelectrolyte could cause better miscibility with perfluorosulfonic polymers and lead to selectivity improvement [35]. In a very recent report, Hasani-Sadrabadi et al. prepared proton exchange membranes based on Nafion and 2-acrylamido-2-methylpropanesulfonic acid (AMPS) modified montmorillonite (MMT). Nanocomposite membranes containing different loading weights of AMPS-MMT as well as Cloisite 15A and unmodified MMT were characterized for their proton conductivity properties. Proton conductivity of all nanocomposite membrane samples is decreased with increasing nanofiller content. Such reducing trend of conductivity is associated with the fact that clay layers baffle proton migration pathways and increase the length of proton transfer routes through polyelectrolyte matrices. However, it was found that incorporation of AMPS-MMT into Nafion matrix has caused the least unfavorable effect on the proton conductivity of corresponding nanocomposite membranes. This indicates that proton migration in the vicinity of AMPS modified MMT is more facilitated compared to unmodified MMT and Cloisite 15A. In other words, more accessible routes for proton conduction might have been formed due to conceivable interactions between sulfonate groups ($-\text{SO}_3^-$) on Nafion chains and above discussed functional groups of adsorbed AMPS molecules onto clay layers. Methanol permeability of prepared membranes compared with corresponding nanocomposite membranes comprising MMT and Cloisite 15A. Methanol permeability of all kinds of nanocomposite membranes is considerably decreased with increasing clay content. Indeed, reduction in permeability has been arisen from formation of longer diffusive pathway against methanol molecules in the presence of impermeable inorganic filler. Clay modification has resulted in a significant decrease of permeability in comparison with unmodified clay. Actually, more effectiveness of organically modified MMTs might be owing to formation of stronger interfacial interactions and obstruction of wiggling routes of methanol molecules around clay nano-layers, and Lower permeability of Nafion/Cloisite 15A at higher contents of Cloisite 15A (>3 wt. %) could be interpreted with the more hydrophobic nature of Cloisite 15A. To determine the optimum composition of AMPS-MMT, membrane selectivity parameter of Nafion/AMPS-MMT membranes at different AMPS-MMT loadings was



calculated. It was found that the maximum selectivity value of about 8.9×10^5 S.sec.cm⁻³ is achieved at 3.0 wt. % AMPS-MMT, which is remarkably higher than that of 4.0×10^4 S.sec.cm⁻³ for Nafion-117. In fact, such a remarkably improved selectivity parameter of Nafion matrices is owing to the effective role of AMPS-modified nanolayers in restricting methanol permeation while maintaining essential proton conduction properties [36].

5- Conclusion

Nafion-based nanocomposite membranes are a very important inclusion in the family of proton exchange fuel cell membranes. By changing the nature of the nanofillers and the processing conditions, some of the physical properties of pure Nafion such as permeability, proton conductivity, etc. have been improved significantly, which was not possible by simple mixing with conventional fillers. On the other hand, Modification of nanofillers also can have significant effect on proton conductivity and methanol permeability. Although a significant amount of work has already been done on various aspects of Nafion-based nanocomposite membranes, much research still remains in order to understand the complex structure-property relationships in various nanocomposite membranes.

6- References

- [1] Mohd Norddin M.N.A., Ismail A.F., Rana D., Matsuura T., Tabe S., The effect of blending sulfonated poly(ether ether ketone) with various charged surface modifying macromolecules on proton exchange membrane performance, *J. Membr. Sci.* 2009, 328, 148-155.
- [2] Munakata H., Yamamoto D., Kanamura K., Three-dimensionally ordered macroporous polyimide composite membrane with controlled pore size for direct methanol fuel cells, *J. Power Sources*, 2008, 178, 596-602.
- [3] Yildirim M.H., Stamatialis D., Wessling M., Dimensionally stable nafion polyethylene composite membranes for direct methanol fuel cell applications, *J. Membr. Sci.*, 2008, 321, 364-372.
- [4] Lufrano F., Baglio V., Staiti P., Arico A.S., Antonucci V., Polymer electrolytes based on sulfonated polysulfone for direct methanol fuel cells, *J. Power Sources*, 2008, 179, 34-41.
- [5] Zhang X., Tay S.W., Hong L., Liu Z., In situ implantation of poly(oxo) blocks in nafion matrix to promote its performance in direct methanol fuel cell, *J. Membr. Sci.*, 2008, 320, 310-318.
- [6] Peoples B.C., In-situ production of polyolefin-clay nanocomposites, Ph.D. dissertation, University of California, 2008.
- [7] Hasani-Sadrabadi M.M., Emami S.H., Moaddel H., Preparation and characterization of nanocomposite membranes made of poly(2,6-dimethyl-1,4-phenylene oxide) and montmorillonite for direct methanol fuel cells, *J. Power Sources*, 2008, 183, 551-556.
- [8] Fu T., Cui Z., Zhong S., Shi Y., Zhao C., Zhang G., Shao K., Na H., Xing W., Sulfonated poly(ether ether ketone)/clay-SO₃H hybrid proton exchange membranes for direct methanol fuel cells, *J. Power Sources* 185 (2008) 32-39.
- [9] Peighambari, S.J., S. Rowshanzamir, and M. Amjadi, Review of the proton exchange membranes for fuel cell applications. *International Journal of Hydrogen Energy*, 2010. 35(17): p. 9349-9384.
- [10] Kim T.K., Kang M., Choi Y.S., Kim H.K., Lee W., Chang H., Seung D., Preparation of Nafion-sulfonated clay nanocomposite membrane for direct methanol fuel cells via a film coating process, *J. Power Sources* 165 (2007) 1-8.
- [11] Gaowen Z., Zhentou Z., Organic/inorganic composite membranes for application in DMFC, *J. Membr. Sci.* 261 (2005) 107-133.
- [12] Lee, S.K., et al., Measuring the relative efficiency of hydrogen energy technologies for implementing the hydrogen economy: An integrated fuzzy AHP/DEA approach. *International Journal of Hydrogen Energy*, 2011. 36(20): p. 12655-12663.
- [13] Kakati, B.K. and V. Mohan, Development of Low-Cost Advanced Composite Bipolar Plate for Proton Exchange Membrane Fuel Cell. *Fuel Cells*, 2008. 8(1): p. 45-51.



- [14] Kakati, B.K. and D. Deka, Differences in physico-mechanical behaviors of resol(e) and novolac type phenolic resin based composite bipolar plate for proton exchange membrane (PEM) fuel cell. *Electrochimica Acta*, 2007. 52(25): p. 7330-7336.
- [14] Aricò, A.S., V. Baglio, and V. Antonucci, Direct Methanol Fuel Cells: History, Status and Perspectives, in *Electrocatalysis of Direct Methanol Fuel Cells 2009*, Wiley-VCH Verlag GmbH & Co. KGaA. p. 1-78.
- [16] Valdez, T.I., et al. Direct methanol fuel cell for portable applications. in *Battery Conference on Applications and Advances, 1997.*, Twelfth Annual. 1997.
- [17] Aricò, A.S., S. Srinivasan, and V. Antonucci, DMFCs: From Fundamental Aspects to Technology Development. *Fuel Cells*, 2001. 1(2): p. 133-161.
- [18] Lamy, C., J.-M. Léger, and S. Srinivasan, Direct Methanol Fuel Cells: From a Twentieth Century Electrochemist's Dream to a Twenty-first Century Emerging Technology, in *Modern Aspects of Electrochemistry*, J.O.M. Bockris, B.E. Conway, and R. White, Editors. 2002, Springer US. p. 53-118.
- [19] Hacquard, A., R. Datta, and D. DiBiasio, Improving and Understanding Direct Methanol Fuel Cell (DMFC) Performance. MS thesis, 2005.
- [20] Lu, G.Q. and C.Y. Wang, Electrochemical and flow characterization of a direct methanol fuel cell. *Journal of Power Sources*, 2004. 134(1): p. 33-40.
- [21] Costamagna, P. and S. Srinivasan, Quantum jumps in the PEMFC science and technology from the 1960s to the year 2000: Part I. Fundamental scientific aspects. *Journal of Power Sources*, 2001. 102(1-2): p. 242-252.
- [22] Gottesfeld, S., et al., Polymer electrolyte direct methanol fuel cells: an option for transportation applications 1996. Medium: ED; Size: 5 p.
- [23] Kerres, J. and W. Cui, Acid-base polymer blends and their application in membrane processes. United States Patent 6300381, 2001.
- [24] Piela, P., et al., Ruthenium Crossover in Direct Methanol Fuel Cell with Pt-Ru Black Anode. *Journal of The Electrochemical Society*, 2004. 151(12): p. A2053-A2059.
- [25] Choi, P., N.H. Jalani, and R. Datta, Thermodynamics and Proton Transport in Nafion: III. Proton Transport in Nafion/Sulfated Zr O₂ Nanocomposite Membranes. *Journal of The Electrochemical Society*, 2005. 152(8): p. A1548-A1554.
- [26] Hensley, J.E. and J.D. Way, The relationship between proton conductivity and water permeability in composite carboxylate/sulfonate perfluorinated ionomer membranes. *Journal of Power Sources*, 2007. 172(1): p. 57-66.
- [27] Kim, J.W., et al., Intercalated polypyrrole/Na⁺-montmorillonite nanocomposite via an inverted emulsion pathway method. *Polymer*, 2003. 44(1): p. 289-293.
- [28] Kim, J.W., et al., *Polymer*, 2003. 44(null): p. 289.
- [29] Jung, D.H., et al., Preparation and performance of a Nafion/montmorillonite nanocomposite membrane for direct methanol fuel cell. *Journal of Power Sources*, 2003. 118 (1-2): p. 205-211.
- [30] Rhee, C.H., et al., Nafion/Sulfonated Montmorillonite Composite: A New Concept Electrolyte Membrane for Direct Methanol Fuel Cells. *Chemistry of Materials*, 2005. 17(7): p. 1691-1697.
- [31] Silva, R.F., S. Passerini, and A. Pozio, Solution-cast Nafion/montmorillonite composite membrane with low methanol permeability. *Electrochimica Acta*, 2005. 50(13): p. 2639-2645.
- [32] Kim, Y., et al., Montmorillonite functionalized with perfluorinated sulfonic acid for proton-conducting organic-inorganic composite membranes. *Journal of Power Sources*, 2006. 162(1): p. 180-185.
- [33] Lin, Y.-F., et al., A novel composite membranes based on sulfonated montmorillonite modified Nafion for DMFCs. *Journal of Power Sources*, 2007. 168(1): p. 162-166.
- [34] Kim, T.K., et al., Preparation of Nafion-sulfonated clay nanocomposite membrane for direct methanol fuel cells via a film coating process. *Journal of Power Sources*, 2007. 165(1): p. 1-8.
- [35] Hasani-Sadrabadi, M.M., et al., Nafion/bio-functionalized montmorillonite nanohybrids as novel polyelectrolyte membranes for direct methanol fuel cells. *Journal of Power Sources*, 2009. 190(2): p. 318-321.
- [36] Hasani-Sadrabadi, M.M., et al., Novel nanocomposite proton exchange membranes based on Nafion and AMPS-modified montmorillonite for fuel cell applications. *Journal of Membrane Science*, 2010. 365(1-2): p. 286-293.



Electrocatalytic activity of graphene- carbon nanotube supported Pt₃Co as an electrocatalyst for oxygen reduction reaction in PEM fuel cell gas diffusion electrodes

Monireh Faraji, Hussein Gharibi

Department of Chemistry, Faculty of Science, Tarbiat Modares University
Monireh.faraji@gmail.com

Abstract

Graphene-supported Pt and Pt₃M (M = Co) alloy nanoparticles are prepared by ethylene glycol reduction method and characterized with X-ray diffraction and transmission electron microscopy. X-ray diffraction depicted the face-centered cubic structure of Pt in the prepared materials. Electron microscopic images show the high dispersion of metallic nanoparticles on graphene/nanotube sheets. The high catalytic performance of Pt₃M alloys is ascribed to the inhibition of formation of (hydr) oxy species on Pt surface by the alloying elements.

Keywords: H₂, Fuel cell, Pt alloy

1 Introduction

Graphene has received tremendous scientific and technological interest with potential applications in various fields, such as electronic devices, energy storage and conversion devices, solar cells, bioscience and biotechnologies. The unique properties, such as good electronic conductivity, surface area, mechanical and/or thermal stability and durability, makes it as a promising electrode/electrode support material for fuel cell applications [1–5]. In comparison with carbon nanotubes (CNTs), graphene not only possesses similar physical properties but also larger surface areas. Additionally, production cost of graphene sheets in large quantities is much lower than that of CNTs [4,6]. Several studies have been carried out to produce graphene nanosheets in bulk quantity by chemical vapor deposition and wet chemical reduction of graphite oxide (GOx) [7–9]. Since abundant functional groups on the surfaces of GOx can be used as anchoring sites for metal nanoparticles [10,11], it is possible to use them as a support to produce graphene-nanoparticle hybrids. Combination of graphene and functional nanoparticles may lead to materials with interesting properties for a variety of applications, and they are specifically expected to have enhanced electrocatalytic activity. Carbon black-supported Pt is widely used as an oxygen reduction electrocatalyst for energy conversion device applications. But the vulnerability toward oxidation of carbon black support hinders its use for electrode applications [12]. It is consequently of increasing interest to develop new support materials that avoid the drawbacks linked to carbon black supports [1,5,13,14]. Recently, graphene has been used as a support for Pt to investigate the electrocatalytic activity and durability towards oxygen reduction reaction (ORR). The results indicate the enhanced electrocatalytic activity and durability of graphene-supported metal electrodes compared with CNT and amorphous carbon supported electrodes [15,16]. This is attributed to the intrinsic graphitization degree of graphene and the enhanced metal-support interaction. Even though the results are encouraging, the overpotential on the Pt/graphene was ca. 300 mV. It has been known that various bimetallic Pt alloys were more catalytically active than Pt for ORR [17–22]. Among the Pt alloys, Pt–Co appear to be the promising ORR catalysts [17–19,21]. Therefore, the Pt alloy nanoparticle-graphene hybrids may enhance the ORR activity and exhibit low overpotential for ORR. In this study, graphene is employed for the first time as a support for bimetallic Pt₃M (M = Co) alloy nanoparticles and their electrocatalytic ORR performance is



investigated.

2 Experimental

2.1. Preparation of graphite oxide (GOx)

GOx was synthesized from graphite powder by Hummers method [23]. The composition (wt.%) is determined to be C:53.4, O: 41.1, H: 3.8 and N: <0.5

2.2. Preparation of graphene-supported Pt₃M alloy catalysts

graphene Pt₃M (M = Co and Cr) alloy nanoparticles are synthesized by ethylene glycol reduction (EG) method following ref's [11] and [24]. In a typical synthesis, stoichiometric amounts of metal precursors (H₂PtCl₆ as Pt precursor, and CoCl₂ as Co precursor, respectively) dispersed in 40ml ethylene glycol solution and 160 mg GOx dispersed in 40ml ethylene glycol solution are mixed together and taken in a 125ml round-bottom flask equipped with a N₂ in/outlet. The resulting suspension is refluxed at 403 K for 3 h. Then it is filtered, washed copiously with acetone and dried at 333 K in a vacuum oven. Finally, the catalysts were heat treated at 573 K under Ar-H₂ (9:1 v/v) gas atmosphere for 2 h. For comparison, graphene-supported Pt is also prepared. The nominal metal content on the graphene is 40 wt.%. Also, GOx is treated in the similar manner to check the complete reduction.

2.3. Characterization techniques

X-ray diffraction (XRD) measurements are performed on a Siemens D5000 X-ray diffractometer using a Cu K α source operated at 30 keV at a scan rate of 0.02° s⁻¹. Raman spectra are obtained using a Jobin-Yvon T64000 spectrometer equipped with a triple-grating monochromator and a Coherent Innova90C Ar-laser at 514.5 nm. The spectra are acquired in a single scan with an acquisition time of 180 s. Transmission electron microscopic (TEM) images are recorded using a JEOL2100 system operated with accelerating voltage 200 kV. Electron microscope equipped with EDX is used to observe composition of the catalysts.

An EG&G Princeton Applied Research Model 273A instrument were used to determine the electrochemical properties of the electrodes. The performances of the GDEs (geometric exposed area 1 cm²) in the reduction of oxygen were investigated in 0.5M H₂SO₄. All measurements were performed at 25 °C in a conventional three-electrode cell, with O₂ flowing at 50 mL min⁻¹. The GDEs were mounted into a Teflon holder that contains a pyrolytic graphite disk as a current collector and has provision for feeding oxygen from the back of the electrode. A glassy carbon electrode immersed in 0.5 M H₂SO₄ was used to perform cyclic voltammetry.

3. Results and discussion

3.1. XRD, Raman and TEM analyses

Fig. 1 shows the XRD patterns recorded for graphite, GOx and reduced GOx, respectively. Graphite exhibited a characteristic (0 0 2) diffraction peak at 26.7°, corresponding to the interspacing between the graphene layers as 3.34 Å. Upon oxidation/exfoliation of graphite with strong acids, the ordering of the graphene layers in graphite was disrupted and a smaller broader peak at 10.75° appeared for GOx (Fig. 1). It indicates the complete oxidation of graphite. The interlayer spacing between the layers is increased from 3.34 to 8.26 Å.

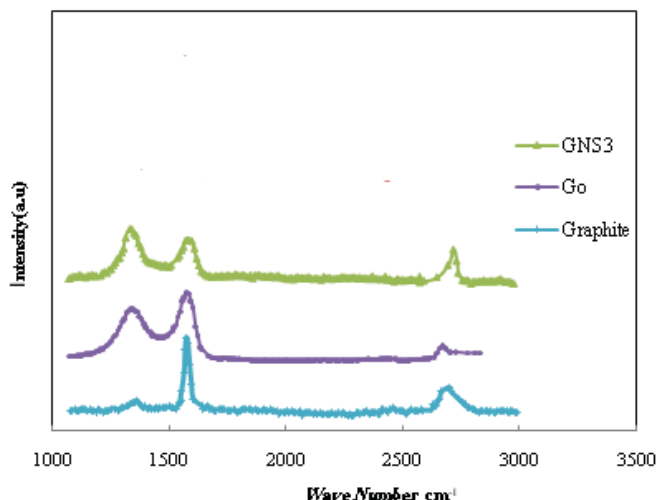


Fig1.XRD patterns Graphite,Go,Graphene nanosheets(GNS)

Fig. 2 shows the Raman spectra recorded for graphite, GOx and reduced GOx, respectively. All the three samples exhibited the characteristic D, G, and 2D peaks at around 1350, 1580 and 2700 cm^{-1} respectively. The appearance of intense G peak in all the three samples indicates the graphitization of the samples. The more intense D peak observed for GOx and graphene samples compared to that of graphite is due to the creation of defect sites by chemical treatment. 2D band, which is a characteristic of graphene usually used to determine the number of layers of graphene in the sample. Broad and less intense 2D band observed for the reduced GOx (Fig. 2) clearly indicates that it has few layers of graphene [5].

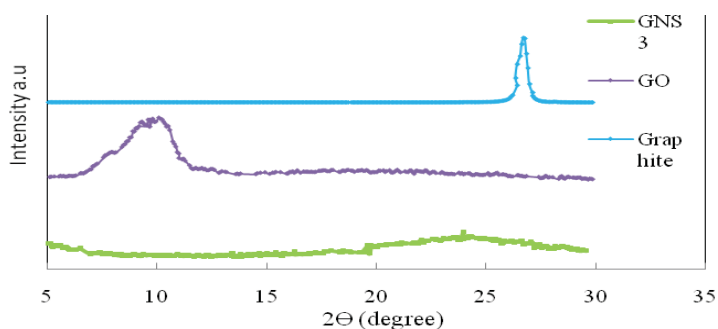


Fig2.Raman spectra of Graphite,Go and Graphene nanosheets

Powder XRD patterns of the chemically reduced GOx and graphene-supported Pt and Pt₃M alloy catalysts recorded in the 2θ range of 10°–90° are shown in Fig. 3. The narrow diffraction peak observed around 2θ = 26° is due to the hexagonal structure of graphene [5]. All the

graphene-supported Pt and Pt₃M alloy catalysts exhibited five characteristic diffraction peaks at 2θ values around 40°, 47°, 68°, 82° and 87° corresponding to the (1 1 1), (2 0 0), (2 2 0), (3 1 1) and (2 2 2) planes of face-centered cubic (fcc) structure of Pt. In the case of Pt₃M/graphene catalysts, diffraction peaks are shifted to higher 2θ values with respect to the corresponding peaks in the Pt/graphene catalysts. It indicates the contraction of lattice by the incorporation of base metal (Co) in the fcc structure of Pt due to alloy formation. The compressed Pt–Pt bond length has been shown to lower the valence band center relative to the Fermi level, reduce the binding strength and/or coverage of oxygenated adsorbates, and enhance ORR activity. The average crystallite size was calculated from Scherrer's equation for the XRD peak assigned to Pt(2 2 0). It is determined to be 3.5, 4.2, and 4.3 nm for the graphene-supported Pt, Pt–Co catalysts, respectively

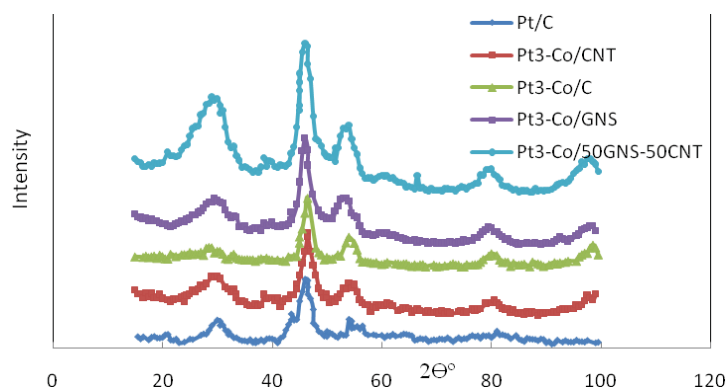


Fig3 Powder XRD patterns of graphene-supported Pt, and Pt₃Co samples

Cyclic voltammograms of graphene-supported Pt, Pt₃Co alloy catalysts in deaerated 0.5 M H₂SO₄ are shown in Fig. 4. Well-defined hydrogen desorption/adsorption peaks in the potential range of \approx 0.05 and +0.3 V vs Ag/AgCl and irreversible pre-oxidation/reduction peaks in the potential range of +0.2 and + 1.2 V vs Ag/AgCl are observed. The electrochemically active surface area (EAS) was determined by assuming a monolayer of adsorbed hydrogen requires 210 μ C/cm² for its oxidation. EAS evaluated from hydrogen adsorption/desorption peaks is calculated to be 65, 57, and 55 m²/g for graphene-supported Pt, Pt₃Co, catalysts, respectively. A comparison of the voltammetry also shows the difference in the onset of oxide formation on Pt (generally accepted as OH_{ads} species formed from oxidation of water on platinum surfaces at around +0.8 V vs Ag/AgCl). The extent of oxide formation on the catalysts is in the order; Pt₃Co < Pt. This is due to the increased donor ability and electropositive nature of alloying elements Co. This may have a beneficial effect on the oxygen adsorption at low overpotential, and thus may lead to an enhancement of the ORR kinetics

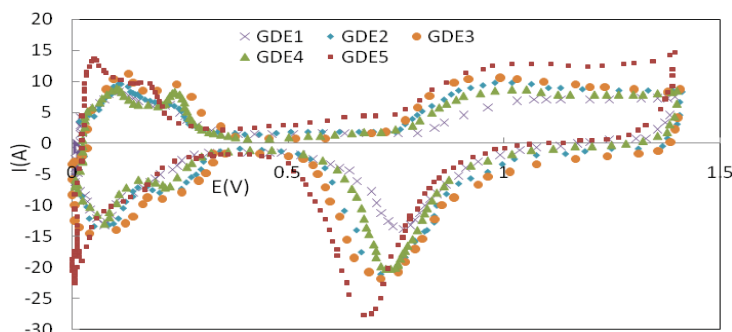


Fig. 4 – A - Cyclic voltammograms (CVs) of graphene-supported Pt, (b) Pt₃Co alloy electrodes in Ar- saturated 0.5 M H₂SO₄; Scan rate – 50mV/s.

4 Conclusions

Two-dimensional layered graphene-supported Pt and Pt₃M alloy nanoparticles were prepared by ethylene glycol reduction method and characterized by XRD and TEM. Pt₃M alloys exhibited 3–4 times higher ORR activity and 45–70mV lower overpotential than that of Pt. The enhanced ORR activity was due to the inhibition of formation of (hydr) oxy species on Pt surface by the presence of alloying elements. The nearly identical Tafel slopes observed for the graphene-supported Pt and Pt₃M alloy electrodes indicate that the mechanism of ORR is similar for these electrodes. The stability of the electrodes was found to be good for 500 cycles. Graphene-supported Pt₃M alloy cathodes exhibit better performance than Pt under fuel cell

References

- [1] Geim AK, Novoselov KS. The rise of graphene. *Nat Mater* 2007;6:183–91.
- [2] Zhu J. New solutions to a new problem. *Nat Nanotechnol* 2008;3:528–9.
- [3] Seger B, Kamat PV. Electrocatalytically active graphene-platinumnanocomposites. Role of 2-D carbon support in PEfuel cells. *J Phys Chem Lett* 2009;113:7990–5.
- [4] Stankovich S, Dikin DA, Dommett GHB, Kohlhaas KM, Zimne EJ, Stach EA, et al. Ruoff RS Graphene-based composite materials. *Nature* 2006;442:282–6.
- [5] Gao W, Alemany LB, Ci L, Ajayan PM. New insights into the structure and reduction of graphite oxide. *Nat Chem*



Study of adsorption of oxygen molecule on the structures of Pt_n/Graphene as an electrode in the PEM Fuel Cell

Rasol Abdullah Mirzaei^{*1}, Javad Beheshtian¹, Aref Gholami¹

1- Fuel cell Research Laboratory, Dep. Of chemistry, Faculty of science, Shahid Rajaei Teacher Training University, Tehran, IRAN
Corresponding Author E-mail: ra.mirzaei@srttu.edu

Abstract

Fuel cell systems have main role in production of clean energy in present century. Many aspects of these systems are investigated by researchers. One of them is using theoretical calculation for better understanding of performance of these systems. Oxygen is common oxidant in low temperature fuel cells. One of the mechanism steps of oxygen reduction reaction in PEM fuel cell is adsorption of oxygen molecule. In this paper, for modeling chemical adsorption of molecular oxygen on the cathode electrode of the fuel cell is used density functional theory and G09 programs. for investigate absorbed reaction of oxygen fuel cell polymer, first, it is considered some structure of GPt_n for cathode electrode and optimized this structures. Basis set for Graphene is 6-31G** and basis set for Pt is Lanl2dz. Then, O₂ molecule is bended to GPt_n and they are optimized with basis set of 6-31G** for C, H, O and Lanl2dz for Pt. Calculated energy of this structure is compared and adsorption energy of a O₂ molecule is obtained. Structure deformation and bending energy is calculated and they are compared and it selected the best state of GPt_n for O₂ molecule adsorption. Charge transfer from platinum to oxygen and conductivity structures is studied and the ultimate structure of the adsorption of molecular oxygen is introduced.

Keywords: Density functional theory, Adsorption energy, PEM fuel cell.

1. Introduction

A fuel cell converts energy produced in a chemical reaction into electricity with better efficiency than other methods. An important goal for basic research and for the development of practical portable electric power sources in the form of hydrocarbon-fed electrochemical fuel cells is the understanding of the factors governing the electrode processes. The biggest problem in the fuel cell industry is the cathodic process of oxygen reduction because of its very slow kinetics leading to a high overpotential and high current flows only at potentials with lower technological interest [1]. For acid-electrolyte fuel cells, the best electrocatalysts for the oxygen reduction reaction (ORR) are platinum and its alloys [2]. This improvement has been attributed to different structural changes caused by Graphene [3-7].

In x-y-z or 3-d space, the bonding between carbon atoms is sigma (σ). In other words, such electrons direct their charges along the bonds within the Graphene sheet, itself—whereas the remaining available electron—one for each atom—lies in the z- or third dimension, above and below the Graphene sheet. Such electrons are called pi (π) electrons, and are highly mobile.

¹. Fuel cell Research Laboratory, Dep. Of chemistry, Faculty of science, Shahid Rajaei Teacher Training University, Tehran, IRAN

Mobile electrons, put into motion, are electricity. In fact, Graphene electron orbitals overlap and unite to form a “conduction band.” This effect is heightened for Graphene by special principles of physics [8]. Platinum is also an important catalyst in the electrochemical reactions. High conductivity, high absorbency and ... of Graphene and catalytic properties in platinum, They give special properties together [3].

Platinum metal strongly catalyzes the decomposition of hydrogen peroxide into water and oxygen gas [8]. However, due to the low reactivity and high price, not the catalyst suitable for absorption of oxygen. So to improve, the different materials is used such as cobalt, gold, Graphene. Much laboratory work has been done in this case but of these two, to absorbent molecular oxygen in polymer fuel cell is not used in computational studies. For this reason, in this paper, we will investigate the structures of GPt_n oxygenated and their properties.

2. Computational Methods

For modeling chemical adsorption of molecular oxygen on the cathode electrode of the fuel cell is used density functional theory and Gaussian 09 program. For carbon and hydrogen and oxygen basis set, 6-31G**, and platinum basis set, Lanl2dz are used in GPt_nO_2 structures [9]. First, Graphene structure and platinum clusters were optimized [table 1]. Then, these structures were connected and were optimized. The reaction of platinum binding to Graphene is:



Second, oxygen molecule were connected to GPt_n structures. The reaction to this step was considered is:



Oxygenated structures differ in energy and structure. So, energy structures, charge distribution, HOMO and LUMO's is compared. Structures that were optimized for this step, are shown in table 2.

3. Results of the calculations

After optimization of the structures in G09, structures energy were compared. This comparison is based on the absorption of energy, binding energy and deformation energy was performed. To obtain these energies, the following formulas were used.

$$E_{(ads)} = E (GPt_nO_2) - E (GPt_n) - E (O_2) \quad (3)$$

$$E_{(bin)} = E (GPt_nO_2) - E (GPt_n)^* - E (O_2)^* \quad (4)$$

$$E_{(deformation)} = E^* - E \quad (5)$$

E^* is structure energy that structural modified forms. Energies where the adsorption, binding, and deformation are shown in figure 1. The highest of binding and adsorption energy is in GPt_9O_2 structure. In these structures, electron transfer from platinum to oxygen occurs, But are different. To investigate these differences, the amount of charge transferred from Pt to oxygen was calculated [Fig. 2]. Thus, in the most of structures, charge transfer is approximately the same, except $GPtO_2$. Conductivity of these structures to the energy difference between HOMO and LUMO orbitals depends. in Figure 3, this energy difference

(Gap) is shown. If the gap is small, the conductivity is more and GPtO₂ has one of the lowest gap.

But these structures should be compared to the Graphene and pure platinum is marked difference between them [fig. 4]. In this form is known that Hussein is better than platinum and pure Graphene.

Table 1. Structures were optimized

Pt	Pt ₂	Pt ₃
Pt ₄	Pt ₅	Pt ₈
Pt ₉	Graphene	GPt
GPt ₂	GPt ₃	GPt ₄
GPt ₅	GPt ₈	GPt ₉

Table 2. Oxygenated structure

PtO ₂	Pt ₂ O ₂	Pt ₃ O ₂
Pt ₄ O ₂	Pt ₅ O ₂	Pt ₈ O ₂
Pt ₉ O ₂	Graphene	GPtO ₂
GPt ₂ O ₂	GPt ₃ O ₂	GPt ₄ O ₂
GPt ₅ O ₂	GPt ₈ O ₂	GPt ₉ O ₂

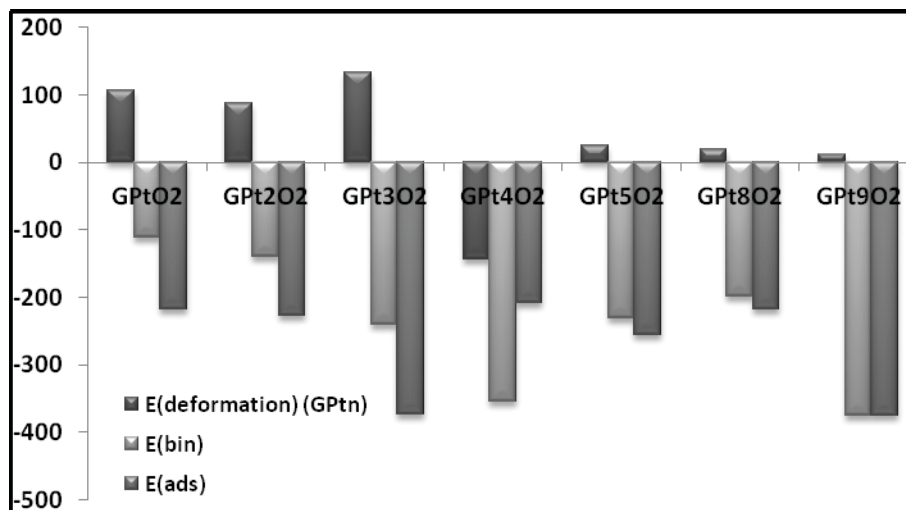


Fig. 1. Graph energy variation in different structures.

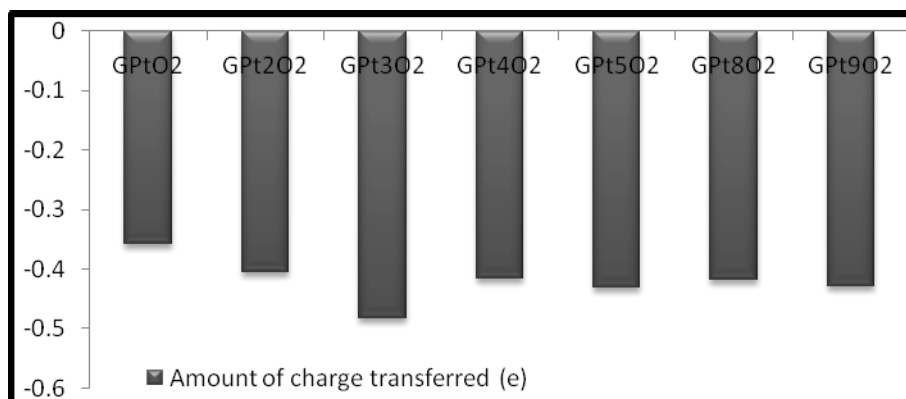


Fig. 2. Graph of charge transferred amount from Pt to oxygen.

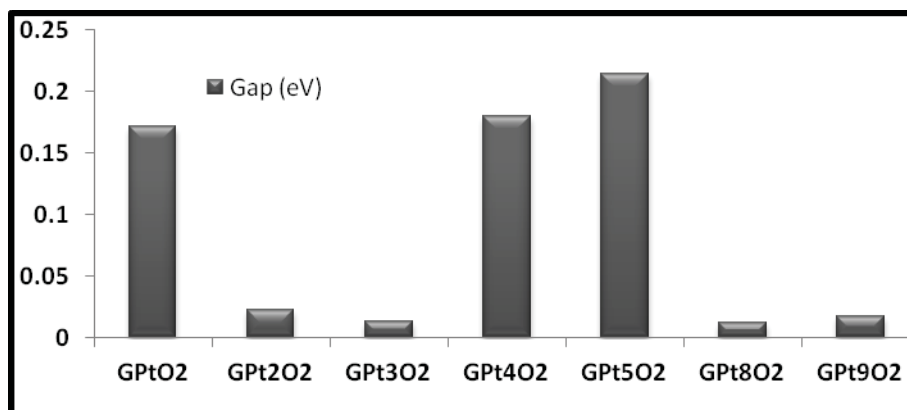


Fig.3. Graph of Gap energy

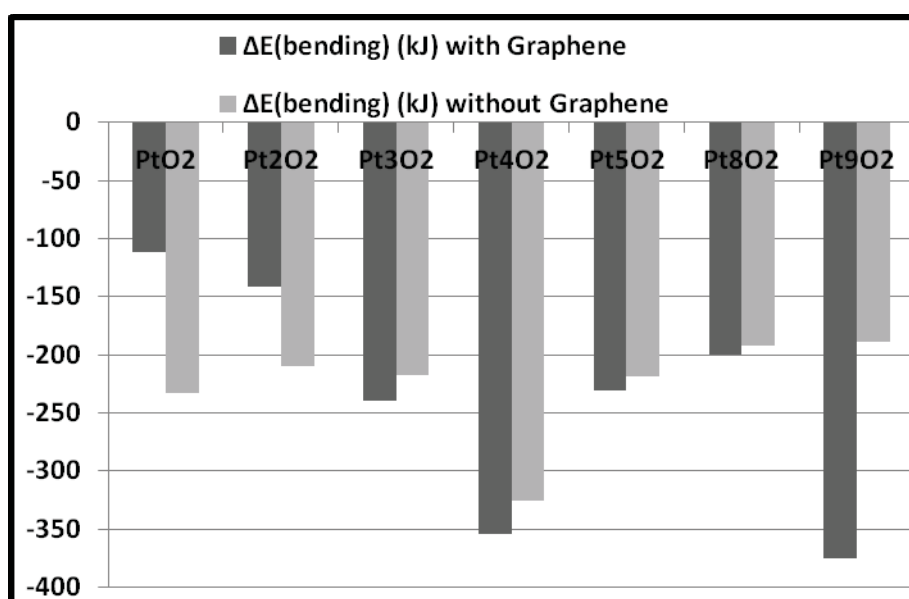


Fig. 4. Comparisons between the structures of oxygenated.

4. Conclusions

Method of modeling the chemical adsorption of molecular oxygen on the cathode electrode fuel cell in this paper is density functional theory and the program used here is G09. Several structures were considered for the cathode electrode and to all structures were connected to the oxygen molecule. The basis set of carbon, hydrogen and oxygen was 6-31G** and basis set for Pt was Lan12dz in $G\text{Pt}_n\text{O}_2$ structure. Then, binding, deformation and absorption energies of these structures were compared with each other. In this step, structure of $G\text{Pt}_9\text{O}_2$ had the highest values

In the next step, the amount of charge transferred from Pt to oxygen was investigated. Again, this structure was one of the the highest values. The last step was to compare the energy of HOMO and LUMO. In this stage as well, $G\text{Pt}_9\text{O}_2$ structure had a little Gap. In other words, This structure was very high conductivity and it is very suitable for electron transfer In fuel cell. Therefore, $G\text{Pt}_9\text{O}_2$ structure and structures such as these, are suitable for modeling the oxygen reduction reaction. Because they have the largest binding energy, attract and deformation of its structure are minimal.

Due to the properties of Graphene for absorption of oxygen, absorption energy of $G\text{Pt}_9\text{O}_2$ is more than Graphene. In addition, absorption energy in this structure is higher than pure



platinum. Thus, the electrode comprises platinum and Graphene, absorption of oxygen is better and between platinum clusters on Graphene, GPt_0 is the best state. Because it is closer to the crystal unit cell.

References

- [1] J.O'M. Bockris, S.U.M. Khan, Surface Electrochemistry, Plenum Press, New York, 1993, p. 319.
- [2] A.B. Anderson, Y. Cai, R.A. Sidik, D.B. Kang, J. Electroanal. Chem. 580 (2005) 17.
- [3] K. Okazaki-Maeda, Structures of Pt clusters on graphene by first-principles calculations, Surface Science, Volume 604, Issue 2, 15 January 2010, Pages 144–154.
- [4] Jianbo Deng, Density functional calculation of transition metal adatom adsorption on graphene, institute of Theoretical Physics, Lanzhou University, Physica B: Condensed Matter, Volume 405, Issue 16, 15 August 2010, Pages 3337–3341.
- [5] Yasuharu Okamoto, Density-functional calculations of graphene interfaces with Pt(1 1 1) and Pt(1 1 1)/Ru_{ML} surfaces, 2005, Chemical Physics Letters, Volume 407, Issues 4–6, 27 May 2005, Pages 354–357.
- [6] Justin Nicolosi, Graphene Production and Future Use: An Investigation Into the Materials Application as a Hydrogen Gas Sensor, Spring 2011.
- [7] Ying Chen, Xiao-chun Yang, Yue-jie Liu, Jing-xiang Zhao, Qing-hai Cai, Xuan-zhang Wang, Can Si-doped graphene activate or dissociate O₂ molecule? Journal of Molecular Graphics and Modelling, Volume 39, February 2013, Pages 126-132,
- [8] A. Geim & K. Novoselov "The rise of graphene" Nature Materials v.6, 183 (2007).
- [9] Feltham, A. M.; Spiro, Michael (1971). "Platinized platinum electrodes". Chemical Reviews 71 (2): 177. doi:10.1021/cr60270a002.



Parametric study and optimization of the cathode catalyst layer in PEM fuel cells

E. Kooshki^a, S. Rowshanzamir^{a,b,*}

^a Fuel Cell Laboratory, Green Research Center, Iran University of Science and Technology, Narmak, Tehran, Iran

^b School of Chemical Engineering, Iran University of Science and Technology, Narmak, Tehran 16846-13114, Iran

Abstract

Extensive research and development efforts are being under taken in recent year in the field of PEM fuel cell (PEMFC) systems to make them commercially viable. The platinum loading is typically about 0.05-0.2 mg.cm⁻² on the anode side and 0.2-0.6 mg.cm⁻² on the cathode side. More platinum is used on the cathode side because of the sluggish oxygen reduction reaction. As many limiting processes take place in the reaction layer, it is important to model this layer. Given the importance and details of this layer, instead of simulation software such as COMSOL, MATLAB was used to solve and simulate the model. A two-dimensional steady state model for a PEM fuel cell cathode is described in this work. All the components in the cathode such as the gas manifold, diffusion layer, micro-porous layer and the catalyst layer are modeled. Concentrations of gaseous components, liquid water saturation in the cathode catalyst layer and ionomer local potential calculated to solve the equations in MATLAB. After comparing the results of the model and experimental data, the design parameters include platinum loading, catalyst layer thickness and ionomer weight fraction was chosen to achieve maximum current density. The optimal values were calculated in both high and low operating voltage.

Keyword: PEM fuel cell, Cathode catalyst layer, Modeling, Optimization.

Introduction

Over the past two decades, proton exchange membrane fuel cells (PEMFCs) have received attention due to increases in energy price and concerns about environmental pollution. Low pollutants emission, high energy conversion efficiency, and low operating temperature are characteristics of the fuel cells that are making this technology attractive. PEMFCs are

* Corresponding author. Fuel Cell Laboratory, Green Research Center, Iran University of Science and Technology, Narmak, Tehran, Iran. Tel./fax: þ98 2177491242.E-mail address: rowshanzamir@iust.ac.ir (S. Rowshanzamir).



considered to be among the most promising candidates for transportation, portable and stationary applications. However, further cost reduction and performance improvement are required to make PEMFCs a commercial success.

The major cost component of a PEMFC is the platinum catalyst. More platinum is used on the cathode side because of the sluggish oxygen reduction reaction. To optimize the performance of the cell, it is necessary to have a better understanding of the various processes that take place inside the cell and also their influence on the cell performance. The performance of PEMFCs is significantly affected by cathode catalyst layer's (CL) performance. Quite often, it is expensive, time consuming, and difficult to study all these processes through experiments. Hence, a detailed mathematical model is needed to simulate various model parameters on the cell performance. The Study of parameters that influence on cell performance and ultimately find the optimal values for the best performance can be achieved by using a reliable model. In this field many models have been presented which have advantages and disadvantages. Most of the models developed earlier have considered the catalyst layer (CL) as very thin and ignored its effect on the performance of the cell.

A two-dimensional steady state model for a PEM fuel cell cathode is described in this work. All the components in the cathode such as the gas manifold, diffusion layer, micro-porous layer and the catalyst layer are modeled. The effect of the liquid water is taken into account in every layer of the cathode and the catalyst layer is characterized as spherical agglomerates. The model is validated using experimental data. The utility of the steady state model for the optimization of the cathode catalyst layer design parameters is also described. The thickness of the catalyst layer, the platinum loading and weight fraction of ionomer inside the catalyst layer has been chosen as design parameters and finally the optimal values for these parameters are obtained that this values maximize the cell current density at a given operating cell voltage.

Model development

The schematic of the PEMFC cathode studied here is shown in Fig. 1. A two-dimensional steady state model for a PEM fuel cell cathode is described in this work. All the components in the cathode such as the gas manifold consists of straight channels with uniform cross-section, diffusion layer, micro-porous layer and the catalyst layer are modeled. The effect of the liquid water is taken into account in every layer of the cathode.

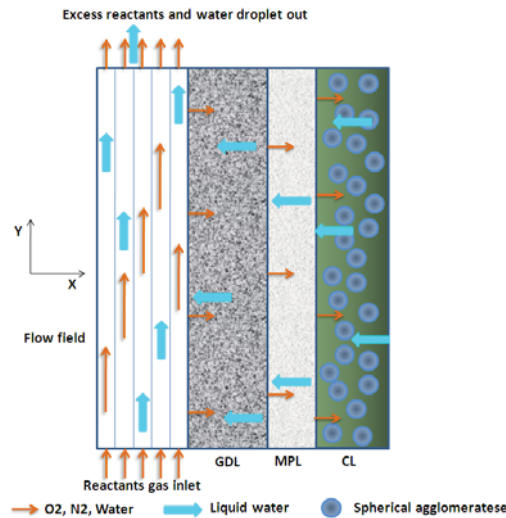


Figure.1: Schematic of PEMFC cathode.

Spherical agglomerate characterization assumes that the catalyst particles form agglomerates that are spherical in shape. Fig. 6 shows the schematic of a single spherical agglomerate in isolation. A thin film of ionomer is also assumed on top of the agglomerate. The following assumptions are considered for setting up the model equations:

- Isothermal conditions are considered through-out the region of interest.
- Pressure gradients in the X direction in all the regions are negligible. Hence, velocities in the X direction are zero.
- Effective diffusivities are assumed for diffusive transport in the gas phase inside the porous regions.
- Butler–Volmer kinetics are considered for the oxygen reduction reaction.
- Potential drop in the solid phase due to resistance to the electron transport is assumed to be negligible.
- The gas mixture inside the region of interest is assumed to behave as an ideal gas.

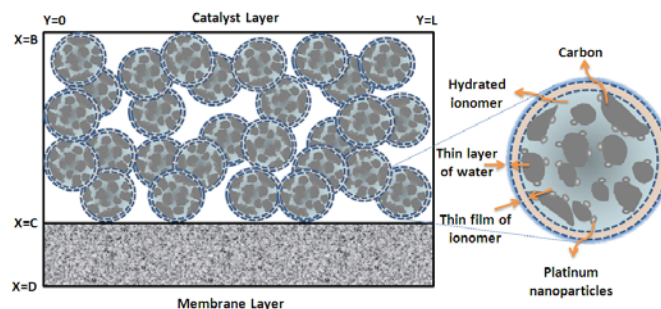


Figure.2: Schematic of a PEM fuel cell catalyst layer and spherical agglomerate.

Governing equations

Gas flow channel:

Gas flow and liquid water transport in the channels can be considered as a plug flow with simultaneous exchange of species at the boundary between the gas flow channels and the backup substrate. The species molar balance equation inside the gas flow channels can be written as:

$$-\frac{\partial}{\partial y} (C_{i,g} u_{inlet}) - \nabla \cdot J_i = 0 \quad (1)$$

$$J_i = -D_{i,eff} \nabla C_{i,d} |_{x=0} \quad (2)$$

For water vapor, an additional term accounting for evaporation/condensation appears in the above species balance equation.

$$-\frac{\partial}{\partial y} (C_{H_2O,g} u_{inlet}) - \nabla \cdot J_{H_2O} - R_W = 0 \quad (3)$$

Diffusion Layer:

Transport of species is governed purely by diffusion due to concentration gradients. Moreover, in order to simplify computations, diffusive transport is defined using Fick's law with an effective diffusivity.

$$-\nabla \cdot (-D_{eff} \nabla C_{i,d}) - R_W = 0 \quad (4)$$

The effective diffusivities of species in porous regions are related to the diffusivities in gaseous regions by Bruggeman equation:

$$D_{i,eff} = \epsilon_k^{1/2} (1 - \epsilon)^{3/2} D_{im} \quad (5)$$

The molar flux of liquid water can be written as:

$$N_W = -\frac{\rho_W K_W(s)}{M_W \mu_W} \left(-\frac{dP_c}{ds} \right) \nabla_s N_W = -\frac{\rho_W K_W(s)}{M_W \mu_W} \nabla (-P_c) \quad (6)$$

Writing a conservation equation for liquid water in the absence of any reaction in the diffusion layer leads to

$$-\nabla \cdot N_W + R_W = 0 \quad (7)$$

Microporous layer

For modeling purposes, the microporous layer is similar to the diffusion layer. The only difference is in the physical parameters such as, the void fraction, pore structure and thickness. Hence, based on the same assumptions considered for writing species conservation equations

for the diffusion layer, the conservation equations for species in gas phase and liquid water inside the microporous layer can be written as

$$-\nabla \cdot (-D_{i,eff} \nabla C_{i,m}) - R_W = 0 \quad (8)$$

$$-\nabla \cdot N_W + R_W = 0 \quad (9)$$

Catalyst layer

The conservation equations inside the catalyst layer for species i can be written by adding the oxygen reduction term.

$$-\nabla \cdot (-D_{i,eff} \nabla C_{i,c}) + R_{O_2} - R_W = 0 \quad (10)$$

$$R_{O_2} = -\frac{a_2 i_0}{n_e F} \frac{C_{O_2,mem}}{C^2_{O_2}} \exp\left(-\frac{\alpha n_e F}{RT_{cell}}\right) \quad (11)$$

From the stoichiometry of the overall reaction, amount of water produced in the cathode catalyst layer is twice the amount of oxygen consumed, hence

$$-\nabla \cdot N_W - 2R_{O_2} + R_W = 0 \quad (12)$$

Hydrogen ions produced at the anode catalyst layer travel through the membrane and reach the active catalyst sites in the cathode catalyst layer. Writing the charge conservation equation inside the catalyst layer leads to,

$$\epsilon^{3/2} K_{mem} \nabla^2 \phi_r + nFR_{O_2} = 0 \quad (13)$$

The cell current density is calculated by integrating the hydrogen ion flux at the cathode catalyst layer and membrane interface. It can be expressed as

$$i_{cell} = \frac{1}{w_{cell} L} \int_{y=0}^{y=L} \left\{ -\epsilon^{3/2} K_{mem} \frac{\partial \phi_r}{\partial x} \Big|_{x=C} \right\} w_{cell} dy \quad (14)$$

Model development

The equations with the specified boundary conditions are discretized using finite difference formulas and converted into a system of non-linear algebraic equations (NAEs). The list of NAEs solved with fsolve in Matlab software.

Optimization

According to the model and approach that has been chosen for the catalyst layer, various parameters of this section can be selected as decision variables. The analysis shows that the

amount of platinum loading, the weight fraction of ionomer and catalyst layer thickness is the best parameters that influence the performance of the cell.

In optimization problems a parametric study for decision variables was used, in this case at first the influence of variables checked in throughout the polarization curve. Different values of the parameters are chosen in case the other parameters are fixed, the output of each of the programs, is a polarization curve. In this manner the effects of relevant parameters are specified in all current densities. Next, to compare the effect of parameters in the upper and lower current density and also the fact that the optimal range for this parameter is whether there is or not, a high voltage and low voltage output of program prepared over the range of the parameter. The range of values for each parameter value, the maximum cathode current density is to be specified.

Results and discussion

The output program is current density and concentration of the gas component, liquid water saturation and the local ionomer potential in all areas too. To verify the results, the model outputs with the experimental results of Rao et al. [7] are compared in Figure 3.

To compare the oxygen concentration profiles in different voltage, these profiles investigated in three operating voltage. The results are shown in Figure 4.

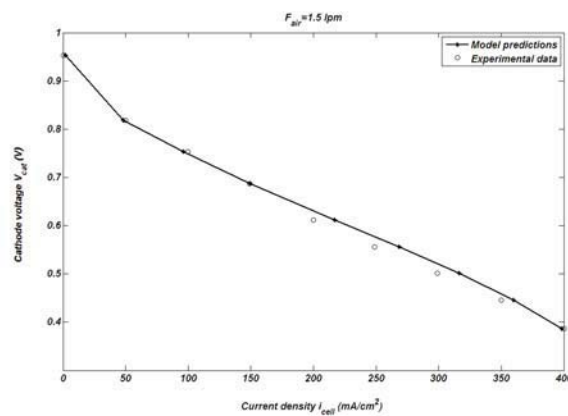


Figure.3: Model predictions vs. experiment. Fair = 1.5 lpm

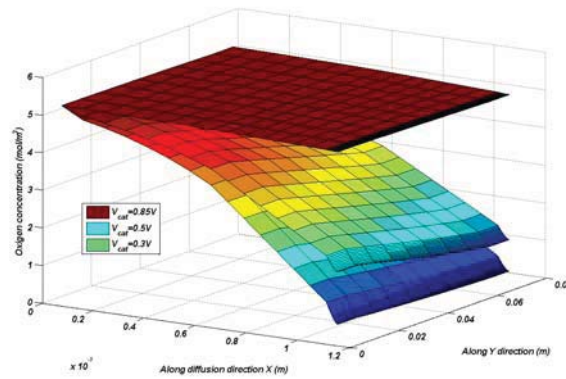


Figure.4: Spatial variation of oxygen concentration in all regions.

Ionomer local potential changes that is result of the proton concentration in the catalyst layer, in three different operating voltages is compared in Figure 5.

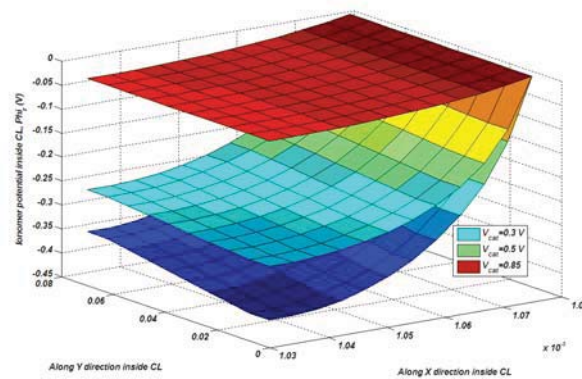


Figure.5: Spatial variation of ionomer potential inside catalyst layer.

Platinum loading

With the increase in platinum loading, the effective area of platinum per unit volume of the reaction layer increases and hence, the rate of oxygen reduction reaction increases. It also results in an increase of the solids (platinum and carbon) and membrane fractions and a decrease in the void fraction. As a result of this, the mass transfer resistance increases. As shown in figure 6, at high and low operating voltages, the current produced first increases and then decreases with an increase in the platinum loading.

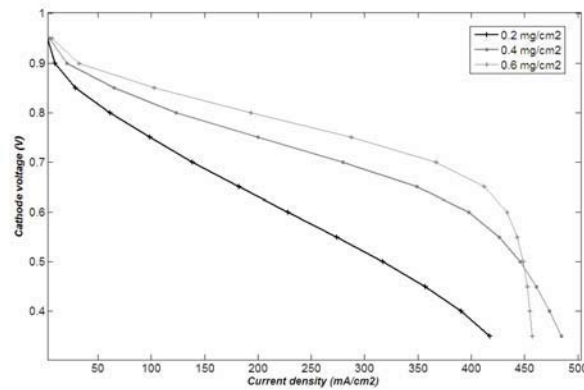


Figure.6: Performance curves at various platinum loadings

To find the optimum values of platinum loading, the current are calculated at more values of this at high and low voltages and the results shown in figure 7.

There is an optimal platinum loading for each operating voltage. For example, at voltage in 0.8 V optimal platinum loading is 0.9 mg/cm^2 .

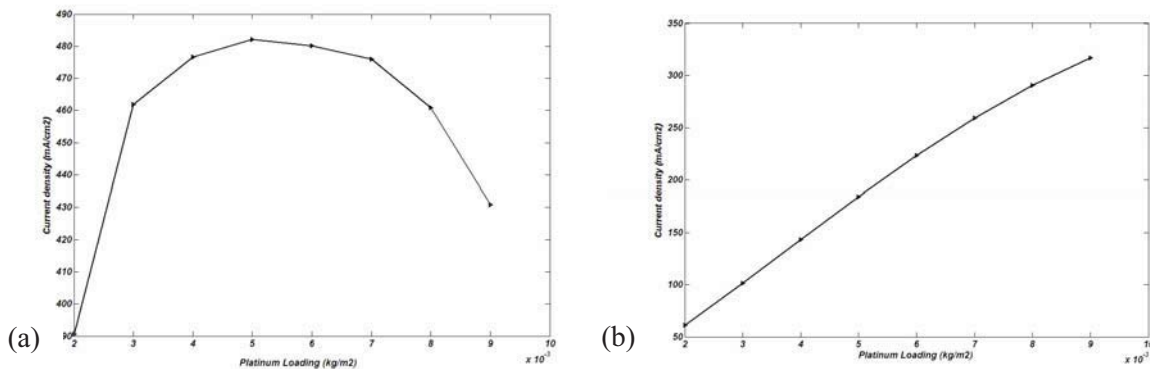


Figure.7: Current density at different values of platinum loading at low (a) and high (b) operating voltage.

Catalyst layer thickness

As the thickness is increased, the effective area of platinum per unit volume of the catalyst layer decreases. With the increase in the reaction layer thickness, the void fraction increases. Hence, mass transfer losses decrease. However, an increase in the thickness increases the diffusion path length. The effect of the reaction layer thickness on the overall performance at low and high voltage is shown in Figure 8a and 8b.

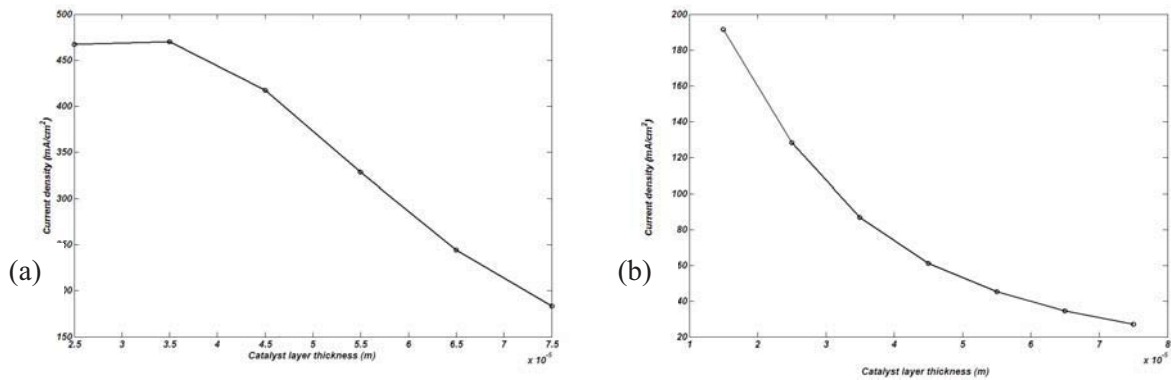


Figure.8: Current density at different values of Catalyst layer thickness at low (a) and high (b) operating voltage.

Fraction of ionomer

An increase in ionomer fraction results in lesser porosity and lesser ionic loss. As a result, mass transfer resistance increases. Since, mass transfer losses are higher at high current densities, increase of ionomer fraction results in larger concentration overpotential. The performance curves for various ionomer fractions are shown in Figure 9.

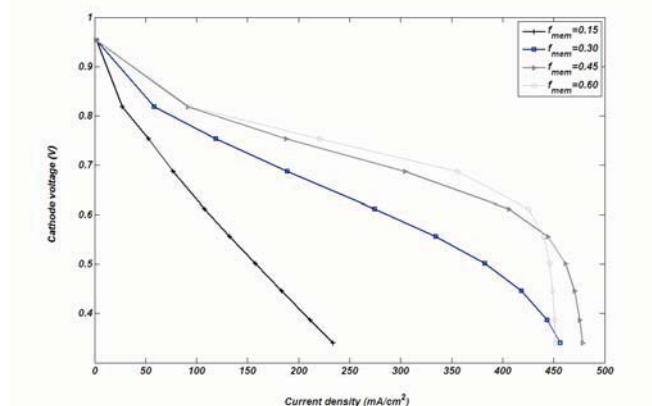


Figure.9: Performance curves at various ionomer fraction.

Figure 10a and 10b shown the optimal performance at voltage in 0.8 and 0.35 V with 50-60 wt.% and 40-50 wt.% of ionomer respectively.

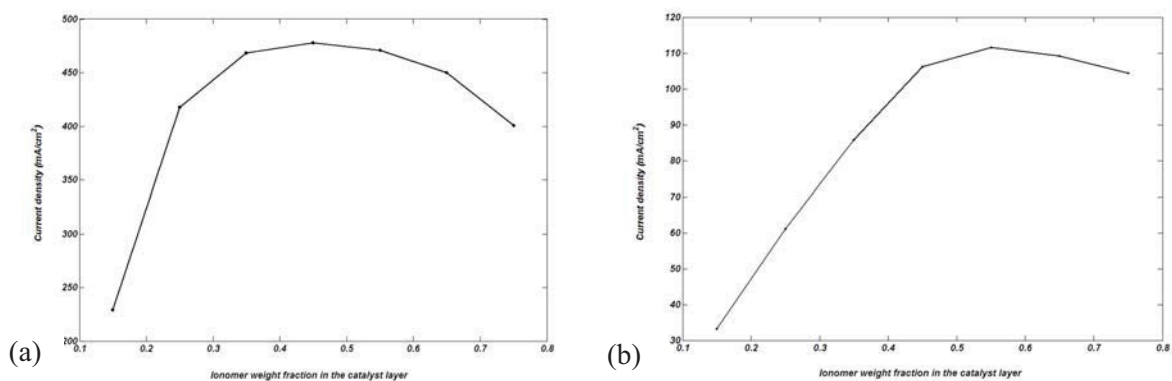


Figure.10: Current density at different values of ionomer fraction at low (a) and high (b) operating voltage.



Conclusions

A two-dimensional steady state model for the cathode of a PEM fuel cell was presented in this work. It was shown that the model predictions using the spherical agglomerate characterization of the catalyst layer fits the experimental data. A sensitivity and optimization studies was carried out with the model. A study is conducted by varying three key design parameters of the CL – platinum loading, thickness of the CL, and fraction of ionomer. Each parameter is varied at a time by keeping others constant. The optimal values were calculated in both high and low operating voltages. The optimal values was 0.9 mg.cm^{-2} , $15 \text{ }\mu\text{m}$ and 55% for platinum loading, CL layer thickness and weight fraction at high voltage respectively, and 0.5 mg.cm^{-2} , $30 \text{ }\mu\text{m}$ and 45% at low voltage.



Characterization and preparation of single wall nanotubes materials for hydrogen storage

Ali naeemy

*Department of Chemistry, Faculty of Science, K.N. Toosi University of
Technology, P.O. Box 15875-4416, Tehran, Iran
a-naeemy@farabi.tums.ac.ir*

Abstract

Carbon single-wall nanotubes (SWNTs) are capable of adsorbing hydrogen quickly, to high density, at ambient temperatures and pressures. We present the details of the cutting procedure here and show that, when optimized, hydrogen storage densities up to 7 wt% can be achieved. We wish to report that we have performed first synthesis experiments with a new laser. Raman spectroscopy indicated that the asproduced materials were ~ 50 wt% pure SWNTs, in contrast to the 20 to 30 wt% usually seen with the previous laser, and the production rate for raw soot appears to be significantly greater than the 150 mg/hr observed previously, even though the current performance is probably far from optimal. We show that hydrogen storage densities can be optimized to values as high as 7 wt%, and present results from experiments designed to elucidate the mechanisms responsible for the unique hydrogen adsorption properties.

Keywords: hydrogen storage, Carbon single-wall nanotubes, thermal gravimetric analysis, Infra Red adsorption

1 Introduction

In the recent years, some works mentioned that hydrogen storage densities on SWNTs made by laser vaporization ranged from 3.5 to extreme 4.5 wt% after a new cutting procedure was performed. Infrared absorption spectroscopy measurements on pristine and H₂-charged samples indicate that no C-H bonds are formed in the hydrogen adsorption process. These experiments are in agreement with an earlier temperature programmed desorption analysis which showed that hydrogen molecules are not dissociated when bound to the SWNT surfaces [1]. This conclusion is further supported by the first neutron scattering measurements which were performed through collaboration with researchers at NIST and University of Pennsylvania [2]. Dillon and co-workers developed methods to tune SWNT diameters during synthesis so that mechanistic aspects of H₂ storage can be probed [3], and learned how to detangle and organize individual tubes to form "superbundles" that will afford high volumetric storage densities [4].

With the 1990 Clean Air Act and the 1992 Energy Policy Act, many of countries trailed United States that recognized the need for a long-term transition strategy to cleaner transportation fuels [5]. This realization comes while the U.S. continues to increase petroleum imports beyond 50% of total oil consumption, with nearly 50% of the total oil consumed being used in the transportation sector⁶. Because of the potential for tremendous adverse environmental, economic, and national security impacts, fossil fuels must be replaced with pollution-free fuels derived from renewable resources. Hydrogen is an ideal candidate as it is available from domestic renewable resources, and usable without pollution. It could therefore provide the long-term solution to the problems created by the Nation's dependence on fossil fuel. Interest in hydrogen as a fuel has grown dramatically since 1990, and many advances in hydrogen



production and utilization technologies have been made. However, hydrogen storage technology must be significantly advanced in performance and cost effectiveness if researchers are to establish a hydrogen based transportation system.

Hydrogen provides more energy than either gasoline or natural gas on a weight basis. It is only when the weight, volume, and round-trip energy costs of the entire fuel storage system and charging/discharging cycle is considered that hydrogen's drawbacks become apparent. New approaches enabling more compact, lightweight, and energy efficient hydrogen storage are required in order for the wide-spread use of hydrogen powered vehicles to become a reality. Research and development geared towards implementation of a national hydrogen energy economy has many indirect economic benefits. In the past decade, with almost 600 million vehicles in the world in 1992 - double the number in 1973 - the conflict between energy requirements, power generation, and environmental concerns is felt on a worldwide basis [7].

Hydrogen can be made available on-board vehicles in containers of compressed or liquefied H₂, in metal hydrides, or by gas-on-solid adsorption. Hydrogen can also be generated on-board by reaction or decomposition of hydrogen containing molecular species [8]. Although each method possesses desirable characteristics, no approach satisfies all of the efficiency, size, weight, cost and safety requirements for transportation or utility use. Gas-on-solid adsorption is an inherently safe and potentially high energy density hydrogen storage method that should be more energy efficient than either chemical or metal hydrides, or compressed gas storage. Consequently, the hydrogen storage properties of high surface area "activated" carbons have been extensively studied [9- 11]. However, activated carbons are ineffective in hydrogen storage systems because only a small fraction of the pores in the typically wide pore-size distribution are small enough to interact strongly with gas phase hydrogen molecules.

The first measurements of hydrogen adsorption on carbon single-wall nanotubes (SWNTs) were performed with highly impure samples. The room-temperature stabilization that was demonstrated at atmospheric pressures suggested the possibility of 5-10 wt % hydrogen storage in SWNT-based systems [1]. Contradictory results from purified SWNTs indicated that such high storage densities could only be achieved with cryogenic temperatures (80 K) and high pressures (158 atm) [12], consistent with theoretical consideration of van der Waals interactions between H₂ and SWNTs [13- 15]. Gennett and cooperators shown that SWNTs can adsorb between 3.5 and 4.5 wt% at room temperature and room pressure when un-optimized preparation procedures were employed [16], and large-diameter SWNTs were recently shown to adsorb 4.2 wt % hydrogen at room temperature and ~100 atm [17].

In this work, we present the details of the new cutting procedure and show that, when optimized, hydrogen storage densities up to 7 wt% can be achieved. Infrared absorption spectroscopy measurements on pristine and H₂-charged samples indicate that no C-H bonds are formed in the hydrogen adsorption process. These experiments are in agreement with an earlier temperature programmed desorption analysis which showed that hydrogen molecules are not dissociated when bound to the SWNT surfaces [1]. This conclusion is further supported by first neutron scattering measurements of hydrogen adsorbed onto SWNTs which were performed through collaboration with researchers at NIST and University of Pennsylvania [2]. We also developed methods to tune SWNT diameters during synthesis so that mechanistic aspects of H₂ storage can be probed [3], and learned how to de-tangle and organize individual tubes to form "superbundles" that will afford high volumetric storage densities [4]. Finally, we wish to report that we have performed first synthesis experiments with a new laser Raman spectroscopy indicated that the as-produced materials were ~ 50 wt% pure SWNTs, in contrast to the 20 to 30 wt% usually seen with the previous laser, and the production rate for raw soot appears to be significantly greater than the 150 mg/hr observed previously, even though the current performance is probably far from optimal.



2. Material and methods

2.1. Pulsed Laser Synthesis of SWNTs

SWNT materials were synthesized by a laser vaporization method similar to that of Thess et al. [19]. A single Molelectron MY35 Nd:YAG laser was used which produced gated laser light ranging in duration from 300 to 500 ns at a frequency of 10 Hz. The gated laser light contained numerous short laser pulses of about 5 to 15 ns. The emission wavelength was 1064 nm at an average power of 20 - 30 W/cm². An electronically rastered beam enabled material generation at rates of 75 - 150 mg / h. Typically, production is ~ 1.5 g / day. It is important to stay in a vaporization regime [20] during synthesis so that graphite particles are not ejected. Targets were made by pressing powdered graphite (~ 1 μ particle size) doped with 0.6 at % each of Co and Ni in a 1 / 8" inch dye at 10,000 psi. Crude soot was produced between 850 - 1200 °C with 500 Torr Ar flowing at 100 sccm. Raw materials were estimated to contain ~ 20 - 30 wt% SWNTs by both a detailed analysis of numerous different TEM images [20] and an accurate thermal gravimetric analysis method. SWNT diameters were between 1.1 - 1.4 nm [3]. Inductively coupled plasma spectroscopy (ICPS) was performed after complete air-oxidation of the carbon soots and thorough digestion of the residue in concentrated HNO₃. The same metal content was found in both the laser-generated crude and the initial target to be ~6 wt%.

2.2. Purification of Laser-generated SWNTs

Approximately 80 mg of the above laser-generated crude was refluxed in 60 ml of 3M HNO₃ for 16 h at 120 °C. The solids were collected on a 0.2 μm polypropylene filter in the form of a mat and rinsed with deionized water. After drying, an ~ 82 wt % yield was obtained.

The weight lost is consistent with the digestion of the metal and an additional ~ 12 wt % of the carbon impurities. The carbon mat was then oxidized in stagnant air at 550 °C for 10 min., leaving behind pure SWNTs. The SWNTs were shown to be > 98 wt% pure with thermal gravimetric analysis. Also, TGA revealed that no significant SWNTs were consumed in the purification process [21].

2.3. Cutting of Laser-generated SWNTs

Purified 1-3 mg samples were sonicated in 20 ml of 4M HNO₃ with a high-energy probe for 10 minutes to 24 hrs at powers ranging from 25 - 250 W/cm². Figure 1 displays a typical transmission electron microscopy (TEM) image of purified SWNTs following ultrasonication in 4M HNO₃ for 16 hrs, and shows that the very long ropes found after purification [21] have been cut and re-assembled. The large-scale cutting observed here is consistent with the generation of cuts and defects that have been observed by others [22- 24]. We find that cutting with a high-energy probe in HNO₃ is necessary to achieve high-capacity ambient H₂ adsorption, explaining why other studies have not seen the high room-temperature capacities observed here [12]. Other TEM images of cut samples revealed metal particles ranging in size from several nanometers to several microns. X-ray patterns of the particles in the cut samples were consistent with an alloy of nominal composition TiAl_{0.1}V_{0.04} as expected for disintegration of the ultrasonic probe.

2.4. Temperature Programmed Desorption

carbon samples weighing ~1 mg were placed in a packet formed from 25 μm thick platinum foil and mounted at the bottom of a liquid nitrogen cooled cryostat. The packet could be resistively heated with a programmable power supply. Pinholes in the foil enable gas diffusion into and out of the packet. An ion gauge and capacitance manometer are employed to monitor pressure. Gas exposures are controlled with a variable conductance leak valve. Isolation gate valves separate the sample compartment during high-pressure gas exposures. A mass spectrometer measures species with an m/e up to 300 a.m.u. and insures that only hydrogen is involved in adsorption/desorption cycles. Signals were sufficiently large that the ion current could provide low-noise spectra without multiplication. The instrument was easily calibrated [25] by thermally decomposing known amounts of CaH₂. The amount of evolved hydrogen was linear

with the weight of decomposed CaH_2 , and the calibrations were performed with amounts of CaH_2 that yielded a TPD signal similar to the SWNT samples. The charged hydrogen could also be desorbed under flowing helium during thermal gravimetric analysis (TGA). The hydrogen uptake measured by TPD and TGA was within 10%. Samples were initially degassed by heating in a vacuum of $\sim 10^{-7}$ torr to 823 - 973 K at 1 K/s. The sample temperature was measured with a thin thermocouple spot-welded to the platinum packet. Room temperature H_2 exposures for ~ 1 minute at pressures between 10–500 torr saturated the hydrogen adsorption. Capacity determinations in the TPD were done by cooling the sample to 130 K prior to evacuation of the chamber.

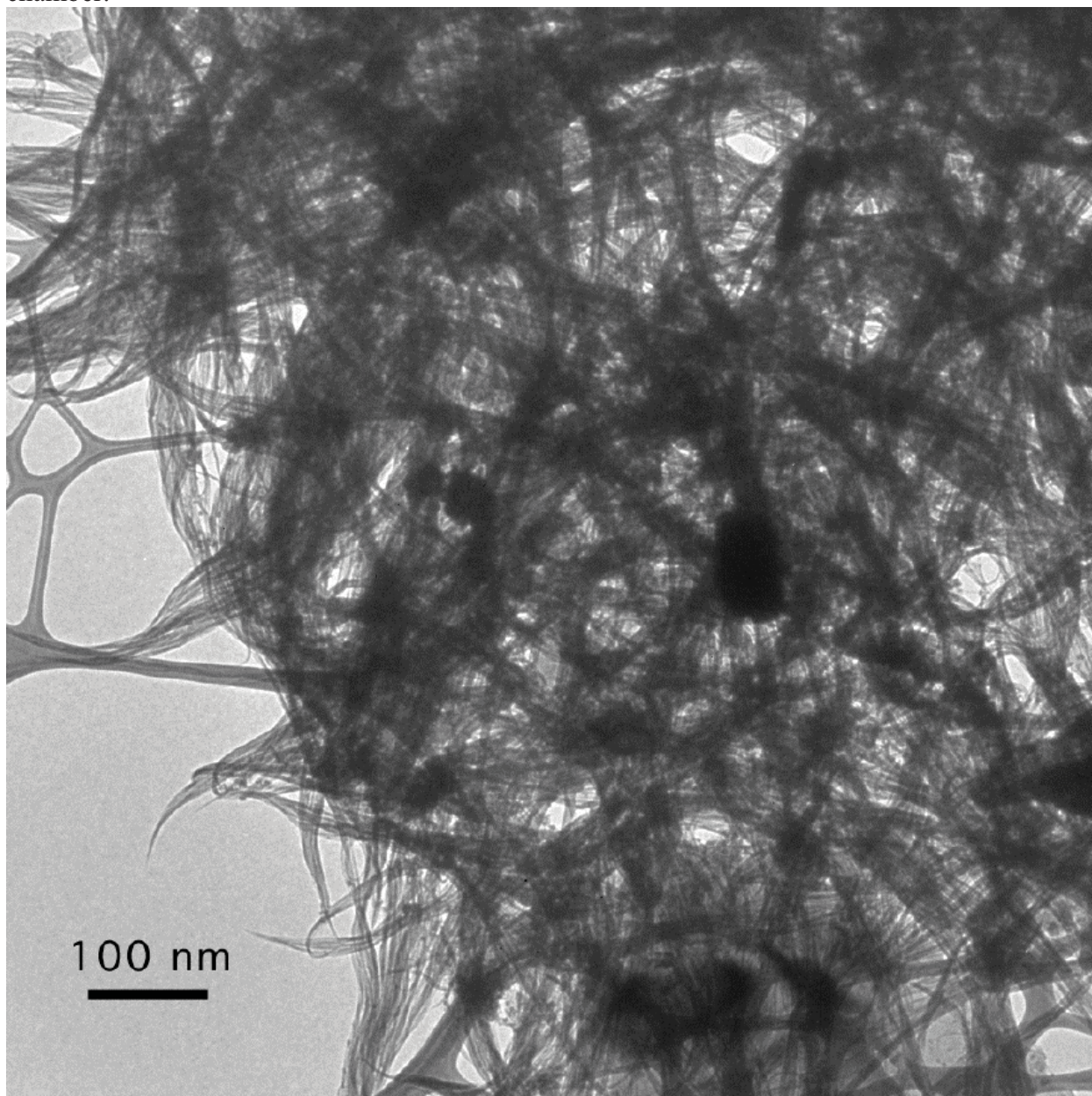


Figure 1: TEM image of purified SWNTs following ultrasonication in 4M HNO_3 for 16 hrs.

2.5. Infrared Absorption Spectroscopy

Transmission Fourier transform infrared (FTIR) studies of single walled carbon nanotubes were performed on a Nicolet 690 spectrometer with a liquid nitrogen cooled MCT-B detector at a resolution of 4 cm^{-1} . Thin SWNT films were prepared employing an Anthem airbrush to spray



SWNT/acetone mixtures onto silicon wafers. Approximately 4 mg of various SWNT materials were suspended in ~ 15 ml acetone by sonication with an ultra sonic probe for several minutes. The resulting solution was sprayed onto the silicon for ~ 10 s. at 30 p.s.i., and the acetone was allowed to evaporate at room temperature in air. A uniform thin SWNT film on the IR transparent silicon substrate was thus obtained. Infrared spectra were ratioed to a background spectrum of a clean silicon wafer. A minimum of 500 scans were collected.

3. Results and Discussion

3.1. Hydrogen Adsorption on Cut SWNTs

Upon degassing the purified cut SWNT samples in vacuum, the high capacity hydrogen adsorption was activated. Figure 2 displays the H₂ TPD spectrum of a degassed sample following a brief room temperature H₂ exposure at 500 torr. The spectrum is characterized by two separate desorption signals peaked at ~ 375 and 600 K indicating at least two different types of sites for hydrogen adsorption. The peak desorption temperatures of these signals can be as much as 100 K lower depending on the SWNT sample and the specific cutting conditions. The hydrogen adsorption capacity, as measured by calibrated TPD, was ~ 6.5 wt% on a total sample weight basis after sonication for 16 hrs at 50 W/cm² and degassing to 825 K. This sample was found to contain ~ 15 wt% TiAl_{0.1}V_{0.04} by combusting the carbon fraction in flowing air and accounting for the oxidation of the metals. In addition to being used in the construction of ultrasonic probes, TiAl_{0.1}V_{0.04} is also employed in fusion reactor components. The latter application has led to numerous studies of the interactions between the alloy and hydrogen. A maximum of ~3 wt % hydrogen is observed [26- 28], while virtually no adsorption is seen for T < 373 K due to poor kinetics²⁸. We generated TiAl_{0.1}V_{0.04} samples with the ultrasonic probe for 16 hrs in 4M HNO₃ without the addition of SWNTs. The generated particles exhibited X-ray patterns consistent with the alloy found in the SWNT samples. After a normal degas and H₂ exposure, the TiAl_{0.1}V_{0.04} sample exhibited only ~ 2.5 wt% hydrogen adsorption as measured by both TPD and volumetric techniques. Assuming that the alloy in the SWNT sample behaves like the pure alloy sample, the hydrogen uptake on the SWNT fraction is ~ 7.2 wt%. Samples with higher alloy contents had reduced overall hydrogen capacities, but the value of ~ 7 wt% on the SWNT fraction was relatively constant. The total adsorption capacity of the cut samples varied between 2-7 wt% depending on the material, the sonication power, sonication time, the hydrodynamics of the sonication vessel and the sample degas temperature. Adjustments in these parameters also affected the temperatures of the hydrogen desorption signals [29]. The storage results were highly reproducible within 10-20% for a given set of experimental conditions. The samples are stable to cycling with no apparent degradation when the vacuum and the hydrogen are relatively clean and the sample temperature does not exceed ~825 K.

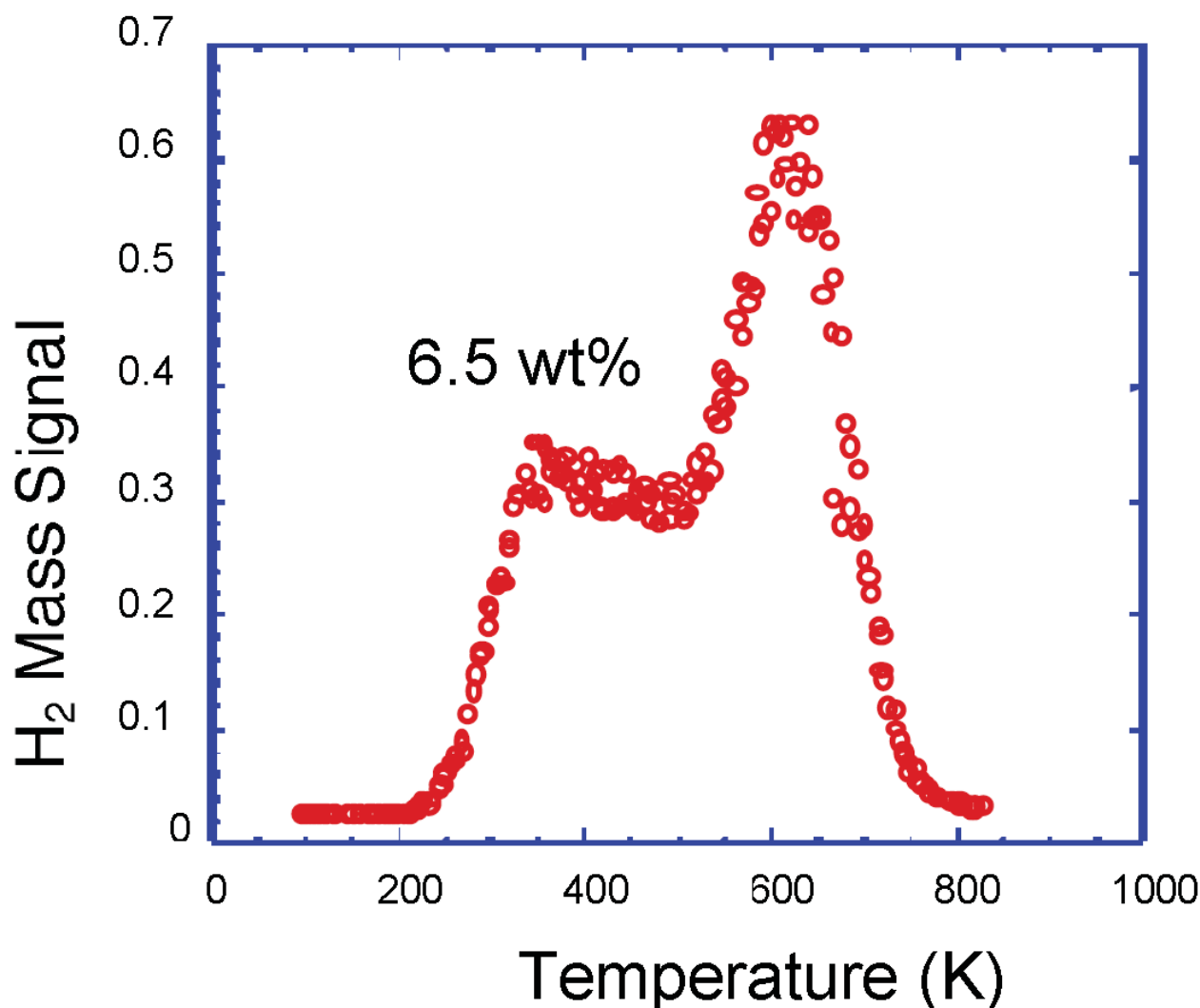


Figure 2: Hydrogen TPD spectrum of a degassed sample following a brief room temperature H₂ exposure at 500 torr. The adsorbed hydrogen corresponds to 6.5 wt%.

3.2. Mechanism of Hydrogen Adsorption

We worked at length this past year to elucidate the mechanism of H₂ adsorption on SWNTs. This type of work is critical to the growing community that has been attempting to understand how SWNTs - as well as other types of nanostructured carbons - interact with hydrogen. There is considerable debate over the issue in the scientific community, and it is important to obtain a deeper understanding so that; (i) accurate theoretical models and predictions may be developed, (ii) specific SWNT diameters and chiralities may be targeted for synthesis, and (iii) capacities and performance characteristics may be optimized. We have previously shown that hydrogen is not dissociated when adsorbed on arc-generated SWNTs even though the binding energy is 19.6 k/mol. In this report we present new evidence that H₂ is non-dissociatively adsorbed on laser generated materials.

All-in-all, we find that the interaction between H₂ and single-wall nanotubes is mid-way between conventional van der Waals adsorption and chemical bond formation. A detailed understanding of the mechanism coupled with a high degree of control during synthesis should allow useful hydrogen adsorbents to be designed and constructed.

Figure 3 displays TPD data from a sample which displays hydrogen desorption peaks at ~ 425 and 600 K. The low-temperature peak occurs at a slightly higher temperature in comparison to



the spectrum in Fig 2. due to the specifics of nanotube diameter and chirality and alterations in the cutting procedure. The hydrogen corresponding to the signal peaked at 425 K can be mostly evolved by holding the sample at room temperature overnight in vacuum, or completely evolved after 1 hr at 373 K (Fig. 3). Also in Fig. 3 it is apparent that all but the most stable hydrogen is liberated after heating in vacuum for 1 hr at 550 K. Qualitatively, the data show a distribution of binding energies for hydrogen, with the existence of at least two different sites. In some papers, this fact investigates that SWNT samples could be removed from vacuum after dosing with hydrogen and that the adsorbed hydrogen was retained on the sample [31]. Consequently, we are now able to perform spectroscopic experiments on H₂ charged samples outside of the controlled environment of the dosing chamber. Figure 4 displays infrared spectra of a cut and a cut, degassed and H₂ charged SWNT film. The spectrum of the cut sample displays a broad infrared absorbance between 942 and 1251 cm⁻¹ consistent with Si-O stretching vibrations due to slightly different concentrations in the native oxide layer of the silicon before and after coating with the cut SWNT film. Features at 1478 and 1630 cm⁻¹ which may be attributed to SWNT vibrational modes are also apparent. The feature at 1317 cm⁻¹ is consistent with an N-O stretching vibration attributed to the presence of intercalated HNO₃ species following cutting in nitric acid. Features between 2810 – 2970 cm⁻¹ consistent with C-Hx stretching vibrations of chemisorbed hydrogen most likely introduced during cutting are also observed. Temperature programmed desorption data of the cut samples indicates that this chemisorbed hydrogen constitutes an amount less than 0.1 wt%. Following infrared spectroscopy the cut SWNT film was loaded into the TPD chamber, degassed to 550 °C and charged with hydrogen at 500 Torr. The amount of adsorbed hydrogen then corresponded to approximately 3.5 wt%. The infrared spectrum subsequently obtained for the charged SWNT sample displays a loss in the N-O stretching feature consistent with the desorption of intercalated nitric acid species during the degas (Fig. 4). However, a significant increase in the C-Hx stretching region is not observed suggesting that the 3.5 wt% adsorbed hydrogen is not chemically bound to the nanotube walls. Changes in the infrared spectrum between 3100 - 3200 cm⁻¹ and at ~1600 cm⁻¹ are consistent with slightly different Si-OH and adsorbed H₂O species present at different locations on the silicon substrate.

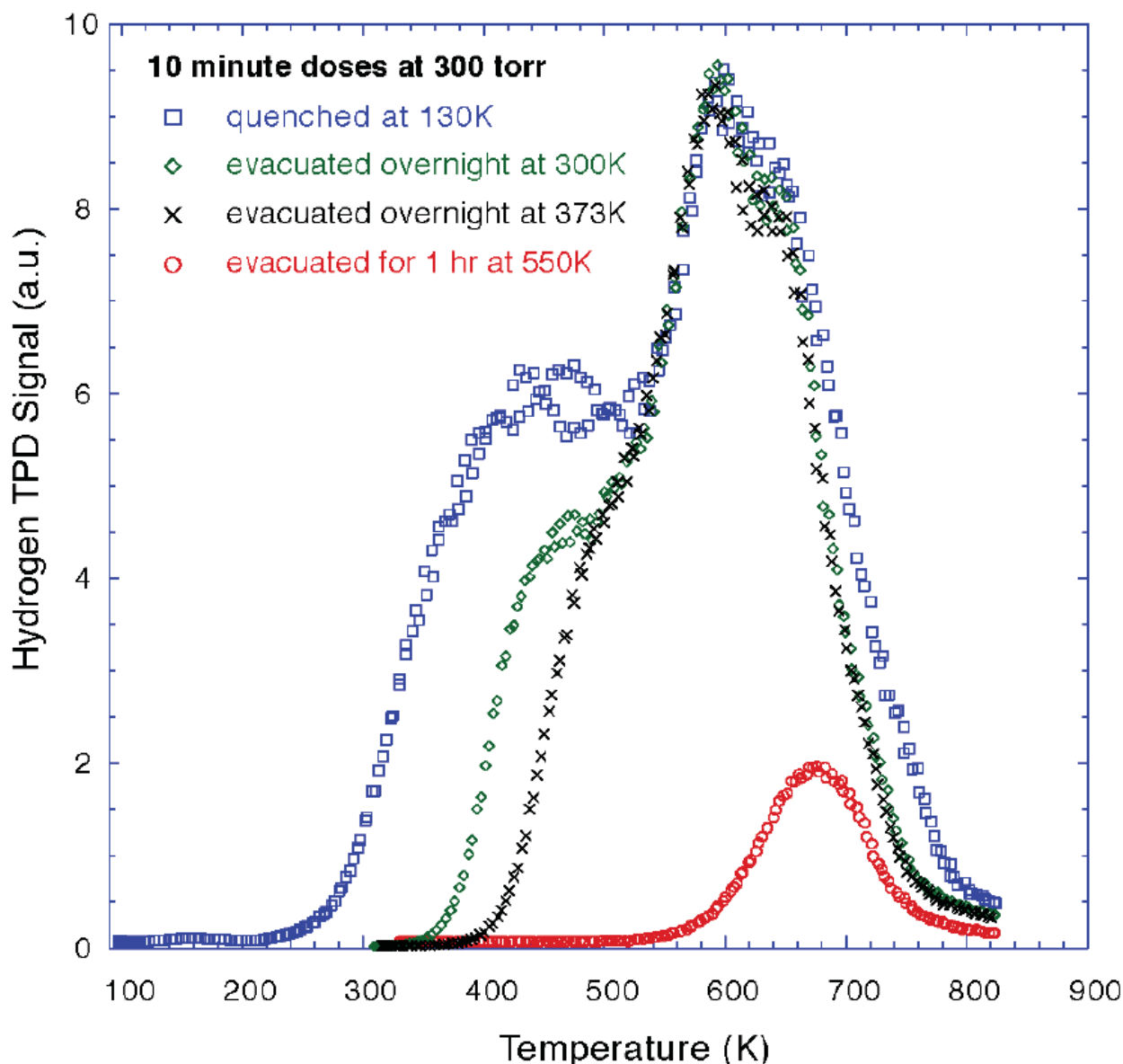


Figure 3: Hydrogen TPD data from an SWNT sample that was exposed to hydrogen at 300 Torr for 10 minutes followed by a variation in postdosing conditions.

Figure 5 shows the signal associated with the ortho to para conversion as a function of temperature for the unprocessed material. Surprisingly the transition is observed at temperatures as high as 65K, indicating a binding energy of ~ 6 kJ/mol. These first measurements were performed on raw (unpurified and uncut) SWNT samples grown by laser vaporization, and the dosing and degassing procedures were not fully controlled. Although we do not expect to see strongly-bound H₂, these experiments serve as a basis for future work on samples which have been more carefully activated and charged with hydrogen. The reader is referred to the publication² for a detailed explanation of these neutron scattering measurements.

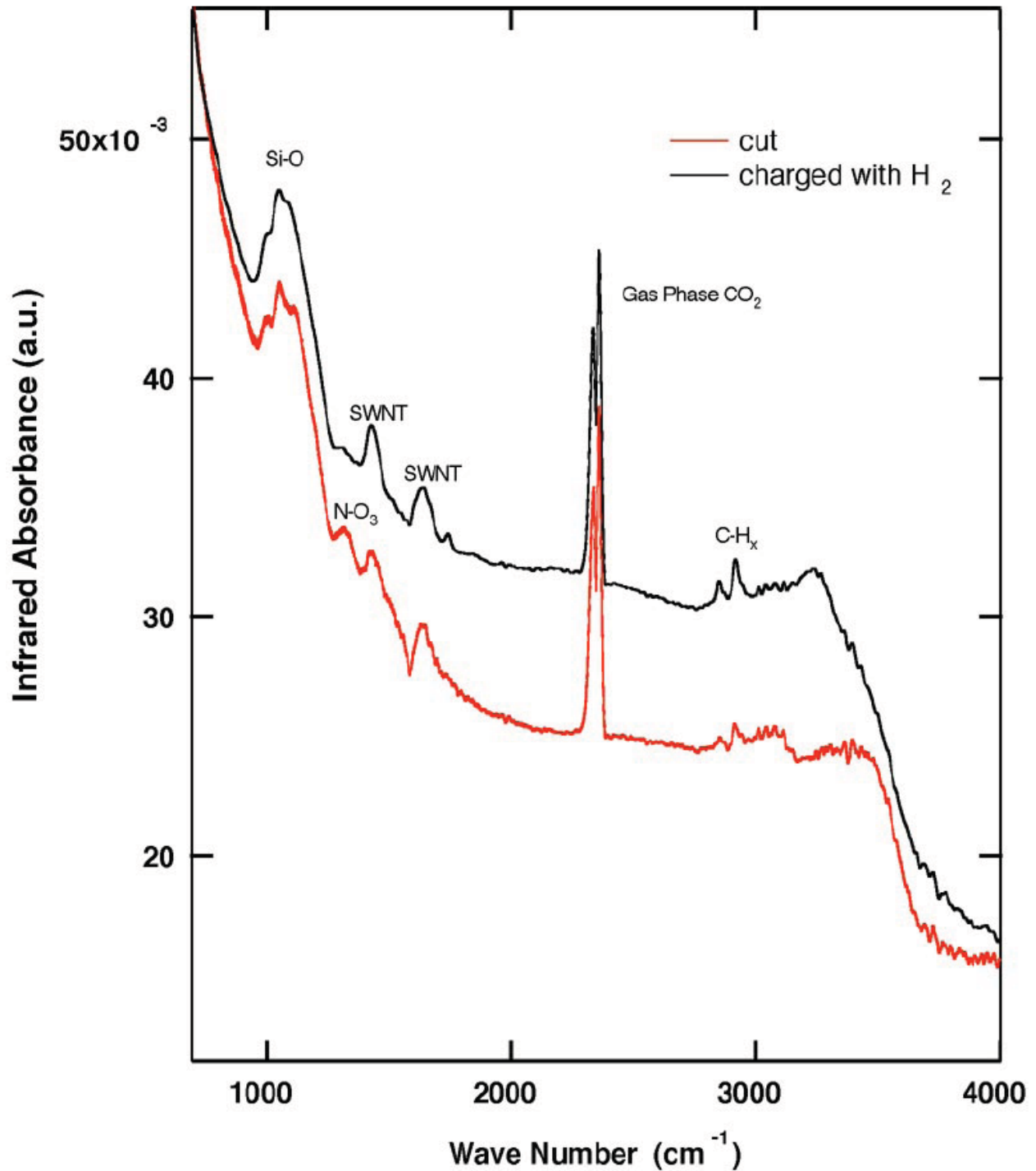


Figure 4: FTIR spectra of a cut and a cut, degassed and H₂ charged SWNT film.

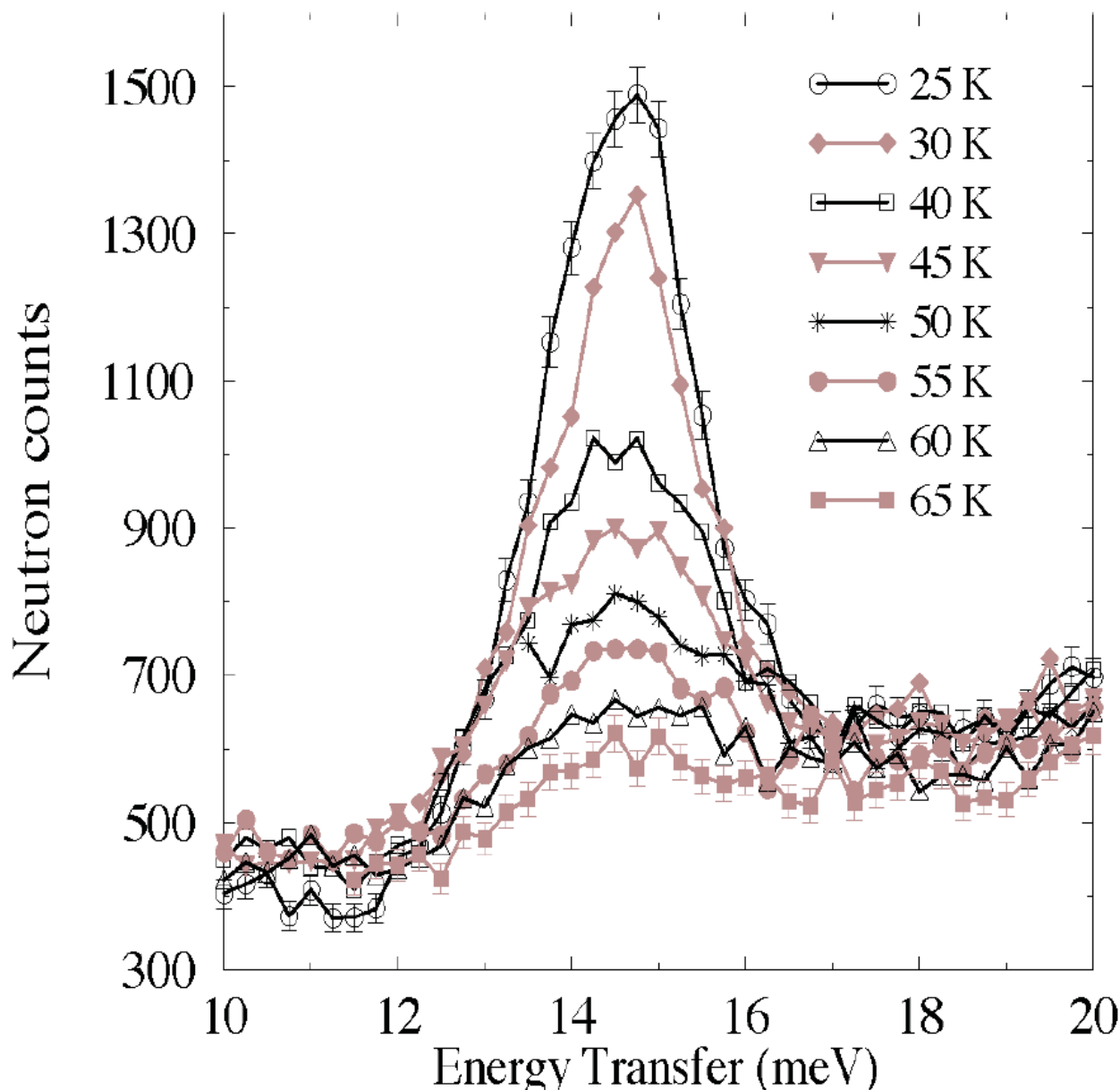


Figure 5: The signal from inelastic neutron scattering measurements on our hydrogen-loaded SWNT samples associated with the ortho to para conversion as a function of temperature.

3.3. Diameter Tuning and Increased Production Rates by Controlled Laser Vaporization

This year we have demonstrated, for the first time, that SWNT diameter distributions can be tuned through variation in laser pulse power. This advance is important to furthering progress towards the goals of the Hydrogen Program since there is growing evidence in our lab as well as in others [17] that the diameter of a given SWNT can affect the capacity, thermodynamics, and kinetics of hydrogen storage. The production of SWNTs was investigated at room temperature with a porous target, and at 1200 °C with a dense target. The tube diameters were shifted to smaller sizes with increasing pulse power in both cases. The SWNT size distributions and yields were studied with Raman spectroscopy and transmission electron microscopy, and the evolution of the material quality with laser energy parameters was investigated. The smaller fragments generated by the higher peak pulse powers result in the formation of smaller tubes. Conversely, larger tubes are generated when larger fragments are produced at lower peak pulse powers. The



overall yield of nanotubes is low unless thermal energy for assembly is provided by an external furnace. The study offers a unique view of SWNT formation mechanisms, and should aid in the development methods for the rational control of SWNTs. The full, peer-reviewed study was previously published in Chemical Physics Letters [3]. Some key findings are reproduced here. A Molelectron Nd:YAG laser was operated in both a Q-switched (10 ns) and long-pulsed (450 ns) mode. The pulse repetition rate was fixed at 10 Hz, and experiments were performed with an external furnace surrounding the target at a temperature of 1200 °C. Figure 6 shows Raman spectra in the radial breathing mode region for SWNT materials produced with three different types of laser pulses. Spectrum 6a shows data from material produced at an average power of 200 W/cm² in long-pulse mode where the pulse power is 45 MW/cm². Three signals are present at 164, 177 and 182 cm⁻¹ consistent with populations of (10,10), (16,0), and (9,9) tubes [32]. Much weaker signals at 193 and 202 cm⁻¹ may also be discerned. The Raman spectrum is dramatically shifted to higher frequencies corresponding to smaller tubes when the average power is maintained at 200 W/cm² but the laser is Q-switched to yield a pulse power of 2 GW/cm² (Fig 6b). The 164 cm⁻¹ peak is no longer observed, and the signals at 177 and 182 cm⁻¹ are significantly reduced in intensity. Two new strong bands found at 202 and 193 cm⁻¹ can be associated with (8, 8) tubes and a slightly larger non-armchair tube such as the (14, 0) tube, respectively. The data is consistent with the shift to smaller tubes seen with increasing peak pulse power in room temperature experiments³. However, with the Molelectron laser, the comparison can be made at different peak powers when the average power and pulse repetition rate are the same. The shift to smaller tubes is clearly due to the increased pulse power. The point is proven further by considering the size distribution of SWNTs when the average power, and thus the pulse power, is reduced while the pulse width and repetition rate are held constant. Figure 6c shows the radial breathing modes for SWNTs produced at an average power of 80 W/cm² and a 10 ns pulse width so the peak power is 0.8 GW/cm². The SWNT size distribution is shifted to larger values in comparison to the distribution obtained at a peak power of 2 GW/cm², and is in fact similar to the size distribution found at an average power of 200 W/cm² in the long-pulse mode. Two major features are present at 164 and 182 cm⁻¹ as expected for (10, 10) and (9, 9) tubes and weaker modes at 193 and 202 cm⁻¹ are also seen.

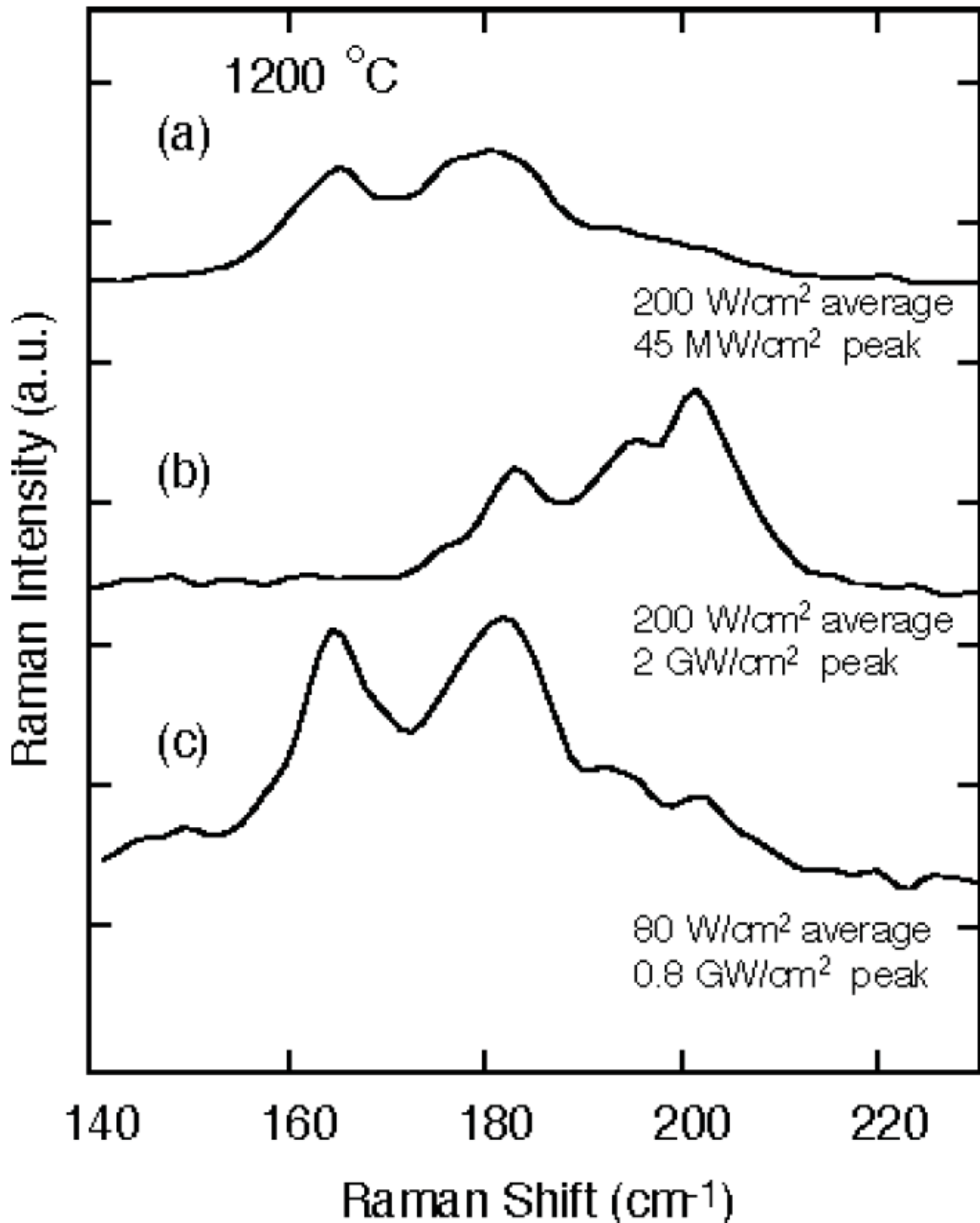


Figure 6: Raman spectra in the radial breathing mode region for SWNT materials produced with three different types of laser pulses.

In addition to learning how to control nanotubes size distributions we have also learned how to de-tangle and order nanotubes on a larger scale. This capability eventually may be important for achieving high packing densities, and therefore high volumetric hydrogen storage densities. Figure 7 shows a SWNT "superbundle" prepared using our methods. The relevant discussion is

beyond the scope of this report, but is reported completely in an article published in Chemistry of Materials [4].

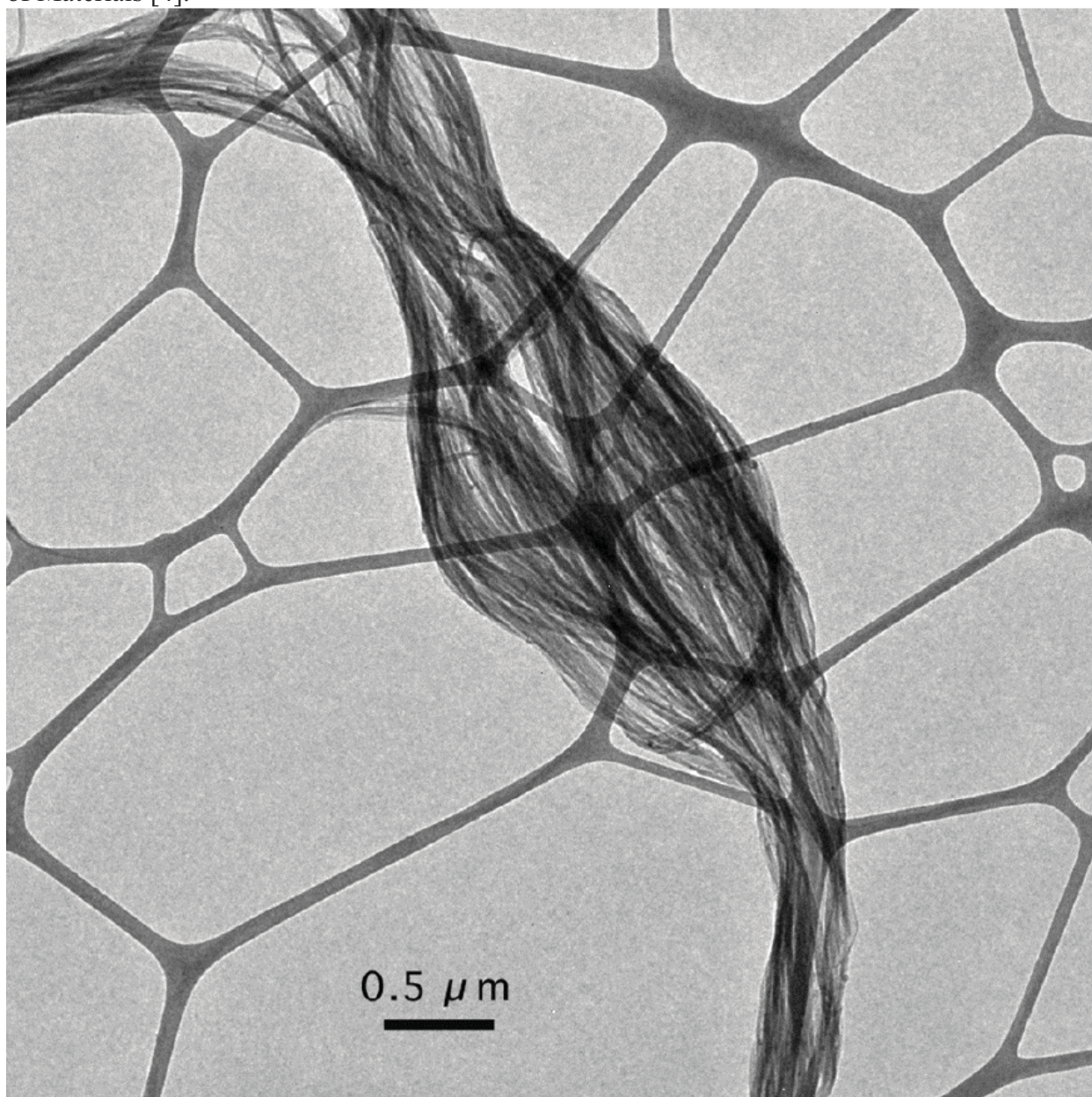


Figure 7 : An SWNT "superbundle". The large bundle of well-aligned tubes should enable higher capacity hydrogen storage.

Finally, we wish to report that we have performed the first synthesis experiments with a new laser. The Molelectron MY35 laser which had been in use was more than 20 years old and had been failing more and more regularly. Additionally problematic was the fact that the laser spot itself was very in homogenous and irreproducible after required flash lamp changes. The TEM images of Figure 8 show the quality of the raw materials produced using a) old Molelectron MY35 and b) the new Light Age, Inc., laser operating at ~ 0.5 J/pulse. Raman spectroscopy indicated that the as-produced materials were ~ 50 wt% pure SWNTs, in contrast to the 20 to 30 wt% usually seen with the Molelectron laser. The new laser will be much more stable and require less maintenance than the Molelectron laser, and the production rate for raw soot appears to be significantly greater than the 150 mg/hr observed previously, even though the current

performance is probably far from optimal. The fact that we can easily produce gram quantities of this quality material everyday will greatly facilitate our development of a carbon nanotube based hydrogen storage system.

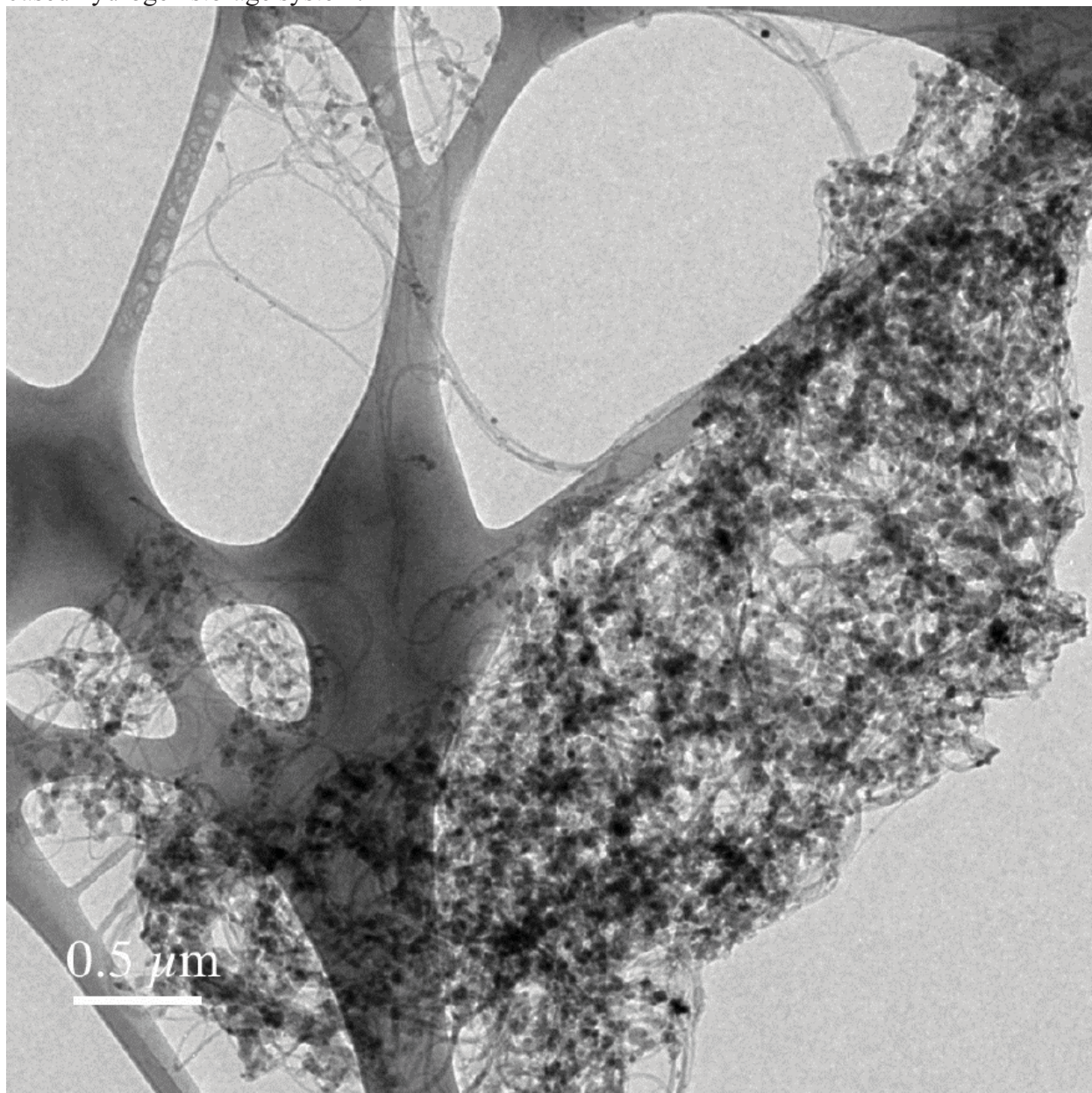


Figure 8: TEM images of the raw materials produced using a) the old Molelectron MY35 laser and b) the new Light Age, Inc. laser. The SWNT density was improved from ~20-30 wt% to 50 wt%.

4. Conclusions

In this work, we have presented the details of our recently developed cutting procedure for laser generated SWNTs and have shown that, when optimized, hydrogen storage densities up to 7 wt% can be achieved. Briefly, purified 1 - 3 mg samples are sonicated in 20 ml of 4M HNO₃ with a high-energy probe for 16 hrs at a power of 50 W/cm². We have employed TPD measurements to show that at least two unique binding sites are present for hydrogen adsorption on SWNTs. We have also employed infrared absorption spectroscopy measurements on pristine and H₂-charged samples to show that no C-H bonds are formed in the hydrogen adsorption



process. These experiments are in agreement with an earlier temperature programmed desorption analysis which showed that hydrogen molecules are not dissociated when bound to the SWNT surfaces [1]. This conclusion is further supported by the first neutron scattering measurements which were performed through collaboration with researchers at NIST and University of Pennsylvania [2]. We also developed methods to tune SWNT diameters during synthesis so that mechanistic aspects of H₂ storage can be probed³, and learned how to de-tangle and organize individual tubes to form "superbundles" that will afford high volumetric storage densities [4]. Finally, we wish to report that we have performed the first synthesis experiments with a new laser which recently arrived at NREL. The as-produced materials are ~ 50 wt% pure SWNTs, in contrast to the 20 to 30 wt% usually seen with the old laser, and the production rate for raw soot appears to be significantly greater than the 150 mg/hr observed previously, even though the current performance is probably far from optimal. The fact that we can easily produce gram quantities of ~ 50 wt% SWNT material everyday will facilitate future large-scale measurements with volumetric techniques. These experiments will more closely simulate the anticipated on-board hydrogen storage system. In the future we will also employ our laser diameter tuning techniques to better establish a correlation between materials properties and hydrogen adsorption behaviors. For example, is the adsorption site that may be depopulated at 300 K for cut and purified laser-generated SWNTs located on larger diameter tubes rather than smaller diameter tubes? Is it also possible that either semi-conducting or metallic SWNTs are better suited for hydrogen adsorption? Raman studies at multiple wavelengths which enable the differentiation between semi-conducting and metallic nanotubes [33] may enable an answer to this question. If a preference is determined, synthetic methods for the production of specifically metallic or semiconducting tubes will need to be developed.

References

- [1] Dillon AC, Jones KM, Bekkedahl TA, Kiang CH, Bethune DS, Heben M.J. *Nature* 1997; 386: 377.
- [2] Brown CM, Yildirim T, Neumann DA, Heben MJ, Gennett T, Dillon AC, Alleman JL, Fischer JE. *Chemical Physics Letters* 2000; 329: 311.
- [3] Dillon AC, Parilla PA, Alleman JL, Perkins JD, Heben MJ. *Chemical Physics Letters* 2000; 316: 13.
- [4] Takagi H, Hatori H, Soneda Y, Yoshizawa N, Yamada Y. *Materials Science and Engineering B* 2004; 108: 143-7
- [5] Cannon JS. *Harnessing Hydrogen*. New York: INFORM, Inc.; 1995.
- [6] Zacharia R, Kim KY, Fazzle Kibria AKM, Nahm KS. *Chemical Physics Letters* 2005; 41(369-375).
- [7] Flavin C, Lessen N. *Power Surge*. New York: W.W. Norton & Co.; 1994.
- [8] Ioannatos Gerasimos E, Verykios Xenophon E. *International Journal of Hydrogen Energy* 2010;35: 622-8.
- [9] Carpetis C, Peschka W.. *International Journal of Hydrogen Energy* 1980; 5: 539.
- [10] Dresselhaus MS, Williams KA, Eklund PC. *MRS Bulletin* 1999; 45-50.
- [11] Pietraß T, Shen K. *Solid State Nuclear Magnetic Resonance* 2006; 29: 125-31.
- [12] Ye Y, Ahn CC, Witham C, Fultz B, Liu J, Rinzler AG, Colbert D, Smith KA, Smalley RE. *Applied Physics Letter* 1999; 74: 2307.
- [13] Wang Q, Johnson JK. 1999; 103: 4809.
- [14] Wang Q, Johnson JK. *Journal of chemical Physics* 1999; 110: 577.
- [15] Rzepka M, Lamp P, de la Casa-Lillo MA. *Journal of Physical Chemistry B* 1998; 102: 10894.
- [16] Schur DV, Tarasov BP, Zaginaichenko SYu, Pishuk VK, Veziroglu TN, Shul'ga Yu M, et



- al. International Journal of Hydrogen Energy 2002; 27: 1063-9.
- [17] Liu C, Fan YY, Liu M, Cong HT, Cheng HM, Dresselhaus MS. Science 1999; 286: 1127.
- [18] Pederson MR, Broughton JQ. Physical Review Letters 1992; 69: 2689.
- [19] Thess A, Lee R, Nikolaev P, Dai H, Pitit P, Robert J, Xu C, Lee YH, Kim SG, Rinzler AG, Colbert DT, Scuseria GE, Tomanek D, Fischer JE, Smalley RE. Science 1996; 273: 483.
- [20] Huang M C, Chou Chia-Huei, Teng H. AIChE; 2002; 48, 8.
- [21] Dillon AC, Gennett T, Jones KM, Alleman JL, Parilla PA, Heben MJ. Advanced Materials 1999; 11: 1354.
- [22] Shelimov KB, Esenaliev RO, Rinzler AG, Huffman CB, Smalley RE.. Chemical Physics Letters 1998; 282: 429.
- [23] Liu J, Rinzler AG, Dai H, Hafner JH, Bradley KR, Boul PJ, Lu A, Iverson T, Shelimov K, Huffman CB, Roderiguez-Macias F, Shon YS, Lee TR, Colbert DT, Smalley R.E. Fullerene Pipes. Science 1998; 280: 1253.
- [24] Lu KL, Lago RM, Chen YK, Green MLH, Harris PJF, Tsang SC. Carbon 1996; 34: 814.
- [25] Wang J, McEnaney B.. Thermochemica Acta. 1991; 190: 143.
- [26] Davis JW, Smith DL.. J. Nuclear Matter 1979; 85: 71.
- [27] Jiao J, Seraphin S.. J. Material Research 1998; 13: 2438.
- [28] Ishiyama S, Fukaya K, Eto M, Miya N. Journal of Nuclear Science and Technology 2000; 37: 144.
- [29] Gayathri V, Devi NR, Geetha R. International Journal of Hydrogen Energy 2010; 35(3):1313-20.
- [30] Yartys VA, Lototsky MV. Hydrogen materials science and chemistry of carbon nanomaterials; 2004: 75-104.
- [31] Lawrence Jeremy, Xu Gu. Applied Physics Letters 2004;84.
- [32] Rao AM, Richter E, Bandow S, Chase B, Eklund PC, Williams KA, Fang S, Subbaswamy KR, Menon M, Thess A, Smalley RE, Dresselhaus G, Dresselhaus MS. Science 1997; 275: 187.
- [33] Brown SDM, Corio P, Marucci A, Dresselhaus MS, Pimenta MA, Kneipp K.. Physical Review B 2000; 61: R5137.



Study of synergism effect in platinum – Gold alloy electrocatalyst for glucose oxidation in direct glucose alkaline fuel cell

Rasol Abdullah Mirzaei^{*1}, Mohammad safi Rahmanifar², Yekta Majidifard¹

1- Fuel cell Research Laboratory, Dep. Of chemistry, Faculty of science, Shahid Rajaei Teacher Training University, Tehran, IRAN

Corresponding Author E-mail: ra.mirzaei@srttu.edu

Abstract:

Glucose can be used as an energy source for production of electricity in daily activities. Bio fuel cell systems can be consumed glucose as a fuel for electricity production. For doing that noble electrocatalysts must be used to facilitate glucose oxidation in anode. Gold and platinum nanoparticles on carbon Vulcan (Au-Pt/ C) are synthesized at various ratios (20:80, 40:60, 50:50, 60:40, 80:20) as the catalyst for the anodic oxidation of glucose for use in a direct glucose alkaline fuel cell (DGAFC). Characterization of the catalyst is carried out using physical and electrochemical methods. It is observed that gold nanoparticles are uniformly dispersed onto the carbon support. Linear Sweep Voltammetry was shown that the prepared Au-Pt/ C catalysts exhibit higher electro-catalytic activity for glucose oxidation than pure catalysts. The synergism effect in 50% platinum electrocatalyst in alloy form can provide the better performance for glucose oxidation in prepared electrocatalysts. It was confirmed by impedance spectroscopy results, also.

Keywords: Bio fuel cell, Alloy electrocatalysts, Gold – Platinum electrocatalyst, synergism

Introduction:

Glucose is an idea renewable fuel because it can be produced by photosynthesis in plants such as sugar cane or corn and by a large amount of waste biomass that is generated by agricultural activities [1,2]. Studies on electro-catalytic oxidation of glucose are of high interest to the fuel cell community for various reasons. Firstly, glucose is easily available, cheap and non-toxic bio-fuel. Electro-oxidation of glucose and fructose on PtRu/C catalyst, are studied using cyclic voltammetry in alkaline medium to study the reason for deactivation of glucose fuel cell. A simple direct glucose fuel cell with PtRu/C as anode and activated charcoal as cathode was constructed and operated to study the effect of different temperature and concentration of glucose and KOH solution [3].

Amore systematic study of the thermodynamics and kinetics of glucose electro-oxidation should provide useful data for better evaluating the energy performances, which will be absolutely necessary to guide the exploitation of the direct glucose oxidation or idiotically catalyzed [4] fuel

¹. Fuel cell Research Laboratory, Dep. Of chemistry, Faculty of science, Shahid Rajaei Teacher Training University, Tehran, IRAN

². Dep. Of chemistry, Faculty of basic science, Shahed University, Tehran, IRAN



cells [5]. The investigation of direct carbohydrate oxidation fuel cells started in 1964 [6] and continued as a promising approach to autonomous energy supply for medical implants [4]. Until the coming of the lithium batteries, a dozen years later.

[8] Mallou and co-workers [7] investigated the glucose oxidation on the alloy electrodes of Pt, Pb, Au, Pd, and Rh, and reported that Pt–Pb alloy catalyzed the glucose oxidation in neutral solutions, generating more stable and larger responses than pure platinum. Electrochemical oxidation of glucose on gold–platinum nanocomposite electrodes and platinum-modified gold electrodes was investigated with cyclic voltammetry. The gold–platinum nanocomposite electrodes display high electrocatalytic activity for the glucose oxidation in alkaline solution. The results of experiments indicate that both gold and platinum act as the dehydrogenation site and gold also functions to regenerate platinum from poisoned platinum [8]. Gold nanoparticles supported on MnO₂-carbon nanocomposite (Au/MnO₂-C) are synthesized as the catalyst for the anodic oxidation of glucose alkaline fuel cell (DGAFC) [9].

Effects of different carbon sources and carbonized carbon contents during carbon riveting process (CRP) on the stability of Pt/C catalysts have been systematically studied. Experimental results show that the carbon riveted Pt/C catalysts treated by different carbon sources have different stability due to different properties of Pt and carbon after the CRP [10].

Experimental:

Materials:

Carbon powder Vulcan XC-72R was used as support. K₂PtCl₄ and HAuCl₄ from Merck were used as platinum and gold precursor, respectively. NaBH₄ (Merck) was used as reducing agent. All aqueous solutions were prepared using ultrapure water during catalyst preparation. Propan-2-ol (>99% purity) (Quailed Fine Chemicals) was used as solvent for making a dilute solution of prepared catalyst. Catalyst-coated carbon paper (Toray 90 T) was used as working electrode. D-glucose (>99% pure) and KOH (>85% assay, flakes purified) (Merck) were used as fuel and electrolyte, respectively.

Preparation of electro catalyst:

Bimetallic Pt-Au/C (metal ratio 1:1, total metal w10% wt.) was prepared by immobilizing platinum and gold sols on carbon [12,11]. Aqueous solutions of HAuCl₄ and K₂PtCl₄ (100 mg/l) were prepared and glucose was added as protecting agent (metal: glucose 1:50 w/w) in the mixture of precursor sols. A freshly prepared 0.1 M NaBH₄ solution was added (metal: NaBH₄ 1:1 w/w) drop wise under vigorous stirring condition and a black colloidal dispersion was obtained. The metal particles were immobilized by adding carbon to the metal dispersion under heater-stirring. The slurry was kept overnight and when the solution became clear, it was filtered. The solid obtained was washed many times with distilled water and air dried for 24 h. The oven in 80°C dried catalyst was used for characterization.

Preparation of the gold-platinum electrode:



The anode was prepared using prepared Pt-Au/C. The loading of catalysts in each electrode is 3 mg cm^{-2} for fuel cell operation. The catalyst slurry was prepared by dispersing required amount of catalyst powder in distilled water and 2-iso propanol with 1:1 ratio and 30%w/w poly tetra flour ethylene mixture for 30 min using an ultrasonic. The fairly well-mixed catalyst slurry was coated on a carbon paper (cut to size of the electrode) using a brush. The catalyst-coated carbon paper was dried in an oven for an hour at a temperature of 200°C . The area of each electrode is 1.13 cm^2 [13].

Electrochemical measurements:

Three-electrode cell assembly connected to potentiostat–galvanostat (Zahner) was used for LSV and EIS studies. Ag|AgCl (saturated with KCl) electrode was used as reference electrode and platinum electrode was used as counter electrode. The catalyst coated carbon paper was used as working electrode (Azar Electrode). The electrodes were dipped into 100 ml 0.5 M KOH solution with 0.2 M glucose

Result & Discussion:

Physical characterization:

XRD analysis:

The crystal structures of prepared Pt-Au/C and Pt/C and Au/C catalyst powders were studied using XRD as shown in Fig. 1. All electro-catalysts showed a broad peak at about $2\theta = 25^\circ$ which is associated with carbon support [11].

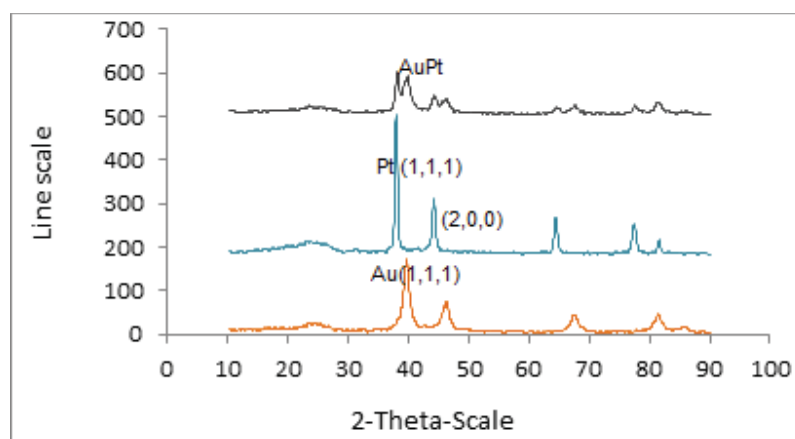


Fig. 1 - XRD pattern of Pt/C, Au/C, AuPt/C catalyst powder samples

The pattern of the AuPt/C, Pt/C and Au/C exhibited diffraction peaks of (1 1 1), (2 0 0), (2 2 0), which indicates that the metals are present in the face centered cubic (fcc) structure [11, 20].



The peaks are found for Au/C at $2\theta = 38.2, 44.4, 64.6, 77.5, 81.8$ and for Pt/C at $2\theta = 40^\circ, 46.2, 67.6, 81.4, 86$. The single diffraction peak of (1 1 1), (2 0 0), (2 2 0), (3 1 1), (2 2 2) at $2\theta = 25^\circ, 40, 46.2, 67.6, 81.4, 86$ for AuPt/C confirms the formation of alloy.

The calculated metal composition for PdPt/C catalysts is 78.8: 21.2, which is very close to the assumed nominal ratio of 3:1 of Au to Pt in Au Pt alloy nanoparticles.

Electrochemical characterization:

LSV analysis:

In the presence of glucose, the usual peak of electrooxidation at platinum electrodes is presented. The glucose molecule is first electrochemically absorbed at the surface of the electrode by dehydrogenation.

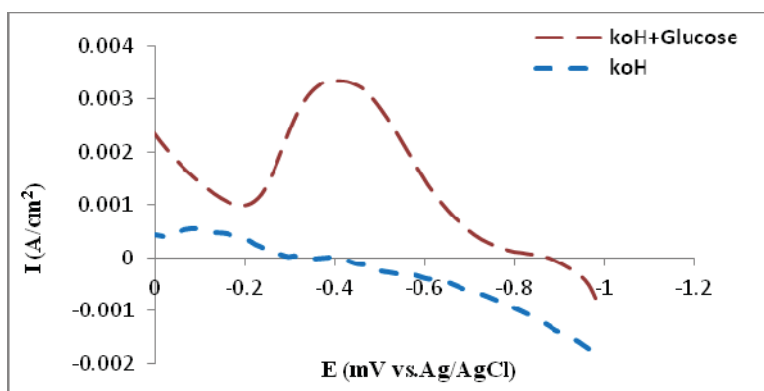


Fig. 2 – Effect of electrolyte in oxidation of glucose in alkaline media

Fig. 2 shows a typical linear sweep voltammogram of glucose electrooxidation in alkaline solution. The LSV from -1 to 0.0V with Ag/AgCl (sat.KCl) reference electrode at 1mVs^{-1} scan rate with Au-Pt/C catalyst in KOH and Glucose electrolyte.

The aim of the present work is to understand the influence of physical synergism in the alloying method.

Electrocatalytic activity of an electrode towards the glucose oxidation is mainly reflected by oxidation potential, i.e., the higher the electrocatalytic activity of the electrode is, the lower the oxidation potential is. The glucose oxidation on the Au-Pt/NPs electrode and the Pt electrode is shown in Fig. 1. The peak potential of the Au-Pt/NPs electrodes appeared at -0.29V , which means about 0.06V negative shift in peak potential as compared with that of the Pt electrodes. The difference in peak potential is remarkable, showing high catalytic activity of the Au-Pt/NPs electrodes. The high catalytic activity of the Au-Pt/NPs electrodes is attributed to platinum and the interaction between gold and platinum species in the reaction, and the detailed mechanism of this reaction needs further investigation. We can see maximum current with 8.22 mA and -0.27 mV related to Ag/AgCl reference electrode.

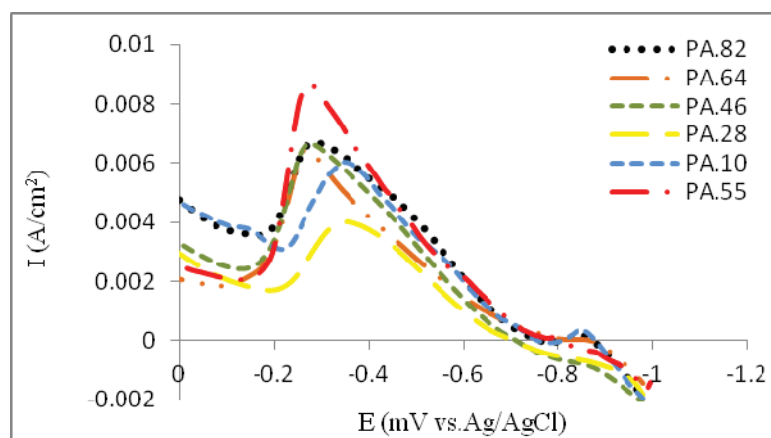


Fig.3 Polarization study of fabricated electrodes at various platinum content for glucose oxidation

EIS analysis:

EIS measurements were used to understand the role of the phosphate buffer on the conductivity of the solution and the mechanism of the reaction. The conductivity of the solution also influences the amount of usable electrode. In fact, a higher conductivity of the solution permits an easier transport of the current inside the electrode and consequently a higher portion of the electrode to be active. The measurement can be used to optimize the thickness of the electrode as a function of the working conditions.

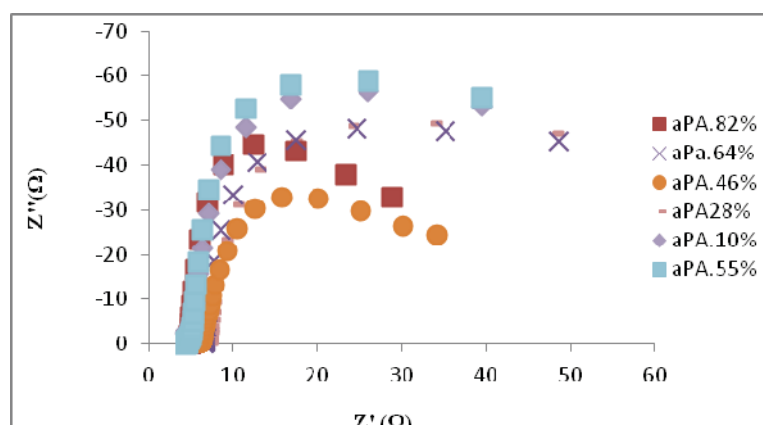


Fig.4 – Impedance Spectroscopy of fabricated electrodes for glucose oxidation in -0.5 v potential



Conclusion:

In this work, alloy method for preparation of electrocatalysts was studied. For these purpose platinum and gold noble metals was used as an alloy form. The simultaneous presence of two metals being together can provide especial situation for creating synergism effect. The percentage of each catalyst in alloy form influences on performance of electrocatalyst for glucose oxidation in gas diffusion electrodes. In this research, the 50:50 proportion percentage of each catalyst is the best ratio for electrocatalytic activity of fabricated electrodes. In this state, the best current density for glucose oxidation reaction was observed. This current density is higher than pure platinum and gold electrocatalysts for desired reaction. Therefore, according our results, the synergism effect was shown in alloy form of platinum and gold electrocatalysts in especial ratio.

Acknowledgment:

The authors would like to acknowledge support of fuel cell research laboratory in Shahid Rajaee teacher training university.

Reference:

- [1] J. Chena,b, C.X. Zhaoa, M. M. Zhia, K.Wanga, L. Denga, G.Xua,* “Alkaline direct oxidation glucose fuel cell system using silver/nickel foams as Electrodes”, *J. Electrochemical Acta*, (2011)
- [2] Jacobus P.H van Wyk “Biotechnology and the utilization of biowaste as a resource for bioproduct development”, *J. of Trends in Biotechnology* , (2001).
- [3] D. Basu, S. Basu “A study on direct glucose and fructose alkaline fuel cell”, *J. of Electrochemical Acta* , (2010). 5775-5779
- [4] S.Kerzenmacher , J.Ducree , R. Zengerle, F. von Stetten “Energy harvesting by implantable abiotically catalyzed glucose fuel cells”, *J. of power sources* , (2008). 1-17
- [5] M. Pastaa,b,* , F. La Mantiab, R. Ruffoc, F. Perid, C. Della Pinaa, C.M. Maric “Optimizing operating conditions and electrochemical characterization of glucose–gluconate alkaline fuel cells”, *J. of power sources* , (2011).
- [6] J.O'M.Bockris , B.J.Piersma , E.Gileadi “Anodic oxidation of cellulose and lower carbohydrates”, *J. of Electrochimica Acta* , (1964).
- [7] Y. Sun, H. Buck, and T. E. Mallou “Combinatorial Discovery of Alloy Electrocatalysts for Amperometric Glucose Sensors”, *J. of Anal. Chem* , (2001).
- [8] Ch. Jin *, Z. Chen “Electrocatalytic oxidation of glucose on gold–platinum nanocompositeelectrodes and platinum-modified gold electrodes”, *J. of Synthetic metals* , (2007).
- [9] L.Li , Keith Scott, E.Hao Yu “A direct glucose alkaline fuel cell using MnO₂–carbon nanocomposite supported gold catalyst for anode glucose oxidation”, *J. of power sources* , (2013).



6th Iranian Fuel Cell Seminar
March 12 & 13 , 2013
Shahid Rajaee Teacher training University
Tehran - Iran



- [10] D. Basu, S. Basu “Electrodeposited gold nanoparticle on carbon nanotube-textile: Anode material for glucose alkaline fuel cells”, J. of Electrochemistry Communications , (2012). [11] D. Basu, S. Basu “Synthesis and characterization of Pt-Au/C catalyst for glucose electro-oxidation for the application in direct glucose fuel cell”, J. of power sources , (2010). [12] C.M, Pina CD, Rossi M “Mono and bimetallic catalysts for glucose oxidation ”. J. of Mol Catal A Chem (2006); 251:89-92.
- [13] D. Basu, S. Basu “Performance studies of Pd-Pt and Pt-Pd-Au catalyst for electro-oxidation of glucose in direct glucose fuel cell ”, J. of power sources , (2011).



Lactose Electrooxidation on the Nickel Oxide Nanoparticles Electrocatalyst Prepared on the Multi-walled Carbon Nanotubes Modified Electrode

Mahsa Behzad, Mehdi Asgari*, Elaheh Lohrasbi

NFCRS, NSTRI, Tehran, Iran

Abstract

The preparation of multi-walled carbon nanotubes-NiO nanoparticles composites (MWCNT-NiO) is presented and the composites were used for modification of glassy carbon electrode for lactose electrooxidation in NaOH. Nickel oxide (NiO) was accumulated on multi-walled carbon nanotubes (MWCNT) by pulsed potential electrodeposition. The structure and nature of the MWCNT-NiO was characterized by and Transmission electron microscopy (TEM) and X-ray diffraction (XRD), the results show that NiO nanoparticles were homogeneously electrodeposited on the surfaces of MWCNTs. Also, the electrochemical behaviour of MWCNTs-NiO nanoparticles composite in an aqueous solution of alkaline solutions of lactose was studied using cyclic voltammetry and chronoamperometry. The peak on the voltammogram for MWCNT-NiO composite electrode in alkaline solutions of lactose is observed which is ascribed to the lactose oxidation in alkaline medium. The results obtained are discussed from the point of view of employment of the MWCNT-NiO composites for the catalytic electrodes of sugar-oxygen fuel cells.

Keywords: Nickel oxide, Nanoparticle, Carbon nanotube, lactose, Electrooxidation, sugar-oxygen fuel cells.

1. Introduction

Carbohydrates, by nature are some of the most abundant compounds as they form more than 80% of the available biomass. The structural architecture of the carbohydrate polymers depends very much on the saccharides, which can be mono-, disaccharides, dextrans or oligosaccharides. The unit composition of a particular polymer will vary according to the nature or origin of the carbohydrate [1].

Lactose is the only disaccharide present in milk; it is a cheap industrial product obtained in abundant tonnage. At the moment, however, its chemical validation is little developed; its only wide application is in the food industry. Thus, only a few fundamental investigations can be found in the literature. They all aim at promoting the selective transformation of lactose to lactobionic acid, as well as the products more interesting than lactose, which have potential applications as food acidulant [2], but could also be used in the pharmaceutical field [3,4] or because of their chelating properties [5,6].

Various reports have described the preparation of nanoparticle based electrodes for different applications [7-9]. The electrocatalytic oxidation of carbohydrates on this type of electrode is attractive because of its sugar-oxygen fuel cell application, as well as its use in sugar sensors for the medical and food industry [10-12].

In the present work, the aim is concentrated on the electrocatalytic oxidation of lactose in aqueous medium on glassy carbon modified by MWCNTs and NiO nanoparticles. The catalysts were prepared by the pulsed potential method on the multi-walled carbon nanotube. The nanoscale catalysts were characterized by TEM and XRD techniques. Lactose electrooxidation



reaction took place by means of electrochemical techniques such as cyclic voltammetry and electrochemical impedance spectroscopy. The performance of nanoscale catalysts was compared with that of corresponding single potential prepared potential catalysts prepared to see whether nanocrystalline materials offer better properties for complete oxidation.

2. Experimental

2.1. Reagents and Apparatus

NiSO₄·7H₂O, Boric acid, Sodium hydroxide and lactose of analytical reagent grade were purchased from Merck and were used without further purification.

MWCNTs with 95% purity (30-50 nm diameters and 3 μm length) were obtained from Timesnano Co. Ltd. (China). Purification and surface activation of MWCNTs were done before use, as follows:

The electrochemical experiments were carried out by means of an Ivium Compactstate Electrochemical Analyzer equipped with a personal computer used for data storage and processing. Cyclic Voltammetric experiments were done in a conventional three-electrode cell using a Glassy Carbon (GC) disk electrode as the working electrode (with 3 mm in diameter). The auxiliary electrode was a platinum wire and the reference electrode was a saturated Ag/AgCl electrode. All measurements were taken at 25°C (±2 °C), the temperature was maintained with a water thermostatic bath.

2.2. Modified electrode preparation

The surface of the GC electrode for each experiment was mechanically polished with 0.05 μm α-alumina powder. The polished surface was rinsed thoroughly with acetone and then with doubly distilled de-ionized water. 16 mg MWNTs were added into the 5 mL acetone. A homogeneous and stable suspension of 3.2 mgmL⁻¹ MWNTs was achieved with the aid of ultrasonication agitation for about 3 min. The GCE was coated by casting 20 μL suspension of MWNT and dried at the room temperature.

The deposition baths were prepared using NiSO₄·7H₂O with a total concentration of 40.0 mM for all solutions. The pH of the bath was adjusted to 2 using boric acid and 2 drops of sulfuric acid. The pulse potential for making Ni nanoparticles on the electrode was applied according to Table 1. The sizes of particles were controlled by changing the number of cycles applied to the depositions. It is clear that the increasing of the pulses caused the formation of a larger particle of modifier on the surface of GC/MWCNT electrode.

The prepared electrode was conditioned in 0.10 M NaOH solution by potential cycling between 100 to 800 mV (vs. Ag/AgCl) for about 10 cycles of potential scans with a scan rate of 100 mVs⁻¹. These parameters were obtained experimentally as optimum values for complete transformation of Ni (II) to Ni (III) and maximum activation of electrode surface towards electrocatalytic oxidation of lactose. All electrochemical investigations were performed at the room temperature.

3. Result and discussions

3.1. Nanostructure of the nanocrystalline NiO-MWCNT composite

In the TEM image of the nanocrystalline NiO-MWCNT composite shown in Fig. 1A, it can be seen that the Nickel nanoparticles are distributed on the MWCNTs surface in the form of single stick. The Nickel oxide nanoparticles can therefore grow by repeated electrodeposition into the MWCNT matrix under a homogeneous distribution (Fig.1A). It can be deduced from these images that aggregation of the NiO nanoparticles is not obvious, and the nanoparticles are widely dispersed on the MWCNTs. Almost NiO particles are coated on MWCNT surface, and the particle sizes for all MWCNT samples are found to be a constant 30–50 nm. The deposition of uniformly dispersed nanoparticles on MWCNTs is believed to be the result of uniform

surface functional sites on all nanotubes that can be created in the chemical-wet oxidation of nitric acid. During the surface modification process, the surface oxides may act as active sites in adsorbing with Ni ions, thus forming intermediate complex in aqueous phase. Consequently, the surface coverage accessible to Ni (II) adsorption depends on the ionic concentration. Within the fixed period, the particles can grow an equivalent size, in different particle densities over the surface of MWCNTs. It is well known that oxygen functional groups impart a surface polarity, i.e. surface electrostatic field, to carbon surfaces [13, 14]. The interaction of the electrostatic field on the surface with dipole moment of water molecules plays a crucial role in determining the saturation of carbons in aqueous solutions.

In order to further support the formation of MWCNTs -NiO composite, the X-ray diffraction (XRD) profile of the prepared nanocomposite was also obtained, the result of which is shown in Fig. 1B. As seen, there is a typical reflection peak (002) for MWCNT at 21.8° in two curves [15]. The other diffraction peaks in NiO/MWCNT composite display peaks of salt structured NiO, which can be assigned to (111), (200) and (220) (2θ) reflections of fcc phase NiO [16, 17], among which the two small diffraction peaks at 44° and 52° are matching Ni (111) and Ni (200) reflections, respectively [18].

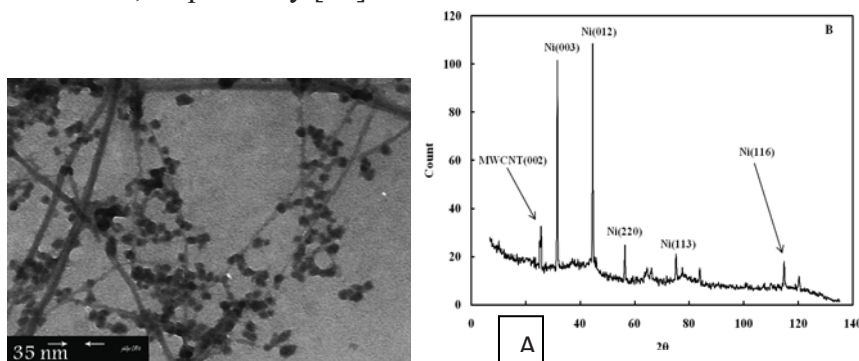


Fig.1. (A)TEM image of the nanocrystalline NiO-MWCNT composite. (B)X- ray diffraction profile of the prepared nanocomposite.

3.2. Electrocatalytic oxidation of lactose on the GC/MWCNT-NiO modified electrode

Fig. 2A represents the cyclic voltammograms of the GC/MWCNTs/NiO modified electrode in 0.10 M NaOH solution recorded at different potential sweep rates in a wide range of 5-800 mVs⁻¹. A pair of well defined peaks with a peak potentials of 530mV appears in the voltammograms, and the peak-to-peak potential separation (at the potential sweep rate of 10mVs⁻¹) is 81mV. The voltammograms shown are similar to those previously reported [14,16,18], and the redox transition involved is attributed to the presence of Ni (II)/Ni (III) species. The peak-to-peak potential separation deviates from the theoretical value of zero and increases at higher potential sweep rates. This result indicates a limitation in the charge-transfer kinetics, which is due to: (a) the chemical interactions between the electrolyte ions and the modifier film, (b) the dominance of electrostatic factors, (c) the lateral interactions of the redox couples present on the surface and/or (d) the non-equivalent sites present in the film.

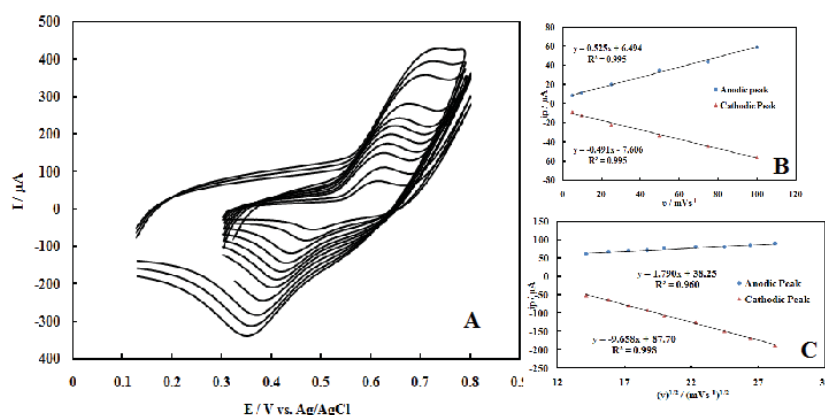


Fig.2. (A) cyclic voltammograms of the GC/MWCNTs/NiO modified electrode in 0.10 M NaOH solution recorded at different potential sweep rates in a wide range of 5-800 mVs⁻¹. (B) Variation of the anodic and cathodic peak currents versus the potential sweep rate values of 5-100mVs⁻¹. (C) Variation of the anodic and cathodic peak currents versus the square root of potential sweep rate values of 200-800mVs⁻¹.

The voltammograms represented in Fig. 2A also show that the anodic and cathodic peak currents are proportional to the potential sweep rate at low values of 5-100mVs⁻¹ (Fig. 2B). This result is attributable to the electrochemical activity of an immobilized redox couple on the surface. From the slope of this line and using [28]:

$$I_p = \left(\frac{n^2 F^2}{4RT} \right) \theta A \Gamma^* v$$

where I_p is the peak current, A is the electrode surface area and Γ^* is the surface coverage of the redox species and taking the average of both cathodic and anodic currents, a total surface coverage of the electrode with the modifier film of about 7.91×10^{-9} mol cm⁻² was derived. In the broad range of potential sweep rates of 200-800mVs⁻¹ (Fig. 2C), this dependency is of square root form, signifying the dominance of a diffusion process as the rate-limiting step in the total redox transition of the modifier film. This limiting-diffusion process, which is also reported for other Ni-based modified electrodes [19-21], may take place for the charge neutralization of the film during the oxidation/reduction process.

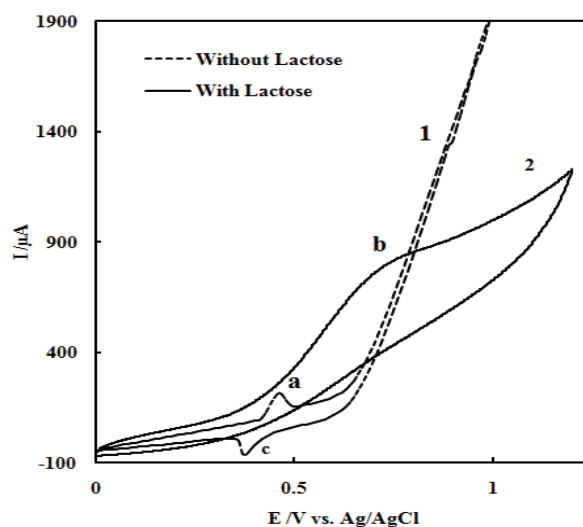


Fig.3. Voltammograms recorded for this electrode in the absence (1) and in the presence of 0.10 M lactose (2).

The modifier layer of MWCNTs/NiO on the electrode acts as a catalyst for the oxidation of lactose in 0.10 M NaOH solution. Fig.3 shows the voltammograms recorded for this electrode in the absence (1) and in the presence of 0.10 M lactose (2). An increase in the anodic peak current for peak (a) followed by the appearance of a new peak (b) at more positive potential (with which these two peaks are overlapped in this figure) and disappearance of the cathodic peak(c) current during the reverse scan are the main effects observed in the addition of lactose to electrolyte. It is obviously seen that the oxidation occurs in two regions of potential which overlap each other. The first region corresponds with the source from where Ni (III) species originate [19-23]. It is noted that the Ni(OH)₂/NiOOH transformation occurs on the nickel electrode reversibly. On the other hand, on GC/MWCNTs/NiO modified electrode, this transformation occurs quasi-reversibly and ultimately NiOOH is formed. At this potential, lactose oxidation appears as an increase in $I_{p,a}$ accompanied with disappear in cathodic peak current in the reverse sweep. This fact clearly shows that the applied modifier in this process participates directly in the electrocatalytic oxidation of lactose. In the second region of potential, where only Ni (III) species exists at the electrode surface, a new anodic peak (b) with a powerful peak current with respect to that of the former one appears. The height of this peak increases linearly with lactose concentration in the solution, showing that it concerns the process in which lactose is involved. In the previous works [23-26], for methanol electrooxidation, the authors noted that the appearance of this new anodic peak (b) leads to the conclusion that methanol oxidation takes place after the complete oxidation of Ni (II) to Ni (III). While, we concluded that lactose can be adsorbed on Ni(III) when Ni(III) starts to form on the electrode surface at the potential of 400 mV. The adsorbed lactose oxidized under a chemical reaction in fast kinetics and produces Ni(II) and other products. In potential sweeps the newly produced Ni(II) oxidized to Ni(III) is materialized again and a new peak (b) appears at the potential of 700 mV. This peak current depending on the lactose concentration, increases in lactose concentration causing an increase in Ni(III) to Ni(II) transformation and then an increasing amount of the newly produced Ni(II) oxidized to Ni(III) emerges once more. The produced Ni(III) in these potentials oxidizes the lactose and in the switching potential, a great amount of Ni(III) is transformed to Ni(II), due to the decrease in this reaction's cathodic peak. Accordingly, the catalytic role of Ni (III) for lactose oxidation can be proposed as follows:



In Fig 4. the steady-state voltammogram recorded in the course of electrocatalytic oxidation of lactose is presented. The typical S-type plot, and charge transfer coefficient (α) were obtained

using potential versus $\log I$ plotting. The slope of such plots is equal to $\frac{2.3 RT}{\alpha F}$. Therefore, the calculated charge transfer coefficient was 0.44.

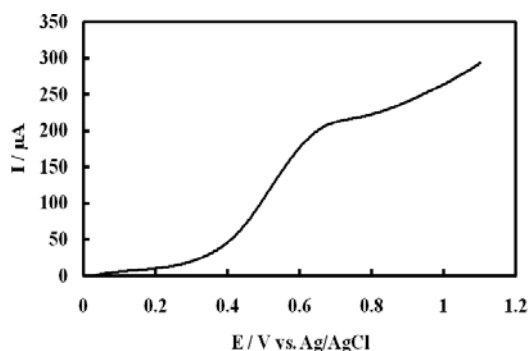


Fig.4. the steady-state voltammogram recorded in the course of electrocatalytic oxidation of lactose

3.2.1. Effect of scan rate

The effect of scan rate on the peak current ratio at GC/MWCNTs/NiO modified electrode in 0.10M NaOH + 0.10M lactose is shown in Fig. 5A. These voltammograms show that the anodic current for lactose oxidation increases rapidly with increasing the potential scan rate. Indeed, the time window for lactose oxidation process at the higher scan rates becomes very narrow avoiding the facile electron transfer between substrate and catalytic sites. However, the peak currents of the oxidation of Ni(OH)₂ and the reduction of NiOOH enhance with increasing the scan rate. Therefore, it can be concluded that the Ni(OH)₂/NiOOH transformation process is much faster than the lactose oxidation. Direct reaction between lactose and NiOOH (that formed on the electrode surface) produces NiO leading to a small increase in the anodic peak current.

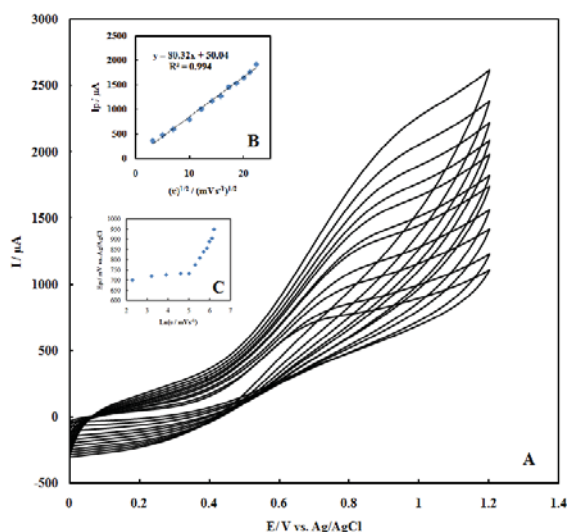


Fig.5. (A) The effect of scan rate on the peak current ratio at GC/MWCNTs/NiO modified electrode in 0.10M NaOH + 0.10M lactose. (B) Variation of the anodic peak currents versus the square root of potential sweep rate. (C) Variation of the anodic peak currents versus the natural logarithm of potential sweep rate.

Fig. 5B exhibits clearly that the anodic peak currents are linearly proportional to the square scan rate up to 250 mV s^{-1} . This figure shows that they are diffusion limited (Cottrell). However, the relationship between anodic peak currents and square scan rates indicates that at the high scan rates, it is a diffusion controlled process. In addition, the value of the charge transfer coefficient can be obtained using the following equation [27]:

$$E_p = \left(\frac{RT}{2\alpha F} \right) \ln v + \text{constant} \quad (4)$$

This equation is valid for a totally irreversible diffusion controlled reaction. Using the dependency of natural logarithm of potential scan rate on the anodic peak potential, the value of charge transfer coefficient obtained is 0.41. This value is in agreement with that obtained from steady-state voltammogram. According to Randles-Sevcik equation and dependency of square root of scan rate on the anodic peak currents, the diffusion coefficient of lactose obtained is $6.27 \times 10^{-5} \text{ cm}^2 \text{ s}^{-1}$. The Randles-Sevcik equation is [28]:

$$I_p = (2.99 \times 10^5) \alpha^{1/2} n^3 / 2 AD^{1/2} v^{1/2} C \quad (5)$$

where I_p is the peak current, A is the electrode surface area, D is the diffusion coefficient and C is the bulk concentration of lactose.

3.2.2. Effect of lactose concentration

Fig. 6 shows the effect of lactose concentration on the anodic peak current at GC/MWCNTs/NiO modified electrode in 0.10M NaOH. It is clearly observed that as the lactose concentration increases, the peak height increases linearly with lactose concentration up to 0.40 M. It can be assumed that the increase is due to the presence of a diffusion-controlled process that appears to play an important role at low lactose concentrations. While the lactose concentration exceeds this limit, the rate of the whole oxidation process seems to be limited by

that of the catalytic process in origin and its rate depends on the reaction between lactose and Ni(III) species, which is present in the film.

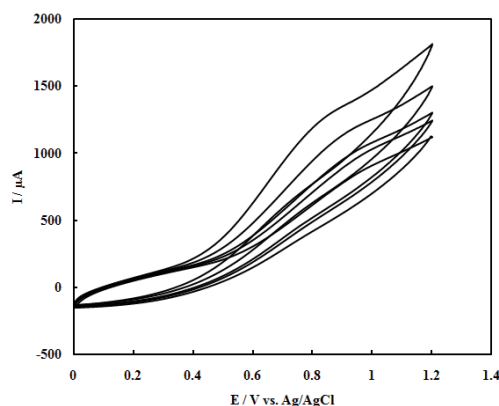


Fig.6. effect of lactose concentration on the anodic peak current at GC/MWCNTs/NiO modified electrode in 0.10M NaOH.

3.2.3. Chronoamperometric study

The electrocatalytic oxidation of lactose on the GC/MWCNTs/NiO modified electrode was studied using chronoamperometry. Double-step chronoamperograms were recorded by setting the working electrode potentials to the desired values used to measure the catalytic rate constant on the modified surfaces. Fig. 7 shows the double-step chronoamperograms for the GC/MWCNTs/NiO modified electrode in the absence and presence of different concentrations of lactose. The applied potential steps were 700 and -200 mV. The current was negligible when the potential decreased to -200 mV, indicating that the electrocatalytic oxidation processes were irreversible.

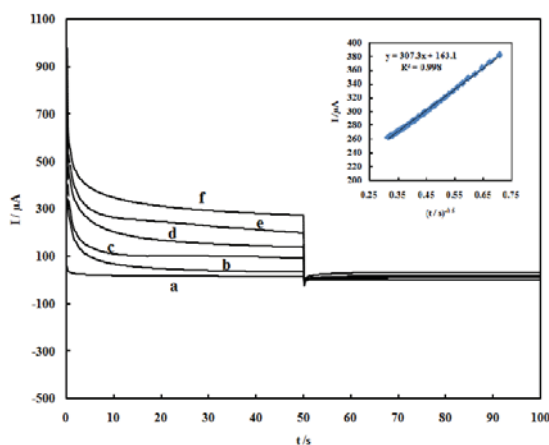


Fig.7. the double-step chronoamperograms for the GC/MWCNTs/NiO modified electrode in the absence and presence of different concentrations of lactose. The applied potential steps were 700 and -200 mV. Inset: plotting the net currents versus the minus square roots of time.

It was found that the current observed from chronoamperograms was in good agreement with the current observed from cyclic voltammetry. Also, the current increased as the lactose concentration increased (curves b to f). This result supported our conclusion about the catalytic



role of NiOOH for lactose oxidation that lactose oxidation started directly after the formation of the first amount of NiOOH on the electrode surface [23,29].

In the inset of Fig. 7, plotting the net currents versus the minus square roots of time results has linear dependencies. Therefore, a diffusion-controlled process is dominant for electrooxidation of lactose, as presented previously utilizing cyclic voltammetry (Fig.5). By means of the slopes of this line, the diffusion coefficients of the lactose can be obtained according to the Cottrell equation [28]:

$$I = \frac{nFAD^{1/2}C}{(\pi t)^{1/2}} \quad (6)$$

where D is the diffusion coefficient, and C is the bulk concentration of lactose. The mean value of the diffusion coefficient for lactose is $6.35 \times 10^{-5} \text{ cm}^2 \text{ s}^{-1}$.

Conclusion:

GC/MWCNT-NiO modified electrode was checked for electro-oxidation of lactose in alkaline medium. The electrode showed electrocatalytic oxidation for lactose. Chronoamperometric works showed a powerful anodic current at the oxidation potential of low-valence nickel hydroxide in further support of the mediated electro-oxidation. Using cyclic voltammetry and chronoamperometry techniques, the kinetic parameters of these drugs, such as charge-transfer coefficient and diffusion coefficient for oxidation, were determined.

References:

- [1] M.P. Coughlan, G.P Hazlewood, Hemicellulose and Hemicellulases, Portland Press, London, 1993.
- [2] J.L. Short, N.Z.J. Dairy Sci. Technol., 13 (1978) 181-185.
- [3] H.V. Udupa, K.S. Udupa, P. Subbiah, K. Jayaraman, T.D. Blakrishham and P. Thirunavakkarasu, Ind. Pat. IN 154413, 1984; Chem. Abstr. 104, 26212m.
- [4] P.J. Simms, K.B. Hicks, R.M. Haines, A.T. Hotchkiss, Jr. and S.F. Osman, J. Chromatogr., 667 (1994) 67-73.
- [5] G.G. Leppard and S. Ramamoorthy, Can. J. Bot., 53 (1975) 1729-1732.
- [6] G.M. Escandar, A.C. Olivier, M. Gonzalez-Sierra and L.F. Sala, J. Chem. Soc., Dalton Trans., 8 (1994) 1189-1192.
- [7] J.W. Slot and H.J. Geuze, Eur. J. Cell Biol. 38 (1985) 87-95.
- [8] M. Tominaga, T. Shiamzoe, M. Nagashima and I. Taniguchi, Electrochem. Commun. 7 (2005) 189-193.
- [9] B. Kutsch, O. Lyon, M. Schmitt, M. Mennig and H. Schmidt, J. Non Cryst. Solid. 217 (1997) 143-149.
- [10] G. Majumdar, M. Goswami, T.K. Sarma, A. Paul and A. Chattopadhyay, Langmuir 21 (2005) 1663-1668.
- [11] G.T.R. Palmore and H.-H. Kim, J. Electroanal. Chem. 464 (1999) 110-116.
- [12] A. Heller, Phys. Chem. Chem. Phys. 6 (2004) 209-212.
- [13] Kinoshita K. Carbon: electrochemical and physicochemical properties. New York: John & Wiley; 1987.
- [14] Hsieh CT, Teng H. , Carbon 2002;40(5): 667-74.
- [15] D. J. Guo, H. L. Li, Carbon, 2005,43, 1259-1263.
- [16] F. B. Zhang, Y. K. Zhou, H. L. Li, Mater. Chem. Phys. 2004, 83,260-265.



- [17] X. M. Liu, X. G. Zhang, *Electrochim. Acta* 2004, 49,229-235.
- [18] C. C. Hu, C. Y. Lin, T. C. Wen, *Mater. Chem. Phys.* 1996, 44, 233-240.
- [19] M. Asgari, M. Ghannadi Maragheh, R. Davarkhah, E. Lohrasbi, *J. The Electrochem. Soc.* 158 (12) (2011) K225-K229.
- [20] A. N. Golikand, M. Asgari, M. Ghannadi Maragheh, S. Shahrokhian, *J. Electroanal. Chem.* 588(2006)155-160.
- [21] A. N. Golikand, S. Shahrokhian, M. Asgari, M. Ghannadi Maragheh, L. Irannejad, A. Khanchi, *J. Power Sources* 144(2005)21-27.
- [22] A. Seghior, J. Chevalet, A. Barhoum, F. Lantelme, *J. Electroanal. Chem.* 442 (1998) 113-119.
- [23] A.A. El-Shafei, *J. Electroanal. Chem.* 471 (1999) 89-92.
- [24] G. Ve'rtes, G. Hora'ny, *J. Electroanal. Chem.* 52 (1974) 47-53.
- [25] P.M. Robertson, *J. Electroanal. Chem.* 111 (1980) 97-102.
- [26] J. Taraszewska, G. Rostonek, *J. Electroanal. Chem.* 364 (1994) 209-214.
- [27] J.A. Harrison, Z.A. Khan, The oxidation of hydrazine on platinum in acid solution, *J. Electroanal. Chem.* 28 (1970) 131-138.
- [28] A.J. Bard, L.R. Faulkner, *Electrochemical Methods*, Wiley, New York, 2001.
- [29] R. M. A. Tehrani, S. Ab Ghani , *Fuel Cells* 9(2009)579-583.



Hydrogen Evolution Reaction on Graphene Supported Pt Hollow Nanospheres

Reza Ojani*, Jahan-Bakhsh Raouf, Roudabeh Valiollahi

*Electroanalytical Chemistry Research Laboratory, Department of Analytical Chemistry,
Faculty of Chemistry, University of Mazandaran, Babolsar, Iran, 47415, P.O. BOX. 416*

E-mail address: fer-o@umz.ac.ir

Abstract

Platinum hollow nanospheres are synthesized by Co nanoparticles as sacrificial template and then immobilized on graphene nanosheets (HNPt/G). The prepared HNPt/G was used as electrocatalyst for hydrogen evolution reaction (HER). For this purpose, GC electrode modified by HNPt/G was fabricated (HNPt/G/GC). Electrochemical studies show that HNPt/G has a good electrocatalytic activity toward the hydrogen evolution reaction.

Keywords: Platinum hollow nanospheres, Graphene, Hydrogen evolution reaction, Electrocatalyst.

1. Introduction

Nowadays, fuel cells become promising power sources due to their environmental affinity and high energy conversion [1]. Comparing to oil, gasoline, methane, and liquefied petroleum gas, hydrogen is of high quality, clean, renewable and thus a promising fuel [2,3]. The product of its oxidation is only water that makes it a clean fuel. The hydrogen evolution reaction, whereby protons and electrons are combined into molecular hydrogen, has been extensively investigated [2,4]. Most of investigations are based on the introduction of new electrocatalyst reducing the overpotential of HER [5-8]. Platinum and platinum-based catalysts are the most effective catalyst toward HER. As the Pt is expensive and its supply is limited, the introduction of Pt catalyst with higher catalytic activity and lower Pt dosage is favorable. On way to reach this goal is a hollow structure construction. Nanoparticles with hollow interiors have advantages such as increased surface area, saving of materials, low density, cost reduction, and interesting special properties compared to their solid counterparts [9,10]. These favorable properties make them effective catalysts. It is well known that the supported metal nanoparticles are more efficient and show higher electrocatalytic activity than unsupported metal due to their large surface area on the supports [11]. Therefore, the support material is an important component of a catalyst.

Graphene, the parent of all graphitic structures ranging from graphite to carbon nanotubes (CNTs) and fullerenes, is a two dimensional material which contains of sp^2 carbon network with a thickness of one atom. It is highly expected as a cheap substitute for CNTs to provide a cost-effective platform for developing hybrid materials containing graphene and metal nanoparticles [12,13]. Graphene unlike rolled structure of CNTs has a two dimensional plane



sheet structure, so both sides of graphene sheets could be utilized as support for catalysts [14]. Therefore, it is expected as a favorable and more promising catalyst carrier.

In this paper, to utilize the advantages of Pt hollow nanospheres and graphene, the graphene supported Pt hollow nanospheres were synthesized and characterized. The electrochemical behavior of as-prepared nanostructure, as an electrocatalyst for HER, was studied.

2. Experimental

2.1. Chemical and reagents

The solvent used for the electrochemical studies was twice distilled water. Graphite powder (particle diameter = 0.1 mm), sodium borohydride, sulfuric acid, sodium nitrate and hexachloroplatinic (IV) acid hexahydrate were purchased from Merck. Sodium hydroxide was purchased from Fluka.

2.2. Instrumentation

The size of Pt solid nanoparticles was determined with an Easyscan2 Flex AFM (Switzerland). Electrochemical studies were performed in a three-electrode cell with HNpT/G/GC or NPt/G/GC as working electrodes, a Pt wire as counter electrode, and saturated calomel electrode (SCE) as reference electrode using a computer-controlled potentiostat/galvanostat (model IVIUM, CompactStat instrument, The Netherlands).

2.3. Preparation of catalyst

Graphene oxide (GO) was prepared with the Hummers method and purified from graphite powder [15], then chemical reduction of GO to graphene, using hydrazine monohydrate, was carried out [16].

Platinum hollow nanospheres were prepared according to the procedure that mentioned elsewhere [17]. For comparison, graphene supported solid Pt nanoparticles were synthesized. The Pt colloidal solution was synthesized according to Ref. [18] by using borohydride as reductant agent.

3. Results and discussion

3.1. Morphology and characterization

Fig. 1 shows TEM images of graphene nanosheets. As can be seen, they are rippled like a silk weave due to extremely small thickness of graphene suggesting a flexible structure of graphene sheets.

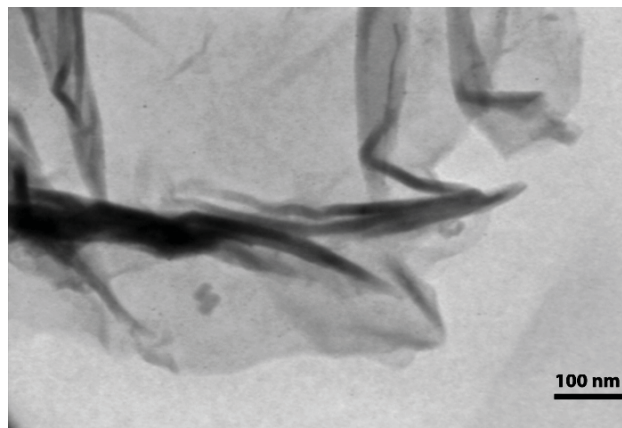


Figure 1. TEM image of graphene nanosheets

Fig. 2 shows the AFM image Pt nanoparticles. As shown, uniformly distributed spherical nanoparticles of Pt with an average diameter ranging from 12 nm to 60 nm, have been synthesized.

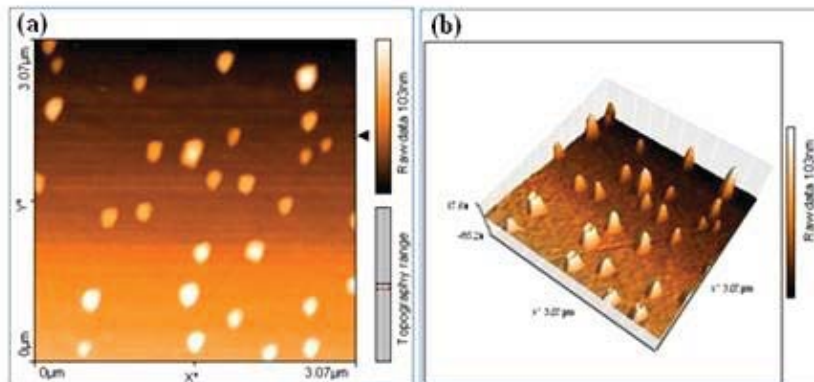


Figure 2. AFM image of (a) Pt nanoparticles, (b) 3D view

3.2. Active surface area estimation

The active surface area was estimated from coulombic charge for the hydrogen adsorption / desorption at the electrodes in H₂SO₄ solution using cyclic voltammetry according to eq. 2:

$$A_r = \frac{Q_H(\mu C)}{210} \quad (2)$$

The value of Q_H is the mean value between the amounts of charge transfer during the hydrogen adsorption / desorption, and 210 is the required charge for the oxidation a monolayer hydrogen adsorption on bright Pt [19]. Cyclic voltammograms of HNpT/G/GC (curve a) and NpT/G/GC

(curve b) are shown in Fig. 3. The real surface area of HNPt/G/GC and NPt/G/GC were estimated as 0.07 and 0.026 cm², respectively.

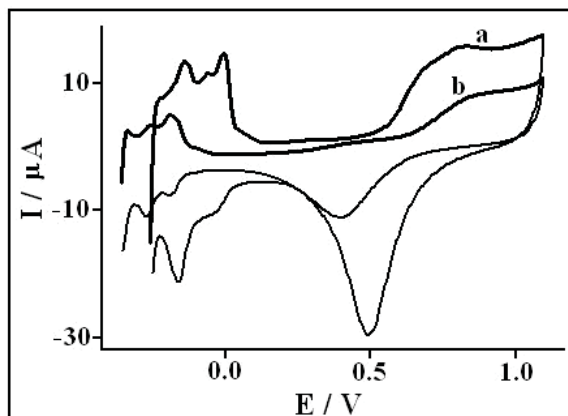


Fig. 3. Cyclic voltammograms of (a) HNPt/G/GC and (b) NPt/G/GC electrodes in 0.5 M H₂SO₄. Sweep rate was 50 mV s⁻¹.

3.3. Electrochemical behavior of [Fe(CN)₆]^{3-/4-} at the modified electrodes

3.3.1. Cyclic voltammetry

Cyclic voltammetry of [Fe(CN)₆]^{3-/4-} at bare GC, G/GC, NPt/G/GC, and HNPt/G/GC electrodes were performed (Fig. 4). As results show, modification of the GC electrode by graphene increases the redox current. This increase is due to the good conductivity of graphene that facilitates the electron transfer. The currents are increased more when the electrode is modified by NPt/G. This is because of the integration of good conductivity of graphene and Pt nanoparticles. The highest currents are achieved at HNPt/G/GC. This increase is due to the higher conductivity of Pt hollow nanostructure than the others that facilitate the electron transfer process.

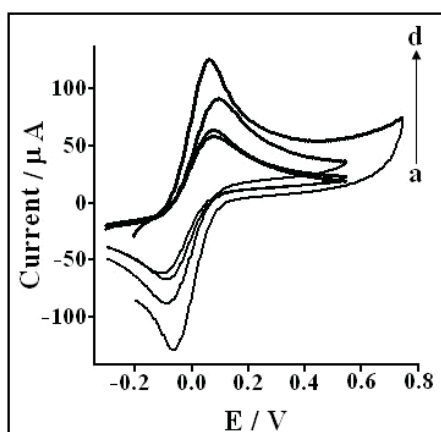


Fig. 4. Cyclic voltammograms of (a) Bare GC, (b) G/GC, (c) NPt/G/GC, and (d) HNPt/G/GC in 0.01 M [Fe(CN)₆]^{3-/4-} + 0.1 M KCl solution. Sweep rate was 0.1 V s⁻¹.

3.3.2. Electrochemical impedance spectroscopy

Fig. 5 shows normalized Nyquist plots for bare GC, G/GC, NPt/G/GC, and HNpT/G/GC electrodes. The slope of plot increases when the electrode was modified by graphene, NPt/G, and HNpT/G. The increase in the slope shows that the electron transfer rate is facilitated. As can be seen in Fig. 5, the best electron transfer is achieved at HNpT/G/GC electrode. These results are in agreement with cyclic voltammograms.

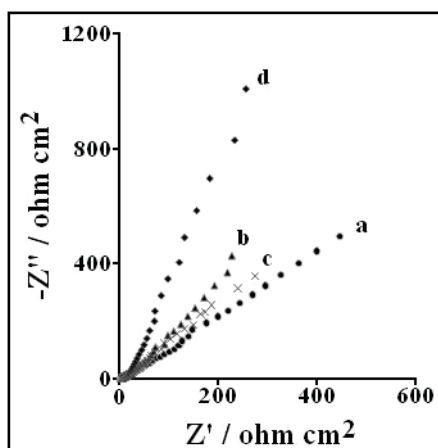


Fig. 5. Normalized Nyquist plots for (a) Bare GC, (b) G/GC, (c) NPt/G/GC, (d) and HNpT/G/GC in 0.01 M $[\text{Fe}(\text{CN})_6]^{3-/4-}$ + 0.1 M KCl solution.

3.4. Electrocatalytic behavior of modified electrodes toward HER

Fig. 6 shows HER at the surface of bare GC (curve a), G/GC (curve b), NPt/G/GC (curve c), and HNpT/G/GC (curve d). As can be seen, when the electrode is modified by graphene, the current density is lightly increased. By modification with NPt/G, the current density is increased and the onset potential is shifted to less negative amounts. This can be attributed to the electrocatalytic activity of Pt nanoparticles toward HER. When the GC electrode is modified by HNpT/G, the current density is the highest and onset potential is the less negative amount than the others. This behavior is due to the better electrocatalytic activity of hollow nanostructure compared with solid nanostructure.

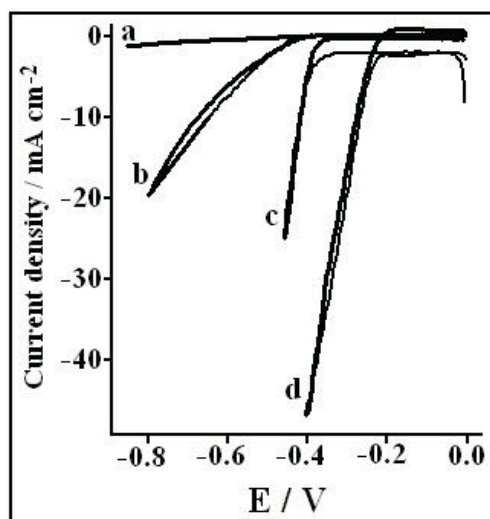


Fig. 6. Cyclic voltammograms of HER at (a) Bare GC, (b) G/GC, (c) NPt/G/GC, and (d) HNpT/G/GC in 0.5 M H₂SO₄ solution. Sweep rate was 50 mV s⁻¹. (Onset potentials: Bare GC: -0.6, G/GC: -4.4, NPt/G/GC: -3.5, HNpT/G/GC: -0.2 V/SCE).

3.5. Linear sweep voltammetry at different concentrations of H₂SO₄

The effect of H₂SO₄ concentration on electrode response was investigated by linear sweep voltammetry technique (LSV). Fig. 7A shows the voltammograms at HNpT/G/GC and Fig. 7B shows the voltammograms at NPt/G/GC. As can be seen, by increasing the H₂SO₄ concentration, the current density increases. The dependence of current density to H₂SO₄ concentration is shown in Fig. 8. The obtained slope at HNpT/G/GC is 1.4 times higher than that of NPt/G/GC. This can be attributed to higher catalytic activity of HNpT than that of NPt.

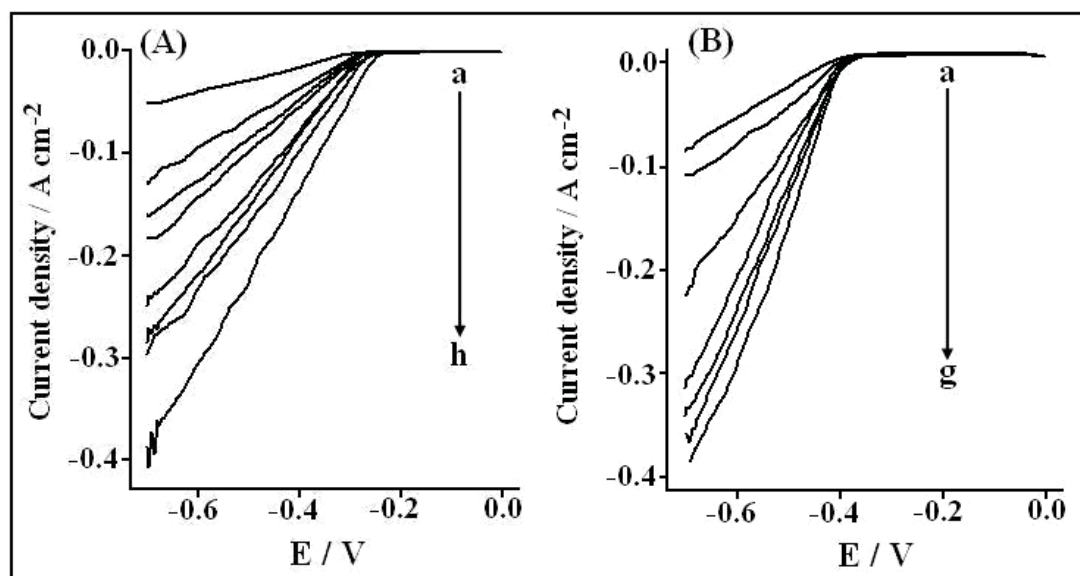


Fig. 7. Linear sweep voltammograms of H₂SO₄ at different concentrations: (A) On HNpT/G/GC; a: 0.1, b: 0.2, c: 0.3, d:0.4, e: 0.5, f: 0.6, g: 0.9, and h: 1 M. (B) On NPt/G/GC; a: 0.1, b: 0.2, c: 0.4, d:0.6, e: 0.7, f: 0.8, and g: 1 M. sweep rate was 50 mV s⁻¹.

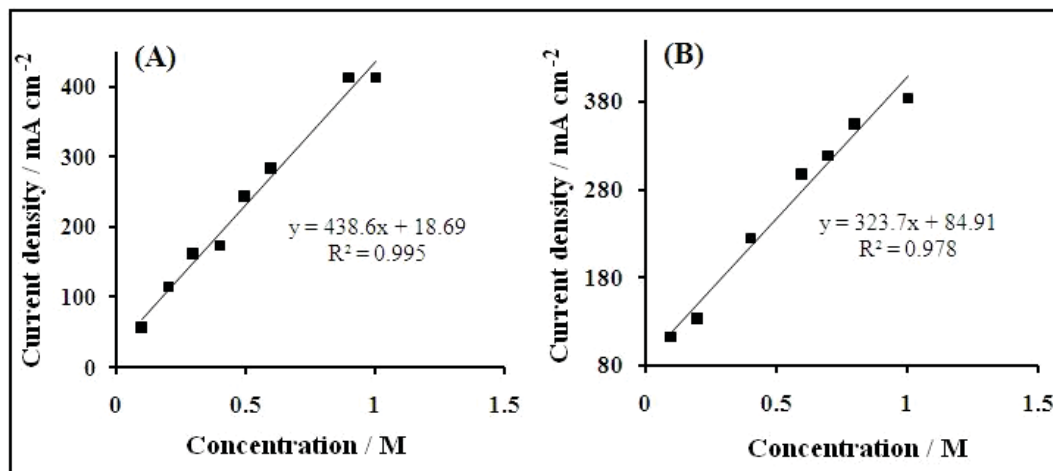


Fig. 8. The peak current density versus H₂SO₄ concentration on (A) HNpT/G/GC and (b) NPt/G/GC. The black squares indicate experimental data; the lines indicate regression.

3.6. Chronoamperometry

For test the electrocatalytic activity and stability of a catalyst, chronoamperometry was employed as a suitable technique. Fig. 9, shows chronoamperograms of 0.5 M H₂SO₄ at HNpT/G/GC and NPt/G/GC. As results show, the steady state of the current density is higher at HNpT/G/GC. This shows the better electrocatalytic activity of HNpT/G. Also, chronoamperometry for long time experiment shows acceptable stability for this catalyst.

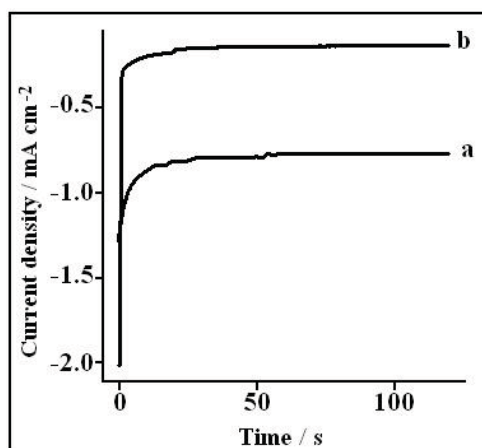


Figure 9. Chronoamperograms of (a) HNpT/G/GC and (b) NPt/G/GC in 0.5 M H₂SO₄ solution.

4. Conclusion

In summery, Pt hollow nanospheres decorated on graphene nanosheets were synthesized and characterized. The as-prepared nanostructure was used as electrocatalyst for HER. Results showed that HNpT/G have a better electrocatalytic activity than NPt/G toward HER.



References:

- [1] B. Liu, H.Y. Li, L. Die, X.H. Zhang, Z. Fan and J.H. Chen "Carbon nanotubes supported PtPd hollow nanospheres for formic acid electrooxidation", *J. Power Sources*, (2009). 186 (1), 62-66.
- [2] E.A. Baranova, A. Cally, A. Allagui, S. Ntais and R. Wüthrich "Nickel particles with increased catalytic activity towards hydrogen evolution reaction", *Comptes Rendus Chimie*, (0).
- [3] A. Abbaspour and E. Mirahmadi "Electrocatalytic hydrogen evolution reaction on carbon paste electrode modified with Ni ferrite nanoparticles", *Fuel*, (2013). 104 (0), 575-582.
- [4] J.B. Raouf, R. Ojani, S.A. Esfeden and S.R. Nadimi "Fabrication of bimetallic Cu/Pt nanoparticles modified glassy carbon electrode and its catalytic activity toward hydrogen evolution reaction", *International Journal of Hydrogen Energy*, (2010). 35 (9), 3937-3944.
- [5] H. Dong, T. Lei, Y. He, N. Xu, B. Huang and C.T. Liu "Electrochemical performance of porous Ni₃Al electrodes for hydrogen evolution reaction", *International Journal of Hydrogen Energy*, (2011). 36 (19), 12112-12120.
- [6] A. Kiani and S. Hatami "Fabrication of platinum coated nanoporous gold film electrode: A nanostructured ultra low-platinum loading electrocatalyst for hydrogen evolution reaction", *International Journal of Hydrogen Energy*, (2010). 35 (11), 5202-5209.
- [7] B. Habibi, M.H. Pournaghi-Azar, H. Razmi and H. Abdolmohammad-Zadeh "Electrochemical preparation of a novel, effective and low cost catalytic surface for hydrogen evolution reaction", *International Journal of Hydrogen Energy*, (2008). 33 (11), 2668-2678.
- [8] M. Wu, P.K. Shen, Z. Wei, S. Song and M. Nie "High activity PtPd-WC/C electrocatalyst for hydrogen evolution reaction", *J. Power Sources*, (2007). 166 (2), 310-316.
- [9] X.-W. Zhou, R.-H. Zhang, Z.-Y. Zhou and S.-G. Sun "Preparation of PtNi hollow nanospheres for the electrocatalytic oxidation of methanol", *J. Power Sources*, (2011). 196 (14), 5844-5848.
- [10] D.-J. Guo, L. Zhao, X.-P. Qiu, L.-Q. Chen and W.-T. Zhu "Novel hollow PtRu nanospheres supported on multi-walled carbon nanotube for methanol electrooxidation", *J. Power Sources*, (2008). 177 (2), 334-338.
- [11] N. Chakroune, G. Viau, S. Ammar, L. Poul, D. Veautier, M.M. Chehimi, C. Mangeney, F. Villain and F. Fiévet "Acetate- and Thiol-Capped Monodisperse Ruthenium Nanoparticles: XPS, XAS, and HRTEM Studies", *Langmuir*, (2005). 21 (15), 6788-6796.
- [12] Q. Cheng, J. Tang, J. Ma, H. Zhang, N. Shinya and L.-C. Qin "Graphene and nanostructured MnO₂ composite electrodes for supercapacitors", *Carbon*, (2011). 49 (9), 2917-2925.
- [13] T.A. Pham, B.C. Choi, K.T. Lim and Y.T. Jeong "A simple approach for immobilization of gold nanoparticles on graphene oxide sheets by covalent bonding", *Applied Surface Science*, (2011). 257 (8), 3350-3357.
- [14] J. Luo, S. Jiang, H. Zhang, J. Jiang and X. Liu "A novel non-enzymatic glucose sensor based on Cu nanoparticle modified graphene sheets electrode", *Analytica Chimica Acta*, (2012). 709 (0), 47-53.
- [15] W.S. Hummers and R.E. Offeman "Preparation of Graphitic Oxide", *Journal of the American Chemical Society*, (1958). 80 1339-1339.
- [16] J. Luo, S. Jiang, H. Zhang, J. Jiang and X. Liu "A novel non-enzymatic glucose sensor based on Cu nanoparticle modified graphene sheets electrode", *Analytica Chimica Acta*, (2012). 709 47- 53.
- [17] L. Yi, Y. Song, W. Yi, X. Wang, H. Wang, P. He and B. Hu "Carbon supported Pt hollow nanospheres as anode catalysts for direct borohydride-hydrogen peroxide fuel cells", *International Journal of Hydrogen Energy*, (2011). 36 11512-11518.



- [18] X. Xiao and A.J. Bard "Observing Single Nanoparticle Collisions at an Ultramicroelectrode by Electrocatalytic Amplification", J. Am. Chem. Soc., (2007). 129 9610-9612.
- [19] L. Yi, Y. Song, W. Yi, X. Wang, H. Wang, P. He and B. Hu "Carbon supported Pt hollow nanospheres as anode catalysts for direct borohydride-hydrogen peroxide fuel cells", International Journal of Hydrogen Energy, (2011). 36 (18), 11512-11518.



Designing H4KIDS software for hydrogen energy teaching to children

Rasol Abdullah Mirzaei¹, Javad Hatami², Farmand Farzin³

*Fuel cell research laboratory, Department of Chemistry, Faculty of Science, Shahid Rajaei teacher training University, Tehran, Iran
mirzai_r@yahoo.com*

Abstract

The use of computer-based methods and tools for teaching is especially important for the development of those new courses related to non-traditional topics. It is predicted that in future, production and consumption of hydrogen as a factor for carrying energy will be transmitted around world economy and "hydrogen economy " will be stabilized. For introducing this new concept to children, H4KIDS software was designed. The goal of this software (H4KIDS) is attractive training of basic concept of hydrogen energy to children and facilitation of their learning. For designing process, Hatami model and Mayer multimedia design principles have been used in designing of this software. Six steps in learning of hydrogen energy concepts were considered. In each step, cognitive, emotional and behavioral dimensions were included. In this paper, it would be discussed more.

Keywords: Instructional multimedia, hydrogen energy education, fuel cell, Hatami model, software, children.

1- Introduction

In 1997, convention of climatic changes proposed Kyoto protocol with the goal of stabilizing greenhouse gases density in atmosphere. According to this protocol, industrial countries have been bound to reduce emission of greenhouse gases density in atmosphere in order to prevent dangerous interference of human activities with climatic system. And such a level will be applicable in suitable time framework because ecosystems adjust themselves with climatic change naturally and it is made sure that there is no threat for food security and economic development is formed constantly. On the other hand, Set of renewable energies is playing more roles in system of supplying world energy increasingly. Therefore, an important role has been devolved upon renewable sources of energy. One of the best renewable energies is hydrogen energy. Hydrogen energy system is a stable, permanent, in destructible, comprehensive and renewable system due to independence from initial sources of energy. Now this question is propounded: "How and when can a step be taken for using renewable energies specially hydrogen energy and fuel cell?" Well, certainly the first step is instruction

¹ - Fuel cell research laboratory, Department of Chemistry, Faculty of Science, Shahid Rajaei teacher training University, Tehran, Iran

² - Dep. Of education , Faculty of Humanities Science Tarbiat Modares University, , Tehran, Iran

³ - M. Sc. student of chemistry education, Shahid Rajaei teacher training University, Tehran, Iran,
farmandfarzin@gmail.com



and culture-making that if it begins from lower levels, then its result will be better in adulthood. Today creative child will be tomorrow active teacher or engineer who can move the wheels of country with his/her new plans and ideas. Importance of training and instruction in initial periods is so remarkable which its reflection is completely clear in all discussions and scientific researches and instructional plans of school. Instruction in childhood is considered in terms of two aspects: first, sensitivity and facilitation of children flexibility from instructional environments. Second, effects permanency and depth of their learning's in this period.

Perhaps, using computer technology can give happiness and enjoyment to classes in elementary schools. Computer helps children of this period to learn lessons details and book contents well. Instruction of hydrogen energy and fuel cells by computer and computer conversations and electronic meetings can help lesson planning and class activities very much. Among educational periods, elementary period is one of the most sensitive instructional periods. Investments of developed countries and employing experienced people in this period prove this claim. [1]

2- Process Integration and computer aided engineering education

Embedding the aspects of Process Systems Engineering within Energy Engineering Education is crucial for achieving adequate educational results. Having in mind the overall importance of computer- aided education; there are several prerequisites for the successful implementation of computer-aided methods and tools. A very important aspect is also the development of new advanced tools, both within professional computer development companies and academic institutions [2]. Very recent techniques in multimedia internet-based teaching and learning [3] combining text, still images, video, animation, and interactivity to enhance both visual and verbal communications, and the development of different cyber-applications, e.g. hub cyber infrastructure for collaboration in research and education [4], a virtual library for process systems engineering as a Pan-American initiative [5], an initiated virtual library at EURECHA [6], and a virtual environment for problem formulations and algorithmic developments (Cyber-MINLP) by Grossmann and co-workers [7], are some of the recent examples of how methods and tools for teaching can be successfully implemented and applied to chemical engineering education[2].

3- Hydrogen in school education

Presentations about hydrogen in the classroom usually bear a spectacular atmosphere. Most pupils will never forget the Knallgas “explosion” and are attracted from the story around the Zeppelin disaster at Lakehurst. However, time changes. Nowadays, hydrogen is not anymore claimed to have caused the Lakehurst disaster. New investigations showed that the painting used was highly flammable and had a low electric conductivity, causing an electrostatic discharge and spread of flames [8] and we are now facing hydrogen as a friendly and clean energy carrier. In fact, modern school education focuses not anymore primarily on the chemical element hydrogen, but often starts to take its new role in energy systems into



account. Additionally, a fast growing and broad range of educational information about hydrogen and fuel cell technology is available from bookstores and the Internet (see for example the Internet presentations of the following organizations: British Columbia Hydro and Power Authority, Canada; FuelCellStore.com, USA; Hydrogen Energy Center, USA; L-B-Systemtechnik GmbH , Germany; Deutscher Wassersto2 Verband , Germany). It should, however, be noted that teaching hydrogen energy technology at middle and high schools is not compulsory yet and only few curricula explicitly mention it [9].

4- Designing software H4KIDS

Multimedia design of software H4KIDS is based on principles of Mayer design. Principles of Mayer multimedia design (2001) have been summarized in table 1 [10].

5- Hatami model for instruction

Hatami model has been designed by Dr.Javad Hatami. This model mainly results from structuralism instructions but it is not limited to that case. The goal of designing this model has been improving quality of perspectives instruction in curriculum of Iran Ministry of education. Among available approaches about theories of learning, structuralism approach is more conformable to discussion of perspectives instruction. Therefore, principal standards in Hatami model are mainly those standards in theories of structuralism learning, but Hatami model is not limited to structuralism approach; it means that although structuralism framework has been considered for its design, but with regard to instruction principles and changing approach factors and dominant rules on it, researcher uses each principle of being Hatami, is an active learner in process of training-learning. One of special features of Hatami model is its emphasis on Initial technique. The mentioned principle is from institutional principles in approach of structuralize learning too. In the past this model has been studied with the goal of instruction of social perspectives as instructional computer program in educational year 83-84 for middle schools with a sample composed of 368 students on both sexes (girl and boy) and in comparison with available model in text book.

Results of the research show that there is no difference between cognitive dimensions of social viewpoints with available model in instruction. But there is a significant difference in influencing on the other approach dimensions (feeling and behavior) and effect of Hatami model is more than available model [11]. The main hypothesis of Hatami model about order and succession of instruction is an instruction based on previous knowledge of learners. Therefore providing internal and external conditions is recommended. After providing a short and brief pre. Organizer learners should confront an issue resulting from in attention to hidden rules and values in the new approach. Proposing issue (problem) should be completely expressive and preferably by audiovisual media. Stated problem should be completely clear and influence emotional and excitable dimension of audience. Of course using techniques and artistic elegances is very necessary for stating the problem more eloquently.

Using examples and analogies can help better learning in cognitive dimension of learners. (Hatami from quotation of Kamradt and Kamradt 1999 page 567) [12].



After making issue (problem) situation method of question and answer can be used as one of the effective methods. With regard to this matter that learners have confronted the problem method of group discussion has been used for cooperation and enjoying the others ideas and increases

Richness of training–learning process. Naturally this process activates method of cooperative learning too. By this way students discover and solve the problems. If instruction is provided by interactive media then forming an interactive environment and techniques of instructional design must be done with the best way and by better artistic techniques like design and proportion of pictures music sound and effect and special effects. Hatami model about general approaches of instruction emphasizes some points such as: instructing practice and feedback of an active student and planning for cognitive approaches of learning.

It is one of the main parts of Hatami model. Initial evaluation as pre- test is very necessary. The goal of pre- test is determination of situation and viewpoint quality of instruction case in learners. In the instruction learners will be evaluated too.it must be said that kind of question or methods of tester in pre-test and post-test should include three dimensions (cognitive, emotional and behavioral). If the results of this evaluation are not satisfactory in terms of reaching to the goals, then step or used cases must be improved. And if appositive feedback emerges, then reinforcement of element and used approaches will be necessary for obtaining a dynamic and optimum model. Figure 1 show elements, steps and processes related to Hatami model.

5-1 Applying Hatami model in software H4KIDS

Hatami model has been presented for different steps of software H4KIDS (the following).

5-1-1- page of pre-test

In this page which is the first page of multi-media, beginning icon emerges after 2 seconds. Student can observe a clip by clicking on it. This clip repeats progressive method in this page. Work method is as follows: student confronts pretest icon after observing clip and closing its window. After participating in test, if he/she acquires score quorum, then he/she can go to the next step. Otherwise, he/she must observe a site and take the key after finding answer of questions. However, in case of non-accessing, he/she can study mobile books or software license, too.



Table1- Based primarily on Mayer's research (2001)

Multimedia Principles	Effect on Learning
Multimedia best use of words & pictures	Adding graphics to words can improve learning. Students learn better from words and pictures, rather than from words alone.
Spatial Contiguity best placement of words & pictures	Placing text near graphics improves learning. Students learn better when corresponding words and pictures are presented near rather than far from each other.
Temporal Contiguity best sequencing of words & pictures	Students learn better when corresponding words and pictures are presented simultaneously rather than successively.
Coherence "less is more"	Using gratuitous visuals, text, and sounds can hurt learning. Students learn better when extraneous words, pictures and sounds are excluded rather than included. Less is more: eye or ear "candy" can distract and actually hurt instruction by causing cognitive overload. <ul style="list-style-type: none"> ▶ Visual: Student learning is hurt when interesting but irrelevant words and pictures are added to a multimedia presentation. ▶ Sound: Student learning is hurt when interesting but irrelevant sounds and music are added to a multimedia presentation. ▶ Words: Student learning is improved when unneeded words are eliminated from a multimedia presentation.
Modality best use of visual and auditory channels	Explaining graphics with audio improves learning. Students learn better from animation and narration, than from animation and on-screen text.
Redundancy best use of text and audio	Explaining graphics with audio and redundant text can hurt learning. Avoid reading on-screen text. Students learn better from animation and narration, than from animation, narration, and on-screen text.
Individual Differences best use of prior knowledge	Design effects are stronger for low-knowledge learners than for high-knowledge learners and for high-spatial learner than than for low-spatial learners. These learners are equipped to use cognitive strategy to work around cognitive overload, distraction, or other effects of poor design.
Practice best interactions for learning	Frequent, distributed, problem-solving, job-context practice improves learning and transfer.
Learner Control vs. Program Control best navigation scheme	Most students learn more under program control. Adult learners require a sense of control to be able to establish a self-paced learning process.
Personalization engaging the learner	Use of conversational tone and pedagogical agents can increase learning

5-1-2- first step: H is sign of hydrogen

According to Hatami model, after doing pre-test, learners must confront the problem. And after providing pre-organizer and discussing without any partiality against initial viewpoints (approaches) and temporary accompaniment with them, real samples related to the topic must be provided to them. After wards, mental unrest is created for learner by asking question and



finally subjects adding up and agreement about correct solutions will be done. In addition, instruction goals in the step of instructional design are completely clear. Goals and instructional components of this step are as follows.

A) Cognitive dimension

- Student understands physical feature of hydrogen.
- Student knows hydrogen sign.
- Student knows structure of water molecule as one of the sources of hydrogen production.

B) Emotional dimension

- Student will be interested in studying about hydrogen.

C) Behavioral dimension

- Student should have skill in using computer and internet.
- Student should have skill in making practical work with simple and every day tools.
- Student uses internet as a tool for communicating with others and for seeking solution of his/her scientific and lesson problems.

In this step which is done after initial pre-test, the following concepts will be learnt by using an instructional clip which has role of a pre-organizer, too.

- Hydrogen is the lightest and the most abundant element in the world.
- Sign of hydrogen is H.
- Hydrogen is an odorless, colorless and tasteless gas.
- Water is made of two atoms of hydrogen.

After observing the clip, student confronts problem situation in a game. Not only, this game shows difference of hydrogen fuel with gasoline but also it causes student to get acquainted with hydrogen sign. With passing this step, student enters album section. Here, he/she must watch pictures in order to think and find similar pictures to H around him/her and share it with his/her friends in chat room in the next steps. The next section of this step is making a handiwork. And if he/she does it with the help of his/her friends, then cooperative learning will happen, too.

In the other section which is assessment of this step, all goals of this chapter will be questioned. If student obtains acceptance quorum in the test, he/she will go to the next step. Otherwise, he/she should go to "more practice" section. There, after observing chat room, he/she can find the answer of his/her question from others or seek it in the site.



If he/she does not have access to the internet, he/she can refer to mobile books or software license for solving his/her problem. In the end part, learner can go to page of receiving letter of appreciation by selecting continuation button. Letter of appreciation can print this step directly or save it its computer. Relevance of parts of this step is clear in figure 3.

5-1-3- second step: why hydrogen?

This step has been designed according to Hatami model (like previous step). All steps of Hatami model are exactly similar to previous step. But the goals and instructional components of this step are as follows:

A) Cognitive dimension

- Student should get acquainted with fuel cell.
- Student should know sources of renewable and non-renewable energy and give some examples for them.

B) Emotional dimension

- student should get acquainted with phenomenon of increasing greenhouse gases and he/she knows that is responsible to solve this global problem.
- After observing pictures related to the earth heat and being informed from its environmental effects, student should consider himself/herself responsible.

C) Behavioral dimension

- Student should have skill in making a handiwork for informing his/her friends about sources of renewable and non- renewable energies.
- Student should have skill in using computer and internet.
- Student should use the internet as a tool for communicating with others and for seeking his/her scientific and lesson solutions.

And some concepts which will be learnt in this step are as follows: fuel cell is a tool which can produce electricity by mixture of hydrogen and oxygen.

-In cycle of gasoline production and consumption, there are many environmental dangers for the environment. (Such as greenhouse gas resulting from gasoline burning and the other fossil fuels and also dangers resulting from emitting raw oil to the sea and)

-greenhouse effect is the name of a phenomenon which is formed due to greenhouse gases like CO₂. CO₂ can be formed due to burning fossil fuels, too. In this phenomenon, greenhouse gases act as greenhouse glass (i.e. they let the sunlight to enter the earth atmosphere but prevent the exit of its heat). Consequently it causes to heat the earth more.



There is greenhouse effect in the earth naturally and the most important advantage of it that if the earth didn't have it, this could cause earth temperature to earth -2°F (instead of 57°F)! On the other hand, increasing greenhouse gases causes to increase the earth very much.

-sources of renewable energy are sources which are referable and their reproduction doesn't need much time , for example: solar energy , wind energy , thermal energy of the earth , biomass , energy of sea waves ,

-sources of non-renewable energy are sources which are not reproducible after consumption or their reproduction spends million years.

-hydrogen is found in the water and air, too. And it can be extracted by renewable energies.

In the step of instructional game, learner gets acquainted with all renewable energies and avoids approaching fossil fuels. Problem situation of this game is very effective on the students. In addition, in album part, learner thinks and controverts about relevant pictures with lesson goals. The other steps are similar to previous step, too .but they have been designed with regard to subject and the goals of this step.

5-1-4- third step: energy measurement

Steps of Hatami model of this step are similar to the previous steps, too. It means that instructional film is as pre organizer and maker of problem situation and album has role of thought and forming controversy and cooperative learning. However, cooperative learning and discovery will be specified clearly in the test section. All steps are similar to previous step with this difference that game step and practical work (handiwork) have been deleted. But students painting have been used in album section. And learners have been requested to draw their ideas about renewable energies and send them to e-mailed address in order to been shown in software backup site. Assessment section unlike the other steps has two tests that student can enjoy an older person or his/her friend for answering them. Using calculator is permissible in this test, too. The rules for passing this test are similar to the previous steps. There is section of receiving letter of appreciation after passing the test (like previous steps) that learners can print it directly or save in their computer.

Goals and in structional components of this step are as follows:

A) Cognitive dimension

-Student should interpret his/her observations correctly.

-Student should get acquainted with the other usages of hydrogen in life.

B) Emotional dimension

-Student should be responsible in group work.

-Based on answers of his/her tests, student should interpret and conclude that hydrogen is more suitable and economical replacement than fossil fuels.



C) Behavioral dimension:

- Student should have skill in using computer and internet.
- Student should use internet as a tool for communicating with others and seeking solution for his/her scientific and lesson problems.

Concepts which will be trained in this step are as follows:

- hydrogen produces the most energy in weight unit than the other fuels.
- Hydrogen is used in making glass, soap, vitamins, toothpaste and herbal oil.

Relevance of sections of this step has been shown in figure5, briefly.

5-1-5- fourth step: Hydrogen economy

The hydrogen economy promises to eliminate environmental problems fossil fuel economy has created worldwide. Specifically, the hydrogen economy may be even more beneficial to developing countries because it will generate economic opportunities, reduce poverty and offer a dramatically cleaner renewable resource. Each individual could become the producer as well as the consumer of their energy. There are good national examples to look at for new energy inspiration. Icelanders are working towards creating the world's first hydrogen society. In addition to various demonstrations of hydrogen and fuel cell technologies, Iceland is utilizing its geothermal energy potential to power its transportation system. Virtually all of its electricity and heating comes from hydroelectric power and the geothermal water reserves. [13]

Step of Hatami model have been performed similar to previous step, too. It means that after forming internal conditions in the test of previous step which is considered as a pre-organizer for this step, external conditions and stimulation of learners' emotional dimension will be formed by a clip in the beginning the step. Of course, no special partiality is done against learners' viewpoint (approaches) which is initial. After observing album, learners find an opportunity to deliberate. And after passing this step of test, if there is problem, they can go to chat room (like the previous step). It causes to reinforce problem-solving skill in student.

Goals and instructional component of this step are as follows:

A) Cognitive dimension:

- student should get acquainted with hydrogen economy and its goals.
- student should get acquainted with advantages of group work from cooperation level with his/her friends to international level and countries cooperation for solving global problems.

B) Emotional dimension.



-After getting acquainted with global problems student should be responsible to their solution.

C) Behavioral dimension

-student should have skill in using computer and internet.

-student should use internet as a tool for communicating with others and seeking solution for his/her scientific and lesson problems.

And concepts of this step are as follows:

Hydrogen economy wants to extract hydrogen by renewable sources and replace hydrogen instead of fossil fuel in future. Some factors which cause hydrogen economy to follow such a goal are as follows:

1- Oil problem and limitation of its sources

2- Air pollution

3- Global environmental dangers.

- Cooperation and interaction among different industries and even different countries are necessary for succeeding in goals of hydrogen economy. For example a company which is producer of hydrogen tanks can cooperate with an automobile – making company and a company which is transferor of hydrogen to the fuel stations and they can found a hydrogen economy together.

You can observe relevance of different sections of this step in figure 6 too.

5-1-6- Fifth step: fueling change

Hatami model of this step is similar to the previous steps too.

Instructional goals and components of instruction in this step are as follows:

A) Cognitive dimension:

- Student should get acquainted with fuels history.

B) Emotional dimension:

Student should evaluate social economical and environmental effects resulting from fossil and hydrogen fuels by collection information.

C) Behavioral dimension:

-Student should have skill in using computer and internet.



- Student should use internet as a tool for communicating with others and seeking solution for his/her scientific and lesson problems.

5-1-7- Sixth step: why hydrogen will fuel the future?

This step is final step of multimedia and it has been founded based on Hatami model (like previous steps) too. After finishing this step title “Hydrogen scientist “is given to the learner.

Instructional goals of this step are as follows:

A) Cognitive dimension:

- Student should predict by information.

B) Emotional dimension:

Student studies hydrogen benefits in using energy source in future by group work and collecting information.

C) Behavioral dimension:

- Student should have skill in using computer and internet.

- Student should use internet as a tool for communicating with others and seeking solution for his/her scientific and lesson problems.

Concepts of this step are as follows:

- Hydrogen is the most abundant element in the world and doesn't have special pollution too.

- Benefits or advantages of using hydrogen in future are as follows:

1- Cleaner environment

2- Improving efficiency and output of energy.

3- Reducing fluctuations of price and economic growth.

6- Discussion and conclusion

Nowadays, thought about some means which help instruction, media and computers has been globalized. And most of the countries have invested in this domain. These means help teaching, cause motivation and answerless, and increases speed of training-learning process. Under present conditions, learning is necessary (i.e. learning which is not limited to age, place and time). Permanent learning means continuous cycle form formal instruction to adulthood and independent learning during life by available opportunities (formal and informal). This powerful strategy is related to all age groups from the old to the young. Prerequisite and main factor of permanent learning is being equipped to information technology and using its tools and multi-sense media is one of their effective forms. Using



computer at schools specially elementary schools opens a new way for training-learning process in Education system. Which according it a special novelty emerges at schools that its result is class attractiveness creativity in selecting lesson content and different teachers method of teaching. According to studies in this research it was specified that using software H4KIDS could transfer its contents to children and also it could provide required skills for preparation to change viewpoint (approach) for adjusting with continuous transformations of knowledge technology expansion and consecutive change in life conditions for children one of these skills is getting acquainted and enjoying electronic means of instruction like cell phone computer and internet by children which all of them are foundations of software.

References

- [1] Seif ,Ali Akbar,(2009)Educational psychology, Tehran· Agah publication.
- [۲] Jaromir Klemeš, J. Kravanja, Z . Sabev Varbanov, P. Loong Lam, H. Advanced multimedia engineering education in energy, process integration and optimization. doi:10.1016/j.apenergy.2012.01.039
- [۳] Klemeš JJ, Kravanja Z, Lam HL, Varbanov PS. The role of structured multimedia internet based teaching programs in sustainability education. In: Proceedings of ICOSSE'11, Tucson, Arizona, Session 12, January 912; 2011.
- [۴] Reklaitis GV. Hub cyber infrastructure for collaboration in research and education. EURECHA session at ESCAPE-18. <bari.upc.es/eurecha/docs/Reklaitis.6.08.pps> [accessed 22.11.11].
- [۵] Grossmann IE. Pan American Advanced Study Institute and Virtual Libraries on PSE. EURECHA session at ESCAPE-19. <bari.upc.es/eurecha/docs/PASIESCAPE_Ignacio_Grossmann.ppt> [accessed 22.11.11].
- [6] The EURECHA. <bari.upc.es/eurecha> [accessed 22.11.11].
- [۷] Grossmann IE. Cyber-MINLP: a virtual environment for problem formulations and algorithmic developments. EURECHA session at ESCAPE-20. <bari.upc.es/eurecha/docs/EURECHA_Session_at_ESCAPE_Ignacio_Grossmann.pdf> [accessed 22.11.11].
- [8] Bain A, Van Vorst WD. The Hindenburg tragedy revisited: the fatal flaw found Int J Hydrogen Energy 1999;24:399–403.
- [9] Wunschiers, R. Lindblad, P. Hydrogen in education—a biological approach. Int J Hydrogen Energy. (2002) 1131 – 1140.
- [10] Mayer, R.E. (2001). Multimedia learning. New York: Cambridge University Press.
- [11] Hatami, Javad. Faredanesh, Hashem. (2006). design of viewpoint society of curriculum in guidance schools. quarterly of curriculum observations.
- [12] Kamradt, T.F, Kamradt, E.J (1999) .Structured Design for Attitudinal Instruction. In C.M.Reigeluth. Instructional Design: Theories and Models (PP.563-590).Mahwah Lawrance Erlbaum Associates.
- [13] Suha Yazici.M. Hydrogen and fuel cell activities at UNIDO-ICHET. Int J Hydrogen Energy doi: 10.1016/j.ijhydene.2009.04.072



Theoretical Study of Hydrogen Bonding in Blend Membranes Based on Sulfonated poly(ether ether ketone)-Sulfonated poly(ether sulfone)

Ghasem Bahlakeh^{1,*}, Manouchehr Nikazar², Ashor Mohamd Paya³, Mahdi Tohidian⁴, Ahmad Lashgar⁵

*Department of chemical engineering, Amirkabir university of technology
ghasem.bahlakeh@gmail.com*

Abstract

Hydrogen bonding characteristics of acid-acid blend membranes based on the sulfonated poly(ether ether ketone) (SPEEK) and sulfonated poly(ether sulfone) (SPES) were investigated under different water content conditions using MD simulations methods. Simulation results have shown that hydrogen bonding interactions were formed between sulfonic acid groups of SPEEK and SPES with water molecules and hydronium ions, and also among water molecules and hydronium ions. With an increase in water content, the number of sulfonic acid-water hydrogen bonds was increased while that of sulfonic acid-hydronium ions was found to decrease. Furthermore, the calculation of water coordination number for water and hydronium ions suggested the formation of hydrogen bond network inside the hydrated structure of SPEEK-SPES blend membrane.

Keywords: Polymeric blend membrane, Sulfonated poly(ether ether ketone), Sulfonated poly(ether sulfone), Hydrogen bonding, Molecular dynamics simulation

1 Introduction

During recent years, thanks to their potential usages in both polymer electrolyte membrane fuel cells (PEMFCs) and direct methanol fuel cells (DMFCs), polymer electrolyte membranes (PEMs) have been subject of extensive research studies [1]. Performance of these PEMs is strongly dependent on their physicochemical properties. Nafion membrane, a perfluorosulfonic PEM with a poly(tetrafluoroethylene) (PTFE) backbone and a sulfonic acid group attached to backbone, is the frequently used PEM due to high ionic conductivity at optimum water uptake and good chemical and mechanical stability [2]. However, major disadvantages of high methanol permeability in DMFCs applications, high cost of membrane production and low conductivity at higher temperatures have limited Nafion applications for fuel cells and motivated research works toward the development of new membranes especially hydrocarbon-type materials like sulfonated poly(2,6-dimethyl-1,4-phenylene oxide) (SPPO), sulfonated poly(ether ether ketone) (SPEEK), sulfonated poly(ether sulfone) (SPES) and so forth [3-4].

¹ -PhD student

² -Professor, Department of chemical engineering, Amirkabir university of technology, Nikazar@aut.ac.ir

³ -MSc student, Islamic azad university, ashorpaya@gmail.com

⁴ -MSc student, Polymer engineering and color technology, Amirkabir university of technology, m.tohidian68@gmail.com

⁵ - MSc, Computer engineering department, University of Tehran, ahmad.lashgar@gmail.com

These alternative polymeric membranes have been utilized in pure form and also in blended form with each other and with Nafion membrane. Tsai et al. studied Nafion–SPEEK and Nafion–nitrated SPEEK blend membranes. They observed lower water swelling and methanol crossover in blend membranes as compared to Nafion [5-6]. Hasani–Sadraabadi et al. investigated acid–acid blend membranes of SPPO and SPEEK incorporated with organically modified montmorillonite (MMT) and reported lower methanol permeability in blend membrane than in Nafion [7]. In another study, Sengül et al. reported that acid–acid blend membranes composed of SPEEK and SPES showed better swelling property compared to the pure SPEEK membrane, although the proton conductivity of blend membrane was lower than that of pure SPEEK and Nafion PEMs [8]. Gao et al. concluded that the methanol permeability of SPEEK–sulfonated phenolphthalein poly(ether sulfone) (SPES–C) blend system is lower than that of Nafion [9]. Moreover, they indicated that with addition of SPES–C to SPEEK material, the conductivity enhanced at increased temperatures.

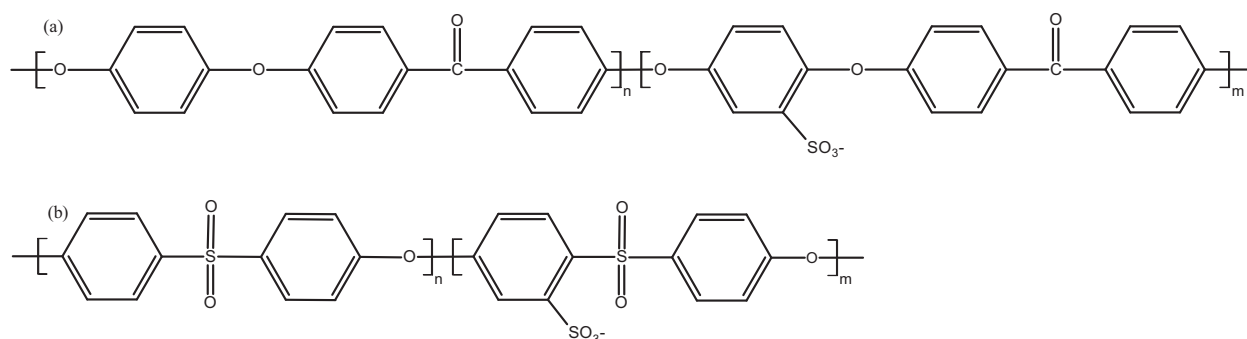


Figure 1: Chemical structure of non-sulfonated and ionized sulfonated (a) PEEK and (b) PES monomer used for MD simulations. Degree of sulfonation (DS) is defined as: $DS = \frac{m}{n+m} \times 100$.

Theoretical methods such as molecular dynamics (MD) simulations are powerful tools that are able to provide molecular level information regarding characteristics of PEM materials that could not be easily attained using experimental studies. These techniques have been recently used to investigate properties of Nafion [10-11] and alternative pure PEMs like SPEEK, SPES, SPPO and so on [12-15]. Therefore, in this work, MD simulations were used to study the characteristics of acid-acid blend membranes based on SPEEK and SPES. Experimental observations about acidic membranes revealed that water content (hydration level) is a parameter that influences membrane performance. On the other hand, it is known that proton conductivity properties of these membranes depend upon their ability to form hydrogen bonds under hydration conditions. For these reasons, current study investigates the hydrogen bonding characteristics of hydrated SPEEK-SPES blend systems under varied water content conditions by using MD simulations. This work is an extension to our recent work in which effects of water content on various properties of SPEEK-SPES blend membranes were examined via MD simulations [16].

2 Details of simulation

2.1 Molecular models and amorphous cell construction

To evaluate the hydrogen bonding characteristics of hydrated SPEEK-SPES blend membranes as a function of water content, MD simulations were carried out for blend membranes containing five hydration levels including $\lambda = 3, 6, 9, 12$ and 15 (here, λ is the ratio of the number of water molecules to the number of sulfonic acid groups). Three-dimensional



amorphous cells which consist of SPEEK and SPES polymeric chains, hydronium ions (H_3O^+) and water molecules were constructed for this objective. 20 SPEEK (degree of sulfonation of 60%) and SPES (degree of sulfonation of 40%) chains each with degree of polymerization of 20 were used. Degree of sulfonation is defined as the ratio of number of sulfonated monomers to the total number of sulfonated and non-sulfonated monomers, as shown in Figure 1. Using these degrees of sulfonation, each SPEEK and SPES chain contains 12 and 8 sulfonated monomers, respectively. Before constructing amorphous cells, it was assumed that sulfonic acid groups attached to polymeric backbones are completely dissociated, as displayed in Figure 1. Therefore, to keep the charge neutrality of the simulation cells, the same number of hydronium ions as the total number of sulfonic acid groups was employed. The number of water molecules was determined by using corresponding hydration level. Table 1 presents the composition of simulated cells. Using the composition for $\lambda = 15$, initial cell for maximum water content was first created at initial density of 0.005 g/cm^3 by means of amorphous cell module of the Materials Studio software [17]. For the case of lower hydration levels, cells were built by successive removal of water molecules from constructed cell with maximum water content.

2.2 Force field parameters and MD simulation

DREIDING and flexible 3-centered (F3C) force fields [18-19] were employed for polymeric (SPEEK and SPES) chains and water molecules, respectively, which have been used in our previous study [15-16]. Partial charges for SPEEK and SPES were assigned using charge equilibration procedure. Potential parameters and charges for hydronium ions were from work of Jang et al. [10].

After construction, all amorphous cells were minimized using conjugate gradient algorithm. Optimized cells were then equilibrated using shrinking box method, as discussed in our previous study [16]. In this method, NPT MD simulations were first performed at 300 K for 10 ps during which operating pressure was increased from 1 to 100 atm. Next, the simulation cells were further compressed from 100 to 150 atm for 1 ns using NPT runs. In these simulations, only the bonded and repulsive non-bonded Lennard-Jones (LJ) interactions were included. Afterwards, NPT simulations were continued at 150 atm for 10 ps with inclusion of both repulsive and attractive parts of LJ interactions, which was followed by another NPT MD run at 150 atm for 50 ps where columbic interactions were also turned on. Subsequently, MD cells were equilibrated for time period of 10 ns in NPT ensemble at 300 K and 1 atm. This equilibration phase of MD simulations was used to accelerate attainment of equilibrated structures. Finally, at the equilibrated densities, NVT simulations were done for 1 ns at 300 K, where trajectories were used every 1 ps for subsequent analyses of hydrogen bonding interactions.

All MD simulations were done by using LAMMPS (large-scale atomic/molecular massively parallel simulator) open-source MD code [20]. Non-bonded interactions were truncated at 12 Å cutoff distance and the long-range electrostatic interactions were computed using particle-particle particle-mesh (PPPM) method [21]. Newton's equation of motion was solved with velocity Verlet integrator using a time step of 1 fs [22]. During simulations, temperature and pressure were controlled via Nose-Hoover algorithm as thermostat and barostat [23-24]. Periodic boundary conditions were imposed in all directions of simulation cells.

Table 1: Composition of the hydrated SPEEK–SPES blend membranes used in MD simulations and calculated average cell size and density for hydration levels of $\lambda = 3, 6, 9, 12$ and 15.

	Hydration level (λ)				
	3	6	9	12	15
No. of SPEEK chains	4	4	4	4	4
No. of SPES chains	5	5	5	5	5
No. of H ₂ O	264	528	792	1056	1320
No. of H ₃ O ⁺	88	88	88	88	88
Total No. of atoms	6546	7338	8130	8922	9714
Cell size ^a (Å)	43.58	44.03	44.72	45.75	46.87
Density ^a (g/cm ³)	1.1977	1.2533	1.2850	1.2819	1.2689

^aResults from our previous study [16].

۳ Results and discussion

The property of hydrogen bonding interactions among various atoms in hydrated structure of SPEEK-SPES blend membrane were evaluated using radial distribution function (RDF) $g_{A-B}(r)$ at different water contents. RDF shows the probability distribution of B atoms around reference A atoms, and is defined as equation (1):

$$g_{A-B}(r) = \frac{\left(\frac{n_B}{4\pi r^2 \Delta r} \right)}{\left(\frac{N_B}{V} \right)} \quad (1)$$

where n_B is the number of B atoms located around A atoms inside a spherical shell of thickness Δr , N_B is the total number of B atoms employed when constructing simulation cell and V is the equilibrated cell volume.

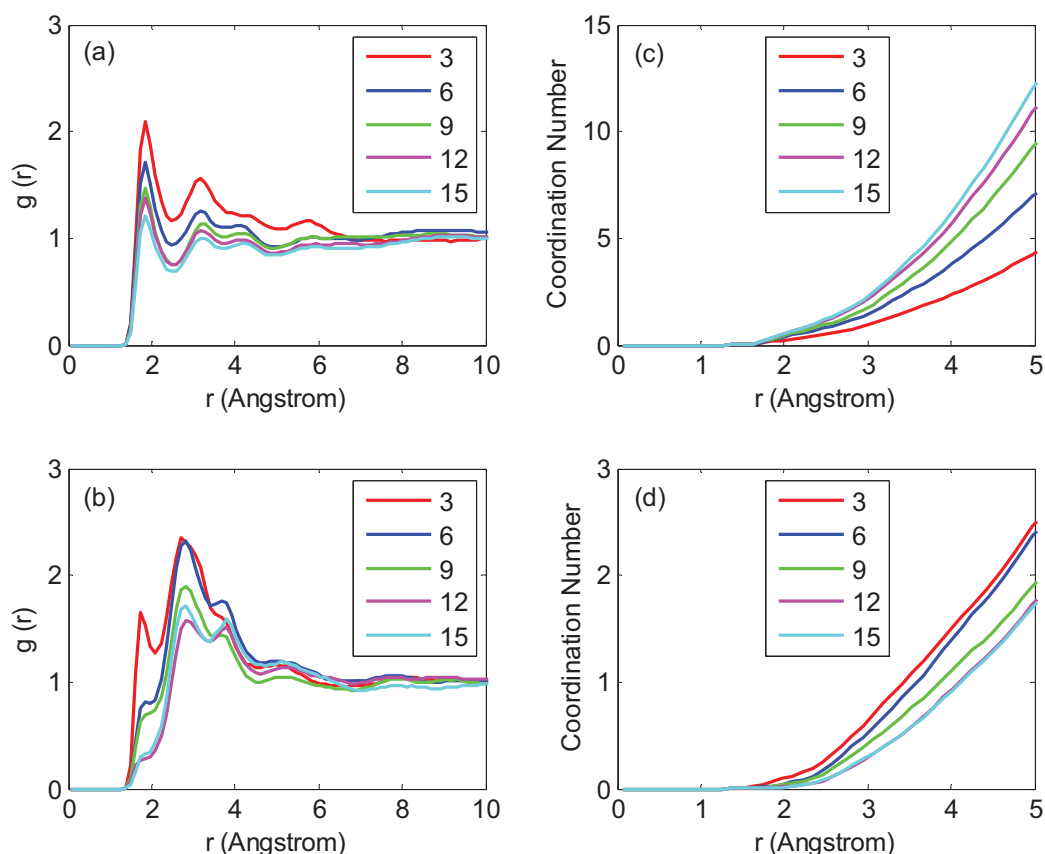


Figure 2: RDFs of (a) oxygen(sulfonic acid group)–hydrogen(water), (b) oxygen(sulfonic acid group)–hydrogen(hydronium ion); coordination number of (c) water and (d) hydronium ion around sulfonic acid groups for hydration levels of $\lambda = 3, 6, 9, 12$ and 15 .

In MD simulations of hydrated PEMs, a hydrogen bond between a hydrogen acceptor atom (A) and a hydrogen atom bonded to a hydrogen donor atom (D) can be defined using geometric criteria. These criteria are based on the donor–acceptor (D...A) or hydrogen–acceptor (H...A) distance and the donor–hydrogen–acceptor (D–H...A) angle. Two hydrogen donor and hydrogen acceptor atoms are considered as hydrogen bonded if the H...A distance is usually less than 2.5 \AA (or the D...A distance is less than 3.5 \AA), and the D–H...A angle is usually greater than 90° . The hydrogen bond in PEMs can also be described in terms of RDF between hydrogen acceptor and hydrogen atom, that is, if the position of peak in RDFs of hydrogen acceptor toward hydrogen (i.e., H...A distance) is within the value of 2.5 \AA , a hydrogen bond has been formed.

In the membrane-water-hydronium ion system considered here, the oxygen atoms of sulfonic acid groups can act as hydrogen acceptor, oxygen atom of hydronium ions can act as hydrogen donor and oxygen atom of water molecules can act as both hydrogen acceptor and hydrogen donor. Therefore, water molecules and hydronium ions can form hydrogen bonds both with sulfonic acid groups of SPEEK and SPES chains and also with each other. These hydrogen bonding characteristics are indicated using the RDF analysis.

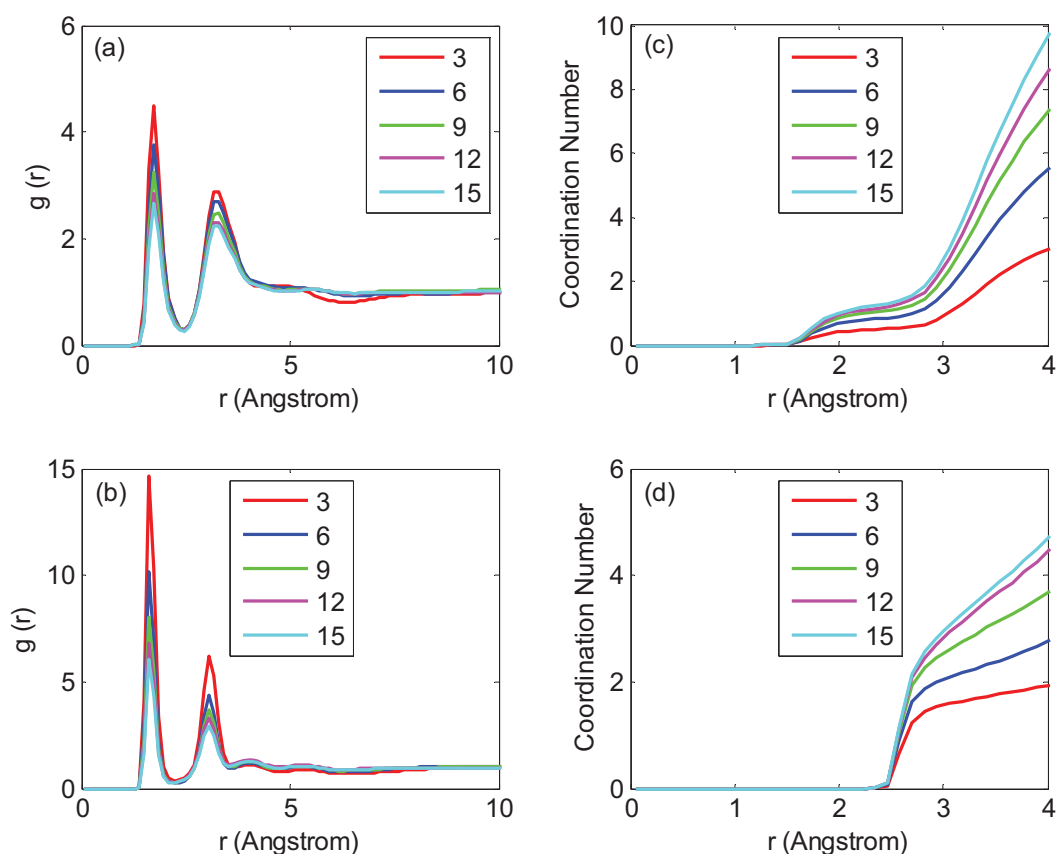


Figure 3: RDFs of (a) oxygen(water)–hydrogen(water) and (b) oxygen(water)–hydrogen(hydronium ion) coordination number of water around (c) water and (d) hydronium ion for hydration levels of $\lambda = 3, 6, 9, 12$ and 15 .

Figure 2 (a) and (b) illustrates the oxygen(sulfonic acid)-hydrogen(water) (Os-Hw), and oxygen(sulfonic acid)-hydrogen(hydronium ion) (Os-Hh) RDFs for all hydration levels studied here, respectively. In Os-Hw RDFs, there is a first peak at 1.86 \AA with a minimum at 2.46 \AA for all hydration levels, which are both within the range of distance required for formation of hydrogen bond. Therefore, from the existence of high peak it can be concluded that water molecules form hydrogen bonding interactions with sulfonic acid groups in hydrated morphology of SPEEK-SPES blend membrane. The peak height decreases with an increase in water content which is owing to the solvent effect of water molecules on water molecules. In the case of Os-Hh RDFs, there are two peaks observed at 1.74 and 2.82 \AA , which indicate the hydrogen bonding of hydronium ions toward sulfonic acid groups. The first peak position in Os-Hh RDFs is occurred at lower distance compared to Os-Hw RDFs. This observation is attributed to strong electrostatic interactions between negatively charged sulfonic acid groups and positively charged hydronium ions. The height of first peak in Os-Hh RDFs with higher hydration levels is insignificant. At increased water contents of membrane, water molecules reduce the sulfonic acid-hydronium ion interactions and so hydronium ions move away from sulfonic acid groups.

Parts (c) and (d) in Figure 2 present the coordination number of water and hydronium ions around sulfonic acid which is computed from integration of corresponding RDFs up to a certain distance. It is seen that with an increase in hydration level, water coordination number around



sulfonic acid groups increases, whereas that of hydronium ion decreases, suggesting that increasing the water content leads to an increase in number of water-sulfonic acid hydrogen bonds, and a decrease in number of hydronium ion-sulfonic acid group hydrogen bonds.

Hydrogen bonding properties between water molecules and between water molecules and hydronium ions were analyzed using RDFs of water oxygen-water hydrogen (Ow-Hw) and water oxygen-hydronium ion hydrogen (Ow-Hh), as provided in Figure 3 (a) and (b). RDFs of Ow-Hw demonstrate a pronounced peak at 1.74 Å which confirms the presence of hydrogen bonds among water molecules. For interaction of oxygen atoms in water molecules and hydrogen atoms in hydronium ions in Ow-Hh RDFs, an intensified peak is seen at 1.62 Å, which is also a distance at which water molecules and hydronium ions can form hydrogen bonds. From comparison of peak height in Os-Hw and Os-Hh RDFs with that in Ow-Hw and Ow-Hh RDFs, it could be concluded that hydrogen bond interactions among water molecules and hydronium ions are stronger than those among water/hydronium ions and sulfonic acid groups. Coordination number for water molecules which surround water molecules and hydronium ions were exhibited in Figure 3 (c) and (d), respectively. As the level of water content is enhanced, both coordination numbers increase which imply that water molecules and hydronium ions are surrounded with greater number of water molecules. Consequently, a hydrogen bond network among water molecules and hydronium ions can exist which is necessary for enhanced proton conductivity of hydrated membrane.

Acknowledgement

The authors gratefully acknowledge the use of High Performance Computing Research Center (HPCRC) of Amirkabir University of Technology.

References

- [1] L. Carrette, K.A. Friedrich, U. Stimming, Fuel cells – fundamentals and applications, Fuel Cells, (2001), 1, 5-39.
- [2] K.A. Mauritz, R.B. Moore, State of understanding of Nafion, Chem. Rev., (2004), 104, 4535-4586.
- [3] M. Rikukawa, K. Sanui, Proton-conducting polymer electrolyte membranes based on hydrocarbon polymers, Prog. Polym. Sci., (2000), 25, 1463-1502.
- [4] H. Ahmad, S.K. Kamarudin, U.A. Hasran, W.R.W. Daud, Overview of hybrid membranes for direct-methanol fuel-cell applications, Int. J. Hydrogen Energy, (2010), 35, 2160-2175.
- [5] J.C. Tsai, H.P. Cheng, J.F. Kuo, Y.H. Huang, C.Y. Chen, Blended Nafion®/SPEEK direct methanol fuel cell membranes for reduced methanol permeability, J. Power Sources, (2009), 189, 958-965.
- [6] J.C. Tsai, J.F. Kuo, C.Y. Chen, Nafion®/nitrated sulfonated poly(ether ether ketone) membranes for direct methanol fuel cells, J. Power Sources, (2009), 194, 226-233.
- [7] M.M. Hasani-Sadrabadi, S.R. Ghaffarian, N. Mokarram-Dorri, E. Dashtimoghadam, F.S. Majedi, Characterization of nanohybrid membranes for direct methanol fuel cell applications, Solid State Ion., (2009), 180, 1497-1504.
- [8] E. Sengül, H. Erdener, R.G. Akay, H. Yücel, N. Baç, I.I. Eroglu, Effects of sulfonated polyether-etherketone (SPEEK) and composite membranes on the proton exchange membrane fuel cell (PEMFC) performance, Int. J. Hydrogen Energy, (2009), 34, 4645-4652.
- [9] Q. Gao, Y. Wang, L. Xu, G. Wei, Z. Wang, Studies on SPEEK/PES-C and SPEEK/SPES-C blend proton-exchange membranes, Acta Polymerica Sinica, (2009), 1, 45-52.



- [10] S.S. Jang, V. Molinero, T. Cagin, W.A. Goddard, Nanophase-segregation and transport in Nafion 117 from molecular dynamics simulations: effect of monomeric sequence, *J. Phys. Chem. B*, (2004), 108, 3149-3157.
- [11] R. Devanathan, A. Venkatnathan, M. Dupuis, Atomistic simulation of Nafion membrane: I. effect of hydration on membrane nanostructure, *J. Phys. Chem. B*, (2007), 111, 8069-8079.
- [12] G. Brunello, S.G. Lee, S.S. Jang, Y. Qi, A molecular dynamics simulation study of hydrated sulfonated poly(ether ether ketone) for application to polymer electrolyte membrane fuel cells: Effect of water content, *J. Renewable Sustainable Energy*, (2009), 1, 033101-033114.
- [13] T. Ohkubo, K. Kidena, N. Takimoto, A. Ohira, Molecular dynamics simulations of Nafion and sulfonated polyether sulfone membranes. I. Effect of hydration on aqueous phase structure, *J. Mol. Model.*, (2011), 17, 739-755.
- [14] G. Bahlakeh, M. Nikazar, M.-J. Hafezi, E. Dashtimoghadam, M.M. Hasani-Sadrabadi, Molecular dynamics simulation study of proton diffusion in polymer electrolyte membranes based on sulfonated poly (ether ether ketone), *Int. J. Hydrogen Energy*, (2012), 37, 10256-10264.
- [15] G. Bahlakeh, M. Nikazar, Molecular dynamics simulation analysis of hydration effects on microstructure and transport dynamics in sulfonated poly(2,6-dimethyl-1,4-phenylene oxide) fuel cell membranes, *Int. J. Hydrogen Energy*, (2012), 37, 12714-12724.
- [16] G. Bahlakeh, M. Nikazar, M. Mahdi Hasani-Sadrabadi, Understanding structure and transport characteristics in hydrated sulfonated poly(ether ether ketone)–sulfonated poly(ether sulfone) blend membranes using molecular dynamics simulations, *J. Membr. Sci.*, (2013), 429, 384-395.
- [17] Accelrys Software Inc. SD, 2009.
- [18] S.L. Mayo, B.D. Olafson, W.A. Goddard, DREIDING: a generic force field for molecular simulations, *J. Phys. Chem.*, (1990), 94, 8897-8909.
- [19] M. Levitt, M. Hirshberg, R. Sharon, K.E. Laidig, V. Daggett, Calibration and testing of a water model for simulation of the molecular dynamics of proteins and nucleic acids in solution, *J. Phys. Chem. B*, (1997), 101, 5051-5061.
- [20] S.J. Plimpton, Fast parallel algorithms for short-range molecular dynamics, *J. Comput. Phys.*, (1995), 117, 1-19.
- [21] R.W. Hockney, J.W. Eastwood, *Computer Simulation Using Particles*, McGraw-Hill, New York, 1981.
- [22] W.C. Swope, H.C. Andersen, P.H. Berens, K.R. Wilson, A computer simulation method for the calculation of equilibrium constants for the formation of physical clusters of molecules: Application to small water clusters, *J. Chem. Phys.*, (1982), 76, 637-649.
- [23] S. Nose, A unified formulation of the constant temperature molecular dynamics methods, *J. Chem. Phys.*, (1984), 81, 511-519.
- [24] S. Nose, An extension of the canonical ensemble molecular dynamics method, *Mol. Phys.*, (1986), 57, 187-191.



Organically Modified Nanoclays and Chitosan– Phosphotungstic Acid Complex Nanocomposites as Polyelectrolytes for Fuel Cells Applications

Mahdi Tohidian¹, Seyed Reza Ghaffarian^{2,*}, Seyed Emadodin Shakeri³, Ghasem Bahlakeh⁴, Erfan Dashtimoghadam⁵, Mohammad Mahdi Hasani-Sadrabadi⁶

*Department of polymer engineering and color technology, Amirkabir
university of technology, sr_ghaffarian@aut.ac.ir*

Abstract

Polyelectrolyte complex (PEC) of chitosan and phosphotungstic acid (PWA) was suggested and evaluated as an alternative membrane to Nafion for direct methanol fuel cells applications (DMFCs). To reduce the methanol permeability, several amounts of unmodified montmorillonite (MMT, trade name: cloisite Na) and organically modified montmorillonite (OMMT, trade names: cloisite 15A and cloisite 30B respectively) were introduced to the system. The X-Ray diffraction (XRD) patterns of nanocomposites proved clay layers were exfoliated lower than 3 wt%. Proton conductivity and methanol permeability were measured. According to selectivity parameter – ratio of proton conductivity to methanol permeability– PEC containing 2wt% MMT 30B (PEC/2wt%MMT 30B) was identified as the optimum composition. The results indicate the optimum nanocomposite membrane as a promising polyelectrolyte membrane (PEM) for DMFC applications.

Keywords: Direct methanol fuel cell, Polyelectrolyte membranes, Proton conductivity, Methanol permeability, Montmorillonite

1. Introduction

Fuel cells are able to convert the chemical energy to electricity via oxidation/redox reactions and generate energy from renewable sources [1,2]. Direct methanol fuel cells (DMFCs) as a member of fuel cell family has attracted lots of interest in stationary and especially in portable power generators. Polyelectrolyte membranes (PEMs), as the key part of such systems, has a crucial role in DMFC as a proton conducting media [3-5]. Perfluorinated ionomers such as Nafion has been identified as a commonly used PEM for DMFCs applications. Although due to high proton conductivity, good mechanical properties and chemical stability, Nafion is a famous option, the utilization of this membrane is restricted due to expensive cost, high methanol permeability and significant reduction in proton conductivity at elevated temperatures or at low

¹ -MSc student, Department of polymer engineering and color technology, Amirkabir university of technology, m.tohidian68@gmail.com

² -Professor,

³ -MSc student, Department of polymer engineering and color technology, Amirkabir university of technology, emzh.1368@gmail.com

⁴ -PhD student, Department of chemical engineering, Amirkabir university of technology, ghasem.bahlakeh@gmail.com

⁵ - PhD student, Department of polymer engineering and color technology, Amirkabir university of technology, erfand.ashtimoghadam@gmail.com

⁶ - PhD student, Department of polymer engineering and color technology, Amirkabir university of technology, mahdi.hasani@gmail.com



humidity. In this regard, based on proton transport concepts there are considerable attempts to develop new PEMs as alternatives to commercial Nafion membranes [6-9].

Generally, oppositely charged polyions can interact electrostatically to form polyelectrolyte complexes (PECs) [10]. Due to remarkable properties such as biocompatibility, nontoxicity and suitable thermal resistance, Chitosan, as a polycation, has attracted a lot of interests, [11,12]. Although, this polymer is mainly used in medicine, it is able to be used as a PEM [13, 14] and due to the presence of polar functional groups; it is able to interact with polyanions and salts electrostatically and form new kinds of PECs [15,16]. Phosphotungstic acid (PWA), $H_3PW_{12}O_{40}$, as an inorganic polyacid, is an excellent proton conductor and it has a high ability to be used in manufacturing of hybrid proton conductor membranes [17-22]. PWA has high water solubility and it leaks out by electrochemically produced water during cell operation which reduces the cell performance [23]. Due to effective powerful interactions between matrix polymer chains and polyacids, which are expected in the case of chitosan and PWA, the dissolution of PWA in electrochemically produced water decreases significantly [40].

Significant reduction in methanol permeability can be achieved through modifying proton transport channels and introducing tortuous pathways [24-34]. As reported previously, tortuous pathways can be achieved by dispersing inorganic fillers such as MMT into polymeric matrix and nanocomposite manufacturing. As the maximum dispersion of MMT is desirable, the normally hydrophilic silicate surface should be converted to an organophilic one. OMMT is made by ion exchange reactions with cationic surfactants, such as alkylammonium or alkylphosphonium cations [7]. Exfoliation of layered silicates into polymeric matrix reduces proton conductivity and methanol permeability simultaneously and also enhances thermal and mechanical stability [35-40].

In this research the goal is producing PEC nanocomposite membranes, based on chitosan and PWA, containing different loading weights of MMT Na as the unmodified MMT, MMT 15A and MMT 30B as OMMT, to achieve PEMs with the ability of suitable proton conductivity and low methanol permeability as alternative membranes to commercial Nafion membranes, for DMFCs applications.

2. Experimental

2.1 Materials

MMT (cloisite Na) and OMMT (cloisite 15A, cloisite 30B) nanoclays were purchased from Southern Clay Products Inc., Gonzales, TX, USA. Methanol, acetic acid, glycerol, sodium hydroxide for neutralization and PWA, all were obtained from Merck Company. High molecular weight Chitosan was purchased from Mahtani chitosan company, India. The catalysts, platinum (Pt) black and Pt/Ru black for the cathode and anode respectively, were purchased from Johnson–Matthey, England. Nafion 117 membrane, 178 μm thickness, from DuPont Company was used to compare the data.

2.2 Membrane preparation

Dried chitosan powder was added to the acetic acid/deionized water (2 v/v%) to prepare chitosan solution (1 w/v%). Furthermore aqueous solution of PWA was prepared (15 w/v%). cloisite Na (MMT Na), cloisite 15A (MMT 15A) and cloisite 30B (MMT 30B) at different loading weights (0, 0.5, 1, 2, 3, 5, 10 w clay/w chitosan%) were added to chitosan solution. The mixtures were stirred at 60 °C by 80 rpm for 36 h and ultra-sonicated for totally 20 min to ensure maximum dispersion of nanoclay layers in the chitosan solution. The resultant viscous mixtures were casted through solution casting method in petri dishes and incubated at 25 °C for a week to achieve dry membranes. To neutralize the membranes, 1N sodium hydroxide solution was

poured on the dry membranes in petri dishes for several times. The neutralized membranes were washed with deionized water for several times and then soaked in PWA solution for 24h. Then the membranes were washed and soaked in a big deionized water container for 24 h to remove physically absorbed PWA. Finally the membranes were dried at 25°C for 48 h and annealed at 60°C for 6 h.

2.3 Membrane characterization

Fourier transform infrared spectroscopy (FTIR)

The IR spectra (4000–500 cm⁻¹, resolution 4 cm⁻¹) were recorded in absorbance mode with a Bruker Vertex 70 RTIR spectrometer.

Stability of PWA in the membranes

A membrane without any nanoclay and another one containing 10wt% of MMT Na were chosen for this work. Concentrated solution of acetic acid in deionized water was poured on these samples and the mixtures were stirred for 48h and filtered to achieve solutions with concentration of 0.25w/v%. The percent weight of tungsten was determined with inductively coupled plasma-mass spectrometry (ICP-MS), POEMS MODEL (TJA Corporation) and finally the concentration of PWA in the membranes was calculated by attending to tungsten concentration.

XRD

Dispersion of MMT (or OMMT) nanoclays in the membranes was detected by XRD (SIEMENS XRD-D5000 diffractometer, Cu-K α). The scanning diffraction angle, 2 θ , was less than 15°.

Water uptake

The fully dried membranes were soaked in deionized water container for 36 h to ensure maximum water absorption. Then after removing surface water, the membranes were weighted quickly and finally, the water uptake was calculated based on equation (1):

$$\text{Water uptake\%} = \frac{M_{\text{wet}} - M_{\text{dry}}}{M_{\text{dry}}} \times 100 \quad (1)$$

Where M_{wet} and M_{dry} are the weights of the membrane in the wet and dry states, respectively.

Proton conductivity

Proton conductivity of fully hydrated membranes (95%RH), as a function of temperature, were measured via 4-point probe conductivity cell. The proton conductivity values were achieved according to equation (2) quantitatively.

$$\sigma = \frac{L}{R \times A} \quad (2)$$

Where L is the membrane thickness (cm), A is the cross sectional area (cm²) of the membrane and R is the resistance (S⁻¹).

Methanol permeability

The methanol permeability was measured by means of two-compartment glass diffusion cell. The first cell contained pure methanol (cell A) and the second one contained deionized water (cell B) and a mixer stirred the solutions continuously to make both cells homogeny. Gas chromatography method was used to measure methanol concentration in cell B at different times. Finally, the methanol diffusion coefficient was determined according to the equation (3):

$$P = \frac{1}{C_a} \times \left(\frac{\Delta C_b(t)}{\Delta t} \right) \times \left(L \times V_b / A \right) \quad (3)$$

Where, P is the methanol diffusion permeability of the membrane ($\text{cm}^2 \text{s}^{-1}$), C_a is the methanol concentration in cell A (mol L^{-1}), $\left(\frac{\Delta C_b(t)}{\Delta t} \right)$ is the slope of the molar concentration variation of methanol in the cell B as a function of time ($\text{mol L}^{-1} \text{s}^{-1}$), V_b is the volume of each diffusion reservoir (cm^3), A is the membrane's area (cm^2) and L is the membrane thickness (cm).

3 Results and discussion

PWA has four characteristic bands, which are depicted in figure 1. These bands are (P–O_a), (W–O_b–W), (W–O_c–W) and (W=O_d) respectively [39, 40].

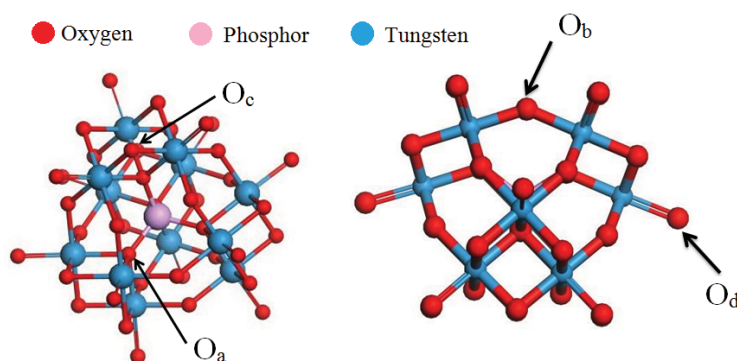


Figure 1: PWA chemical structure in two sides of view.

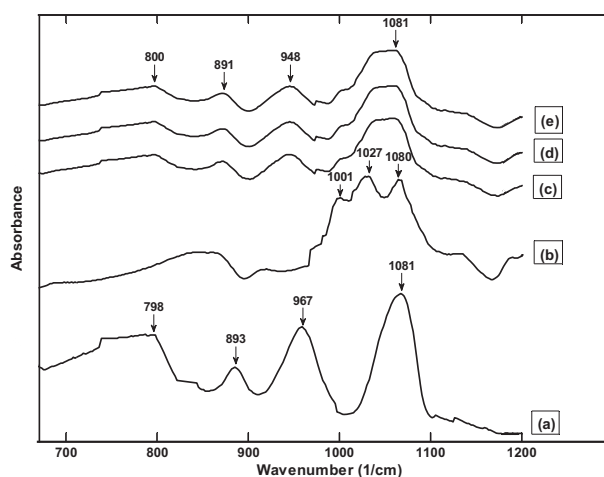


Figure 2: The FTIR spectra ($700 - 1200 \text{ cm}^{-1}$) of PWA (curve a), chitosan (curve b), PEC/3 wt% MMT Na (curve c), PEC/3 wt% MMT 15A (curve d), PEC/3 wt% MMT 30B (curve e).

FTIR spectroscopy was investigated for different nanocomposite membranes, containing 3 wt% nanoclay loading weight, pure chitosan and PWA (Keggin-type) and chitosan/PWA complex (PEC), to detect stable PWA in these samples. Figure 2 presents the IR spectra of PWA, chitosan, PEC and nanocomposite membranes. The IR spectrum of PWA in Figure 2 shows four characteristic bands at 1081 (P–O_a), 967 (W=O_d), 893 (W–O_b–W) and 798 cm⁻¹ (W–O_c–W) [39, 40]. All of these characteristic bands of PWA are also presented in the spectra of nanocomposite membranes, which indicate the stable PWA in these membranes. For example in the sample of PEC/3 wt% MMT 30B, the FTIR spectra has the peaks at 1081, 948, 891 and 800 cm⁻¹, which are attributed to (P–O_a), (W=O_d), (W–O_b–W) and (W–O_c–W) of adsorbed PWA in nanocomposites of PEC/MMT(or OMMTs) membranes, respectively. In the case of chitosan the bands at 1001, 1027 and 1080 cm⁻¹ are assigned to the saccharide structure [38, 40].

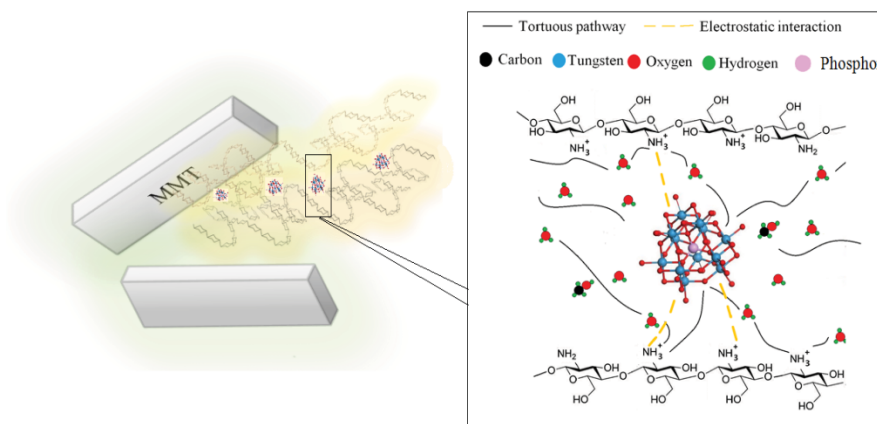


Figure 3: Schematic of tortuous pathways through the membrane.

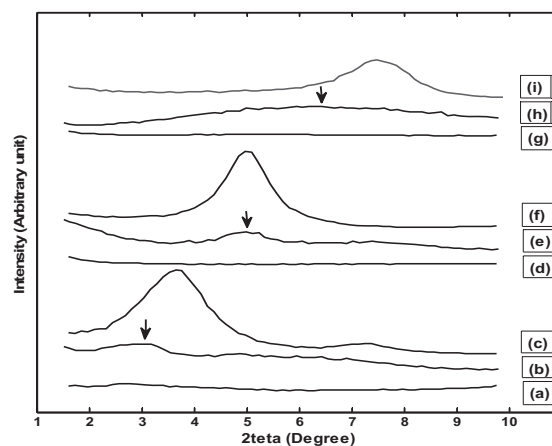


Figure 4: XRD patterns of PEC/3 wt% MMT 15A (curve a), PEC/5 wt% MMT 15A (curve b), MMT 15A (curve c), PEC/3 wt% MMT 30B (curve d), PEC/5 wt% MMT 30B (curve e), MMT 30B (curve f), PEC/3 wt% MMT Na (curve g), PEC/5 wt% MMT Na (curve h), MMT Na (curve i).

To reduce the methanol crossover in PEC membrane, proton pathways were modified via introducing several amounts of MMT Na, 15A and MMT 30B to the system and forming tortuous pathways. The clay layers have negative charge on their surfaces and some cations are existed between these layers and make tactoids. chitosan chains have positive charge they are able to diffuse between clay layers and make tortuous pathways. Figure 3 shows the tortuous

pathways through the nanocomposite membranes, chitosan and PWA chemical structures schematically.

The X-ray diffraction patterns of MMT Na, MMT 15A, MMT 30B and PEC/3 and 5 wt% MMT (or OMMTs) nanocomposites are illustrated in figure 4. As seen, MMT and OMMTs show one crystalline peak around 3.5° , 5° and 7.5° for MMT 15A, MMT 30B, MMT Na respectively. The membranes, containing 3 wt% clay showed the plateau curve in XRD patterns, which indicates that by diffusing chitosan chains through the limited space of MMT (or OMMTs) interlayers, the clay layers were dispersed in the PEC matrices completely. But in the case of membranes, containing 5 wt% of MMT (or OMMT), the XRD patterns showed an obvious peak. This proved the presence of nanoclay agglomerations for high loading weights of MMT (or OMMTs).

As the water adsorption in polymeric membranes plays an essential role in the operation of PEMs, the effect of nanoclay loading weight on the water uptake behavior of the prepared PEC/MMT (or OMMTs) nanocomposite membranes has been studied. Figure 5 shows that with increase in the nanoclay content, water uptake decreases. This effect is not only due to the mass of nanoclay layers, but also it is related to a significant reduction in water diffusivity constant through the nanocomposite membranes in comparison with neat PEC.

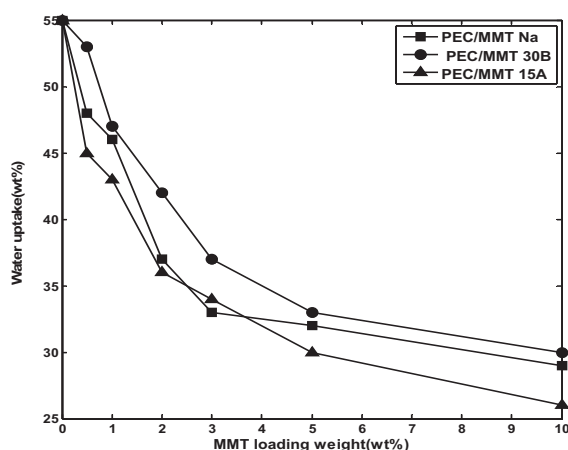


Figure 5: Water uptake (wt%) in PEC/MMT (or OMMTs) nanocomposites containing different loading weights of MMT against MMT (or OMMTs) loading weight (wt%).

ICP results showed that the percentages of tungsten in the dried membranes were 15.7 and 7.5 wt% for PEC and PEC containing 10 wt% MMT Na, respectively. This indicates that the total amount of stable PWA in the PEC and PEC containing 10 wt% MMT Na is 20.3 and 9.7 wt% respectively. The results proved that the presence of nanoclays decreases the total amount of adsorbed PWA in the membranes and it can be related to the decrease in water up take of nanocomposite membranes.

Figure 6 shows the proton conductivity versus the temperature for the nanocomposite membranes, containing different types of MMT (or OMMTs) and various loading weights for each type. The proton conductivity of the PEC/MMT (or OMMTs) nanocomposite membranes was measured at ten different temperatures. Generally the nanocomposite membranes showed significant increase in proton conductivity with increase in temperature, before 100°C . At elevated temperature close to boiling point of water, unlike increase in oxidation of fuel, due to water evaporation the rate of increase in proton conductivity becomes slower and in some cases the proton conductivity decreases at higher temperatures. As we reported the proton conductivity of pure chitosan in our previous research [14], it is obvious that by introducing the

PWA to chitosan, the proton conductivity increases significantly. The higher proton conductivity can be related to the presence of anionic sites on PWA, in addition to hydroxyl and amine groups present in chitosan, which increase hydrophilicity [14]. As it is obvious from figure 6, due to the presence of nanoclay layers in the systems which forms tortuous pathways, the proton conductivity of the nanocomposite membranes, similar to water uptake behavior, decrease with increase in the loading weight of MMT (or OMMTs) in the system. Furthermore, the conductivity of Nafion17 membrane at different temperatures was reported in our previous research [42].

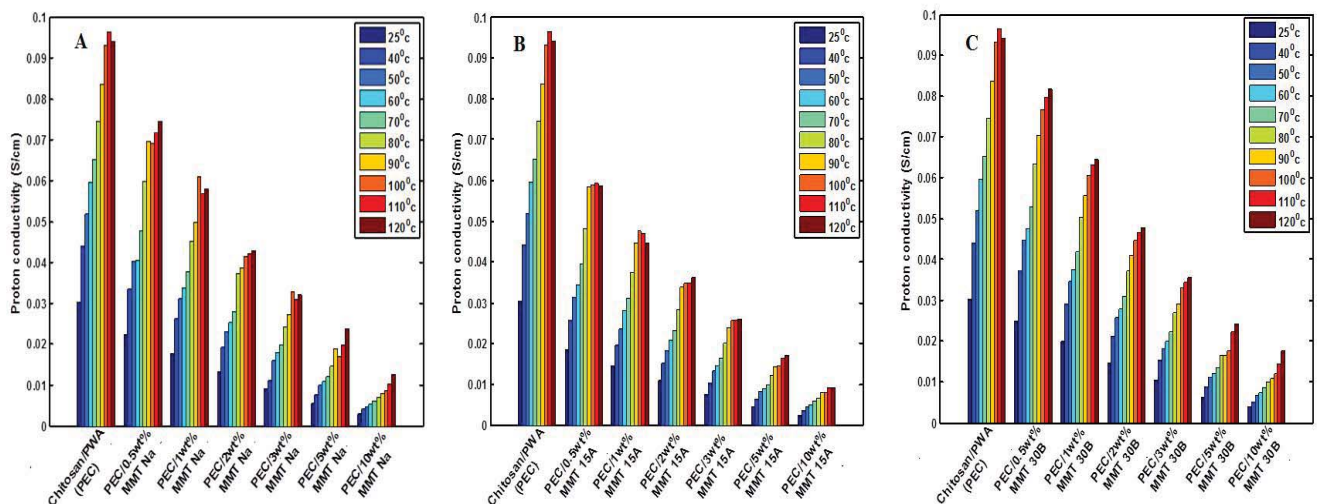


Figure 6: Proton conductivity for PEC/MMT Na(A), MMT 15A (B), MMT 30B (C) nanocomposites, containing different loading weights of MMT (or OMMTs) and at different temperatures.

In addition to proton conductivity, the methanol permeability of the PEC/MMT (or OMMTs) nanocomposite membranes were measured at various temperatures and the results are shown in figure 7. As shown, with increase in the temperature, methanol permeability increases and by introducing the nanoclay layers to the system, due to formation of tortuous pathways the methanol permeability, in comparison with neat PEC decreases significantly. The methanol-cross over surprisingly increases, with increase in the MMT (or OMMTs) loading weight more than 3 wt%. Alexandre et.al [43], who studied the water barrier properties of polyamide 12/montmorillonitenanocomposite, attributed this effect to nanoclays aggregations. They reported that, the existence of nanoclays aggregates in partially intercalated nanocomposite membranes, should probably favor the diffusivity of water molecules along a new pathway including a percolation path through the clay/polymer interface. According to figure 4, nanocomposite membranes containing 5 wt% MMT (or OMMTs) did not prove completely exfoliated structure. So the probable nanoclay agglomerations can be the cause of increase in methanol cross over for the membranes, containing more than 5 wt% MMT (or OMMTs). Furthermore the methanol permeability of neat Nafion17 and chitosan were reported in our previous researches [14, 42]. The PEC and all of the nanocomposite membrane showed lower methanol permeability in comparison with Nafion 117 and pure chitosan. This fact is related to physical crosslinking of chitosan by PWA and formation of tortuous pathways.

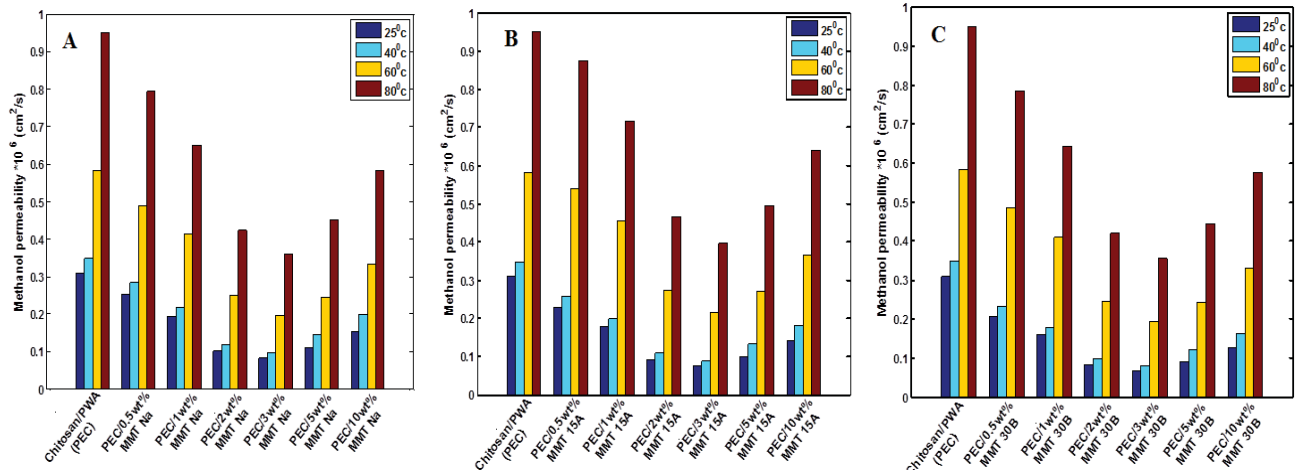


Figure 7: Methanol permeability for PEC/MMT Na (A), MMT15 (B), MMT 30B (C)nanocomposites, containing different loading weights of MMT (or OMMTs) at different temperatures.

Membrane selectivity parameter which is defined as the ratio of proton conductivity to methanol permeability is commonly used to evaluate electrochemical performance of poly electrolyte membranes. Since introducing the nanoclays affects both proton conductivity and methanol permeability, as it was discussed before, to determine the optimum composition of PEC and MMT (or OMMTs), membrane selectivity parameter at different MMT (or OMMTs) loading weights was calculated and displayed in figure 8 at 25°C . At all loading weights of MMT (or OMMTs) the selectivity of nanocomposite membranes which are containing MMT 30B, was higher than the others, containing MMT 15A and MMT Na. Because the better formation of clay/polymer interface (no void at the interface) causes lower methanol permeability [43] and on the other hand, higher water absorption causes higher proton conductivity in most cases, we believe that due to higher gallery space between MMT 30B layers and higher tendency of chitosan chains to MMT 30B, chitosan chains can diffuse through the MMT 30B layers easier than the other two types of MMT and finally the result is better dispersion of MMT 30B layers, better formation of polymer/clay interface and lower methanol permeability. As it was shown in figure 5, membranes containing MMT 30B have the highest water absorption and it seems that the higher proton conductivity of these membranes, is related to their higher water tendency. Due to these reasons the membranes, containing MMT 30B showed higher selectivity. Furthermore current discussions seem to be true for the comparison of membranes which are containing MMT Na and MMT 15A. As it is obvious from figure 8, at 25°C the PEC/2 wt% MMT (or OMMTs) nanocomposite membranes have the highest selectivity in all types of investigated MMT and OMMTs, which were introduced to the system and finally the PEC/2 wt% MMT 30B by the selectivity of 175903 S s cm⁻³ showed the highest selectivity among the whole of investigated membranes in this research, while the selectivity of pure Nafion117 is 40500 S s cm⁻³ at this temperature.

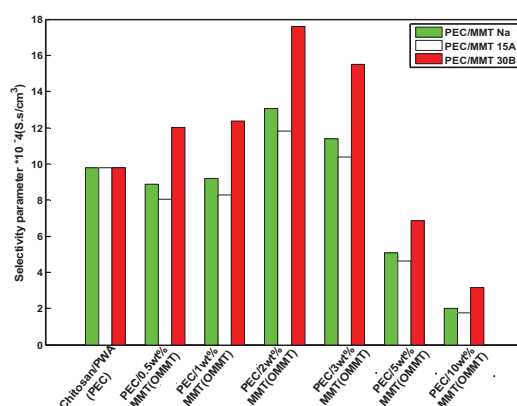


Figure 8: Selectivity parameter for Nafion117 and PEC/MMT (or OMMTs) nanocomposite membranes, containing different loading weights of clays.

References

1. Rees NV, Compton RG (2011) *J Solid State Electrochem* 15:2095-2100
2. Silva VS, Weisshaar S, Reissner R, Ruffmann B, Vetter S, Mendes A, Madeira LM, Nunes SJ (2005) *Power Sources* 145:485-494
3. Haghighi AH, Hasani-Sadrabadi MM, Dashtimoghadam E, Bahlakeh G, Shakeri SE, Majedi FS, HojjatiEmami S, Moaddel H (2011) *Int J Hydrogen Energy* 36:3688-3696
4. Kreuer KD (2001) *J MembrSci* 185:29-39
5. Smitha B, Sridhar S, Khan A (2004) *Macromolecules* 37:2233-2339
6. Xue S, Yin G (2006) *ElectrochimActa* 52:847-853
7. Hasani-Sadrabadi MM, Dashtimoghadam E, Sarikhani K, Majedi FS, Khanbabaei GJ (2010) *J Power Sources*. 195:2450-2456
8. Hasani-Sadrabadi MM, Emami SH, Moaddel H (2008) *J Power Sources* 183:551-556
9. Brandon NP, Skinner S, Steele BC (2003) *Annu Rev Mater Re* 33:183-213
10. Sakiyama T, Tsutsui T, Masuda E, Imamura K, Nakanishi K (2003) *Macromolecules* 36:5039-5042
11. Arora S, Lal S, Kumar S, Kuma M, Kumar M (2011) *Scholars Research Library* 3:188-201
12. Mirzadeh H, Yaghoobi N, Amanpour S, Ahmadi H, Mohagheghi MA, Hormozi F (2002) *Iran Polym J* 11:63-68
13. Ma J, Choudhury NA, Sahai Y, Buchheit RG (2011) *J Power Sources* 196:8257-8264
14. Dashtimoghadam E, Hasani-Sadrabadi MM, Moaddel H (2010) *PolymAdvTechnol* 21:726-734
15. Yi H, Wu LQ, Bentley WE, Ghodssi R, Rubloff GW, Culver JN, Payne GF (2005) *Biomacromolecules* 6:2881-2894
16. Gumusoglu T, Albayrak Ari G, Deligoz H (2011) *J. Membr. Sci.* 376:25-34
17. Yamada M, Honma I (2006) *J PhysChem B* 110:20486-20490
18. Uma T, Nogami M (2007) *Chem Mater* 19: 3604-3610
19. Xu W, Lu T, Liu C, Xing W (2005) *ElectrochimActa* 50:3280-3285
20. Honma I, Nomura S, Nakajima H (2001) *J MembrSci* 185:83-94
21. Staiti P, Minutoli M, Hocevar S (2003) *J Power Sources* 90:231-235
22. Uma T, Nogami M (2007) *J ElectrochemSoc B* 154:845-851
23. Li L, Xu L, Wang Y (2003) *J Mater Sci Letters* 22:1595-1597
24. Miyake N, Wainright JS, Savinell RF (2001) *J ElectrochemSoc A* 148: 898-904
25. Chen Z, Holmberg B, Li W, Wang X, Deng W, Munoz R, Yan Y (2006) *J Chem Mater* 18:5669-5675
26. Alonso RH, Estevez L, Lian H, Kellarakis A, Giannelis EP (2009) *Polymer* 50:2402-2410



27. Thomassin JM, Pagnouille C, Bizzari D, Caldarella G, Germain A, Jerome R (2005) *Polymer* 46:11389-11395
28. Song MK, Park SB, Kim YT, Kim KH, Min SK, Rhee HW (2004) *ElectrochimActa* 50:639-643
29. Felice C, Ye S, Qu D (2010) *IndEngChem Res* 49:1514-1519
30. Rhee CH, Kim HK, Chang H, Lee JS (2005) *Chem Mater* 17:1691-1697
31. Kim Y, Lee JS, Rhee SH, Kim HK, Chang H (2006) *J Power Sources* 162:180-185
32. Hasani-Sadrabadi MM, Dashtimoghadam E, Majedi FS, HojjatiEmami S, Moaddel H (2011) *Int J Hydrogen Energy* 36:6105-6111
33. Jiang SP, Liu Z, Tian ZQ (2006) *Adv Mater* 18:1068-1072
34. Shao Z, Wang X, Hsing IM (2002) *J MembrSci* 210:147-153
35. Hasani-Sadrabadi MM, Dashtimoghadam E, Majedi FS, Kabiri K (2009) *J Power Sources* 190:318-321
36. Hasanabadi N, Ghaffarian SR, Hasani-Sadrabadi MM (2011) *Int J Hydrogen Energy* 36:15323-15332
37. Peckham TJ, Holdcroft S (2010) *Adv Mater* 22:4667-4690
38. Cui Z, Xing W, Liu C, Liao J, Zhang H (2009) *J Power Sources* 188:24-29
39. Janik MJ, Campbell KA, Bardin BB, Davis RJ, Neurock M (2003) *ApplCatal A: General* 256:51-68
40. Cui Z, Liu C, Lu T, Xing W (2007) *J Power Sources* 167:94-99
41. Hasani-Sadrabadi MM, Ghaffarian SR, Mokarram-Dorri N, Dashtimoghadam E, Majedi FS (2009) *Solid State Ion* 180:1497-1504
42. Hasani-Sadrabadi MM, Dashtimoghadam E, Majedi FS, Kabiri K, Solati-Hashjin K, Moaddel H (2010) *J MembrSci* 365:286-293
43. Alexandre B, Langevin D, Médéric P, Aubry T, Couderc H, Nguyen QT, Saiter A, Marais S (2009) *J Membrane Sci* 328:186-204
44. Yoon K, Sung H, Hwang Y, Noh SK, Lee D (2007) *Appl Clay Sci* 38:38-48



Using the electrode based on various core- shell electrocatalyst in polymer electrolyte fuel cells.

M. Javaheri^{*,a}, Z. Khakpour^a

a Department of ceramic, Materials and Energy Research Center, karaj, iran.

*Javaheri54@yahoo.com

Abstract

Recently the core@shell structures are attractive. Researchers were attention to these structures for electrocatalytic applications. Many methods have been reported for synthesis of core@shell. In this work, we attempt to discuss the several studies including: different metal that using as a core or shell, synthesis techniques, and finally electrochemical performance and physical characterization of synthesised electrocatalyst. In addition to, a number of examples are presented to illustration the various applications of such structures and impart the enhancement of electrocatalytic performance due to core@shell structures.

1. Introduction

Fuel cells are receiving increased recognition as notable alternatives to our present power sources because they exhibit high operational efficiencies and impressive environmental acceptability. Polymer electrolyte fuel cell (PEMFC) has great potential for use both in stationary power generation and vehicular power sources [1].

Platinum has a wide range of catalysis applications due to its unique chemical and physical characteristic [2-5]. However, a critical problem for Pt catalysts is the high cost due to limited supply. Pt- based elrcrocatalysts are usually employed in PEMFC as cathode electrocatalysts for oxygen reduction reaction in relatively low temperature [6]. The major challenge in this field at present is to reduce the fuel cell energy cost by developing low cost materials, processes and components, which paves way for the massive introduction of this technology for the common people [7].

Bimetallic nanocrystals consisting of two distinct metals are attractive for a wide variety of catalytic and electrocatalytic applications as they can exhibit not only a combination of the properties associated with both metals but also enhancement or synergy due to a strong coupling between the two metals [8,9]. Many methods have recently been demonstrated for the synthesis of bimetallic



nanocrystals having a wide variety of different structures in the form of alloys, dendrites, core–shells, multi-shells, and monolayers.

(NATURE MATERIALS)Considerable progress has been made on Pt-based bi- and tri-metallic electrocatalysts, such as alloying Pt with 3d-transition metals, including Fe [8-13], Co [8, 14-18), Ni [8,16,17,19,20], Cu [21-23], Cr [16,24] and Mn [25,26]. To maximise Pt utilisation, the ideal structure of a Pt-based catalyst is where the total available Pt atoms are distributed on the electrochemical reaction interface. Following this consideration, the core-shell structure should represent an effective structure model where a monolayer or a few layers of Pt are arranged on inexpensive core materials. More importantly, it is rationally expected that the physical and chemical properties of the Pt shell can be effectively tuned by the underlying core material. This imparts significant room for improvement of the electrocatalytic performance of the Pt shell.[Energy Environ. Sci., 2011, 4, 2736–2753]

[48] Core–shell nanostructure is an effective way to increase the utilization efficiency of precious metal electrocatalysts. By replacing the core of the nanoparticles of electrocatalysts with less expensive or non-precious metals and/or by producing Pt nanosphere shell with high surface-to-volume ratios, the high catalytic activity and utilization efficiency of Pt electrocatalysts and low Pt loading and consequently reduced cost can be achieved [27-29,31-36].

[40] The core@shell can be regarded as a kind of phase separation of an alloy into a core surrounded by the shell composed of a metal [30,40]. This new class of catalysts can be tailored to show significantly enhanced oxygen reduction reaction (ORR) and methanol oxidation reaction (MOR) kinetics, and at the same time possess improved stability of Pt under typical fuel cell operating conditions [37,38].

In this review, we begin with a brief discussion on the possible structures of core@shell nanocrystals, followed by an account of recent progress on synthetic approaches to such nanocrystals. In addition to the experimental procedures and mechanistic studies, a number of examples are presented to highlight the use of such core@shell nanocrystals as catalysts or electrocatalysts for various applications with enhanced performance relative to their mono or bimetallic counterparts.



2. Preparation techniques of core@shell /support electrocatalyst

This section gives a general viewpoint of core-shell electrocatalyst, including support materials, the various metals that using for core or shell and techniques for the preparation of such electrocatalyst.

Recently, variety of carbon materials have been explored as the catalyst supports in PEMFC. The materials that used in these studies consists: carbon Vulcan [39- 45, G. Zhang et al. / *Applied Catalysis B: Environmental* 132–133 (2013) 183– 194] Ti₄O₇ [46] Glassy carbon [47,48] single wall nanotube [49] Multiwall carbon nanotube [50, Chem. Commun., 2010, 46, 2085–2087, H. Zhao et al. / *Electrochemistry Communications* 10 (2008) 1527–1529] TiO₂@C [51]. Each of them support was used for specific purpose.

In order to synthesise core@shell the various transition metals were used as the electrocatalyst. The most research contains the platinum that applied as a core or shell. The metals that in these researches were used including the Ru-Pt [46, Chem. Commun., 2010, 46, 2085–2087, H. Zhao et al. / *Electrochemistry Communications* 10 (2008) 1527–1529] , Au-Pt [47, 43], Pt-Fe [49], Pd/Pt [48, G. Zhang et al. / *Applied Catalysis B: Environmental* 132– 133 (2013) 183– 194], Ru@Pt_xPd_y [39], M-Pt (M = Ru, Fe₃O₄, Pd) [52], PdCu-Pt [40], Ag-Pt [50], PdM@PdPt/C (M = Pt, Ni, Co, Fe, and Cr) [42], Co@Pt [44, H. Zhao et al. / *Electrochemistry Communications* 10 (2008) 1527–1529], Pt/TiO₂@C[51] and Cu/Pt [45].

In order to dispersion the electrocatalyst on catalyst support exist the several techniques. Some methods that are reported contain: the impregnation method; electrochemical method, pyrolysis method, Micro wave irradiation, colloidal synthesis, ultrasonic agitation, magnetron sputtering technique and so on [39-52]. Among these, the main approach employed in most of the studies was a successive two-step reduction; at first, the core part is formed by an appropriate reduction

method, and then a precursor metal ion for the shell part is successively reduced onto the core metal. Impregnation method is widely used rather than the others methods to obtain fuel cell catalyst [39, 40, 42-44, 50, 51, G. Zhang et al. / *Applied Catalysis B: Environmental* 132– 133 (2013) 183– 194, H. Zhao et al. / *Electrochemistry Communications* 10 (2008) 1527–1529]. In impregnation method, a solution of metal salts are prepared and mixed with the material support. Of course precursor mixing with support and reduction the metallic ions was carried out step by step. First process, contained reduction of the metal that selected as a core, after prepared the core/support, in the second process, the shell metal has been reduction on the preformed catalyst.



Now the core@shell/support is synthesised. In this technique, resulting catalyst must be washed and need heat treatment, under either inert or reducing gas streams, in order to removed impurities [39, 40, 42-44, 50, 51].

3. *Catalyst characterization*

The synthesis catalyst can be characterised with recording x-ray diffraction (XRD) patterns, transmission electron microscopy (TEM) measurement and the practical composition of the catalysts was evaluated by using inductively coupled plasma (ICP).

The electrochemical measurements of catalysts were performed using an electrochemical work station (various potentiostat /galvanostat instrument). A common three-electrode electrochemical cell was used for the measurements. The counter and reference electrode were a platinum plate/ wire and an Ag/AgCl electrode, respectively. The working electrode usually was a glassy carbon disk. In almost case, with the aim of making the catalyst ink, for electrochemical studying, the synthesis catalyst was dispersion in solvent and added nafion solution and eventually done electrochemical tests.

4. *Core-shell catalytic application*

The core–shell structures have been widely used as catalysts, and the functions of the core or the shell vary among different reactions. Generally, the core–shell catalysts can be divided into three groups: (1) the core serves as the support and the shell is the active site, (2) the core is the active site and the shell works as the protector, and (3) both core and shell are active sites. In the follow, we will provide a brief review on the catalytic applications of core–shell structures.

Pd and Pt nanoparticles (NPs) have been used as catalysts for many reactions. The active parts of the catalysts are the surface of the NPs and the large part of the expensive metal in the core is a waste. Introducing the cheaper metals as the core such as Ni and Cu is an effective way to economize the catalyst production cost. Furthermore, the introduction of the cheaper core such as Ni within the Pd shell NPs was reported to enhance the catalytic efficiency in the Sonogashira coupling reaction [S. U. Son, Y. Jang, J. Park, H. B. Na, H. M. Park, H. J. Yun, J. Lee and T. Hyeon, J. Am. Chem. Soc., 2004, 126, 5026.]. The Ni–Pd core–shell NPs (3.9 nm) show a much better catalytic effect than the pure Pd NPs (3.5 nm) with a comparable particle size. The enhanced catalytic activity is due to the large number of Pd atoms on the particle surface as compared with the same amount of pure Pd NPs. The Ni@Pd core@shell NPs have also demonstrated a similar catalytic effect on the CO oxidation as the pure Pd NPs, but totally different from that of the pure Ni NPs, Fig. 1. Pure Ni NPs are active

only at higher temperatures. The deactivation was not observed in the Ni@Pd core shell NPs indicating that the core@shell structure is stable and does not form an alloyed structure during the catalytic reaction process. The very close CO oxidation behavior between the core@shell NPs and the pure Pd NPs provides the advantage of the core@shell structural NPs to save the more costly Pd core for the catalysts. [S. Sao-Joao, S. Giorgio, J. M. Penisson, C. Chapon, S. Bourgeois and C. Henry, J. Phys. Chem. B, 2005, 109, 342] The supported Ni catalysts such as Ni/Al₂O₃, Ni/MgO–Al₂O₃ with a core@shell structure have also been proven to be promising in all types of methane reforming reactions, such as partial oxidation of methane, steam reforming, and CO₂ reforming (Fig. 1). In many catalytic reactions, although the metal NPs were reported to be active, their long-term stability either in solutions or at high temperature conditions is always a critical problem. Especially when the reaction temperature is high, tiny NPs start to melt and agglomerate together, yielding larger particles. [Nanoscale, 2011, 3, 4474–4502]

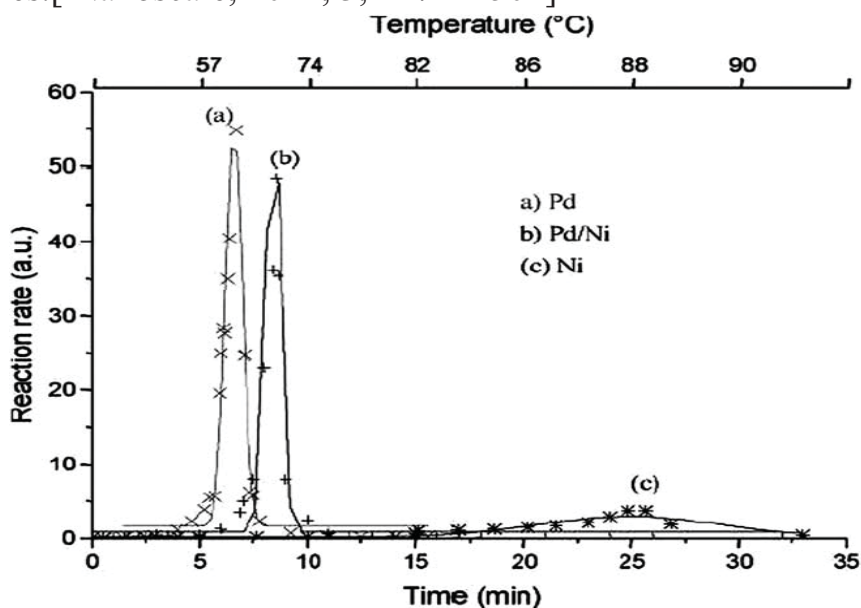


Fig. 1 CO₂ production rate in the reactor as a function of the time, during heating from room temperature to 100 °C for the pure Pd, Ni@Pd core@shell, and pure Ni NPs.

5. Results and discussion

In core-shell structure, the catalytic properties are generally determined by the shell on the surface. When compared with a nanocrystal of the same volume but made of pure Pt, an M@Pt core@shell structure is advantageous for reducing the cost while maintaining the catalytic performance. When the Pt shell is relatively thin (e.g., only a few atomic layers thick), the electronic coupling associated with the M core and the Pt shell may also enhance the performance of such nanocrystals in a specific catalytic reaction. Seeded growth has proven to be a facile and versatile approach to the synthesis of M@Pt core@shell nanocrystals,



where the epitaxial relationship between M and Pt allows for the formation of Pt shells smooth on the surface. By controlling the molar ratio between the Pt precursor and the M seeds, the thickness of Pt shells can be increased from a few atomic layers to several and even tens of nanometers. The epitaxial relationship also helps maintain the proportions of different facets exposed on the surface unless a very thick shell or a strong capping agent for Pt is involved. In general, the shapes of M@Pt core@shell nanocrystals can be controlled by starting with M nanocrystals in different shapes as the seeds. [*Chem. Soc. Rev.*, 2012, **41**, 8035–8049].

As reported in [*Chem. Soc. Rev.*, 2012, **41**, 8035–8049], developed a facile approach to the synthesis of Pd@Pt core@shell nanoplates with hexagonal and triangular shapes through layer-by-layer epitaxial growth of Pt on Pd nanoplates. This synthesis was conducted by reducing H_2PtCl_6 with citric acid (CA) in the presence of Pd nanoplates as seeds and PVP as a stabilizing agent in an aqueous solution. The TEM image in Fig. 2A shows that the product was consisted of a core being a hexagonal or triangular Pd nanoplate and the shell being made of a thin, uniform Pt shell, demonstrating the layer-by-layer epitaxial growth of Pt on Pd nanoplates [B. Lim, J. Wang, P. Camargo, M. Jiang, M. Kim and Y. Xia, *Nano Lett.*, 2008, 8, 2535.]. They believe that the close matching between the lattice constants of Pd and Pt and the slow reduction rate associated with the weak reducing power of CA played a key role in achieving the epitaxial growth of Pt shells on Pd nanoplates. This claim was supported by the observed formation of Pd@Pt nanodendrites when ascorbic acid AA rather than CA was used as a reducing agent. They also systematically investigated the epitaxial growth of Pt on well-defined Pd nanocrystals with different shapes such as regular octahedrons, truncated octahedrons, and cubes. The epitaxial growth of Pt shells on regular and truncated octahedrons of Pd at slow reduction led to the formation of Pd–Pt core–shell octahedrons (Fig. 1B and C). However, an incomplete octahedral Pt shell was formed when the Pt cube was used as a seed (Fig. 1D). [*Chem. Soc. Rev.*, 2012, **41**, 8035–8049]

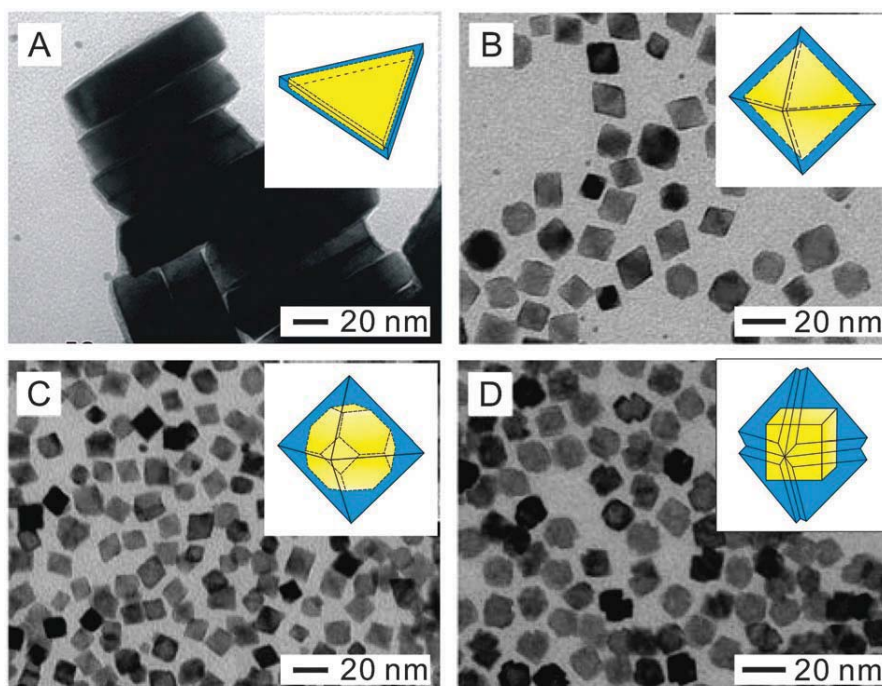


Fig. 1 TEM images of Pd–Pt core–shell nanocrystals that were obtained by reducing K_2PtCl_4 with citric acid (CA) as a reducing agent in the presence of Pd seeds with different shapes: (A) plate-like (B) octahedral, (C) truncated octahedral, and (D) cubic

Geng Zhang et al, made use of commercial 20% Pd/C catalysts as substrate and Pt is deposited onto the Pd nanoparticles by a chemical reduction method. The obtained Pd-Pt/C catalysts have a Pd@Pt core@shell structure. They explain the XRD pattern of Pd@Pt/C, they believe, because Pt and Pd have the same crystal structure (FCC) and very close lattice parameter, the sets of diffraction peaks of Pt and Pd are overlapped. The diffraction peaks of Pd@Pt/C are remarkably strengthened in comparison to Pd/C, indicating good crystallinity of the Pd@Pt/C catalysts. Furthermore, one can be observed that the peaks of Pd@Pt/C locate between that of Pd/C and Pt/C, which is consistent with the results of core@shell structured nanoparticles reported in literature where the diffraction peaks of core-shell structure locate between the individual core and shell metals. [G. Zhang et al. / Applied Catalysis B: Environmental 132– 133 (2013) 183– 194]

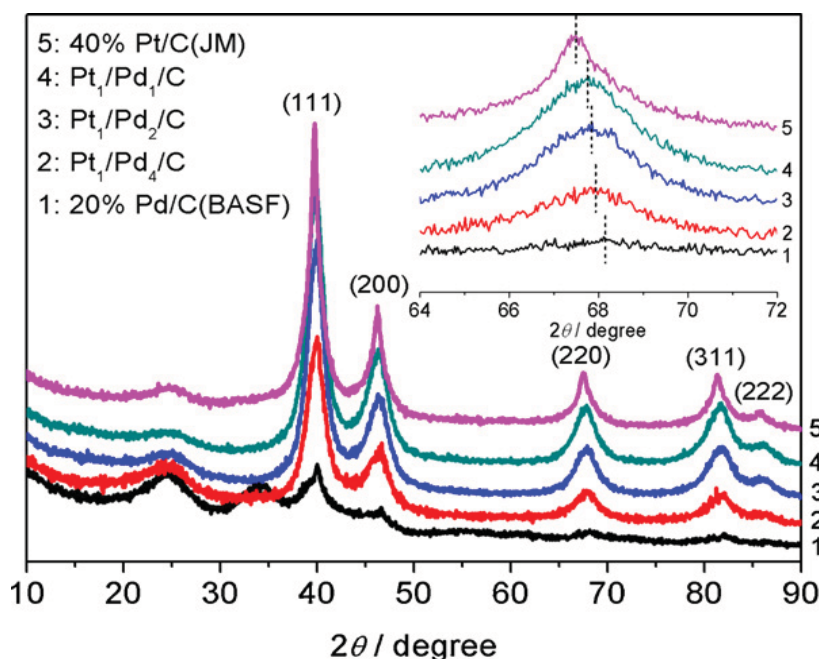


Fig. 3 XRD patterns of 20% Pd/C (BASF), 40% Pt/C (JM), Pd₁@Pt₁/C, Pd₂@Pt₁/C and Pd₄@Pt₁/C; the insert shows the detailed lines of FCC (2 2 0) peaks.

Haili Gao and coworkers[39] report the preparation and characterizations of core-shell structured Ru@Pt_xPd_y/C nanoparticles for formic acid electro-oxidation. Ruthenium was selected as the core element because very small and highly dispersed Ru nanoparticles can be easily prepared, hopefully yielding highly stable and high noble metal utilization catalyst. Another gained advantage for the usage

of Ru core is the expected catalytic activity enhancement between Ru and Pt due to the modified reaction kinetics. Electrochemical evaluation by cyclic voltammetry, indeed, confirmed the beneficial effect of Ru core and Ru@Pt_xPd_y/C registered high catalytic activity for formic acid oxidation. Their results indicate that carbon supported core-shell structured Ru@Pt_xPd_y/C catalysts have been developed by deposition of Pt_xPd_y on the pre-formed Ru/C catalysts. TEM observation found that the particle population of Ru@Pt_xPd_y/C was similar to that of the pre-formed Ru/C except for particle grown-up, an indication of core-shell structure formation. The catalytic activity toward formic acid oxidation of the catalysts was evaluated by half-cell evaluation (cyclic voltammetry and chronoamperometric) and single cell measurements. It was found that Ru@Pt_xPd_y/C displayed enhanced catalytic activity, improved stability and enhanced cell performance. In fact, it is reasonable to suggest that Pt and Pd would be reduced on the small Ru particles based on the following: (i) the interaction between the metals are stronger than the interaction between metal and



carbon, (ii) aging effect can make small Pt_xPd_y particles migrate to the surface of Ru particles.

Hwang et al. reported that Pt-decorated Ru catalysts had higher mass activity for MOR than commercial Pt–Ru catalysts. The enhancement of the electrocatalytic activity was ascribed to the high degree of electron transfer and the long-range ordered hexagonally close-packed structure. [Energy Environ. Sci., 2011, 4, 2736–2753] These results clearly demonstrate that catalysts containing small amounts of Pt on the surface of a less expensive metal may represent a useful approach to reduce cost. [Energy Environ. Sci., 2011, 4, 2736–2753]

In the works of Stamenkovic and co-workers [V. R. Stamenkovic, B. S. Mun, M. Arenz, K. J. J. Mayrhofer, C. A. Lucas, G. F. Wang, P. N. Ross and N. M. Markovic, Nat. Mater., 2007, 6, 241–247, V. R. Stamenkovic, B. S. Mun, K. J. J. Mayrhofer, P. N. Ross and N. M. Markovic, J. Am. Chem. Soc., 2006, 128, 8813–8819] a fundamental insight into ORR activity of three pure Pt surface layers (i.e., Pt-skin, Ptskeleton, and pure polycrystalline Pt) was revealed. The kinetic current of ORR was shown to increase in the order of pure polycrystalline Pt surface < Pt-skeleton < Pt-skin. In line with the order of activity, the Pt-skin was found to possess the maximum positive-shift in reduction potential of oxide and the maximum down-shift in the d-band centre versus the Fermi level. According to d-band centre theory, the down-shifted d-band centre of Pt versus the Fermi level can lead to weaker oxygen binding energy, which is believed to be a key factor to improved Pt ORR activity. [Energy Environ. Sci., 2011, 4, 2736–2753]

6. Conclusion

As mentioned to the previous sections, from the TEM, XRD, ICP, ... technique can be observe that the core@shell structure was synthesise by several researchers, and electrochemical tests indicate that the core@ shell structures have an appropriate electrocatalyst activity and by using these structure the cost of fuel cells decreased; whereas, the catalyst utilization increased.

In the foreseeable future, the area of bimetallic nanocrystals will ontinuously expand in terms of development of new methodologies; variation in materials; control of size, shape, structure, and composition; understanding of the structure–property relationship; and exploration of applications.



Reference

- [1] (electrochemical acta 46 2001 1657-1663) zooncan
- [2] Li WZ, Sun KQ, Hu Z, Xu BQ. Characteristics of low platinum Pt-BaO catalysts for NO_x storage and reduction. Catal Today 2010;153:103-10.
- [3] Liu P, Wang J, Zhang X, Wei R, Ren X. Catalytic performances of dealuminated Hb zeolite supported Pt catalysts doped with Cr in hydroisomerization of n-heptane. Chem Eng J 2009;148:184e90.
- [4] Ali J, Priscilla A, Sylvie L, Josette OF, Jumas JC. Effect of indium in trimetallic Pt/Al₂O₃SnIneCl naphtha-reforming catalysts. J Catal 2010;272:275e86.
- [5] Matsumoto T, Komatsu T, Arai K, Yamazaki T, Kijima M, Shimizu H, et al. Reduction of Pt usage in fuel cell electrocatalysts with carbon nanotube electrodes. Chem Commun 2004;7:840e1.
- [6] (power sources 139 2005 73-78) zooncan
- [7] (international journal of hydrogen energy 29 2004 915- 920) zooncan
- [8]. Stamenkovic, V. R. et al. Trends in electrocatalysis on extended and nanoscale Pt-bimetallic alloy surfaces. Nature Mater. 6, 241_247 (2007).
- [9]. Yano, H., Kataoka, M., Yamashita, H., Uchida, H. & Watanabe, M. Oxygen reduction activity of carbon-supported Pt_M (MDV, Ni, Cr, Co, and Fe) alloys prepared by nanocapsule method. Langmuir 23, 6438_6445 (2007).
- [10]. Antolini, E., Salgado, J. R. C. & Gonzalez, E. R. The stability of Pt_M (MDfirst row transition metal) alloy catalysts and its effect on the activity in low temperature fuel cells_a literature review and tests on a Pt_{Co} catalyst. J. Power Sources 160, 957_968 (2006).
- [11]. Rao, C. V. & Viswanathan, B. ORR activity and direct ethanol fuel cell performance of carbon-supported Pt_M (MDFe, Co, and Cr) alloys prepared by polyol reduction method. J. Phys. Chem. C 113, 18907_18913 (2009).
- [12]. Kim, J., Lee, Y. & Sun, S. H. Structurally ordered FePt nanoparticles and their enhanced catalysis for oxygen reduction reaction. J. Am. Chem. Soc. 132, 4996_4997 (2010).
- [13]. Malheiro, A. R., Perez, J. & Villullas, H. M. Well-alloyed PtFe/C nanocatalysts of controlled composition and same particle size: Oxygen reduction and methanol tolerance. J. Electrochem. Soc. 156, B51_B58 (2009).
- [14]. Stamenkovic, V. R., Mun, B. S., Mayrhofer, K. J. J., Ross, P. N. & Markovic,

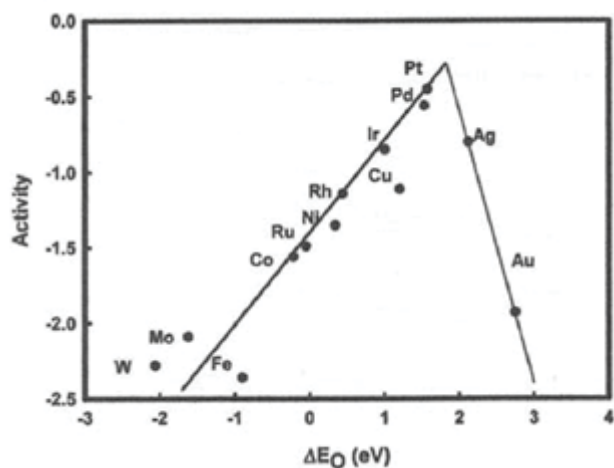


- N. M. Effect of surface composition on electronic structure, stability, and electrocatalytic properties of Pt-transition metal alloys: Pt-skin versus Pt-skeleton surfaces. *J. Am. Chem. Soc.* 128, 8813_8819 (2006).
- [15]. Hwang, S. J. et al. Ternary Pt_Fe_Co alloy electrocatalysts prepared by electrodeposition: Elucidating the roles of Fe and Co in the oxygen reduction reaction. *J. Phys. Chem. C* 115, 2483_2488.
- [16]. Min, M. K., Cho, J. H., Cho, K. W. & Kim, H. Particle size and alloying effects of Pt-based alloy catalysts for fuel cell applications. *Electrochim. Acta* 45, 4211_4217 (2000).
- [17]. Stamenkovic, V., Schmidt, T. J., Ross, P. N. & Markovic, N. M. Surface composition effects in electrocatalysis: Kinetics of oxygen reduction on well-defined Pt₃Ni and Pt₃Co alloy surfaces. *J. Phys. Chem. B* 106, 11970_11979 (2002).
- [18]. Xin, H. L. et al. Atomic-resolution spectroscopic imaging of ensembles of nanocatalyst particles across the life of a fuel cell. *Nano Lett.* 12, 490_497 (2012).
- [19]. Wu, J. B. et al. Truncated octahedral Pt₃Ni oxygen reduction reaction electrocatalysts. *J. Am. Chem. Soc.* 132, 4984_4985 (2010).
- [20]. Zhang, J., Yang, H. Z., Fang, J. Y. & Zou, S. Z. Synthesis and oxygen reduction activity of shape-controlled Pt₃Ni nanopolyhedra. *Nano Lett.* 10, 638_644 (2010).
- [21]. Strasser, P. et al. Lattice-strain control of the activity in dealloyed core_shell fuel cell catalysts. *Nature Chem.* 2, 454_460 (2010).
- [22]. Mani, P., Srivastava, R. & Strasser, P. Dealloyed Pt-Cu core_shell nanoparticle electrocatalysts for use in PEM fuel cell cathodes. *J. Phys. Chem. C* 112, 2770_2778 (2008).
- [23]. Srivastava, R., Mani, P., Hahn, N. & Strasser, P. Efficient oxygen reduction fuel cell electrocatalysis on voltammetrically dealloyed Pt_Cu_Co nanoparticles. *Angew. Chem. Int. Ed.* 46, 8988_8991 (2007).
- [24]. Jeon, M. K., Zhang, Y. A. & McGinn, P. J. A comparative study of PtCo, PtCr, and PtCoCr catalysts for oxygen electro-reduction reaction. *Electrochim. Acta* 55, 5318_5325 (2010).
- [25]. Mukerjee, S., Srinivasan, S., Soriaga, M. P. & McBreen, J. Role of structural and electronic-properties of Pt and Pt alloys on electrocatalysis of oxygen reduction- an in-situ XANES and EXAFS investigation. *J. Electrochem. Soc.* 142, 1409_1422 (1995).
- [26]. Kang, Y. & Murray, C. B. Synthesis and electrocatalytic properties of cubic



- Mn_Pt nanocrystals (nanocubes). *J. Am. Chem. Soc.* 132, 7568_7569 (2010).
- [27] S.J. Guo, Y.X. Fang, S.J. Dong, E.K. Wang, *J. Phys. Chem. C* 111 (2007) 17104.
- [28] J.H. Zeng, J. Yang, J.Y. Lee, W.J. Zhou, *J. Phys. Chem. B* 110 (2006) 24606.
- [29] R. Tena-Zaera, A. Katty, S. Bastide, C. Levy-Clement, *Chem. Mat.* 19 (2007) 1626.
- [30] Kobayashi H, Yamauchi M, Kitagawa H, Kubota Y, Kato K, Takata M. Hydrogen absorption in the core/shell interface of Pd/Pt nanoparticles. *J Am Chem Soc* 2008;130:1818-9.
- [31] Yang JH, Zhou WJ, Cheng CH, Lee JY, Liu ZL. Pt-decorated PdFe nanoparticles as methanol-tolerant oxygen reduction electrocatalyst. *ACS Appl Mater Interfaces* 2010;2:119-26.
- [32] Shimizu K, Cheng IF, Wai CM. Aqueous treatment of singlewalled carbon nanotubes for preparation of Pt-Fe core-shell alloy using galvanic exchange reaction: selective catalytic activity towards oxygen reduction over methanol oxidation. *Electrochem Commun* 2009;11:691-4.
- [33] Chen Y, Yang F, Dai Y, Wang W, Chen S. Ni@Pt core-shell nanoparticles: synthesis, structural and electrochemical properties. *J Phys Chem C* 2008 ; 112:1645-9.
- [34] Sarkar A, Manthiram A. Synthesis of Pt@Cu core-shell nanoparticles by galvanic displacement of Cu by Pt⁺⁴ ions and their application as electrocatalysts for oxygen reduction reaction in fuel cells. *J Phys Chem C* 2010;114:4725-32.
- [35] Koh S, Strasser P. Electrocatalysis on bimetallic surfaces: modifying catalytic reactivity for oxygen reduction by voltammetric surface dealloying. *J Am Chem Soc* 2007;129:12624-5.
- [36] Whittingham MS, Savinell RF, Zawodzinski T. Introduction: batteries and fuel cells. *Chem Rev* 2004;104:4243-4.
- [37] Wang G, Wu H, Wexler D, Liu H, Savadogo O. Ni@Pt core-shell nanoparticles with enhanced catalytic activity for oxygen reduction reaction. *J Alloys Compd* 2010;503:L1-4.
- [38] Zhang JL, Vukmirovic MB, Sasaki K, Nilekar AU, Mavrikakis M, Adzic RR. Mixed-metal Pt monolayer electrocatalysts for enhanced oxygen reduction kinetics. *J Am Chem Soc* 2005;127:12480-1.
- [39] *Electrochimica Acta* 56 (2011) 2024–2030,
- [40] *international journal of hydrogen energy* 36 (2011)83-848
- [41] *Journal of Power Sources* 196 (2011) 9117– 9123

- [42] Journal of Catalysis 291 (2012) 26–35.
 [43] Journal of Colloid and Interface Science 344 (2010) 132–136.
 [44] Journal of Power Sources 223 (2013) 190-198.
 [45] Journal of Power Sources 180 (2008) 84–91.
 [46] Applied Energy 103 (2013) 507–513.
 [47] Electrochimica Acta 87 (2013) 432– 437’
 [48] Electrochemistry Communications 10 (2008) 1575–1578.
 [49] Electrochemistry Communications 11 (2009) 691–694.
 [50] International journal of hydrogen energy 37 (2012)13365-13370.
 [51] Materials Chemistry and Physics 137 (2013) 704-708.
 [52] international journal of hydrogen energy article in press (2 0 1 2)



Trends in oxygen reduction activity plotted as a function of both the O and the OH binding energy [44]. (Reprinted with permission from J Phys Chem B 2004;108:17886–92. Copyright 2004 American Chemical Society.) [44] Norskov JK, Rossmeisl J, Logadotir A, Lindqvist L, Kitchin JR, Bligaard T, et al. Origin of the overpotential for oxygen reduction at a fuel cell cathode. J Phys Chem B 2004;108:17886– 92.



Investigation of Electrolyte Conductivity on Performances of Sediment Microbial Fuel Cell

Zahra Najafgholi¹, Mostafa Rahimnejad^{*2}, Ghasem Najafpour³, Mostafa Ghasemi⁴
and Paniz Izadi⁵

Biotechnology Research Lab., Faculty of Chemical Engineering, Noshirvani University, Babol, Iran

z.najafgholi@gmail.com

Abstract

Sediment microbial fuel cells (SMFCs) are promising technology for viable source of energy. SMFC is considered to be an alternative renewable energy sources for small devices. In this research, a laboratory-scale SMFC was fabricated to bioelectricity generation from organic compound in Shallow sediment that was gathered from Mahmudabad River. The initial SMFC voltage was less than 150 mV but the voltage gradually increased and reached to maximum steady state condition (450 mV) after 6 days. Effect of electrolyte conductivity on SMFC performance was investigated. Electrical conductivity adjusted at 4 different levels (19.5, 26.2, 38.5 and 54.6 $\mu\text{S}/\text{cm}$) by addition of several concentration of NaCl (0.25, 0.5 0.75 and 1 M). With addition of cathode solution conductivity, SMFCs performance improved about 6 fold. Maximum generated power and current density, 49.84 mW/m^2 and 596.41 mA/m^2 , respectively, obtained at NaCl.

Keywords: Sediment Microbial Fuel Cell, Bioelectricity, Conductivity, Power density.

1. Introduction

A microbial fuel cell (MFC) is a device that is able to directly convert chemical energy existing in organic or inorganic matters to bioelectricity by active bacterial oxidation [1-3]. Sediment microbial fuel cell (SMFC), recently appears in fuel cell family, is a simple configuration of MFC which generate electricity from aquatic environment[4-8]. SMFC involves an embedded anode in anoxic sediment which allows electrons resulting from degradation of organic/inorganic matter, contained in the sediment, to pass via external circuit to the cathode located in oxic above liquid column [4]. At cathode surface electrons react with dissolved oxygen at the cathode solution and the results is water. Because of the presence of natural gradient in sediment, the anaerobic environment exists and the membrane that commonly used

¹ MS. student

² Assistant professor of chemical engineering, Babol Noshirvani university, rahimnejad@nit.ac.ir

³ Professor of chemical engineering, Babol Noshirvani university, Naafpour@nit.ac.ir

⁴ Assistant professor of chemistry, UKM university, Malaysia, mostafghasemi@gmail.com

⁵ MS student of chemical engineering, Babol Noshirvani university, paniz_izadi@yahoo.com



in MFC is not necessary. Furthermore, due to the existence of bacteria, such as *Geobacteraceae*, which are capable of transferring electrons directly to electron acceptor (anode)[9] mediators that are toxic and have negative effect on environment are not used. Based on the related literature it has been proven that SMFC has several benefits [10-15]. In addition, continuous replacement of organic matter into sediment by the above liquid column helps this device to be used as viable power supplier [11]. Therefore, SMFCs receive significant attention recently. In general, SMFCs, due to scanty content of organic matter and mass transfer limitation in sediment, generate low electricity[16]. In spite the fact that they generate low electricity, some researcher successfully use this technology for electrification of low power equipments. Donovan et al have used SMFC to power wireless sensor [17]and Tender et al. also used it in meteorological buoy[11].

Several factors have been investigated [18-21]and a lot of effort has been made to improve power generation. Rezaei et al illustrated with addition of chitin and cellulose as substrate mass transfer limitation can be overcome [22]. Zhene et al used rotating cathode to increase the power generation in SMFC [23]. Research in this field of fuel cell must be continued to improve SMFC performances.

Since it is expected to reach higher power generation with the increase of electrolyte conductivity, which results in a low electrolyte resistance, the objective of this study is investigate effect of electrolyte conductivity on power generation. To increase electrolyte conductivity NaCl with several concentrations were selected as a cheap, abundant and easy available substance.

2. Materials and Methods

2.1. Sediment

Shallow sediment (0-15 cm under the water/sediment interface) were gathered from Mahmudabad River estuary located Mahmudabad in the north of Iran. Also the water collected from the similar location at the same time. Sediment mechanically mixed in the laboratory to sure that composition of sediment is homogeneous and used without any pretreatment in SMFCs. Water electrical conductivity was determined 855 μ S/cm.

2.2 SMFC configuration and operating conditions

Fabricated SMFCs were of cylindrical shape and made of polycarbonate with an inner diameter of 8cm and height of 15cm. SMFCs were assembled as soon as samples arrival. In this study used graphite plate as anode (4 cm* 3cm*0.36cm) and cathode (2 cm* 3cm*0.36cm) electrodes and electrodes applied without catalysts on it. SMFC filled with 400 ml wet sediment. The anode entombed 8 cm below the sediments surface. After then SMFC filled with 200 ml rivers water and cathode placed 2 cm below water/air interface. As depicted in Figure 1 electrodes connected to datalogger by electrically insulated copper wire which connected to computer subsequently. Sediment MFCs were operated in duplicate to ensure that the results are trustworthy.

During the experiment SMFC were operated at ambient temperature (8-17 °C) and temperature was not controlled throughout the operation. Water lost from evaporation was manually replenished with distilled water to constant level of dissolved oxygen concentration, electrical conductivity, pH and salinity identical to the nature environment.

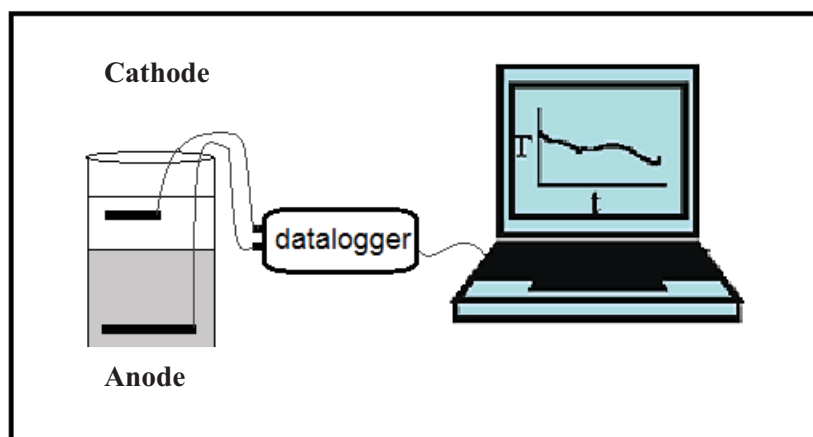


Figure 1 : Schematic diagram from fabricated sediment microbial fuel cell.

2.3. Analyses

The open circuit voltage of SMFC were measured by multimeter and recorded at 12 h intervals. The performance of the MFC system was evaluated by polarization curve. Polarization curves were obtained by an external resistance. Power and current were calculated based on the following equations:

$$P=I \cdot E \quad (1)$$

$$I=(E/R_{ext}) \quad (2)$$

Where P is the generated power; E is the measured cell voltage; R_{ext} is the external resistance and I is the produced current. The produced current and power normalized by the surface area of the used membrane were recorded online every 4 minutes using analog digital data acquisition system. The system had measurements for variable resistances ($65535-1 \Omega$) which were imposed to the MFC. The current in MFC was recorded, dividing the obtained voltage by the defined resistance. Then, the system provides power calculation by multiplication of voltage and current. Moreover, the online system demonstrates polarization graphs for power generation and MFC voltage with respect to the current. The online system had the ability to operate automatically or manually. While it operates in auto-mode, the assembled relays were able to regulate automatically the resistances. Voltage of MFC was amplified and then data was transmitted to a microcontroller by an accurate analog to digital converter. The microcontroller was also able to send the primary data to a computer by serial connection. In addition, a special function of MATLAB software (7.4, 2007a) was used to store and synchronically display the obtained data.

In order to calculate power and current density this values normalized with surface area of the cathode[4]. Electrical conductivity of electrolyte measured with conductivity meter (Mettler Toledo* FG-3,Switzerland).

3. Results and discussion

Initially, the river SMFC was operated at room temperature. After operating for 3 days the maximum generated open circuit voltage (OCV) was 307 mV at an external resistance of 2000Ω . Subsequently, this peak potential increase up to 457 mV in the following 6 days due to

increased conductivity. SMFC operated for 12 days and effect of electrolyte conductivity on power generation was investigated three days after inception of operation when the (OCV) reached a relatively stable level (307 mV). Thereafter, the experiment stopped to ensure that NaCl addition has no negative effect on bacterial activity. After 9 day, when voltage had no sharp drop, it is proven that this amount of NaCl has no negative effect and experiment continued (Figure 2). The obtained OCV was stable for the entire operation time.

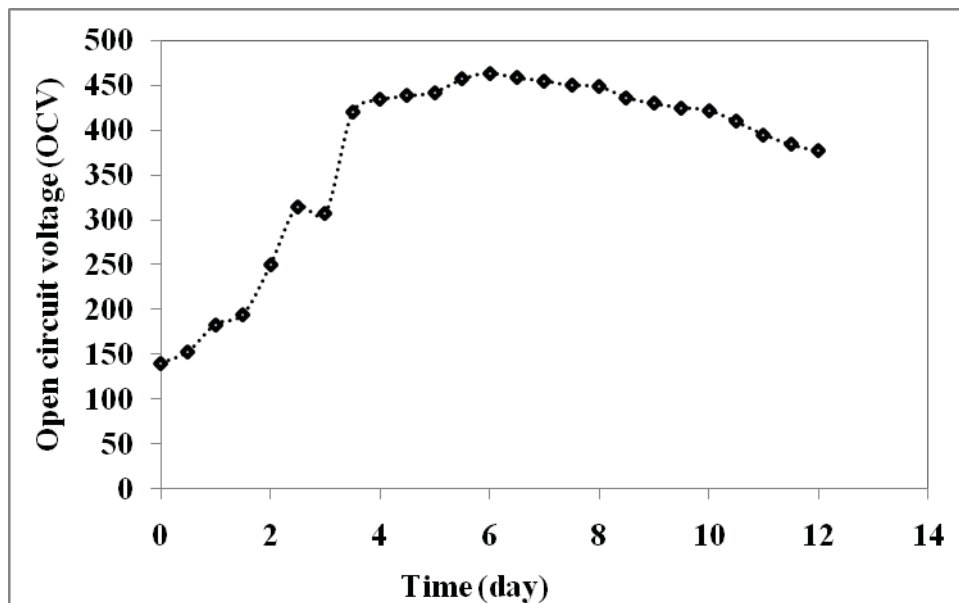


Figure 2 : OCV curve of SMFC for duration of 12 days of operation time.

In any power supply, the main important goal is to increase output power and then to acquire the highest current density under this situation of the maximum power density. In this aim, electrical conductivity was increased to 4 levels (15.5, 26.2, 38.5 and 54.6 $\mu\text{S}/\text{cm}$) by NaCl addition (0.25, 0.5 0.75 and 1 M). At first conductivity have been increased to 15.5 $\mu\text{S}/\text{cm}$ and 26.2 $\mu\text{S}/\text{cm}$ (0.5). As shown in Figure 3 it is clear that the power improved with respect to increase of conductivity. Afterwards conductivity has been enhanced to 38.5 $\mu\text{S}/\text{cm}$ and then to 54.6 $\mu\text{S}/\text{cm}$. It can be seen that with conductivity adjusted at 54.6 $\mu\text{S}/\text{cm}$ power increased and maximum power and current density obtained 49.84 mW/m^2 and 596.41 mA/m^2 , respectively. But when conductivity increased from 38.5 $\mu\text{S}/\text{cm}$ to 54.6 $\mu\text{S}/\text{cm}$ the power has not significantly improved.

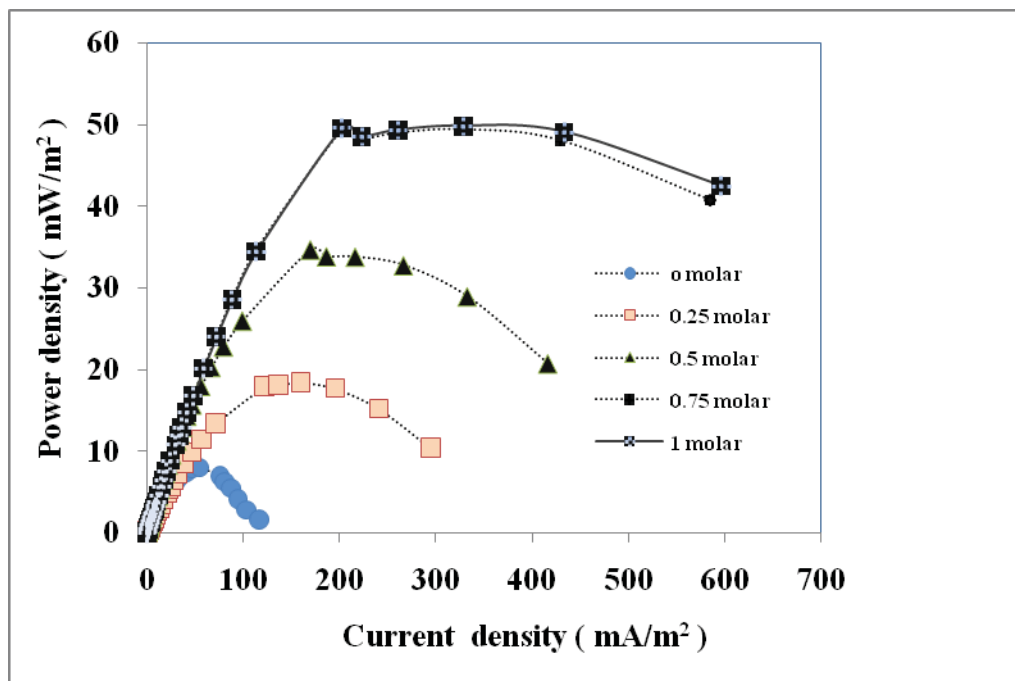


Figure 3 : Generated power density curves at different concentration of NaCl in cathode compartment.

The maximum power and current density at the each concentration of used NaCl are summarized in table 1. This table indicated conductivity of cathode solution is important parameter in SMFC. With NaCl addition which is a cheap and economic substance, the performance of SMFC was improved. Also table 1 indicated NaCl with concentration of 0.75 M has the best ability for transferring produced protons to cathode surface. This concentration of NaCl in aerobic cathode compartment increased produced power more than 6.25 times greater than when NaCl not used in SMFC.

Table 1 : Maximum generated power and current density obtained from this study at several concentrations of NaCl

NaCl molarities (M)	0	0.25	0.5	0.75	1
Maximum power density (mW/m ²)	8.005	18.436	34.68	49.315	49.609
Maximum current density (mA/m ²)	117.062	295.237	416.713	584.764	596.912

Polarization curve slope show the internal resistance such that as slope descents the internal resistance decreases. Figure 4 demonstrates that with increase of conductivity the internal resistance decreased and power density improved.

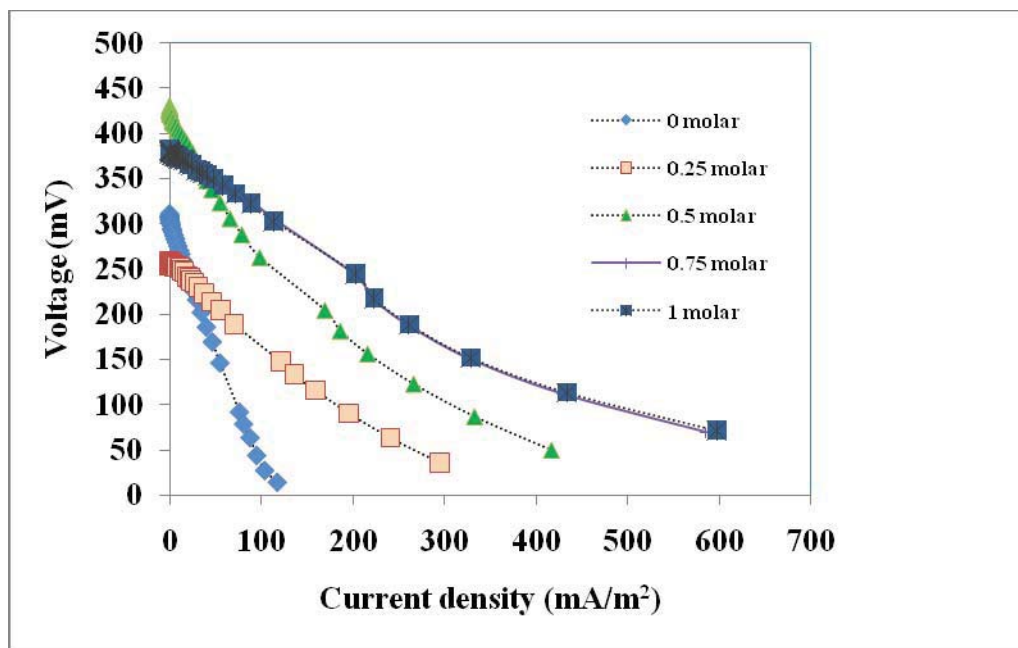


Figure 4: Polarization curves at various concentration of NaCl (0, 0.25, 0.5, 0.75 and 1 M) as increasing conductive agent.

4. Conclusions

In this research, the obtained results demonstrated that SMFC performance was enhanced by increasing electrical conductivity. The enhanced power density confirms that power increase with increasing electrolyte conductivity which attributed to reduction of internal resistance. Increasing conductivity by NaCl could be economic way to enhance power generation from SMFCs. Maximum generated power and current density were 49.315 mW/m² and 584.764 mA/m², respectively. The maximum condition was obtained at 0.75 M NaCl concentration.

Acknowledgement

The authors wish to acknowledge Biotechnology Research Center, Babol Noshirvani University of Technology, Babol, Iran for the facilities provided to accomplish this research.

References

1. Logan, B.E., et al., *Microbial fuel cells: methodology and technology*. Environmental Science & Technology, (2006). **40**(17): p. 5181-5192.
2. Lovley, D.R., *Microbial fuel cells: novel microbial physiologies and engineering approaches*. Current Opinion in Biotechnology, (2006). **17**(3): p. 327-332.
3. Venkata Mohan, S., et al., *Bioelectricity generation from chemical wastewater treatment in mediatorless (anode) microbial fuel cell (MFC) using selectively enriched hydrogen producing mixed culture under acidophilic microenvironment*. Biochemical Engineering Journal, (2008). **39**(1): p. 121-130.



4. Reimers, C.E., et al., *Harvesting energy from the marine sediment-water interface*. Environmental Science & Technology, (2001). **35**(1): p. 192-195.
5. Bond, D.R., et al., *Electrode-reducing microorganisms that harvest energy from marine sediments*. Science, 2002. **295**(5554): p. 483-485.
6. Holmes, D., et al., *Microbial communities associated with electrodes harvesting electricity from a variety of aquatic sediments*. Microbial ecology, (2004). **48**(2): p. 178-190.
7. Reimers, C., et al., *Microbial fuel cell energy from an ocean cold seep*. Geobiology, (2006). **4**(2): p. 123-136.
8. Donovan, C., et al., *Power management system for a 2.5W remote sensor powered by a sediment microbial fuel cell*. Journal of Power Sources, (2011). **196**(3): p. 1171-1177.
9. Bond, D.R. and D.R. Lovley, *Electricity production by Geobacter sulfurreducens attached to electrodes*. Applied and environmental microbiology, (2003). **69**(3): p. 1548-1555.
10. Huang, D.-Y., et al., *Enhanced anaerobic degradation of organic pollutants in a soil microbial fuel cell*. Chemical Engineering Journal, (2011). **172**(2-3): p. 647-653.
11. Tender, L.M., et al., *The first demonstration of a microbial fuel cell as a viable power supply: Powering a meteorological buoy*. Journal of Power Sources, (2008). **179**(2): p. 571-575.
12. Morris, J.M. and S. Jin, *Enhanced biodegradation of hydrocarbon-contaminated sediments using microbial fuel cells*. Journal of Hazardous Materials, (2012). **213-214**(0): p. 474-477.
13. Jeon, H.J., et al., *Production of algal biomass (Chlorella vulgaris) using sediment microbial fuel cells*. Bioresource Technology, (2012). **109**(0): p. 308-311.
14. Yan, Z., et al., *Enhanced degradation of phenanthrene and pyrene in freshwater sediments by combined employment of sediment microbial fuel cell and amorphous ferric hydroxide*. Journal of Hazardous Materials, (2012). **199-200**(0): p. 217-225.
15. De Schamphelaire, L., et al., *Outlook for benefits of sediment microbial fuel cells with two bio-electrodes*. Microbial Biotechnology, (2008). **1**(6): p. 446-462.
16. Tender, L.M., et al., *Harnessing microbially generated power on the seafloor*. nature biotechnology, (2002). **20**(8): p. 821-825.
17. Donovan, C., et al., *Batteryless, wireless sensor powered by a sediment microbial fuel cell*. Environmental Science & Technology, (2008). **42**(22): p. 8591-8596.
18. An, J., et al., *Determination of effects of turbulence flow in a cathode environment on electricity generation using a tidal mud-based cylindrical-type sediment microbial fuel cell*. Journal of Environmental Management, (2010). **91**(12): p. 2478-2482.
19. Song, T.-S. and H.-L. Jiang, *Effects of sediment pretreatment on the performance of sediment microbial fuel cells*. Bioresource Technology, (2011). **102**(22): p. 10465-10470.
20. Scott, K., et al., *Power from marine sediment fuel cells: the influence of anode material*. Journal of Applied Electrochemistry, (2008). **38**(9): p. 1313-1319.
21. Scott, K., et al., *Fuel cell power generation from marine sediments: Investigation of cathode materials*. Journal of Chemical Technology and Biotechnology, (2008). **83**(9): p. 1244-1254.
22. Rezaei, F., et al., *Substrate-enhanced microbial fuel cells for improved remote power generation from sediment-based systems*. Environmental science & technology, (2007). **41**(11): p. 4053-4058.



6th Iranian Fuel Cell Seminar
March 12 & 13 , 2013
Shahid Rajaei Teacher training University
Tehran - Iran



23. He, Z., H. Shao, and L.T. Angenent, *Increased power production from a sediment microbial fuel cell with a rotating cathode*. *Biosensors and Bioelectronics*, (2007). **22**(12): p. 3252-3255.



Synthesis and characterization of PVA/sulfonated graphene oxide nanocomposite membranes for used in PEMFC

Hossein Beydagh^{*1}, Mehran Javanbakht²

Department of Chemistry, Amirkabir University of Technology, Tehran, Iran

Hossein.beydagh@gmail.com

Abstract

A series of crosslinked organic–inorganic nanocomposite membranes have been prepared from poly (vinyl alcohol) (PVA) and sulfonated graphene oxide (SGO). The surface of the graphene oxide nanoparticles is modified by aryl diazonium salt of sulfanilic acid. The synthesized sulfonated graphene oxide and composite membranes were characterized using X-ray diffraction, FT-IR, SEM, DSC and impedance spectroscopy. Interestingly, sulfonated graphene oxide particles with a high surface area and small particle size showed the best results: good water uptake, long membrane life time under oxidative conditions, good thermal and mechanical stability and high proton conductivity.

Keywords: Nanocomposite membrane, Sulfonated graphene oxide, PEM Fuel cells

1. Introduction

Proton exchange membrane fuel cell (PEMFC) is potentially suitable for the power supply to all kinds of dynamoelectric vehicles, because it exhibits high efficiency and is friendly to environment [1]. Membranes of perfluorosulfonic acid (PFSA) have emerged as the state-of-the-art proton exchange membrane (PEM) material for fuel cells [2] as well as water electrolyzers [3] operating up to about 80 °C. However, the high cost, high methanol permeability [4] and low conductivity at low humidity or high temperature [5] have limited its further application. Composite membranes consisting of this polymer backbone and inorganic materials have also been studied because of controllable chemical and physical properties produced by combining different components, may be suitable for developing alternate proton exchange membranes. Organic-inorganic composites have attracted much interest as polymer electrolyte membranes (PEMs) for fuel cells, since inorganic particles in a polymer matrix might improve mechanical strength, thermal stability, proton conductivity, fuel barrier properties and membrane durability [6]. The alternative materials such as sulfonated poly (aryl ether ketone) (SPAEK) [7], polybenzimidazole (PBI) [1], sulfonated polyimide (SPI) [8,9] have been rapidly explored for PEM usages.

Presently, our groups mainly focused on the study of new type of proton exchange membranes based on poly vinyl alcohol. Poly (vinyl alcohol), PVA, is a cheap polymer with a high density of functional -OH groups, it also has potential for chemical cross-linking. Indeed it is well known that under acidic conditions the hydroxyl groups of PVA react with aldehydes to form acetal or hemi-acetal linkages. Compared to blend polymers, cross-linked networks offer greater chemical stability [6].

Graphite oxide (GO), formerly called graphitic oxide or graphitic acid, is a compound of carbon, oxygen, and hydrogen in variable ratios. Hydrophilic graphene oxide disperses readily in most polar solvents such as water, breaking up into macroscopic flakes, which are mostly one layer thick. Recently, materials based on graphene

¹ - Department of Chemistry, Amirkabir University of Technology, Tehran, Iran

²- Department of Chemistry, Amirkabir University of Technology, Tehran, Iran, Mehranjavanbakht@gmail.com



oxide as inorganic fillers in polymer composites have been attracting attention as a result of the potential for applications in electronics and nanocomposites, due to their extremely high aspect ratio, high conductivity, high mechanical strength, unique graphitized plane structure and electrically insulating property [10,11]. Upon incorporation in PFSA, the unique structure and high surface area of the GO may provide more proton transport channels and hold more water, which could be beneficial for the improvement of the proton conductivity and mechanical properties of the membranes [12].

In the present work, the effects of functionalized graphene oxide (F-GO) nanosheets have been investigated as inorganic fillers in a PVA/SGO nanocomposite membrane, fabricated by a simplistic solution casting method. The structure, morphology, thermal stability and water uptake properties of new hybrid membranes were investigated.

2. Experimental

2.1. Material

Poly (vinyl alcohol), PVA, 99+% hydrolyzed, with an average molecular weight of 130,000 was used as supplied by Sigma-Aldrich. The cross-linking agent was a 25 wt% solution of glutaraldehyde (GLA) in water (Sigma-Aldrich). All of another materials and solvents (Merck) were used without more purification.

2.2. Syntheses of GO and SGO

The graphene oxide (GO) nanosheets were produced from natural graphite flakes by the modified Hummer's method [13]. Firstly, graphite powders (1g) were placed in cold (0-5 °C) concentrated H₂SO₄ (23 ml) and then 3 g of KMnO₄ was slowly added. Then the solution was transferred to a 35 ± 2 °C water baths and stirred for about 1 h, and then 46 mL distilled water was added and the solution was stirred for 30 min while the temperature was raised to 90 ± 2 °C. Finally, distilled water (140 ml) and 30% H₂O₂ solution (10 ml) were added after the reaction. The product was then filtered and washed with copious amounts of 5% hydrochloric acid (HCl) and distilled water, after which it was centrifuged several times until the excess HCl was removed, collected by filtration, and dried in an oven at 70 °C overnight.

The water-dispersible SGO were synthesized from GO according to the reported method with minor modifications [14]. Three steps are involved in this process: (a) pre-reduction of GO with sodium borohydride; (b) sulfonation with the aryl diazonium salt of sulfanilic acid (c) post-reduction with hydrazine to remove epoxy functionality completely. The pre-reduction of GO is essential: (i) to enable the sulfonation reaction by increasing the domain size of sp² carbon for reaction with aryl diazonium salt and (ii) it also helps to achieve complete reduction during hydrazine treatment after sulfonation. The later reduction is necessary to get more sp² carbon atoms in the graphene and hence to get extended conjugation in the graphene [14]. First, 75 mg dried GO was dispersed in 75 ml water via sonication for 30 min. After the dispersion was centrifuged at 4000 rpm, a clear and brown dispersion of GO was formed. Then, 600 mg sodium borohydride in 15 ml water was added into the dispersion of GO after its pH value was adjusted to 9–10 with 5 wt% sodium carbonate solution. Then 15 ml sodium borohydride solution (4%, w/v) in water is mixed with the GO dispersion and is kept at 80 °C for 1 h under constant stirring. The partially reduced product is washed with water until its pH becomes 7 and it is re-dispersed in water for diazonium coupling. For this purpose 46 mg sulfanilic acid and 10 mg sodium nitrate are dissolved in 10 ml water with the addition of 1 ml 12 N HCl at ice cooled condition. The mixture is then added to the RGO dispersion at 0 °C and is kept for two hrs with stirring. It is centrifuged, washed repeatedly with water until pH becomes 7. The product is then redispersed in 100 ml water for final reduction with 2 ml



hydrazine hydrate solution under refluxed condition for 24 h at 100 °C. Finally it is washed with water and dried in vacuum at 60°C.

2.3. Preparation of membranes

Three membranes (PVA/GLA, PVA/GLA/GO and PVA/GLA/SGO) were synthesized and named M₁, M₂ and M₃. The PVA-based membranes were prepared by dissolving appropriate amounts of PVA and GO, in distilled water, to produce a 10 wt% solution. The solution was stirred for 1 h at 80-90°C in order to obtain a transparent low-viscous liquid. Then 1 ml of a diluted GLA solution was gradually added. The solution was left to stir for another hour, before the temperature was slowly decreased to 25°C. At this time approximately 60 mg of 2 M H₂SO₄ was added to the solution as a catalyst for the cross-linking reaction. The transparent solution was then casted on a Petri-glass dish. The cast solution underwent freeze-thaw cycles in order to gain high mechanical strength and elasticity. This freeze-thaw procedure is widely used for PVA based on membranes and described in depth elsewhere. The PVA-based membranes with a thickness of about 100 μm were kept in humid cells until the experiments were performed.

2.4. Apparatus

The IR spectra (resolution 4 cm⁻¹) were recorded with a Bruker Equinox 55 with ultra dry compressed air. The differential scanning calorimetric (DSC) measurements were performed on the dried samples using a Mettler DSC 823. The scanning rate was 10°C min⁻¹ in nitrogen flow. The membrane morphologies were investigated by XL300 philips scanning electron microscopy. The membrane samples were sputtered with gold. The measurements of proton conductivity, σ (S/cm), of the membranes were carried out via AC impedance spectroscopy over the frequency of 10–10⁷ Hz with 50–500 mV oscillating voltage and 10 mV amplitude.

2.5. Water uptake Measurements

The membranes were dried in a vacuum oven at increased temperature, weighed, soaked in deionized water for 12 h at room temperature and reweighed. Water uptake was calculated from following formula:

$$SW = \frac{m_{wet} - m_{dry}}{m_{dry}} \times 100 \%$$

(1)

Here, m_{wet} is the weight of the wet membranes and m_{dry} the weight of the dry membranes.

2.6. Conductivity Measurement

Proton conductivities of membranes were measured at room temperature by AC impedance method. The sample was cut into sections 1.6 cm × 0.8 cm and sandwiched between two electrodes on the cell. Before running the test, the membranes were soaked in water for 24 h until got sufficiently wet and saturated. The conductivity was calculated from the following equation: $\sigma = L/RA$, where σ is the proton conductivity (S/cm), L is the membrane thickness (cm), A is the surface area of membrane (cm²) and R is the membrane resistance (Ω).

3. Results and discussion

3.1. XRD

The XRD analyses of as-prepared GO is shown in (Figure1). Natural graphite shows a very sharp diffraction peak at $2\theta = 26.6^\circ$ corresponding to the (002) plane, indicating a highly organized crystal structure with a layer-

to-layer distance (d-spacing) of 0.33 nm [15]. As for GO, the peak (001) is observed at $2\theta = 12^\circ$, which indicates that the interlayer spacing is about 0.75 nm calculated using Bragg's law ($\lambda = 2d\sin\theta$). Such value is much larger than that of natural graphite due to the generation of oxygen-containing functional groups between layers [16].

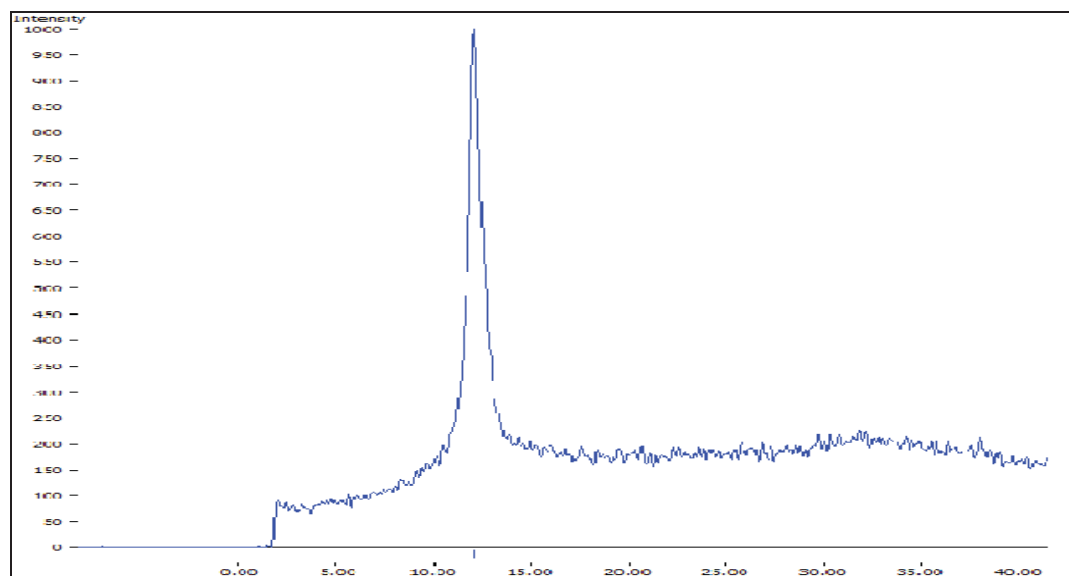


Figure 1. XRD patterns of GO.

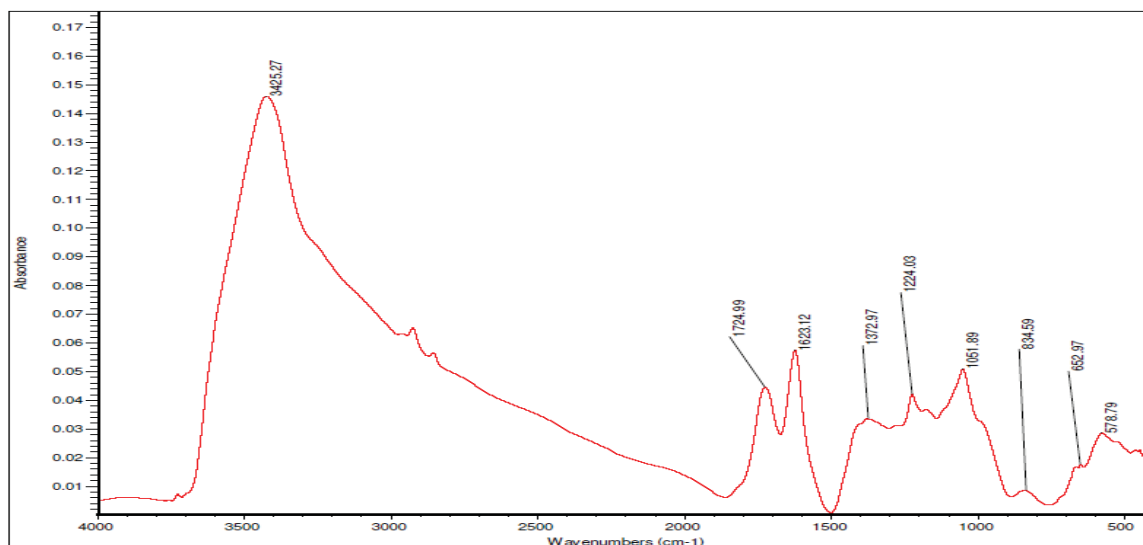
3.2. FTIR

The structure of nanoparticles was characterized by FTIR spectroscopy. The infrared spectrum of GO and SGO are shown in Figure 2. In the FT-IR spectrum of GO, we observe a strong and broad absorption at 3425 cm^{-1} due to O-H stretching vibration. The peaks at 1372 cm^{-1} and 1224 cm^{-1} in Figure 2 (a) correspond to the skeletal vibrations of C-OH and C-O-C in unoxidized graphitic domains and C=O and C-O stretching vibration bands of COOH groups are at 1724 cm^{-1} and 1051 cm^{-1} [17]. The peak at 1623 cm^{-1} may be from skeletal vibrations of unoxidized graphitic domains.

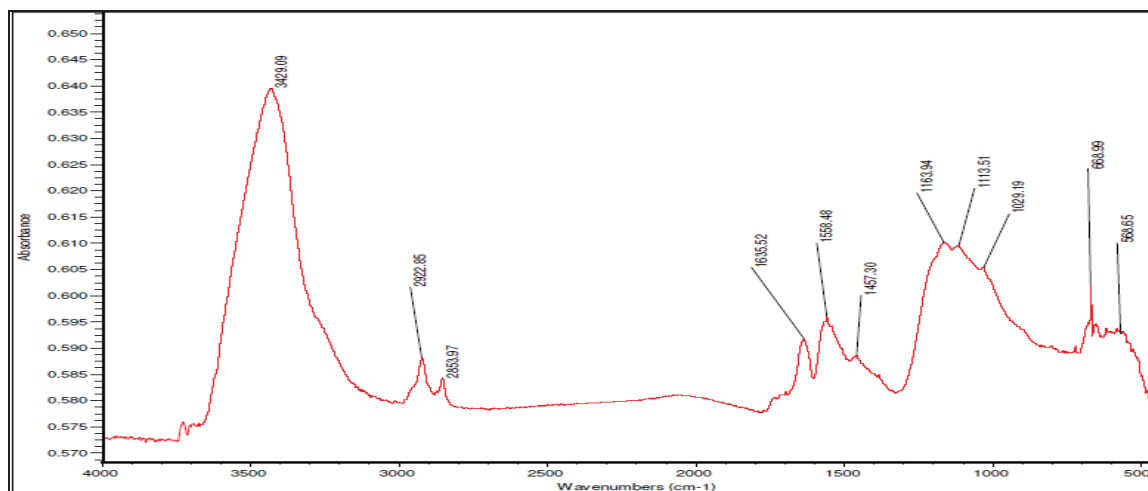
After prereduction and sulfonation (Figure 2 b), The peaks at 1163 cm^{-1} , 1113 cm^{-1} , and 1029 cm^{-1} (two $\nu_{\text{S-O}}$ and one $\nu_{\text{s-phenyl}}$) confirm the presence of a sulfonic acid group, and the peaks at 830 cm^{-1} (out-of-plane hydrogen wagging) is characteristic vibrations of a *p*-disubstituted phenyl group[18]. The absorption peak at about 1724 cm^{-1} is due to the C=O group in either carboxylic or carbonyl moieties in GO. After reduction by the present method, this band apparently diminishes, demonstrating the successful reduction of GO to reduced graphene.

In the FTIR spectra of the PVA/GLA and PVA/GLA/SGO membranes (Figure 2 c,d), the presence of an intense O-H stretching absorption between 3000 and 3500 cm^{-1} indicated the existence of strong intermolecular and intramolecular hydrogen bonding [6]. This absorption is shifted to a lower wavenumber as the SGO is added, and the band corresponding to C-OH stretching (around 1096 cm^{-1}) displays a similar. Both of those phenomena indicate the existence of hydrogen bonding between the -OH in PVA and the remaining oxygen-functional groups in SGO. The absorption at 1716 cm^{-1} , corresponding to the stretching vibration of C=O ester groups formed between the carboxylic acid groups of SGO and the alcohol groups of PVA. Bands at $2800\text{-}3000$

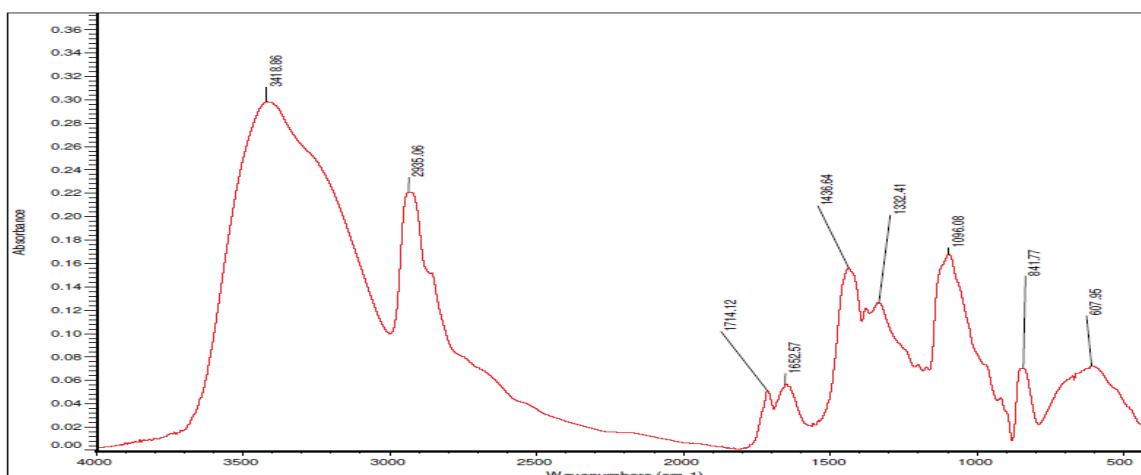
cm^{-1} were due to stretching vibrations of the CH and CH_2 groups and bands present at 1300-1500 cm^{-1} range were attributed to the CH/ CH_2 deformation vibrations.



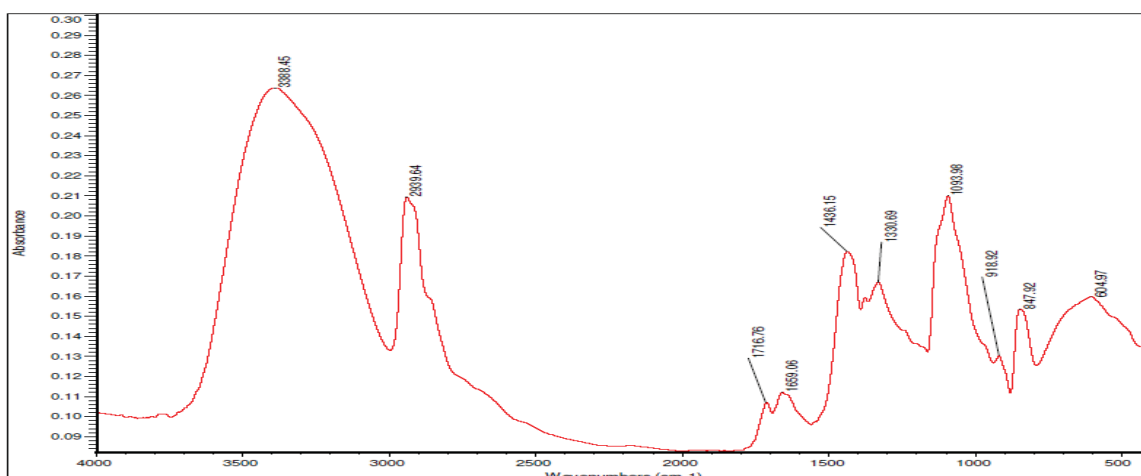
A) GO



B) SGO



C) PVA/GLA



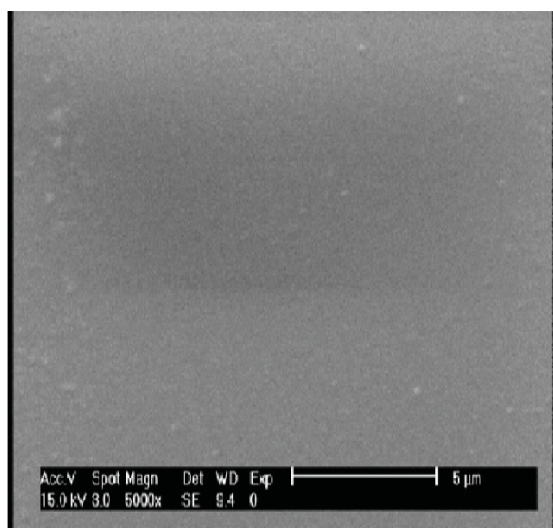
D) PVA/GLA/SGO

Figure 2. FTIR spectra of A)GO B)SGO C)PVA/GLA D) PVA/GLA/SGO.

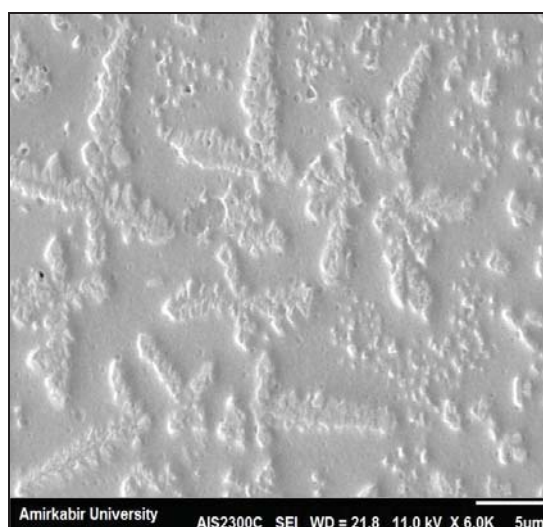
3.3. SEM

Figure 3 shows SEM images for the surfaces of hybrid membranes (M_1 and M_3). The effect of SGO on the membrane morphology was clearly observed in these SEM images. With addition of SGO in the membrane matrix, an incensement in the membrane porosity was observed. From the SEM images, it can be clearly known that, the surface in M_1 membrane is smooth; whereas the M_3 membrane surface is distributed with little mounds, which are related to SGO particles.

These images display a layered structure for the composites (as indicated by arrows in Figure 3b) comparing with the smooth fracture surface for neat PVA matrix (see Figure 3a). Such a layered structure indicates that the SGO sheets were coated with PVA matrix and the presence of strong interaction between SGO sheets and PVA chains through the hydrogen bonding between residual oxygen-functional groups on the SGO sheets and PVA chains. Those SGO sheets coated with PVA matrix could be single or multi-layers.



a) PVA/GLA

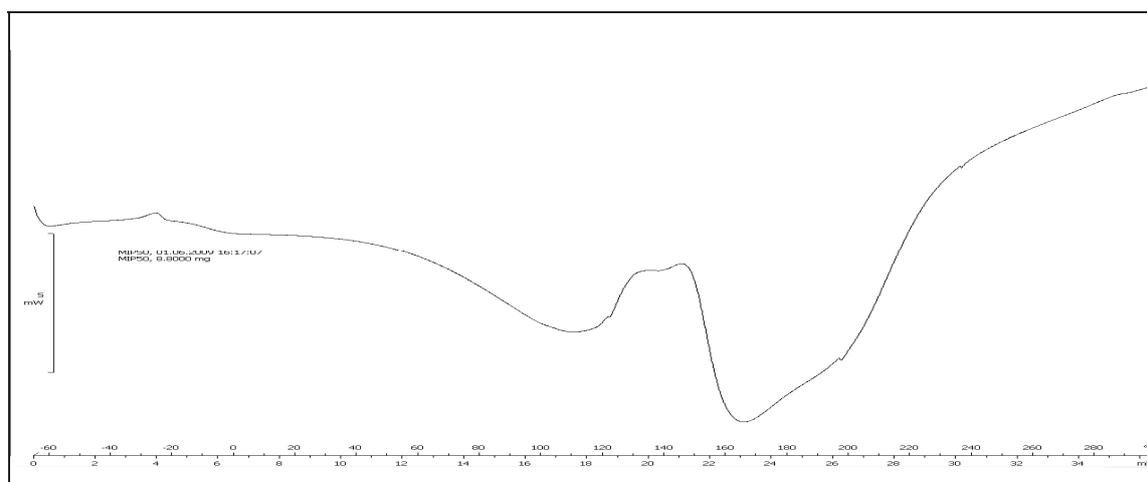


b) PVA/GLA/SGO

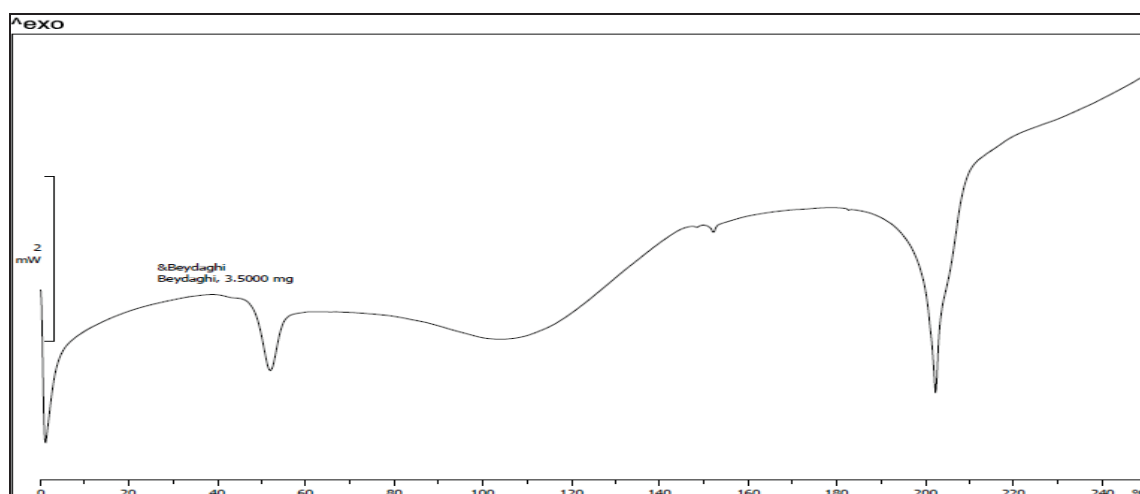
Figure 3. SEM images of the surfaces morphology of M₁ and M₃ composite membranes.

3.4. DSC

The differential scanning calorimetry (DSC) thermograms of the nanocomposite PVA membranes are shown in Figure 4. The melting temperature depression of a crystalline component means that the formation of a crystal is suppressed by the interaction between two blend components. The endothermic peaks located between 110 and 215°C correspond to the melting of the crystalline phases of membranes. These peaks show that membranes have several melting points and indicate different crystal structures in membranes. The higher temperature peak is for the melting of PVA crystal entrapped between the SGO nanostructures. As shown in Figure 4, final T_m for M₁ and M₃ membranes are 165 and 205°C respectively. It was found that the melting temperature, T_m , of the PVA composite membrane slightly shifts toward higher temperature when SGO is added into the PVA polymer matrix.



A) PVA/GLA



B) PVA/GLA/SGO

Figure 4. DSC thermograms of the composite membranes.

3.5. Water Uptake

It is well known that water in proton exchange membranes plays an important role in proton conducting because the adsorbed water can facilitate the transport of protons. That is, the available acid groups in the membrane and their capacity to dissociate in water determines the proton conductivity [16]. The water uptake of the membranes was tested and the results are shown in Table 1.

Graphene oxide has a high surface area (2630 m²/gr). It can be observed that an increase in functionalized GO content in the hybrid membrane leads to a substantial increase in water uptake of the membrane because of the increase in density of functional groups as well as the porous volume in the membrane phase [16].

The membranes with sulfonic acid functionalized GO show higher water uptakes in compare to the membranes with non-functionalized GO. The -SO₃H groups of GO nanoparticles, which are present in the membrane interior, attracted the -OH groups of PVA to reverse the -SO₃H groups to the membrane interior. The high surface of GO was responsible for the enhancement in water uptake. It is for the presence of hydrophilic sulfonic acid groups on the surface of functionalized GO. The high hydrophilic character of the -SO₃H groups, the high surface area of GO and the stronger interactions between the absorbed water and the modified matrix, contribute to increase the water uptake.

3.6. Proton Conductivity

Generally, two principle mechanisms of Vehicle mechanism and Grotthus (hopping) mechanism describe proton diffusion through the membrane. It is possible that the bound water participates in the Grotthus mechanism, and the free water takes part mostly in vehicle mechanism [19,20]. It shows that the enhanced proton conductivity is attributed to the retention of water.

Table 1 provides a comparison proton conductivity of the three membranes. It can be observed that the incorporation of functionalized GO into the matrix of PVA has significantly increased the proton conductivity. This phenomenon may suggest that there is an interaction between sulfonic acid groups on



the SGO and those in the PVA membrane. The bound water facilitates the proton transport ability through the Grotthuss mechanism, originating by generation of a continuous proton conductive pathway [21]. With enhance of water uptake in composite membranes, vehicle mechanism is improved and proton conductivity is increased.

Membrane	Water Uptake (%)	R (Ω)	Proton Conductivity (S/cm)
PVA/GLA	75	65	0.0007
PVA/GLA/GO	90	42	0.0014
PVA/GLA/SGO	97	5	0.0090

Table1. Water uptake and proton conductivity of membrane

4. Conclusions

Organic-inorganic hybrid membranes based on PVA/SGO hybrids, in which $-SO_3H$ groups are introduced by co-condensation as hydrophilic inorganic modifier have been investigated. Enhancement of physicochemical and electrochemical properties due to addition of glutaraldehyde (GLA) as cross-linking agent in a PVA matrix have been studied. The characterizations of the blend membranes were examined and verified by FTIR technique. The membrane structure was confirmed by SEM. With addition of SGO, the nanocomposite membranes show higher water uptake, thermal stability, mechanical stability and proton conductivity.

References

- [1] H. Zhang, X. Li, Ch. Zhao, T. Fu, Y. Shi, H. Na, J. Membr. Sci. 308 (2008) 66
- [2] S. Banerjee, DE. Curtin, J Fluorine Chem 125. (2004) 1211
- [3] P. Millet, F. Andolfatto, R. Durand, Int J Hydrogen Energy 21 (1996) 87
- [4] J. St-Pierre, D.P. Wilkinson, AIChE J. 47 (1998) 1482
- [5] P. Jannasch, Curr. Opin. Colloid Interface Sci. 8 (2003) 96
- [6] H. Beydaghi, M. Javanbakht, H. Salar Amoli, A. Badiei, Y. Khaniani, M R. Ganjali, P. Norouzi, M. Abdouss, Int J Hydrogen Energy 36 (2011) 13310
- [7] P.X. Xing, G.P. Robertson, M.D. Guiver, S.D. Mikhailenko, S. Kaliaguine, Polymer 46 (2005) 3257
- [8] H.B. Park, C.H. Lee, J.Y. Sohn, Y.M. Lee, B.D. Freeman, H.J. Kim J. Membr. Sci. 285 (2006) 432
- [9] L. Wang, B.L. Yi, H.M. Zhang, Y.H. Liu, D.M. Xing, Z.-G. Shao, Y.H. Cai, J. of Power Sources 164 (2007) 80
- [10] I. Jung, D. A. Dikin, R. D. Piner, R. S. Ruoff, Nano lett 8 (2008) 4283
- [11] M. A. Raza, A. Westwood, A. Brown, N. Hondow, C. Stirling, Carbon 49 (2011) 4269



- [12] A. Yu, I. Roes, A. Davies, Z. Chen, Appl. Phys. Lett. 96 (2010) 253105
- [13] W. Hummers, R. Offeman, J. Am. Chem. Soc. 80 (1958) 1339
- [14] Y. Si, E.T. Samulski, Nano Lett 8 (2008) 1679
- [15] J. Guo, L. Ren, R. Wang, Ch. Zhang, Y. Yang, T. Liu, Composites 42 (2011) 2130
- [16] H.L. Guo, X.F. Wang, Q.Y. Qian, F.B. Wang, X.H. Xia, ACS Nano 3 (2009) 2653
- [17] H. Gu, Y. Yu, X. Liu, B. Ni, T. Zhou, G. Shi, Biosens Bioelectron 32 (2012) 118
- [18] N. B. Colthup, L. H. Daly, S. E. Wiberley, Introduction to Infrared and Raman Spectroscopy, 3rd ed.; Academic Press: London, 1990
- [19] D.S. Kim, B. Liu, M.D. Guiver, Polymer 47 (2006) 7871
- [20] C.M.B. Rodriguez, M.G.A.R. Paleta, J.A.R. Marquez, J.R.G. Delavega, Int. J. Electrochem. Sci. 5 (2010) 414
- [21] K.D. Kreuer, Chem. Mater. 8 (1996) 610



Dynamic Response Analysis of Two Conventional Types of SOFCs to the Inlet Air Mass Flow Rate Variation

Ebrahim Afshari¹, Yasser Mollayi Barzi²

1- Mechanical Engineering Department, Faculty of Engineering, University of Isfahan, Isfahan, Iran, e.afshari@eng.ui.ac.ir

2- Mechanical Engineering Department, Islamic Azad University, Kashan branch, Kashan, Iran

Abstract

The purpose of present study is to investigate the dynamic response of two conventional types of solid oxide fuel cells to the inlet air mass flow rate variation. A dynamic compartmental model is developed for two typical planar and tubular SOFC designs. The model accounts for heat and mass transfer processes, electrochemical processes, activation and ohmic polarizations, among others. Using developed model the dynamic response of the cell to the step change of the air feed stream conditions is investigated. The results show an almost slow electrical response of the cell to the air flow rate step variation that is estimated to be about one hour. Moreover, the effect of the inlet airflow conditions on a tubular solid oxide fuel cell performance is more noticeable than its effects on a planar SOFC.

Keywords: Solid oxide fuel cell, Tubular cell, Planar cell, Dynamic simulation, Time constant

1- Introduction

Solid oxide fuel cell systems have been proposed for electric utility power generation in both large central station power plants and distributed generation stations [1]. High operating temperature of SOFCs creates some desirable points, for example in that expensive catalysts are not required for the electrochemical reaction and the high temperature means that a gas turbine can be effectively combined with an SOFC in a hybrid manner to form a single unit for self-sustainable distributed energy system [2].

To function efficiently, a SOFC needs to maintain a high operating temperature, which facilitates the ion conductance of the solid oxide. However, too high temperature may lead to localized "hot spots", electrode sintering and a chemical reaction between the electrode and the electrolyte [3]. Therefore, the temperature of a SOFC has to be controlled within a narrow range for safety and efficiency. An issue that can improve a SOFC's performance includes optimization of the fuel-oxidant ratio or the stoichiometry of the oxidant. In addition, the air mass flow rate should be large enough to maintain effective cooling of the cell as well as to reduce the concentration polarization of the cathode side. Therefore, properly thermal management of the cell could be provided via the inlet mass flow rate controlling [2]. Generally, the input airflow conditions might be a proper controlling parameter for the cell temperature and the other output characteristics of the cell. To carry out the dynamic effects of the input airflow conditions, detail analysis of the dynamic phenomena occurring inside the SOFC is required. Therefore, a suitable mathematical model must be established to consider the complicated multi-physic dynamic phenomena occurring inside the fuel cell.

Haynes [4] observed that the thermal transients typically occur within of tens of minutes,

¹ Assistant professor

² Assistant professor, Islamic Azad University, Kashan branch,



whereas electrical and anodic mass transfer transients occur within seconds and fractions of seconds, respectively. Sedghisigarchi and Feliachi [5] simulated output voltage response of a stand-alone fuel cell to a step load change and a fuel flow step change to illustrate the dynamic behavior of SOFC for fast and slow perturbations. Xue et al. [6] considered a model for heat and mass transfer simulation assuming an electrical circuit includes the Ohmic resistances and capacitors for the energy storage mode of operation. In other research conducted by Aguiar et al. [7] the temperature control of a stack-level SOFC model was presented. A PID controller was adopted to maintain the outlet fuel temperature and the fuel utilization during load changes by varying the airflow rates. Qi et al. [8] obtained and solved a non-linear set of differential equations for the heat and mass transfer as well as electrical and electrochemical variables and calculated the cell time response to the load change. Gemmen and Johnson [9] investigated a variety of transient cases, including representative load increase and decrease and system shutdown. Ford [10] enhanced the SOFC transient modeling and simulation via characterization of the electrical and mass transfer time constants using a quasi-steady state 1-D model. Chaisantikulwat et al. [11] developed a SOFC dynamic model and a feedback control scheme that can maintain output voltage despite load changes for a counter flow planar SOFC. Wang et al. [12] investigated the steady state and transient behavior of a co-flow planar solid oxide fuel cell with the volume-resistance characteristic modeling technique. Serincana et al. [13] developed a two-dimensional, axisymmetric transient model for an intermediate temperature micro-tubular solid oxide fuel cell, which incorporates mass, species, momentum, energy, ionic and electronic charge conservation. In two literatures published by present authors [14, 15], the heat-up and start-up behavior and load change response of a tubular SOFC is studied using a 2-D transient numerical model.

In this study, the dynamic response of the solid oxide fuel cells to the inlet air mass flow rate is investigated theoretically for two conventional types of SOFCs and the results are compared to each other. For this purpose, the typical experimented tubular and planar SOFC designs is considered to explore the dynamic effects of the inlet airflow perturbations [16, 17]. Understanding these phenomena is applicable for control of the cell temperature and electrical characteristics of the SOFC via the inlet air conditions adjustment.

2- Geometry and configuration of SOFC models

2.1 Tubular solid oxide fuel cell

Fig. 1 shows a schematic view of a single tubular solid oxide fuel cell in a cell stack. Each single cell is separated from the other cells by two symmetry lines in both sides of the cell tube. The computational domain and the flow streams of fuel and oxidant in a typical tubular SOFC are highlighted on the figure. Due to symmetry, only half of the cell unit (between the cell symmetry axis and the symmetry line between two adjacent cells) is considered. The closed end of the cell is assumed to be flattened for numerical model simplification.

Fig. 2 shows the detailed view of the axis-symmetric computational domain and the cell overall heat and mass flow. The computational domain includes the air and fuel channels, anode, cathode, electrolyte and the supporting tube layers. The fuel entrance is at the closed end of the cell. Table 1 presents the geometrical characteristics of the tubular SOFC [16].

Table 1 – Geometrical characteristics of the tubular SOFC unit[16]

	Thickness (μm)
Supporting tube	1500
Cathode	1000
Electrolyte	50
Anode	150
	Radius (mm)
Inner side of air-inducing tube	4.0
Outer side of air-inducing tube	4.5
Inner side of supporting tube	6.9
Outer side of Anode	9.6
Outer boundary of fuel channel	14.6
	Length(mm)
Tubular cell unit	500

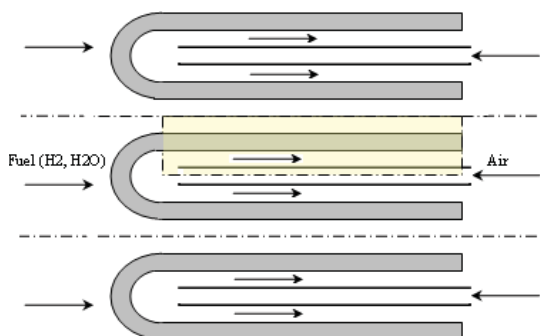


Figure 1 – Schematic diagram of a tubular SOFC and the computational domain

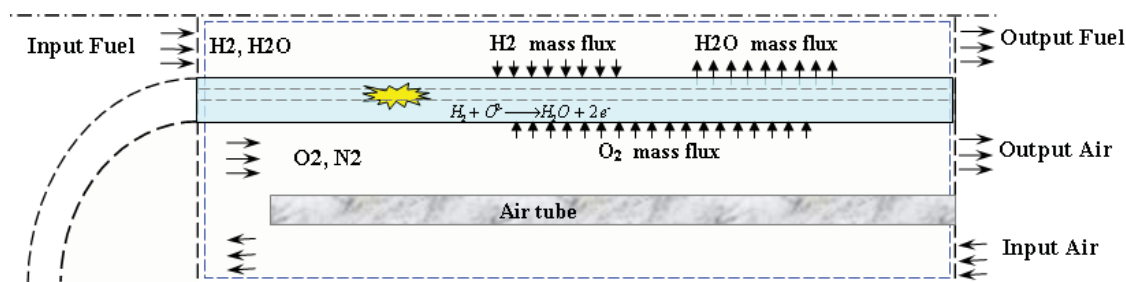


Figure 2 – Schematic of flow field in the computational domain

2.2 Planar solid oxide fuel cell

The geometrical characteristics of the under-study planar SOFC stack are depicted in Fig. 3. Fig. 3 shows a unit of a counter flow solid oxide fuel cell stack (interconnects, gas channels and MEA) tested experimentally by Keegan et al. [17]. To prevent very heavy numerical works, a slice of the stack unite is taken as the geometrical model and it is assumed that all the slices in the whole stack work in the similar conditions. As shown in the figure, a 3-D model is used for the transient behavior analysis of the planar solid oxide fuel cell. It is because that all three-dimensional effects of heat and mass transfer are noticeable in a planar solid oxide fuel cell especially for a transient analysis.

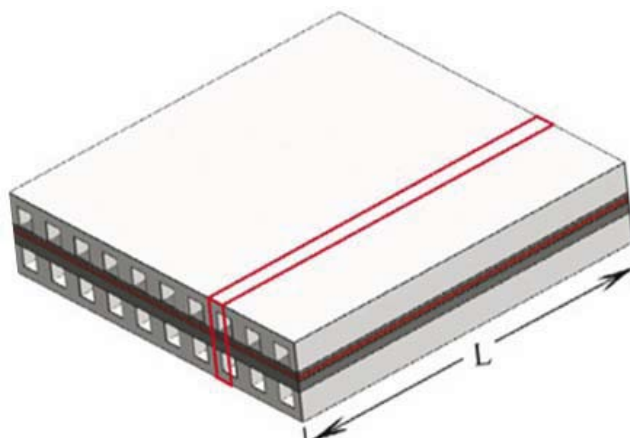


Figure 3 – Geometrical specifications of a counter flow planar SOFC stack unit

3- Physical properties of solid materials

The core of the tubular SOFC consists of a porous cathode (LSM), an electrolyte (yttria stabilized zirconia or YSZ), a porous anode (i.e. Nickel-YSZ) and a ceramic supporting tube assembly in tubular shape. Reference [18] gives the tubular cell components properties like heat conductivity, heat capacity, density and the ionic and electric resistivity [2]. The planar SOFC components include anode/electrolyte/cathode assembly of Ni-YSZ/8YSZ/LSM and interconnect made of metal alloys. The cell components material properties are presented in reference [18].

4- Mathematical model

In some published literatures, we presented the transient form of the governing equations used in our dynamic model to investigate the load current change response of a SOFC unit cell [18, 19]. In addition, the steady state and transient results of the model are evaluated and examined in these literatures. In the present study, we use the same transient model and governing equations to investigate dynamic behavior of two kinds of SOFC stack units for the inlet air mass flow rate and temperature variations and compare their responses to these input perturbations. Generally, the mathematical model includes electrochemical, electrical and heat and mass transfer sub-models which is explained briefly in the following sections.

4.1. Electrochemical and Electrical model

In the simulation process, the cell ideal voltage, activation polarization and heat and mass sources (resulted from the electrochemical reaction of hydrogen and oxygen), is calculated by the electrochemical model. In such a model, the concentration polarization due to the non-uniform distribution of the species existing in the air and fuel flow passages and the diffusion of the species within the porous electrodes is automatically taken into the account by the mass transfer model.

The electrical model calculates the voltage distribution and electrical current in the conductive regions in coupled with the other equations. In this study, an equivalent electrical circuit is used to calculate the cell current and voltage distribution in a specified load current. The circuit includes a set of electrical resistances and local electrical power sources. In order to calculate the current and voltage distribution in a specified load current, Kirchhoff's law is applied to each node. For each node, an equation associating the potential of the central grid point P with the potentials of its neighboring points (east, west, north, and south) and the corresponding grid P in the cathode is obtained. Then a set of equations for local potentials is created with all of the equations written for the discretized grids in both cathode and anode sides, The voltage in cathode connector is set to be zero (as a reference voltage) and the total



current taken out from the cell is prescribed. Then the potentials in each node and in the anode connector are calculated by solving the matrix of potential equations.

4.2. Heat and mass transfer model

All aspects of fluid flow, heat transfer and mass transfer in the flow channels and porous electrodes are considered in present dynamic model. The transient form of mass, momentum and energy conservation equations in porous and gas channels and also the boundary conditions are described elsewhere [19, 22]. It should be noted that for the tubular SOFC a two dimensional axis-symmetric computational domain in cylindrical coordinate is considered, while a three-dimensional geometrical models is adopted for the planar SOFC unit.

The heat sources include the Ohmic and activation over potential power dissipations beside the thermodynamic heat generation. In mass transfer equations the mass sources is considered at the interfaces of the electrodes and electrolyte.

5- Simulation procedure of the cell transient operation

The simulation is based on a finite volume based code that uses separate modules for each sub-model (electrical, electrochemical and heat and mass transfer sub-models). Initially steady state operation of the cell is simulated by the developed code. Then the steady state operation results of the cell are set as initial values for the transient analysis. At each time step an internal iteration is performed and continues until convergence. Then the code proceeds to the next time step utilizing previous results.

The governing transient transport equations (momentum, energy and species conservation equations) are solved by the SIMPLE algorithm. In this method, the time steps do not affect the stability of the solution; however, it affects the accuracy of the results. All transport and thermo-physical properties ρ , μ , C_p , λ and D_{ij} of the fuel and air are calculated as functions of the local temperature, pressure, and species concentrations. The gaseous components are assumed to behave as perfect gases and the local properties of the gas mixture are calculated according to the relations given in reference [2].

The computational domain is discretized by 140600 grids in radial and longitudinal directions for 2-D tubular SOFC model and 86300 grids for the 3-D planar SOFC model. The grid independency of the results is examined and insured. The grids are non-uniform in direction perpendicular to the electrodes plate. This is due to very low thickness of the electrodes and electrolyte layers in compare with the air and fuel channel width.

6- Results and discussion

For verification purpose, the electrochemical model empirical parameters are calibrated to fit the output electrical data of the experimental work of Hagiwara et al. (1999) (for tubular cell) and the test data of Keegan et al. (2002) (for planar cell) with the same geometries and test setups. The polarization curve results of the current model have been evaluated elsewhere in references [19, 20] and the capabilities of the mathematical model and the code were discussed there.

To calculate the response time of the cell to an input perturbation, we have to define a time constant to be able to evaluate and characterize different results and to compare different time scales. To date, no unique criterion is specified in the literature, for time constant of the cell dynamic response to an input perturbation. This criterion should be applicable for different types of input perturbations and a various output operating characteristics of the solid oxide fuel cells like species concentration, temperature and electrical power (output voltage and current). In addition, the time constant definition should be enough inclusive to cover different order of time scales for various parameters.

In this study, we suggest the time constant criterion of reaching 90% difference between initial

and final steady state values. We hope that it could be used in further studies on the dynamic behavior of the solid oxide fuel cells as a unique criterion for analogy and application of the experimental and theoretical results.

6.1 Tubular cell response to the input air mass flow rate

To investigate the dynamic effects of the input air mass flow rate, the cell dynamic response to a 5% increase in the air mass flow rate in a constant electrical load is analyzed for two kinds of solid oxide fuel cells. It is assumed that the load current is constant during transition while the effect of inlet air mass flow rate increase on the cell output voltage and performance is investigated.

Fig. 4. shows the longitudinal profiles of the cell temperature in different time steps up to the final steady state conditions. It is clear that with increasing the air mass flow rate, the heat transfer rate from the cell body increases and thereby the cell temperature decreases, especially in the closed end of the cell. As shown in the figure, the cell maximum temperature decreases less than 22 oC (2%) when the air mass flow rate increases 5%. In addition, the cell maximum temperature position shifts about 5 cm toward the air flow downstream. It is reasonable that the hot spot shifts toward the downstream region when the mass flow rate increases, because the cooling effect of the air flow is dominant in the cell closed end. In addition, the air flow convective heat-transfer is the primary means to remove the generated heat and to avoid the occurrence of a hot spot in tubular solid oxide fuel cells.

Fig. 5 shows how the oxygen mole fraction distribution along the cell is changed during the input air mass flow rate increase. Despite very fast response of the oxygen concentration (less than 1s), very low variation of the oxygen mole fraction is observed. It is well documented that the effect of the air mass flow rate on the oxygen concentration and consequently on the cell performance is less noticeable in high mass flow rates (lower utility factors, e.g. 0.167 in this case study) [14]. However, its effect on the oxygen concentration distribution would be more important in lower air mass flow rate ranges (higher oxygen utility factors).

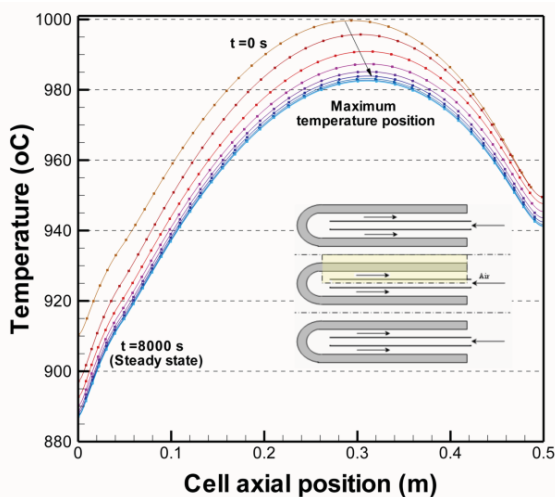


Figure 4 – The cell temperature profiles with time for 5% increase of the air mass flow rate

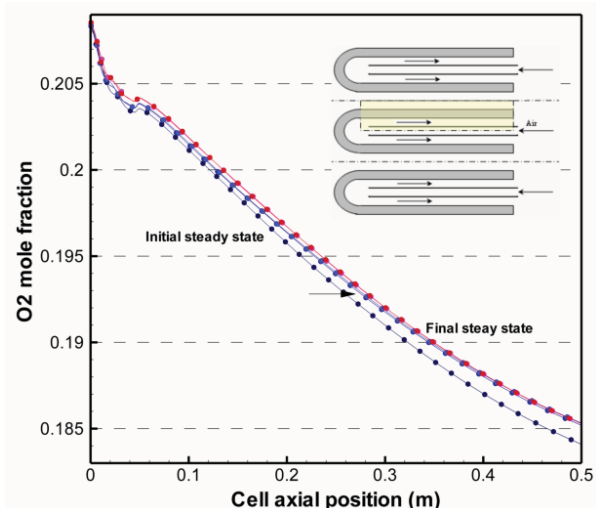


Figure 5 – The oxygen mass fraction profiles along the cell with time for 5% increase of the air mass flow rate

The voltage and temperature time response of the cell to the inlet air mass flow rate is shown in Fig. 6. As mentioned before the average operating temperature of the cell decreases with increase of the air mass flow rate as a cooling fluid (at 600°C) and leads to decrease of the

output voltage and generated power. The electrical response time is calculated about 4150s (69 min) up to the new steady state condition (based on the above defined criterion). In addition, it is observed that the cell output voltage reduces about 2.5% (0.017 V) with 5% increase of the air mass flow rate. This voltage lost is just because of the cell temperature decrease and consequently increase of the internal voltage losses. As shown in the figure, the time variation of the cell voltage is simultaneous with the temperature variation because the temperature is the main reason of the output voltage variation with time constant of about 4200s or 70 min. Moreover, the other factor which influences the cell output voltage is the cathode oxygen concentration that affected by the inlet air mass flow rate. However, about 22oC decrease in the cell temperature has the dominant effect on the cell output voltage despite the oxygen concentration raise.

6.2 Planar cell response to the input air mass flow rate

Figs. 7 and 8 show the longitudinal distribution of the planar SOFC temperature and oxygen mass fraction respectively due to 5% inlet air mass flow rate increase. As shown by figure 8 the cell temperature decreases about 6°C uniformly gradually due to the excess heat removal from the cell surface. Furthermore, figure 9 shows maximum about 0.01 increase in the oxygen mass fraction in cathode-electrolyte interface due to the inlet air mass flow rate raise.

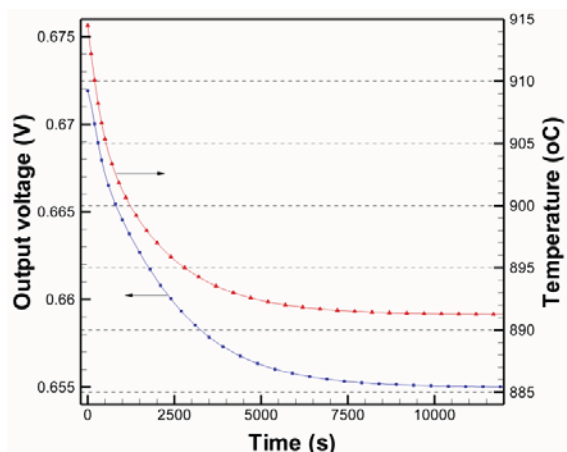


Figure 6 – The voltage and temperature time response of the tubular cell to the inlet air mass flow rate change

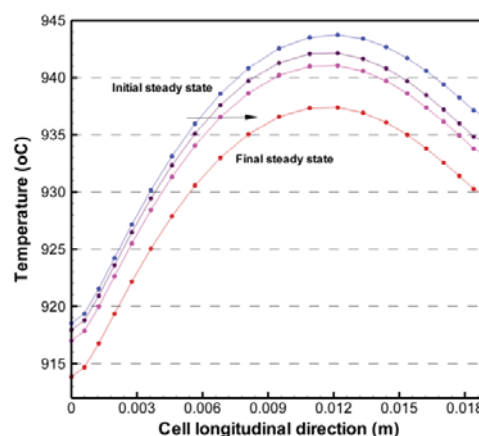


Figure 7 – Longitudinal distribution of the electrolyte temperature in various time steps

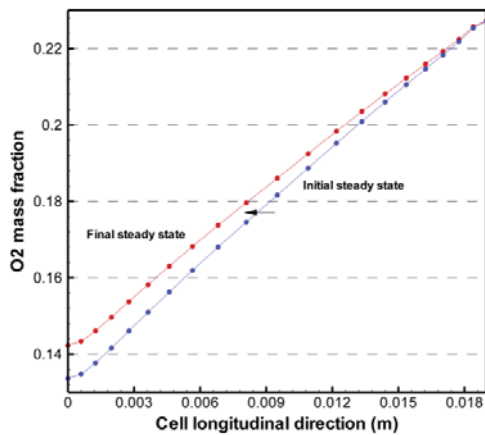


Figure 8 – Longitudinal distribution of the cathode side oxygen mass fraction in various time steps

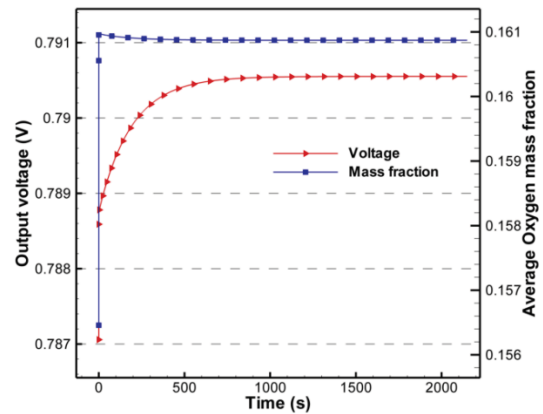


Figure 9 – Output voltage and Oxygen mass fraction time variation with the inlet air mass flow rate step up

The general effect of the inlet air mass flow rate on the cell output voltage together with the time variation of oxygen mass fraction in cathode-electrolyte interface is depicted in Fig. 9. As shown in figure 9, the voltage response time is about 300 s (5 min) for a planar cell unit that is 14 times smaller than the tubular cell unit (figure 6). It could be observed that the output voltage has a sudden increase initially while it rises slowly after this fast response. The fast response part of the output voltage (up to 50% of total voltage change) is related to the effect of oxygen concentration variation on the cell voltage, whereas the slow part of the voltage response is due to the slow temperature variations during transition.

Although the oxygen mass fraction time response is very fast (less than 0.1 s), the cell voltage follows the temperature time scale.

Generally, in lower inlet air mass flow rates (higher utility factors, e.g. higher than 40% utility factors in this case study) effect of the air mass flow rate on the voltage is dominant via the oxygen concentration variation. However, in higher inlet air mass flow rates (lower utility factors) the air mass flow rate effect on the voltage is dominant via the cell temperature variation. Anyway, it also depends on the inlet air temperature. When the inlet air temperature is very low (in compare with the cell operating temperature) it is clear that the effects of the inlet air variations on the cell temperature will play the main role on the cell performance and its effects on the oxygen concentration will lie on the next priority.

7- Summery and conclusions

Generally, the following remarks can be extracted from the present study.

- In this study, we considered the time constant criterion of reaching 90% difference between initial and final steady state values. It could be used in further studies on the dynamic behavior of the solid oxide fuel cells as a univalent criterion for analogy and application of the experimental and theoretical results. This criterion is applicable for different input perturbations as well as output operating characteristics of the solid oxide fuel cells like species concentration, temperature and electrical power (output voltage or current).
- The inlet air mass flow rate change affect the cell performance via two factors of the cell temperature and the cathode oxygen concentration. In tubular solid oxide fuel cells, the air flow convective heat-transfer is the primary means to remove the generated heat and



- to avoid the occurrence of a hot spot. However, in planar type of SOFCs the inlet air flow has less effect on the cell temperature than the tubular types.
- The output voltage response time (to the inlet air flow change) depends on the above-mentioned time constants. The initial fast response of the output voltage is related to the effect of oxygen concentration variation on the cell voltage; whereas the slow part of the electrical response, is due to the slow temperature variations during transition.
 - Generally, the inlet air flow effect on the tubular solid oxide fuel cells performance is sorely more prominent than the planar SOFCs. Moreover, it can be concluded that the effect of the inlet air flow conditions on a tubular solid oxide fuel cell performance is more noticeable than its effects on a planar SOFC.
 - The electrical response time of a tubular SOFC is about 10 times greater than a planar type. This is due to thicker support layer and also bigger active area of a tubular cell unit in compare with a unit of planar cell that leads to slower diffusion of heat, species and electrical current. The mass transfer response time in a planar SOFC is estimated to be on the order of fractions of second and in a tubular SOFC it is on the order of seconds.

M.amirinejad, S. rowshanzamir and M.H.Eikani "Effects of operating parameters on performance of a proton exchange membrane fuel cell", J. of Power Sources, (۲۰۰۶). ۱۶۱(۲), ۲۴-۳۲

8- References

- [1] S.C. Singhal "Solid oxide fuel cells for stationary, mobile, and military applications", Solid State Ionics; (2002). 152–153, 405– 410.
- [2] B. Sunden and M. Faghri "Transport Phenomena in Fuel Cells", WITPRESS, 2005.
- [3] S.C. Singhal "Advances in solid oxide fuel cell technology", Solid State Ionics, (2000). 135, 305-313.
- [4] C. Haynes "Simulating process settings for unslaved SOFC response to increases in load demand" J. Power Sources, (2002). 109(2), 365-371.
- [5] K. Sedghisigarchi and A. Feliachi "Dynamic and transient analysis of power distribution systems with fuel cells", IEEE Transactions on Energy Conversion, (2004). 19(2), 423–428.
- [6] X. Xue, J. Tang, N. Sammes and Y. Du "Dynamic modeling of single tubular SOFC combining heat/mass transfer and electrochemical reaction effects", J. Power Sources, (2005). 142, 211–222.
- [7] P. Aguiar, C. Adjimana and N. Brandon "Anode-supported intermediate temperature direct internal reforming solid oxide fuel cell. II: Model-based dynamic performance and control", J. Power Sources, (2005). 147, 136–147.
- [8] Y. Qi and Luo B. Huang "Dynamic modeling of a finite volume of solid oxide fuel cell: The effect of transport dynamics", J. Power Sources, (2006). 61, 6057 – 6076.
- [9] R.S. Gemmen and C.D. Johnson "Effect of load transient on SOFC operation– current reversal on loss of load", J. Power Sources, (2005). 144, 152–164.
- [10] J. C. Ford Ms thesis, "An enhanced transient solid oxide fuel cell performance model, Georgia Institute of Technology", December 2006.
- [11] A. Chaisantikulwat, C. Diaz-Goano and E.S. Meadows "Dynamic modelling and control of planar anode-supported solid oxide fuel cell, Computers & Chemical Engineering, (2008). 8, 154-162.
- [12] L. Wang and S. Weng "Modeling and simulation of solid oxide fuel cell based on the volume–resistance characteristic modeling technique", J. Power Sources, (2008). 177, 579–589.
- [13] M. F. Serincana, U. Pasaogullaria and N.M. Sammes "A transient analysis of a micro-tubular solid oxide fuel cell (SOFC)", J. Power Sources, (2009). 194, 864–872.



- [14] Y. Mollayi Barzi, M. Ghassemi and M.H. Hamedei 2009, “Numerical analysis of start-up operation of a tubular solid oxide fuel cell”, *Int. J. Hydrogen Energy*, (2009). 34, 2015-2025.
- [15] Y. Mollayi Barzi, M. Ghassemi and M.H. Hamedei “A 2D transient numerical model combining heat/mass transport effects in a tubular solid oxide fuel cell”, *J. Power Sources*, (2009). 192, 200–207.
- [16] A. Hagiwara, H. Michibata, A. Kimura, M.P. Jaszcar, G.W. Tomlins and S.E. Veyo “Tubular solid oxide fuel cell life tests” In: *Third International Fuel Cell Conference*. (1999). Nagoya, Japan.
- [17] K. Keegan, M. Khaleel, L. Chick, K. Recknagle, S. Simner and J. Deibler “Analysis of a planar solid oxide fuel cell based automotive auxiliary power unit”, *SAE Technical Paper Series* (2002). 2002–01-0413.
- [18] Y. Mollayi Barzi, A. Raoufi, N. Manafi Rasi and S. Davari “Three Dimensional Simulation of a Counter-flow Planar Solid Oxide Fuel Cell”, *ECS Transactions*, (2011). 35 (1), 1021-1033.
- [19] Y. Mollayi Barzi, M. Ghassemi, M.H. Hamedei and E. Afshari “Numerical Analysis of Output Characteristics of a Tubular SOFC with Different fuel Compositions and Mass Flow Rates”, *ECS Transaction*, (2007). 7, 1119-1125.



6th Iranian Fuel Cell Seminar
March. 12 & 13 , 2013
Tehran - Iran



Problems, components and methods for making polymer fuel cell electrodes and applying nanotechnology to solve their problems

Marziyeh Azadfalah^{1*}, Seyed Saber Mirhosseini²

Malayer University, Malayer, Iran

marziyeh_azadfalah@yahoo.com

Abstract

Fuel cells have a significant role in reducing environmental pollution and Due to the lack of mechanical parts often do not make noise. Polymer membrane fuel cells is one of the most attractive in terms of design and performance of a fuel cell. Most of the platinum catalyst is used in this fuel cell, that's high prices have prevented widespread use of fuel cell. Using nanotechnology electrodes can be light, thin and inexpensive to produce better yields than conventional electrodes. In the field of Nano-carbon fibers, carbon nanotubes, or compounds that are Nano scale pores have used. The new research used instead of platinum cathode materials with carbon nanotubes doped with nitrogen and transition metals cobalt and iron are used to facilitate electron transfer and catalytic properties. This paper also examines the various components of PEM fuel cells as the electrode, electrolyte, etc. PEM electrode manufacturing methods are discussed.

Keywords: PEM fuel cells, Carbon Nano-materials, PEM fuel cell components, Electrode

Introduction

Energy has long been recognized as the driving force of human societies. And the importance of human development and its impact on human life has increased. Combination of various factors including the limited fossil resources, the negative environmental impacts, use of hydrocarbon resources, increasing the price of fossil fuels, political conflict and its effects on the provision of sustainable energy are among the reasons that many politicians and experts in energy and environmental issues to move toward building a new structure based on providing energy security, protect the environment, and enhance performance of energy has forced. Therefore best options for playing the role of energy carriers in the energy of this new system is hydrogen [1]. And In the not too distant future, humanity will experience the hydrogen age [1, 2]. Operation of chemical energy of hydrogen into the electrical energy done by machine

¹ Graduate student of Ceramics engineering

² Graduate student of Characterization & Selection of Engineering Materials, mirhosseini@mut-es.ac.ir

called fuel cell. According to their structural properties and applications, fuel cells are classified into different types [3]. Fuel cells have a significant role in reducing environmental pollution and due to the lack of mechanical parts often do not make noise and due to directly processes produce electricity have higher efficiency by other devices such as combustion engines. Fuel cell, essentially a device that converts the chemical energy of fuel directly into electrical energy [4, 6, 7]. Hydrogen gas is due to the high reactivity and high energy density as ideal fuel for the fuel cell is used, although other fuels such as methanol, natural gas, gasoline and etc. is also used. A fuel cell is series of electrolyte, electrodes and bipolar plates. In fuel cell (for example type of solid polymer electrolyte) hydrogen from an anode and oxygen from a cathode is entered. Hydrogen loses electrons at the anode and like protons through the electrolyte to the cathode move. Electrons leads through the external circuit to the cathode. Oxygen is converted to water with receive electrons and protons. Electrons move from the anode to the cathode, creating an electrical current is used in electronic devices. The water at the cathode can be reused [4].

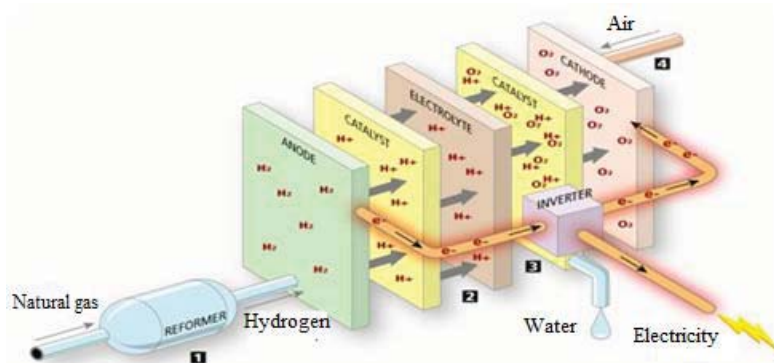


Figure 1: General view of a fuel cell [8]

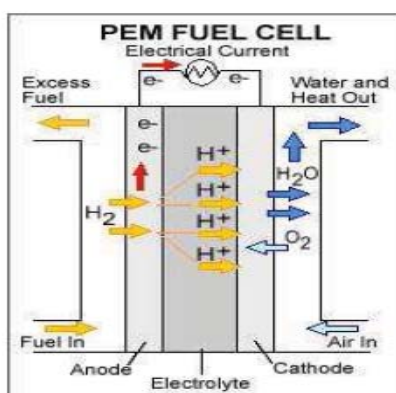
Fuel cells from different perspectives are classified, such as fuel type and consumption of oxidizer, fuel conversion system (internal or external adapter), type of electrolyte, operating temperature, etc. General categories according to the type of fuel cell is the electrolyte which consists of five categories: 1. Alkaline fuel cell (AFC), 2. Phosphoric acid fuel cell (PAFC), 3. Molten carbonate fuel cell (MCFC), 4. Solid oxide fuel cell (SOFC), 5. Polymer electrolyte fuel cell or proton exchange membrane (PEFC) [4, 9].

Of course there are other types of fuel cells. A subset of these cells of which: Proton ceramic fuel cells, methanol, microbial, and etc.

1. The proton exchange membrane fuel cells

Proton membrane fuel cells (polymer) was used for the first time in 1960 for NASA's Gemini program. This type of fuel cell is one of the most attractive in terms of design and application of fuel cell types. Polymer fuel cell having polymer electrolyte with a thin flexible sheet such as, sulfuric acid, Nafion, etc., that conductor of hydrogen ions (protons) but it is not

electrically conductive and set between two porous electrodes are made of carbon. For optimum performance it is necessary electrolyte is saturated with water [4]. The cell operating temperature is 80°C. Oxygen reduction reaction in polymer fuel cell is slower reaction (This response is three times slower than the hydrogen oxidation reaction). Most of the platinum catalysts used in the fuel cell and the amount of catalyst used in fuel cell electrodes of this type of fuel cell is higher than other types. The electrical efficiency of this type fuel cell is about 40-50%. PEM fuel cells require pure hydrogen is used in fuel therefore, the fuel cell for conversion of methanol fuels or gasoline to hydrogen is needed to converter. This type of fuel cell power density is higher than other types of fuel cell. The predicted lifetime for PEM fuel



cell of over 40,000 hours. Carbon monoxide in the fuel cell due to catalyst poisoning. Symbolic gestures of a PEM fuel cell is shown in Figure 2 [4, 10].

Figure 2: The proton exchange membrane fuel cells [10].

2. PEM fuel cell components

PEM fuel cell components, including electrodes, electrolytes, electro catalytic, gas diffusion layers and bipolar plates and etc. Symbolic gestures of these components can be seen in Figure 3.

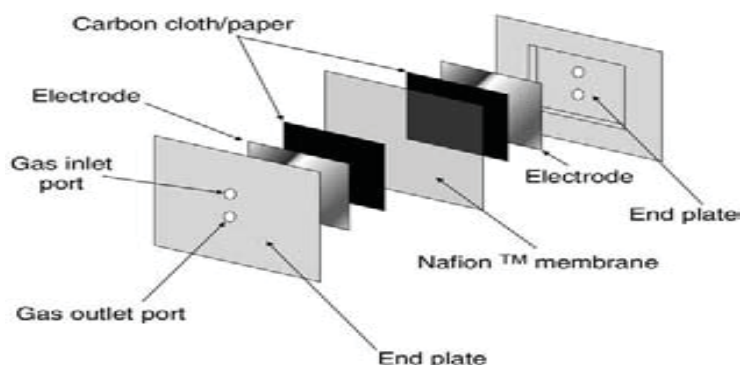


Figure 3: Components of PEM fuel cells [8].

2.1. Electrode

Electrodes in fuel cell are reactions place and catalyst is located in this section. The anode and cathode (electrodes) are on either side of the membrane [8]. To increase the contact area of reactant with catalyst is necessary porous electrode structure and Levels available and covered

by the catalyst is high relative to the size of the electrode. In porous fuel cell electrode plates duties include:

1. Creating an active area for the electrochemical reactions on the surfaces is performed.
2. Conduction of ions into or out of the three phase exchange reaction and transport of electrons produced in the external circuit (electrodes should have good electrical conductivity).

Polymer membranes for fuel cells are currently the best catalyst for both of side platinum. In fact catalyst layer consists of a porous layer of carbon that very small particles of platinum as a catalyst surrounds them. Because these layers are made of porous materials, reactants gas diffusion electrodes and the electrochemical reaction can be done at a higher level [8, 10, 12]. Electrochemical reaction rate increases with increasing temperature, so catalytic properties of electrodes at low temperature fuel cells is more important than high-temperature fuel cell [12].

2.2. Electrolyte

In fact, membrane is the heart of the fuel cell. Membrane is same electrolyte, which in each type of fuel cell has a specific profile. Of which can be a barrier to the flow of electricity, enabling the passage fuel of ions and prevent the passage and contact reactant gases named. Polymer fuel cell membranes from a solid polymer material, which is now mainly a Nafion. Due to the limited thermal stability and ionic conductivity of the material is better that cell operating temperature not higher than 85°C. Electrolyte with conduct ions between the electrodes causes of the fuel cell electrical circuit is completed [12, 13]. The proton conductivity of the membrane must have the following characteristics: Inexpensive, accessible, high oxygen solubility, mechanical strength appropriate.

Each cell produces about 0.7 volts of electricity. To produce higher voltages some of these cells are connected in series and the structure of the fuel cell are collection.

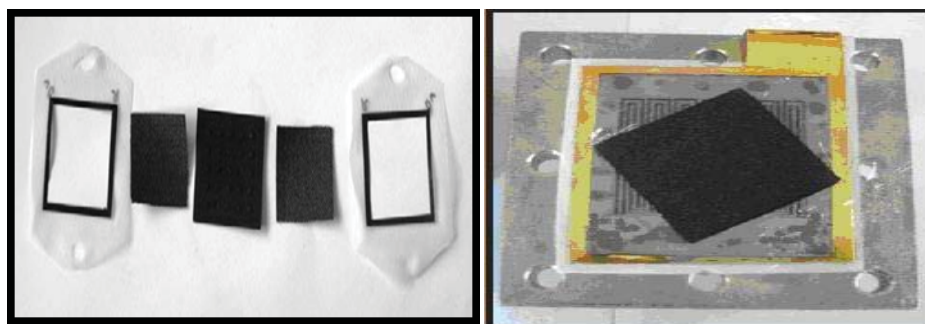


Figure 4: Collection of electrolyte and electrode MEA

2.3. Electrocatalysts

Electrocatalyst substances that are not consumed during the reaction while increases electrochemical reaction rate. Electrocatalyst divided into two homogeneous and heterogeneous categories, that electron transfer reactions in homogeneous is performed inside solution and electrons cannot be transferred directly from the electrode to the reagents. While, in heterogeneous, reagents to the electrode surface and electron transfer between the two phases (electrode and solution) is done. Heterogeneous electrocatalyst used in the fuel cells [12].

2.4. Gas diffusion layer (GDL)

Consists of a porous environment that can provide uniform distribution of gases on the catalyst. According to the fuel cell channels and the channel wall, if the catalyst is directly exposed to the gas, part of the catalyst on the channel walls would be useless. To prevent this act gas diffusion layer is used. Gas diffusion layers are playing key role in improving fuel cell performance. And based on the three concepts of higher conductivity, better water management and higher gas Permittivity are designed. Carbon paper, carbon cloth and metal sintered are widely used as gas diffusion layer. The most important gas diffusion layers that are used today in commercial scale are made of carbon fiber (carbon paper and carbon cloth). For use paper and carbon cloth substrates in fuel cell as these structures hydrophobic GDL was initially and then placed on a layer of MPL, But the use of nanomaterial including carbon nanotubes and carbon Nanofibers Cause Reduce the contact resistance, improve gas distribution and water management is better[10,12].

Other components such as end plates, bipolar plates, sealing materials (gaskets), voting systems humidity or damp instruments are used. Be seen in Figure 5.

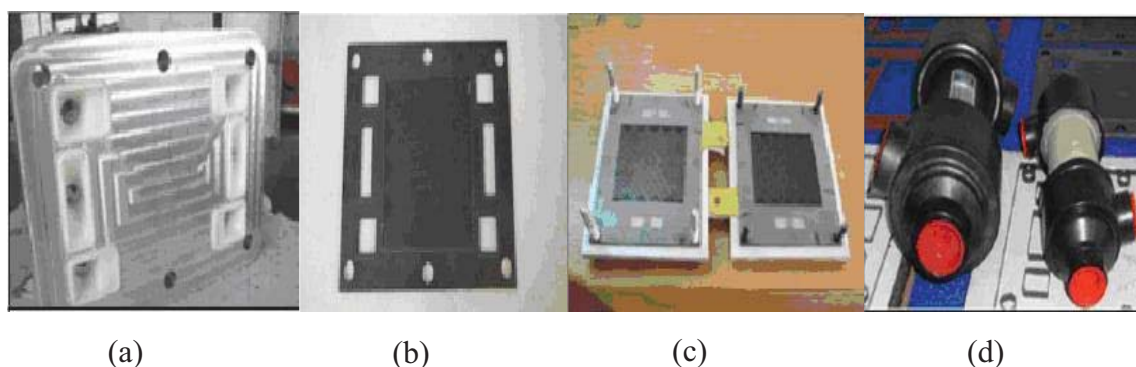


Figure 5: a. End plates, b. Bipolar plates, c. sealing of single cell, d. The wet polymer fuel cell maker [14]

3. Methods for fuel cell electrodes ion exchange of protons

Build issues like reducing the electrode catalyst layer, carbon Nano-sized platinum particles on the nanometer scale is considered. Here, various methods of coating Teflon emulsion-based methods, thin film, thin film recovered, electro spray deposition, measured using ion sputter, plasma, spray deposition, electron beam loss, Ion sputter assisted deposition and plasma samples discussed are useful [9].

3.1. Teflon emulsion based methods

Before the development of thin-film catalyst layers, catalyst layers made with this method were very common. In this way, the catalyst particles are surrounded by the hydrophobic PTFE. Due to ion transfer process, Operation by spraying or brushing the catalyst layers are saturated with Nafion. However, the use of platinum in about 20% remains. This method has the ability to reduce this rate 10 times.

3.2. Thin film method

Conventional methods for making PEM fuel cell catalyst layer is thin film. In 1993, Wilson, Such a method for making the catalyst layer PEM with platinum loading of less than 0.35 mg/cm^2 provided. In this method, instead of using PTFE hydrophobic of hydrophilic monomers (Nafion) is used [9].

3.3. Electro spray

The advantages of this method is simple and does not require temperature special conditions and vacuum or growth and morphology of the films with high uniformity is appropriate. Electrostatic interactions between charged particles and the surface layer during the deposition process, by spraying method prevent the mass formation and adhesion layer and in addition, there is the possibility of using a jet for rapid growth.

3.4. Spray deposition method

Because of the many advantages of this technique over the past decade as a method for PEMFC fuel cell electrodes have been used. These advantages are: 1. Preparation of electrode with the specific platinum and thickness and Fine morphology, 2. the smaller the particle size increased activity levels, and the activity of platinum is used, 3. Facilitate the construction of Nano-scale layers of platinum with the uniform distribution, 4. Easy fabrication process, 5. Scaling capability, Platinum deposition capability in different layers of the fuel cell like Gas diffusion layer, Not catalytic membrane layer. Efficiency obtained by this method is strongly dependent on the catalyst Layer thickness. The optimum thickness is 5-10nm [9].

3.5. Electron beam reduction method

Electrodes prepared process by this method is shown in Figure 6.

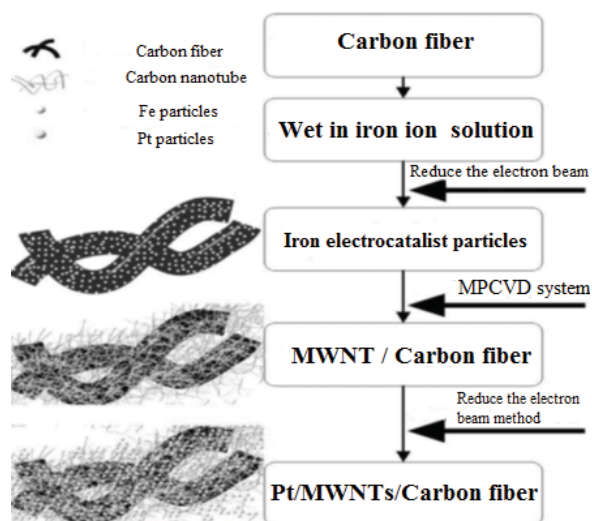


Figure 6: Preparation of electrodes by reducing the electron beam



3.6. Precipitation method using ion sputtering

This process is a combination of ion sputtering and physical vapor deposition method. Atoms that they are coated on a substrate, the vapor phase produced by electron evaporator and then deposited on the substrate. Subsequently ions ejected and accelerated in the precipitation films. Ion sputtering is the key to control characteristics in sediment film, so part of energy is imported into covers and part of that imported into the layer surface. The advantages of this method is produces denser layer with more uniformly, also heat treatment without changing the bulk properties. The important parameters in this process are: Cover materials, Evaporation rate, Types of ions, Ion energy and Ion beam current density. In this way, platinum only deposited at high levels gas diffusion layer, Sedimentary thickness increases, and the value is high [9].

3.7. Plasma

The other method is plasma deposition that its advantage is Concentration depth profiles control. It is observed that the cells derived from these methods have similar behavior with commercial electrodes except at high current density. In this region the plasma electrode voltage, the intensity drops. The reasons for this behavior can be expressed as follows:

1. May be due to environmental impurities, electrode poisoning.
2. Platinum precipitation may increase, decrease pore size and thus cell efficiency decrease [9].

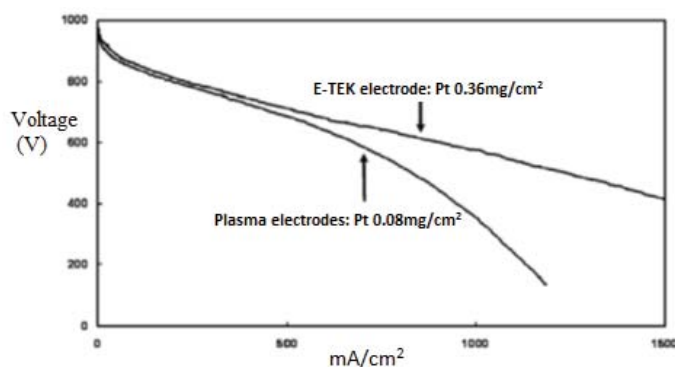


Figure 7: Efficiency of fuel cells with plasma electrodes [10].



Table2: A summary of the advantages and disadvantages of different methods of making electrodes [10].

Method	Loading quantity (Mg _{Pt} /Cm ²)	q _{Pt} /kW	Advantage	Disadvantages
Teflon emulsion	0.4	0.093	Simple , Reduce loading to 10 times	The high usage of platinum.
Thin film	0.2	0.13	22-45% increase active surface, Improve Pt utilization	
Improved thin film	0.1	0.14	Reduce loading and Relatively economical process.	Non-uniformity sediment in Large-scale, Size control Complexity
Electro spray	0.15	0.45	sediment in membrane	Relatively complex process and relatively high loading.
Spray deposition	0.04	1.21	The best Efficiency in the gas diffusion layer deposition, Possibility of constructing Nano scale.	Sensitive to the thickness of the sediment layer, Low adhesion to the substrate and low Stability.
Electron beam reduction	0.06	1.34	No loss of material during production, Rapid particle production, Particle homogeneous morphology, Appropriate strength.	Need to vacuum
Precipitation using ion sputtering	0.04	0.297	Relatively low loading	Low-density sediment, Complex process, Large number of steps, Low specific energy density.
Plasma	0.08	0.98	Control of the concentration depth profiles.	Require expensive equipment.



4. Problems polymer fuel cell and nanotechnology achievements

Recently PEMFC are from solely research phase close to phase commercialization. But there is still the challenge of reducing cost and high technology. To reduce costs, the following solutions are suggested:

- Research on ways to build and improve electro catalyst.
- Improved methods for the preparation of controlled deposition of platinum particles.
- Research in the field of high temperature membranes.
- Research in the field of catalysts with higher activity, Cheaper and more stable than platinum.

The proposed solution catalyst with higher activity, cheaper and more stable than platinum Research has been done. Polymer fuel cell electrode catalyst used in the past often made of platinum and electrodes price directly depended on the platinum price and its high cost prevented widespread use of fuel cell. So platinum on both fuel cell electrodes must be replaced and more comparable effect of the substitution at the cathode. Because oxygen reduction reaction (ORR) at the electrode is slow and need more platinum [15].but today, because of two reasons don't use platinum as PEM Electrode.

1. In this electrodes a large amount of platinum used and PEM fuel cell prices were very expensive.
2. Platinum catalyst can accelerate the reaction in the fuel cell only where it is in contact with the electrode and electrolyte. This points called "three-phase boundary" (Figure 8) because the number of molecules of platinum in three-phase boundary was low, efficiency of fuel cell is low, too.

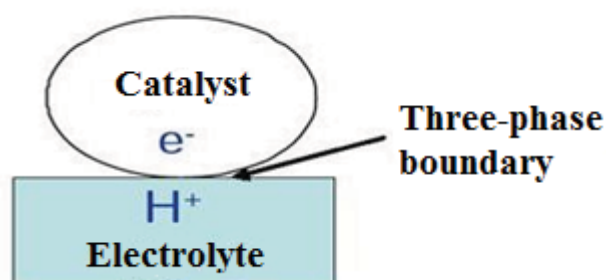


Figure 8: Three-phase boundary in fuel cells

To solve this problem, three issues must be resolved: 1. the amount of platinum used in fuel cell manufacturing decreased, 2. higher levels of platinum molecules were available, 3. Platinum catalyst was replaced. One way to solve these problems was distributed Platinum on the material that has a lot of surface. This was the name of the substrate in addition to having a high level, must be conductor. Today, different types of carbon using as a substrate of PEM fuel

cells. The main reason for choosing carbon as substrate unique characteristics of this material note the examples of cheap, high electrical conductivity, high corrosion resistance, good chemical stability. With Distribute platinum on carbon, platinum particle size is about 2nm or less. As we know when the particles reach the nanometer scale, Contact area is increased significantly, the distribution of platinum on a carbon substrate much less platinum can be achieved much more surfaces. It also decreases the amount of platinum while more platinum surface will be available. Due to reactions between Pt and the substrate, Electronic structure of platinum atoms could be improved this slight increase catalytic activity. In addition, this interaction, which is the platinum particles are trapped on substrate, the platinum particles are later hunk. Hunk of platinum particles reduced the levels of contact [17]. (Figure 9)

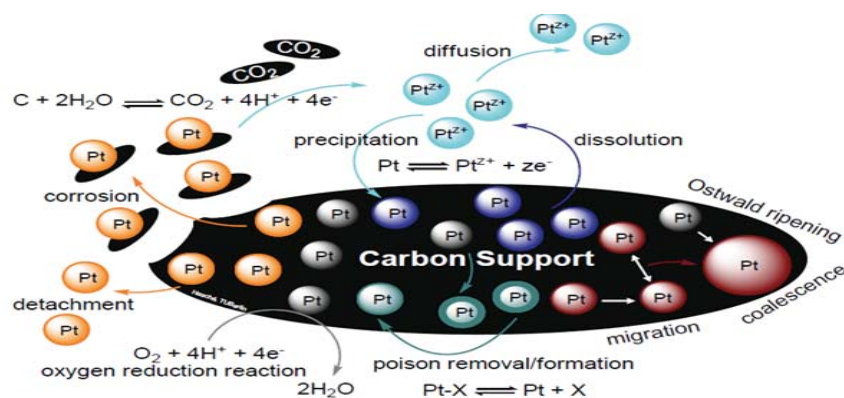


Figure 9: Distribution processes of platinum nanoparticles on carbon substrate [16].

4.1. Achievements in nanotechnology

Using nanotechnology can be produce light, thin and inexpensive electrodes that Better performance than conventional electrodes. In this regard, carbon Nano fibers, carbon nanotubes, or compounds that are nanometer-sized pores can be used (Fig 10). Carbon nanotubes are considered Most of the other cases. Carbon nanotubes are a new form of carbon which can be single-walled or multi-walled as a catalyst for the deposition of metals onto carbon nanotubes are used. The catalysts were deposited on carbon substrate (Pd, Rh, Pt, Ru for example) show high activity in many chemical reactions. Carbon nanotubes are superior other than routine for reasons Specific interaction between metal and support, higher electrical conductivity and lower organic impurities in them. Platinum catalysts with small particle sizes are distributed evenly on a variety of carbon substrate. Despite the lower metal sediment show the high catalytic activity [17].

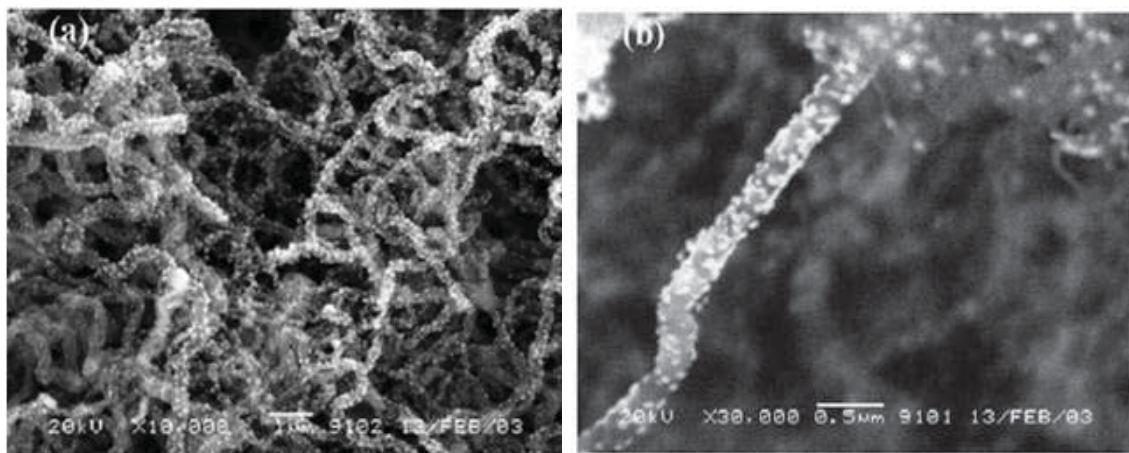


Fig 10: Distribution of platinum on carbon Nano-fibers [17].

Figure 11 shows that carbon nanotubes that Platinum is placed on them. As seen in figure 11 by putting platinum on carbon, platinum particles are small.

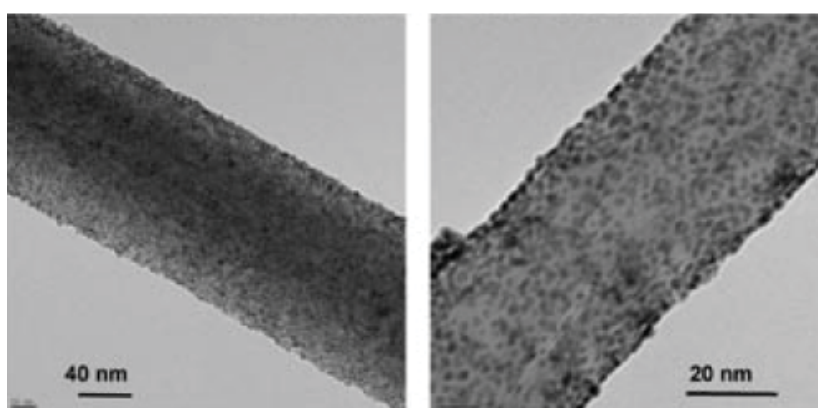


Figure 11. Distribution of platinum on carbon nanotubes [6].

Carbon nanotubes can be used to help lower the amount of platinum to a large contact area ties. This case the amount of platinum and the price of fuel cell is less [16, 17].

Recently, instead of use platinum in cathode, Carbon nanomaterial doped with nitrogen and transition metals (Co,Fe) to facilitate electron transfer and catalytic properties have been used [15,18,19]. However, the high efficiency the resulting material, manufacturing methods is complex and production efficiency is low. So the method looks expensive. Hence new production methods for carbon-based material, and similar materials need to investigate further.

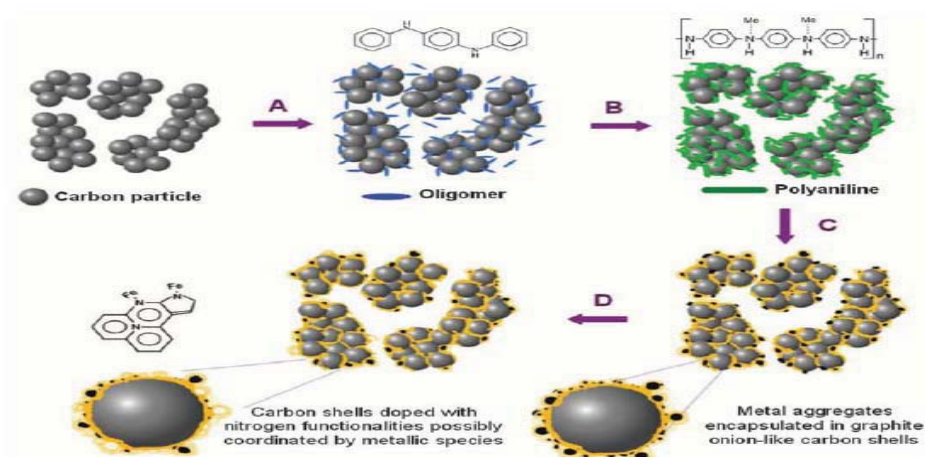


Figure 12. A schematic of the catalysts synthesized PANI-M-C

Conclusion

According to what was said, hydrogen can be considered as an alternative fuel in the future. Tool of this work is full cell. Hence the development of these systems as a means of producing electricity is important. For the commercialization of fuel cells should be trying to bring down their prices. Nanotechnology can play an important role in this field and can help producing fuel cells with lower prices and higher efficiency. Nano carbon fiber, carbon nanotubes or compounds with nanometer-sized pores are Nanotechnology proposals to improve the performance of fuel cells.

References

- [1] M. B. Salehi "Technical analysis of the economic development of the fuel cell application As vehicle driving force by emphasis on nanotechnology", M.Sc. Thesis of Industrial Engineering, Sharif University of technology, 2009
- [2] B. Cook "An introduction to fuel cells and hydrogen technology" , Heliocentris North America, 2001
- [3] S. Prip Beier, P. Dybdahl Hede "Essentials of chemistry", 2010.
- [4] EG&G Technical Services, Inc. "Fuel Cell Handbook", U.S. Department of Energy Office of Fossil Energy National Energy Technology Laboratory P.O. Box 880 Morgantown, 7th Edition, 2004.
- [5] S. Basu "Recent Trends in Fuel Cell Science and Technology", Springer, USA, 2007.
- [6] E. Budevski "Structural Aspects of fuel cell electrodes", Journal of Optoelectronics and Advanced Materials, 2003.
- [7] A. Rashidi Mohammadi "Study and fabrication of polymer electrolyte fuel cell", M.Sc. Thesis of Material Engineering, Tehran University, 1995.
- [8] www.fcc.gov.ir



6th Iranian Fuel Cell Seminar
March. 12 & 13 , 2013
Tehran - Iran



- [9] G.Mclean, S.Litster1 "PEM fuel cell electrodes" , Journal of Power Sources 130 ,2004
- [10] F. Yousefi rad "Polymer membrane fuel cell", M.Sc. Thesis of Material Engineering, Malek Ashtar University of Technology, 2006.
- [11] N. Ohio, Introduction to Fuel Cells, Hocking College, ppt, 2007.
- [12] G. Karimi Moghaddam "Effects of different bipolar plate channels patterns in fuel cell polymer membranes performance", M.Sc. Thesis of Energy Engineering, Sharif University of technology, 2009.
- [13] M. Ciureanu "Effects of Nafion Dehydration in PEM Fuel Cells", Journal of Applied Electrochemistry, 2004.
- [14] M. Gholami "Polymer fuel cell package of technology transfer to Iran to help determine the readiness", the first national conference on hydrogen and fuel cell, 2007.
- [15] Gang Wua, Karen L. More, chirstina M. jahnston and Piotr Zelenaya "High performance electrocatalysts for oxygen reduction drived from polyaniline iron and cobalt", science 2011.
- [16] "Activity, stability, and degradation mechanisms of platinum and platinum alloy nanoparticle PEM fuel cell electrocatalysts", genehmigte Dissertation, 2012.
- [17] H. Mokarrami ghartavol "Electrochemical deposition of platinum nanoparticles on carbon nanotubes", M.Sc. Thesis of Corrosion Engineering, Sharif University of technology, 2010
- [18] G. Wua, Z. Chena, K. Artyushkovab, F. H. Garzona, and P. Zelenaya, Polyaniline "derived Non-Precious Catalyst for the Polymer Electrolyte Fuel Cell Cathode", The Electrochemical Society, 2008.
- [19] G. Wu , Ch. Dai , D. Wang , D. Li and N. Li , "Nitrogen-doped magnetic onion-like carbon as support for Pt particles in a hybrid cathode catalyst for fuel cells", Journal of Materials Chemistry, 2010.



Electrochemical characterization of binary carbon supported Pd₃Co nanocatalyst for oxygen electroreduction reaction in direct methanol fuel cells

Farhad Golmohammadi¹, Hussein Gharibi² and Mehdi Kheirmand³
*Department of Chemistry, Faculty of Science, Tarbiat Modares University,
Tehran, Iran
GolmohammadiFarhad@gmail.com*

Abstract

In this paper, we report the use of binary carbon supports for fabricating membrane electrode assembly (MEA) of passive direct methanol fuel cells (PDMFCs) and their detailed electrochemical characterization. Electrocatalytic properties for the oxygen reduction reaction (ORR) were evaluated by polarization curves and electrochemical impedance spectroscopy (EIS) in a PDMFC. The binary-support electrode exhibits better performance than the single-support electrode, and the best performance is obtained when the mass ratio of multi-walled carbon nanotubes (MWCNTs) and Vulcan XC-72 (VC) is 27:75. An eight-hour lifetime test was performed for the single cell to evaluate the durability, in which the MEA was done using MWCNT: VC with the mass ratio of 25:75. The test results show that formation of the optimal combination of MWCNT and VC support is favorable to improve the stability and durability.

Keywords: Binary carbon supports; Cell performance; Electrochemical stability.

1. Introduction

Direct methanol fuel cells (DMFCs) offer lots of promise as the next-generation power source for portable devices [1]. In particular, a passive air-breathing DMFC system consisting of an anode that absorbs methanol from the built-in reservoir and a cathode that “breathes” from the ambient atmosphere works without any auxiliary devices such as heat exchangers, humidifiers, fuel pumps, gas blowers/compressors, etc. [2]. However, further development of the DMFC is still facing some technical issues, among which methanol crossover is the most significant obstacle. However, the permeation of methanol through the membrane produces a loss of efficiency and a decrease of the fuel cell voltage due to parasitic methanol oxidation at the cathode, which remain one of the major problems for the DMFC performance [3]. In DMFCs, when Pt is used as the cathode catalyst, the problems are exacerbated by methanol crossover from the anode that results in a mixed potential at the cathode [4]. Therefore, a non-Pt catalyst with high activity and selectivity toward ORR is urgently required. Recently, extensive studies have been carried out on the feasibility of replacing Pt with alternative metals such as Pd, the cost of which is only one-fifth of Pt [5]. In particular, PdCo/C electrocatalysts have been identified as promising alternatives to Pt catalysts for ORR, and the use of these electrocatalysts is thought to be a possible solution to the methanol crossover problem in direct methanol fuel cells (DMFCs) [6]. Apart from activity of the electrocatalyst, type and properties of the carbon support, such as its hydrophobicity [7], surface area, electronic conductivity [8], and surface functional groups [9], all contribute to the overall performance of the GDE [10].



Carbon is not only used to conduct electrons in a GDE, but also should result in the presence of macro- and microscopic pores [11] and helps to stabilize the three-phase boundary and morphology [12]. The Vulcan XC-72 carbon black has been the most used carbon support in fuel cells. However, blocking of the oxygen transportation reduces the reactive sites to obtain high current densities. Carbon nanotubes (CNTs) have been demonstrated to possess excellent electronic properties, good chemical stability, and large surface areas. These unique properties make carbon nanotubes very useful for supporting metal nanoparticles in many potential applications ranging from advanced catalytic systems to very sensitive electrochemical sensors to highly efficient fuel cells. However, when using a single carbon support, it may be difficult to obtain the optimal parameters needed for enhancing the gas diffusion performance of the ORR, as well as to obtain optimized ionic and electronic conductivity, good morphology, surface area, electron diffusion, and product removal. Sakaguchi et al. [13] and Watanabe et al. [14] first reported the use of binary carbon supports in liquid electrolyte fuel cells. Wang et al. [15] and Gharibi et al. [16-18] reported the use of binary carbon supports with different surface areas.

In this paper, MWCNTs are first used as a secondary carbon support of Pd₃Co catalyst layers at different mass ratios in order to determine the best mass ratio of these types of carbon in acid media at the presence and absence of methanol and afterwards for fabricating membrane electrode assembly (MEA) in passive direct methanol fuel cells (PDMFCs). The role of binary carbon supports in the catalyst layer is evaluated and characterized through measurement of polarization curves and electrochemical impedance spectroscopy (EIS). It will be shown that by using two carbon supports, the electrochemical performance of as-formed MEA can be enhanced. This improvement is further exemplified by enhanced electrode kinetics of ORR in the presence of methanol for binary-support electrode compared to that with single support. Finally, durability of electrodes was also examined in PDMFC and compared with that of the commercial Pt/C electrocatalyst.

2. Experimental Section

2.1. Materials and synthesis of electrocatalysts

The chemical compounds of concentrated sulfuric acid, Pd [NO₃]₂.2H₂O, Co [NO₃]₂.6H₂O, ethylene glycol, methanol, 2-propanol were bought from Merck; Nafion solution 5% from Aldrich; Vulcan XC-72 (VC) from Cabot, and multi-walled carbon nanotubes (MWCNTs) from Plasma Chem. GmbH. Since MWCNTs are chemically inert, the MWCNTs (5-20 nm) were functionalized by pretreatment with 70% nitric acid in order to introduce surface oxides before preparation of the composites [19-21]. In our study, the MWCNTs were refluxed under constant agitation at 120 °C in concentrated nitric acid for 12 hours. The solid phase filtered and washed with distilled water, and the recovered functionalized MWCNTs were then dried at 80 °C for 12 hours.

2.2. Ink Preparation

For the diffusion layer, a mixture of 30 %wt PTFE and 70 %wt VC in 2-propanol and water was sonicated for 30 min with a sonicator (Misonix model S-3000) to produce a homogeneous suspension. The suspension was painted onto the carbon paper (TGPH-0120T) (Toray), and the electrode was dried in oven at 120 °C for 1 hour and then finally sintered at 300 °C for 30 min. The loading of diffusion layer in each electrode was fixed at 1.0 mg cm⁻².

To prepare the catalyst layers in GDEs, a homogeneous suspension containing the desired amounts of Pd₃Co/support/Nafion composite (20 %wt), 2-propanol, and water was sonicated for 20 min. The loading of Nafion in the catalyst layer was fixed at 15 wt%.



2.3. Stability of the passive direct methanol fuel cell performance

The home-made, oxygen-breathing DMFC with stainless steel (SS316) current collectors was used to evaluate the electrochemical performance of synthesized supported Pd₃Co electrocatalysts in comparison with the commercial Pt/C. A pretreated Nafion 115 membrane with a thickness of 125 μm was employed in this work. Prior to modification, the Nafion 115 membranes were treated by sequentially boiling for 1.5 hours in each of the following solutions: 5 Vol% H₂O₂, washing in DI water, boiling in 0.5 M H₂SO₄, and washing in DI water at 80 °C. The pretreated membranes were kept in the DI water prior to the fabrication of MEAs. Carbon paper was used as the backing support of anode and cathode electrodes. The following four membrane electrode assembly (MEA) samples were tested in this experiment. MEA-1: 20 wt% Pd₃Co on 25% MWCNT + 75% VC, MEA-2: 20 wt% Pd₃Co on MWCNT, MEA-3: 20 wt% Pd₃Co on VC, and MEA-4: 20 wt% commercial Pt/C used as cathode and anodes based on 10 wt% commercial Pt/C were prepared and MEA catalyst loadings for both the anode and cathode were 3 mg_{metal} cm⁻². The active area of MEAs was 4.75 cm² and the methanol reservoir volume was 12.5 mL. In order to estimate the durability of the as-prepared electrocatalyst, the experiment was devoted to the operation of a passive direct methanol fuel cell for 8 hours. Current-voltage (I-V) curves, power curves, and EIS spectra were measured to trace the performance of the cell.

3. RESULTS AND DISCUSSION

3.1. Passive Direct Methanol Fuel Cells (PDMFCs) performance

Figure 1a. shows polarization and power density curves of the MEAs: 1, 2, 3, and 4, in which MEA 1: 20 wt% Pd₃Co on (25% MWCNT + 75% VC), MEA 2: 20 wt% Pd₃Co on MWCNT, MEA 3: 20 wt% Pd₃Co on VC and MEA 4: 20 wt% commercial Pt/C electrocatalyst as cathode in PDMFC under the identical testing conditions were filled with 1.0 M methanol solution. The polarization curves recorded for these PDMFCs have the same characteristic shape of typical fuel cells, with kinetically, ohmic, and mass transport limited regions. Better performance of MEA-1 with 25% MWCNT + 75% VC supported Pd₃Co cathode confirms the above obtained parameters (conventional three electrode system), and suggests that Pd₃Co electrocatalyst with a MWCNT: VC mass ratio of 25:75 as cathode has high catalytic activity for oxygen reduction in a PDMFC. From the viewpoint of tailoring surface properties, owing to the high surface area and capability to absorb water, MWCNT powder offers a better contact with electrolyte ionomer than does VC, helping VC carbon retain sufficient water to enhance the ionic conductivity of the electrode. The combination of increased electronic and ionic conductivity contributes to better cell polarization characteristics of MEA with binary-support electrode. The values for the peak power density, maximum current density, and open circuit potential are presented in Table 1.

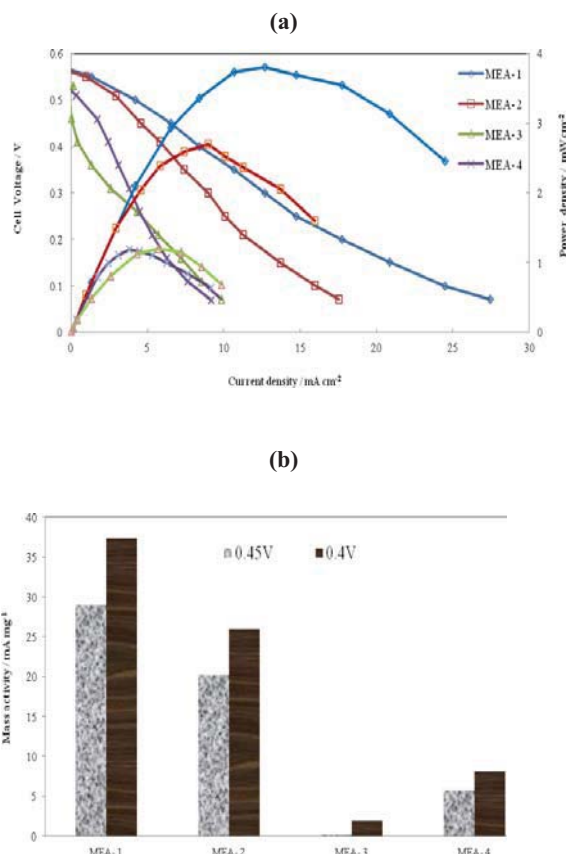


Figure1: PDMFC polarization curves obtained for MEAs: 1, 2, 3 and 4 (a) Comparison of the mass activities at various potentials for binary and single support of Pd₃Co alloy electrocatalysts and commercial Pt/C as cathodes at PDMFCs (b).

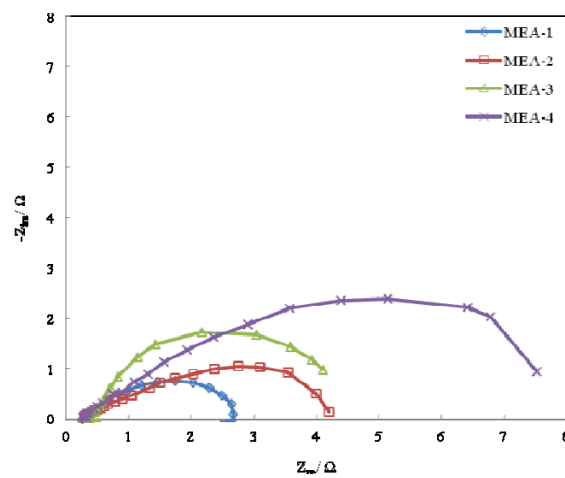
Figure 1b compares the mass activity for oxygen reduction of the four MEAs. At 0.45 and 0.4V, the MEA-1 exhibits 1.44 and 4.82 times higher mass activity than MEA-2 and MEA-4, respectively. The results obtained in PDMFCs are consistent with those obtained in conventional three electrodes in this work.

Table 1: Peak power density and current density of the PDMFC for four cathodes configurations.

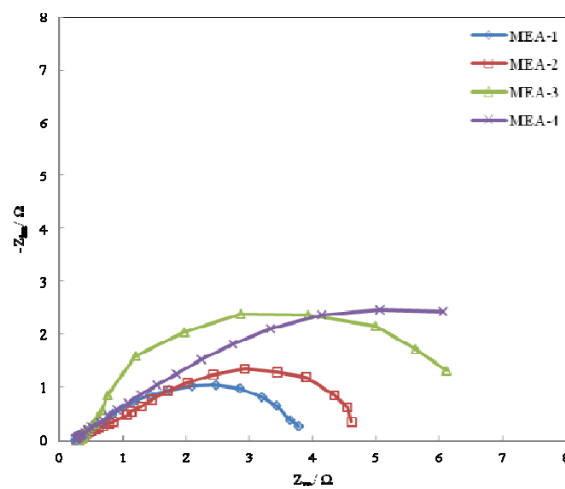
Pd ₃ Co/25%MWCNT+75%VC			Pd ₃ Co/VC		
E _{max} / V	I _{max} / mA cm ⁻²	W _{max} / mW cm ⁻²	E _{max} / V	I _{max} / mA cm ⁻²	W _{max} / mW cm ⁻²
0.57	27.46	3.81	0.52	11.40	1.20
Pd ₃ Co/MWCNT			Commercial Pt/C		
E _{max} / V	I _{max} / mA cm ⁻²	W _{max} / mW cm ⁻²	E _{max} / V	I _{max} / mA cm ⁻²	W _{max} / mW cm ⁻²
0.56	20.85	2.53	0.51	11.12	1.20

Electrochemical impedance spectroscopy (EIS) is a powerful diagnostic testing method for fuel cells because it is nondestructive and provides some useful information about fuel cell performance [22]. EIS was used to measure the intrinsic properties of the electrodes caused by the electrocatalyst in this experiment, including the ohmic resistance, charge-transfer resistance, and mass-transfer resistance in the catalyst layer. Nyquist plots of EIS may include one, two, or three arcs: low, medium, and high frequency semicircles. These semicircles are related to the mass transport resistance, charge transfer resistance combined with double layer capacitance within the catalyst layer, and the structural features of MEA, respectively [23]. However, in some researches, the internal ohmic resistance and the contact capacitance in the granular electrode structure have been stated to be responsible for the high frequency semicircle [24].

(a)



(b)



(c)

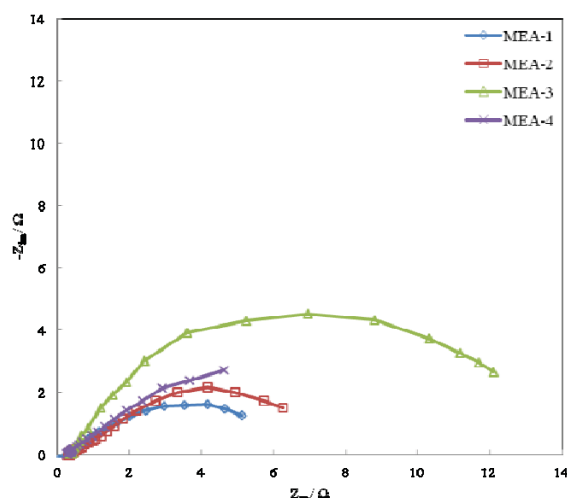


Figure 2: Nyquist diagrams of a Passive DMFC for MEAs: 1, 2, 3 and 4 using different E (V vs. NHE): (a) 0.1V, (b) 0.2V and (c) 0.3V.

EIS measurement was performed as described in Figure 2, which is the Nyquist representation of EIS measurements of the single cell. The high frequency (HF) interception on the real impedance axis of the Nyquist plot represents ohmic resistance of the cell (RHF), which contains the ohmic resistance of the cell components, such as the membrane, catalyst layer, backing layer, end plate, as well as the contact resistance between each of them [25]. The diameter of the kinetic semicircle, which corresponds to the charge-transfer resistance of fuel cell, defined as the difference between low frequency and high frequency intercepts of the curve. The values for the electric elements, which were obtained from the fit and the values of ohmic and charge transfer resistances, are presented in Table 2.

Table 2: Parameters obtained from EIS diagrams with the equivalent circuit shown in Figure 8 for MEAs: 1, 2, 3 and 4 using different potentials: (a) 0.1V, (b) 0.2V and (c) 0.3V, using nonlinear least-squares fitting (Zview, ver. 2.0).

MEA	0.1V		0.2V		0.3V	
	R_{ohmic} / Ω	R_{ct} / Ω	R_{ohmic} / Ω	R_{ct} / Ω	R_{ohmic} / Ω	R_{ct} / Ω
1	0.27	2.80	0.27	4.12	0.25	6.34
2	0.31	4.20	0.31	4.67	0.31	7.54
3	0.23	5.51	0.23	7.31	0.23	14.33
4	0.26	7.32	0.25	11.57	0.25	24.69

MEA-1: 20 % wt Pd₃Co on MWCNT:VC with a mass ratio 25:75, **MEA-2:** 20 % wt Pd₃Co on MWCNT, **MEA-3:** 20 % wt Pd₃Co on VC and **MEA-4:** 20 % wt commercial Pt/C used as cathode and anodes based on 10 % wt commercial Pt/C were prepared.

3.2. Durability test of PDMFCs for binary and single support electrodes and comparison of their with a commercial Pt/C

Since MEA-1 with a MWCNT: VC mass ratio of 25:75 in the cathode catalyst layer significantly improves PDMFC performance, it is necessary to investigate its durability under constant current or voltage discharge for a long-term operation. Figure 3 shows variation of the cell current density as a function of time at a constant voltage of 0.15 V under a normal operating condition without any recovery process. In this set of experiments, a time period of 8 hours has been chosen since substantial performance loss occurred during the first few hours in discharge operating modes. It was found that during the first 1 hour operation, performance of the fuel cell decreased slightly. After that, the performance kept stable. The decay of the performance was not significant during the 8-hour operation process. Compared with MEA-2, MEA-3, and MEA-4, MEA-1 exhibits much higher current density and slower current density decay, indicating better catalytic activity and stability for PDMFCs.

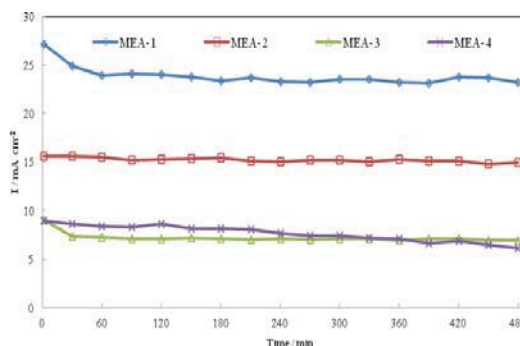


Figure 3. Current density – time behavior of MEAs: 1, 2, 3 and 4 in PDMFC at a constant voltage of 0.15 V.

The difference between the PDMFC test using a membrane electrode assembly (MEA) and the ADT test is that in case of MEA, only the catalyst, which is in contact with the membrane is active. Also, the proton electromigration and diffusion are limited due to the presence of a solid polymer electrolyte interfacing the cathode and anode. In the case of ADT, the entire active surface of the catalyst is exposed and high proton mobility in the liquid results in more severe catalyst corrosion than that observed in the MEA [26, 27].

4. Conclusions

Compared with single-support electrode, the binary-support electrode demonstrates improved polarization performance. It is believed that introduction of MWCNTs in the catalyst layer not only provides high accessible surface area, but also enhanced ORR kinetics. This observation is also supported by the decreased activation energy for ORR with binary-support electrode from analysis of Arrhenius plots. The best performance is observed on the electrode in which the catalyst layer is composed of MWCNT and VC at a mass ratio of 25:75, as the cell generates a maximum power density of 3.81 mW cm⁻² at 0.30 V. These results imply that introduction of MWCNTs as a secondary support of the catalyst layer may be a candidate for carbon support; as MEA fabrication in oxygen reduction is an important practical consideration in passive direct methanol fuel cells. The synergism between MWCNT and VC in Pd₃Co electrocatalyst is favorable to improve the stability, which was proved by durability testing and electrochemical characterization.



References

- [1] C.K. Dyer "Fuel cells for portable applications", *J. of Power Sources*, (2002), 106, 31-34.
- [2] Y.-L. He, Z. Miao, W.-W. Yang "Characteristics of heat and mass transport in a passive direct methanol fuel cell operated with concentrated methanol", *J. of Power Sources*, (2012), 208, 180-186.
- [3] J.R.C. Salgado, F. Alcaide, G. Álvarez, L. Calvillo, M.J. Lázaro, E. Pastor "Pt–Ru electrocatalysts supported on ordered mesoporous carbon for direct methanol fuel cell", *J. of Power Sources*, (2010), 195, 4022-4029.
- [4] J. Zhao, A. Sarkar, A. Manthiram "Synthesis and characterization of Pd-Ni nanoalloy electrocatalysts for oxygen reduction reaction in fuel cells", *Electrochim. Acta*, (2010), 55, 1756-1765.
- [5] D.N. Son, K. Takahashi "Selectivity of Palladium–Cobalt Surface Alloy toward Oxygen Reduction Reaction", *J. Phys.Chem. C*, (2012), 116, 6200-6207.
- [6] C.A. Bessel, K. Laubernds, N.M. Rodriguez, R.T.K. Baker "Graphite Nanofibers as an Electrode for Fuel Cell Applications", *J. Phys. Chem. B*, (2001), 105, 1115-1118.
- [7] E. Passalacqua, P. Staiti, L. Pino, M. Vivaldi, N. Giordano, E.J. Taylor, G. Wilemski "Influence of the morphological-absorptive properties upon the performance of phosphoric acid fuel cell gas diffusion electrodes", *Int. J. Hydrogen Energy*, (1992), 17, 771-776.
- [8] B. Rajesh, K. Ravindranathan Thampi, J.M. Bonard, H.J. Mathieu, N. Xanthopoulos, B. Viswanathan "Electronically conducting hybrid material as high performance catalyst support for electrocatalytic application", *J. of Power Sources*, (2005), 141, 35-38.
- [9] S.-I. Pyun, S.-B. Lee "Effect of surface groups on the electrocatalytic behaviour of Pt–Fe–Co alloy-dispersed carbon electrodes in the phosphoric acid fuel cell", *J. of Power Sources*, (1999), 77, 170-177.
- [10] X. Wang, I.M. Hsing, P.L. Yue "Electrochemical characterization of binary carbon supported electrode in polymer electrolyte fuel cells", *J. of Power Sources*, (2001), 96, 282-287.
- [11] M. Watanabe, M. Tomikawa, S. Motoo "Preparation of a high performance gas diffusion electrode", *J. Electroanal. Chem. Int. Electrochem.* (1985), 182, 193-196.
- [12] X. Xu "polymer/carbon blend electrodes and polyphosphonate membrane for PEM fuel cells", Thesis, state university of New York, NY, (1993).
- [13] C.T. Hsieh, W.Y. Chen, I.L. Chen, A.K. Roy "Deposition and activity stability of Pt–Co catalysts on carbon nanotube-based electrodes prepared by microwave-assisted synthesis", *J. of Power Sources*, (2012), 199, 94-102.
- [14] M. Sakaguchi, K. Uematsu, A. Sakata, Y. Sato, M. Sato "Correlation between wettability of carbon carriers and activity of porous electrodes", *Electrochim. Acta*, (1989), 34, 625-630.
- [15] M. Watanabe, K. Makita, H. Usami, S. Motoo "New preparation method of a high performance gas diffusion electrode working at 100% utilization of catalyst clusters and analysis of the reaction layer", *J. Electroanal.Chem. Int. Electrochem.* (1986), 197, 195-208.
- [16] H. Gharibi, R.A. Mirzaie "Fabrication of gas-diffusion electrodes at various pressures and investigation of synergetic effects of mixed electrocatalysts on oxygen reduction reaction", *J. of Power Sources*, (2003), 115, 194-202.
- [17] M. Kheirmand, H. Gharibi, R. Abdullah Mirzaie, M. Faraji, M. Zhiani "Study of the synergism effect of a binary carbon system in the nanostructure of the gas diffusion electrode (GDE) of a proton exchange membrane fuel cell", *J. of Power Sources*, (2007), 169, 327-333.
- [18] H. Gharibi, M. Javaheri, R.A. Mirzaie "The synergy between multi-wall carbon nanotubes and Vulcan XC72R in microporous layers", *Int.J. Hydrogen Energy*, (2010), 35, 9241-9251.
- [19] C.G. Hu, W.L. Wang, S.X. Wang, W. Zhu, Y. Li "Investigation on electrochemical properties of carbon nanotubes", *Diam. Relat. Mater.* (2003), 12, 1295-1299.



- [20] C.G. Hu, W.L. Wang, K.J. Liao, G.B. Liu, Y.T. Wang “Systematic investigation on the properties of carbon nanotube electrodes with different chemical treatments”, *J. Phys. Chem. Solids*, (2004), 65, 1731-1736.
- [21] K.M. Lee, L. Li, L. Dai “Asymmetric End-Functionalization of Multi-Walled Carbon Nanotubes”, *J. Am. Chem. Soc.* (2005), 127, 4122-4123.
- [22] D.j. Guo, H.l. Li “Electrochemical synthesis of Pd nanoparticles on functional MWNT surfaces”, *Electrochem. Commun.* (2004), 6, 999-1003.
- [23] R. Lin, C. Cao, T. Zhao, Z. Huang, B. Li, A. Wieckowski, J. Ma “Synthesis and application of core-shell Co@Pt/C electrocatalysts for proton exchange membrane fuel cells”, *J. of Power Sources*, (2013), 223, 190-198.
- [24] T. Romero-Castañón, L.G. Arriaga, U. Cano-Castillo “Impedance spectroscopy as a tool in the evaluation of MEA’s”, *J. of Power Sources*, (2003), 118, 179-182.
- [25] A. Fischer, J. Jindra, H. Wendt “Porosity and catalyst utilization of thin layer cathodes in air operated PEM-fuel cells” *J. Appl. Electrochem.* (1998), 28, 277-282.
- [26] B. Li, R. Lin, D. Yang, J. Ma “Effect of driving cycle on the performance of PEM fuel cell and microstructure of membrane electrode assembly”, *Int. J. Hydrogen Energy*, (2010), 35, 2814-2819.
- [27] H.R. Colón-Mercado, B.N. Popov “Stability of platinum based alloy cathode catalysts in PEM fuel cells”, *J. of Power Sources*, (2006), 155, 253-263



Hydrogen storage: A DFT investigation of adsorption hydrogen Molecule on born nitride nanofullerens like structure

Sima Mehdi Shishvan, Javad Beheshtian*

Department of Chemistry, Shahid Rajaei Teacher Training University, P.O. Box 16875-163, Tehran, Iran

j.beheshtian@srttu.edu

Abstract

The purpose of the present work is to investigate hydrogen gas storage and adsorption it on the BN nanoclusters i.e. $B_{16}N_{16}$ and $B_{24}N_{24}$, $K^+@B_{16}N_{16}$ and $K^+@B_{24}N_{24}$. In the next stage we compare two these groups from the point view of adsorption energy. The K^+ adding into nanofulleren like increases adsorption energy about 100 percent in hydrogen storage process.

Keywords: boron nitride nanofulleren, Density functional theory, adsorption, H_2 .

1-Introduction

Hydrogen is attractive as a fuel because its use creates neither air pollution nor greenhouse-gas emissions [1–3]. The use of hydrogen requires an effective, safe, and stable storage medium. However, how to store hydrogen easily and cheaply is still one of the key challenges in developing hydrogen economy [4,5]. Considerable attentions have been focused on porous materials such as metal–organic frameworks (MOF's), carbon nanotubes, fullerenes and organic hosts as possible materials for hydrogen storage [6–11]. Non-carbon nanosystem comprised of light elements such as boron and nitrogen atoms also have been noticed [12,13]. Boron nitride nanostructures have a wide range of attractive properties, such as high-temperature stability, a low dielectric constant, large thermal conductivity, and oxidation resistance, leading to a number of potential applications as a structural or electronic material [14–16]. The heteropolar nature in the BN nanostructures offers higher binding energy for hydrogen storage compared to the carbon based materials [17]. It has been found experimentally that at 10 MPa the BN nanotubes can store as much as 2.6 wt.% of hydrogen and that collapsed BN nanotubes exhibit an even higher storage capacity (4.2 wt.%) [18,19]. Takeo Oku et al in 2004 showed that H_2 gas storage in $B_{36}N_{36}$ cluster, Their work also indicates that BN fullerene materials could be a one of the possible candidates as hydrogen gas storage materials[20].

¹Sima Mehdi Shishvan, student at Shahid Rajaei Teacher Training University in Tehran Iran
,e-mail:sima_mehdishishvan@yahoo.com

²Javad Beheshtian, Department of Chemistry, Shahid Rajaei Teacher Training University, P.O. Box:16875-163, Tehran, Iran,
e-mail: j.beheshtian@srttu.edu

2. Computational details

All computations were performed at M062x/6-311G(d,p) level of density functional theory with the Gaussian 09 program packages. The convergence criteria for structure optimizations and energy calculations in this work were set to default values in the package. The frontier molecular orbital (FMO) analyses, and energy calculations. The adsorption energy of H₂ molecule on the pure B_nN_n cluster was obtained using the following equation,

$$E_{\text{ads}} = E(\text{B}_n\text{N}_n/\text{H}_2) - E(\text{B}_n\text{N}_n) - E(\text{H}_2)$$

where E (B_nN_n/H₂) is the total energy of B_nN_n/H₂ complex and E (B_nN_n) or E (H₂) is referred to the energy of an isolated B_nN_n or H₂ molecule, respectively.

3- Results

In the first we optimized H₂ molecule and K⁺ cation with M062x/6-311G(d,p) level of density functional theory. We carried out full structural optimization of the B₁₆N₁₆ and B₂₄N₂₄ K⁺@B₁₆N₁₆ and K⁺@B₂₄N₂₄ nanoclusters with and without H₂ gas molecule and to examine the energetic, structural, and electronic properties. Optimized structures of stable H₂ molecule & K⁺, B₁₆ N₁₆, B₂₄ N₂₄, A1, A2, B1, B2 shown in Figs.1 and 3.

The highest occupied molecular orbital (HOMO) and the lowest unoccupied molecular orbital (LUMO) is also desired structures shown in Figs. 2 and 4.

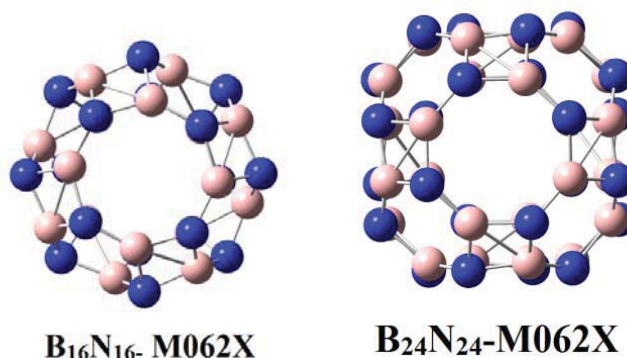


Fig.1 Optimized structure of stable B₁₆ N₁₆ and B₂₄ N₂₄ nanocluster.

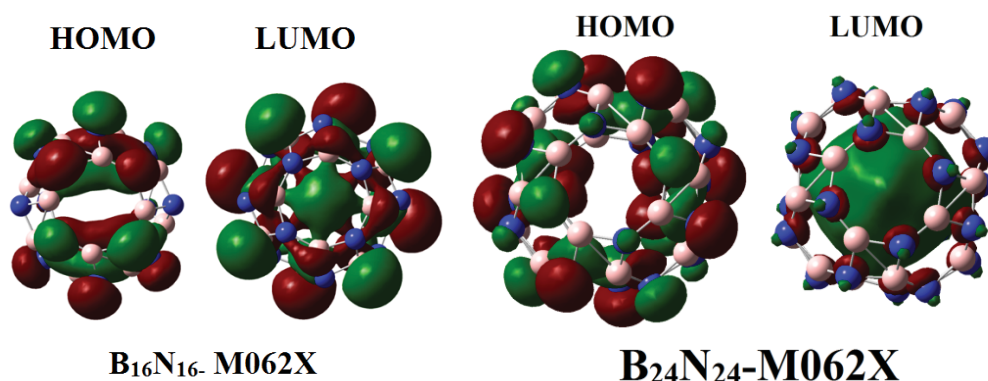


Fig.2 HOMO and LUMO MOs from left to right respectively for B₁₆N₁₆ nanocluster

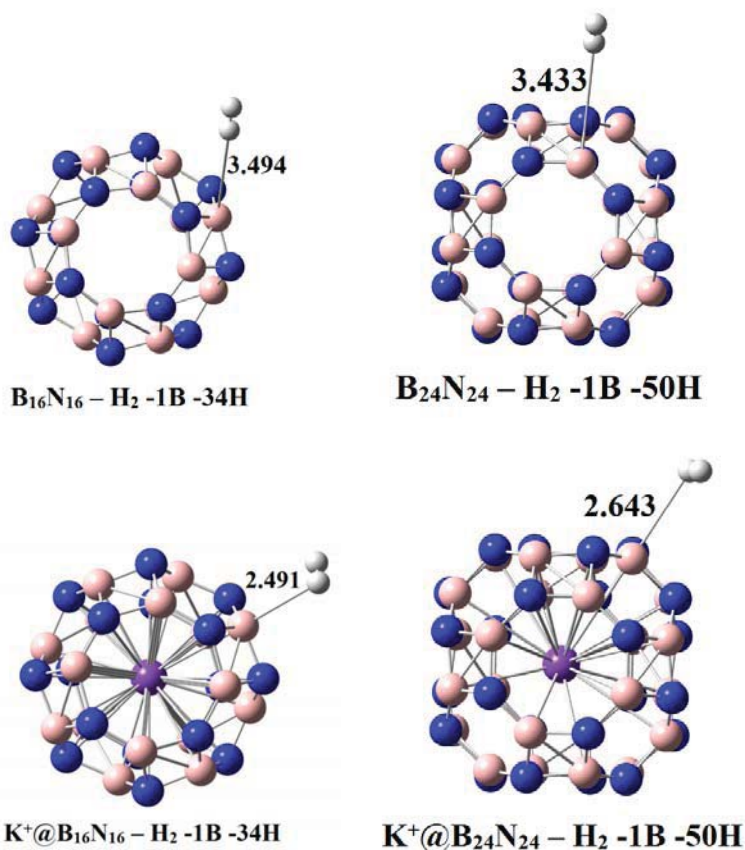


Fig. 3 The optimized structures of stable complex. Distances are in Å°

Table.1 The HOMO–LUMO gap(eV) upon the adsorption process, The adsorption energy (E_{ads}), Dipole Moment (Debye), charge transfer (electron).

Configuration	Adsorption mode	E_{ads} (eV)	HOMO	LUMO	Gap(eV)	Dipole Moment	Q_{H_2}
$\text{B}_{16}\text{N}_{16}$	$\text{B}_{16}\text{N}_{16}$	-	-0.3486	-0.0137	9.114	0.0084	-
$\text{B}_{24}\text{N}_{24}$	$\text{B}_{24}\text{N}_{24}$	-	-0.3371	-0.0153	8.757	0.0046	-
A ₁	$\text{B}_{16}\text{N}_{16}\text{-H}_2$	-0.0269	-0.3488	-0.0141	9.107	0.0805	-0.005
A ₂	$\text{B}_{24}\text{N}_{24}\text{-H}_2$	-0.0238	-0.3374	-0.0153	8.766	0.1451	-0.01
B ₁	$\text{B}_{16}\text{N}_{16}\text{-K-H}_2$	-0.077	-0.479	-0.154	8.841	1.6033	0.059
B ₂	$\text{B}_{24}\text{N}_{24}\text{-K-H}_2$	-0.052	-0.454	-0.142	8.494	1.4543	0.033

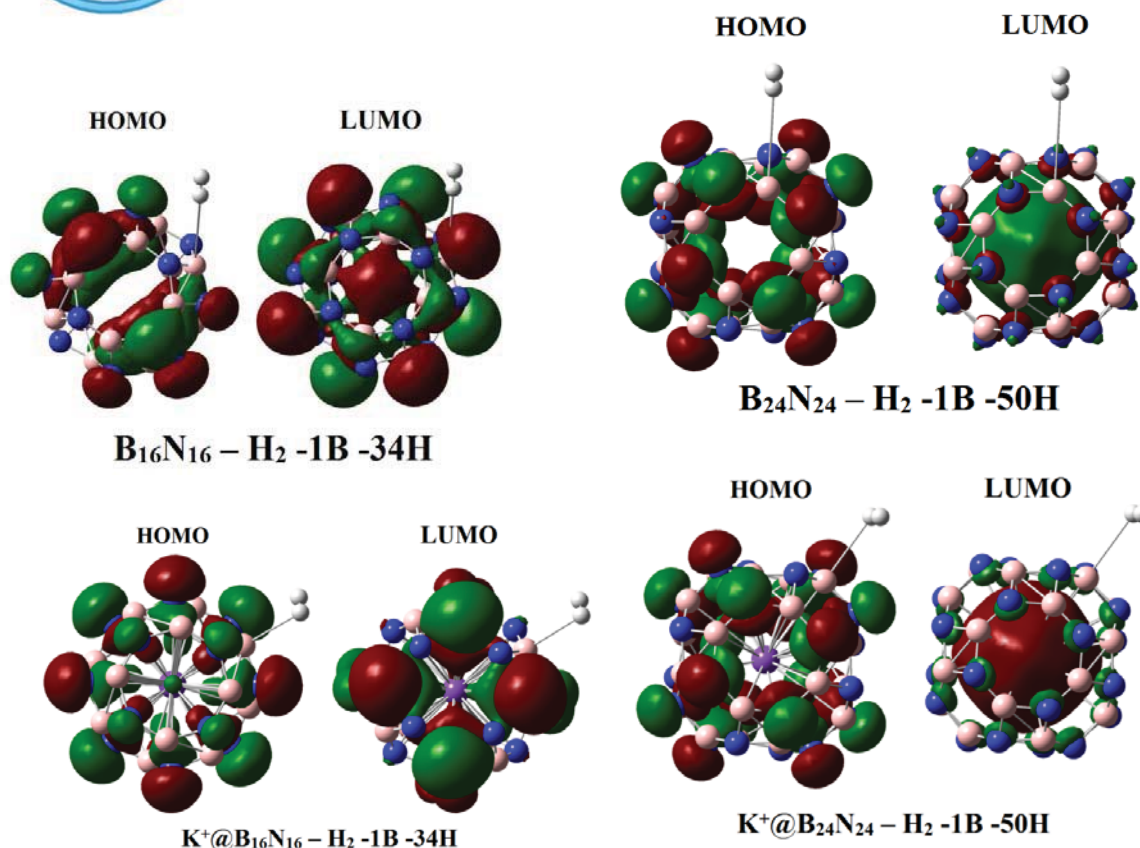


Fig.4 HOMO and LUMO MOs from left to right respectively for adsorption of H₂ Molecule on BN nanocluster.

4. Conclusions

With respect to data, it can be inferred that B₁₆N₁₆ and B₂₄N₂₄ nano-cages function as a gas sensor device against H₂ molecule. In respect to Gap(eV) A₁, A₂, B₁, B₂ all of them are insulator. According to the tables 1, charge transfer in the A₁, A₂ has been happened from B₁₆N₁₆ and B₂₄N₂₄ to the H₂ molecule and in B₁, B₂ configurations has been happened opposite i.e from H₂ to K⁺@ B₁₆ N₁₆, K⁺@B₂₄N₂₄ respectively.

According to the Tables 1 can be seen by placing K⁺ within B₁₆N₁₆ and B₂₄N₂₄ nano fullerenes like structures, the adsorption energy is much than to the case 1 where the K⁺ cation is not. Diag.1, shows comparison of A₁, A₂, B₁, B₂ absorbed energies. If we compare absorbed energies in Diags.1, it can be seen that configuration B₁ has the highest absorbed energy among them. Perhaps cation as K⁺ adding into nanofulleren like increases adsorption energy in hydrogen storage process. In this study the adsorption energy increases about 100 percent compare BN nanofulleren like pristine.

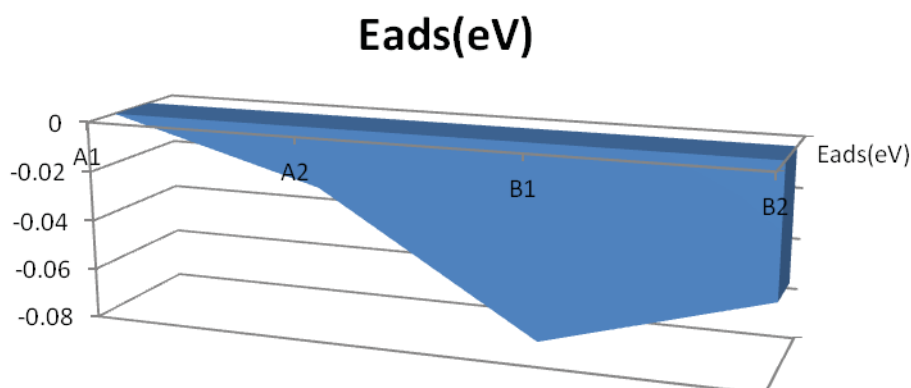


Diagram 1. Comparison of A_1 , A_2 , B_1 , B_2 absorbed energies.

References

- [1] R.D. Cortight, R.R. Davada, J.A. Dumesic, Nature 418 (2002) 964.
- [2] J. Alper, Science 299 (2003) 1686.
- [3] L. Schlapbach, A. Züttel, Nature 414 (2001) 353.
- [4] B. Sakintuna, F.L. Darkrim, M. Hirscher, Int. J. Hydrogen Energy 32 (2007) 1121.
- [5] A.W.C. van den Berg, C.O. Areal, Chem. Commun. (2008) 668.
- [6] (a) N.L. Roshi, J. Eckert, M. Eddaoudi, D.T. Vodak, J. Kim, M. O’Keeffe, O.M. Yaghi, Science 300 (2003) 1127; (b) J.L.C. Rowsell, A.R. Millward, K.S. Park, O.M. Yaghi, J. Am. Chem. Soc. 126 (2004) 5666; (c) X. Lin, J. Jia, P. Hubberstey, M. Schröder, N.R. Champness, CrystEngComm 9 (2007) 438.
- [7] (a) W. Struzhkin, B. Militzer, W.L. Mao, H.K. Mao, R.J. Hemley, Chem. Rev. 107 (2007) 4133; (b) M.H.F. Sluiter, H. Adachi, R.V. Belosludov, V.R. Belosludov, Y. Kawazoe, Mater. Trans. 45 (2004) 1452.
- [8] R. Ströbel, J. Garche, P.T. Moseley, L. Jörissen, G. Wolf, J. Power Sources 159(2006) 781.
- [9] P.O. Krasnov, F. Ding, A.K. Singh, B.I. Yakobson, J. Phys. Chem. C 111 (2007) 17977.
- [10] Q. Sun, P. Jena, Q. Wang, M. Marquez, J. Am. Chem. Soc. 128 (2006) 9741.
- [11] (a) N.S. Venkataramanan, R. Sahara, H. Mizuseki, Y. Kawazoe, J. Phys. Chem. C



- 112 (2008) 19676; (b) H. Woolf, I. Brown, M. Bowden, *Curr. Appl. Phys.* 8 (2008) 459.
- [12] E. Fakioglu, Y. Yurum, T.N. Veziroglu, *Int. J. Hydrogen Energy* 29 (2004) 1371.
- [13] T. Umegaki, J.M. Yan, X.B. Zhang, H. Shioyama, N. Kuriyama, Q. Xu, *Int. J. Hydrogen Energy* 34 (2009) 2303.
- [14] R.T. Paine, C.K. Narula, *Chem. Rev.* 90 (1990) 73.
- [15] T. Oku, T. Hirano, M. Kuno, T. Kusunose, K. Niihare, K. Suganuma, *Mater. Sci. Eng. B* 74 (2000) 206.
- [16] T. Oku, M. Kuno, H. Kitahara, I. Nartia, *Int. J. Inorg. Mater.* 3 (2001) 597.
- [17] G. Mpourmpakis, G.E. Froudakis, *Catal. Today* 120 (2007) 341.
- [18] R.Z. Ma, Y. Bando, H.W. Zhu, T. Sato, C.I. Xu, D.H. Wu, *J. Am. Chem. Soc.* 124 (2002) 7672.
- [19] C.C. Tang, Y. Bando, X.X. Ding, S.R. Qi, D. Golberg, *J. Am. Chem. Soc.* 124 (2002) 14550.
- [20] T. Oku, M. Kuno, I. Narita, Hydrogen storage in boron nitride nanomaterials studied by TG/DTA and cluster calculation, *Journal of phys. & Chem. of solides* 65(2004)549-552.
- [21] J. Beheshtian, M. Kamfiroozi, Z. Bagheri, A.Ahmadi, *Computational Materials Science* 54 (2012), 115-118.
- [22] J. Beheshtian, A.Ahmadi, Z. Bagheri, M. Kamfiroozi, *Struct Chem* (2012), 1-6.



Proton exchange membrane fuel cell modeling based on harmony search algorithm

S. Ahadpour*, S. Ranjbaryan¹,
M. Shabaninezhad²

*Department of Physics, University of Mohaghegh Ardabili, Ardabil, Iran
e-mail: ahadpour@uma.ac.ir*

Abstract

Concerns due to depletion of fossil fuel energies from one side and their major share in environmental pollutions on the other hand has changed the efficiency and energy consumption toward using high efficient electricity production equipments such as fuel cells. Since the primary costs of these equipments is decreasing every year, their entrance to international market is predictable. In this way, many attempts have conducted toward the optimization of fuel cells including Proton Exchange Membrane Fuel Cells (PEMFC). Among the many methods we can refer to new heuristics optimization methods. In this study the proposed algorithm is harmony search algorithm that is one of the new heuristics methods. In comparison to other algorithms that are applied for the optimization process of PEMFC's, this algorithm has presented the best results in less time, but we are searching for more appropriate algorithms with better and more acceptable results.

Keywords: Fuel cell, Optimization, Harmony search algorithm.

Introduction

Fuel cells are electrochemical devices that convert chemical energy to electricity without the combination process, which is one of the inspiring energy technologies for sustainable future with high energy efficiency and compatible with natural environment, when the world is facing the global warming. Among different types of fuel cells, proton exchange membrane fuel cells (PEMFC) have many excellent characteristics such as pretty low, output temperature, fast reaction, longer durability, high power density, high modularity, and zero emission. In addition to these aspects, PEMFC's are considered as more promising candidature devices in order to produce future force, especially in automobile industry, production of distributed energy, and portable electronic applications [1].

As a result, optimization in engineering design of fuel cells has always been very important and useful in solving the real-world design issues. Basically, the optimization process discusses about finding a collection of quantities for a vector of design variables, in such a way that it results in an optimized quantity of cost or objective function [2]. So, at the present time there are diverse models for deeper understanding of PEMFC efficiency, its evaluation characteristics and the optimization of fuel cell system that aren't definite. The algorithms that are available for optimizing the model parameters are included:

- The simulated annealing algorithm (SAA)
- The seeker optimization algorithm (SOA)
- The adaptive focusing particle swarm optimization (AFPSO) algorithm

These algorithms have acquired desirable effects but still have some faults. For example, it is possible that the result of optimization process being trapped in relative extremum [3].

¹ Email: saeideh.ranjbar@yahoo.com

² Email: shabani.ms@gmail.com

So, we are searching for more appropriate algorithms in order to modeling the optimized PEMFC. Therefore, we introduce the harmony search algorithm (HSA). It can be referred to Reference 18 for more analysis.

The paper is organized as follows. The section 2, includes the explanation of fuel capacitor. The section 3, considers the fundamentals of the harmony search algorithm, In section 4, we use the HAS for optimizing the parameters of PEMFC model. Finally, section 5, presents the conclusion.

۲ The principle of the PEMFC

In a fuel cell, two semi-reactions occur simultaneously, The Oxidation reaction (electron repulsion) in Anode and Reduction reaction (electron adsorption) in Cathode. These two reactions form the oxidation-reduction reaction (redox) in a fuel cell. During this process hydrogen and oxygen gases and water are produced. Anode and Cathode are separated by an electrolyte that allows ions to be transferred from one side to the other side. The electrolyte of a PEM fuel cell is a solid acid within the membrane [4]. The stages of the process and its fundamental reactions are illustrated in figure 1.

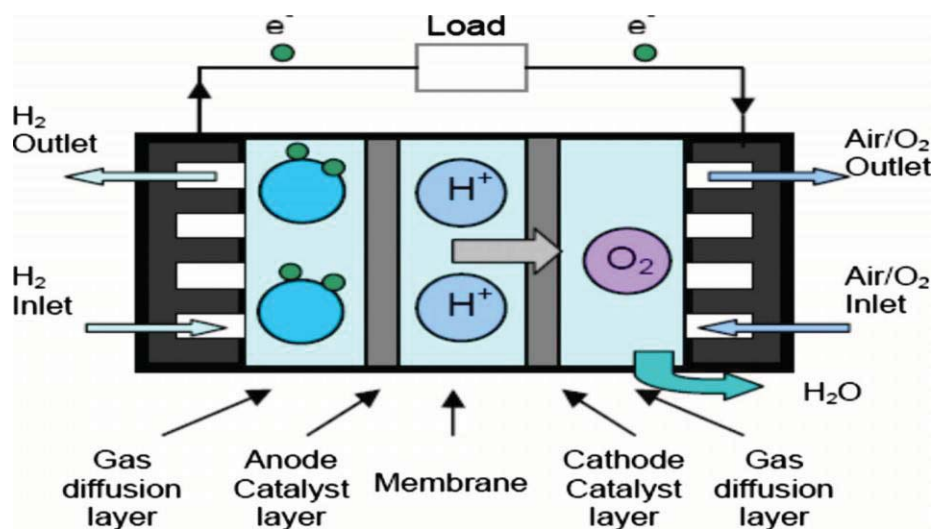


Figure 1: The work process and reaction principle of the PEMFC.

The basic term for the voltage of a fuel cell is as the following [5,6]:

$$U_{cell} = E_{Nernst} - \eta_{act} - \eta_{ohmic} - \eta_{con} \quad (1)$$

Where, E_{Nernst} is the thermodynamic potential, η_{act} are activation losses, η_{ohmic} are ohmic losses, and η_{con} are concentration losses.

For n cells connected in series and forming a stack, the voltage U_s , can be calculated by [7]:

$$U_s = n U_{cell} \quad (2)$$

$$E_{nernst} = 1.229 - (8.5 \times 10^{-4})(T - 298.15) + (4.308 \times 10^{-5})T \quad (3)$$

Where T , is cell temperature, P_{H_2} effective partial pressure of hydrogen, P_{O_2} and shows effective partial pressure of oxygen.

The activation loss of PEMFC is conducted by sluggish kinetics of performed reactions on the active surface of electrodes that can be illustrated as the following relation:

$$\eta_{act} = \xi_1 + \xi_2 T + \xi_3 T [\ln(C_{O_2})] + \xi_4 T [\ln(JA)] \quad (4)$$

Where J is the actual current density of the PEMFC, A is the activation area of the membrane, $\xi_1, \xi_2, \xi_3, \xi_4$ are the model coefficients based on electrochemistry, thermodynamics, and fluid mechanics, and C_{O_2} is dissolved oxygen concentration in the interface of the cathode catalyst. According to Henry's law we would have:

$$C_{O_2} = \frac{P_{O_2}}{5.08 \times 10^6 \exp\left(\frac{-4998}{T}\right)} \quad (5)$$

For the PEMFC which operated on air, the relationship among P_{O_2} , P_{H_2} , and P_{H_2O} can be expressed as [8,9]:

$$\log(P_{H_2O}) = 2.95 \times 10^{-2}(T - 273.15) - 9.18 \times 10^{-3}(T - 273.15)^2 + 1.44 \times 10^{-7}(T - 273.15)^3 - 2.18 \quad (6)$$

$$P_{N_2} = \frac{0.79}{0.21} P_{O_2} \quad (7)$$

$$P_{O_2} = P_c - P_{H_2O} - P_{N_2} \exp\left(\frac{0.291J}{T^{0.892}}\right) \quad (8)$$

$$P_{H_2} = 0.5 P_{H_2O} \left[\left(\exp\left(\frac{1.625J}{T^{1.934}}\right) \times \left(\frac{P_{H_2O}}{P_a}\right) \right)^{-1} - 1 \right] \quad (9)$$

Where P_{H_2O} is the saturation pressure of water vapour (atm), P_{N_2} is the N_2 partial pressure at the cathode gas flow channel (atm), and P_a and P_c are the anode and cathode inlet pressures (atm).

In this distinctive model of empirical relation, the ohmic losses are voltage losses that are created by R_M and R_C . The voltage loss due to R_C is because of connection resistance between membrane and electrodes, bipolar plates and electrodes themselves. Ohmic losses are defined by the following relation:

$$\eta_{ohmic} = JA(R_M + R_c) \quad (10)$$

The equivalent membrane impedance is acquired from Ohm's law:

$$R_M = \frac{r_M \lambda l}{A} \quad (11)$$

Where l is membrane thickness, which is obtained by $128\mu\text{m}$ in this model. The special resistance of Nafion series proton exchanging membrane are defined by the following relation:

$$r_M = \frac{191.6 \left[1 + 0.02J + 0.062 \left(\frac{T}{303} \right)^2 J^{2.8} \right]}{[\lambda - 0.634 - 3J] \exp \left[4.18 \left(\frac{T - 303}{T} \right) \right]} \quad (12)$$

Where λ is the water content of the membrane, it is an adjustable parameter of the relative humidity of the gas in the anode.

In this model, the concentration losses are considered unlike other models. The concentration losses due to mass transfers become apparent at high density currents. This is the reason why these losses are describable in the area of stack operation (where the concentration losses are high (low efficiency)).

If stack works in the high current density, contents this phrase. Concentration loss is described the following relation[9] :

$$\eta_{con} = -b \ln \left(1 - \frac{J}{J_{max}} \right) \quad (13)$$

where b is a parametric coefficient (V) that depends on the cell and its operation state. J_{max} is the maximum value of J .

3 the principle of the harmony search algorithm (HSA)

The HSA have been composed of five basic steps as described below (its diagram has been shown in Fig. 2:

Step 1. Initializing harmony search parameters

The HSA parameters are included:

Harmony memory matrix (HMM), harmony memory size (HMS), harmony memory considering rate (HMCR), pitch adjusting rate (PAR), number of iteration (NI), which has been used as a stopping factor in this algorithm, and distance bandwidth (BW).

Step 2. Initializing harmony memory matrix (HMM):

In HSA, each row of HMM contains the values of design variables which are randomly selected feasible solutions from the design pool for that particular design variable. HMS is the number of harmony vectors simultaneously stored in HMM.

Step 3. Improvising new harmony memory matrix:

HSA can obtain new solution and the parameters of HMCR and PAR are introduced to allow the solution to escape from local minimum and to improve the global optimum prediction of

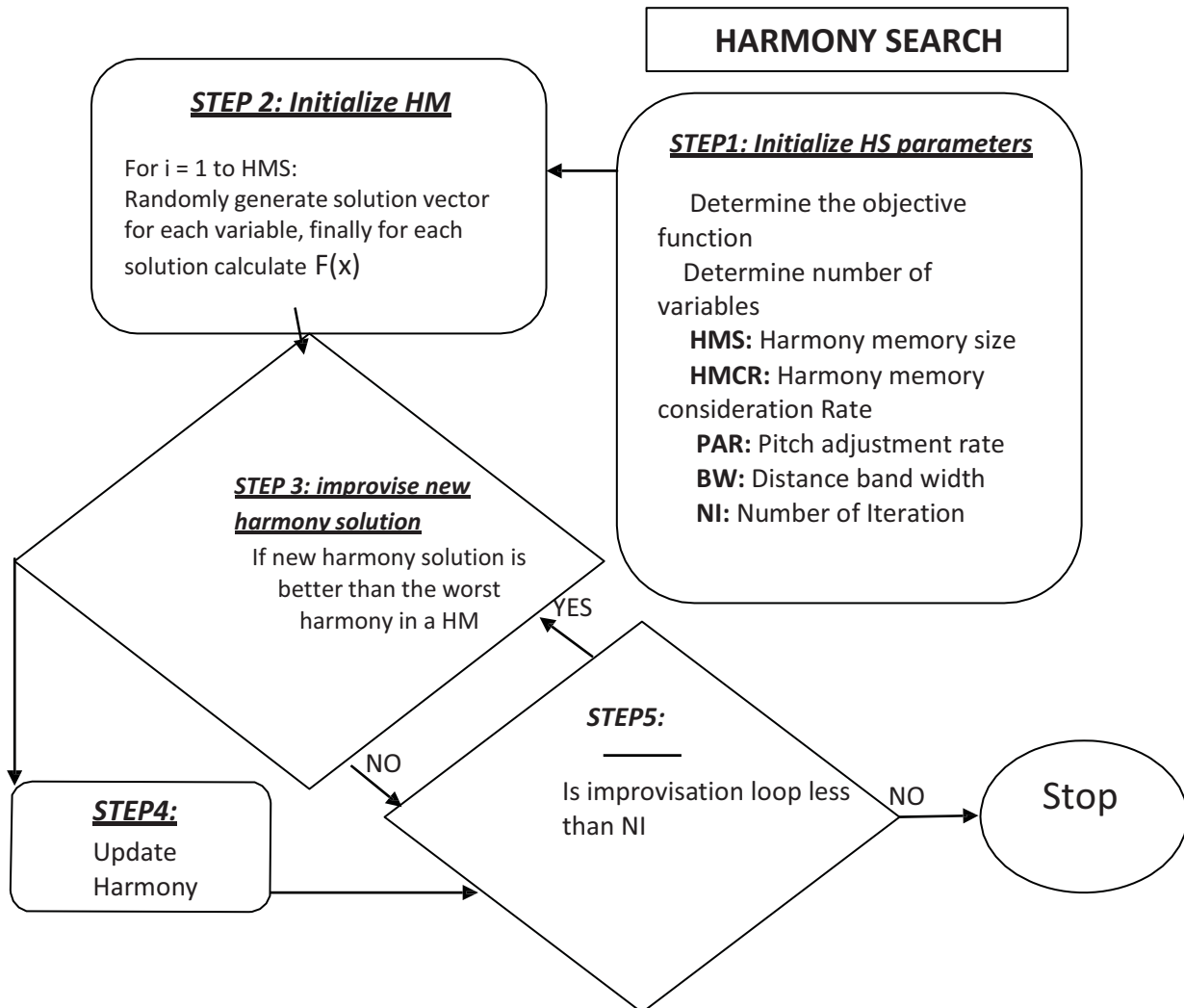


Figure 2: Flowchart of the harmony search algorithm

the algorithm. In this algorithm, HMCR which can be select between 0 and 1 is the probability of choosing one value from the historic values stored in the HMM, and (1-HMCR) is the probability of randomly choosing one feasible value not limited to those stored in the HMM. After a value is chosen from the HMM, the Pitch adjusting process will be performed for each component of the new vector. In this procedure, a value moves to its neighboring value with probability of PAR, or just stays in its original value with probability (1-PAR).

Step 4. Updating the harmony memory. After improvising a new harmony and evaluating the new one if it is better than the worst one in the HMM in terms of the objective function value, the generated harmony vector replaces the worst harmony in the HMM (harmony memory). The HM is then sorted by the objective function value.

Step 5. The stopping criterion (generally the number of iterations) is checked. If it is satisfied, computation is terminated; Otherwise, Steps 3 and 4 are repeated.

3 Discussion

The optimization problem that has been investigated in this paper is mean square error (MSE) in fuel cells which is defined as below:

$$MSE = \frac{\sum_{i=1}^N (U_{ik} - U_{cell})^2}{N} \quad (14)$$

In Eq. (14), N is the number of experimental data, U_k is the voltage value of experiment, and U_{cell} is the output voltage of the PEMFC from Eq. (2). In this algorithm, MSE as an objective function depends $(\xi_1, \xi_2, \xi_3, \xi_4, \lambda, b, R_c)$. Therefore, these parameters in order to find minimum MSE will from solution vectors in HMM:

$$X_i = [\xi_1^i, \xi_2^i, \xi_3^i, \xi_4^i, \lambda^i, b^i, R_c^i] \quad (15)$$

Which X_i is representative of i th row in HMM. In the PEMFC mechanism model, each of optimization parameters has lower and upper bounds [8] and they randomly have been chosen in those ranges (see Table 1).

Table 1: Bounds of model parameters [8].

Model parameter	ξ_1	ξ_2	ξ_3	ξ_4	λ	b	R_c
Lower Bound	-1.2	8.00×10^{-4}	3.50×10^{-2}	-3.00×10^{-4}	10	0.01	8.00×10^{-2}
Upper bound	-0.8	6.00×10^{-3}	1.00×10^{-4}	-8.00×10^{-2}	24	0.06	9.90×10^{-4}

Based on the above equation (1)-(13), the PEM fuel cell stack model can be built up easily. The known parameters of the PEM fuel cell stack adopted in current work are shown in Table2.

parameters	Value	parameters	Value
n	24	$W(W)$	250
$A(cm^2)$	27	$P_a(bar)$	1.0 - 3.0
$l(\mu m)$	127	$P_o(bar)$	1.0 - 5.0
$J(A\ cm^{-2})$	0.86	$T(K)$	343.15 - 353.15

Table 2: Kown parameters of the PEMFC stack model [8]

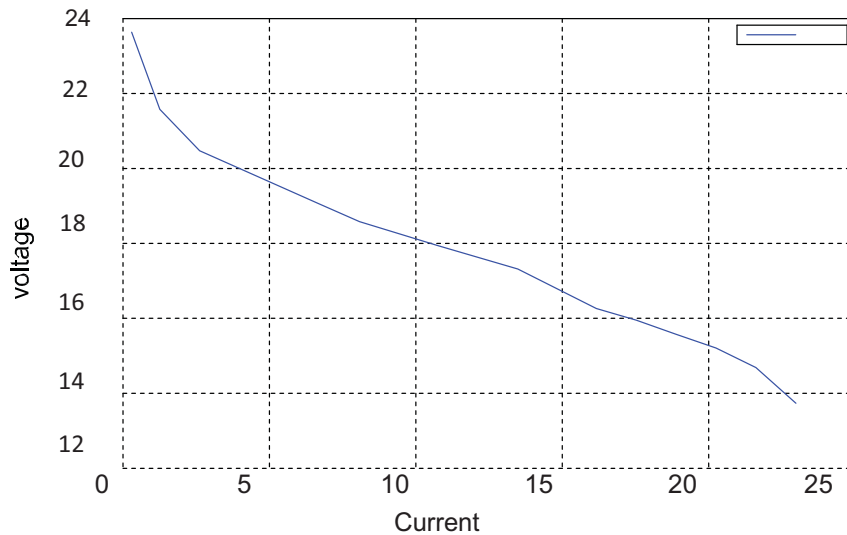


Figure 3: the current-voltage curve

In this approach, we calculated minimum MSE for different amount of HMCR and its result has been shown in Fig 4. According to this curve, after successful runs the algorithms achieve the best MSE of 0.0108 for HMCR=0.85, and worst MSE of 0.0581 for HMCR=0 within the maximum, iterations of 20000. The result which has obtained in $HMCR = 0$ is better than other algorithms outcomes [3,8]. As a result, HSA has more validity and advantage for optimizing the parameters of the PEMFC mechanism model. As Figure 5 shows, at the beginning of the searching process MSE is larger because of random startup, but diminishes quickly and then approaches the optimization solution during the increasing numbers. Furthermore, the result of optimum parameters for these

HMCR	0.55	0.65	0.75	0.8	0.85	0.90
MSE	0.0142	0.0132	0.0126	0.0110	0.0108	0.0114
$MSE/24^2$	2.463×10^{-5}	2.2917×10^{-5}	2.1875×10^{-5}	1.9097×10^{-5}	1.8750×10^{-5}	1.9792×10^{-5}
ξ_1	-1.11362	-1.0888	-0.8000	-0.9929	-0.9000	-1.625
ξ_2	0.0037	0.0030	0.0020	0.0035	0.0032	0.0037
ξ_3	8.5263×10^{-5}	4.3949×10^{-5}	3.5×10^{-5}	1.000×10^{-4}	1.000×10^{-4}	1.000×10^{-4}
ξ_4	-1.3406×10^{-4}	-1.332×10^{-4}	-1.445×10^{-4}	-1.364×10^{-4}	-1.394×10^{-4}	-1.463×10^{-4}
λ	11.3080	12.1863	13.5712	11.3826	11.4626	13.3841
b	0.0100	0.0100	0.0114	0.0100	0.0100	0.0160
R_c	8.0×10^{-5}	9.9000×10^{-4}	9.900×10^{-4}	1.5966×10^{-4}	8.000×10^{-5}	8.000×10^{-5}

HMCRs are arranged in Table 3.

Table 3: Results of optimized parameters for HMCR= 0.55, 0.65, 0.75, 0.80, 0.90

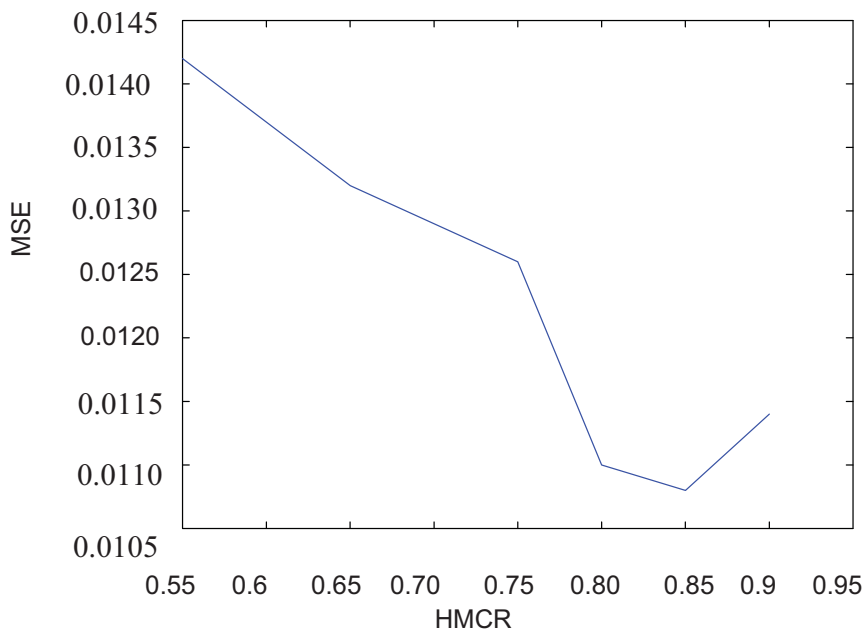


Figure4: Results of optimized MSE parameters for HMCR=0.55, 0.65, 0.75, 0.80, 0.90

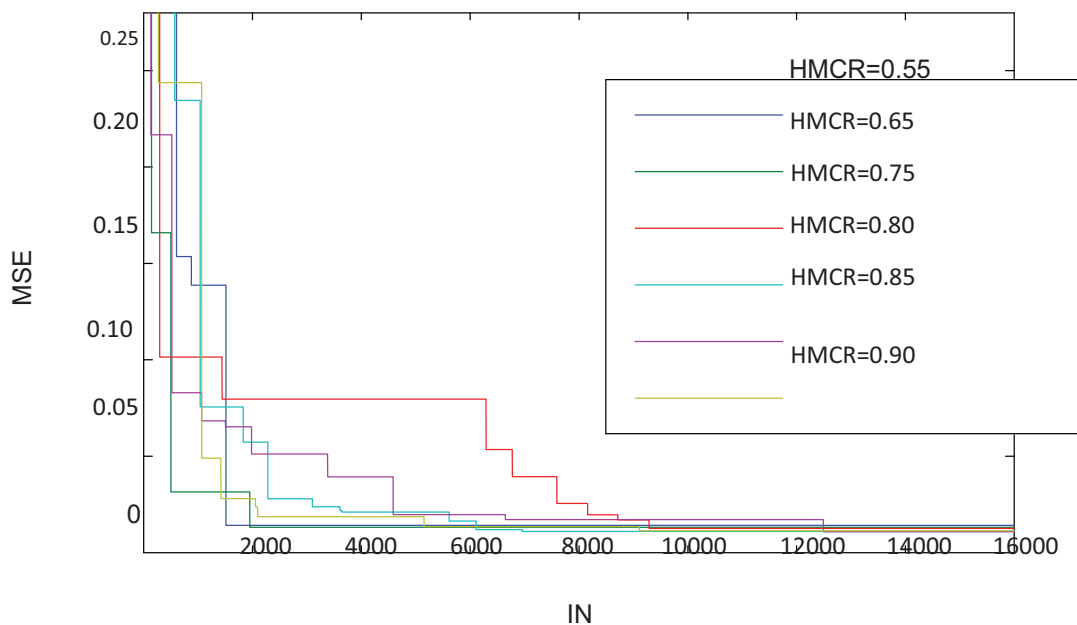


Figure 5: Trend of MSE with iteration number



4 Conclusion

Nowadays fuel cells are considered as one the most important sources of energy in the world, on which many works are being done to enhance their efficiency. Of those fuel cells are PEMFC's that have attracted a great deal of attention because of their low performance temperature. One of the optimization techniques is heuristic method in which lessons are learned from natural and artificial phenomena. HS algorithm is also a current method of this technique. In this article, using matlab software, the proposed algorithm is run and mean deviation function for cell output is optimized and it is compared with other algorithms. It is seen that this algorithm provides the minimum mean deviation in the shortest time compared to others.

References

- [1] Dai Chaohua, Zhu Yunfang, Chen Weirong, Seeker optimization algorithm for global optimization: A case study on optimal modelling of proton exchange membrane fuel cell (PEMFC), *International Journal of Electrical Power and Energy Systems*, 33 (2011), pp. 369-376.
- [2] Abolfazl Khalkhali, Mohamadhosein Sadafi, Javad Rezapour, Hamed Safikhani, Pareto based multi-objective optimization of solar thermal energy storage using genetic algorithms, *Transactions of the Canadian Society for Mechanical Engineering*, 34 (2010), pp. 463-474.
- [3] Li Qi, Chen Weirong, Jia Junbo, Cham Yew Thean, and Han Ming, Proton exchange membrane fuel cell modeling based on adaptive focusing particle swarm optimization, *J. Renewable Sustainable Energy* 1, 013105 (2009), pp. 1-10.
- [4] Brian Cook, *An introduction to fuel cells and hydrogen technology*, Heliocentris, (2001), pp. 17-22.
- [5] Amphlett JC, Baumertr M, Mannr F, Performance modeling of the Ballard mark IV solid polymer electrolyte fuel cell: Empirical model development, *J. Electrochem Soc*, 142 (1995), pp. 1-8.
- [6] Lee S, Kim J, Srinivasan S, Modelling of proton exchange membrane fuel cell performance with an empirical equation, *J. Electrochem Soc* 142 (1995), pp. 2670- 2674 .
- [7] Correˆa JM, Farret FA, Popov VA, Simoes MG. Sensitivity analysis of the modeling parameters used in simulation of proton exchange membrane fuel cells. *IEEE T Energ Conver*, 20 (2005), pp.
- [8] Shipin Yang, Ning Wang, A novel P systems based optimization algorithm for parameter estimation of proton exchange membrane fuel cell model, *International Journal of hydrogen energy*, 37 (2012), pp. 8465-8476.
- [9] Chaohua Dai, Weirong Chen, Yonghua Song, Zhu Yunfang, Seeker optimization algorithm: a novel stochastic search algorithm for global numerical optimization, *J. Syst Eng Electron*, 21 (2010), pp. 300-311.
- [10] Z.W. Geem, J.H. Kim, G.V. Loganathan, A new heuristic optimization algorithm: harmony search, *Simulation*, 76 (2001), pp. 60-68.
- [11] Kim J. H, Geem Z. W, Kim E. S, Parameter Estimation of the Nonlinear Muskingum Model using Harmony Search, *Journal of the American Water Resources Association*, 37 (2001), pp. 1131-1138.
- [12] Geem Z. W, Kim J. H, Loganathan G. V, Harmony Search Optimization: Application to Pipe Network Design, *International Journal of Modelling and Simulation*, 22 (2002), pp. 125-133.



6th Iranian Fuel Cell Seminar
March 12 & 13 , 2013
Shahid Rajaei Teacher training University
Tehran - Iran



[13] Kang S. L, Geem Z. W, A New Structural Optimization Method Based on the Harmony Search Algorithm, Computers and Structures, 82 (2004), pp. 781-798.



Study design and construction techniques and types of bipolar plates used in fuel cell stack

Ali Asfia¹ , Alghar abdollahi¹

Shahid Rajaei Teacher Training University, Lavizan, Tehran, Iran

Abstract

Stack fuel cell today, in various industries such as power plants, industry, military, automotive and ... Has been used. Bipolar plates are one of the main components of the fuel cell stack that is. Work with bipolar plates of the fuel cell stack , cost, weight and volume is reduced and the efficiency of stack increases. Therefore, different methods have been developed for the design and manufacture of bipolar plates. In this article we will cover some common bipolar plate design and the advantages and disadvantages, and it'll. In this paper, the design and testing of the graphite bipolar plates of dimensions 90 * 75 * 5mm in Catia software model , and CNC 3-axis machine is built we will explain it.

Key Words

Bipolar plates , Fuel Cell Stack , Proton exchange membrane (PEM)

Introduction

Bipolar plates of the basic components of all types of fuel cell proton exchange membrane (PEM) is one of several key functions in the fuel cell is responsible. Bipolar plates hydrogen and oxygen should be evenly distributed on the cell surface can affect the flow of electricity and heat from one unit to another unit to Conductivity. Because the sample cell to produce electricity from hydrogen and oxygen is used, these pages should be able to prevent gas leakage to the outside environment, while the mixing of two gases, hydrogen and oxygen (air) to prevent. Bipolar plates contributes effectively reduced size, weight and cost of a cell will be set. Therefore a suitable material for bipolar plates in fuel cell output and the final price will be effective.

The main functions of bipolar plates:

- 1 - The distribution of hydrogen and oxygen into the cell
- 2 - Facilitate water management within the cell
- 3 - Conduct electric current in the external circuit cell
- 4 - Transfer of heat generated inside the cell to the environment and overall cell thermal management
- 5 - Creating pathways for mass transfer of oxygen and hydrogen inside the cell
- 6 - Connection single cell in order to achieve higher voltages
- 7 - A runner for fluid cooling

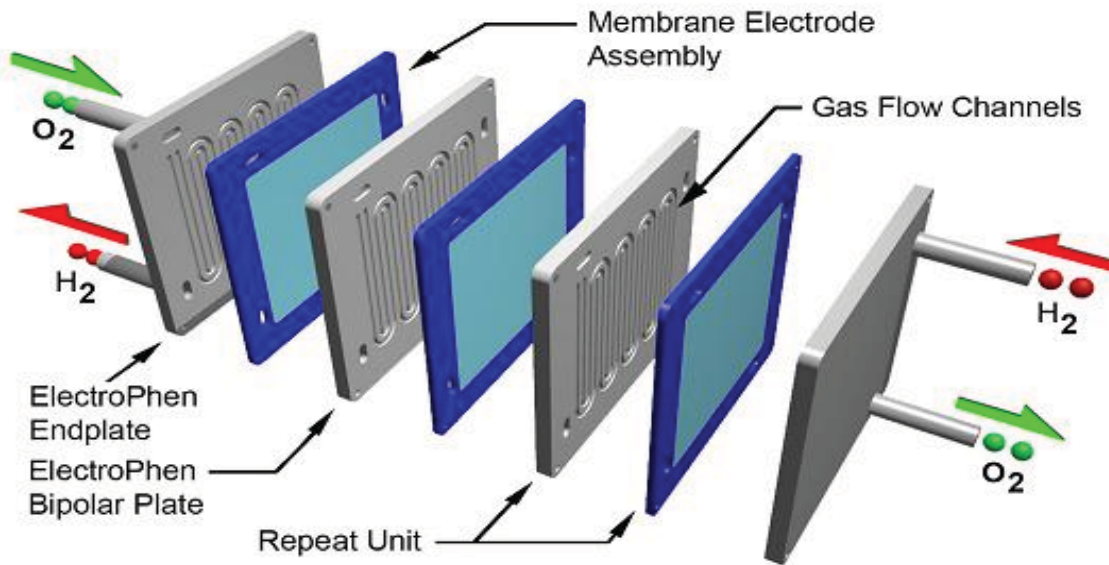


Figure 1 - The structure and method of making fuel cell bipolar plates in

Introducing the bipolar plates and the description of its function

To produce electricity in a fuel cell has three main requirements which include; Gas transfer plates, proton exchange membrane (PEM) and anchoring plates (End plate). Each of the components are introduced into the production process of electric current to the task. Hydrogen fuel cell, hydrogen and oxygen gas transfer in graphite is usually used. Use of Graphite, being lighter, better heat transfer, electrical transmission and the car is working well. The disadvantages of graphite gases can penetrate the layers of graphite and graphite leakage and corrosion after long pointed. Many research laboratories and fuel cell manufacturers to make use of graphite bipolar plates.

For hydrogen gas in the unit cell (Single Cells) on one side of the Graffiti screen machines and gas stations to make. And to transport oxygen-screen machines and other graffiti gas channels have been created. With the proton exchange membrane (PEM) fuel cell unit is created between the pages of a graphic that you can put an electrical load on the electric current between two graphite (Fig. 2).

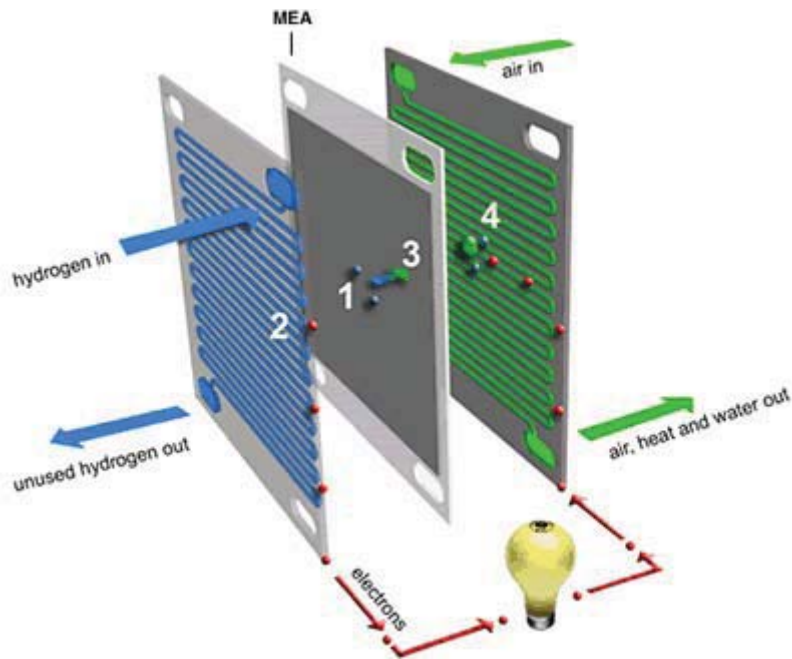
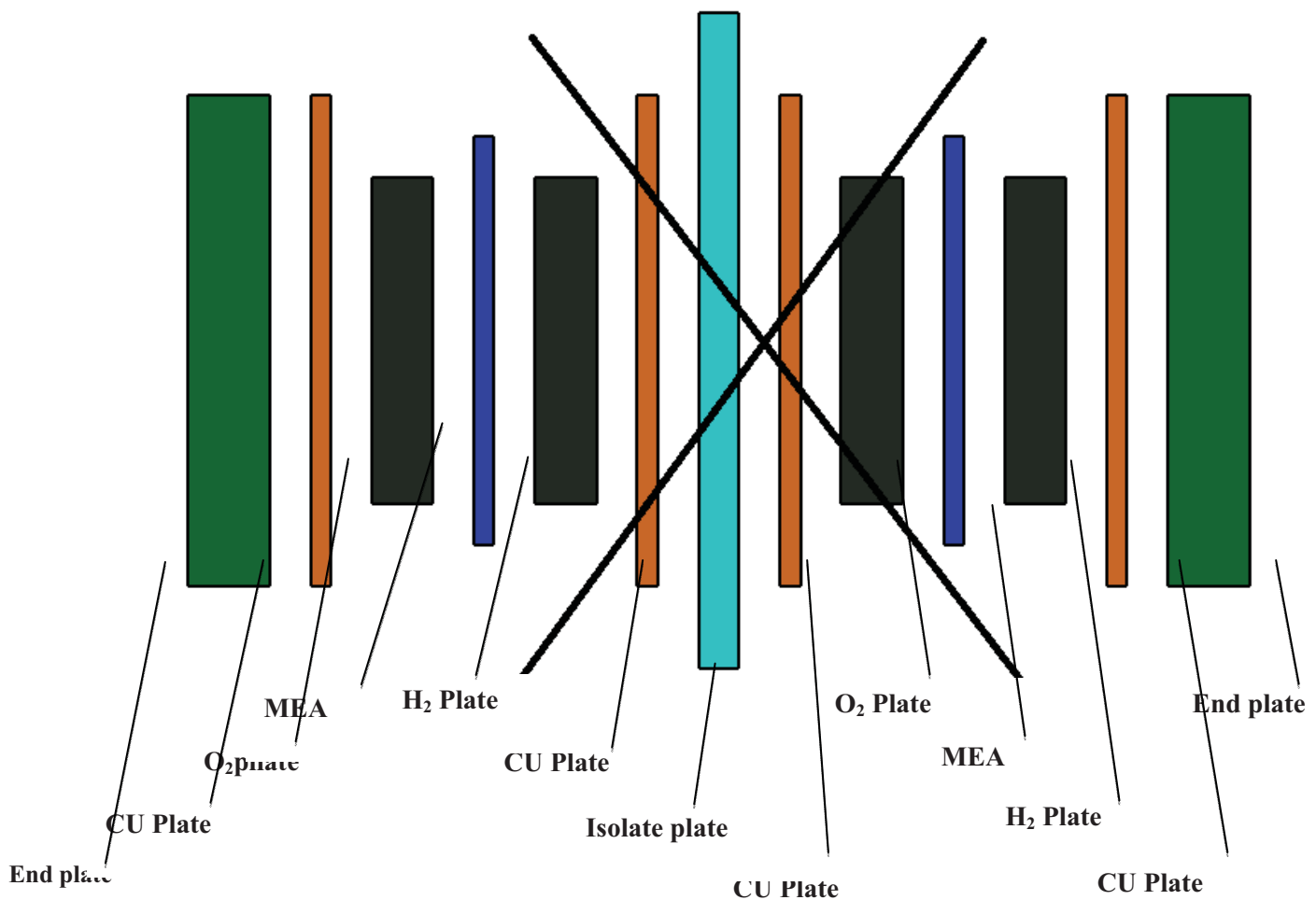


Figure 2 - The usage of hydrogen fuel cell

If you build a fuel cell stack to put together the use of fuel cells, Size, weight and cost will increase greatly. To resolve this issue Bipolar plates are used in this collection. As can be seen in Figure 3. If you use the bipolar plates 4 members (2 Sheets, Graphite oxygen barrier and screen) will be removed per unit. The reduction in weight, volume and cost effective to stack.



Fi

Figure 3 - Dismantling a hydrogen fuel cell stack

Bipolar plate, graphite is a the two sides are working car. On one side of the bipolar plate hydrogen gas and oxygen gas flows on the other side Each si The gas and electricity transmission to consumer leads.de of a bipolar, is a fuel cell unit.

The main methods of manufacturing bipolar plates

Common methods of manufacturing bipolar plates; build pages using graphite machining, forming and casting is. Bipolar plates made by machining .

Bipolar plates made by machining

In this approach using the CNC, the gas slots on both sides of the page are a Graphite. This method is commonly used to make bipolar plates with gas slots are easy to use.

As can be seen in Figure 4, , The first gas transmission slots on wood samples using CNC machines have created and then we have the ultimate example of graffiti on the screen.



Figure 4 - Typical wood machining by CNC machine

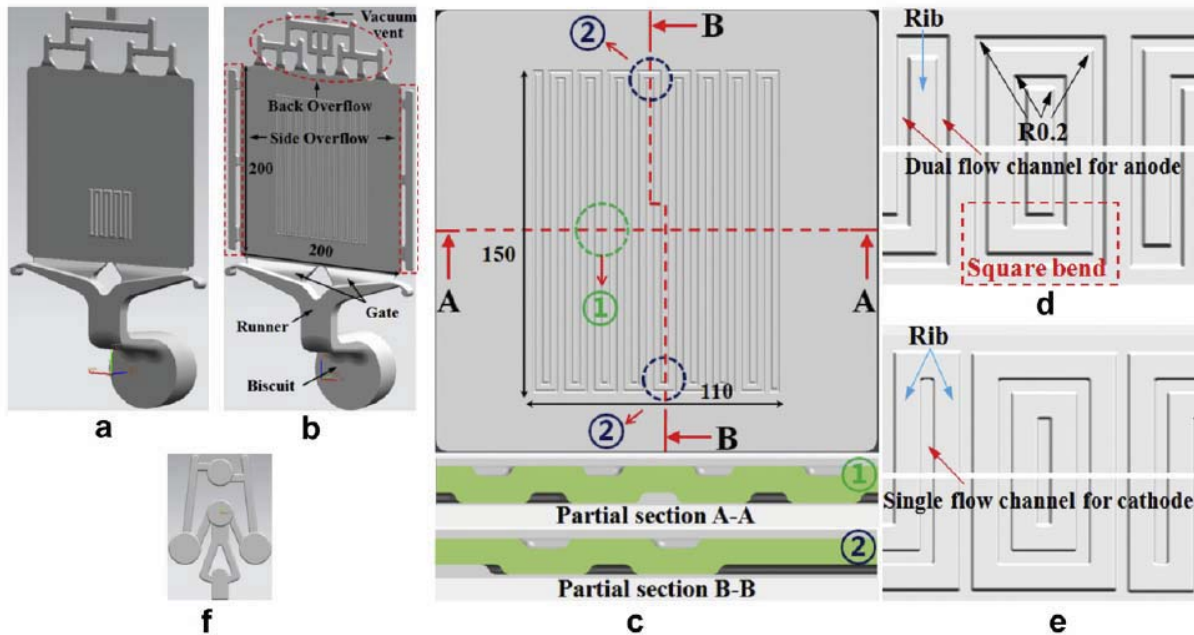
Bipolar plates made by casting



Among manufacturing methods for bipolar plates, vacuum die casting is an ideal process because arbitrarily complicated shapes and mass production is possible with a high production rate. We report on the fabrication of bipolar plates with micro-channel arrays on both sides by vacuum die casting for use in proton exchange membrane (PEM) fuel cells. The formability, mechanical properties, and microstructures of samples fabricated under various experimental conditions (molten metal temperature, injection velocity, and vacuum assistance) are investigated, and the experimental and simulation results are compared.

vacuum die casting is suitable for the high precision mass production of metallic bipolar plates, and is thus more advantageous than conventional die casting. Machining and cutting processes for metallic bipolar plates are not used for mass production because of the high costs involved, even though these processes can provide the required high precision. In addition, metal forming processes such as stamping and hydroforming, which can be used for mass production, have the forming limit problem. Other processes such as welding and sealing are also required to fabricate the micro-channel's net shape, formed on both sides. High pressure die casting (HPDC) is widely used because a near-net shape can be obtained for complex geometries, and a small wall thickness (3 mm) can be achieved. Furthermore, high production rates and low production costs can be achieved [24]. However, this process induces casting defects in the products such as gas porosity (20e30 cc/100 g) and oxide films because of air entrapment in the turbulent flow of the molten metal; this turbulent flow is in turn due to the high injection speed in the die cavity [25]. Because of this problem, heat treatment and welding are almost impossible. Vacuum die casting is a possible solution to the aforementioned problems. This method yields products with good surface conditions, good welding characteristics, and high mechanical strength, as well as very low gas porosity (2e5 cc/100 g), because air is evacuated from the die cavity. Furthermore, short cycle times are typical in this process; hence, a net-shaped component can normally be cast in less than 15 s [26]. Despite these advantages, very little research has been carried out on the use of vacuum die casting for fabricating thin plates because it is difficult to manufacture thin-walled parts (wall thickness <1 mm) using this process.

Illustration of bipolar plate die casting: (a) previous die design [23], (b) new modified die design, (c)
ca



...vity part (bipolar plate area), (d) top detail view of channel (dual channel for anode), (e) bottom detail view of channel (single channel cathode), (f) vacuum block (units in mm).

Conclusions

1. Bipolar plates eliminate 4 members (2 per page \times page insulated copper and graphite plane oxygen) in a typical fuel cell stack is placed.
2. The two side panels are graphite bipolar plates for ways CNC machining and casting have been produced by Forming.
3. A bipolar plate on one side of the page, hydrogen gas and oxygen in the gas flow is used as a fuel cell unit.

References

- [1] for use in a fuel cell bipolar plates made of polymer, using conductive polymer composites. M. Rezaei, Sina Nafisi, begotten SH, Faghieh Imani B, M. Gholami. 1,387.
- [2] Fabrication by vacuum die casting and simulation of aluminum bipolar plates with micro-channels on both sides for proton exchange membrane (PEM) fuel cells. Chul Kyu Jin a, Chung Gil Kang. 2012.
- [3] Designing and Building Fuel Cells. Colleen Spiegel. 2007.
- [4] Fabrication by vacuum die casting and simulation of aluminum bipolar plates with micro-channels on both sides for proton exchange membrane (PEM) fuel cells. Chul Kyu Jin a, Chung Gil Kang. 2012.



Numerical Simulation of a PEM fuel cell with partially blocked channel

Nasser Baharlou Houreh^{1*}, Ebrahim Afshari^{2*}

**Department of Mechanical Engineering, Faculty of Engineering, University of Isfahan, Isfahan, Iran*

1- E-mail address: Nasser.baharloo@yahoo.com

2- E-mail address: e.afshari@eng.ui.ac.ir (E. Afshari)

Abstract

The attempt is made to apply a structure for cathode gas channel of PEM fuel cell that is partial blocked by one or more baffle plates. In order to investigate the effects of the selected shape, size and the number of baffle plates on the oxygen transport in the gas diffusion layer a two - dimensional simulation is carried out in 27 cases. A dimensionless number called CHB is introduced to represent channel blocking, as a criterion for choosing the optimum cases that cause maximum oxygen concentration in the catalyst layer and minimum pressure drop along channel. By installing three large rectangular baffles in one attempt and then two large rectangular baffles in another , the least amount of CHB ranked the first and second, respectively. Installing three large semicircle baffles in the same channel is ranked the third, where CHB is slightly higher than its value in the best condition with a lower pressure drop in specific. So when there is restriction in securing pressure in fuel cell, installing the semicircle baffle is better than the rectangular one. By installing the triangle baffle, the CHB will increase significantly.

Keywords: Proton exchange membrane fuel cell; Baffle plate, Oxygen transport, Channel blocking number

1 Introduction

The bipolar collector/separator plates in a PEM fuel cell stack typically include separated flow channels to supply hydrogen and oxygen reactant gases to anode and cathode electrodes. The flow field geometry is one of the most important enhancing factors for gases transported from GDLs into catalyst layers. Most PEM fuel cells made to date use straight gas flow channel configurations, whereas serpentine flow channels and interdigitated flow field are commonly used in many fuel cell flow field designs. Several studies have attempted to improve PEM fuel cell performance through flow field design such as straight[1-3], serpentine[4&5] and many other novel combinations[6] of these conventional types in recent years. Some literatures investigated Three-dimensional simulation of PEM fuel cell [7-10]. Partially blocked channels with baffle plates being transversely inserted in the channels can increase the reactant gases flow rate to the catalyst layer and the removal of water vapor produced, therefore improving PEM fuel cell performance [11&12]. The local current density generation, can be enhanced by the presence of the baffle(s) [13]. From the literature, it is clear that very few studies have investigated the effect of baffle shape, size and number of baffles on gas transport into GDL and effective area of catalyst layer. Moreover, little attention has been given to the optimization of channel blocking in order to create the most oxygen diffusion in GDL and less pressure drop in the cell.

In order to enhance cell performance, this study proposes a new configuration of partially blocked oxygen channel and investigates the effect of various shapes of baffle plates

transversely inserted in the channel consisting of rectangular, triangle and semicircle, various sizes and numbers of plates on the oxygen transport to find the best configuration of partially blocked channel that have maximum oxygen transfer in the GDL and minimum pressure drop in the cell. A half-cell, two-dimensional, single-phase, non-isothermal and single-domain is modeled.

2 Mathematical modeling

The model domain consists of the following subregions: the gas channel, gas diffusion layer (GDL) and catalyst layer for the cathode side, with rectangular, triangle or semicircle baffle plate(s) along the transverse section of the flow channel as shown in Fig. 1. Air flow through channel is distributed into cathode and Oxygen reduction reactions occur only within the active catalyst layer.

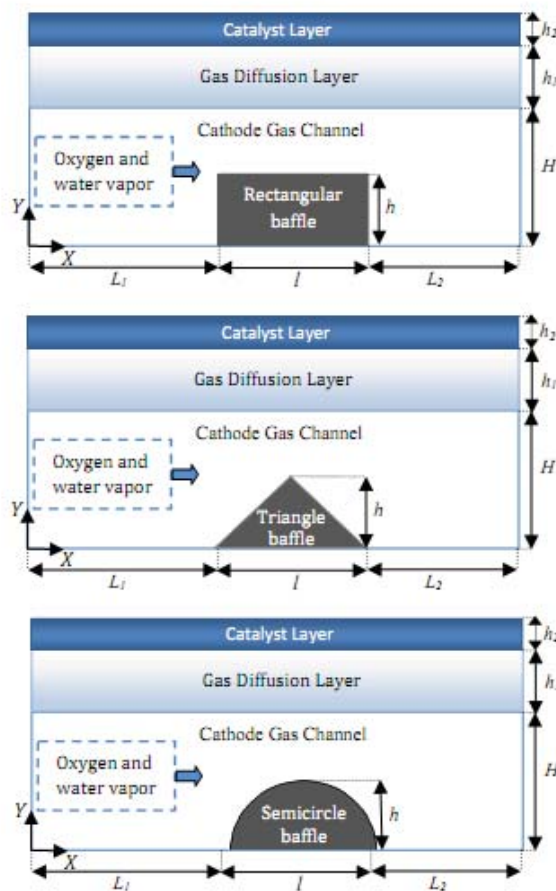


Figure 1. Two-dimensional geometry and computational modeling for PEM fuel cell cathode. Three cases for blocking with plate(s), equal length in amidst of channel

2.1. Assumptions

The following assumptions are made in implementing the single-phase model: (i) two-dimensional, (ii) steady-state flow, (iii) ideal gas mixtures, (iv) laminar and incompressible flow with low Reynolds numbers and pressure gradients, (v) no contact resistance at the interfaces between GDL and catalyst layers, (vi) constant viscosity of gas mixture is calculated for the inlet condition, (vii) isotropic and homogeneous electrode and catalyst layer are characterized by effective porosities and permeabilities and (viii) the operating temperature of fuel cell is 80° C.

2-2 Governing equations

In contrast to the usual approach which employs a separate differential for different sub-regions, here a unified single-domain approach with a single set of governing equations is applied to all sub-regions. In the developed single-domain method, one set of conservation equations is considered for different regions of PEM fuel cell cathode electrode [14]. Thus, under the above mentioned assumption, the model has a set of coupled non-linear partial differential equations. The relevant equations are presented in Table 1.

Table1. Governing equations for a two-dimensional model.

	Conservation equation	Source term	Number
Mass	$\nabla \cdot (\varepsilon \rho \vec{u}) = 0$	-	(1)
Momentum	$\frac{1}{\varepsilon^2} \nabla \cdot (\rho \vec{u} \vec{u}) = -\nabla p + \nabla \cdot (\mu \nabla \vec{u}) + S_u$	$S_u = -\frac{\mu}{K} \vec{u}$	(2)
Species	$\nabla \cdot (\vec{u} C^i) = \nabla \cdot (D^{i,eff} \nabla C^i) + S_k = 0$	$S_{k,O_2} = -\frac{I}{4F} M_{O_2}$ $S_{k,H_2O} = \frac{I}{2F} M_{H_2O}$	(3)

In these equations, \vec{u} , ρ , p and μ are mixture velocity, density, pressure and gas mixture viscosity, respectively. ε is volume fraction of GDL layer and catalyst layer. C^i is the total concentration of species i and $D^{i,eff}$ is the effective diffusivity of species i in gas mixture. Diffusivity in channel is a function of pressure and temperature [15]. The source term of momentum equation, Eq.3, is employed to consider Darcy's law under the limiting condition [16]. The proportionality factor K in Darcy's model is the permeability of the porous medium. The source terms in the species conservation equation, S_k , is equal to zero everywhere except in the catalyst layer, where the species are consumed or generated in the electrochemical reactions. I is the current density and F is Faraday constant. The distribution of current density is characterized by a descending trend along the channel length due to oxygen consumption with axial location X . In the present study, the current density distribution was obtained from measured experimental data presented by Perng et al [11]

2-3 Boundary conditions

Equations of conservations of mass, momentum, and species, form a complete set of governing equations for four unknowns: u , v , p and C^i . Solving these equations needs to specify the suitable boundary conditions. No-flux condition is applied to the equations for flow and transport at all boundaries except inlet and outlet channel. The inlet velocity in the gas channel is expressed by the respective stoichiometric flow ratio. In this model, inlet velocity is considered 1 meter per second. Fully developed flow with a given back pressure is assumed to take place at the outlet.

2-4 Numerical procedures

The geometry is given in Fig. 1 with the specifications listed in Table 2. The governing equations were discretized using a finite-volume method and solved using a computational fluid dynamic code. In this code, the pressure and velocity fields are treated with the SIMPLE pressure correction algorithm, where a single-domain model is used. Stringent numerical tests were carried out to ensure that the solution was independent of grid size. 200 grids along the channel and 50, 40 and 10 grids along the thickness of each channel width, GDL and catalyst layer, were used respectively. The coupled set of equations was solved iteratively, and the

solution was checked to be convergent when the relative error in each field between the two consecutive iterations was less than 10^{-6} .

Table 2. Physical and dimensional parameters and transport and material properties

Description	Unit	Value
Dimensional parameters		
Baffle height, h	mm	0.15, 0.25, 0.35
Flow channel height, H	mm	0.5
Gap size, H-h	mm	0.35, 0.25, 0.15
Gas diffusion layer thickness, h_1	mm	0.2
Catalyst thickness, h_2	μm	10
Flow channel length, L	mm	10
Baffle plate thickness, l	mm	2
Upstream channel length, L_1	mm	4
Downstream channel length, L_2	mm	4
Operating conditions		
Cell temperature, T	K	353.15
Cathode pressure, P	atm	1
Cathode stoichiometry		1.1
Cathode dry gas mole fraction		79
Transport parameters		
Faraday's constant, F	C/mol	96487
Cathode gas viscosity, μ	Pa.s	1.88×10^{-5}
O_2 diffusivity in the cathode gas channel, D	m^2/s	1.81×10^{-5}
H_2O diffusivity in the cathode gas channel, D	m^2/s	2.236×10^{-5}
Material properties		
GDL and catalyst layer porosity, ε		0.6
GDL and catalyst layer permeability, K	m^2	10^{-12}

3 Results and discussion

For validation purpose, the axial velocity distribution from this model at midway of the gap region ($X/L = 0.5$) is compared with analytical results, as shown in Fig. 2. For the small values of the porosity, the Darcy law gives a uniform flow solution in porous layer. So, the obtained results from this model show a very good agreement with the analytical results and deviation is less than 5%.

Also, the maximum pressure drop across the channel length obtained from the case without blocking plates is compared with analytical data for laminar flow in square channel that is as follows:

$$\Delta P = f \frac{l}{d} \frac{V^2}{2} \quad (4)$$

where f, L, d, v and are friction coefficient, channel length, hydraulic diameter and average velocity in channel where the Reynolds number is about 29. The deviation between maximum pressure drops obtained from Eq. (4) (about 14.1Pa) and the present numerical study (about 12Pa) is less than 14.5%, showing a good agreement.

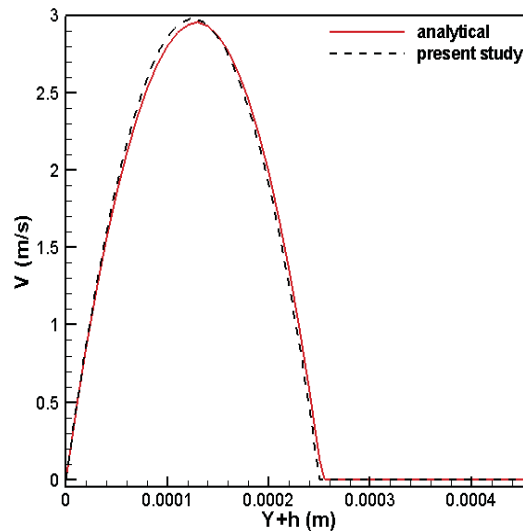


Fig. 2. Comparison of numerical and analytical results of axial velocity distributions in the gap region GDL layer

Flow velocity along the channel in the cathode GDL/catalyst layer interface and oxygen concentration in this interface is shown in Figs. 3 and 4. An abrupt change of velocity occurs at the gap region and the gas flow is forced into the GDL by the installation of a rectangular plate in the flow channel. This causes a larger amount of oxygen to move into the GDL around the region above the plate therefore, the reaction at the catalyst layer can be enhanced. However, the baffle plate causes a larger pressure drop (about 4 times the case without a plate) and needs a higher pumping power for delivery of the oxygen.

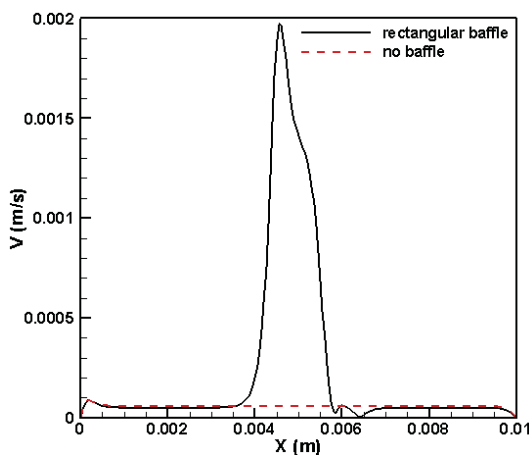


Figure. 3. Comparison flow velocity in the cathode GDL/catalyst layer interface along the channel between cases with and without rectangular baffle in the channel

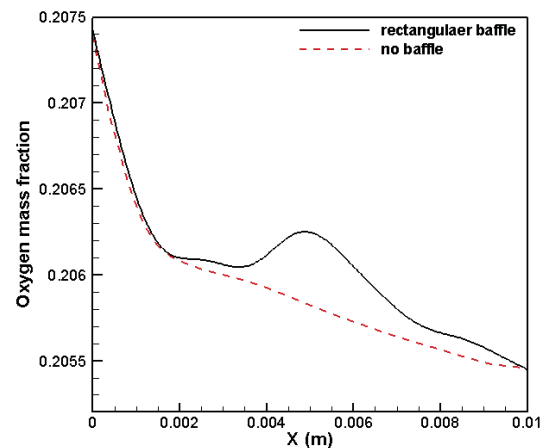


Figure. 4. Comparison oxygen concentration in the cathode GDL/catalyst layer interface along the channel between cases with and without rectangular baffle in the channel

An appropriate design of the flow channel has been reached by installed baffle plate(s) with various shapes, sizes, numbers and locations of plates in the channel. It can be expected that the change in the parameters mentioned may have a considerable influence on the mass transport. with considering both the maximum of oxygen concentration in the GDL and catalyst layer (or maximum velocity), and minimum pressure drop along the channel to arrive

at a better quantified evaluation of the effects of installation of baffle plate(s) we define an index, CHB, an abbreviated channel blocking, as follows:

$$CHB = \frac{\Delta P}{\rho \bar{V}^2} \quad (5)$$

ΔP is pressure drop along channel, ρ is gas (oxygen) density and \bar{V} is average velocity of reactant gases in the cathode GDL/catalyst layer interface, which is defined as:

$$\bar{V} = \frac{1}{L} \int_0^L V dx \quad (6)$$

where L is channel length and V is velocity distribution along the channel in the cathode GDL/catalyst layer interface.

It should be noted that channel should be designed to have smaller CHB value.

In the present study, we investigated the effect of shape of baffle plate that consisted of rectangular, triangle and semicircle baffle on the oxygen transfer in the GDL and pressure drop in the cathode side. For each shape, the effect of size and number of plates in the channel was investigated. Therefore, modeling was accomplished for 27 different cases. Table 3 shows the results of numerical solution of fuel cell cathode.

Table 3. The results of numerical solution of fuel cell cathode velocity and pressure drop for 27 blocking cases.

Shape, height and number of baffles	No. blocking case	baffle height (mm)	Pressure drop(Pa)	$\bar{V} \times 10^5$ (m/s)	CHB $\times 10^9$	Rank
	1	0.15	13.9	7.0254	2.816	22
	2	0.15	15.3	7.8002	2.515	20
	3	0.15	17.3	8.9208	2.174	16
	4	0.25	18.8	9.8533	1.936	14
	5	0.25	26.5	14.3010	1.296	9
	6	0.25	43.3	18.4668	0.966	7
	7	0.35	42	23.6994	0.748	5
	8	0.35	86.5	50.1282	0.344	2
	9	0.35	125	72.4184	0.238	1
	10	0.15	13.6	6.7830	2.956	24
	11	0.15	14.1	6.3072	3.544	27
	12	0.15	14.9	6.8340	3.190	26



	13	0.25	15	6.8781	3.171	25
	14	0.25	15.5	7.9180	2.472	19
	15	0.25	18.1	9.4356	2.033	15
	16	0.35	19.8	10.2975	1.867	13
	17	0.35	32.1	16.8530	1.130	8
	18	0.35	37.5	20.7513	0.871	6
	19	0.15	13.6	6.7891	2.951	23
	20	0.15	14.7	7.4361	2.658	21
	21	0.15	16.1	8.2196	2.383	18
	22	0.25	16.5	8.4676	2.301	17
	23	0.25	21	11.0498	1.720	12
	24	0.25	25.9	13.8864	1.342	10
	25	0.35	22.8	12.3	1.507	11
	26	0.35	46.4	25.2988	0.725	4
	27	0.35	63.5	35.3157	0.509	3

With the consideration of both maximum velocity (maximum concentration of oxygen in the GDL) and minimum pressure drop, minimum CHB, the rank of each 27 cases of optimum performance is shown in the seventh column. As seen in Table 3, by comparison of cases 1, 10 and 19, which investigate the effects of shape, it is observed that the least CHB is for rectangle, semicircle and triangle baffle, respectively. In all cases, the effect of the increase in plate height is more remarkable than the increase in the number of plates on the CHB.

The results indicate that the blocked channel with three large rectangular baffles, case 9, gives the least CHB and therefore, the most optimal blocking plate. Even with reducing the number of large rectangular plates, CHB obtained from 2 large rectangular baffles plate, case 8, is smaller than the other cases and allocated to rank 2. With installing three large semicircle baffles, case 27, CHB is slightly higher than case 9, but the pressure drop is much lower. The apparent pressure drops increase the pumping power requirement for operating a fuel cell system. So, when there is restriction in the pumping power, installing the semicircle baffle is

better than the rectangular baffle. By installing the triangle baffle, the CHB number will increase significantly. So installing triangle baffle does not seem to be appropriate.

Fig. 5 illustrates oxygen concentration in cathode for 3 baffle shapes consisting of rectangle, triangle and semicircle plate. As shown in Fig. 5, the maximum oxygen concentration in GDL layer occurs beneath the rectangular plate

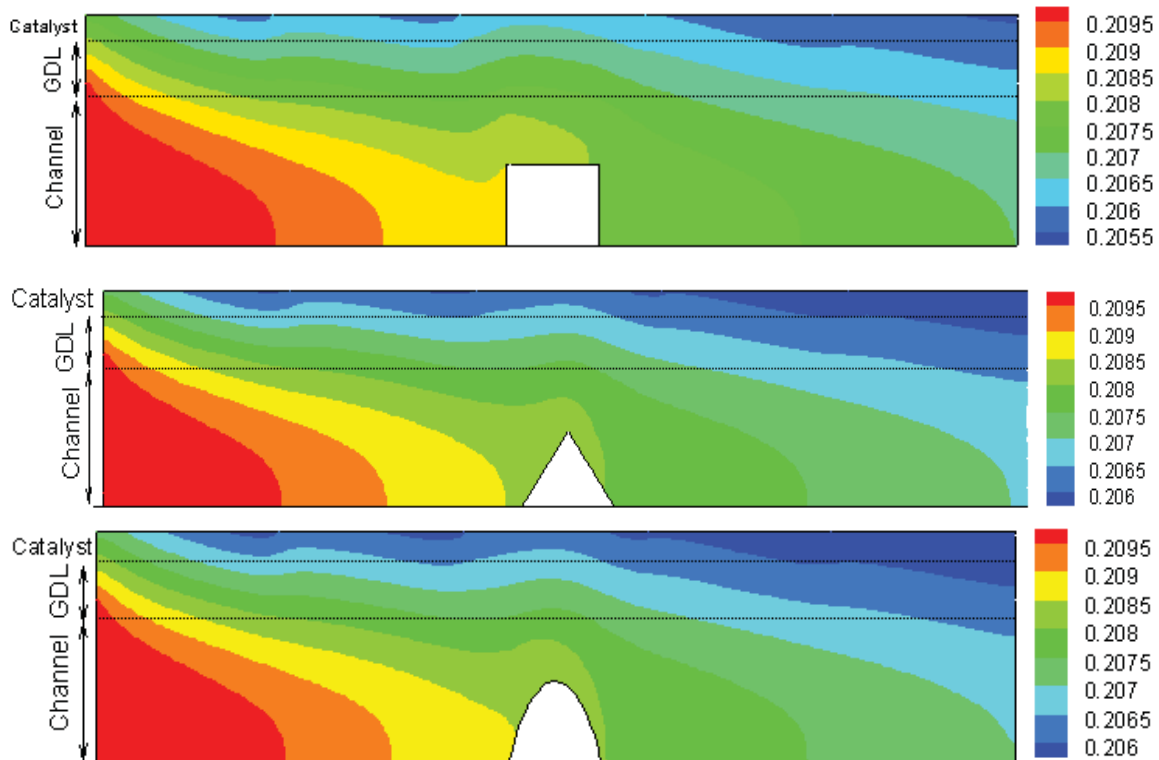


Figure. 5. Oxygen concentration contour for 3 blocking cases with rectangular, triangle and semicircle baffles in terms of Pascal

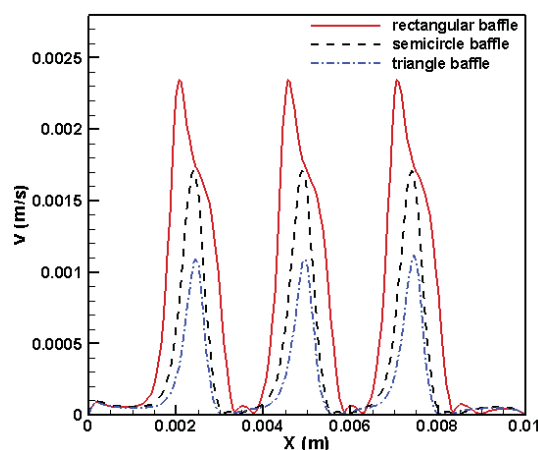


Figure. 6. Velocity distribution in the GDL/catalyst layer interface, three rectangular baffles, three semicircle baffles, three triangle baffles

The effects of baffle shape type on velocity distribution, oxygen concentration in GDL/catalyst layer interface and pressure drop along the channel are shown in Figs, 6, 7 and 8, respectively. In these figures, three rectangular baffles, three semicircle baffles and three triangle baffles are installed in flow channel.

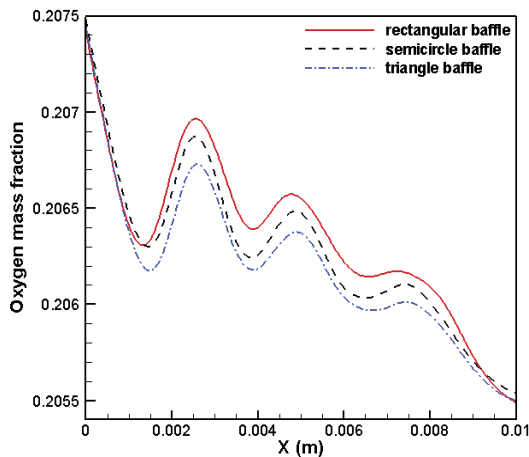


Figure 7. Oxygen concentration distribution in the GDL/catalyst layer interface, three rectangular baffles, three semicircle baffles, three triangle baffles

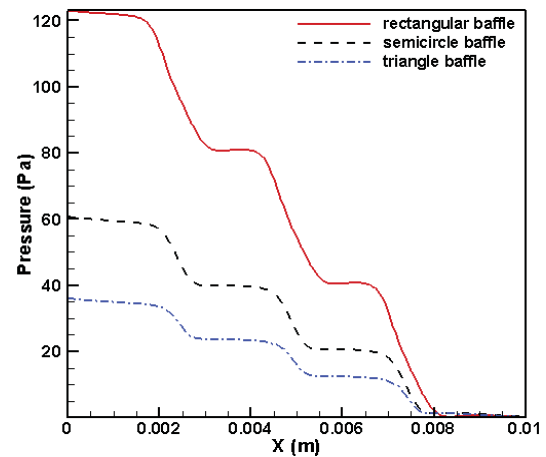


Fig. 8. Pressure variation along the channel, three rectangular baffles, three semicircle baffles, three triangle baffles

3 Conclusion

A two-dimensional model has been developed for a PEM fuel cell cathode electrode with partially blocked channel to investigate the effect of plate shape, size and the number of baffle plates on transport phenomena in gas diffusion layer. The following conclusions are drawn:

- By installing the baffle plate, flow velocity in the gap between the baffle and the GDL is increased; causing more oxygen to be diffused into GDL and increasing reaction rate in catalyst layer, however, pressure drop along the channel is increased too. Therefore, it should be chosen as optimum case.
- To compare different blocking cases, we introduced a dimensionless number as the ratio between pressure and squared velocity and called CHB.
- According to CHB definition, the best blocking case between 27 investigated cases is installing three rectangular baffles with the height of 0.35 mm.
- By installing three semicircle baffles with the height 0.35 mm, CHB number was found to be slightly higher than its value in the best condition, but the pressure drop was much lower. So when there is restriction in securing pressure in fuel cell, installing the semicircle baffle is better than the rectangular one.
- By the increase in the number of baffles and also baffle height, CHB is decreased. However CHB is more sensitive than the height.
- By installing the triangle baffle, the CHB will increase significantly. So installing triangle baffle is not recommended

Acknowledgments

The authors are grateful for the financial support of the Renewable Energy Organization of Iran [SUNA].

References

- 1- E. Birgersson and M. Vynnycky, "A Quantitative Study of the Effect of Flow-Distributor Geometry in the Cathode of a PEM Fuel Cell" J. Power Sources, (2006). 153, 76–88.



- 2- G. Squadrito, O. Barbera, I. Gatto, G. Giacoppo, F. Urbani and E. Passalacqua, "CFD analysis of the flow-field scale-up influence on the electrodes performance in a PEFC." J. Power Sources, (2005). 152, 67–74.
- 3- S. Maharudrayya, S. Jayanti and A.P. Deshpande, "Flow distribution and pressure drop in parallel-channel configurations of planar fuel cells" J. Power Sources, (2005). 144, 94–106.
- 4- P.T. Nguyen, T. Berning and N. Djilali," Computational model of a PEM fuel cell with serpentine gas flow" J. Power Sources, (2004). 130, 149–157.
- 5- L. Wang and H. Liu," Performance studies of PEM fuel cells with interdigitated flow fields" J. Power Sources, (2004). 134, 185–196.
- 6- W.M. Yan, H.C. Liu, C.Y. Soong, F. Chen and C.H. Cheng, "Numerical study on cell performance and local transport phenomena of PEM fuel cells with novel flow field designs" J. Power Sources, (2006). 161, 907–919.
- 7- G. Hu, J. Fan, S. Chen, Y. Liu and K. Cen, "Three-dimensional numerical analysis of proton exchange membrane fuel cells (PEMFCs) with conventional and interdigitated flow fields." J. Power Sources, (2004). 136, 1–9.
- 8- W.M. Yan, H.Y. Li and W.C. Tsai, "Three-Dimensional Analysis of PEMFCs with Different Flow Channel Designs" J. Electrochem., (2006). 153, 1984–1991.
- 9- X. Liu, W. Tao, Z. Li and Y. He, "Three-dimensional transport model of PEM fuel cell with straight flow channels" J. Power Sources, (2006). 158, 25–35.
- 10- J.K. Kuoa, T.H. Yen and C.K. Chen, "Three-dimensional numerical analysis of PEMFCs with straight and wave-like gas flow fields channels" J. Power Sources, (2008). 177, 96–103.
- 11- S.W. Perng, H.W. Wub, T. Jue and K.C. Cheng, "Numerical predictions of a PEM fuel cell performance enhancement by a rectangular cylinder installed transversely in the flow channel" Applied Energy, (2009). 86, 1541–1554.
- 12- C.Y. Soong, W.M. Yan, C.Y. Tseng and H.C. Liu, "Analysis of reactant gas transport in a PEM fuel cell with partially blocked fuel flow channels" J. Power Sources, (2005). 143, 36–47.
- 13- H.C. Liu, W.M. Yan, C.Y. Soong and F. Chen, "Effects of baffle-blocked flow channel on reactant transport and cell performance of a proton exchange membrane fuel cell" J. Power Sources, (2005). 142, 125–133.
- 14- E. Afshari and S.A. Jazayeri, "Analyses of heat and water transport interactions in a proton exchange membrane fuel cell", J. Power Sources, (2009). 194, 423–432.
- 15- J.J. Hwang, "A complete two-phase model of a porous cathode of a PEM fuel cell." J. Power Sources, (2007). 164, 174–181.
- 16- C.Y. Wang and P. Cheng, "Multiphase Flow and Heat Transfer in Porous Media" J. Adv. Heat Transfer, (1997). 30, 93–196.



Hydrogen storage: A DFT investigation of adsorption of hydrogen Molecule on $\text{Si}_{16}\text{C}_{16}$ and $\text{Si}_{24}\text{C}_{24}$ nanofulleren like structures : A comparison with adsorption of hydrogen molecule on $\text{Si}_{16}\text{C}_{16}@\text{Li}^+$ and $\text{Si}_{16}\text{C}_{16}@\text{K}$

* *Elham Zarorati*¹, Javad Beheshtian²

Department of Chemistry, Shahid Rajaei Teacher Training University, P.O. Box 16875-163,
Tehran, Iran¹⁻²

*elhamzaroorati@yahoo.com**

Abstract

The purpose of the present work is to investigate hydrogen gas storage and adsorption it on the SiC nanoclusters i.e. $\text{Si}_{16}\text{C}_{16}$ and $\text{Si}_{24}\text{C}_{24}$ and $\text{Si}_{16}\text{C}_{16}@\text{Li}^+$ and $\text{Si}_{16}\text{C}_{16}@\text{K}$. We performed DFT calculations to study adsorption of H_2 on nanoclusters. It is suggested that, It can be inferred that $\text{Si}_{16}\text{C}_{16}$ and $\text{Si}_{24}\text{C}_{24}$ nano-cages function as a gas sensor device against H_2 molecule, However, lithium cation within the $\text{Si}_{16}\text{C}_{16}-\text{H}_2$ structure, the energy absorption is increased. Maybe there are other elements within the structures, they can be a suitable sensor.

Keywords: Carbon Silicon nanocluster, Density functional theory, Adsorption, H_2 .

Introduction

Hydrogen gas is a new source of energy as fuel in fuel cell with no pollution and it is an ecological fuel that should be remembered. Nowadays We are face to face with complications of fossil fuels such as: (heating of the atmosphere, air pollution, expiration of all the underground hydrocarbon storage, etc.). Hydrogen are recognized as a viable solution but it is the basic problem in the usage and storage of hydrogen gas, if the condition is not perfect and safe. It can not enough gas being stored in a given specified volume because there is the explosion hazard of it. so the study of hydrogen adsorption on various materials has been regarded by many scientists in this field. Many research papers has been published in this field. But the basic problem is the usage of hydrogen storage. Next problem is the danger of explosion in the gas from used channels [1-5]. Non-carbon nanosystem comprised of light elements such as silicon and nitrogen atoms and etc, also have been noticed. Silicon carbide (SiC) is a compound of silicon and carbon with a chemical formula SiC. SiC nanomaterials may be promising semiconductors for preparation of nanoelectronic devices for high-temperature, high-power, and high-frequency applications[6-8]. We performed DFT calculations to study adsorption of H_2 on $\text{Si}_{16}\text{C}_{16}$ and $\text{Si}_{24}\text{C}_{24}$ fullerene-like nanoclusters and investigated corresponding different electronic properties.

Computational methods

All calculations were performed using DFT within M062X level calculation which has been widely used in the nanostructure studies. The basis set were set to be 6-311G** for the optimization, frontier molecular orbital (FMO) analyses, and energy calculations. The adsorption energy of H₂ molecule on the pure Si_nC_n cluster obtained using the following equation:

$$E_{\text{ads}} = E(\text{Si}_n\text{C}_n/\text{H}_2) - E(\text{Si}_n\text{C}_n) - E(\text{H}_2)$$

, where $E(\text{Si}_n\text{C}_n/\text{H}_2)$ is the total energy of Si_nC_n/H₂ complex and $E(\text{Si}_n\text{C}_n)$ or $E(\text{H}_2)$ is the energy of an isolated Si_nC_n or H₂ molecule, respectively. All calculations were implemented in GAUSSIAN 09 package.

Results

We carried out full structural optimization of the Si₁₆C₁₆ and Si₂₄C₂₄ and Si₁₆C₁₆@Li⁺ (Lithium cation) and Si₁₆C₁₆@k (Potassium atom) nanoclusters with H₂ gas molecule to examine the energetic, structural, and electronic properties. To find the most favorable adsorption configurations, the adsorbate is placed at different positions freely above the cluster surface having different orientations.

Optimized structures shown in Fig.1. Detailed information are listed in Table1. The highest occupied molecular orbital (HOMO) and the lowest unoccupied molecular orbital (LUMO) is also desired structures were drawn. The total electronic densities of states (DOS) analysis was performed using GaussSum program, to verify the effects of the adsorption of H₂ molecule on the nanocluster electronic properties.

Table.1 The adsorption energy (E_{ads}) of H₂ on the Si₁₆C₁₆ and Si₂₄C₂₄ and Si₁₆C₁₆@Li⁺ and Si₁₆C₁₆@k nanoclusters, Mulliken charge transfer (the charge on the molecule after its adsorption (QT) on the cluster), and the change of Si₁₆C₁₆ and Si₂₄C₂₄ HOMO–LUMO gap (ΔE_{gap}) upon the adsorption process.

Configuration	E_{ads} (kJ/mol)	ΔE_{gap} (ev)	Q_{T} (e)
Si ₁₆ C ₁₆ -H ₂	-0/0.01	2/19	0/0.03
Si ₂₄ C ₂₄ -H ₂	-0/0.09	2/0.8	0/0.23
Si ₁₆ C ₁₆ -H ₂ @Li ⁺	-0/0.8	2/0.1	0/0.73
Si ₁₆ C ₁₆ -H ₂ @k	-0/0.3	-0/54	0/0.02

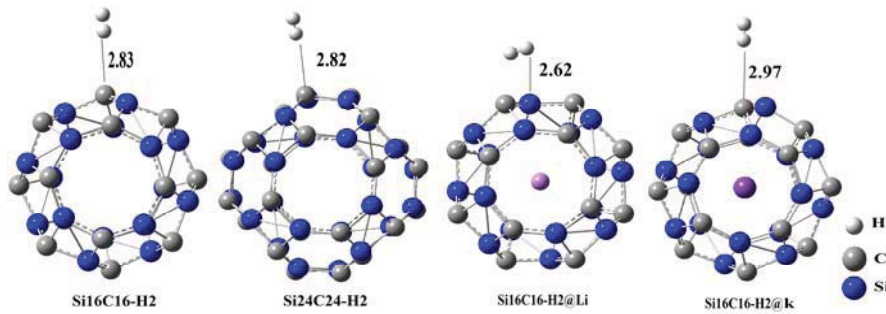


Fig.1 Optimized structures of stable H₂/ Si₁₆ C₁₆ and Si₂₄C₂₄ complexes. Distances are in Å .

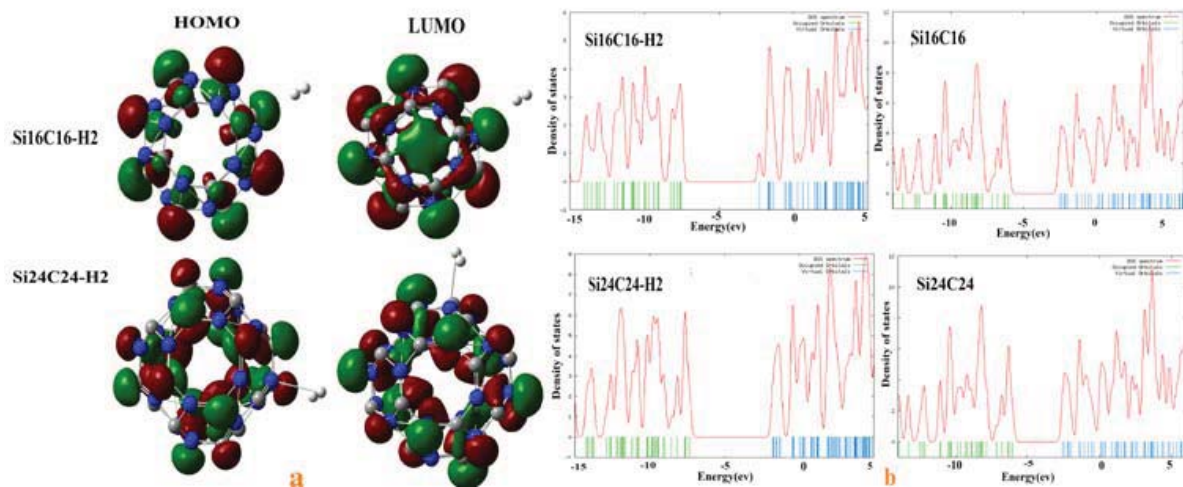


Fig.2 a HOMO and LUMO of stable nano-cages . b DOS plot of structures .

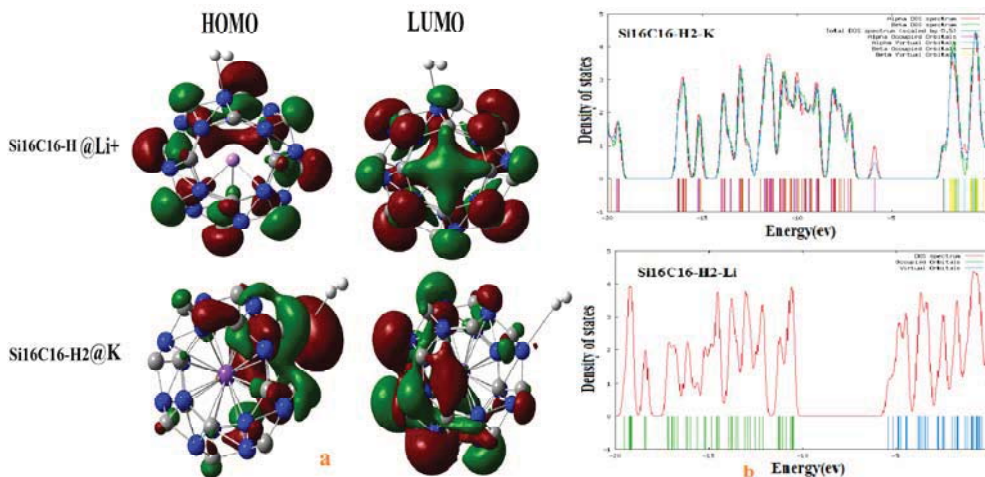


Fig.3 a HOMO and LUMO of stable nano-cages . b DOS plot of structures .

With respect to data, it can't be inferred that Si₁₆C₁₆ and Si₂₄C₂₄ nano-cages function as a gas sensor device against H₂ molecule, However, Lithium cation within the Si₁₆C₁₆-H₂ structure, the energy absorption is increased. Maybe there are other elements within the structures, they can be a suitable sensor.

Reference

[1] R.D. Cortight, R.R. Davada, J.A. Dumesic, Nature 418 (2002) 964.



- [2] B. Sakintuna, F.L. Darkrim, M. Hirscher, *Int. J. Hydrogen Energy* 32 (2007) 1121.
- [3] R. Ströbel, J. Garche, P.T. Moseley, L. Jörisen, G. Wolf, *J. Power Sources* 159(2006) 781.
- [4] J. Beheshtian, M. Kamfiroozi, Z. Bagheri, A.Ahmadi, *Computational Materials Science* 54 (2012),115-118.
- [5] J. Beheshtian, A.Ahmadi, Z. Bagheri, M. Kamfiroozi, *Struct Chem* (2012), 1-6.
- [6] M.N.Huda and A.K.Ray, "Novel silicon-carbon fullerene cage " *Eur. Phys. J. D* 31. 63-68(2004).
- [7] J. Li, Y. Xia, M. Zhao, X. Liu, C. Song, L. Li, F. Li, B. Huang, *Chemical Physics Letters*, 442, (2007), 384-389.
- [8] L. I. Ovsyannikova, V. V. Pokropivny, V. L. Bekenev, *Physics of the Solid State*, Vol. 51, No. 10 (2009), 2199–2206.



Electrochemical impedance study on methyl orange and methyl red as power enhancing electron mediators in glucose fed microbial fuel cell

Mir Ghasem Hosseini¹, Iraj Ahadzadeh^{2*}, Mehdi Abdolmaleki³

Electrochemistry Research Laboratory, Department of Physical Chemistry, Faculty of Chemistry, University of Tabriz, Tabriz, Iran

mg-hosseini@tabrizu.ac.ir

Abstract

Methyl orange and methyl red are studied as electron mediators in a glucose-fed microbial fuel cell. Maximum output power levels of the cell are about $106 \mu\text{W}\cdot\text{cm}^{-2}$ in the absence of any added mediator, $164 \mu\text{W}\cdot\text{cm}^{-2}$ and $207 \mu\text{W}\cdot\text{cm}^{-2}$ in the presence of 1 mM of methyl orange and 1 mM of methyl red in the anolyte, respectively, normalized to anode geometric surface area. Also addition of these organic mediators increases the open circuit potential and short circuit current of the cell from 425 mV and $1.12 \text{ mA}\cdot\text{cm}^{-2}$ to 512 mV and $1.51 \text{ mA}\cdot\text{cm}^{-2}$ for methyl orange and 585 mV and $1.51 \text{ mA}\cdot\text{cm}^{-2}$ for methyl red. Impedance measurements are performed for the microbial fuel cell in a two electrode configuration. From impedance spectra it is found that the main factor resulting in an increased power level of the cell is the decrease in the anodic charge transfer resistance.

Keywords: Microbial fuel cell, Biofilms, Membrane, Electrochemical impedance spectroscopy, electron mediator

1 Introduction

Microbial fuel cells (MFCs) are currently considered as renewable energy production and also potentially economic wastewater treatment systems that generate electric energy from any biodegradable organic materials through micro-organism assisted oxidation processes. From biochemical engineering point of view, use of MFCs as novel robust wastewater treatment approach is highly interesting because it combines the simultaneous benefits of producing useful electrical power and at the same time removing the organic material [1-2]. However, at this time, due various factors such as slow reaction kinetics and high internal ohmic and kinetic losses, power output level and also organic material removal capability of these fuel cells is very low [3, 4]. One of the suggested and well practiced methods to enhance the output power

¹*Electrochemistry Research Laboratory, Department of Physical Chemistry, Faculty of Chemistry, University of Tabriz, Tabriz, Iran*

²*Electrochemistry Research Laboratory, Department of Physical Chemistry, Faculty of Chemistry, University of Tabriz, Tabriz, Iran, irajahadzadeh@gmail.com*

³*Electrochemistry Research Laboratory, Department of Physical Chemistry, Faculty of Chemistry, University of Tabriz, Tabriz, Iran, m_iust2004@yahoo.com*



level of these cells is the use of the so called "electron shuttles" or mediators. Mediators are usually bacteria self-secreted and/or organic compounds which deliberately added to the anodic compartment of a microbial fuel cell with the aim of accelerating the electron extraction from the micro-organism cell internal biological reaction pathways through cell membrane and transferring the extracted electrons to the anode electrode and from there to the external circuit to produce electric power. For a material to act as an efficient electron mediator, some general requirements should met, i.e. it should exhibit least toxicity and high bio-compatibility to the micro-organisms, it should has long term stability capable of performing its function in a reversible cycle and itself not be consumed [5, 6]. In this regard, various organic compounds have been extensively studied in related literature, for example Humic acids (HA) [7], Neutral Red [8], and flavin [9], all of them resulting in a significant increase in the output power level of the MFC systems investigated. But detailed mechanism(s) and electro-biochemical pathways through which these mediators enhance the electron transfer from inside of the micro-organism cells to the anode are rather poorly understood and detailed directed studies must be performed [8, 9]. Therefore, gaining insight to electrochemical processes taking place at the surface of the anode electrode during the employment of these electron mediators is of critical importance for further development, enhancing the performance and promoting the output level of MFCs with the aim of proper tailoring of these systems for biochemical engineering applications. Electrochemical impedance spectroscopy (EIS) is among the most powerful and well-established electrochemical methods to study the fuel cells in general and microbial fuel cells in particular, for example for non-intrusive detection of extra-cellular mediators in microbial Fuel Cells, to determine the internal resistance of the fuel cell, to study the spatial distribution of the internal resistance on fuel cell components such as cathode, anode and electrolyte, to investigate the electro-catalytic activity of the electrodes [10-15]. For this purpose, in the current study, EIS was applied to investigate methyl orange and methyl red as power enhancing electron mediators in a glucose-fed microbial fuel cell with graphite anode, FlemionTM membrane and Platinum sheet cathode. Anaerobic activated sludge was used as bacterial medium.

2 Experimental

2.1 Materials and Methods

Main features of microbial fuel cell construction is as follows: the homemade cell set-up consists of two polycarbonate plastic cylinders each of about 0.125 L separated by a 3.1cm² FlemionTM cation exchange membrane (250 μm thickness, Asahi Glass Company, Japan). Anode in the shape of a rectangle with a total geometrical area of 24.3 cm² was made of commercial electrical grade graphite plate. All chemicals used throughout the study were of analytical grade provided by Merck (Germany) unless otherwise stated and used as received without any further treatment. Double distilled water was used to all solution preparation and rinse purposes. Prior to the experiments, fuel cell setup was immersed in a KMnO₄ solution (3 gL⁻¹) for 24 h in order to disinfect the anode and cathode chambers. After three times rinse with double distilled water, cation exchange membrane was fitted between anodic and cathodic parts using three stainless steel screws. Catholyte and anolyte solution composition was as follows: 60 mM biological phosphate buffer solution (PBS) with pH=7.4, MgSO₄ (0.9 gL⁻¹) and NH₄Cl (1 gL⁻¹) and 0.1 mL L⁻¹ trace essential elements solution (contained per liter: 23 mg MnCl₂.2H₂O, 30 mg MnCl₄.H₂O, 31 mg H₃BO₃, 36 mg CoCl₂.6H₂O, 10 mg CuCl₂.2H₂O, 20 mg NiCl₂.6H₂O, 50 mg ZnCl₂, and 30 mg Na₂MoO₄.2H₂O). Prior to the insertion of the graphite anode into the anolyte, the biofilm was formed on graphite anode in a batch procedure. Briefly, in a batch procedure, the graphite anode was immersed in a solution with the composition of the anolyte along with 1 gL⁻¹ glucose as feed and 1 mL of urban waste water (Tabriz) sludge as



mixed culture bacterial source, while kept stirred for 24 h in anaerobic condition. Anaerobic condition was achieved by bubbling pure nitrogen gas into the solution for 0.5 h after which the setup was kept sealed using proper gas tight miniature taps. Stirring was aimed to produce a gentle shear on the surface of the anode with the hope of obtaining a more compact and active biofilm. After fitting the anode covered with biofilm and adding 100 mL of the anolyte solution containing 1 gL^{-1} glucose into the anodic section, anaerobic condition was further observed in that compartment by sealing all apertures around the anode by water-proof silicone sealant. During the study of the effect of methyl orange ($\text{C}_{14}\text{H}_{14}\text{N}_3\text{NaO}_3\text{S}$, $\text{MW}=327.33 \text{ g.mol}^{-1}$) and methyl red ($\text{C}_{15}\text{H}_{15}\text{N}_3\text{O}_2$, $\text{MW}=269.3 \text{ g.mol}^{-1}$) mediators, the concentration each mediator in the anolyte was adjusted to be 1 mM. It should be mentioned methyl orange is difficultly soluble in water at room temperature so in order to dissolve methyl orange, hot (about $80 \text{ }^\circ\text{C}$) solution of the blank anolyte was used and after cooling down to the room temperature, the solution was added to the anodic compartment of the MFC. Cathode electrode was a highly pure Platinum sheet with a geometric surface area of 15 cm^2 .

2.2 Polarization measurements

Polarization measurements were performed by successive lowering the value of externally connected homemade precision-resistor box to the anode and cathode via some length of wire and two crocodile clips, and at the same time recording the potential drop across the load resistor. Variation range of the resistor box was from $2 \text{ M}\Omega$ to 10Ω in a logarithmic scale. All potential records were performed using a high input impedance ($10 \text{ M}\Omega$) commercial 3.5 digit voltmeter. Sufficient time interval, typically 5 min, was observed after each change in resistor box value to obtain a stable potential reading. Short circuit current was measured using a 3.5 digit commercial ammeter with 20 mA full range.

2.3 Electrochemical impedance

Electrochemical impedance spectrum was recorded for different anolytes i.e. anolyte without mediator, anolyte with 1mM added methyl orange and anolyte with 1mM added methyl red. Impedance measurements were performed using an EG&G (Princeton Applied Research) Parstat 2263 Advance Electrochemical System (USA) in the frequency range of 100 kHz down to 0.01 Hz. To measure the impedance of whole microbial fuel cell, use was made of a two-electrode configuration in which counter and reference electrodes of the impedance measuring apparatus were connected to the anode and working electrode was electrically fixed to the cathode of the fuel cell.

3 Results and Discussion

3.1 Polarization measurements

Figures 1 and 2 show the voltage-current density (V - J) polarization and power-current density (P - J) curves of the cell after 24 h operation with a 1 k Ω external constant resistor, respectively.

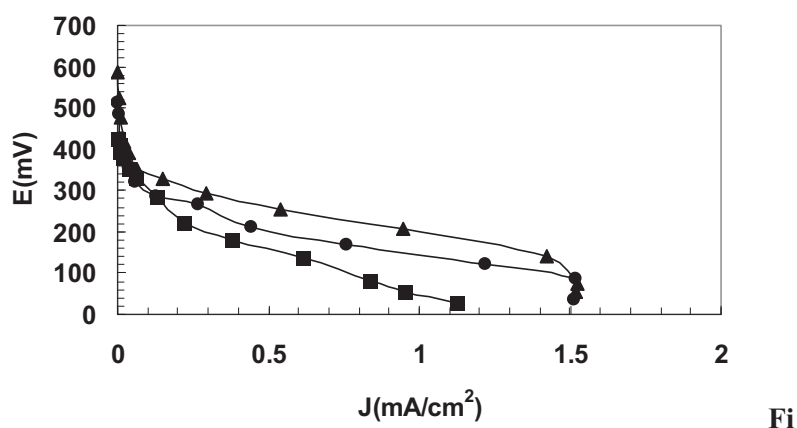


Figure 1. Polarization (V - J) curves of microbial fuel cell after 24 h operation with an external 1 $k\Omega$ resistor. (■) mediator-less, (●) with 1 mM Methyl orange, and (▲) with 1mM methyl red. Parameter J indicated the current density (mA cm^{-2}) normalized to the geometric surface area of the anode.

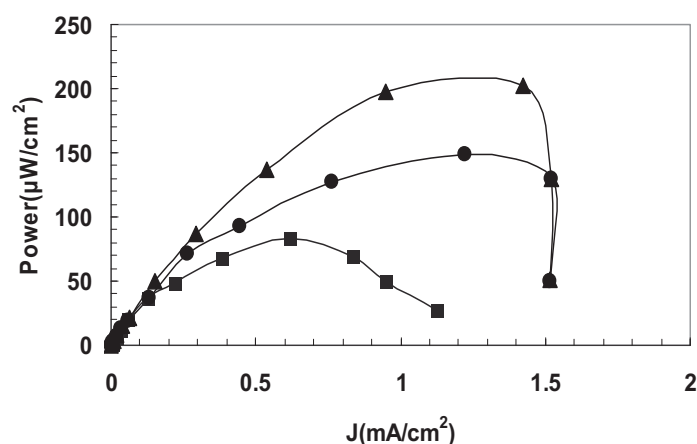


Figure 2. Power (P - J) curves of microbial fuel cell after 24 h operation with an external 1 $k\Omega$. (■) mediator-less, (●) with 1 mM Methyl orange, and (▲) with 1 mM methyl red.

As can be seen from Figs.1 and 2, after 24 h operation, maximum output power levels of the cell were about $83.5 \mu\text{W cm}^{-2}$ in the absence of any added mediator, $150 \mu\text{W cm}^{-2}$ and $202 \mu\text{W cm}^{-2}$ in the presence of methyl orange and methyl red in the anolyte, respectively, normalized to anode geometric surface area. Also addition of these organic mediators increased the open circuit potential (OCP) and short circuit current density (J_{sc}) of the cell from 425 mV and 1.12 mA.cm^{-2} to 512 mV and 1.51 mA.cm^{-2} for methyl orange and 585 mV and 1.51 mA.cm^{-2} for methyl red, respectively.

3.2 Electrochemical impedance spectroscopy

Fitting and analysis of the EIS data were performed by ZSimTM software. Nyquist complex impedance plots of the fuel cell with three anolytes after 24 operation with a 1 $k\Omega$ external constant resistor are shown in Figures 3 along with their proper electrical equivalent circuit in Figure 4.

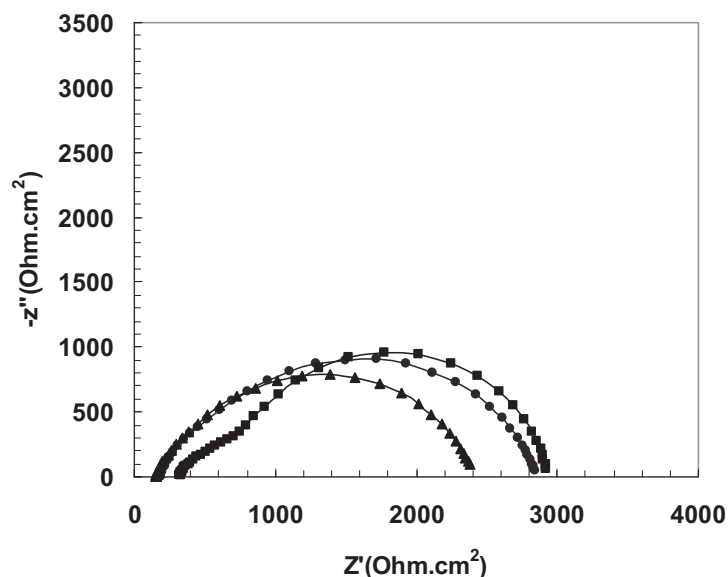


Figure 3. Fitted Nyquist impedance spectra of the microbial fuel cell at after 24 h operation with an external 1 k Ω resistor. (■) mediator-less, (●) with 1mM Methyl orange, and (▲) with 1 mM methyl red. The frequency range is extended from 100 kHz down to 0.01 Hz.

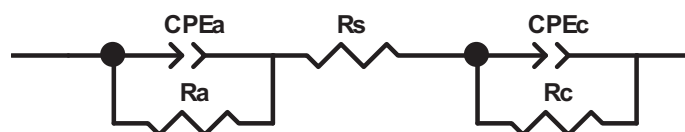


Figure 4. Electrical equivalent circuit employed to analyze the experimental impedance data, mediator-less, (●) with 1 mM Methyl orange, and (▲) with 1 mM methyl red.

Impedance parameters for each experiment were derived by fitting the experimental data on the electrical equivalent circuit. The electrical equivalent circuit modeling is one of the most fundamental approaches in EIS. In this approach, an electrical circuit containing passive (lumped) electrical elements such as resistors (R), capacitors (C), constant phase elements (CPE), Warburg diffusion elements (W) and so, is designed according to the physicochemical model of the system under study and each element and its value(s) are related to a real physicochemical phenomenon in the electrochemical system; for example, charge transfer kinetics (Faradic impedance) and bulk as well as interfacial conductances are modeled by resistors and CPE and in some cases, capacitances are used to model interfacial double layer capacitances [16].

In the electrical equivalent circuits depicted in Figure 4, the resistor R_s is an indication of the internal ohmic resistance i.e. resistance of the anolyte and catholyte solutions and membrane toward transfer of H^+ produced at the anode to the cathode, R_c and R_a are cathodic and anodic respective charge transfer resistances which are inversely proportional to the chemical reaction rate at the cathode and anode respectively. The constant phase elements CPE_c and CPE_a are corresponding electrical double layer pseudo-capacitances of the cathode/catholyte and anode/anolyte electrochemical interfaces, respectively. These electrical equivalent circuits was designed on the basis of achieving the best fit for the observed experimental EIS data and also

physicochemical model of the fuel cell composed of a cathode electrode and an anode electrode both in contact with electrolyte solution separated by a membrane [12, 16]. Impedance of a constant phase element (*CPE*) is defined as below:

$$Z_{CPE} = (1/T)(j\omega)^{-n} \quad (1)$$

where T is the admittance parameter; j and ω are the $\sqrt{-1}$ imaginary number and the angular frequency ($\omega = 2\pi f$, f being the frequency) of the perturbing sinusoidal voltage, respectively. For different values of n , *CPE* can represent the impedance of a variety of circuit element, namely, $n=1$, ideal capacitor; $n=0$, ideal resistor; $n=-1$, ideal inductor; $n=0.5$, Warburg diffusion impedance. Thus by including *CPE* element in the equivalent circuit, high level of flexibility can be achieved in fitting the EIS experimental data. But the main problem is the inconsistency of the arguments on the physical concept of the parameter n . In some studies, the value of the parameter n was related to some microscopic characteristics of interface such as surface roughness and/or surface fractal dimension, but at present, there is not a coherent agreement on the physical meaning of the n power [16]. Keeping above mentioned notes in mind we have chosen *CPE* element instead of ideal capacitor to design the electrical equivalent circuit and fit the experimental EIS data. But it should be mentioned that for comparative purposes, the ideal capacitance equivalent value of a *CPE* must be used which is given by well-known Brugg's formula [17]:

$$C = T^{1/n} (1/R_s + 1/R_{ct})^{n-1} \quad (2)$$

In which C denotes the ideal plane capacitance value ($F \cdot cm^{-2}$) and T , n , R_s and R_{ct} are *CPE* admittance, *CPE* power (as given in Equation 1), solution resistance and charge transfer resistance respectively. So having in hand T , n , R_s and R_{ct} for cathode and anode after fitting experimental EIS data on proper equivalent circuit (Figure 4), C_c and C_a (cathodic and anodic capacitance, respectively) can be calculated with results shown in Table 1 after 24 h operation with a 1 k Ω external resistor.

Table 1. Impedance parameters of the data presented in Fig. 3 after 24 h operation of the cell. (R_s : Ohm; R_a and R_c : $Ohm \cdot cm^2$; $n-a$, $n-c$ and $W-n$: dimensionless parameters; CPE_a-T and CPE_c-T : $Ohm^{-1} \cdot s^n \cdot cm^{-2}$; $W-T$: $Ohm^{-1} \cdot s^{0.5}$, "s" denotes the time in seconds and C_a and C_c : $\mu F \cdot cm^{-2}$).

<i>Anolyte</i>	R_s	R_a	R_c	CPE_a-T $\times 10^{-5}$	CPE_c-T $\times 10^{-5}$	$n-a$	$n-c$	C_a	C_c
<i>Without Mediator</i>	321	470.7	2143	2.30	4.36	0.73	0.90	1.2	24
<i>With Methyl Orange</i>	182	330	2344	4.50	4.50	0.80	0.81	7.9	9.5
<i>With Methyl Red</i>	153	176	2082	7.74	5.25	0.82	0.81	18	11

As can be seen from Table 1, values of the parameter R_c which is inverse indication of the cathodic reaction rate, change little during the addition of mediators to the anolyte of the cell while R_a values show considerable decrease in the presence of mediators in such a way that decrease in R_a is more profound for methyl red. Thus it can be said that the main role played by the mediators is to decrease the anodic charge transfer resistance and thereby facilitate the oxidation reaction of the glucose by micro-organisms and extract more electrons from the micro-organisms cell membranes. In order to evaluate the long term stability and thus practical applicability of the studied mediators, output power of the cell with three anolytes was monitored for a 200 h time interval under an external constant load of 1 k Ω in two feed renewal cycles. Results are depicted in Figure 5.

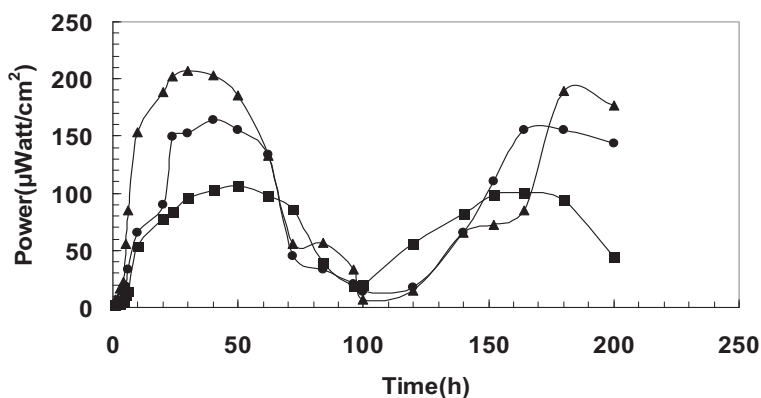


Figure 5. Power-time trend of the MFC during a two cycle feed renewal operation. (■)

Fall of the power level after about 75 h is a direct consequence of the consumption of glucose in the anolyte. After renewal of the anolyte with fresh feed at 100 h of operation, power level increases again showing the same trend as the first cycle of operation. Therefore it may be concluded that employed mediators are not consumed during cell operation instead it is proposed that they undergo red-ox cyclic reactions and can express their power enhancing capabilities for a much prolonged time. In a complementary set of confirmation and reproducibility tests, whole of the experimental procedure and electrochemical measurements were twice repeated in nominally identical conditions with newly prepared anodic biofilm. Summary of the results of polarization measurements are given in Table 2.

Table 2. Polarization results of the MFC in three successive runs after 24 h operation with 1 k Ω external resistor.

Run	Conditions	Jsc(mA.cm ⁻²)	OCP(mV)	Power(μ W.cm ⁻²)
1	Without Mediator	1.12	425	83.5
	Methyl Orange	1.51	512	150
	Methyl Red	1.51	585	202
2	Without Mediator	0.96	422	88.1
	Methyl Orange	1.66	523	150
	Methyl Red	1.41	580	188
3	Without Mediator	1.10	417	75.4
	Methyl Orange	1.61	506	167
	Methyl Red	1.48	592	210

From Table 2, it can be seen that the performance of the fuel cell and the power enhancing effect of studied electron mediators are reasonably reproducible regarding the inherent complexities associated with mixed-culture bacterial biofilm of the anode.

Although on an equi-molar basis, in this study, methyl red shows a rather better performance as a mediator compared with methyl orange, extensive complementary electrochemical studies are needed to interpret the results in a more solid molecular basis possibly in terms of mediator structure-bacteria interaction and mediator electrochemical redox potential and to identify the underlying biological pathways of the anodic reactions. Application of this mediator- enhanced MFC system to study organic material removal capability and its further development as a wastewater treatment bio fuel cell is underway as a subsequent study.

4 Conclusions

From polarization data and impedance spectra it was found that the main factor resulting in an increased power level of the cell after application of the mediators is the decrease in the anodic charge transfer resistance. It is suggested that this decrease is a direct consequence of more feasible micro-organism assisted anodic oxidation and electron transfer reaction in the anodic compartment in the presence of mediators. Although on an equi-molar basis, methyl red shows a better performance compared with methyl orange, complementary studies are needed to interpret the results in a more solid basis. Also, EIS can be used to study various potentially applicable mediators and to select most suitable compounds.

References

- [1] Antonopoulou G, Stamatelatou K, Bebelis S, Lyberatos G. Electricity generation from synthetic substrates and cheese whey using a two chamber microbial fuel cell. *Biochemical Engineering Journal* 2010; 50:10-15.



- [2] Liu ZD, Li HR. Effects of bio- and abio-factors on electricity production in a mediatorless microbial fuel cell. *Biochemical Engineering Journal* 2007;36:209-214.
- [3] Zhou M, Chi M, Wang H, Jin T. Anode modification by electrochemical oxidation: A new practical method to improve the performance of microbial fuel cells. *Biochemical Engineering Journal* 2012;60:151-155.
- [4] Hosseini MG, Ahadzadeh I. A dual-Chambered microbial fuel cell with Ti/nano-TiO₂/Pd nano-structure cathode. *Journal of Power Sources* 2012;220:292-297.
- [5] Rabaey K, Boon N, Siciliano SD, Verhaege M, Verstraete W. Biofuel Cells Select for Microbial Consortia That Self-Mediate Electron Transfer. *Applied and Environmental Microbiology* 2004;70:5373–5382.
- [6] Rabaey K, Boon N, Hofte M, Verstraete W. Microbial Phenazine Production Enhances Electron Transfer in Biofuel Cells. *Environ Sci Technol* 2005;39:3401-3408.
- [7] Huang L, Angelidaki I. Effect of humic acids on electricity generation integrated with xylose degradation in microbial fuel cells. *Biotechnology and Bioengineering* 2008;100:413-422.
- [8] Park DH, Zeikus JG. Electricity Generation in Microbial Fuel Cells Using Neutral Red as an Electronophore. *Applied and Environmental Microbiology* 2000;66:1292–1297.
- [9] Velasquez-Orta SB, Head IM, Curtis TP, Scott K, Lloyd JR, von Canstein H. The effect of flavin electron shuttles in microbial fuel cells current production. *Appl Microbiol Biotechnol* 2010; 85:1373-1381.
- [10] Liang P, Fan MZ, Cao XX, Huang X, Wang C. Composition and measurement of the apparent internal resistance in microbial fuel cell. *Chinese J Environ Sci* 2007;28:1894–1898.
- [11] Liang P, Huang X, Fan MZ, Cao XX, Wang C. Composition and distribution of internal resistance in three types of microbial fuel cells. *Appl Microbiol Biotechnol* 2007; 77:551–558.
- [12] Ramasamy RP, Gadhamshetty V, Nadeau LJ, Johnson GR. Impedance Spectroscopy as a Tool for Non-Intrusive Detection of Extracellular Mediators in Microbial Fuel Cells. *Biotechnology and Bioengineering* 2009; 104:822-891.
- [13] Ouitrakul S, Sriyudthsak M, Charojrochkul S, Kakizono T. Impedance analysis of bio-fuel cell electrodes. *Biosens Bioelectron* 2007;23:721–727.
- [14] Manohar AK, Bretschger O, Nealon KH, Mansfeld F. The use of electrochemical impedance spectroscopy (EIS) in the evaluation of the electrochemical properties of a microbial fuel cell. *Bioelectrochemistry* 2008;72: 149–154.
- [15] Strik DPBTB, ter Heijne A, Hamelersa HVM, Saakesa M, Buismana CJN. Feasibility Study on Electrochemical Impedance Spectroscopy for Microbial Fuel Cells: Measurement Modes & Data Validation. *ECS Transactions* 2008;13:27-41.
- [16] Barsoukov E, Macdonald JR. Impedance spectroscopy, Theory Experiment and Applications. Chichester: Wiley- Interscience; 2005.



6th Iranian Fuel Cell Seminar
March 12 & 13 , 2013
Shahid Rajaei Teacher training University
Tehran - Iran



[17] Brug GJ, van den Eeden ALG, Sluyters-Rehbach M, Sluyters JH. The Analysis of Electrode Impedances Complicated by the Presence of a Constant Phase Element. J Electroanal Chem 1984; 176:275-295.



Electrochemical Study of the Energy Generation Performance of Glucose, Lactose, Sucrose and Starch as Substrates in a Mixed Culture Microbial Fuel Cell

Mir Ghasem Hosseini¹, Iraj Ahadzadeh^{2*}

Electrochemistry Research Laboratory, Department of Physical Chemistry, Faculty of Chemistry, University of Tabriz, Tabriz, Iran

mg-hosseini@tabrizu.ac.ir

Abstract

In this research, energy generation performance of glucose, lactose, sucrose and starch as substrates in a mixed culture microbial fuel cell was studied by polarization measurements and electrochemical impedance spectroscopy. Results showed that after operation with a 1000 Ω external resistance, normalized to the anode geometric surface area, output open circuit potential and power levels of the microbial cell are highest for glucose (488mV and 25.3 $\mu\text{W}/\text{cm}^2$) followed by lactose (352 mV and 7.5 $\mu\text{W}/\text{cm}^2$) then sucrose (302 mV and 5.1 $\mu\text{W}/\text{cm}^2$) and finally, starch shows considerably lower output power (158 mV and 2.1 $\mu\text{W}/\text{cm}^2$). In other words, for an anodic biofilm which was batch cultured using glucose as the initial substrate, with increasing the complexity of digestion metabolism of the employed hydrocarbon substrates, power levels of the microbial fuel cell significantly decrease which can be attributed to the feasibility of the simple hydrocarbons for biochemical digestion.

Keywords: Microbial Cell (MFC), Simple Hydrocarbons, polysaccharides, Electrochemical Impedance Spectroscopy, Ion Exchange Membrane, Mixed Culture

1 Introduction

Microorganisms naturally present at different environments can form biofilms on conductive electrode surfaces and oxidize organic matter using the electrode as direct electron acceptor. In a microbial fuel cell (MFC) any biodegradable organic material is biochemically converted to electric energy by micro-organism assisted electro-oxidation processes (Dumas et al., 2008, Thygesen et al., 2009). By the way, currently, this novel bioenergy conversion technology has many limitations such as low power output level of MFCs which is mainly due to slow reaction kinetics and high internal ohmic losses (Davis and Higson, 2007; Min and Logan, 2004; Gil et al., 2003; Liang et al., 2007). In order to enhance output power level of an MFC, study of the electrochemical processes taking place at the surface of both anode and cathode electrodes

¹Electrochemistry Research Laboratory, Department of Physical Chemistry, Faculty of Chemistry, University of Tabriz, Tabriz, Iran

²Electrochemistry Research Laboratory, Department of Physical Chemistry, Faculty of Chemistry, University of Tabriz, Tabriz, Iran, irajahadzadeh@gmail.com



through well-developed electrochemical methods and design of new material combinations for the manufacture of anode and cathode electrodes as well as choice of more efficient organic material as carbon source (substrate) are of great importance (Cheng et al., 2006a; Wei et al., 2012). MFCs can handle vast biodegradable organic materials as substrate by their anodic biofilms among them are hydrocarbons, organic simple and long chain alcohols and acids, fatty acids as well as proteins. Vast diversity of carbon sources are employed and studied in the MFCs (Mohanakrishna et al., 2010; Chae et al., 2009; Zhuang and Zhou, 2009; Pant et al., 2010; Sharma and Li, 2010). Applicability of a given source of carbon as a MFC substrate depends on its availability, bio-digestibility by the microorganisms employed and most importantly on the output power level of the MFC. Therefore it is of significant research and application interest to address the effect of changing of substrate on the performance of the MFCs with the aim better understanding of the role played by anodic biochemical reactions on the characteristics of MFC systems (Sharma and Li, 2010). In order to tackle this problem, electrochemical impedance spectroscopy (EIS), as an advanced monitoring technique, would be of great value because it can bring us with some electrochemical parameters such as anodic charge transfer resistance and electrical double layer capacitance and etc which remain inaccessible by other electrochemical methods (Guo et al., 2003; He et al., 2006;). Keeping above mentioned issues in mind, in this research, energy generation performance of α -D-glucose ($C_6H_{12}O_6$), lactose ($C_{12}H_{22}O_{11}$, a disaccharide), sucrose ($C_{12}H_{22}O_{11}$, a disaccharide) and starch (a long chain polysaccharide) as organic substrates in a mixed culture microbial fuel cell was studied by polarization measurements and electrochemical impedance spectroscopy. Anaerobic activated sludge was as mixed-culture bacterial medium and a platinum sheet was employed as the cathode.

2 Materials and Methods

2.1. Chemicals and Fuel Cell setup

Figure 1 shows one of the homemade MFC setups constructed for this research. This configuration consists of two polycarbonate plastic cylinders each of about 125 cm^3 volume with a 3 cm wide O-ring fitted aperture between them to set a 3.1 cm^2 area Flemion[®] cation exchange membrane (250 μm thickness, provided by Asahi Glass Company, Japan). Anode in the shape of a rectangle with a total geometrical area of 24.3 cm^2 was made of commercial electrical grade graphite plate. Distance between cathode and anode was 8.5 cm. All chemicals used throughout the study were of analytical grade provided by Merck (Germany) and used as received without any further treatment. Double distilled water was used to all solution preparation and rinse purposes.

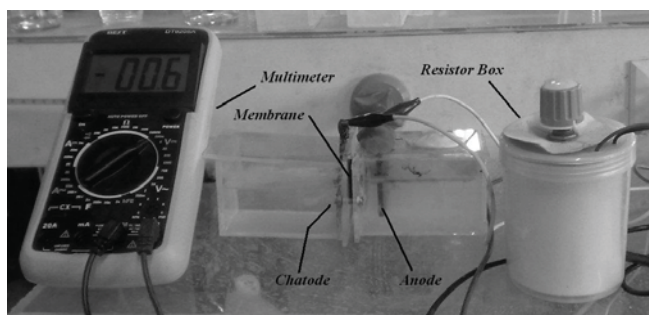


Figure 1. Photo of the homemade dual-chambered MFC setup.

2.2. Preparation of the Anode

Before initiation of the experiments, fuel cell setups was immersed in a KMnO_4 solution (3 gL^{-1}) for 24 h in order to disinfect the anode and cathode chambers prior to any bacterial inoculation in the anode compartment. After three times rinse with double distilled water, cation exchange membrane was fitted between anodic and cathodic parts using three stainless steel screws. Catholyte and anolyte solution composition was as follows: 60 mM biological phosphate buffer solution (PBS) with $\text{pH}=7.4$, MgSO_4 (0.9 g/L) and NH_4Cl (1 g/L) and 0.1 ml/L trace essential elements solution. Prior to the insertion of the graphite anodes into the anolyte, the biofilm was formed on graphite anodes in a batch procedure as follows: The graphite anodes were immersed separately in a solution with the composition of the anolyte along with 1 g/L glucose as the initial substrate and 1 ml of urban waste water (Tabriz) sludge as mixed culture bacterial source, while kept stirred for 24 h in anaerobic condition. Aerobic condition was achieved by bubbling pure nitrogen gas into the solution for 0.5 h after which the setup was kept sealed using proper gas tight miniature taps. Stirring was aimed to produce a gentle sheer on the surface of the anode with the hope of obtaining a more compact and active biofilm. After fitting the anodes covered with biofilm and adding 100 mL of the anolyte solution containing respectively 1 g/L of glucose, lactose, sucrose and starch, into the anodic sections of the four MFC setups, anaerobic condition was further observed in the anodic compartments by sealing all apertures around the anode by water-proof silicone sealant. The cathodic chamber was air-bubbled by an air-stone dispenser at a rate of about 1 L/min using an aquarium fish pump. All of the fuel cells were kept at room temperature of $27 \pm 1^\circ\text{C}$. A platinum sheet with a geometric area of about 25 cm^2 was employed as the cathode which catalyses the reduction reaction of the dissolved oxygen at the cathode.

2.3. Polarization measurements

Polarization measurements were performed using an externally connected homemade precision (1% tolerance)-resistor box to the anode and cathode of the MFC and recording the potential drop across the load resistor. Variation range of the resistor box was from $2 \text{ M}\Omega$ to 10Ω . All potential records were performed using a high input impedance ($10 \text{ M}\Omega$) commercial 3.5 digit voltmeter. Sufficient time interval, typically 10 min, was observed after each change in resistor box value to obtain a stable potential reading. Short circuit current was measured using a 3.5 digit commercial ammeter with 2 mA full range. It should be mentioned that due to large electrical load imposed on the cell during short circuit conditions, immediately after each

measurement of the short circuit current, cell was allowed to work with highest external resistor (2 M Ω) for a sufficient time, typically 30 min, to reach the previous steady state ready to other subsequent polarization measurements.

2.4. Electrochemical impedance

Electrochemical impedance spectrum was recorded at different operation intervals using an EG&G Princeton applied Research Parstat 2263 advance Electrochemical System (USA) from frequency of 100 kHz down to 0.02 Hz at open circuit (external resistor load disconnected) condition. Impedance measurements were performed for the anode of the microbial fuel cell. In order to measure impedance of the anode, the working and counter terminal of the EIS instrument were connected to the anode and cathode, respectively while a saturated Calomel electrode (SCE) was inserted into the anodic compartment, i.e. a conventional three-electrode configuration was adopted.

3 Results and discussion

3.1. Polarization measurements

Figures 2 and 3 respectively show the voltage-current density (V - J) and power-current density (P - J) polarization curves of the MFC with various hydrocarbon sources, after 36 h operation with 1000 Ω external resistor.

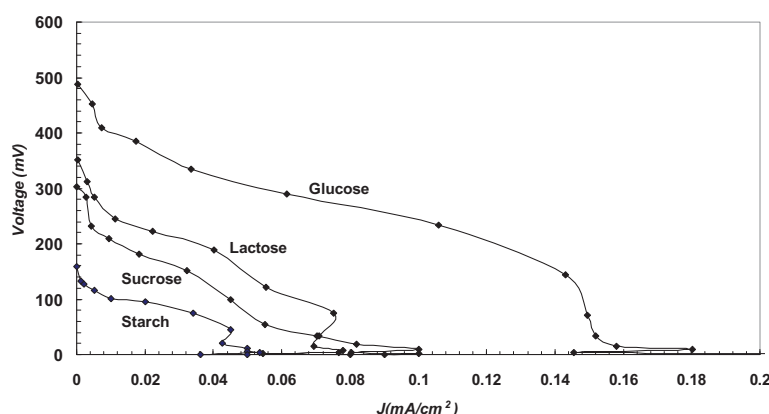


Figure 2. Potential polarization curves of the MFCs with different substrates after 36 h operation with a 1000 Ω external resistor.

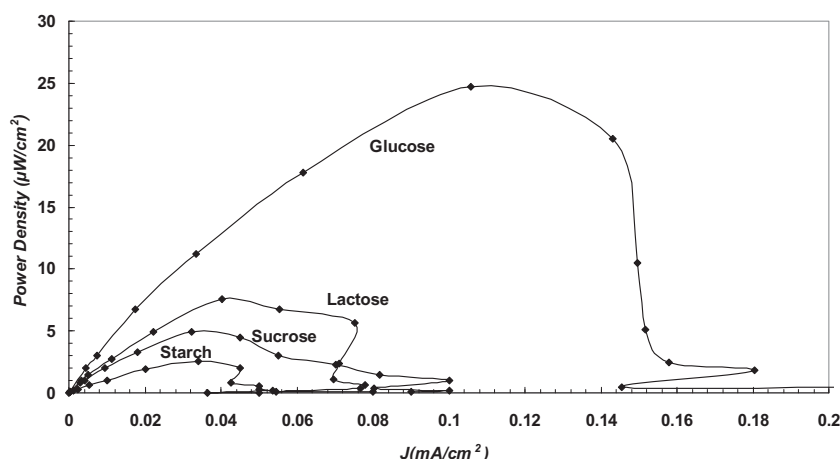


Figure 3. Power polarization curves of the MFCs with different substrates after 36 h operation with a 1000 Ω external resistor.

Also values of MFC open circuit potential (OCP), short circuit current density (J_{sc}), and power density (P) for the studied cathodes are reported in Table 1.

Table 1. Polarization results of the four MFC setups with different feeds.

Feed	OCP (mV)	J_{sc} (mA/cm ²)	P (μ W/cm ²)
Glucose	488	0.162	25.3
Lactose	352	0.092	7.5
Sucrose	302	0.088	5.1
Starch	158	0.051	2.1

Also, Figures 4 and 5 show time variations of current density and power density of the MFC, respectively. From Figures 2 and 3 and according to Table 1, one can see that glucose substrate exhibits highest J_{sc} and OCP so the maximum output power level. The next one is the lactose substrate followed by sucrose and finally starch substrate results in much lower J_{sc} and OCP so the minimum output power level. As indicated in Table 1, the maximum output power levels of the MFCs are about 25.3 mW/cm² for glucose, 7.5 mW/cm² for lactose, and 5.1 mW/cm² for sucrose and finally 2.1 mW/cm² for starch normalized to the anode geometric surface area. Open circuit potential and output power level of glucose substrate with Pt cathode as studied in this research is in accordance with those reported for other rather similar MFC setups in the literature, i.e. 309 mW/m² for anode surface area with Pt doped carbon cloth (0.5 mg, 10% Pt), 3.9 mW/m² again normalized to anode surface area for solid graphite cathode (Cheng et al., 2006b).

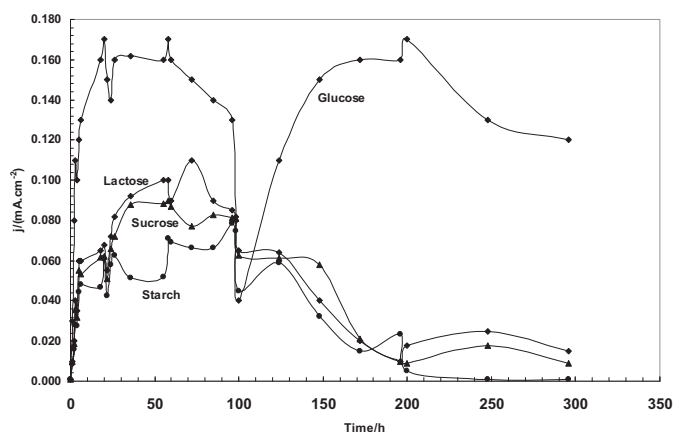


Figure 4. Time variation of short circuit current density of the MFCs with different substrates operated with a 1000 Ω external resistor.

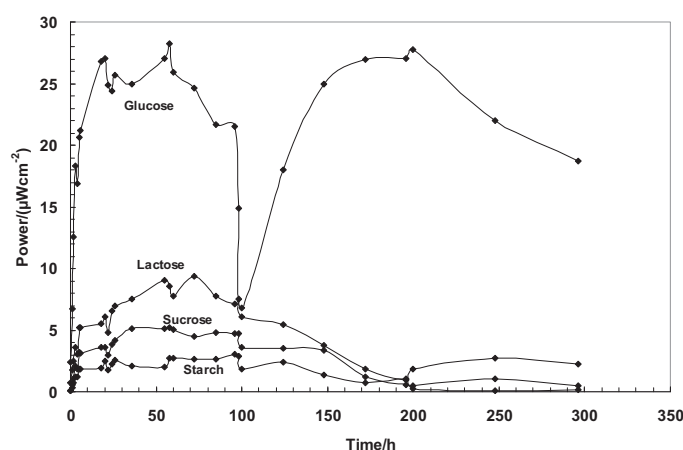


Figure 5. Time variation of power density of the MFCs with different substrates operated with a 1000 Ω external resistor.

From Figures 4 and 5, it is clear that the MFC with glucose substrate reaches its maximum current and power levels much faster than other substrates. Also, it can be seen from Figures 4 and 5 that current and power levels of the MFC with glucose substrate start to decline after about 70 h. After draining of anodic solution and filling the anodic compartment with fresh anolyte at 72 h, both current density and power of the MFC start to increase again reaching roughly previous peak values after about 200 h of operation. According to Figures 4 and 5, a similar trend is not observed for other substrates. These findings can be attributed to the fact that glucose as a light substrate can be easily oxidized and therefore applied by anodic biofilm microorganisms as an organic fuel, so it is consumed in a rather short time. On the other hand, in comparison with glucose, heavier substrates and particularly starch which is a long chain polysaccharide are not easily consumable by microorganisms, so they produce much lower current and power and also due to their slow anodic kinetics, their biodegradation takes longer time to proceed.

3.2. Electrochemical impedance spectroscopy

Nyquist complex impedance plots of the anodes of the MFCs with different substrates are given in Figure 6. Performance parameters such as solution ohmic resistance (R_s) i.e. resistance of the anolyte solution between anode and reference electrode, anodic charge transfer resistances (R_a) and its corresponding anodic electrical double layer pseudo-capacitances (Constant Phase Elements i.e. CPE_a) were extracted after fitting of the impedance data on the circuit shown in Figure 7 which is the system's electrical equivalent circuit.

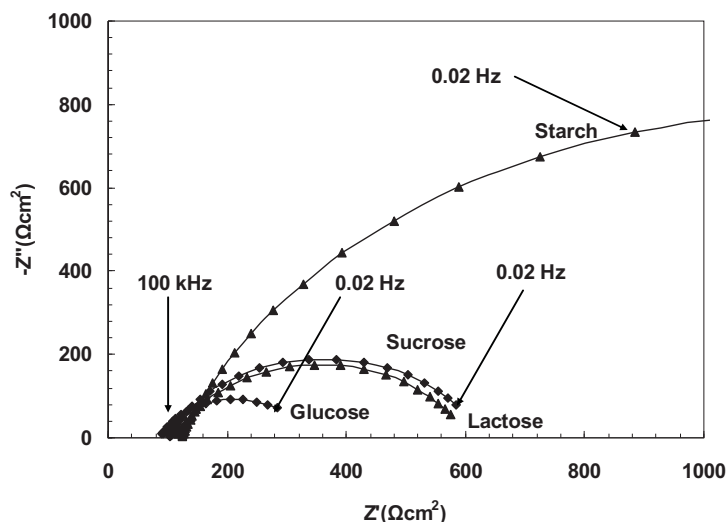


Figure 6. Fitted Nyquist impedance spectra of the MFCs after 36 h work with 1000Ω external resistance.

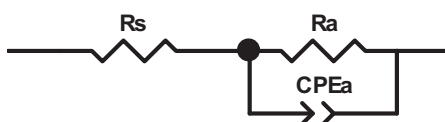


Figure 7. Electrical equivalent circuit (EEC) of the anode electrode of the MFCs which used for analysis of EIS spectra.

This electrical equivalent circuit was designed on the basis of physicochemical model of the anode of a microbial fuel cell composed of an anode electrode in contact with electrolyte solution (Ouitrakul et al., 2007). Table 2 shows the values of electrical circuit elements derived by fitting the experimental data on the electrical equivalent circuit of the Figure 7. Fitting and analysis of the EIS data were performed by ZSimTM software.

Table 2. Electrochemical impedance parameters of the four MFC setups with different feeds after 36 h work with 1000 Ω external resistance.

Feed	R_s (Ω)	R_a ($\Omega \cdot \text{cm}^2$)	$CPEc-T$ $\times 10^4$	$CPEc-n$
Glucose	88	252	3.17	0.93
Lactose	115	485	3.12	0.81
Sucrose	103	522	2.95	0.91
Starch	126	2133	3.18	0.89

From EIS data analysis some interesting remarks could be extracted. As it can be seen from Table 2, the $CPEa-T$ values, which are direct indications of the anode/solution interface capacitance magnitude, are rather similar for all four studied substrates. Similar behavior can be seen for the values of the $CPE-n$ parameter which is inversely proportional to the non-homogeneity and roughness of the anode electrode surface covered with biofilm. At this time, due to inherent complexity of the anode/biofilm/solution interfaces and lack of detailed knowledge about microorganism/ anode interactions, we are unable to account for this trend in the variation of anodic double layer capacitance parameters and therefore further research is needed to understand this corner (Lanthier et al., 2007). As is clear from Figure 6 as well as Table 2, values of the anodic charge transfer resistances for the anode/electrolyte interface (R_a), which are inversely proportional to the substrate bio-assisted oxidation reaction rate, show an increasing trend from glucose to lactose and then to sucrose and, finally, starch shows the highest anodic charge transfer resistances. These EIS-based findings support the trend of the variation of power level as indicated by polarization measurements and also time trend of the variations in current and power densities of the MFCs. Also this trend of variation of power density for different substrates and its interpretation in terms of increasing metabolism complexity was observed and supported by similar studies on glucose, xylose and acetate with humic acid as a mediator (Thygesen et al., 2009).

4 Conclusions

The main conclusions of the present study are as:

- 1) The power density and open circuit cell potential obtained from Glucose substrate is significantly higher than other hydrocarbons in particular the starch which is a heavy polysaccharide. This fact can be in principle attributed to the adaptation of the anode microorganisms to the glucose substrate which was initially used for bath culture. Also these findings can be interpreted in terms of the simplicity and more feasible metabolism of the monosaccharide and disaccharides compared with high molecular weight polysaccharides.



2) Trend of the variation of power density as measured by polarization measurements are in accordance with the EIS findings. In other words for an easily oxidizable substrate like glucose which produces highest power density, the anodic charge transfer resistance as measured by EIS is the least and for starch which results in the lowest power density the corresponding anodic charge transfer resistance has the highest value. Therefore anodic charge transfer resistance which is a part of the MFC total internal resistance has an inverse effect on the power level of the MFC.

3) EIS reveals itself as a promising electrochemical tool to study the effect(s) of any modification and/or enhancement of materials on the power density of MFC systems and to find the most efficient substrate-microorganism combination in terms of MFC output power level and durability.

References

Chae, K.J., Choi, M.J., Lee, J.W., Kim, K.Y., Kim, I.S., 2009. Effect of different substrates on the performance, bacterial diversity, and bacterial viability in microbial fuel cells. *Bioresour. Technol.* 100, 3518-3525.

Cheng, S., Liu, H., Logan, B.E., 2006a. Increased performance of single-chamber microbial fuel cells using an improved cathode structure, *Electrochem Commun.* 8, 489-94.

Cheng, S., Liu, H., Logan, B.E., 2006b. Power densities using different cathode catalyst (Pt and CoTMPP) and polymer binders (Nafion and PTFE) in single chamber microbial fuel cells. *Environ. Sci. Technol.* 40, 364-9.

Davis, F., Higson, S.P.J., 2007. Biofuel Cells—recent advances and applications, *Biosens. Bioelectron.* 22, 1224-35.

Dumas, C., Mollica, A., Féron, D., Basseguy, R., Etcheverry, L., Bergel, A., 2008. Checking graphite and stainless anodes with an experimental model of marine microbial fuel cell. *Bioresour. Technol.* 99, 8887-8894.

Gil, G.C., Chang, I.S., Kim, B.H., Kim, M., Jang, J.K., Park, H.S., Kim, H.J., 2003. Operational parameters affecting the performance of a mediator-less microbial fuel cell. *Biosens. Bioelectron.* 18, 327-334.

Guo, J.W., Mao, Z.Q., Xu, J.M., 2003. Studies on the electrochemical behavior of polymer electrolyte membrane fuel cell (PEMFC) by AC impedance method. *Chem. J. Chin. Univ.* 24, 1477-1481.

He, Z., Wagner, N., Minteer, S.D., Angenent, L.T., 2006. An upflow microbial fuel cell with an interior cathode: assessment of the internal resistance by impedance spectroscopy. *Environ. Sci. Technol.* 40, 5212-7.

Lanthier, M., Gregory, K.B., Lovley, D.R., 2007. Electron transfer to electrodes with high planktonic biomass in *Shewanella oneidensis* fuel cells. *Microbiol. Lett.* 278, 29-35.

Liang, P., Huang, X., Fan, M.Z., Cao, X.X., Wang, C., 2007. Composition and distribution of internal resistance in three types of microbial fuel cells. *Appl. Microbiol. Biotechnol.* 77, 551-558.



- Min, B., Logan, B.E., 2004. Continuous electricity generation from domestic wastewater and organic substrates in a flat plate microbial fuel cell. *Environ. Sci. Technol.* 38, 4900–4904.
- Mohanakrishna, G., Mohan, S.V., Sarma, P.N., 2010. Bio-electrochemical treatment of distillery wastewater in microbial fuel cell facilitating decolorization and desalination along with power generation. *J. Hazard. Mater.* 177, 487-494.
- Ouitrakul, S., Sriyudthsak, M., Charojrochkul, S., Kakizono, T., 2007. Impedance analysis of bio-fuel cell electrodes. *Biosens. Bioelectron.* 23, 721–727.
- Pant, D., Bogaert, G.V., Diels, L., Vanbroekhoven, K., 2010. A review of the substrates used in microbial fuel cells (MFCs) for sustainable energy production, *Bioresour. Technol.* 101, 1533-1543.
- Sharma, Y., Li, B., 2010. The variation of power generation with organic substrates in single-chamber microbial fuel cells (SCMFCs). *Bioresour. Technol.* 101, 1844-1850.
- Thygesen, A., Poulsen, F.W., Min, B., Angelidaki, Irini., Thomsen, A.B., 2009. The effect of different substrates and humic acid on power generation in microbial fuel cell operation. *Bioresour. Technol.* 100, 1186–1191.
- Wei, L., Yuan, Z., Cui, M., Han, H., Shen, J., 2012. Study on electricity-generation characteristic of two-chambered microbial fuel cell in continuous flow mode. *Int. J. Hydrogen Energy* 37, 1067-1073.
- Zhuang, L., Zhou, S., 2009. Substrate cross-conduction effect on the performance of serially connected microbial fuel cell stack. *Electrochem. Commun.* 11, 937-940.

Design and constructing DC-DC convertor with Ripple-mitigating for fuel cell system

Mahnaz , Hamid ChaychiAmir khiz, Davoud BageriAzarfam, Farid Jafazadeh, Jafar Agazadeh shahsavari

Tabriz, Iran·Young Researchers and Elite Club, Tabriz Branch, Islamic Azad University

Agazadeh_Jafar@yahoo.com

Abstract:

Proton exchange membrane system of fuel system needs ripple mitigation and influence of ventilation system to be used in residential applications. The main issue to achieve this goal is to design and control a DC-DC convertor. According to traditional convertors theoretical and experimental analysis, this article is to propose a DC-DC convertor balanced circuit of complete series Pole (P-SFB) and improves that design phase change. More over in this article we proposed a new controller to low frequencies stream of applied ripple in convertor. Confirming experimental results show peak efficiency of DC-DC convertor up to 95.5% as a result maximum efficiency of PCS reaches to 92.9%. And input undulated current is reduced drastically with new controllers.

Key words: efficient, undulated, mitigation, convert

Introduction:

Environmental and economical concerns regarding power production and energy consumption have been increased and photo volatile panels and fuel piles are replaced with electrical energy sources. These sources are small and the basic solution distributed generation. Although this creates similarly low range and Different DC voltage with depending load, in applications connected to network or separated ones; power generator needs a change in output generator from a standardized power generator. Hence power generator has other characteristics including power quality improvement and ipmroves using electrical energy generators.

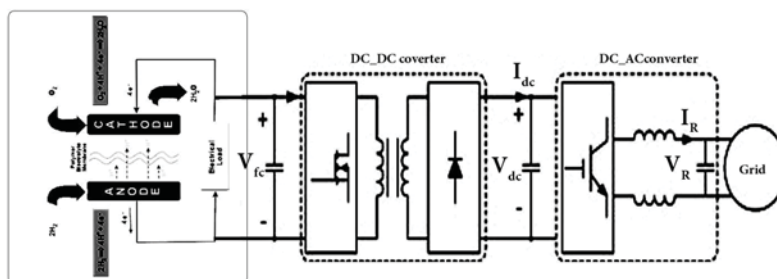


figure 1. Block diagram of PEMFC PCS in residential application

Stack output of fuel pile proton exchange membrane and ventilation system power output and lower DC voltage is accompanied with vast diversity. So in ventilation system power there is a need to connection between mound and load. To

convert lower DC voltage to 60 Hz and 240/120 v we need AC voltage. More over in diagram block, ventilation system power was proposed to residential applications. As an example it has been shown in figure1.

At first stage step by step till DC-DC convertor of lower voltage fuel pile increase to DC voltage link was almost 350 volt and in second stage DC-AC convert investors are changed to DC voltage link and Ac voltage. Electricity network is connected to invertors output to be supported.

Dc-DC convertor is to achieve efficient PCS and reduce in ripple. Most DC-DC converters have been proposed and investigated during last decades. A supporting voltage with complete pile, relatively high transformor along with a rectifier diode has been proposed to fuel cell applications in figure2.

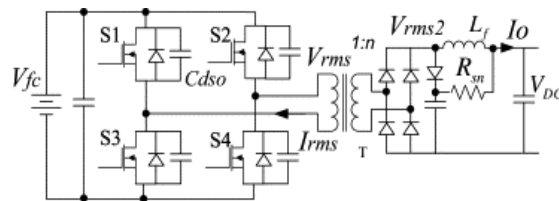


Fig 2. FB converter topology

It is believed that suitable complete typology is used in green power applications to medial power. Figure 3

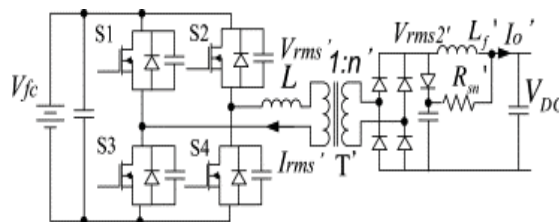


Fig 3. PSFB converter topology

Indicates complete pile phase change (PSFB) of convert typology. This FB converter has been attached to main circuit along with leakage inductance. In this method it is expected that switching wastes which are reduced after zero voltage switching would be obtained after transmitting modulation phase. In this article we have provided upper complete pole analysis and power waste PSFB convert in fuel pile applications with theoretical and experimental coordinates at first stage. Using results, we have provided new design of balanced and full bridge series (P-SFB) of DC-DC convertor. New convertor efficiency is valid. More over both theoretically and experimentally it has been used at 1.2 kilo vat of fuel cell. Now the main issue related to DC-DC convertor is that of low frequency impeding rippling.

$$\frac{1}{2} L_{\sigma} I_{rms}^2 > C_{dso} V_{fc}^2 + \frac{1}{2} C_{TR} V_{fc}^2$$

Fuel Cell DC-DC convertor control has been presented to prevent lower frequencies rippling. This controller is composed of two rings including a control ring outside DC link voltage and



another has been installed inside control link of inductance output current. Two ringed control of some mitigation ripple currents is different from DC link voltage aspect compared to common ringed control.

Now in this article we have provided ripple mitigation, DC-DC convertor control. At present time using DC-DC input convertor with one ring to control, suppresses currency rippling.

Comparing waste power of FB and PSFB convertor:

Power waste in FB and PSFB convertors is mainly of transistor semiconductor metal oxide, transformers field effect, rectifier diode and side and back circuit type. MOSFET wastes can be divided into conducting wastes and switching wastes. PSFB phase change modulation and goal or target convert has been carried out to reduce MOSFET switching wastes. At same time it mitigates the convert. Power transition convertor capability is due to leakage inductance. Hence we have increased currency and power and Trans torsion. These above mentioned greater amounts of wastes will result in lower input voltage and higher current of cell pile. In this section we will compare higher power waste and then will evaluate efficiency degree of PSFB convertor on FB convertor when PEMFC is used in 1.2 kilo vat of PCS. In PSFB convertor to carry out ZVS procedure and to compensate L6 we need to use following equation. (1)

$$\Delta D = \frac{2L_{\sigma}}{n^2 V_{fc} T_s} \left[2I_{\sigma} - \frac{V_{fc}}{L_f} (1-D) \frac{T_s}{2} \right]$$

This shows that higher L and lower C DSO is suitable for expanding ZVS domain. In spite of this, L6 results in wastes of convertor coefficient ratio. This has been shown in figure 2.

$$P_{CU-T}' = (I_{rms})^2 \cdot R_{wire-T}' > P_{CU-T} = (I_{rms})^2 \cdot R_{wire-T}$$

$$P_{CM}' = I_{TMS}^2 \cdot R_{ms} > P_{CM} = I_{TMS}^2 \cdot R_{ms}$$

Paying attention to formula (2) power transition capability from PSFB has been reduced. Hence transformer convert ratio needs increase in N'. Increase in transformer copper wastes ratio is bigger than first side MOSFET conduct wastes. These have been shown in figures 3, 4. Wastes higher that rectifier diode and side circuit have been shown in following figure. This is specially grater for fuel pile PCS drastically.

Theoretical and experimental derivations are confirmed in this section. Used parameters in experiment have been shown in table (1).

V_{FC}	30-70 V
V_{DC}	350 V
power	1.2 Kw
I_{FC}	40 AMAX
F	30 Khz
L_{σ}	20 μ H
L_F	500 μ H
Diod	1200 V
Ron	6 m Ω

Table (1): Fuel cells convert settings.

Experimental results have been shown in figure 4. Just 3w of whole switching wastes are mitigated by phase change modulation in ZVS range of 1200 w convertor. So PSFB convertor just improves efficiency through little amount and just when power is larger than 1 kW.

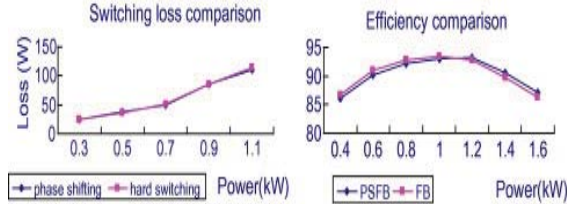


Fig 4. Switching loss and total efficiency compare

3. Converter design and waste comparison with PSFB. According to researches carried out, we have proposed an efficient method and P-SFB has been shown in figure 5.

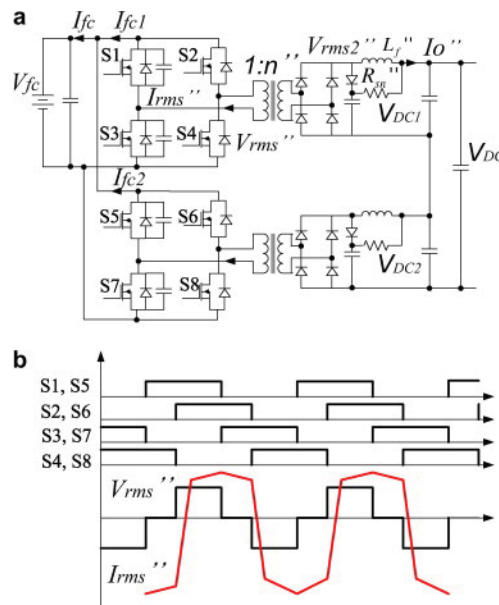


Fig 5. P-SFB topology and phase shifting signal. (a) Topology and (b) phase shifting modulation

Main power stage is composed of two traditional FB balance convertors in DC entry and a set in connected rectifier output. As it can be seen in figure 5 modulation phase change is for setting output voltage. Each bridge function in switching frequencies moves towards half of output process neck to neck to phase change. More over two capacitors balance with our two is to reduce switching wastes respectively.

It is a proposed unique typology in which modulation phase change is used without installing leakage inductance. Since wastes ratio in P-SFB and transformer change ratio (N) in side little convertors is less than N/2, so current peak and secondary side voltage reduces. Voltage amount in rectifier diodes can be increased from 600 w to 1200 w in PSFB convert. So as it can be seen wastes in transformer, rectifier diode and side circuit reduces.

Wastes of switching diode rectifiers are expressed as following relation.

$$(9) P_{S,RFD}^w = \frac{Q_{rr2} V_{jc} t_{rr}^e}{2T} < \frac{P_{S,RFD}^c}{2}$$

Side circuit wastes reduce.

$$(10) P_{SK}^w = \frac{V_{SK}^2}{R_{SK}} < \frac{P_{SK}^c}{2}$$

4-Ripple mitigation to control P-SFB convert

1-4 Low PCS ripple dispersion

Now it is believed that output dispersion and production of inverter at lower frequency ripples has been shown in figure 6.

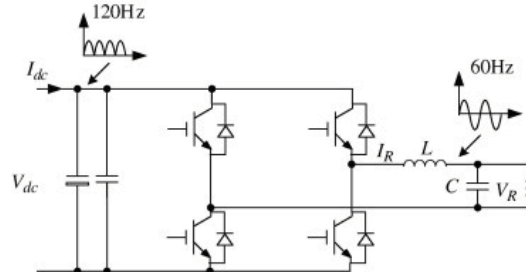


Fig 6. Low frequency ripple current generated by H-bridge inverter

Output self inverter is a sinus linear load as output voltage, while it is input voltage and DC current components. This is while I_{dc} current involves 120 hertz and a wave obtained from power wave of single phase inverter. More over now rippling is continuously carried out through DC-DC convertor and has been dispersed through turning to fuel cells. Using a sample experiment of designed 1.2 PCS, this experiment indicates that observed peak to peak ripple equals 30%. Unlike other PCS now current rippling leads not only in reduce of PCS output capability, but also it results in fuel consumption. If rippling speed is 30% it shows that fuel has been consumed 15% more. More over it is believed that current ripple is harmful to fuel cell longevity.

2-4 Lower frequency method in controlling DC-DC converts in ripple mitigation

In this controller DC-DC convertor is controlled by a ring in output. This is to achieve quick and accurate response and reduce in ripple. More over D-Q output current controlling inverter is used in rotational coordinates which is to complete DC voltage link and inverter controlling output current. Figure 7 shows diagram block of PCS controller wave, controlling input current in sampled I_{fc} 7 and follows fuel pile current structure.

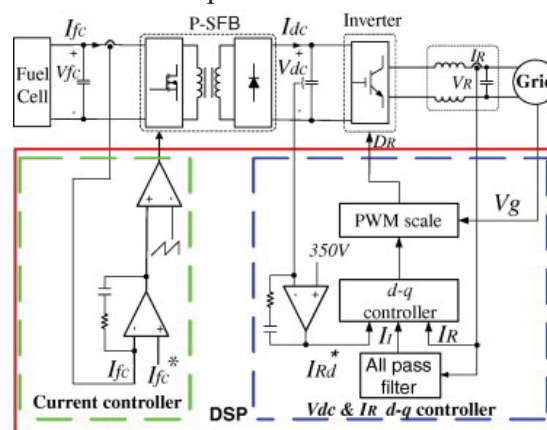


Fig 7. Block diagram of ripple current suppressing PCS controller.

Doing so currently rippling in DC side is lower. It is expected that from downward input DC current is traced directly to upward side or current. P-SFB is calculated neck to neck with

angle phase change through DSP according to D output capacity, PI compensating input is currently shown as following relation in figure 8.

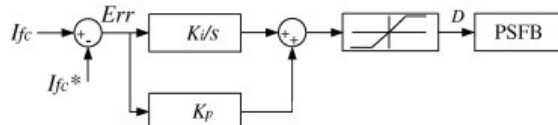


Figure 8: P-SFB controlling

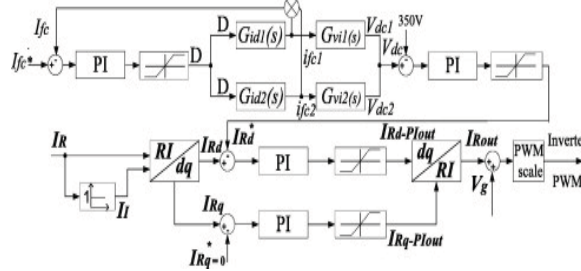


Fig9. The novel ripple current suppressing PCS controller.

Simulation enables almost 350 volt to connect inverter to electricity network. Sampling IR current inverter output and 90 degree toward after phase and creating a filter to produce a virtual current of I₁ from DQ we need at least two variables Figure9: suppressing ripple of PCS control

5. Small signal and analyzing P-SFB convertor function

So tank circuit equity of each convertor can be easily recognized and we will carry out circuit condition analysis almost during switching priod.

Using la plus convert, we can control function rings of convert transition small signals. (15)

$$G_{mi}(S) = \frac{\hat{i}_{fc1}}{\hat{d}} = \frac{V_{fc} \cdot R \cdot (-RLCS^2 - LS - R + 1)}{R(RLCS^2 + LS + R)}$$

DC voltage link to function input of small transition signal (16)

$$G_{mi}(S) = \frac{\hat{V}_{dc1}}{\hat{i}_{fc1}} = \frac{R}{(-RLCS^2 - LS - R + 1)}$$

Regarding to V convertor transition function of has been shown in figure 17.

Under input current stimulation of C_{DC} achieves 350 volt and then we can connect inverter to power network. At the same time DC output voltage link compensating PI on D basis is added as inverter instruction. (18)

$$I_{ref}^* = \left[\frac{R \cdot I_{fc}}{(-RLCS^2 - LS - R + 1)} - 350 \right] \cdot C_1(S)$$

6. Experimental results

One primary sample of PCS PEMFC 1.2 k v convertor has been developed. Presented typology has been investigated and mitigation ripple has been controlled. DC-DC convertors have been carried out using 100 volt switches and MOSFET. This has some advantages which operates at 30 kilo hertz of switching frequencies and each transformer ratio is converted with high frequencies whose ratio is 12:13 Complete Bridge of inverter from 600 volt has IGBT which uses PWM mono polar modulation in 15 hertz frequencies. Allowed voltage for fuel pile is 40 V_{fc} while operation voltage range is 30-70 volt. Proposed controller in this article

has been programmed and has been platformed to TMS320F2808 DSP. Efficiency measurement has been carried out by 3000 wt analysis power.

Figure 11: Leading leg MOSFET switching signals and loss

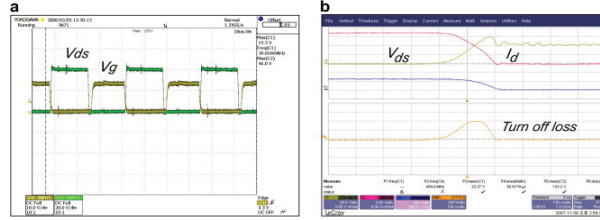


Figure 12: Lagging leg MOSFET switching signal and loss

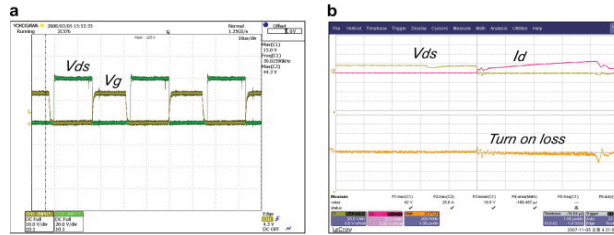


Figure 13: Leading leg MOSFET turn off loss reduced by C_{dso} . (a) $C_{dso} = 3 \text{ nF}$ (b) $C_{dso} = 15 \text{ nF}$ (c) $C_{dso} = 40 \text{ nF}$

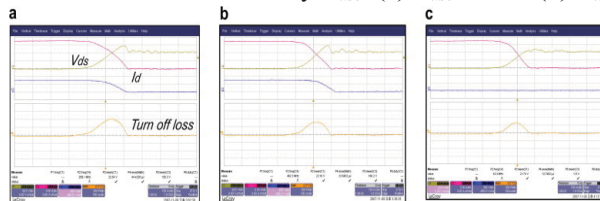


Figure 14: P-SFB efficiency test results

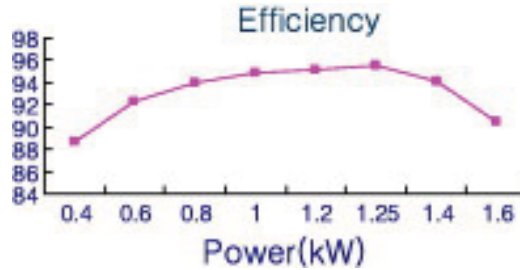
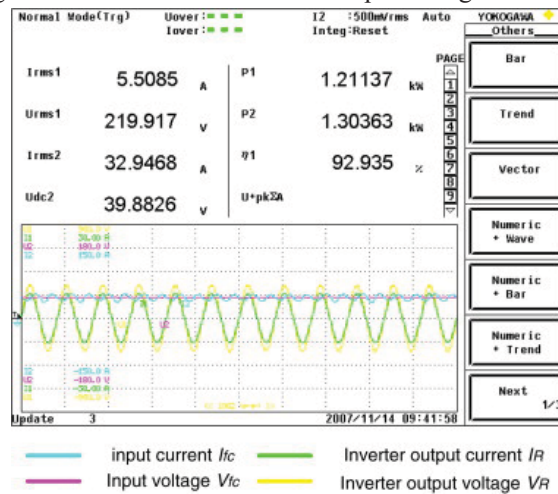


Figure 15: dc-dc sub-converter 1 output voltage and current



The experimental results for efficiency test have been indicated in figure 14. This shows that P-SFB convert efficiency is higher than FB or PSFB compared to figure 4 has higher improved

efficiency power range and extends it to maximum efficiency of 95%. Hence maximum 92.2 efficiency in 1.2 kilo watt has been shown in figure 16.

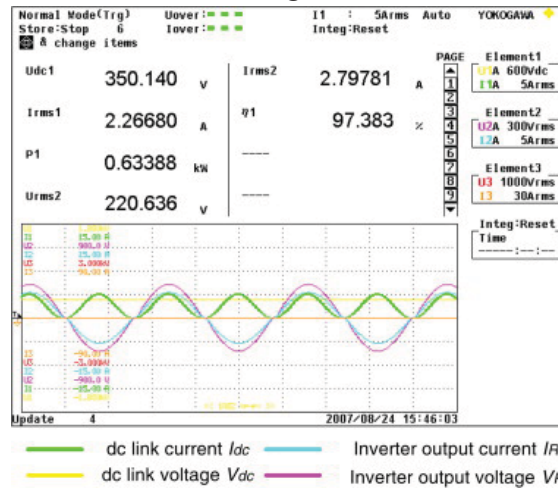
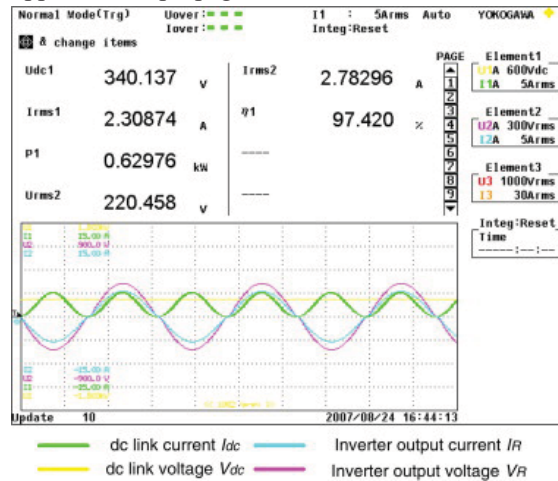


Figure (16): Ripple current propagation to fuel cell with conventional controller



Figures 17: Ripple current propagation to dc link with conventional controller

Indicate current output ripple through inverter and common controlling of PCS convertor. Here DC-DC convertor has been controlled with DC voltage link ring and inverter through output ring. DC switches ripple shape shows 7-5 or almost 80% of rippling. Hence ripple amount is almost 30% in I_{fc}

7. Conclusion:

In this article we have examined and calculated power waste analysis from complete bridge when it is located at a residential PEMFC system. According to experimental results and theoretical derivation we have proposed higher efficiency of DC-DC convertor called complete balanced series bridge and we have proposed a new method to control and omit ripple used on it. Maximum efficiency of DC-DC convertor reached at 95.5 and maximum total efficiency of PCS reaches at 92.2%. Input current ripple with lower frequency reduced from 30% to 3%. So it provides DC-DC convert ripple influence and reduce in residential fuel pile applications.

References:

[1] J. Wang, F.Z. Peng, J. Anderson, A. Joseph, R. Buffenbarger Low cost fuel cell converter system for residential power generation IEEE Trans Power Electron, 19 (5) (2004), pp. 1315–1322



- [2] Averberg A, Mertens A. Analysis of a voltage-fed full bridge DC–DC converter in fuel cell systems. In: IEEE 38rd power electronics specialists conference (PESC'07). Orlando, USA; June 2007.
- [6] Wang J, Reinhard M, Peng F.Z, Qian Z. Design guideline of the isolated dc–dc converter in green power applications. In: Power electronics and motion control conference. Xi'an, China; August 2004.
- [7] H. Xu, L. Kong, X. Wen Fuel cell power system and high power dc–dc converter IEEE Trans Power Electron, 19 (5) (2004), pp. 1250–1255
- [8] S. Moisseev, K. Soshin, M. Nakaoka Tapped-inductor filter assisted soft-switching pwm dc–dc power converter IEEE Trans Aerospace and Electron Syst, 41 (1) (2005), pp. 174–180
- [9] Choi W, Enjeti PN, Howze JW. Development of an equivalent circuit model of a fuel cell to evaluate the effects of inverter ripple current. In: Applied power electronics conference. Anaheim, USA; February 2004.
- [10] De Caro, Testa S, Triolo A, Cacciato D, Consoli M. Low input current ripple converters for fuel cell power units. In: 2005 European conference on power electronics and applications. Dresden, Germany; September 2005.
- [11] C. Liu, J.S. Lai Low frequency current ripple reduction technique with active control in a fuel cell power system with inverter load IEEE Trans Power Electron, 22 (4) (2007), pp. 1429–1436
- [12] Roshan Arman, Burgos Rolando, Baisden Andrew C, Wang Fred, Boroyevich Dushan. A $d-q$ frame controller for a full-bridge single phase inverter used in small distributed power generation systems. In: Applied power electronics conference. Anaheim, USA; February 2007.
- [13] Zhang R, Cardinal M, Szczesny P, Dame M. A grid simulator with control of single-phase power converters in D-Q rotating frame. In: Power electronics specialists conference. Cairns, Australia; June 2002.



Studies of DFT modeling of methanol oxidation in fuel cell.

Javad Beheshtian ,Elena Yashmi ,Rasol Abdullah Mirzaie

Dep of chemistry, Faculty of science, Shahid Rajaee Teacher Training University, Tehran, Iran

Abstract:

Increasing demand for energy ,energy security and the need to minimize the impact on the environment related to the energy are the major drivers for the research and development of alternative energy technologies. In order to these reasons we research to the polymer electrolyte membrane fuel cell (PEM) that emphasizes density functional theory which calculates methanol oxidation on Pt₄

Keywords:Platinum; methanol; Density functional theory; Computational method.

Introduction:

Fuel cells are electrochemical cells in which both fuel and oxidant are fed in a continuous supply to the electrodes. They are attractive sources of electrical power since the production of electrical energy can be maintained as long as the reactants are supplied to the electrodes. This concept was first proposed in 1839 by Sir W. R. Grove, and direct conversion of chemical to electric energy in a hydrogen/oxygen fuel cell was demonstrated. Although hydrogen/oxygen fuel cells are used in spaceships, wider applications in traction-based vehicles (for example, electric cars) are limited by unsolved problems such as transport and storage of hydrogen. Liquid fuels would solve this problem; however, extracting molecular hydrogen from a liquid fuel requires a reformer. This greatly increases the overall cost of the cell, reducing the fuel conversion efficiency.

An alternative to H₂ is the use of a liquid fuel such as methanol supplied directly to the anode and electrooxidized to CO₂. Indeed, recent results for model direct methanol fuel cells (DMFCs) show that critical performance parameters for commercial use are now achievable with modern catalytic formulations and cell designs. A simple schematic of the DMFC is shown in Figure 1. The fuel (methanol and water) is passed through the anode, and the oxidant (O₂ in air) flows through the cathode. The two electrodes are separated by a proton exchange membrane such as Nafion. Platinum-based electrodes demonstrate the highest



catalytic activity and cleanest combustion products. Since engines operate at high temperatures, this whole system will be in an “oven-like” setting. The design and Fuel cells are electrochemical cells in which both fuel and oxidant are fed in a continuous supply to the electrodes. They are attractive sources of electrical power since the production of electrical energy can be maintained as long as the reactants are supplied to the electrodes. This concept was first proposed in 1839 by Sir W. R. Grove, and direct conversion of chemical to electric energy in a hydrogen/oxygen fuel cell was demonstrated. Although hydrogen/oxygen fuel cells are used in spaceships, wider applications in traction-based vehicles (for example, electric cars) are limited by unsolved problems such as transport and storage of hydrogen. Liquid fuels would solve this problem; however, extracting molecular hydrogen from a liquid fuel requires a reformer. This greatly increases the overall cost of the cell, reducing the fuel conversion efficiency. An alternative to H₂ is the use of a liquid fuel such as methanol supplied directly to the anode and electrooxidized to CO₂. Indeed, recent results for model direct methanol fuel cells (DMFCs) show that critical performance parameters for commercial use are now achievable with modern catalytic formulations and cell designs.¹ A simple schematic of the DMFC is shown in Figure 1. The fuel (methanol and water) is passed through the anode, and the oxidant (O₂ in air) flows through the cathode. The two electrodes are separated by a proton exchange membrane such as Nafion. Platinum-based electrodes demonstrate the highest catalytic activity and cleanest combustion products. Since engines operate at high temperatures, this whole system will be in an “oven-like” setting. The design and construction of high-performance DMFCs is already undergoing optimization.[1] An obvious advantage of the DMFC over the internal combustion engines is to avoid the environmental damage caused by the latter. The alternative use of batteries could, in principle, operate a vehicle without unwanted emissions; however, current batteries also have environmental problems and require constant recharging. The DMFC, on the other hand, can provide a continuous supply of electrical energy as long as there is available fuel. Renewable liquid fuel alternatives such as methanol also allow use of the current infrastructure for petroleum. However, the DMFC does have disadvantages, the primary problem being a low power density. High over-potentials at the anode catalyst combined with the necessity of using low temperatures severely reduces the conversion efficiency. Thus high loadings of noble metals are required to enhance the performance of the anode, increasing costs. In addition, the membrane properties need to be improved with respect to

water balance sensitivity (six protons at the anode produced per methanol molecule) and inhibition of methanol crossover. Diffusion of methanol across the membrane leads to depolarization of the cell and loss of activity. Recently, advances have been made in two significant areas:(1) the use of solid polymer electrolyte (SPE) technology now allows increased operating temperatures, thereby improving efficiency² and (2) improved electrocatalysts have been identified that increase reaction activity, allowing reduction of the noble metal loading. This decreases the cost and generates higher power densities. This paper will focus on the latter area. The progress in developing improved DMFCs has been hindered by the lack of a detailed reaction mechanism. Relevant mechanistic were discussed by Leger and Lamy,³ and recently reviewed by Hamnett,⁴ while Parsons and VanderNoot⁵ provide an earlier review of fuel cell research.

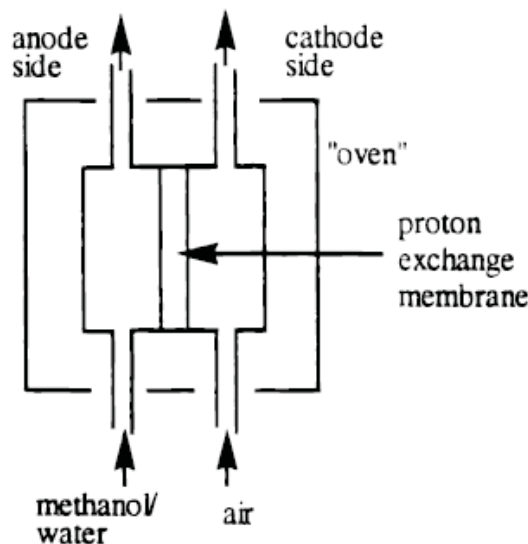


Figure 1. Schematic of a direct methanol fuel cell.

2. Review of Mechanistic Understanding for Direct

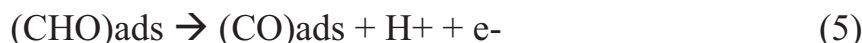
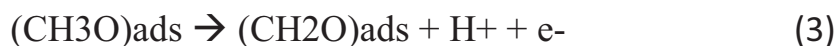
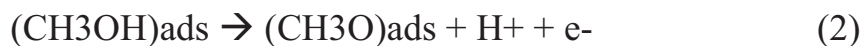
Methanol Oxidation

There are several different plausible pathways for the oxidation of methanol. Water is required for the overall conversion of methanol to carbon dioxide^[2]

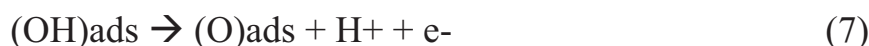
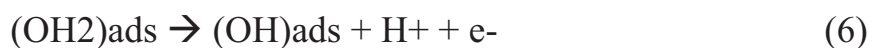




Methanol adsorbed on the electrode surface can undergo successive dehydrogenation, as indicated in steps 2-5. However, the exact structure of the adsorbed intermediates is unknown except for (CO)_{ads}.



Our computational results (*vide infra*) suggest which particular isomers are the adsorbed species. Water may also dehydrogenate successively to form adsorbed OH and O atom as in steps 6 and 7.



Formation of a second C-O bond is then required to remove (CO)_{ads} from the surface in the form of CO₂ as in



Equation 8a assumes complete dehydrogenation for both CH₃OH and H₂O takes place to form CO_{ads} and O_{ads} which then forms CO₂, which desorbs from the surface. However, it is possible that partially dehydrogenated species could recombine and then dehydrogenate (either simultaneously or in a successive step) to form CO₂ as in



The recombination of partially dehydrogenated species could also produce compounds such as HCOOH, HCOOCH₃, and CH₂(OCH₃)₂.

we also study small clusters which is intrinsically interesting because they often exhibit structures and properties different from those of the bulk, due to their high ratio of surface area to volume. Transition metal clusters are of special interest because they are used to catalyze reactions; for example, small clusters of Pt, Rh, and Pd are used in automotive exhaust systems to reduce toxic pollutants such as CO, NO, and hydrocarbons. Pt clusters are considered to be one of the most

important materials for the heterogeneous catalysis of hydrogenation because of their small hydrogenation energy compared with other metal clusters [3]. Determining the shape and the microstructure of small metal particles is important because it is a major feature in controlling the catalyst's activity. In particular, it is possible that very small transition metal clusters have unusual structures and therefore unusual activities. Quantum mechanical theoretical studies of Pt clusters are however scarce, reflecting the difficulty of treating the compact d orbitals present in transition metals[4]. The purpose of this letter is to provide a systematic ab initio study of the structure and adsorption energy of small Pt_n clusters for n =4

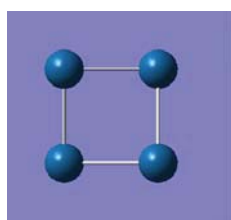
3.computational method:

All calculation were performed with Guassian 03 code .we employ the hybride B3LYP functional to explore the stationary points on the potential energy surfaces (PESs).we used the Los Alamos LANL2DZ effective core pseudo potential (ECP).The C,H and O atoms were treated with the 6-31G(d,p) basis set.The adsorption energy of methanol on the pure Pt₁₅ cluster was obtained The adsorption energy for molecule of CH₃oh and CH₂oh and Choh and Cho and Co on Pt₄ cluster obtained using the following equation for example :

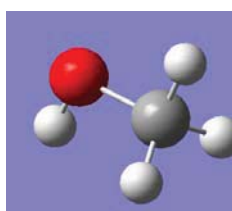
$E_{ads}=E(Pt_4 \text{ CH}_3\text{oh}) -E(Pt_4)-E(\text{CH}_3\text{oh})$ where $E(Pt_4\text{CH}_3\text{oh})$ is the total energy of complex(Pt₄ch₃oh) and $E(Pt_4)$ and (ch_3oh) is the energy of isolated atom .

4.Result and disscution :

We carried out full structural optimization of Pt₄ with Co and Coh and Co₂h and Co₃h gas molecule to examine the energetic and structural and electronic properties .to find the most favorable adsorption configuration we demonstrate these optimize structure for Pt₄ .These result show that adsorption energy of pt4choh is the most favorable .we calculated it around -21.973407ev.



Pt4



Ch3oh



Pt4ch3oh

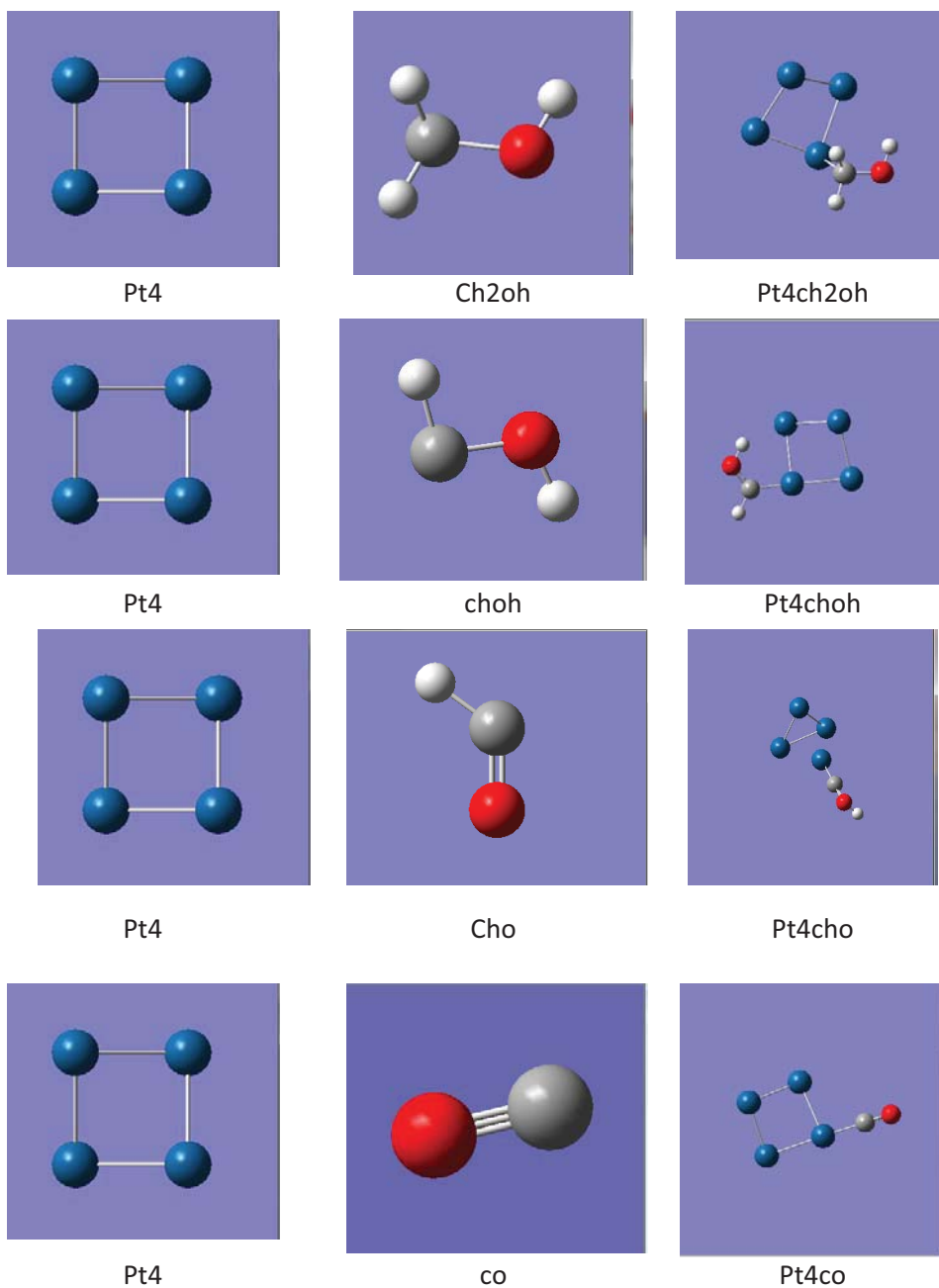


Figure2: of pt4 optimized structure on Ch3oh and Ch2oh and Choh and co



	Pt4Ch3oh	Pt4Ch2oh	Pt4choh	Pt4cho	Pt4co
E adsorption	-18.611	-19.94563	-21.973407	-21.648871	-21.746769
ΔH	-18.519	-19.81338	-20.952750	-21.50316731	-19.3768216
ΔG	-18.108	-19.37186	-20.473574	-20.39767437	-18.9717982

Table1:calculated adsorption energy and ΔH and ΔG for Pt4 on Ch3oh and Ch2oh and Choh and Coh and co

5.References:

1. Hogarth, M.; Christensen, P.; Hamnett, A.; Shukla, A. *J. Power Sources* **1997**, *69*, 113.
2. Balasubramanian K 1987 *J. Chem. Phys.* **87** 6573
3. M.D. Esrafil, F. Elmi, N.L. Hadipour, *J. Phys. Chem. A* **111** (2007) 963
4. T. Frosch, J. Popp, *J. Mol. Struct.* (2009),
 doi:10.1016/j.molstruc.2008.12.019



Fabrication of MEA based on sulfonic acid functionalized carbon supported platinum nanoparticles for oxygen reduction reaction in PEMFCs

Fatemeh Yasi¹, Hussein Gharibi² and Ahmad Heydari³

Department of Chemistry, Faculty of Science, Tarbiat Modares University,
Tehran, Iran
fatemeh.yasi@gmail.com

Abstract

To improve the utilization and activity of cathodic catalysts for oxygen reduction reaction (ORR), platinum nanoparticles were loaded on the mixture of Vulcan XC72 and MWCNTs, which were functionalized in the mixture of 96% sulfuric acid and 4-aminobenzenesulfonic acid using sodium nitrite to produce intermediate diazonium salts from substituted anilines. The ORR performance of the fabricated membrane electrode assembly (MEA) was studied using polarization curves and electrochemical impedance spectroscopy (EIS) in a proton exchange membrane fuel cell (PEMFC). It is suggested that the improvement of the performance of the PEMFC is facilitated not only by enlarging the three-phase boundary in the catalyst layer, but also by providing ionic-conduction paths as well as by imparting negative charge to platinum sites with concomitant oxidation of sulfur present in the carbon support.

Keywords: Sulfonic acid functionalized carbon; Cell performance; Electrochemical stability.

1. Introduction

Polymer electrolyte membrane fuel cells (PEMFCs) are attractive alternative power sources due to their safe emission, high conversion efficiency, and high energy density [1]. For PEMFCs, electrode performance relies critically on the three phase boundary formations in the membrane-electrode-assembly (MEA) [2]. A high performance electrode can provide effective proton conduction, electron conduction, and transfer path for reactant and product to or from the catalyst layer. In thin-film electrode designs, the electrode typically consists of three different layers, i.e. backing, microporous layer (MPL), and catalyst layer (CL) [2]. In this method, hydrophobic polytetrafluoroethylene (PTFE) is added into the gas diffusion layer to enhance water management, whereas Nafion ionomer is mixed with the CL to improve the utilization of platinum (Pt) catalyst. The Nafion ionomer fails to penetrate the small pores in the carbon agglomerate. Besides, Nafion often affects the efficiency of the platinum electrocatalyst by blocking the active sites restricting the gas permeability of the catalyst layer as well as its electronic conductivity. Accordingly, there is a limitation in the quantity of Nafion that needs to be added without affecting the cell performance [3]. Several studies have been focused on the enhancement of the catalyst utilization in the PEMFC electrodes through extending the so-called triple-phase boundaries [4-19]. Among them, sulfonation of carbon-supported catalysts as mixed electronic and protonic conductors has been reported to be an efficient way to increase the triple-phase boundaries. Recently, CNTs, as innovative catalyst supports, have drawn a great deal of attention due to their unique surface structures, excellent mechanical and thermal properties, high electric conductivity, and large surface areas. However, the current on the



single-CNT support electrode had little change at low overpotentials, but deteriorated rapidly at high overpotentials. The difference in the polarization features might be associated with the wettability and structural properties of the used carbon support materials. As CNTs have a hollow tubular structure and the CNT support electrode has many micro or nanosized pores, the catalyst layer was much easily penetrated by electrolyte solution under the action of capillarity. As a result, the decreased interfacial area of the gas–liquid–solid phase at the reaction sites and larger flooding may happen for the single-CNT support electrode [20]. In this work, functionalized MWCNTs were used as a secondary carbon support of Pt catalyst at different mass ratios in order to determine the best mass ratio of these types of carbon in acid media and afterwards for fabricating membrane electrode assembly (MEA) in proton exchange membrane fuel cells (PEMFCs). The well dispersed reduction of Pt nanoparticles on the surface of benzenesulfonic functionalized MWCNTs and Vulcan XC-72R was demonstrated from H_2PtCl_6 aqueous solution by using $NaBH_4$ as a reductive agent. The role of binary carbon supports in the catalyst layer is evaluated through polarization curves and electrochemical impedance spectroscopy (EIS). It will be shown that by using binary functionalized carbon supports, the electrochemical performance of as-formed MEA can be enhanced.

2. Experimental Section

2.1. Anchoring phenyl-sulfonic groups to Vulcan XC-72R using *p*-amino phenyl-sulfonic acid

The process of preparation of benzenesulfonic functionalized Vulcan XC-72R has been reported elsewhere [5]. In a typical experiment of synthesis of f-Vulcan XC-72R, Carbon support was mixed with hot aqueous solution of *p*-amino phenyl sulfonic acid (Merck, Germany) to form slurry. The required amount of concentrated hydrochloric acid was added drop wise to the carbon slurry with constant stirring at 80°C. The resulting suspension was cooled below 20°C. Subsequently, the aqueous solution of sodium nitrite was added with stirring forming 4-sulfobenzendiazonium salts in situ that reacted with carbon support. The mixture was stirred for 30 min, filtered, washed copiously with hot distilled water to remove the unbounded residues, and then dried in an air oven at 120°C for 2 h.

2.2. Purification of raw MWCNTs (*p*-MWCNTs)

The MWCNTs were refluxed with concentrated nitric acid at 120°C for 12 h, then washed and filtered with deionized water. The steps introduced oxygen containing groups, mainly carboxyl groups to the MWCNTs [21]. We denoted them as *p*-SWCNT in the following text. The filtrate cake was dried in air at 80 °C for 12 h [22].

2.3. Functionalization of MWCNTs (*f*-MWCNTs)

The procedures of benzenesulfonic functionalized MWCNTs have been described elsewhere [7]. A typical experiment consisted of dispersing *p*-SWNT in 96% H_2SO_4 and $(NH_4)_2S_2O_8$ with magnetic stirring (6h). When the mixture was visibly dispersed, the substituted 4-aminobenzenesulfonic acid was added and homogenization was continued for 2 h in order to effectively disperse the aniline throughout the mixture. This was followed by addition of solid $NaNO_2$ and slow addition of di-tert-butylperoxide (AIBN and di-tert-butylperoxide produced similar results). The mixture was stirred at 80°C and homogenization was continued for 6 h. The resulting product was filtered and washed with deionized water, acetone, and fresh N,N-



dimethylformamide (DMF) in order to remove any impurity and then dried at 30°C for 24 h in a vacuum oven.

2.4. Preparation of carbon-supported platinum catalyst

The modified catalysts with different ratios of f-MWCNTs and f-VulcanXC-72R were synthesized at 80°C by using NaBH₄ as a reductive agent. The w/o of phenyl sulfonic acid group anchored to Vulcan XC-72R was 5. The mixture of f-VulcanXC-72R and f-MWCNTs were impregnated with Pt particles through adding H₂PtCl₆ salt in water followed by sonication of the suspension for 30 min. Excess quantities of 0.1 M NaBH₄ solution were added dropwise to the suspension with vigorous stirring at 80°C. The mixture was stirred for 24 h at 80°C to permit the complete reduction of Pt from its metal salt. Finally, the resulting material was washed with distilled water several times and dried at 70°C. The metal loading was determined by ICP to be 10 wt%.

2.5. Fabrication of membrane electrode assembly

Nafion-115 (DuPont) used as the proton electrolyte membrane, was treated in 30 w/o H₂O₂ for 1.5 h followed by its rinsing and washing in distilled water. It was then boiled in 0.5M H₂SO₄ for 1.5 h followed by washing with distilled water.

Both anode and cathode comprise a gas diffusion layer and a reaction layer. To prepare the gas-diffusion layer, Vulcan-XC72R carbon and PTFE (6% solution by weight) are suspended in isopropyl alcohol: distilled water (2:1) and sonicating the mixture for 30 min at room temperature. The amount of PTFE in the diffusion layer was 30% (by weight), and the loading in the carbon and PTFE composite was 1 mg/cm². The resultant slurry was spread on a carbon paper and sintered in a furnace at 350°C for 30 min. To prepare the reaction layer, the required amount of the catalyst (modified or unmodified) and Nafion (Dupont) solution were agitated for 1 h. The resulting ink was coated onto the treated 115-Nafion membranes. The MEAs were assembled with gas diffusion electrodes and placed in 4.25 cm² Paxi-tech single-cell fuel cell for electrochemical testing. Both anode and cathode contain platinum loading of 0.5 mg cm⁻² and Nafion loading of 1 mg/cm².

3. RESULTS AND DISCUSSION

3.1. Temperature Effect

Temperature is one of the most important operating parameters that need to be properly controlled. The major effect of temperature is to change the reaction kinetics of the ORR in the fuel cell; The other effect is to change the fuel cell's water management. Temperature can also affect proton transport inside the membrane, resulting in membrane conductivity change.

The following membrane electrode assembly (MEA) samples were tested in this experiment. MEA-1: 10 wt% Pt on 75% MWCNT + 25% Vulcan XC-72 C used as cathode and 10 wt% commercial Pt/C used as anodes, MEA-2: 10 wt% commercial Pt/C used as cathode and anodes. MEA catalyst loadings for both the anode and cathode were 0.5 mg_{metal} cm⁻². The polarization and power curves for MEA 1 is illustrated in Fig. 1. The MEA was initially activated at 0.6 V for 2 h at 100% relative humidity (RH); the voltage scan measurements were performed between 0.05 and 1.2 V at a scan rate of 50 mV/s [23]. The humidification temperatures of the anode and cathode gases were varied, the flow rates were 300 ml/min for hydrogen and 500 ml/min for O₂.

According to the polarization curves obtained at 50°C, 60°C, 70°C, 80°C, the best performance is obtained at 80°C. In the high current density range, all performances dropped rapidly, which was typical of mass transfer limitation. However, an increase in temperature makes a huge difference in the high current density range, due to improvements in mass transfer at higher temperatures. Table 1 shows the kinetic parameters obtained for the MEA 1 from polarization curves. As shown in Table 1, the kinetic parameters of the MEA 1 improved considerably in comparison with MEA 2 (Pt/C Electrochem 10%). It indicates that the current density improved in the presence of functional group in the support.

As was mentioned, increasing the temperature will speed up the ORR. This is reflected in EIS in such a way that the kinetic arc in a Nyquist plot is larger at low temperatures than at high temperatures, as shown in Fig. 2. However, the high frequency intercept value (membrane resistance) of the kinetic loop can be significantly affected by changing fuel cell temperature. Increasing temperature can reduce membrane resistance, thereby improving fuel cell performance. As shown in Fig. 2, at lower temperatures, the arc radius in a low frequency range (mass transfer arc) can be significantly reduced by increasing fuel cell temperature as more liquid water may accumulate at the cathode, resulting in a mass transfer problem.

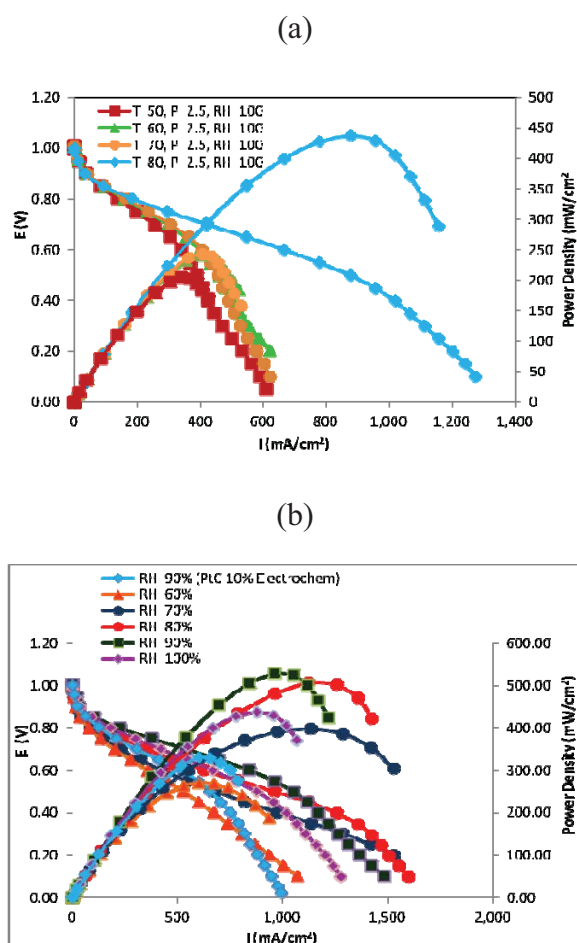
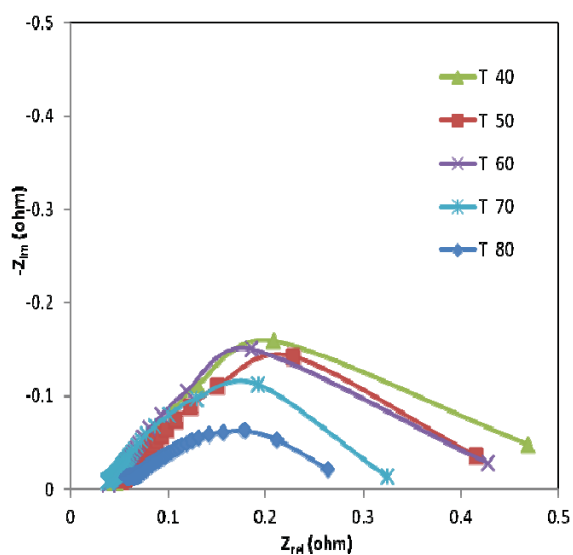


Fig. 1. (a) Effect of temperature on single cell performance (H_2/O_2 gases with 100% relative humidity) (b) Polarization curves of single cell at 80°C and different relative humidities of cathode and anode; MEA active area: 4.25 cm^2 , anode gas flow rate 300 ml min^{-1} , cathode gas flow rate 500 ml min^{-1} , and the gas pressure at the back of the electrodes was 1.5 atm.

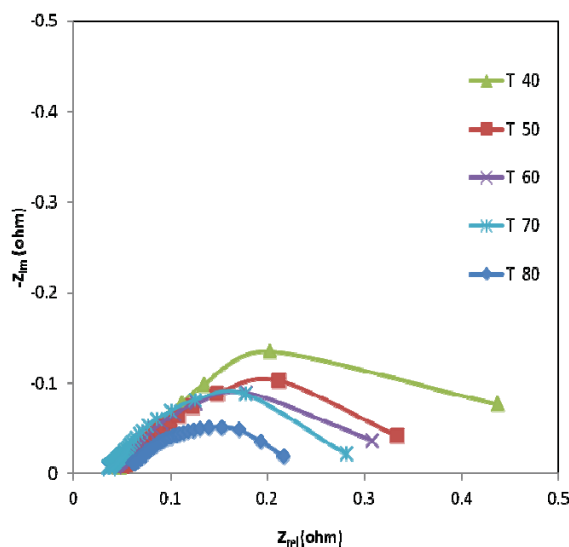
Table 1. The kinetic parameters obtained from the polarization curves for MEAs at different relative humidity with flow rates of 300 ml/min of hydrogen and 500 ml/min of oxygen. The cell was maintained at 353 K, and the gas pressure at the back of the electrodes was varied between 1 and 1.5 atm.

MEA	Cell Temperature (°C)	Absolute back pressure (atm)	Relative humidity (%)	i_0 (A cm ⁻²)
MEA 1	80	2	90	8.22×10^{-4}
	80	2.5	60	3.28×10^{-3}
	80	2.5	80	4.64×10^{-3}
	80	2.5	90	7.30×10^{-3}
	80	2.5	100	5.68×10^{-3}
MEA 2 (Pt/C 10% Electrochem)	80	2.5	90	3.60×10^{-3}

(a)



(b)



(c)

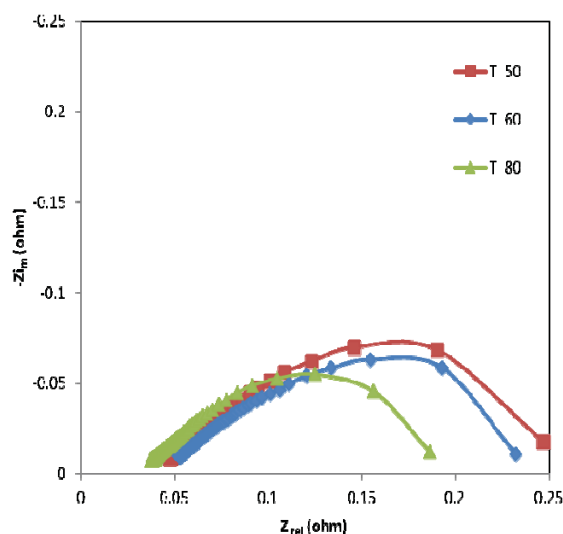


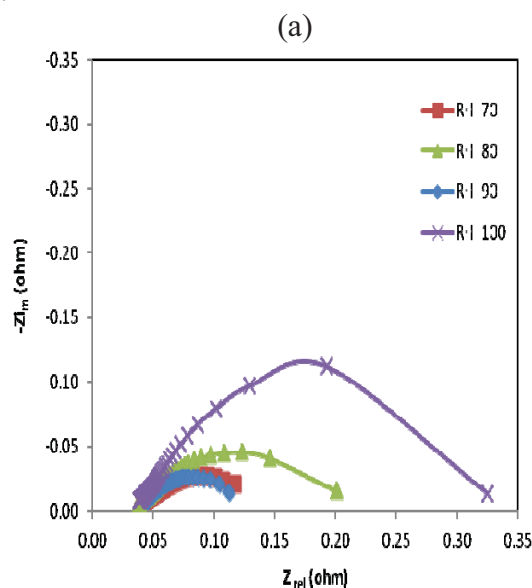
Fig. 2. Impedance spectra from 1 mHz to 1000 kHz, 100% relative humidity, different cell temperatures and 1.5 atm back pressure for the anode and cathode. The flow rates are 300 ml/min for hydrogen and 500 ml/min for oxygen (a) at 0.3V (b) at 0.5 V (c) at 0.7 V.

3.2. Humidity Effect

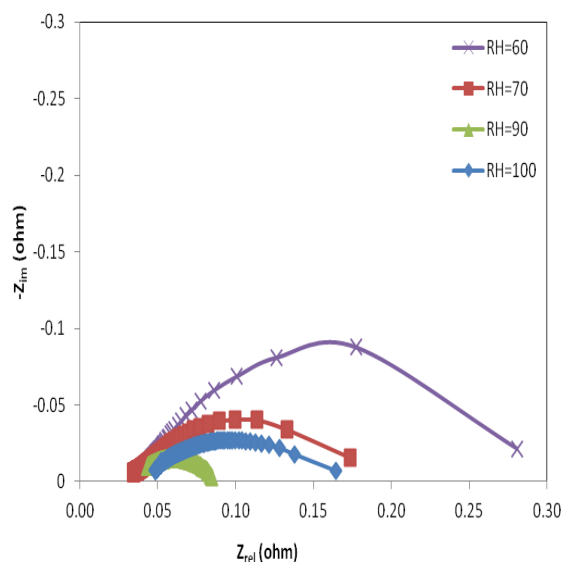
Water management is an important issue in the performance of PEM fuel cells. Water content at the interface contributes to the transport of the involved species in many different ways. At one extreme, a high water level can block oxygen transport. If water content is elevated due to its generation at the cathode, it can directly affect the ORR kinetics and also contribute indirectly to the state of contact between the Pt catalyst and the ionomer. If there is not enough water at the reaction interface, the ionomer will shrink, reducing both the surface contact of the catalyst

with the ionomer and the proton conductivity of the ionomer. With respect to this, the amount of humidity in the reactant stream may affect the cell performance. Fig. 1 (b) shows the polarization curves of single cell at 80°C and RHs of 60%, 70%, 80%, 90%, and 100%. The cell performance was strongly enhanced at higher relative humidity; the best result was obtained at 90% RH. At higher relative humidity the cell performance decreased due to the increased hydrophilic nature of the catalyst in the presence of phenyl-sulfonic acid group in the support, which led to flooding. As shown in Table 1, the maximum exchange current density of the MEA belongs to the relative humidity of 90%.

It is widely reported that humidity can influence the high-frequency intercept at the real axis, which is associated with membrane resistance. The conductivity of the membrane in a PEM fuel cell is directly related to its water content, which depends on: (1) the water carried by the humidified reactant gases; (2) the water generated by the cell reaction at the cathode; (3) the electroosmotic drag – that is, water carried by the protons that are transported from anode to cathode; and (4) back-diffusion of water from the cathode to the anode. As we know, the fuel cell EIS primarily represents the cathode behaviour. Therefore, cathode humidification can greatly affect the whole impedance spectra. The humidification at the cathode causes a large difference in both the membrane resistance and the kinetic resistance. This result is reflected in EIS Nyquist plot in Fig 3.



(b)



(c)

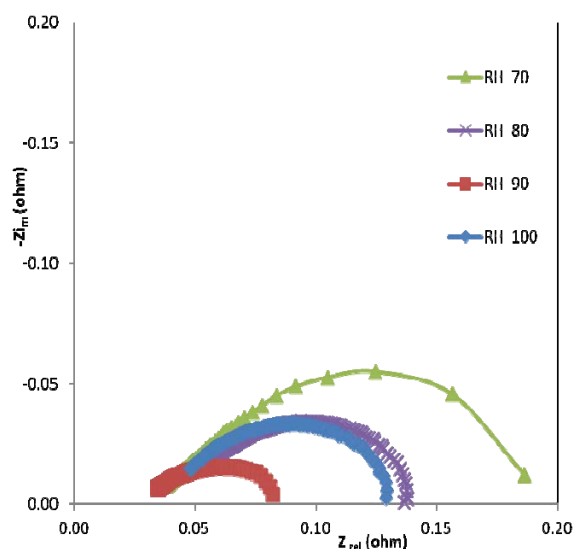


Fig. 3. Impedance spectra, from 1 mHz to 1000 kHz, for different relative humidities, cell temperature 80°C and 2.5 atm absolute back pressure for the anode and cathode. The flow rates are 300 ml/min for hydrogen and 500 ml/min for oxygen (a) at 0.3V (b) at 0.5V (c) at 0.7V.

4. Conclusion

It is suggested that anchoring the phenyl-sulfonic group on the carbon support of the platinum catalyst enhances the performance of PEFC. The goal of this work was to investigate the synergism effect of the functionalized supports on the performance of PEMFCs. According to the single cell data, the synergism between phenyl-sulfonic group and Nafion ionomer affected



the cell performance due to the increasing ion-conducting path in the catalyst layer and so enhanced catalyst utilization in the PEFC electrodes by extending the so-called triple-phase boundaries. The related MEAs exhibited enhanced fuel-cell performance under optimum RH conditions; however, further increase in phenyl sulfonic acid loading decreases Pt utilization possibly due to the increased hydrophilic nature of the catalyst layer, which leads to flooding albeit the amelioration exhibited by negative charged platinum sites that help repelling water molecules.

References

1. Eom, K., et al., *Effects of residual oxygen partial pressure on the degradation of polymer electrolyte membrane fuel cells under reverse current conditions*. Journal of Power Sources, 2012. **198**(0): p. 42-50.
2. Therdthianwong, A., P. Saenwiset, and S. Therdthianwong, *Cathode catalyst layer design for proton exchange membrane fuel cells*. Fuel, 2012. **91**(1): p. 192-199.
3. Selvarani, G., et al., *A phenyl-sulfonic acid anchored carbon-supported platinum catalyst for polymer electrolyte fuel cell electrodes*. Electrochimica Acta, 2007. **52**(15): p. 4871-4877.
4. Du, C.Y., T.S. Zhao, and Z.X. Liang, *Sulfonation of carbon-nanotube supported platinum catalysts for polymer electrolyte fuel cells*. Journal of Power Sources, 2008. **176**(1): p. 9-15.
5. Kim, H., W. Lee, and D. Yoo, *Functionalized carbon support with sulfonated polymer for direct methanol fuel cells*. Electrochimica Acta, 2007. **52**(7): p. 2620-2624.
6. Sun, Z.-P., et al., *A simple approach towards sulfonated multi-walled carbon nanotubes supported by Pd catalysts for methanol electro-oxidation*. Journal of Power Sources, 2008. **185**(2): p. 801-806.
7. Yang, S., et al., *Pd nanoparticles supported on functionalized multi-walled carbon nanotubes (MWCNTs) and electrooxidation for formic acid*. Journal of Power Sources, 2008. **175**(1): p. 26-32.
8. Sun, Z.-P., et al., *Sulfonation of ordered mesoporous carbon supported Pd catalysts for formic acid electrooxidation*. Journal of Colloid and Interface Science, 2009. **337**(2): p. 614-618.
9. Sun, Z.-P., et al., *A facile approach towards sulfonate functionalization of multi-walled carbon nanotubes as Pd catalyst support for ethylene glycol electro-oxidation*. Journal of Power Sources, 2009. **191**(2): p. 366-370.
10. Pak, C., et al., *Direct sulfonation of ordered mesoporous carbon for catalyst support of direct methanol fuel cell*, in *Studies in Surface Science and Catalysis*, S.Q.Y.T. Dongyuan Zhao and Y. Chengzhong, Editors. 2007, Elsevier. p. 401-404.
11. Tominaka, S., et al., *Ionic conductivity improvement in primary pores of fuel cell catalyst layers: Electropolymerization of m-aminobenzenesulfonic acid and its effect on the performance*. Journal of Power Sources, 2009. **192**(2): p. 316-323.
12. Hung, T.-F., et al., *Sulfonation of graphene nanosheet-supported platinum via a simple thermal-treatment toward its oxygen reduction activity in acid medium*. International Journal of Hydrogen Energy, 2012. **37**(19): p. 14205-14210.
13. Carmo, M., et al., *Enhanced activity observed for sulfuric acid and chlorosulfuric acid functionalized carbon black as PtRu and PtSn electrocatalyst support for DMFC and DEFC applications*. International Journal of Hydrogen Energy, 2011. **36**(22): p. 14659-14667.
14. Choi, Y., et al., *A composite electrolyte membrane containing high-content sulfonated carbon spheres for proton exchange membrane fuel cells*. Carbon, 2011. **49**(4): p. 1367-1373.



15. Cheng, N., et al., *Enhanced life of proton exchange membrane fuel cell catalysts using perfluorosulfonic acid stabilized carbon support*. *Electrochimica Acta*, 2011. **56**(5): p. 2154-2159.
16. He, D., S. Mu, and M. Pan, *Perfluorosulfonic acid-functionalized Pt/carbon nanotube catalysts with enhanced stability and performance for use in proton exchange membrane fuel cells*. *Carbon*, 2011. **49**(1): p. 82-88.
17. Carmo, M., et al., *A novel electrocatalyst support with proton conductive properties for polymer electrolyte membrane fuel cell applications*. *Journal of Power Sources*, 2009. **191**(2): p. 330-337.
18. Zhiqiang Xu, Z.Q., and Arthur Kaufman, *Superior Catalysts for Proton Exchange Membrane Fuel Cells Sulfonation of Carbon-Supported Catalysts Using Sulfate Salts*. *Electrochemical and Solid-State Letters*, 2005. **8**(6): p. A313-A315.
19. Zhiqiang Xu, Z.Q., and Arthur Kaufman, *Advanced Fuel Cell Catalysts: Sulfonation of Carbon-Supported Catalysts Using 2-Aminoethanesulfonic Acid*. *Electrochemical and Solid-State Letters*, 2003. **6**(9): p. A171-A173.
20. Huang, H., et al., *Carbon nanotubes as a secondary support of a catalyst layer in a gas diffusion electrode for metal air batteries*. *Journal of Colloid and Interface Science*, 2005. **284**(2): p. 593-599.
21. Yu, H., et al., *Synthesis and characterization of sulfonated single-walled carbon nanotubes and their performance as solid acid catalyst*. *Journal of Solid State Chemistry*, 2008. **181**(3): p. 432-438.
22. Wu, G., Y.-S. Chen, and B.-Q. Xu, *Remarkable support effect of SWNTs in Pt catalyst for methanol electrooxidation*. *Electrochemistry Communications*, 2005. **7**(12): p. 1237-1243.
23. Jae Hyung Cho, J.M.K., Joghee Prabhuram, Sang Youp Hwang, and H.Y.H. Dong June Ahn, Soo-Kil Kim, *Fabrication and evaluation of membrane electrode assemblies by low-temperature decal methods for direct methanol fuel cells*. *Journal of Power Sources*, 2009. **187**: p. 378-386.



Fabrication and modification of graphene Supports for Platinum Electro catalyst using in Proton Exchange Membrane Fuel Cells

Ahmad Heydari¹, Hussein Gharibi² and Fatemah Yasi³

*Department of chemistry, faculty of basic sciences tarbiat modares university
ahmad.heydari1@gmail.com*

Abstract

Proton exchange membrane fuel cells (PEMFCs) are one of the most promising clean energy conversion devices due to their high conversion efficiency, low/zero emission, and high power/energy densities. Nitrogen doping has been an effective way to tailor the properties of graphene and render its potential use for various applications. We developed a simple chemical method to obtain bulk quantities of N-doped, reduced graphene oxide (GO) powder through thermal annealing of GO in ammonia and hydrazine. Oxygen reduction and nitrogen doping were achieved simultaneously under the hydrothermal reaction. Electrochemical measurements show that the graphene support and especially nitrogen doped graphene support has the better activity than Vulcan.

Keywords: PEMFC, graphene, N-doped, Pt nanoparticle

1 Introduction

Fuel cells are able to convert chemical energy to electrical energy with little pollutant emission and high energy conversion efficiency. Despite these advantages, the performance of fuel cells depends largely on oxygen reduction reaction (ORR), which is substantially affected by the activity of the cathode catalyst. Since the sluggish kinetics of ORR is the major factor impeding large-scale application of fuel cells, most research focuses on developing efficient catalysts for ORR. The ORR process can occur in a four-electron pathway to directly produce water or a less efficient two-electron pathway involving the formation of hydrogen peroxide as an intermediate. Platinum (Pt) serves as the most efficient catalyst for the ORR in a direct four-electron pathway, yet its unstable catalytic activity, poor durability, and high cost have limited the commercial prospect of fuel cells. Consequently, a number of techniques have been explored to enhance catalytic activity and to reduce the usage of Pt. For example, there have been considerable efforts at employing carbon nanotubes (CNTs) and graphene as supporting materials to efficiently disperse catalyst particles. Carbon nanotubes, one dimensional structures having a large surface area, possess good conductivity and high carrier densities when used as a supporting material for metal catalysts. Graphene, a mono-atomic sheet of hexagonally arranged carbon atoms, has exhibited excellent electrical conductivity and extremely high specific surface area (2600 m²/g) and therefore, demonstrates its potential as a supporting material for catalyst particles. It has been reported that both CNTs and graphene can enhance electrocatalytic activity of metal catalysts when acting as catalyst supports. Recently, nitrogen (N) and other elements have been successfully doped into graphene sheets. In comparison to pristine graphene, the incorporation of nitrogen atoms within carbon structures contributes to greater electron mobility and more active sites for catalytic reactions. Both N-doped graphene and CNTs have demonstrated high catalytic activity for ORR via a direct four-electron pathway



in alkaline solution and showed the potential to replace noble metals as electrocatalyst. It has been reported that the high activity may arise from the positive charge density on the adjacent carbon atoms created by the introduction of nitrogen atoms, and the bonding configurations of nitrogen atoms in graphene structure can contribute to the enhanced activity for ORR. Moreover, N-doped graphene may increase the durability and catalytic activity of metal catalysts when used as a supporting material. Nevertheless, no systematic investigation of N-doped graphene, used as either a catalyst or a catalyst support for ORR in both acidic and alkaline solutions, exists in the literature to our knowledge. Herein, we synthesized graphene and N-doped graphene by a solvothermal method and studied their electrocatalytic activity as catalysts and catalyst supports in both acidic solution. We found that N-doped graphene exhibits higher electrocatalytic activity for ORR in both acidic solution in contrast with graphene and Vulcan. Moreover, to our knowledge, the current work, for the first time, shows that when employed as supporting materials, graphene and N-doped graphene demonstrate differences in facilitating electrocatalytic activity of Pt nanoparticles in acidic solution.

Experimental section

Synthesis of graphene oxide:

Graphene oxide (GO) was made by a modified Hummers method. using expandable graphite flake (Graftech) as starting material. Expandable graphite flake (3 g) was ground with NaCl (50 g) for 30 min. NaCl was dissolved in water and removed by filtration (~15% carbon was lost during this step). The remaining ground expandable graphite flake (~2.55 g) was stirred in 98% H₂SO₄ (70 mL) for 28 h. KMnO₄ (15 g) was gradually added while keeping the temperature <20 °C. The mixture was then stirred at 35–40 °C for 60 min, and then at 65–80 °C for 90 min. Next, water (200 mL) was added and the mixture heated at 98–105 °C for 15h. The reaction was terminated by addition of distilled water (520 mL) and 30% H₂O₂ solution (50 mL). The mixture was washed by repeated centrifugation and filtration, first with 5% HCl aqueous solution, and then distilled water. Water (480 mL) was added to the final product and vortexed well to make a uniform suspension for storage.

Synthesis of nitrogen doped graphene:

Using hydrazine hydrate to prepare graphene from GO is a widely used method. In this work, N-graphene has been obtained by reducing GO in the NH₃ and N₂H₄ mixed solution. The nitrogen content reaches up to 5 at. % when the reduction temperature is 80 °C; however, the absorbed N₂H₄ takes a non negligible proportion in the total nitrogen content. If the reaction temperature rises to 160 °C or higher, the N₂H₄ will be desorbed and the nitrogen content decreases to ~4 at. %. Interestingly, the morphology of N-graphene also changes with the temperature. The relative flat N-graphene is generated if GO is reduced at low temperature (≤120 °C), whereas the obvious agglomeration in N-graphene will occur if the temperature is higher.

Preparation of Pt/Support:

In this work we used graphene, nitrogen doped graphene and Vulcan as support and Pt ion solution in the form of H₂PtCl₆. we mixed support and ion platinum with methanol:water (1:1) solution and then ultrasonicated them in 20min. The mixture refluxed in 90 °C in Ar atmosphere and NaBH₄ reducing agent was added to mixture to reduce Pt ion. after 24h, the mixture was filtered and washed with distilled water and dried in vacuum oven.

Electrochemical characterization:

For determination of the electrochemical performance and stability of supports and catalysts, a conventional three-electrode electrochemical cell was employed. All the electrochemical measurements were carried out in 0.5M H₂SO₄ solution at 25 °C, and ultra-pure N₂ (Air Products) was passed through a 0.5M H₂SO₄ solution and 0.5M ethanol + 0.5 M H₂SO₄



solution for 30 min before the electrochemical measurements, a platinum electrode was the counter electrode, and a Ag/AgCl(KCl (s)) electrode was the reference electrode. For convenience, all potentials measured are referred to as the normal hydrogen electrode (NHE). A polished glassy carbon disk electrode (3mm diameter) was used as the substrate for the supported catalysts (or supports). The working electrode was fabricated as follows : 5mg of the catalysts (or supports) was dispersed in 2mL of deionized water: isopropyl alcohol (1:2) and then mixed with 17.65mg of 5 wt.% Nafion solution. The mixture was sonicated for 6min to obtain an ink like slurry. 10 μ l of this slurry was spread onto the flat surface of the glassy carbon disk using Hamilton; and then glassy carbon was dried in oven.

Results and discussion:

References:

- [1] Haibo Wang, Thandavarayan Maiyalagan, and Xin Wang. ACS Catal. 2012, 2, 781–794
- [2] Zhengzong Sun, Dustin K. James, and James M. Tour. J. Phys. Chem. Lett. 2011, 2, 2425–2432
- [3] C. Jeyabharathia, P. Venkateshkumarb, M. Sankara Raoa, J. Mathiyarasua, K.L.N. Phania Electrochimica Acta 74 (2012) 171– 175
- [4] Jincheng Bai a,b, Qianqian Zhu a, Zhexin Lv a, Hongzhou Dong a, Jianhua Yu a, Lifeng Dong. International journal of hydrogen energy 38(2013) 1413 -1418

¹ - phd student of physical chemistry, tarbiat modares university

² - phd degree and teacher in tarbiat modares university, h.gharibi@gmail.com

³ - phd student of physical chemistry, tarbiat modares university, fatemeh.yasi@gmail.com



Pt-Sn-SnO₂/C Electrocatalysts for Ethanol Oxidation in Acidic Media

Sadegh Sadeghi¹, Hussein Gharibi²

*Department of physical chemistry, Faculty of Science, Tarbiat Modares University, Tehran, Iran
E-mail: Sadegh.sd@gmail.com*

Abstract

Pt-Sn-SnO₂ and Pt-Sn catalysts supported on carbon were synthesized by a modified polyol method. An electrochemical study showed that the Pt-Sn-SnO₂/C catalyst had a better performance compared with the Pt-Sn/C catalyst. Chronoamperometry experiments of the as-prepared catalysts shows that the activity for ethanol oxidation of Pt-Sn-SnO₂/C is higher than that of Pt-Sn/C.

Keywords: Tin Oxide, Ethanol Oxidation, DAFC.

1 Introduction

Low molecular weight alcohols as methanol and ethanol are widely proposed as possible fuels for fuel cells for mobile applications such as electric vehicles. Direct ethanol fuel cells (DEFCs) have attracted great interest as a power source in numerous applications because ethanol is a nontoxic and high density energy carrier, which is widely available from the reformation of various kinds of biomass [1]. The best binary catalyst for the ethanol oxidation reaction (EOR) in acid environment is Pt-Sn. However, these kinds of alloys usually show relatively low selectivity for CO₂ formation compared with Pt alone. Jang et al. [2] compared the catalytic activity of a partially alloyed Pt-Sn catalyst with that of a quasi non-alloyed PtSnO_x catalyst. From the analysis of results of chronoamperometry of the performance of direct ethanol fuel cells, the PtSnO_x catalyst showed higher catalytic activity for ethanol electro-oxidation than the Pt-Sn alloy. They deduced that the unchanged lattice parameter of Pt in the PtSnO_x catalyst is favorable to ethanol adsorption and meanwhile, tin oxide in the vicinity of Pt nanoparticles could conveniently provide oxygen species to remove the CO-like species of ethanolic residues to free Pt active sites. Zhu et al. [3] synthesized PtSnO₂ and PtSn alloy catalyst. The analysis of the products shows that addition of SnO₂ enhanced the total oxidation to CO₂ but from the analysis of results of the performance of direct ethanol fuel cells, the PtSnO₂ catalyst showed lower catalytic activity for ethanol electro-oxidation than the Pt-Sn alloy.

In this work, we synthesized SnO₂ by an ex situ method and made a ternary catalyst by adding a tin oxide to PtSn alloy and its performance compared with PtSn.

^{1,2} Department of physical chemistry, Faculty of Science, Tarbiat Modares University, Tehran, Iran
Email: H.Gharibi@gmail.com

2 Material and methods

2.1 SnO₂ synthesis

The steps involved in the synthesis of SnO₂ were: i) addition of the required SnCl₄ · 4H₂O to 50cc of water ii) add the 2M KOH solution to the mixture until the solution were opaque iii) after 6h the mixture was filtered and washed with water 3 times and drying of the solid at 80 °C for 24 h iv) finally, the solid was heated up to 500 °C for 4 h in the stove under ambient gasses to complete oxidation of tin oxide to SnO₂.

2.2 Catalyst synthesis

PtSn alloy nanoparticles were deposited on Vulcan XC-72R by using the modified polyol method [4]. The steps involved in the preparation were: i) incorporation of a predetermined amount of carbon, i.e. Vulcan, to 15 cc of ethylene glycol, and then sonicated the whole mixture for 30 min; ii) addition of the required precursors, i.e. H₂PtCl₆, SnCl₂, and SnO₂, to the composite mixture in the stoichiometric amount required and sonicated for 30min ; iii) 45cc of ethylene glycol was added and sonicated for 30 min; iv) increasing the temperature up to 120 °C, and then keeping it constant for 16 h to allow the nucleation and growth of the alloy metal on the carbon support; v) cooling the suspension down to room temperature; vi) separation of the solid by filtration, subsequent thorough rinsing with water and drying of the solid at 80 °C for 24 h in a oven. The atomic ratio of catalysts were PtSn(1:1) and PtSnSnO₂(1:0.5:0.5) with 10% of metal and metal oxide loading.

2.3 Electrochemical characterization

For the electrochemical characterization, a conventional three-electrode cell was employed. The working electrode was a glassy carbon of 0.031415 cm² geometric area, covered by a thin layer of catalyst imbedded in a Nafion polymer electrolyte film. A Pt foil of 1 cm² geometric area was used as counter electrode and a saturated calomel electrode as reference electrode. The electrolyte was a 1 M C₂H₅OH in 0.5 M H₂SO₄ solution. Most of the electrochemical experiments were carried out at room temperature. The real active electrode area was determined from the CV in acidic media at 50 mV s⁻¹ in 0.5 M H₂SO₄. Chronoamperometric measurements for EO were also recorded at 0.7 V for 120 min. Electrochemical impedance spectra were taken by polarizing in a constant voltage mode at 0.3V, sweeping the frequency from 100 KHz to 100 mHz with an amplitude of 5 mV.

3 Results and discussion

3.1 XRD

The XRD patterns were obtained at a scanning rate of 1°/min with a step size in the 2θ scan of 0.02° in the range 20-80°. Fig.1 Show the tin oxide was synthesized and the sample was pure.

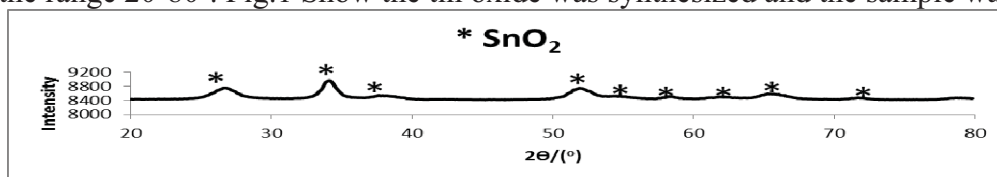


Fig.1. XRD patterns of SnO₂.

3.2 cyclic voltammograms

Fig.2 shows cyclic voltammograms of Hydrogen desorption on Pt-Sn/C and Pt-Sn SnO₂/C catalysts.

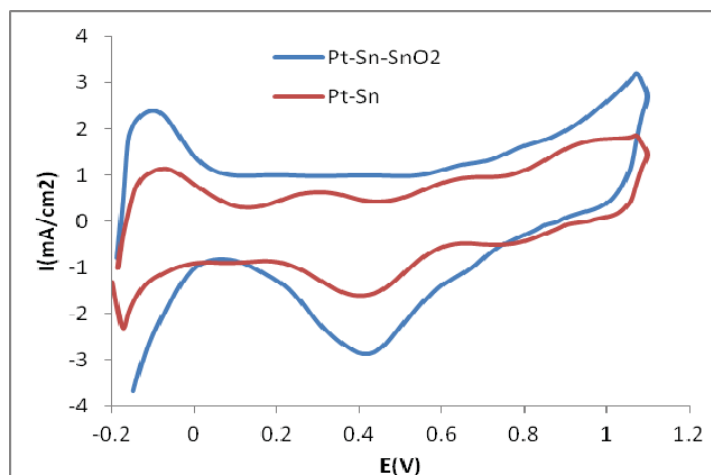


Fig.2. CV scans of PtSn/C(1:1) and PtSnSnO₂/C(1:0.5:0.5) catalysts in 0.5M H₂SO₄ under an argon atmosphere and Potential scan rate:50mVs⁻¹

From the CVs, the electrochemically active surface area (SEAS) is determined by integration of the anodic current corresponding to hydrogen desorption reaction with the correction of double layer region. The SEAS values which can be calculated from Eq. (1):

$$S_{EAS} (m^2 g^{-1}) = \frac{Q_H (\mu C / cm^2)}{210 \times L (g / m^2)} \quad (1)$$

Where Q_H ($\mu C cm^{-2}$) represents the charges corresponding to desorption of hydrogen on the Pt surface, L ($g m^{-2}$) is the Pt loading on the electrode surface, $210 \mu C / real cm^2$ is the charge required to oxidize a monolayer of hydrogen on the Pt surface. Results from table 1 shows PtSnSnO₂ have a higher EAS than PtSn. Maybe in PtSn alloy, some tin particles coverage the Pt and reduce EASA.

Sample	$Q_H (\mu C)$	EAS(m^2 / gr)
Pt-Sn/C	130.8	40
Pt-Sn-SnO ₂ /C	234.3	71

Table1. The EAS values of different catalyst samples determined by hydrogen electroadsorption

3.3 Electrochemical activity of the catalysts for ethanol oxidation

The catalytic activities of the carbon-supported PtSnSnO₂ and PtSn catalysts for ethanol electrooxidation are investigated at ambient temperature by cyclic voltammetry (CV) at a scan rate of $50 mV s^{-1}$ in 1 M EtOH + 0.5 M H₂SO₄(aq) solution (Fig. 3).

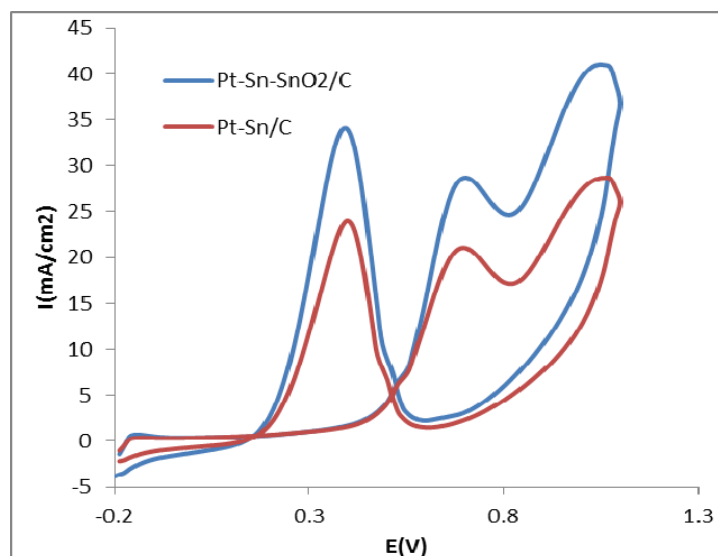


Fig.3. Cyclic voltammograms of the PtSn/C(1:1) and PtSnSnO₂/C(1:0.5:0.5) in 0.5M H₂SO₄+ 1M ethanol solution at the 50th cycle with a scan rate of 50mVs⁻¹.

It is observed that PtSnSnO₂/C catalyst exhibited significantly enhanced catalytic activities for ethanol oxidation relative to PtSn/C catalyst.

3.4 Chronoamperometry

To evaluate both the EOR activity and the stability of the active sites under continuous operation conditions, chronoamperometry was carried out at 0.7 V versus Ag/AgCl for 2 h. Figure 4 shows the current decay curves for the EOR in 0.5 mol/L H₂SO₄ containing 1 mol/L ethanol with a holding potential of 0.7 V at room temperature. The ternary Pt-Sn-SnO₂/C electrocatalyst shows better performance than binary Pt-Sn/C, confirming the beneficial effect of the addition of SnO₂ onto Pt-Sn for the EOR.

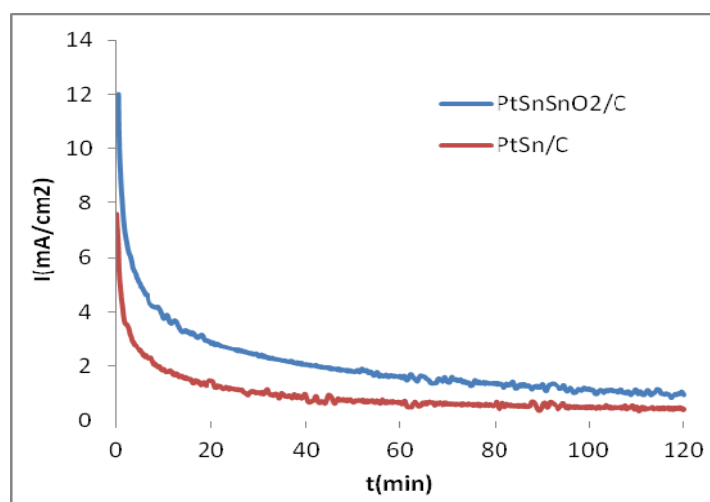


Fig 4. Current-time curves at 0.7V for PtSn/C(1:1) and PtSnSnO₂/C(1:0.5:0.5) in 0.5M H₂SO₄+1M ethanol solution.

3.5 Electrochemical impedance analysis

The AC impedance spectroscopy was further used to investigate the electrochemical behavior of catalysts. The results show that Pt-Sn-SnO₂/C catalyst has a smaller diameter of semi-circle than Pt-Sn/C. The smaller diameter of spectrum in EIS shows a small charge transfer resistance.

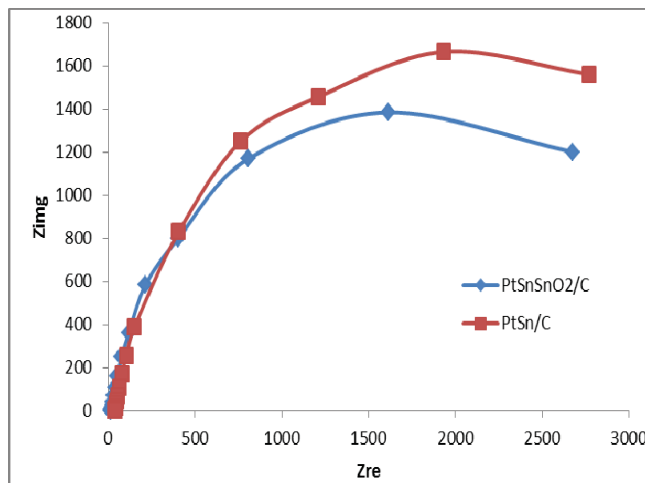


Fig 5. Nyquist plots of EIS for EOR in 0.5 M H₂SO₄+1 M EtOH solution at 0.3 V.

4. Conclusions

The Pt-Sn-SnO₂ catalysts studied here display electrocatalytic activity with respect to ethanol oxidation as evidenced by voltammetric and chronoamperometric measurements. When using PtSnSnO₂ electrodes, higher current density values at constant potentials are obtained for EO in acid media. The results show that using SnO₂ in gives a better performance in ethanol oxidation reaction in three electrode system.

5. References

- [1] C. Lamy, E.M. Belgsir, J.-M. Léger, J. Appl. Electrochem. 31 (2001) 799.
- [2] L. Jiang, G. Sun, S. Sun, J. Liu, S. Tang, H. Li, B. Zhou, Q. Xin, Electrochim. Acta 50 (2005) 5384.
- [3] Zhu M, Sun G, Xin Q. Effect of alloying degree in PtSn catalyst on the catalytic behavior for ethanol electro-oxidation. Electrochim Acta 54 (2009)1511e8.
- [4] Chen M, Xing Y. Polymer-mediated synthesis of highly dispersed Pt nanoparticles on carbon black. Langmuir 21(2005) 9334.



Study of some construction parameters on the Air electrode performance of Zinc-Air semi fuel cell

Rasol Abdullah Mirzaie^{1*}, Mohammad safi Rahmanifar², Nasrin Farshadi¹

1- Fuel cell Research Laboratory, Dept. Of chemistry, Faculty of science, Shahid Rajaei Teacher Training University, Tehran, IRAN

Email address: ra.mirzaei@srttu.edu

2- Faculty of Basic Science, Shahed University, Tehran, IRAN

Abstract:

In this study effect of construction parameters such as KOH amount, pressure and pressing duration on efficiency of gas diffusion electrode (GDE) in Zinc-Air semi fuel cell (ZAsFC) was investigated. For this propose Linear Sweep Voltammetry (LSV) and Electrochemical Impedance Spectroscopy (EIS) were used for comparing electrodes that constructed with different conditions. The results revealed that the pressure has important role on oxygen reduction and evolution reaction. In optimized condition exchange current for oxygen reduction and evolution were improved for 4 and 10 times respectively.

Keywords: Oxygen reduction/evolution reactions, gas diffusion electrode, Zn-air semi fuel cell.

Introduction:

The oxygen reduction reaction (ORR) occurring at the cathode plays a key role in metal-air batteries [1, 2]. ORR in aqueous solutions occurs mainly by two pathways: the direct 4-electron reduction pathway from O₂ to H₂O, and the 2-electron reduction pathway from O₂ to hydrogen peroxide (H₂O₂). In non-aqueous aprotic solvents and/or in alkaline solutions, the 1-electron reduction pathway from O₂ to superoxide (O₂⁻) can also occur [4].

Zn-air semi fuel cell have many advantages including high specific energy, competitive cost, abundant resources, and environmentally benign property, it is expected to be a promising power source and energy storage device in the near future [5]. It is an electro-chemical system powered by the reaction of zinc with oxygen from the air in a basic electrolyte[6]. The key problem the development of Zn-air semi fuel cell is the oxygen-diffusion electrode.

At this study, effect of some construction parameter such as pressing pressure and duration, amount of KOH and pressing frame were investigated.



Material and methods:

Preparation of gas-diffusion electrodes:

A gas-diffusion electrode is composed of a gas-supplying layer and a catalyst layer with a stainless steel mesh. The gas supplying layer is composed of 10% (W/W) polytetrafluoroethylene (PTFE), 7% (W/W) CMC, 60% (W/W) graphite and 5% (W/W) MnO₂ that were mixed well by mortar. After mixing different volume of KOH (9 M) was added and mixed well. The produced paste was rolled on steel mesh and pressed with various pressure and duration. Then electrode was dried in 200 °C oven.

KOH amount: Effect of KOH amount on electrode response was considered. For this purpose effect of KOH amount in electrode was investigated in three levels of 0.09, 0.06 and 0.03 ml of 9 M KOH. Then LSV test results were considered for each electrode with different KOH amounts. For

Pressure: To evaluation of pressure effect on electrode response, the pressure of 30, 40, 50, 60, 70, 80, 90 and 100 Bar were considered. The LSV test results of electrode with different pressure were comprised.

Pressing duration: effect of pressing duration was investigated in three levels of 10, 15, 20 and 30 minutes

Electrochemical testing:

The electrochemical properties of as prepared electrodes were studied by Linear Sweep Voltammetry (LSV) method and Electrochemical Impedance Spectroscopy (EIS) with a three electrode system contain a Ag/AgCl electrode as the reference electrode, a Pt electrode as a counter electrode in 9M OH electrolyte at ambient temperature.

Results:

Figure. 1 shows the LSV of KOH contents on GDE electrode in cathodic (A) and anodic (B) directions. Electrical potential of the LSV test was selected -0.9 to 0 and 0 to 0.5 v for reduction and oxidation, respectively. By increase in potential for reduction, electrical current converged to zero and a peak is seen in - 0.4 v. By potential sweep in anodic direction current is increased too. For investigation of variation of KOH content on LSV current at potential of -0.8 and 0.3v was selected. The results show that the anodic and cathodic current of electrode with KOH amount of 0.03 ml has the maximum values.

For more investigation tafel analysis was performed by polarizing ± 250 mV based on open circuit potential to get exchange current. As it is depicted in Table 1 the KOH amount of 0.03 ml is the optimized value.

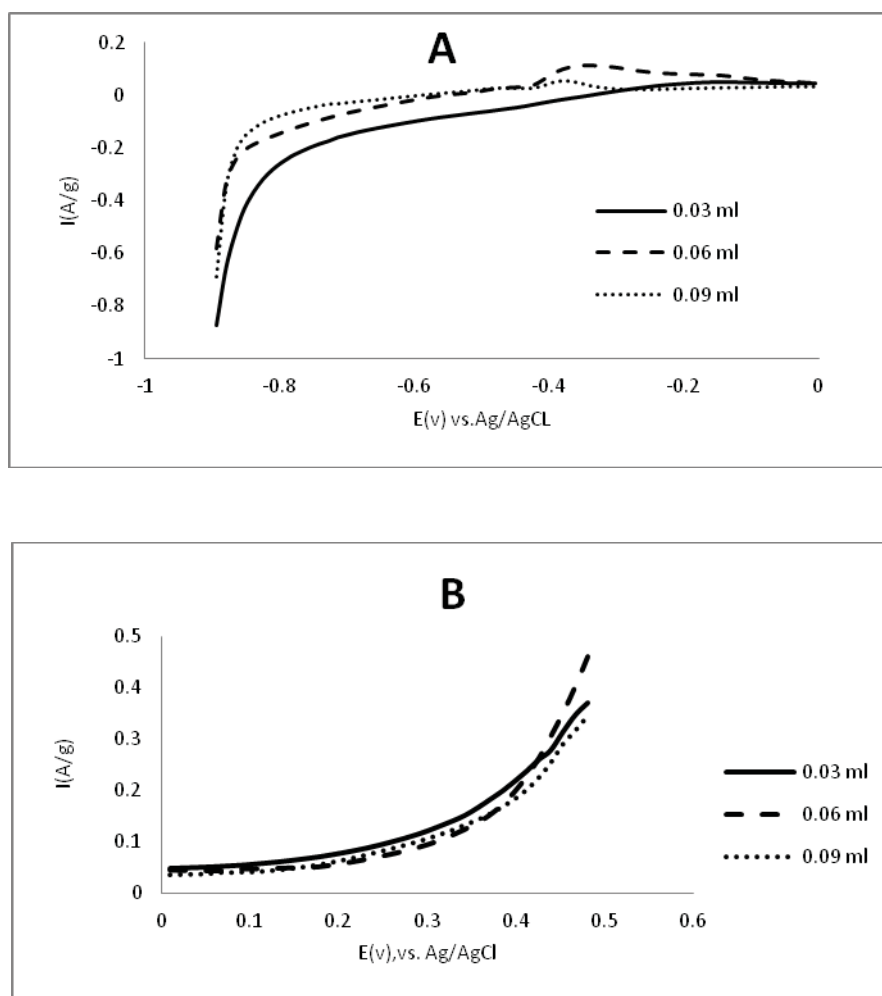


Figure 1: Effect of KOH amount on GDE preparation (A) cathodic direction (B) anodic direction in 9M KOH at scan rate 1 mV/s

Table 1: Effect of KOH content on anodic and cathodic exchange current of GDE

KOH content	I_{0c} mA/g	I_{0a} mA/g	Ocv
0.03 mL	44	27	-0.339
0.06 ml	13.4	4.3	-0.436
0.09 ml	29	36	-0.339

Effect of pressure on GDE was investigated (Figure. 2). Electrical potential of the LSV test was selected -0.9 to 0 volt and 0 to 0.5 volt for reduction and oxidation, respectively. By increase in potential for reduction, current converged to zero and a peak is seen in - 0.4 volt, Figure. 2 A. By increase in potential in oxidation current is increased too, Figure. 2 B.

As it is depicted in table 2, the electrode made under 50 Bar is the best one but the difference between current of electrode prepared under different pressure is low. Optimization criteria

were reduction current at potential of -0.8v was selected also current at 0.3v was selected for oxidation optimization. The LSV curve of electrode (Figure 2) made under 50 bar show that the anode and cathode current of electrode made under is the highest

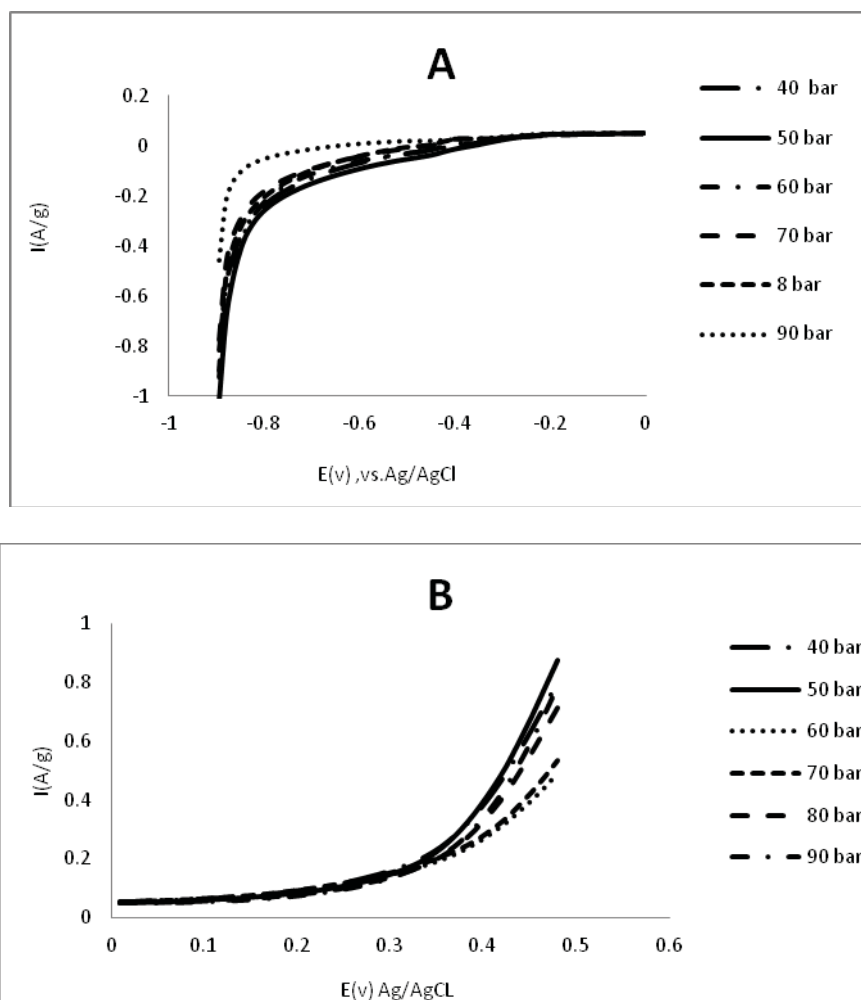


Figure 2: Effect of pressure on GDE preparation (A) cathodic direction (B) anodic direction in 9M KOH at scan rate 1 mV/s

The effect of pressing duration on the performance of GDE is shown in Figure.3. The pressing duration in electrode construction was investigated in different duration time. As it is represented in Table 3 the pressing duration of 15 minute is the optimized value. As mentioned before voltamograms was performed in anodic and cathodic direction for evaluation of pressing duration. By increase in potential for reduction, current converged to zero and a peak is seen in - 0.4 volt. By increase in potential in oxidation current is increased too. For optimization reduction current at potential of -0.8v was selected also current at 0.3v was selected for oxidation optimization. For optimization reduction current at potential of - 0.8v was selected also current at 0.3v was selected for oxidation optimization.

Table 2: Effect of pressure on anodic and cathodic exchange current of GDE.

	I_{0C} mA/g	I_{0a} mA/g	ocv
90 bar	10.7	15.3	-0.644
80 bar	19.5	21.6	-0.45
70 bar	22.1	42.3	-0.464
60 bar	26.4	14.2	-0.408
50 bar	40.7	55.1	-0.352
40 bar	9.3	0.28	-0.422

The LSV curve of electrode (Figure 3) made by pressing duration show that the anode and cathode current of electrode made with the pressing duration is the highest

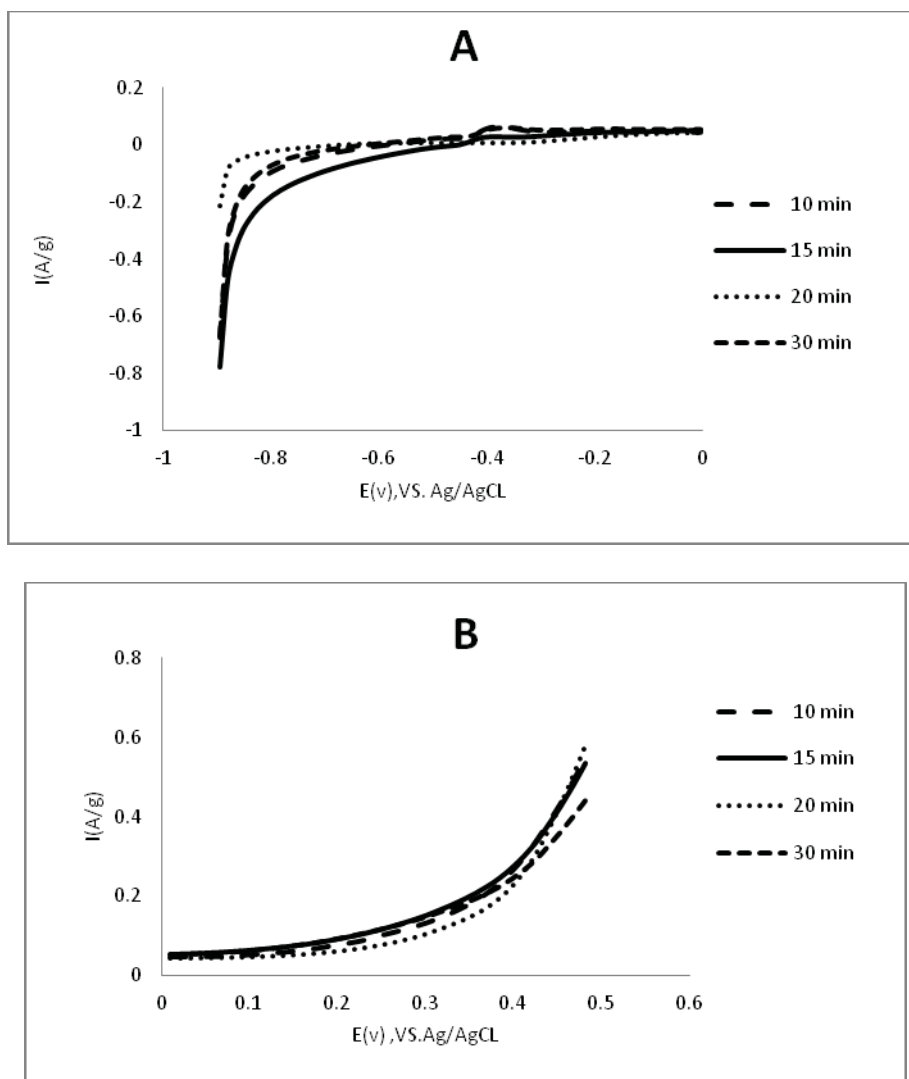


Figure 3: Effect of pressing duration on GDE preparation (A) cathodic direction (B) anodic direction in 9M KOH at scan rate 1 mV/s

Table 3: Effect of pressure duration on anodic and cathodic exchange current of GDE.

pressure duration (min)	I_{0C} mA/g	I_{0a} mA/g	Ocv
10	10.9	11.1	-0.589
15	22.1	42.3	-0.464
20	6.4	5.0	-0.627
30	8.7	10.9	-0.616

The effect of optimization on assembled GDE was investigated further using electrochemical impedance spectroscopy (EIS), with complex impedance plots as shown in Figure 4. The intercept with the real axis at high frequency corresponds to the solution resistance R_s , a result of the combination of electrolyte ionic resistance, the intrinsic resistance of the active materials and binder in the electrodes, contact resistances of the electrodes to current collectors and contacts of the test cells to instrumentation. Moving to lower frequencies, a depressed semi-circle was observed in all cases, assigned to charge transfer processes occurring at the electrode-electrolyte interface; the diameter of this semi-circle gives an indication of the interfacial charge transfer resistance. This was followed at lower frequencies by a curve tending from 45 to 90° at the characteristic “knee” frequency, indicative of a semi-infinite Warburg component with capacitive behavior as a result of electrolyte diffusion within the electrode pores. The results show that charge transfer resistance after optimization reduced also R_s of optimized GDE is lower than that before optimized condition.

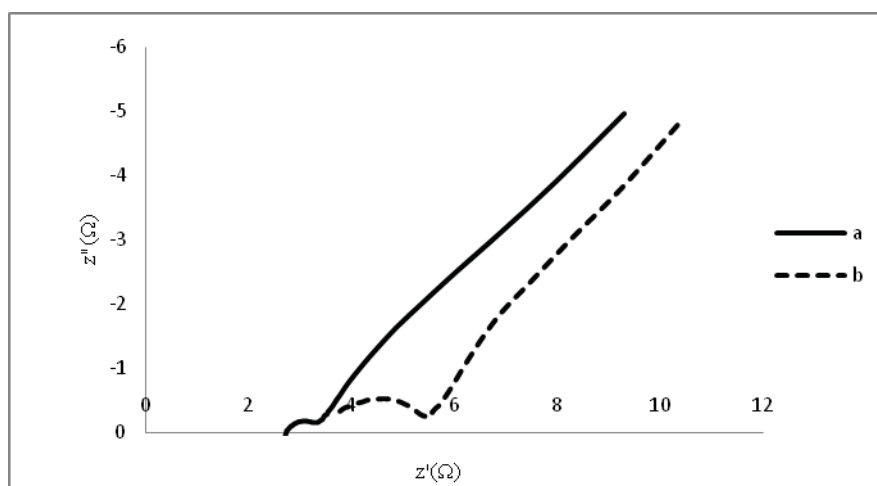


Figure 4: EIS of GDE (a) before and (b) after optimization in 9 M KOH at OCV

Finally the optimized electrode prepared by 0.03 ml KOH (9M), 50 bar pressure and pressure duration 15 min compared with non optimization GDE. It was shown that the optimized electrode has higher performance than non optimized one. The LSV of electrode (Figure 5) shows that the anode and cathode current of electrode before and after of optimization.

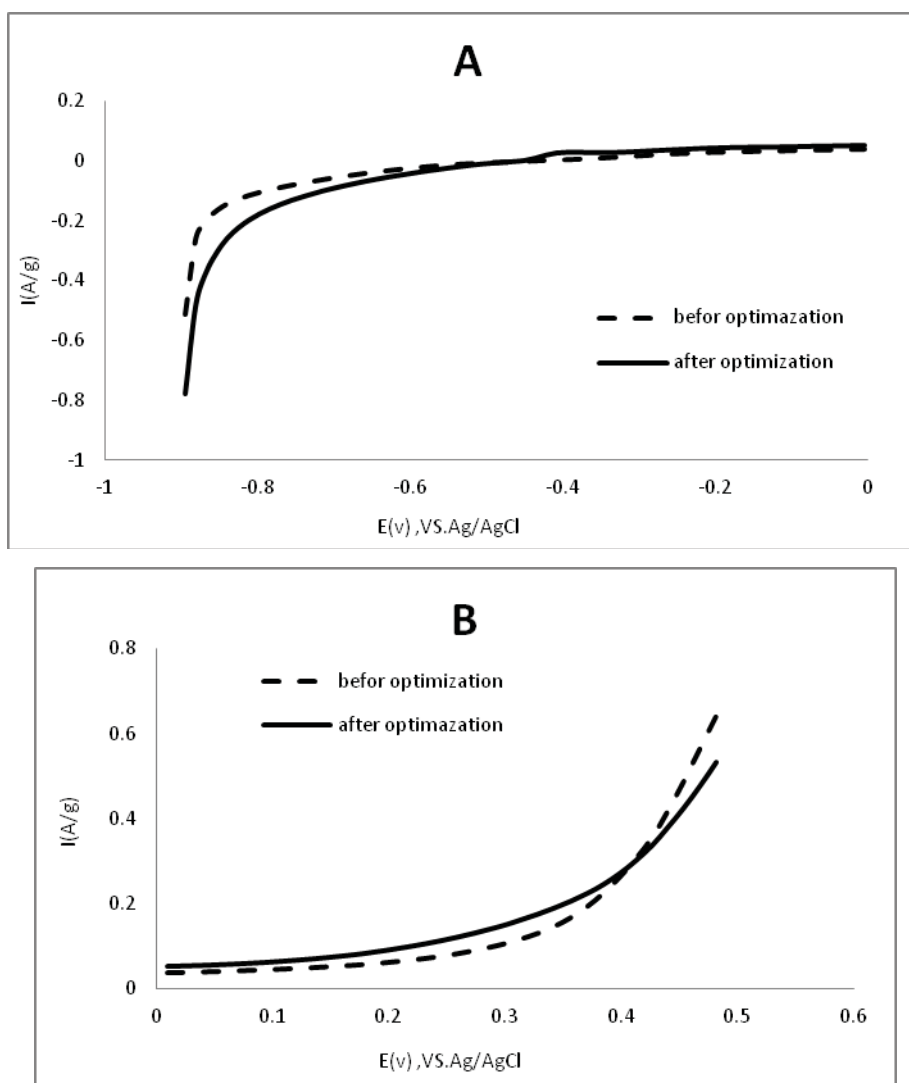


Figure 5: LSV of GDE (A) cathodic direction (B) anodic direction before and after optimization in 9 M KOH at scan rate 1 mV/s

The LSV experiment results for the GDE before and after optimization are shown in Table 4. I_{0c} after optimization improved around 4 times and I_{0a} more than 10 times.

Table 4: effect of optimization on exchange current of GDE.

	I_{0c} mA/g	I_{0a} mA/g	Ocv
Before optimization	6.4	4	-0.408
After optimization	22.1	42.3	-0.464



Conclusions;

Effect of construction variable such as KOH content, pressure and pressure duration on GDE performance has been investigated. When we use optimization condition, the gas diffusion electrode has the best output in produced flow and less resistance. Results show that in optimized condition exchange current for oxygen reduction and evolution were improved for 4 and 10 times respectively.

References:

- 1- C.C. Yang, Int. J. Hydrogen Energy, 29(2004)135.
- 2- V. Neburchilov, H.J. Wang, J.J. Martin, W. Qu, J. Power Sources ,195(2010)1271.
- 3- Zhang L, Zhang J, Wilkinson DP, Wang H. Progress in preparation of non-noble electrocatalysts for PEM fuel cell reactions. J Power Sources,156(2006)171–82.
- 4- Ying Wang , Yu Liu, Xiaojian Lu, Zuopeng Li, Haining Zhang, Xinjiang Cui, Yan Zhang, Feng Shi, Youquan Deng. Silver-molybdate electrocatalysts for oxygen reduction reaction in alkaline media, Electrochemistry Communications, 20(2012) 171–174.
- 5- Xianyou Wang, P.J. Sebastian, Mascha A. Smit, Hongping Yang, S.A. Gamboa, Studies on the oxygen reduction catalyst for zinc–air battery electrode, Journal of Power Sources, 124(2003)278–284.
- 6- Sang-Heon Lee, Yongjoo Jeong, Sihyoun Lim, Eun-Ah Lee, Cheol-Woo Yi., and Keon Kim. The Stable Rechargeability of Secondary Zn-Air Batteries: Is It Possible to Recharge a Zn-Air Battery?" J. Korean Electrochem. Soc., 13(2010) 45-49.



Study of catalyst layer degradation mechanism in proton exchange membrane fuel cell

F. Mirzaei^a, S. Rowshanzamir^{a,b,*}

^a Fuel Cell Laboratory, Green Research Center, Iran University of Science and Technology, Narmak, Tehran, Iran

^b School of Chemical Engineering, Iran University of Science and Technology, Narmak, Tehran 16846-13114, Iran

Abstract

The Department of Energy (DOE) Hydrogen Program supports research and development that has substantially improved the state-of-the-art in fuel cell technology, especially with regard to the major technical hurdles to fuel cell commercialization - durability, performance, and cost of fuel cell components and systems. Catalyst layer degradation has become an important issue in the development of proton exchange membrane fuel cells (PEMFCs). Their performance decrease during operation is attributed, amongst others, to the loss of electrochemical surface area occurring during long-term ageing. These losses are mainly due to catalyst metal degradation and carbon-support corrosion, which are continuous irreversible processes that can dramatically reduce the fuel cell lifetime. This paper reviews the most recent research on degradation and durability issues in the catalyst layers including: (1) platinum catalysts, (2) carbon supports, and (3) Nafion ionomer and interfacial degradation. The review aims to provide a clear understanding of the link between microstructural/macrostructural changes of the catalyst layer and performance degradation of the PEM fuel cell fueled with hydrogen.

Keywords: Durability, Degradation, Catalyst layer, Carbon corrosion, PEM fuel cell.

Introduction

In proton exchange membrane fuel cells (PEMFCs), cost, reliability and durability are important issues that need to be solved before their commercialization [1]. Increasing the durability of proton exchange membrane fuel cells is a major challenge and a growing focus of research attention. So far there remains a wide gap between the ideal and the reality of state-of-the-art PEMFC technology. The operational lifetime for real life applications does not satisfy the requirements for state-of-the-art technologies, e.g., 5000 h for cars, 20,000 h for buses, and 40,000 h for stationary applications[2]. To improve the lifetime of PEM fuel cells, a profound understanding of failure modes for each component as well as the corresponding mitigation strategies is urgently required. In the past few years, numerous papers have been published that focus on the degradation issues of PEM fuel cells. As a result, studies have shown that several

* Corresponding author. Fuel Cell Laboratory, Green Research Center, Iran University of Science and Technology, Narmak, Tehran, Iran. Tel./fax: þ98 2177491242. E-mail address: rowshanzamir@iust.ac.ir (S. Rowshanzamir).



factors can affect the durability of a PEM fuel cell. These factors include PEM thinning, catalyst layer (CL) degradation due to platinum sintering or carbon support corrosion, and gas diffusion layer (GDL) degradation. Among these, CL degradation is one of the most critical factors. More and more experimental results have shown severe catalyst degradation in both automotive and stationary applications. Increasing CL durability is becoming a major challenge and a growing focus of research attention in PEM fuel cell durability studies [3].

According to the currently understood decay mechanisms, a high-durability PEM fuel cell in practice requires the development of a catalyst with proper resilience to sintering and corrosion under universal working conditions. Therefore, current work on improving the durability of PEMFC electrocatalyst is focused mainly on using Pt-alloy catalysts, lowering Pt loading, improving dispersion of Pt particles on the carbon support, improving the stability of the carbon support, and optimizing the fuel cell operating conditions [4].

Catalyst degradation mechanism

According to experimental results, degradation of catalyst layers (CLs) during long-term operation includes cracking or delamination of the layer, catalyst ripening, catalyst particle migration, catalyst washout, electrolyte dissolution (Nafion ionomer), and carbon coarsening. All of these effects, which result either from change in the catalyst microstructure or loss of electronic or ionic contact with the active surface, can result in apparent activity loss in the catalyst layer. It is generally believed that the electrochemical surface area (ECSA) of Pt is one of the most important parameters for characterizing the apparent catalytic activity of PEM fuel cells. Widely used methods to determine ECSA include cyclic voltammetry (CV), CO stripping voltammetry, and CO gas-phase chemisorption. Microstructural changes in catalyst layers are usually examined postmortem through transmission electron microscopy (TEM) and scanning electron microscopy (SEM) [4].

Platinum degradation

Under a combination of different aggressive conditions, such as nanoscale particles, strong acidic environments, oxidizing conditions, reactive intermediates, durative flow of liquid and gas, high electric currents, and large potential gradients, the CL components tend to experience subtle changes and function losses during the operation of PEM fuel cells. For example, Pourbaix diagrams show that Pt is unstable at a potential range of 1.0–1.2 V vs. SHE (Standard Hydrogen Electrode) and at a pH of less than or equal to 1. These imperceptible changes will accumulate and result in a gradual decline in power output during the long-term operation of a PEM fuel cell [3].

Platinum degradation mechanisms

Direct reasons for Pt catalyst degradation include: (1) Pt particle agglomeration and particle growth, (2) Pt loss and redistribution, and (3) poisonous effects aroused by contaminants. All these effects will lead to either a loss of effective catalytic active sites or a loss of electronic contact with conductors, resulting in apparent activity loss in the CL during long-term operation [3].



Platinum agglomeration and particle growth

As demonstrated by many researchers, agglomeration and particle growth of the nanostructure of Pt is the most dominant mechanism for catalyst degradation in PEM fuel cells. First of all, it is believed that nanosized structural elements are able to show size-dependant properties different from bulk elements. Nanoparticles have the inherent tendency to agglomerate into bigger particles to reduce the high surface energy. As particles grow, their surface energy decreases and the growth process slows. The preparation method of the membrane electrode assembly (MEA) could be a cause of agglomeration and particle growth. This can be proven by examining the agglomeration of Pt particles in fresh MEAs. However, during long-term or accelerated stress tests, the Pt/C catalysts can experience more severe agglomeration compared to normal inherit nanoscale Pt particle agglomeration. Ferreira et al. analyzed degraded MEAs after 2000 h of operation under open-circuit voltage (OCV) in a H₂/air cell and explained that small Pt particles dissolve in the ionomer phase and redeposit on larger particles that are separated from each other by a few nanometers, forming a well dispersed catalyst, called “Ostwald ripening”. Virkar and Zhou explained that Ostwald ripening, involving coupled transport of electrically charged species, is the main reason for particle growth in Pt/C catalysts, where the Pt is transported through the liquid and/or through the ionomer and the electrons through the carbon support. Other groups believed that two other mechanisms are predominately responsible for degradation during the potential cycling process: (1) Pt particles detaching from the support and dissolving into the electrolyte without redeposition, and/or (2) a combination of Pt particle coalescence and Pt solution/re-precipitation within the solid ionome. In addition, the agglomeration of Pt can also be affected by many other operating conditions such as temperature or relative humidity. Whatever mechanism the particle growth follows, dissolution of Pt is an important step during the catalyst degradation process. The lower the Pt ion concentration, the lower the degradation kinetics for the Pt/C catalyst. Different electrode aging process may reveal different dissolution reactions taking place at the anode and the cathode. Using the rotating ring-disk electrode (RRDE) experiment following different sweep protocols, Kawahara et al. proved that for a slow anodic triangular wave sweep, the Pt dissolution mechanism is $\text{Pt} \rightarrow \text{Pt}^{4+} + 4\text{e}^-$ or $\text{PtO}_2 + 4\text{H}^+ \rightarrow \text{Pt} + 2\text{H}_2\text{O}$.

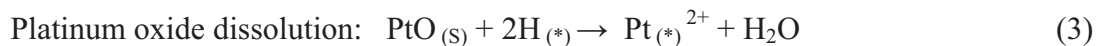
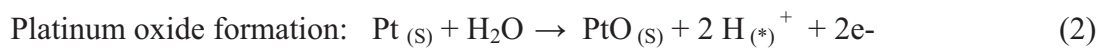
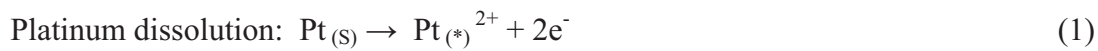
While for a cathodic sweep, the Pt dissolution mechanism is $\text{PtO}_2 + 4\text{H}^+ + 2\text{e}^- \rightarrow \text{Pt}^{2+} + 2\text{H}_2$. Potential values also play an important role during the Pt degradation process. Higher potentials can accelerate Pt dissolvability. Wang et al. suggested that the concentration of dissolved Pt increased monotonically from 0.65 to 1.1 V, and then decreased at potentials higher than 1.1 V due to the formation of a protective oxide film. Therefore, the potential limit for Pt catalyst degradation is generally lower than 1.0 V to avoid the possibility of carbon support corrosion. Yoda et al. also proposed that the Pt electro-catalysts were dissolved even under standard operating conditions [3].

Platinum loss and migration

Pt loss during operation is another major source of CL degradation. This can be caused by many



factors such as Pt dissolution and wash-out. Luo et al. conducted an experiment involving a 10-cell stack operating for 200 h under ambient humidity, ambient pressure and 60°C. Pt content in the Pt/C CL was determined by AAS. The results showed that the Pt content was only 13.5% compared to the original value of 20%, which proved that there are serious Pt losses during the aging process. By weighing and using inductively coupled plasma combined with mass spectrometer (ICP-MS), respectively, Mitsushima et al. and Ball et al. also measured Pt loss from the Pt/C catalyst in acidic electrolyte systems after potential cycling. Pt migration within MEA has been observed to have the same effect as Pt loss. Many groups have reported the presence of Pt particles inside the PEM as well as enrichment of Pt in the CL/PEM interface under different conditions. Fig. 1 shows Pt catalyst particles observed within the PEM and near the CL/PEM interface after degradation. These Pt particles originate from the dissolved Pt species, which diffuse in the ionomer phase and subsequently precipitate in the ionomer phase of the electrode or in the membrane. The precipitation occurs via the reduction of Pt ions by hydrogen that has crossed over from the anode, and thus it is called the “micrometer-scale diffusion process”. The redistribution of Pt nano-particles is actually a complex process involving (1) Pt dissolution, (2) formation of Pt^{z+} species, and (3) reduction to Pt particles by the crossover H₂ from anode to cathode. Considering the potential effect on Pt dissolution, the process of Pt dissolution most likely occurs on the cathode side. Darling and Meyers’ three-step dissolution model for Pt particles in the CL under stressed environments can be a good explanation of the Pt dissolution process:



where (*) denotes ionic species present in water or in the ionomer phase.

In the second stage, faster electro-oxidation of Pt into Pt^{z+} is also possible under higher potentials. Guilminot et al. observed simultaneous Pt²⁺ and Pt⁴⁺ by ultraviolet (UV) detection, which proved the high mobility of Pt contained species. Also, the trans-port of Pt ions can be facilitated by the presence of species contained counter ions, such as F⁻ or SO_x⁻. The migration direction of the species may cross over from the cathode to the anode through the membrane driven by electro-osmotic drag and chemical diffusion. In the third stage, the Pt^{z+} species are chemically and electro-chemically reduced to Pt particles by H₂ that has crossed over the PEM and cathode:



The mechanism described above is a representational hypothesis based on the phenomenon of Pt redistribution during the aging processes. Concerning the direction and degree of the Pt particle migration and redistribution, the result presented in current literature is not always consistent. For example, when conducting a square-wave potential experiment between 0.87

and 1.2 V vs. RHE, Bi and Fuller found that Pt migrated into the PEM near the cathode. However, Ferreira et al. and More et al. observed Pt enrichment at the cathode/membrane interface, while Xie et al. and Guilminot et al. observed Pt enrichment at the anode/membrane interface. The main reason for the diversity of results is that Pt migration and redistribution is a complex process affected by many factors such as potential, operating time, potential cycle numbers, cell operating conditions, gas permeability of the membrane, and other component conditions. Therefore, more detailed explanations of the Pt redistribution and its degradation effect on cell performance are needed for a more profound understanding of the specific characteristics of Pt catalyst behavior during operation.

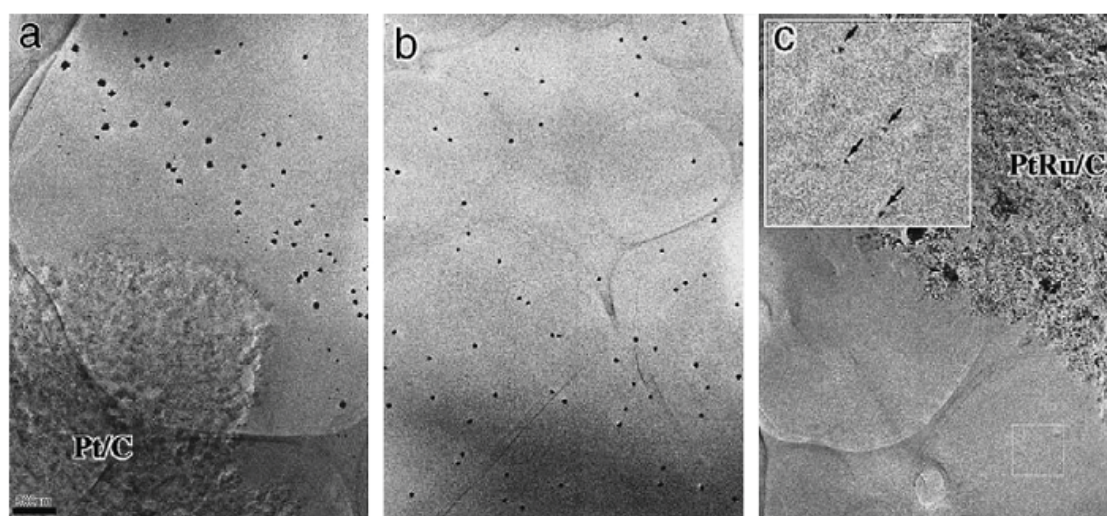


Fig. 1: Cross-sectional TEM images of a MEA after 1.0 V potential holding for 87 h, (a) near the interface of cathode CL and PEM, (b) PEM 10 μ m from the CL, and (c) near the interface of anode CL and PEM [3].

Active sites contamination

Another likely cause of severe degradation of the CL in PEM fuel cells is contamination. In general, contamination can be categorized into two groups based on the sources: the first source includes gas contaminants from the fuel and the air (such as CH₄, CO, CO₂, H₂S, NH₃, NO, NO₂, SO₂, SO₃, and O₃); and the second source includes system-derived contaminants, such as trace amounts of metal ions or silicon from system components (e.g., bipolar metal plates, membranes, and sealing gaskets). Depending on effective time, poison dose, and the reversibility of the poison effect, different contaminants exhibit different poisonous characteristics on Pt catalysts in PEM fuel cells. In literature, the most extensively investigated contaminant is CO. CO can adsorb preferentially on the Pt catalytic active sites and thus block access of H₂ to these sites and decrease the activity of the catalyst. Even trace amounts of these impurities from the reactant gas are likely to reduce fuel cell performance due to kinetic losses of the anode, especially during long-term operation. Some sulfur-containing species are also contaminants that can create irreversible effects on the catalyst and have a strong negative



impact on cell performance. For example, Garzon et al. observed that the cell performance had almost completely deteriorated after 21 h of operation at a constant voltage of 0.5 V when 1 ppm H₂S was added in the anode hydrogen feed. CV results showed the presence of sulfur species chemisorbed onto the Pt surface. Mohtadi et al. also detected two sulfur species formed on the Pt cathode by CV after exposure to either SO₂ or H₂S. They were identified as strongly and weakly adsorbed sulfur on Pt. For some contaminants in the feeding gas, such as NO₂, the negative influence on the fuel cell is reversible. The experimental results of Mohtadi et al. showed that fuel cell performance decreases as a result of NO₂ impurities could be recovered by applying clean air after exposure to the contaminated air. CV spectra of the clean and poisoned MEAs indicated that the poisoning mechanism of NO₂ is not catalyst related. Fig. 4 shows the recovery of the cell after NO₂ poisoning. The contamination mechanism could be an ionomer effect and/or a catalyst–ionomer interface effect due to the formation of NH₄ from NO₂. Other impurities such as Cl⁻ contained anions are also possible contaminants that can induce negative effects on Pt catalyst and performance of PEM fuel cells. These contaminants might come from the preparation of the catalyst or from the feed-stream of the fuel cell. Schmidt et al. investigated that the ORR activity of Pt catalysts with different anions decreased in the order of ClO₄⁻ > HSO₄⁻ > Cl⁻. This order is consistent with the increasing adsorption bond strength of the anions. By using TEM, CV, and EPMA, Matsuoka et al. also proved that the Cl⁻ caused performance changes. The authors described the poison mechanism of Cl⁻ in two steps: (1) Cl⁻ promotes the dissolution of Pt and produces Pt ions ([PtCl₄]²⁻ or [PtCl₆]²⁻) in the inlet-side of the cathode, and (2) the Pt produced ions are reduced into metal Pt by the crossover H₂ and deposited in the PEM to form a Pt band [3].

Carbon support degradation

Nano-scaled Pt particles are usually distributed on carbon support materials to obtain a maximum utilization ratio and to decrease the cost of fuel cells. However, under prolonged operation at high temperatures, high water content, low pH, high oxygen concentration, existence of the Pt catalyst and/or high potential, carbon support is prone to degrade both physically and chemically, which is called carbon oxidation (or carbon corrosion). Carbon oxidation weakens the attachment of Pt particles to the carbon surface, and eventually leads to structural collapse and the detachment of Pt particles from the carbon support, resulting in declines of the catalyst active surface area and fuel cell performance. In Sato et al.'s study, it was proven that no performance degradation occurred when a Pt-black catalyst was applied as the anode electrode catalyst. Under the same hydrogen starvation operation, however, the Pt/C catalyst based fuel cell experienced severe degradation. Generally, carbon corrodes under three conditions: (1) normal operating potentials, (2) gross fuel starvation at the anode, and (3) partial hydrogen coverage at the anode [3].



Carbon corrosion mechanisms

Carbon corrosion may occur as a chemical or an electrochemical process. More specifically, carbon oxidation takes place along two pathways that are believed to proceed by electron transfer, followed by hydrolysis and CO₂ production: (1) incomplete oxidation leading to the formation of surface groups (Eqs. (5) and (6) ; and (2) complete oxidation leading to gaseous carbon dioxide (Eq.(7))



The subscript “s” denotes the surface species. For instance, according to Baumgartner et al.’s report, CO and CO₂ were detected from both the anode and cathode exhausts during degradation test. Carbon corrosion is sensitive to many factors such as potential, carbon surface area, and relative humidity within the fuel cell. Among these factors, potential is the most aggressive. Kangasniemi et al. showed evidence of surface oxidation occurring on Vulcan carbon when potentials were greater than 0.8 V at 65°C and greater than 1.0 V at room temperature. Therefore, carbon corrosion on the cathode is more serious than that on the anode during normal steady-state operation. This was proven by an observed thickness decrease after long periods of operation, especially at high potentials such as OCV and idle conditions. When undergoing unprotected and frequent startup/shutdown of a fuel cell, local cathode potentials can reach up to 1.5 V due to non-uniform distribution of fuel to the anode, accelerating carbon corrosion. Moreover, carbon is prone to be oxidized at lower potentials in the presence of Pt. Roen et al. measured the CO₂ emissions of pure carbon and Pt-catalyzed carbon by on-line mass spectrometry. Their results showed that the presence of Pt in the electrode layer could accelerate the carbon corrosion rate at low temperatures. Also, the magnitude of the CO₂ peaks with respect to cell potential depended on the Pt content in the electrode as well [3].

Ionomer degradation and interfacial degradation

Typically, carbon supported Pt or modified/alloyed Pt catalysts are partially embedded in a proton conducting polymeric ionomer, such as a recast Nafion ionomer, which mediates proton migration as well as water transport inside its pore system. Fig. 2 shows a model of a Pt/ionomer/C microstructure that creates the critical 3-phase interface. Except the Pt catalyst and the carbon support, Nafion ionomer also plays an important role in the CL to influence the structure and performance. The distribution of the ionomer, as well as its content in the CL, can directly impact the ionic/electronic conductivity of the CL. Both chemical/physical degradation and dissolution of the recast ionomer in CL could lead to a decrease in ionic/electronic conductivity and mass transport ability of the MEA. Another aspect concerning the ionic/electronic conductivity and mass transport on a macroscopic scale is the interfacial

components alternation of CL/PEM and CL/GDL during the aging process, which is also a source of performance degradation of PEM fuel cell, especially under extreme conditions.

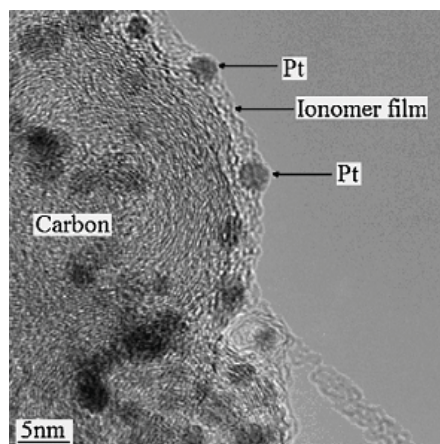


Fig. 2: A TEM image showing model structure of Pt/ionomer/C microstructure that creates the critical 3-phase interfaces [3].

Ionomer degradation

It is known that the hydrogen peroxide, OH radicals or other contaminants produced during the fuel cell reaction are all potential species that damage the functionality and integrity of the Nafion membrane by attacking the perfluorosulfonic acid (PFSA). The same damage could happen to the recast Nafion ionomer employed in the CL during the aging process. The major difference of the ionomer degradation in the CL from that in the PEM is two-sided. On the one hand, the Nafion ionomer in the CL is located adjacent to the fuel cell reaction active sites. Nafion ionomer degradation at these locations can accordingly be slower than that in the membrane, since some of the radical species might be scavenged by the Pt catalyst. On the other hand, the recast Nafion ionomer in the CL is exposed to more water (from both product water generation and inlet water flow) and intermediates under operating conditions. Therefore, the dissolution and chemical degradation of the recast ionomer in the CL might be more severe than that in the PEM. However, there is no sufficient data so far to determine which of the two aspects is weightier than the other. More work is still needed to quantitatively determine the ionomer degradation in both the CL and the PEM. Many research groups addressed that the ionomer degradation/loss might be one of the critical factors that lead to the reduced performance of the CL after long-term operation or AST. Generally, the actual Nafion ionomer network within the CL was not as easily distinguished imaged as Pt and carbon support, when using traditional morphology characterization methods. However, some research groups have made a remarkable progress in confirming the Nafion ionomer degradation in CLs recently. Using cell impedance trends, Xie et al. revealed the degradation of the recast ionomer network in the CL after 500 h of operation under high humidity and constant current. In another quantitative analysis performed with XPS, Zhang et al. detected the CL ionomer degradation (or decrease in concentration) after 300 h of fuel cell operation. According to their report, the CL



surface concentration of fluorine reduced from 50.1% to 38.9%, consistent with a decrease of CF_3 and CF_2 species and an increase in oxidized forms of carbon, which undoubtedly was a proof for the Nafion ionomer change. And with EIS, Hou et al. measured the ionic resistances of the CL at different current densities after the PEM fuel cell suffered from sub-freezing condition. The authors explained that the change of the ionic resistance profile, which was not even across the entire CL, was induced by the ice formation when the temperature reached -10°C . Since the ionic resistance of the cell has been shown to depend primarily on the CL recast ionomer, it is reasonable to conclude that ionomer network degradation is the main reason for the CL degradation in this case. Based on a microstructure reconstruction simulation using statistical information from experimental images of the CLs, Rong et al. also suggested that the competition between the delamination energy accumulated on the interface between Nafion ionomer and the Pt/C agglomerate and the plasticity energy accumulated in the Nafion ionomer plays a key role in microstructure changes during PEM fuel cell aging. However, the understanding of ionomer degradation inside the CL is not thorough enough corresponding to its high importance. Further efforts on the degradation mechanisms of the Nafion recast ionomer on both the anode and the cathode CL, as well as more advanced testing methods and mitigation methods, are urgently required [3].

Interfacial degradation

As the microstructural changes inside the CL accumulate with time, they will undoubtedly lead to a decrease in connection between different solid phases and even mechanical damage to the MEA. As mentioned by Kundu et al., these delamination could cause increased resistance, loss of apparent catalytic activity, and development of flooded areas and pinholes, etc. Guilminot et al. reported an obvious separation and cracks at aged cathode/membrane interfaces during a 529-h constant-power test (0.12 W cm^{-2}). They proved that delamination and cracks between the CL and the PEM or GDL occur more easily due to relative humidity and temperature changes during load cycles. These interfacial degradations have been considered unrecoverable and permanent compared with the recoverable and temporary changes due to water content changes. The most serious interfacial degradation for PEM fuel cells occurs during subzero startups and freeze/thaw cycling. During cold startups in subzero environments, water produced in the CL may freeze instantaneously in the pore systems, covering the electrochemical active sites, hence reducing reaction capability and damaging the interface structure. Yang et al. characterized the cross-sectional samples of the aged MEAs after 110 cold startup cycles. By using TEM and XRD, they confirmed that interfacial delamination between the CL and PEM and the cathode CL pore collapse were among the degradation mechanisms resulting from cold startups. They also explained that the damage degree to the MEA was related to the settling startup current density. CL delamination from both the PEM and the GDL was also observed by Yanetal. During cold startup studies under a wide range of operating conditions. Results showed that when the cell cathode temperature fell below -5°C during the operation,



irreversible cell performance losses were found due to the internal component damages. Similarly, under frequent freeze/thaw cycles, a shear force induced by phase transition between water and ice will cause uneven mechanical stress for different components, resulting in interfacial delamination and damages. For instance, Kim et al. reported interfacial delamination between the CL and GDL after 100 freeze/thaw cycles from -40°C to 70°C . These delamination caused by the ice formation will in turn significantly deform the GDL. Since ice formation is the main reason for structural and performance degradation during exposure to sub-zero temperatures, attention has been paid to minimize the negative effects brought by water. Currently, the most effective way to mitigate interfacial degradation under subzero conditions is to control the water content in the MEA [3].

Conclusion

CL degradation during long-term operation under universal conditions is a complex process that includes many mechanisms that occur in parallel. This paper provides a structural understanding of the significant factors affecting CL degradation including: Pt catalyst ripening, electrocatalyst loss or redistribution, carbon corrosion, electrolyte (Nafion ionomer) degradation, and interfacial degradation. Studies of degradation mechanisms of CL under long-term operation are equally as important as studies of simulated accelerated stress conditions. Extensive effort has been put into this study for half-cells, single cells, and stacks. It is worth noting that each system level of research is valuable and irreplaceable because of its own characteristics. Therefore, conclusions must be drawn cautiously based on a comprehensive research that considers both the real fuel cell operation and the effects of interactions between different materials. Currently, improvements to traditional CL materials are important to the commercialization of PEM fuel cells in the near future. At the same time, research on novel materials is also a key aspect in dealing with issues related to CL degradation. Attractive materials that are in development include: Pt catalysts with highly ordered and optimized structure, non-platinum catalysts, and non-carbon supports with excellent characteristics. Also, more attention should be paid to ionomer and interfacial degradation to investigate fundamental mechanisms with respect to their significant influences on the CL degradation.

[1] N. Yousfi-Steiner, Ph. Moc, otéguy, D. Candusso, D. Hissel, “A review on polymer electrolyte membrane fuel cell catalyst degradation and starvation issues: Causes, consequences and diagnostic for mitigation”, *J. Power Sources* (2009), 194, 130–145.

[2] Jinfeng Wu, Xiao Zi Yuan, Jonathan J. Martin, Haijiang Wang, Jiujun Zhang, Jun Shen, Shaohong Wu, Walter Merida, “A review of PEM fuel cell durability: Degradation mechanisms and mitigation strategies”, *J. Power Sources* (2008), 184, 104–119.

[3] Shengsheng Zhang, Xiao-Zi Yuan, Jason Ng Cheng Hin, Haijiang Wang, K. Andreas Friedrich, Mathias Schulze, “A review of platinum-based catalyst layer degradation in proton exchange membrane fuel cells”, *J. Power Sources* (2009), 194, 588–600.

[4] Shengsheng Zhang, Xiaozhi Yu, Haijiang Wang, Walter Merida, Hong Zhu, Jun Shen, Shaohong Wu, Jiujun Zhang, “A review of accelerated stress tests of MEA durability in PEM fuel cells”, *J. hydrogen energy* (2009), 34, 388–404.



Chemical and Oxidative Stability of Self-humidifying Membranes Based on sPEEK for Proton Exchange Membrane Fuel Cell Applications

S. Rowshanzamir^{1,2}, S. J. Peighambaroust^{*3}, Gh. R. Amirkhanlou¹

¹ School of Chemical Engineering, Iran University of Science and Technology (IUST), Tehran, Iran

² Fuel Cell Section of Renewable Energy Research Laboratory, Green Research Centre, Iran University of Science and Technology, Tehran, Iran

³ Department of Chemical Engineering, University of Tabriz, Tabriz, Iran
j.peighambaroust@tabrizu.ac.ir

Abstract

In this work, the effect of Pt-Cs_{2.5} addition on the durability of nanocomposite membranes has been investigated. The Fenton's test and OCV measurements were used for evaluation of the chemical and oxidative stability of these membranes. The residual weight of nanocomposite membrane having 15 wt.% catalyst increase to over 40 percent after the Fenton's test. Also, in the OCV measurements, a 16 % decrement observes in voltage loss. These results indicate that by addition of Pt-Cs_{2.5} nanoparticles into sPEEK polymer matrix, the oxidative durability of nanocomposite membranes has been improved.

Keywords: Sulfonated poly(ether ether ketone), nanocomposite, proton exchange membrane fuel cell, durability, membrane degradation.

1- Introduction

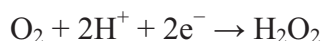
Proton exchange membrane fuel cells (PEMFCs) are promising alternative energy conversion devices for transportation and stationary applications due to their high energy conversion efficiency and environmental benefits. Currently, the development of key materials, the PEMs and the electrocatalysts, is now considered as the impediment to the success of the PEM fuel cell technology and thus should be given high priority [1-4]. The heart of PEM fuel cells is the proton exchange membrane (PEM) which separates catalyzed cathode and anode electrodes. Various efforts were made along different directions aimed to develop alternative membranes which are more economical, have higher operating temperatures, higher proton conductivity and low methanol permeability [5]. Among the appropriate polymers, PEEK which as a new generation of polymers with good mechanical properties and high thermal stability, can be converted to sPEEK, by electrophilic substitution of the sulfonic acid groups in the polymer backbone which is called sulfonation reaction [6,7]. To realize self-humidification operation of PEM fuel cells, most of the literature focuses on development of the functional PEMs, e.g., self-humidifying membranes [8-11]. Heteropolyacids (HPAs) with Keggin anion structures such as PW₁₂O₄₀³⁻ have received the most attention due to their simple preparation and strong acidity in development of composite membranes for PEMFCs [12-15]. But the major factor limit the application of HPAs is their extremely high solubility in aqueous media. For solving this problem, the cesium salt of 12-tungstophosphoric acid, Cs_{2.5}H_{0.5}PW₁₂O₄₀ which is insoluble in water and organic solvents are used [16,17]. Membrane degradation can be classified into three categories: mechanical, thermal, and chemical/electrochemical [18,19]. During fuel cell operation, the overall dimensional change due to non-humidification, low humidification, and relative humidity (RH) cycling are also detrimental to mechanical



durability. The migration and accumulation of the catalysts and the decomposition of the seal into the membrane also negatively affect membrane conductivity and mechanical strength, significantly reducing ductility [20-23]. It has been proposed that chemical degradation leading to ionomer damage and loss in PEM functionality and integrity results from a chemical attack initiated by active oxygen species. Such species as HO• and HOO• originate from the hydrogen peroxide that is generated through incomplete reduction in the oxygen reduction reaction (ORR) [24,25]. Membrane failure could also result from a combination of chemical attack, thermal attack, and mechanical stresses when the fuel cell is subjected to specific extreme conditions. Further investigation has also revealed that the generation of these radicals as well as the chemical degradation of the membrane is accelerated when the fuel cell is operated under open circuit voltage (OCV) and low humidity conditions [26]. Several mechanisms have been proposed, with conflicting views on whether the radicals are formed at the anode, at the cathode, or on both sides of the membrane. The membrane is subjected to both a harsh chemically oxidizing environment on the cathode side and chemically reducing environment on the anode side. The chemical degradation of PEM membranes is mainly attributed to these attacks. There are two proposed mechanisms for the formation of these radicals. General Electric proposed the following [27,28]:

- (1) $H_2 \rightarrow 2H\cdot$ (via Pt catalyst).
- (2) $H\cdot + O_2$ (diffused through PEM to anode) $\rightarrow HO_2\cdot$
- (3) $HO_2\cdot + H\cdot \rightarrow H_2O_2$ (can diffuse into PEM, especially at points where degradation has already begun)
- (4) $H_2O_2 + M^{2+} \rightarrow M^{3+} + HO\cdot + OH^-$
- (5) $HO\cdot + H_2O_2 \rightarrow H_2O + HO_2\cdot$ (hydrogen peroxide radical attacks PEM).

Pozio et al. [29] suggest that the peroxide may also form from incomplete reduction of oxygen on the platinum surface:



The peroxide radicals formed in the MEA are generally accepted to be the cause of membrane degradation. Depending on the type of membrane, the HO• and HOO• radicals generated during the reaction can attack the α -carbon of an aromatic group, the ether links, or the branching points of the polymer. Hydrogen abstraction can also occur. Any H-containing terminal bonds present in the polymer can be attacked by radicals, especially at low relative humidity conditions and temperatures above 90°C. These types of bonds are often introduced during manufacture, for example CF₂COOH [30]. Pianca et al. [31] discuss the methods or reactions which can introduce these endgroups into a fluoropolymer, and some mechanisms of their reactions and degradation. Linden et al. [32] describe several of the reactions that polymers (in general "P") can undergo in the presence of peroxide radicals. The initiation step (1) involves the abstraction of hydrogen from the polymer, which can be followed by numerous propagation steps (2) - (5):

- (1) $PH + HO\cdot \rightarrow P\cdot + H_2O$
- (2) $P\cdot + O_2 \rightarrow PO_2\cdot$
- (3) $PO_2\cdot + PH \rightarrow POOH + P\cdot$
- (4) $PH + HO_2\cdot \rightarrow P\cdot + H_2O_2$
- (5) $PH + HO_2\cdot \rightarrow H\cdot + HO_2\cdot + P\cdot$

In this study, the prepared sPEEK/Pt-Cs_{2.5}H_{0.5}PW₁₂O₄₀ self-humidifying nanocomposite membranes in our previous work were used for the evaluation of nanocomposite membranes'



durability. For investigation of the effect of Pt-Cs_{2.5}H_{0.5}PW₁₂O₄₀ addition on the chemical and oxidative degradation of self-humidifying nanocomposite membranes, Fenton's test and OCV measurements were used.

2- Experimental

2-1- Materials

Aromatic polymer polyether ether ketone was obtained from Sigma-Aldrich Company. The membrane solvent, N,N-dimethyl acetamide, 12-tungstophosphoric acid (H₃PW₁₂O₄₀·29H₂O) as a heteropolyacid materia, the cesium carbonate salt (Cs₂CO₃), chloroplatinic acid hexahydrate, (H₂PtCl₆·6H₂O), the ferrous sulfate heptahydrate (FeSO₄·7H₂O) and hydrogen peroxide (H₂O₂) were totally received from Merck Co.

2-2- Preparation of sPEEK based self-humidifying nanocomposite membranes

In this work, polyether ether ketone polymers were used for preparation of sPEEK membranes by sulfonation reaction of PEEK with concentrated sulfuric acid (95-98%) at 50°C under N₂ atmosphere which was carried out according to the method described in our previous work [11]. Then, sPEEK membranes were prepared by dissolving the sPEEK in conventional solvents such as N,N-dimethylacetamide (DMAc), and then casting the polymer solutions onto clean glass. For preparation of the self-humidifying nanocomposite membranes, the sPEEK with optimum degree of sulfonation, DS_{opt.}, which was obtained from proton conductivity and mechanical properties of sPEEK membranes in our previous work [11], was dissolved in DMAc at temperature of 45°C to prepare a 10 wt% solution. Prior to incorporation of catalyst particles into the sPEEK matrix, the polymer solution were filtered. Then required quantities of Pt-Cs_{2.5} catalyst, which was synthesized by a titration method as described in our previous work [11], was added to the polymer solution and stirred with a magnetic stirrer for 4 h to obtain the homogenous polymer-catalyst solution. For further stirring of the polymer-catalyst solution, this mixture was vigorously sonicated with ultrasonic homogenizer for 30 min. The obtained solution was cast onto a clean flat glass (or petri-dish) and then put at 60°C for 12 h followed by further drying at 120°C under vacuum. The thickness of the nanocomposite membranes was controlled by mild membrane drying and measured by a digital micrometer provided by Mitutoyo. For comparison, the plain sPEEK membrane was fabricated with the same method and same thickness.

2-3- Durability measurement of prepared nanocomposite membranes

For durability evaluation of sPEEK and sPEEK/Pt-Cs_{2.5} nanocomposite membranes, the different experiments has been done. These experiments are classified based on the degradation methods of proton exchange membrane such as chemical and oxidative degradation. Chemical and oxidative degradation has been studied with Fenton's test and OCV measurements. For Fenton's test, the membrane samples were cut into 2*2cm. The initial dry membrane sample weight was first measured and recorded; the sample was next soaked in a beaker containing 100 mL of 3% H₂O₂ aqueous solution at 68°C with stirring. Then enough ferrous ammonium sulfate, Fe(NH₄)₂(SO₄)₂·6H₂O, was added to the 68°C H₂O₂ solution to yield a peroxide solution containing 4 ppm Fe²⁺ (Fenton's reagent). After a 1 h, the membrane samples were removed from the solution and washed in deionized water in order to quench the degradation reaction, followed by drying at 60°C for 12 h prior to weighing. With obtaining the residual weight percent of samples from the following equation, the amount of chemical degradation was evaluated:

$$RW = \frac{W_i - W_f}{W_i}$$

where RW , W_i and W_f are residual weight percent, initial and final weights of samples respectively. When the fuel cell operated in OCV condition, the degradation process of membrane and analysis of its results is very simple. For fuel cell performance evaluation in OCV condition, different membrane electrode assemblies were made with Nafion-117, sPEEK membranes and their nanocomposites. Membrane samples were hot-pressed between two electrodes to form the membrane electrode assembly. In all MEAs, the active electrode area was 5 cm^2 with catalyst loading of 0.4 mg.cm^{-2} for both anode and cathode side of PEM cell. A single PEM fuel cell (Biologic, FCT-150S) with active electrode area of 5 cm^2 was used to investigate the performance of the MEAs including different membranes.

3- Results and discussion

To verify the effect of Pt- $\text{Cs}_{2.5}$ catalyst particles addition on chemical degradation of sPEEK based membranes and also comparison between their durability and Nafion-117 membrane, it has been used from ex-situ Fenton test and in-situ OCV measurement. Table 1 show that the residual weight percents of examined membranes after carrying out of Fenton test for 1 h. It can be seen that after 1 h from test starting, more than half of pure sPEEK has been degraded. By addition of Pt- $\text{Cs}_{2.5}$ nanoparticles into membrane structure, the degradation amount of this membrane in Fenton's solution to some extent will decrease. The results indicated that the chemical properties of sPEEK membranes improve in presence of Pt- $\text{Cs}_{2.5}$ nanoparticles but, we cannot judge the effect of different amount of catalysts due to the near degradation amount of nanocomposite membranes with different weight percents of catalysts. Even with decrease the degradation of nanocomposite membranes based on the sPEEK and Pt- $\text{Cs}_{2.5}$, the chemical durability of these membranes is not comparable with chemical stability of Nafion-117.

Table 1. Residual weight percents of examined membranes after carrying out of Fenton's test for 1 h

Membrane	Amount of Catalyst (wt.%)	Residual weight (%) of membranes after 1 h
Nanocomposite – 1	10	63 ± 3
Nanocomposite – 2	15	65 ± 3
Nanocomposite – 3	20	57 ± 3
Pure sPEEK with DS=65.12 %	0	46 ± 3
Pure Nafion – 117	0	99

Fig. 1 shows that the durability test results of OCV measurements on sPEEK and their nanocomposite membranes with 10, 15 and 20 wt.%. As it can be seen from Fig. 1, the results from OCV test confirm that the Fenton's test results based on the increasing of membrane durability in sPEEK membranes with addition of Pt- $\text{Cs}_{2.5}$ nanoparticles into membrane network structure. In addition, with increasing the amounts of catalyst into membranes up to 20 wt.%, the fuel cell performance intensively decrease and near to the pure sPEEK performance approximately.

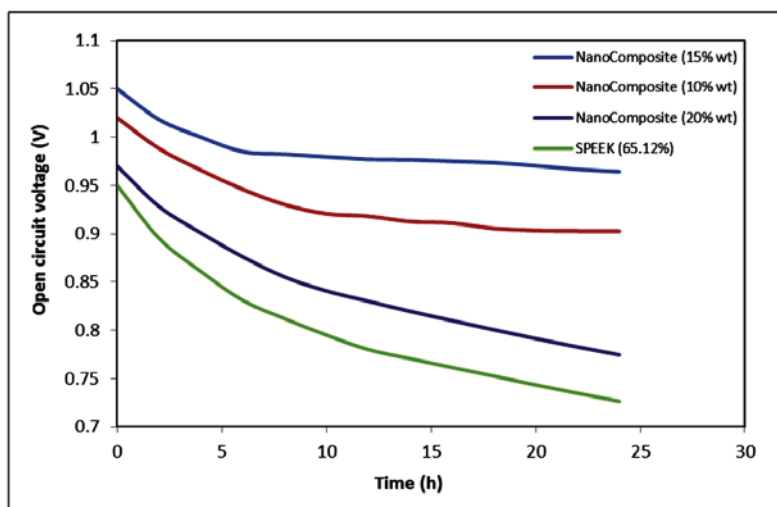


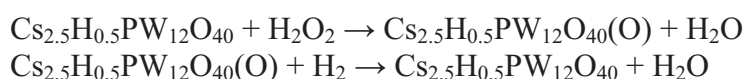
Fig. 1. Durability test results of OCV measurements on sPEEK and their nanocomposite membranes with 10, 15 and 20 wt.%

The OCV decrease amount after 24 h from test starting has been shown in table 2. As it can be seen in table 2, the OCV of nanocomposite membrane with 15 wt.% of catalyst after 24 h from test starting decreases about 8 %, while this OCV decrement excess of 20 % for sPEEK membrane that is a considerable amount. The heteropolyacids in addition to their proton conduction is to be able the grab of hydrogen peroxide and convert to the water.

Table 2. OCV decrease amount after 24 h from test starting

Membrane	Amount of Catalyst (wt.%)	Residual weight (%) of membranes after 1 h
Nanocomposite – 1	10	63 ± 3
Nanocomposite – 2	15	65 ± 3
Nanocomposite – 3	20	57 ± 3
Pure sPEEK with DS=65.12 %	0	46 ± 3
Pure Nafion – 117	0	99

It can be predicted that the chemical degradation decrement of nanocomposite membranes is due to the reaction between heteropolyacid salt with hydrogen peroxide and crossoverable hydrogen from membranes based on these following reactions:



Based on this procedure, the decrease of destructive radicals' production caused to decrease the membrane degradation. This procedure has been proposed by Li et al [33] and Wang et al [34]. The reactant gases crossover through the membrane can be a criterion for evaluation of the membrane chemical degradation. The presence of the Pt sites after incorporation of the Pt-C_s_{2.5}H_{0.5}PW₁₂O₄₀ catalyst in the self-humidifying membrane can effectively suppress the reactants crossover by chemically catalyzing the reaction between the permeable H₂ and O₂, and result in a higher OCV value and improved membrane chemical durability. In Fig. 2, the overall scheme of the self-humidification effect of nanometer size Pt on the hygroscopic

proton conductors for preparation of the self-humidifying nanocomposite membranes has been shown.

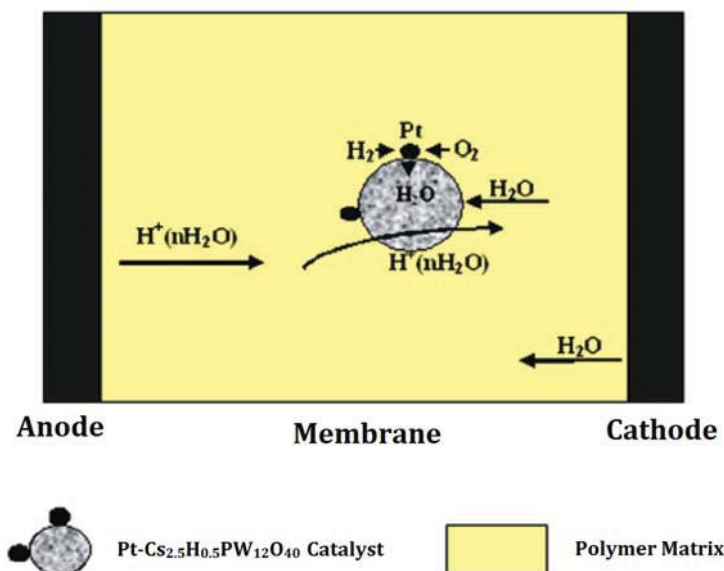


Fig. 2. The overall scheme of the self-humidification effect of nanometer size Pt on the hygroscopic proton conductors

As it can be seen in table 2, the OCV of nanocomposite membranes improves with increasing of the catalyst amount from 10 to 15 wt.% under dry operation conditions. The reason of this behavior is attributed to the proton conductivity increasing of sPEEK/Pt-C_{2.5}H_{0.5}PW₁₂O₄₀ self-humidifying nanocomposite membranes with catalyst amount which was consistent with the proton conductivity results of this type of nanocomposite membranes as described in previous work [11]. But by further increasing of the catalyst amount into nanocomposite membranes up to 20 wt.%, the OCV has been slightly decreased and thus the membrane chemical durability has also been reduced. The reason of this fact can be attributed by existence of the phasic segregation in microstructure of nanocomposite membrane morphology at higher concentrations of catalysts and then the membrane performance is deteriorating. As can be seen by SEM studies in our previous work [11], the whole membrane cross-section has a no segregation of Pt-C_{2.5}H_{0.5}PW₁₂O₄₀ catalyst particles and polymeric matrix phase in nanocomposite membrane with 15 wt.% of catalyst. It means that the interfacial adhesion and compatibility between polymeric and inorganic phases are suitable in this wt.% of catalyst in nanocomposite membrane and there is a no aggregation of nano-size catalyst particles in observed morphology for these nanocomposite membranes. Whereas, in SEM image of nanocomposite membrane (not shown here) with 20 wt.% of catalyst, we can see the segregation of Pt-C_{2.5}H_{0.5}PW₁₂O₄₀ catalyst particles and polymeric matrix phase are occurred and the different morphology of polymeric matrix and catalyst particles are observed. This phase segregation is the result of the catalyst particles' aggregation and caused to the different properties of nanocomposite membrane with 20 wt.% of catalyst and then the membrane performance is deteriorating due to decrease of the homogeneity of nanoparticles' distribution. Really, with phase separation occurrence into nanocomposite membranes, active area of Pt nanoparticles and heteropolyacid salt is reduced and the water production reaction's efficiency is slightly sustained sensible drop. With the loss of the catalytic role of Pt nanoparticles in water production, the self-humidifying property of membrane is also loosed and the membrane performance is deteriorated. With regards to these results, at the high



temperature fuel cells the nanocomposite membranes containing 15 wt.% of catalysts shows the better chemical durability than the other membranes.

4- Conclusion

In this research, the effect of Pt-C_s_{2.5}H_{0.5}PW₁₂O₄₀ addition on the durability of self-humidifying nanocomposite membranes has been investigated. For this purpose, the Fenton's test and OCV measurements were used for evaluation of the chemical and oxidative stability of these nanocomposite membranes. The residual weight of nanocomposite membrane having 15 wt.% catalyst increased to over 40 percent compared to the plain sPEEK after the Fenton's test. Also, in the OCV measurements, a 16 % decrement was observed in voltage loss. These results indicated that by addition of Pt-C_s_{2.5} nanoparticles into sPEEK polymer matrix, the oxidative durability of nanocomposite membranes has been improved for acceptable amount. It can be predicted; this suitable effect of Pt-C_s_{2.5} nanoparticles on the durability of nanocomposite membrane is due to its crystalline structure and self-humidifying properties.

5- Conclusion

- [1] A.M. Pivovar, B.S. Pivovar, J. Phys. Chem. B 109 (2005) 785.
- [2] M.K. Kadirov, A. Bosnjakovic, S. Schlick, J. Phys. Chem. B 109 (2005) 7664.
- [3] M. Saito, K. Hayamizu, T. Okada, J. Phys. Chem. B 109 (2005) 3112.
- [4] E. Spohr, P. Commer, A.A. Kornyshev, J. Phys. Chem. B 106 (2002) 10560.
- [5] M.N.A. Mohd Norddin, A.F. Ismail, D. Rana, T. Matsuura, A. Mustafa, A. Tabe-Mohammadi, Journal of Membrane Science 323 (2008) 404.
- [6] S.J. Peighambaroust, S. Rowshanzamir, M. Amjadi, Int. J. of Hydrogen energy 35 (2010) 9349.
- [7] K. Palanichamy, P. Jin-Soo, K. Chang-Soo, Journal of Membrane Science 279 (2006) 220.
- [8] M. Watanabe, H. Uchida, Y. Seki, M. Emori, P. Stonehart, J. Electrochem. Soc. 143 (1996) 3847.
- [9] M. Watanabe, H. Uchida, M. Emori, J. Electrochem. Soc. 145 (1998) 1137.
- [10] M. Watanabe, H. Uchida, M. Emori, J. Phys. Chem. B 102 (1998) 3129.
- [11] S.J. Peighambaroust, S. Rowshanzamir, M.G. Hosseini, M. Yazdanpour, Int. J. of Hydrogen energy 35 (2011) 10940.
- [12] B.R. Limoges, R.J. Stains, J.A. Turner, A.M. Herring, Electrochim. Acta 50 (2005) 1169.
- [13] N. Giordano, P. Staiti, S. Hocevar, A.S. Arico, Electrochim. Acta 41 (1996) 397.
- [14] S. Malhotra, R. Datta, J. Electrochem. Soc. 144 (1997) L23.
- [15] B. Tazi, O. Savadogo, Electrochim. Acta 45 (2000) 4329.
- [16] G.B. McGarvey, J.B. Moffat, J Catal 130 (1991) 483.
- [17] K. Na, T. Okuhara, M. Misono, J Chem Soc. Chem. Commun. (1993) 1422.
- [18] A. Collier, H. Wang, X. Yuan, J. Zhang, D.P. Wilkinson, Int. J. Hydrogen Energy 31 (2006) 1838.
- [19] A.B. LaConti, M. Hamdan, R.C. McDonald, W. Vielstich, H.A. Gasteiger, A. Lamm, 3 (2003) John Wiley & Sons Ltd., 647.
- [20] F.N. Büchi, S. Srinivasan, J. Electrochem. Soc. 144 (1997) 2767.
- [21] J. Yu, T. Matsuura, Y. Yoshikawa, M.N. Islam, M. Hori, Phys. Chem. Chem. Phys. 7 (2005) 373.
- [22] E. Endoh, S. Terazono, H. Widjaja, Y. Takimoto, Solid-State Lett. 7 (2004) A209.
- [23] X. Huang, R. Solasi, Y. Zou, M. Feshler, K. Reifsnider, D. Condit, S. Burlatsky, T. Madden, J. Polym. Sci. B Polym. Phys. 16 (2006) 2346.
- [24] F.N. Büchi, B. Gupta, O. Haas, G.G. Scherer, Electrochim. Acta 40 (1995) 345.
- [25] H. Wang, G.A. Capuano, J. Electrochem. Soc. 145 (1998) 780.



- [26] E. Endoh, S. Terazono, H. Widjaja, Y. Takimoto, *Electrochem. Solid-State Lett.* 7 (2004) A209.
- [27] A.B. LaConti, M. Hamdan, R.C. McDonald, In: W. Vielstich, A. Lamm, H. Gasteiger, editors. 3 (2003) Chichester, England: Wiley, 647.
- [28] J. Xie, D.L. Wood, D.M. Wayne, T.A. Zawodzinski, P. Atanassov, R.L. Borup, *J Electrochem Soc* 152 (2005) A104.
- [29] A. Pozio, R.F. Silva, M. De Francesco, L. Giorgi, *Electrochim Acta* 48 (2003) 1543.
- [30] D.E. Curtin, R.D. Lousenberg, T.J. Henry, P.C. Tangeman, M.E. Tisack, *J Power Sources* 131 (2004) 41.
- [31] M. Pianca, E. Barchiesi, G. Esposito, S. Radic, *J Fluorine Chem.* 95 (1999) 71.
- [32] L.A. Linden, J.F. Rabek, H. Kaczmarek, A. Kaminska, M. Scoconi, *Coord. Chem. Rev.* 125 (1993) 195.
- [33] M. Li et al, *Electrochemical and Solid-State Letters*, 9 (2004) A92.
- [34] L. Wang, B.L. Yi, H.M. Zhang, D.M. Xing, *Electrochimica Acta* 52 (2007) 5479.



Highly Active Ni-Pt /carbon paper electrode for Methanol Electro oxidation for DMFC applications

Rasol Abdullah Mirzaii*¹, Mohammad Safi Rahmanifar², Abolfath Eshghi¹

¹Fuel Cell research Lab. Department of Chemistry, Faculty of science, Shahid Rajaei Teacher Training University, Tehran, Iran

²Shahed University, Tehran, Iran
(Email: ra.mirzaei @ srttu.edu)

Abstract:

This study deals with the oxidation of methanol in alkaline media. For this purpose, First doping of nickel-platinum particles on carbon paper substrates using electroplating with galvanic deposition method. Then, The morphology of the metal particle coatings on the carbon paper were studied by scanning electron microscopy. The catalytic properties of electrode for methanol oxidation were studied using electrochemical methods such as cyclic voltammetry and chronoamperometry. Therefore Ni-Pt/carbon paper electrode is a good candidate as an anode for direct methanol fuel cells.

Keywords: Nickel, Platinum, Carbon paper, Electro-catalysis, direct methanol fuel cell

Introduction:

Direct methanol fuel cells (DMFCs) are now being considered as attractive power sources for portable power and electric vehicle applications. In a DMFC, it is methanol oxidation at the anode catalyst rather than oxygen reduction at the cathode catalyst that limits the performance of the fuel cell. However, the fuel cells could not reach the stage of commercialization due to the high cost which was mainly associated with the noble [1,2]. Nowadays, all pre-commercial, low-temperature fuel cells use supported Pt and Pt alloys as electro-catalysts. Critical properties to consider when choosing an electro-catalyst support include its electrical conductivity, surface area, microstructure, corrosion resistance and cost. In order to reduce the amount of noble metal loading and also for enhancement of electro-catalytic activity of electrodes, there have been considerable efforts to increase the dispersion of the metal particles on the support. In the present study, we pretreated carbon paper and prepared electro-catalysts, and then characterized these supporting Ni- Pt electro-catalysts in order to find out better catalysts for DMFC [3,4]. The electro-activity of these electro-catalysts for the methanol oxidation in alkaline solutions was studied by different electrochemistry methods.

Experimental

Methanol (Merck, 99.8% purity) and KOH (Merck, 84% purity) were used as received. All other chemicals were of analytical grade and used without further purification. Distilled water was used throughout. The electrochemical experiments were performed in a three-electrode cell

¹ - Fuel cell Research Laboratory, Dep. Of chemistry, Faculty of science, Shahid Rajaei Teacher Training University, Tehran, IRAN

2- Dep. Of chemistry, Faculty of basic science, Shahed University, Tehran, IRAN

arrangement. A platinum sheet was used as counter electrode, while all potentials were measured with respect to Ag/AgCl electrode. Electrochemical experiments were carried out using Zahner and EG&G PARSTAT 2263 Advanced Electrochemical systems.

Treatment of carbon support

a Carbon paper was used as a gas diffusion layer for fabricating gas diffusion electrode which was a circle with the diameter of 11 mm. in order to remove fat and redundant, carbon paper was rinsed in de ionized water and acetic acid with equal ratio and the dried at 200C.

Preparation of electrode

Nickel-platinum particles deposited on carbon paper substrates by using electroplating with galvanic deposition method.

Result and discussion

Ni-Pt particles were deposited on the carbon paper with galvanic deposition method. SEM images of new electro-catalysts show that the Ni- Pt particles are distributed on the surface of the carbon paper. The Cyclic voltammetry method was used to estimate the behavior of the electro-catalysts. The results indicate these improve the electro-catalytic activity for methanol oxidation greatly and confirmed the good electro-catalytic activity and stability of these electro-catalysts.

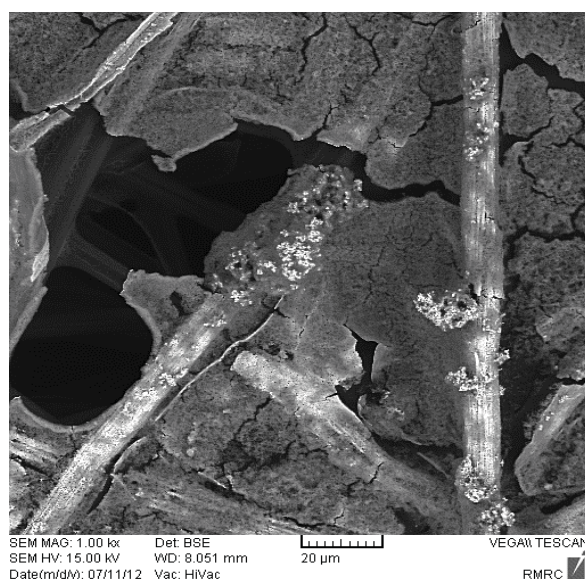


Figure1: The surface morphology of Ni-Pt /carbon paper electrode.

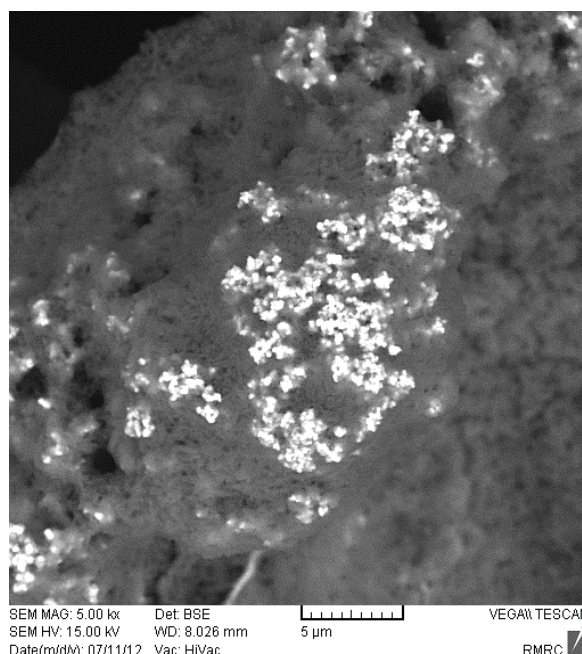


Figure2: The surface morphology of Ni-Pt /carbon paper electrode.

Figures 1, 2 show images of the carbon paper substrates after loading with the Ni-Pt particles are distributed in an almost homogeneous manner at the surface of the carbon paper substrates.

Oxidation of methanol on Ni-Pt/carbon paper

To understand the electrochemical activity of Ni-Pt/carbon paper, the cyclic voltammetric responses of the electrode was recorded. Cyclic voltammetry data were recorded for a 0.25 cm² Ni-Pt/carbon paper electrode in 0.5 M KOH aqueous solution at a scan rate of 20 mV s⁻¹ in the presence of 1 M methanol, as shown in figure 3.

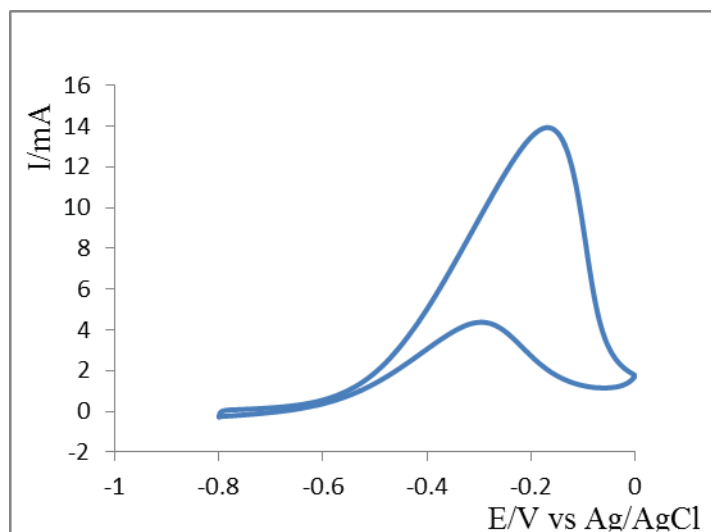


Figure3: Cyclic voltammograms on Ni-Pt /carbon paper electrode in 0.5 M KOH + 1 M methanol at 25° with a scan rate of 20 mV/S.

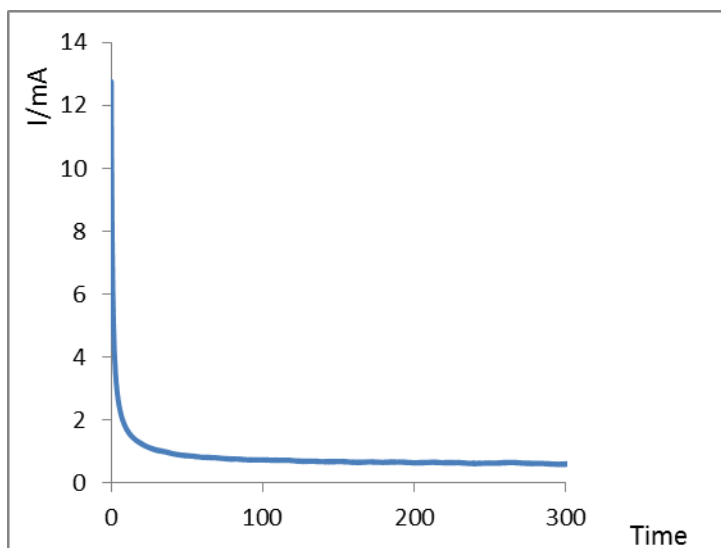


Figure4: Current-time curves for methanol oxidation on Ni-Pt/carbon paper electrode in 0.5 M KOH + 1 M methanol solution.

In order to evaluate the stability of the electro-catalytic activity of the Ni-Pt/carbon paper electrodes towards methanol, chronoamperometric measurements were performed. figure 4 shows the chronoamperometric curves of 1 M methanol + 0.5 M KOH solution on Ni-Pt/carbon paper electrode at for 300s. It was found that the current on the Ni-Pt/carbon paper decreased with time and reached at 300 s to 0.04 mA. These results show that the current represent less decay at the applied constant potential on the Ni-Pt/carbon paper for a long duration (300s), indicating that Ni-Pt/carbon paper exhibits a steady-state electrolysis activity for methanol oxidation.



Conclusion

Ni-Pt/carbon paper with good electro-catalytic property has been successfully fabricated. The morphology and surface analysis of electro-catalysts were investigated by SEM. The electro-catalytic activity of these electro-catalysts for methanol oxidation was evaluated by various electrochemical methods. These electro-catalysts showed high currents for methanol oxidation and good electro-catalytic activity. The Ni-Pt/carbon paper exhibits a steady-state electrolysis activity for methanol oxidation. So it can be said that this electro-catalysts show great prospect in the applications of alcohol fuel cells.

Acknowledgement

We gratefully acknowledge the support of this work by Fuel Cell research Laboratory of Shahid Rajaei Teacher Training University.

References

- [1] Wang, Y., Wang, C.Y., Chen, K.S. (2007). Elucidating differences between carbon paper and carbon cloth in polymer electrolyte fuel cells. *Electrochim Acta*, 52, 3965-3975
- [2] Otomo J, Nishida S, Takahashi H, Nagamoto H. (2008). Electro-oxidation of methanol and ethanol on carbon-supported Pt catalyst at intermediate temperature, *Journal of Electroanalytical Chemistry*, 615 : 84–90.
- [3] Assiongbon K.A, Roy D. (2005) Electro-oxidation of methanol on gold in alkaline media: Adsorption characteristics of reaction intermediates studied using time resolved electro-chemical impedance and surface Plasmon resonance techniques. *Surface Science*, 594:99–119.
- [4] S.M.S.I. Dulal, M.S.Won, Y.B. Shim, J. *Alloys Compound* 494 (2010)463.
- [5] D. Profeti, P. Olivi, *Electrochim. Acta* 49 (2004) 4979.
- [6] M.A. Abdel Rahim, R.M. Abdel Hameed, M.W. Khalil. (2004). Nickel as a catalyst for the electro-oxidation of methanol in alkaline medium. volume 134, *Journal of Power Sources*, pp:160–169
- [7] Wang J, Xib J, Bai Y (2007). Structural designing of Pt-CeO₂/CNTs for methanol electro-oxidation, *Journal of Power Sources* 164: 555–560.
- [8] Bockris JO'M, Veziroglu TN (1983) *Int J Hydrog Energy* 8:323.



Study of Graphite addition on electrochemical activity of platinum on zinc oxide electrocatalyst for oxygen reduction reaction in PEM fuel cell

Rasol Abdullah Mirzaie^{*1}, Mohammad safiRahmanifar², Fatemeh Hamedi¹

1- Fuel cell Research Laboratory, Dep. Of chemistry, Faculty of science, Shahid Rajaei Teacher Training University, Tehran, IRAN

Corresponding Author E-mail: ra.mirzaei@srttu.edu

Abstract:

A fuel cell is an electrochemical device for production of energy from fuel and oxidant. Platinum is the most commonly used catalyst for PEMFC. Catalysts in PEMFC are commonly supported on conductive and porous materials. Carbon is common support for platinum electrocatalyst. Using other materials as supports is attracted researchers for preparing effective electrocatalysts. The preparation of a Pt /zno electrocatalyst for the oxygen reduction reaction in PEM fuel cells was studied in this work. For preparation of electrocatalysts combined process of impregnation and seeding methods were used. The effect of adding Graphite to electrocatalyst and the electrode performance for oxygen reduction reaction was evaluated by three electrode systems. The linear sweep voltammetry (LSV), cyclic voltammetry and impedance Spectroscopy was used for kinetic study of oxygen reduction reaction. Our results show the nano ZnO can be used as a substrate for preparation of platinum electrocatalyst. Also, adding Graphite to the reaction layer improve the electrode performance for oxygen reduction reaction. The optimized concentration of Graphite in the reaction layer is 50%.

Key words: Oxygen reduction reaction; fuel cell; gas diffusion electrode; electrocatalysts; platinum on zinc oxide , non-carbon substrate

Introduction:

Today, fuel cells are widely considered to be efficient and non-polluting power sources offering much higher energy densities and energy efficiencies compared to other current/conventional systems. A fuel cell is an 'electrochemical' device that converts the chemical energy of a fuel (e.g. hydrogen, methanol, etc.) and an oxidant (air or pure oxygen) in the presence of a catalyst into electricity, heat and water. The main objective in fuel cell technologies is to develop lowcost, high-performance and durable materials. A good interaction between the catalyst and the support not only improves catalyst efficiency and decreases catalyst loss but also governs charge transfer. The support can also assist in sufficiently enhancing the catalyst performance and durability by reducing catalyst poisoning (e.g. CO, S, etc.); and in some cases it affects the catalyst particle size. Hence, the choice of support material is vital and highly influential in determining the behavior, performance, longevity and cost effectiveness of the catalyst and the overall fuel cell. However, a multitude of materials other than CBs have been investigated as catalyst supports for PEMFCs. Over the last decade or so, the focus has shifted towards nanostructured supports as they enable

¹. Fuel cell Research Laboratory, Dep. Of chemistry, Faculty of science, Shahid Rajaei Teacher Training University, Tehran, IRAN

².Dep. Of chemistry, Faculty of basic science, Shahed University, Tehran, IRAN



faster electron transfer and high electrocatalytic activity. Broadly, these may be classified into two main categories: (i) carbon based/carbonaceous supports and (ii) non-carbonaceous supports. Among non-carbonaceous based materials, Titanium oxide, Silicon dioxide, Tin oxide, Indium tin oxide nanostructures have been investigated. The search for non-carbonaceous based supports is particularly essential to deal with the issue of carbon corrosion, which is suffered by all carbon supports. Corrosion of the support inherently leads to further issues like loss of catalyst, which drastically affects the overall performance of the fuel cell [1-5,8]. Huang et al. prepared titania supported Pt electrocatalyst for PEMFC cathode. Accelerated degradation test (ADT) studies revealed 10-fold higher ORR for Pt/TiO₂ compared to commercial Pt/C (45.9 wt.% TKK). The authors concluded that Pt/TiO₂ was found to be highly durable and stable as cathode catalyst for PEMFC [6]. Studies conducted by Matsui et al. revealed that when SnO₂ supported Pt catalysts were heat-treated at various temperatures under oxidizing or reducing atmospheres, their catalytic activity for electrochemical oxidation of CO were enhanced because of their peculiar microstructure and metal-support interactions [7].

In this study among different transition metals, the use of ZnO as a substrate has attracted interest because Zinc oxide is one of the most important semiconductor material with direct band gap (3.37 eV or 375nm), good transparency and high electron mobility (>100 cm²/v.s). It has attracted increasing attention due to excellent electrical properties, inexpensiveness, relative abundance, chemical stability towards air. Since ZnO is an important trace element for humans, it is environment friendly and suitable for in vivo application. So we study of Graphite addition on electrochemical activity of platinum on zinc oxide electrocatalyst for oxygen reduction reaction in PEM fuel cell.

Experimental section:

Synthesis nano ZnO powder:

First, 1.0 mmol Zn(CH₃COO)₂·2H₂O was poured in an agate mortar. Then, 4 mmol NaOH was added to the sample and ground for 60 min at room temperature. Finally, the white mixture was transferred to a beaker and washed fully with distilled water and ethanol for several times and dried at room temperature [9].

Electrocatalyst preparation:

Initially, the Pt solution was obtained by H₂PtCl₆ (Fluka) and then adjusting the solution pH with 1 M NaOH, as required, to the desired value. The Zinc oxide slurry was prepared by dispersing of Zinc oxide in de-ionized water, sonicating for 10 min. For the seeded electrocatalyst was prepared by mixing approximately 10% (v/v) of the Pt solution with the Zinc oxide slurry and sonicated for 30 min. The seeded powder was obtained by the reduction of the previous solution with 0.1 M NaBH₄, sedimented by centrifugation and the pellet was harvested and dried by oven. Thereafter, the obtained powder, covered by the seeded Pt, was dispersed in de-ionized water, sonicated for 30 min and then added to the remaining Pt solution (90%) to the required metal loading on Zinc oxide substrate (12.0–35.8% (w/w)). The mixture was again reduced with 0.1 M NaBH₄ under sonication to obtain the catalyst powder, which settled from the solution. The electrocatalyst solution was filtered, washed thoroughly with de-ionized water and dried overnight at 110 °C [10].



Preparation of electrodes:

For the electrode, the catalyst ink was obtained from mixing 1.0 ml of 2-propanol, 1ml distilled H₂O with 30 wt.% of polytetrafluoroethylene solution and 3 mg of electrocatalyst, sonicating them at room temperature for 30 min to obtain the ink which was then coated onto a carbon paper and dried at 200°C for 60 min. This electrode is labeled Pt/zno. Other electrodes are fabricated at various content of Graphite [10].

Electrochemical analysis:

All the electrochemical measurements were carried out using a potentiostat at 27°C in a three electrode system. All the electrode potentials in this work are related to the reference Ag/AgCl electrode in a 0.5 M H₂SO₄ aqueous solution electrolyte. The working electrode was amount of synthesized electrocatalyst powder was coated on Carbon paper and Pt electrode as a counter electrode was used. Linear sweep voltamograms (lsv) were recorded from 0.8 to -0.2 V vs Ag/AgCl in oxygen saturated electrolyte. Cyclic voltammetry technique (CV) in nitrogen saturated electrolyte was performed to calculating the electrode surface area from 0.8 to -0.2 V at 50 mVs⁻¹ scan rate. The electrochemical active surface area (ECAS) is an important parameter in the characterization of Pt electrocatalysts. The ECAS was determined from CV data in the hydrogen adsorption-desorption region using EQ (1). L_{Pt} loading of Pt

$$ECSA(m^2 / g Pt) = \frac{Q_H}{L_{Pt} Q_F} \times 10^{-4} \quad \text{and } Q_F \text{ is } 0.21 \text{mc.} \quad (1)$$

Impedance spectroscopy is an electrochemical technique with broad applications that is growing in importance. Measurement of current and potential under a steady state yields some information concerning a given system. By adding frequency dependence to the macroscopic measurements, impedance spectroscopy expands the information that can be extracted from the measurements. Impedance measurements, however, are not sufficient. Additional observations are needed to gain confidence in the model identification. this technique was used and nyquist plots were recorded at 10 mHz to 100 KHz frequency.

Results and discussion:

Linear sweep voltamograms (lsv) were obtained under O₂ at 27°C , at a scan rate of 1 mV/s in a 0.5 M H₂SO₄ solution from 0.8 to -0.2 V vs Ag/AgCl. The lsv of fabricated electrodes are shown in the Figure 1, as it was seen the ORR current is increasing with decreasing the potential for all of them. By adding Graphite to the electrodes, the performance of electrodes is improved. So that in 50% Graphite in reaction layer of electrodes, the maximum current density was obtained.

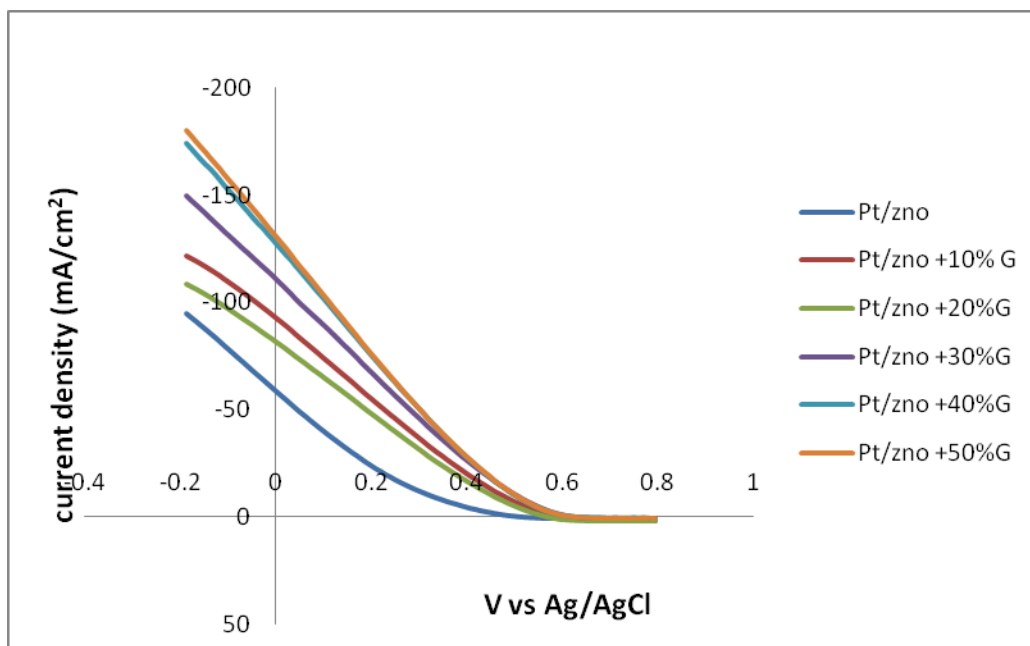


Figure1: polarization plot of 6 electrodes under O₂ at 27°C , at a scan rate of 1 mV/s in a 0.5 M H₂SO₄ solution from 0.8 to -0.2 V vs Ag/AgCl

Figure.2 is shown the Nyquist plots of fabricated electrodes for ORR. According to these results, the best performance of fabricated electrodes for ORR is observed in 50% Graphite in reaction layer.

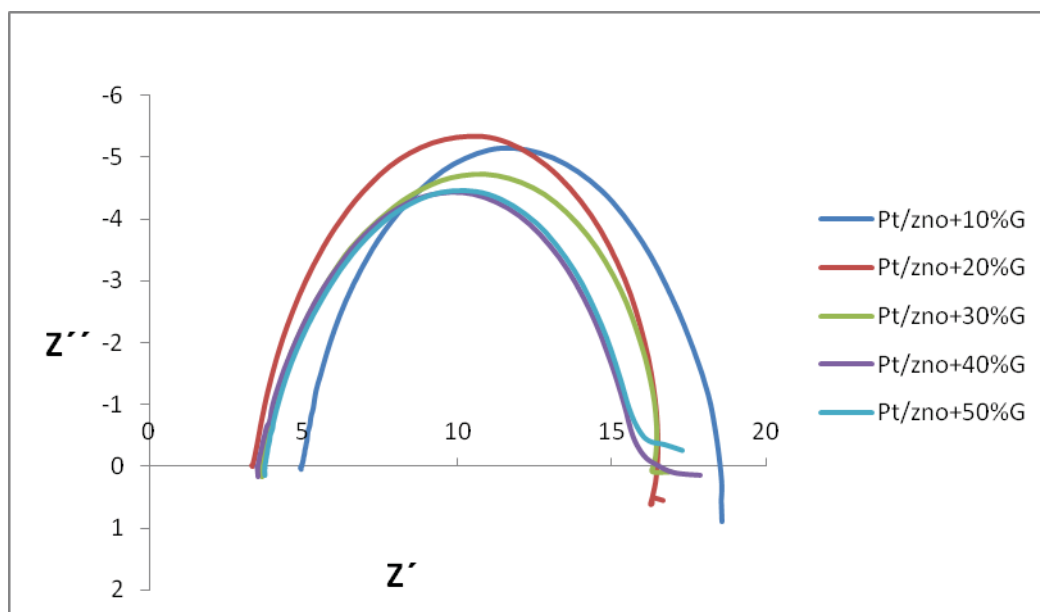


Figure 2: Nyquist plot of 5 electrodes under oxygen at 27°C at 0.5V in a 0.5 M H₂SO₄ solution

The electrochemical surface area of electrodes can be achieved by cyclic voltammetry technique (figure.3). It can be realized the maximum surface area is belonged to 50% Graphite in electrode.

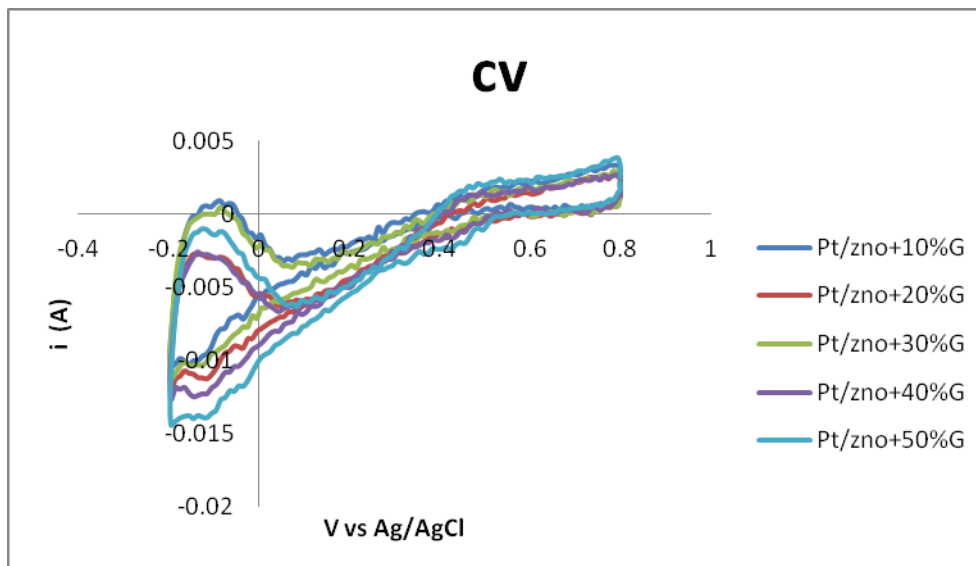


Figure3: cyclic voltammograms of electrodes in H₂SO₄ 0.5 M electrolyte at 50 mV/s and 27°C

Conclusion:

Electrocatalyst substrates play a vital role in ascertaining the performance, durability and cost of PEMFC systems. Pt/zno electrocatalyst was prepared by a combined process of impregnation and seeding methods and prepared electrocatalyst showed an enhancement of electrocatalytic activity toward the ORR process in acid medium. The electronic changes are related to an apparent strong interaction of Pt centers with zinc oxide. On the other hand, in this work adding Graphite to Pt/zno electrocatalyst was studied, according our results, adding Graphite to the reaction layer of fabricated electrodes can improve performance of electrode and increase ORR current and exchange current density. The optimized concentration was found in 50% Graphite in the reaction layer.

References:

- [1] N. Rajalakshmi, N. Lakshmi, K.S. Dhathathreyan "Nano titanium oxide catalyst support for proton exchange membrane fuel cells", *Int. J. Hydrogen Energy* 33 (2008) 7521–7526
- [2] H.P. Bennetto, J.L. Stirling, K. Tanaka, C.A. Vega, " Anodic reactions in microbial fuel cells" *Biotechnol. Bioeng.* 25 (1983) 559–568.
- [3] E. Ticianelli, C. Derouin, A. Redondo, S. Srinivasan, "Methods to Advance Technology of Proton Exchange Membrane Fuel Cells", *J. Electrochem. Soc.* 135 (1988) 2209.
- [4] O. Yamamoto, Y. Takeda, R. Kanno, M. Noda, "Perovskite-type oxides as oxygen electrodes for high temperature oxide fuel cells", *Solid State Ionics* 22 (1987) 241–246.
- [5] Y. Lin, X. Cui, C. Yen, C.M. Wai, " Platinum/Carbon Nanotube Nanocomposite Synthesized in Supercritical Fluid as Electrocatalysts for Low-Temperature Fuel Cells", *J. Phys. Chem. B: Conden. Phase* 109 (2005) 14410–14415.
- [6] S.Y. Huang, P. Ganesan, B.N. Popov, Appl. "Titania supported platinum catalyst with high electrocatalytic activity and stability for polymer electrolyte membrane fuel cell" *Catal. B: Environ.* 102 (2011) 71–77.



- [7] T. Matsui, T. Okanishi, K. Fujiwara, K. Tsutsui, R. Kikuchi, T. Takeguchi, et al., " Effect of Reduction-Oxidation Treatment on the Catalytic Activity over Tin Oxide Supported Platinum Catalysts." *Sci. Technol. Adv. Mater.* 7 (2006) 524–530.
- [8] S. Sharma, Bruno G. Pollet, " Support materials for PEMFC and DMFC electrocatalysts", *J. Power Sources Support materials for PEMFC and DMFC electrocatalysts* 208 (2012) 96–119
- [9] R. Abdullah Mirzaie, F. Kamrani, A. AnarakiFirooz, A. Ali Khodadadi, "Effect of γ -Fe₂O₃ addition on the morphological, optical and decolorization properties of ZnO nanostructures" *Materials Chemistry and Physics*, 133 (2012) 311-316
- [10] W. Trongchuanvij, K. Pruksathorn, M. Hunsom. "Preparation of a high performance Pt–Co/C electrocatalyst for oxygen reduction in PEM fuel cell via a combined process of impregnation and seeding" *Applied Energy*, 88 (2011) 974-980



Cetyltrimethyl Ammonium Bromide Effect on Improved Hydrogen Evolution onto Pt Modified Glassy Carbon Electrode

Jahan-Bakhsh Raouf*, Sayed Reza Hosseini, Seyedeh Zeinab Mousavi-sani

Department of Analytical Chemistry, Faculty of Chemistry, University of Mazandaran, 3rd Kilometer of Air Force Road, Postal Code: 47416-95447, Babolsar, Iran

* *Corresponding author E-mail address: j.raouf@umz.ac.ir (J.-B. Raouf).*

Abstract

In this work, a novel, cost-effective and simple catalyst based on platinum supported onto glassy carbon electrode (GCE) using cetyltrimethyl ammonium bromide (CTAB) as a cationic surfactant is reported. At first, amphiphilic molecules of CTAB are adsorbed onto GCE by immersing the electrode in CTAB solutions. The hydrophilic layer with positive charge is used for accumulation and complexation of hexachloroplatinate anions by immersing the electrode in K_2PtCl_6 solution. The modified electrodes are characterized by scanning electron microscopy, energy dispersive spectroscopy, electrochemical impedance spectroscopy and electrochemical methods. Electrocatalytic activity of Pt particles towards hydrogen evolution reaction (HER) has been investigated. The results show that CTAB significantly enhances the catalytic efficiency of Pt particles on the HER in an aqueous acidic solution.

Keywords: Cetyltrimethyl ammonium bromide; Hydrogen evolution reaction; Platinum



1. Introduction

The hydrogen evolution reaction (HER) is one of the most widely studied reactions in electrochemistry and is important for the development of water hydrolysis and fuel cell technologies [1-4]. For development of the hydrogen-based fuel cell systems as power sources for emission-free electric vehicles, preparation of an active electrocatalyst is still the main subject. Platinum (Pt) is regarded as ideal catalyst for electrochemical production of hydrogen from acidic aqueous solution. Unfortunately, Pt is extremely expensive and therefore it is highly beneficial to reduce the amount of Pt required in processes where it is essential.

The search for new and less expensive alternative materials for HER has been a topic of current interest. Dispersion of Pt micro-particles in polymer matrix [5,6], and less expensive metal materials such as tungsten [7], titanium [8] and tantalum [9] are one of the workhorses of electrochemical technology that reduced the cost of anode materials in the industrial applications. Also, some of them suffer from difficulty in the fabrication of Pt particles.

Surfactants (surface active agents) are a class of molecules that form thermodynamically stable aggregates of inherently nanoscale dimensions both in solution and at interfaces. In solution, surfactant self-assembly has been investigated both theoretically and experimentally, in part because of the importance of such ordered templates in the synthesis of nanometer to micron scale structures with controlled dimensions. Due to the specific amphiphilic structure of surfactants, these molecules can be adsorbed in the interfaces and surfaces. Cetyltrimethyl ammonium bromide (CTAB) as a cationic surfactant have been widely used in electro-analytical chemistry and electrochemical fields [10-15] to change the electrochemical process through adsorption at interfaces or aggregation into supramolecular structure.

Because of difficulty in construction of Pt modified electrodes, it is more advantageous to have a porous electrode of Pt particles fabricated by a novel and very simple method, which deposits the active material directly onto the substrate at room temperature. Recently, we have reported some modified electrodes based on Pt particles by construction of n-Au@Pt/SAM/GFE [16], Pt/n-Cu foam/Cu [17] and n-Pt/Cu-p(8-HQ)/GCE [18], which can successfully catalyze the HER in acidic media. Our literature survey indicates that, there is no report as yet on the usage of the CTAB a commercially available cationic surfactant for accumulation of Pt at the surface of GCE. Thus, in this communication, we report the study of HER on the deposited Pt onto GCE as a low cost electrocatalyst in H₂SO₄ solution.

2. Experimental

2.1. Materials

The solvent used in this work was double distilled water. CTAB and K₄Fe(CN)₆ were obtained from Merck. H₂SO₄, K₂PtCl₆, KCl and K₃Fe(CN)₆ were of analytical grade purchased from Fluka.

2.2. Instrumentation

Electrochemical measurements were performed using a potentiostat and galvanostat (model Autolab, PGSTAT30, Eco Chemie, Netherlands) with FRA software for impedance spectroscopy and GPES software for cyclic voltammetry. All measurements were carried out in a three electrode cell. The utilized three-electrode system was composed of saturated calomel electrode (SCE) as reference electrode, a platinum wire as auxiliary electrode, and glassy carbon disk (0.1 cm in diameter) as working electrode substrate. The surface morphology and elemental analysis of the deposits were evaluated by scanning electron



microscope (model VEGA-Tescan, Razi Metallurgical Research Center) equipped with an energy dispersive spectrometer.

2.3. The electrode modification

Prior to modification of the GCE, it was polished carefully with alumina slurries on a polishing cloth to a mirror finish and then ultrasonically cleaned for 2.0 min in ethanol. Then, the electrode was rinsed thoroughly with distilled water. The Pt deposits were subsequently prepared as follows: The GCE was placed in a well-stirred 3.0 mM CTAB solution. After 2.0 min (optimum time), the obtained CTAB-GCE was rinsed with distilled water, and then the electrode was immersed in 4.0 mM K_2PtCl_6 solution for 5.0 min (optimum time). The unmodified GCE was prepared in the same way without adding CTAB to be used for comparison purposes denoted as Pt/GCE. For HER experiments potentials were cycled between 0.0 to -0.5 V vs. SCE at $v = 50 \text{ mVs}^{-1}$. All experiments were carried out at ambient temperature. In the presence of CTAB, the electrode surface may form hydrophilic films with positive charges. This hydrophilic layer increases the local concentration of $[PtCl_6]^{2-}$ at the surface. It was also assumed that immersion of the CTAB-GCE in the Pt salt solution leads to the formation of a complex containing both Pt ion and CTA^+ .

3. Results and discussion

3.1. Electrochemical properties of the CTAB-GCE

The cyclic voltammogram of $K_4Fe(CN)_6$ solution at the surface of bare GCE give an anodic and corresponding cathodic peak of $Fe(CN)_6^{3-/4-}$ redox system (Figure 1A (a)). However, the voltammetric response is apparently improved at the surface of CTAB-GCE, reflected by the enlargement of the peak currents and the decline of the potential difference (Figure 1A (b)). CTAB can form a surface complex with $Fe(CN)_6^{4-}$ through electrostatic interaction and can also be adsorbed at the interface between the hydrophobic surface and aqueous solution.

For further evaluation of CTAB adsorptive behavior, electrochemical impedance spectroscopy (EIS) was employed. The results of EIS study were in agreement with the cyclic voltammetry results. For the diffusive species, the EIS includes a semicircle part and a linear part, which the semicircle part at high frequencies corresponds to the electron transfer limited process and the linear part at low frequencies corresponds to the diffusion process. Figure 1B (a) shows the EIS of bare GCE which composed of a high-frequency semicircle and a low-frequency straight line. However, a straight line appears at the surface of CTAB-GCE, very different from that bare GCE. This result reflects the fact that the electron-transfer process is facile.

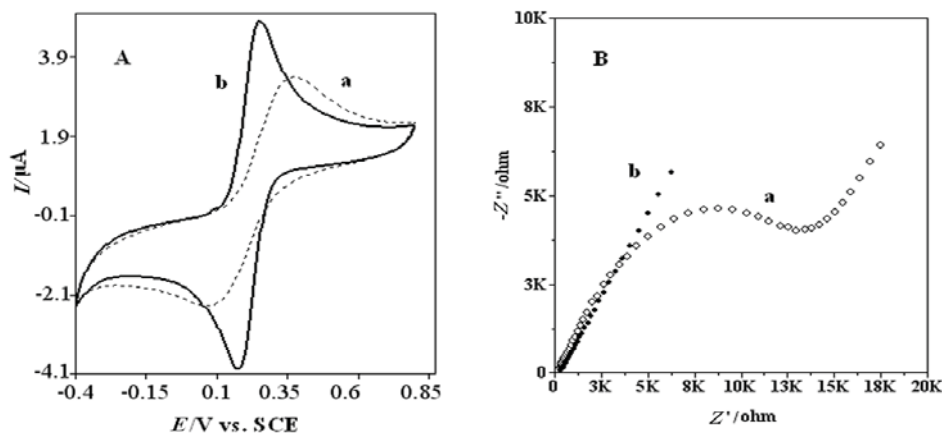


Fig. 1

Figure 1 *A* Cyclic voltammogram of 1.0 mM $K_4Fe(CN)_6$ in 0.1 M KCl solution at the (a) bare GCE and (b) CTAB-GCE at $v=0.05 \text{ V s}^{-1}$. *B* Nyquist plot (Z_{im} vs. Z_{re}) for the Faradaic impedance measurements performed at (a) bare GCE and (b) CTAB-GCE in the presence of 1.0 mM solution of 1:1 $K_3[Fe(CN)]_6/K_4[Fe(CN)]_6$ mixture upon biasing the working electrode at 0.21 V.

3.2. The surface morphology and elemental analysis

Figure 2a shows the morphology of a bare GCE after cleaning process. As can be seen in this image, there are some defects at the surface obtain during the electrode polishing. From the above discussions, it is conceivable that surface morphology of the GCE is influenced by the adsorption of CTAB. The SEM image of the CTAB-GCE shows small aggregates with average size under 100 nm which is beneficial for accumulation of hexachloroplatinate anions (Figure 2(b)). As typical example, image 2(c) shows the morphology of the Pt/CTAB-GCE which it is composed of the small Pt particles. The energy dispersive spectrum (EDS) was used to characterize the surface composition of the CTAB-GCE and Pt/CTAB-GCE (Figure 3). Elemental analysis data given from EDS spectra were listed in Table 1. From the EDS results, N and O are the major elements. C is derived from glassy carbon, N and Br may come from the surfactant. Also, it should be noted that Pt loading in the case of Pt/CTAB-GCE is about 2.5 W%.

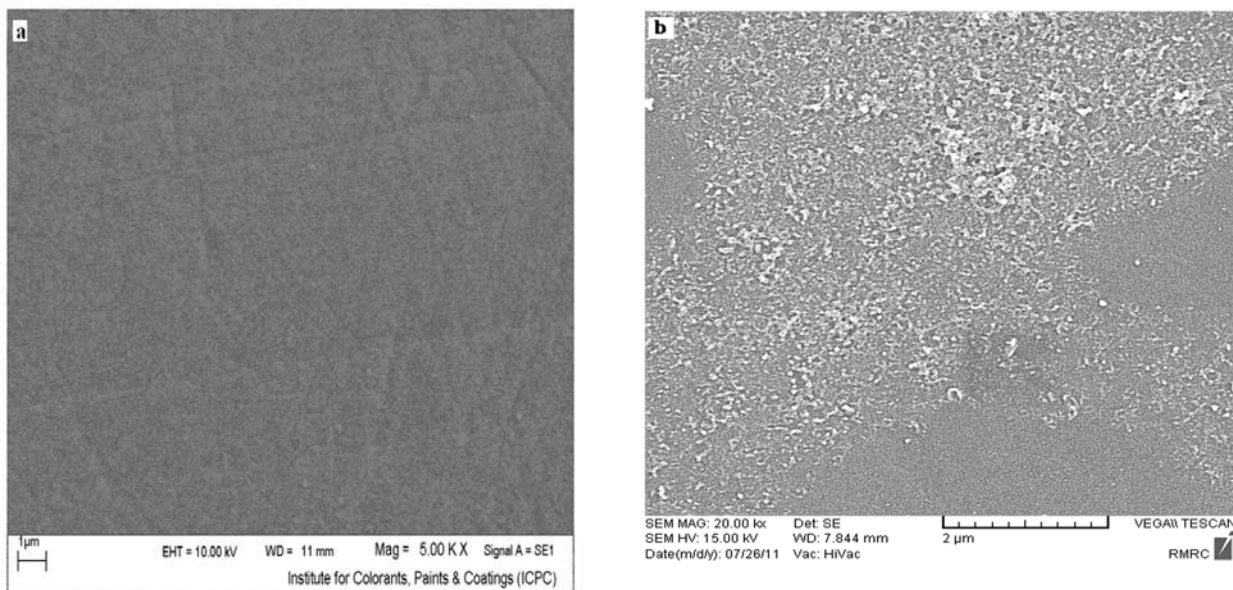


Fig. 2

Fig. 2

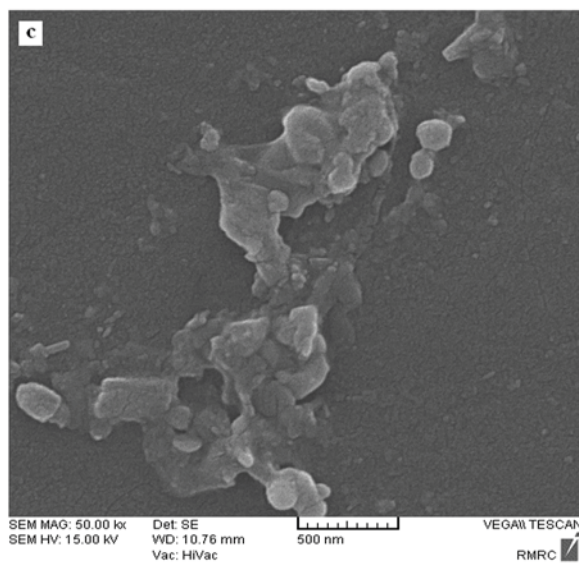


Fig. 2

Figure 2. SEM images of the (a) bare GCE, (b) CTAB-GCE, and (c) Pt/CTAB-GCE.

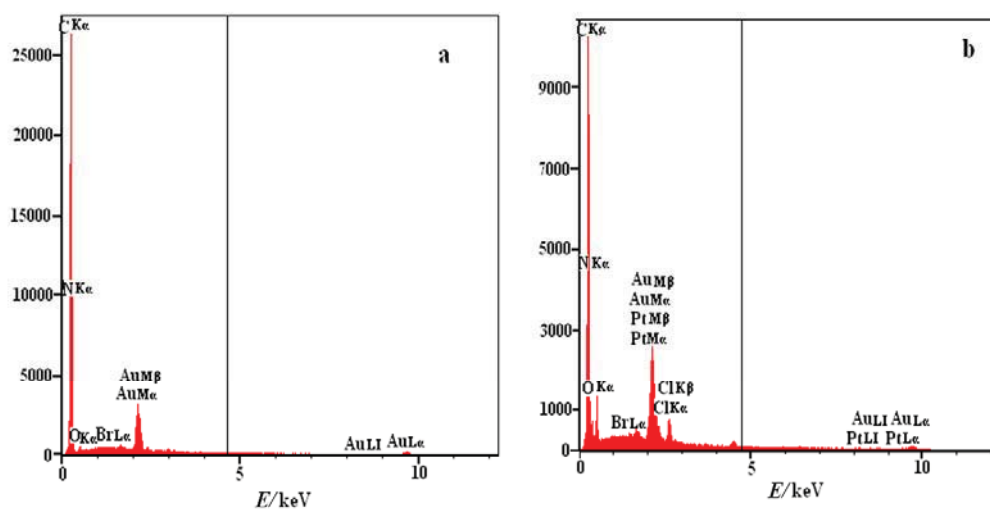


Fig. 3

Figure 3. EDS pattern of the (a) CTAB-GCE and (b) Pt/CTAB-GCE.

Table 1 Elemental analysis data of the CTAB-GCE and Pt/CTAB-GCE from their EDS spectra.

Table 1

Element	CTAB-GCE		Pt/CTAB-GCE	
	Wt %	At %	Wt %	At %
C	71.99	90.13	49.66	66.87
Pt	0.00	0.00	2.53	0.21
Br	0.08	0.01	0.07	0.01
N	5.98	6.42	18.19	21.01
O	2.03	1.91	9.85	9.96
Cl	0.00	0.00	0.86	0.39
Au	19.92	1.52	18.83	1.55
Total	100	100	100	100

3.3. Electrocatalytic activity of the Pt/CTAB-GCE towards HER

The electrocatalytic activity of Pt/CTAB-GCE towards HER was studied in H₂SO₄ solutions by using cyclic voltammetry method. To comparison, overlaid cyclic voltammograms of the HER at a bare GCE, CTAB-GCE, Pt/GCE and Pt/CTAB-GCE were shown in Fig. 4. As can be seen in this figure, CTAB hydrophilic layer enhances electrocatalytic activity towards HER (curve (b)). CTAB can be adsorbed on hydrophobic surface to form surfactant film, which may alter the over-voltage of the electrode reaction and influence the rate of electron transfer. On the Pt/CTAB-GCE, the onset potential of HER occurs at about -0.23 V vs. SCE and is indicated by an increase in the cathodic current (curve (d)). Anodic peak at backward sweep is also attributed to the oxidation of molecular hydrogen. The HER follows the same sequence of reactions reported for polycrystalline smooth Pt electrode [19-21], where the second reaction is the rate-determining step. The performance of this modified electrode towards HER is comparable with our recent work [16].

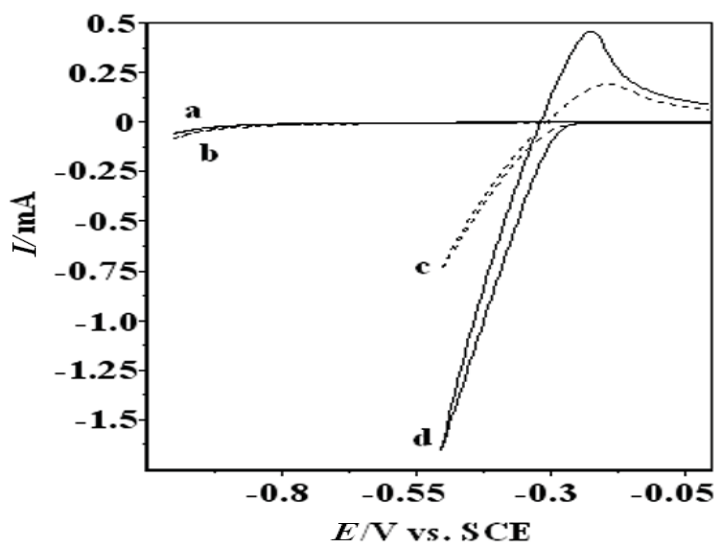
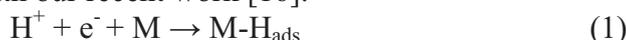


Fig. 4

Fig. 4 Cyclic voltammogram of the HER at the surface of (a) bare GCE, (b) CTAB-GCE, (c) Pt/GCE, and (d) Pt/CTAB-GCE in 0.1 M H₂SO₄ solution at $\nu=0.05 \text{ V s}^{-1}$

4. Conclusion

In this work, we have demonstrated a unique, simple and rapid approach to prepare Pt particles at a solid electrode substrate using a two-step process. The results show that CTAB exhibit a type of adsorptive behavior at the electrode surface. Also, CTAB aggregates at the surface of GCE have a positive influence on HER due to increasing in electron transfer rates. The electrocatalytic activity for HER on the Pt/CTAB-GCE was compared with those at bare GCE, CTAB-GCE and Pt/GCE under the same conditions. It is found that the Pt/CTAB-GCE exhibits superior electrocatalytic activity towards HER.



References

- [1] Hernandez F, Baltruschat H (2007) *J Solid State Electrochem* 11:877-885.
- [2] Mentus S, Mojovic Z, Cvjeticanin N, Tesic Z (2003) *Fuel Cells* 3:15-20.
- [3] Shibli SMA, Dilimon VS (2007) *J Solid State Electrochem* 11:1119-1126.
- [4] Torabi M, Dolati A (2010) *J Appl Electrochem* 40:1941-1947.
- [5] Sun L, Ca DV, Cox JA (2005) *J Solid State Electrochem* 9:816-822.
- [6] Pournaghi-Azar MH, Habibi B (2005) *J Electroanal Chem* 605:136-144.
- [7] Stoychev D, Papoutsis A, Kelaidopoulou A, Kokkinidis G, Milchev A (2001) *Mat Chem Phys* 72:360-365.
- [8] Hao Yu E, Scott K, Reeve RW, Yang L, Allen RG (2004) *Electrochim Acta* 49:2443-2452.
- [9] Mahe E, Devilliers D, Groult H, Pouilleau J (1999) *Electrochim Acta* 44:2307-2315.
- [10] Hosseinzadeh R, Sabzi RE, Ghasemlu K (2009) *Coll Sur B: Biointer* 68:213-217.
- [11] Ghaemi M, Khosravi-Fard L, Neshati J (2005) *J Power Sour* 141:340-350.
- [12] Li C (2007) *Coll Sur B: Biointer* 55:77-83.
- [13] Hu C, Hu S (2004) *Electrochim Acta* 49:405-412.
- [14] He Q, Dang X, Hu C, Hu S (2004) *Coll Sur B: Biointer* 35:93-98.
- [15] Wang F, Fei J, Hu S (2004) *Coll Sur B: Biointer* 39:95-101.
- [16] Raoof JB, Ojani R, Rashid-Nadimi S (2010) *J Electroanal Chem* 641:71-77.
- [17] Raoof JB, Ojani R, Kiani A, Rashid-Nadimi S (2010) *Int J Hydrogen Energy* 35:452-458.
- [18] Raoof JB, Ojani R, Asghari-Esfeden S, Rashid-Nadimi S (2010) *Int J Hydrogen Energy* 35:3937-3944.
- [19] Habibi B, Pournaghi-Azar MH, Razmi H, Abdolmohammad-Zadeh H (2008) *Int J Hydrogen Energy* 33:2668-2678.
- [20] Conway BE, Bai L (1986) *J Electroanal Chem Inter Electrochem* 198:149-175.
- [21] Parsons R (1958) *Trans Farady Soc* 54:1053-1063.



Ni/PMT(TX-100)/MCPE as Anode Catalyst for Direct Ethanol Fuel Cells

Reza Ojani*¹, Jahan-Bakhsh Raoof², Mona Goli³

*Electroanalytical Chemistry Research Laboratory, Department of Analytical Chemistry,
Faculty of Chemistry, University of Mazandaran, Babolsar, Iran
First author E-mail (Fer-o@umz.ac.ir)*

Abstract

Poly (m-toluidine) (PMT) was prepared by oxidation of PMT in acidic aqueous solution in the presence of Triton X-100 (TX-100) at the surface of carbon paste electrode (CPE). Then transition metal of nickel was incorporated into the polymer by electrodepositing of Ni(II) from NiSO₄ acidic solution using potentiostatic technique. The electrocatalytic oxidation of ethanol was studied by cyclic voltammetry and chronoamperometry methods at the surface of obtained Ni/PMT(TX-100)/MCPE. The electrochemical characterization of this electrode exhibits redox behavior of Ni(III)/Ni(II) couple in alkaline medium. It has been shown that PMT/TX-100 film on the surface of the CPE improves efficiency of the catalyst toward the ethanol electrooxidation. The anodic peak current of ethanol oxidation increases with increasing ethanol concentration up to 0.4 M. Finally, the catalytic rate constant (k) for the ethanol oxidation reaction was calculated $3.87 \times 10^4 \text{ cm}^3 \text{ mol}^{-1} \text{ s}^{-1}$ by using a chronoamperometric technique.

Keywords: Fuel cells, Ethanol electrooxidation, Nickel particles, Poly (m-toluidine), Triton X-100

1 Introduction

Fuel cells are considered as green and efficient power generation assembly due to their high efficiency and little or no pollution [1–4]. Among various types of fuel cells, the direct fuel cells which take small organic molecules as fuels have attracted much attention as power sources for portable electronic devices and fuel-cell vehicles owing to its high energy density and low operating temperature [5]. Low molecular weight alcohols such as methanol, ethanol and ethylene glycol have been generally proposed as the fuel for proton exchange membrane fuel cells (PEMFC) due to high mass energy density, simple set-up and availability of the liquid fuel (easy handling, storage and distribution). However, methanol has some disadvantages, for example, it is relatively toxic, has a low boiling point (65 °C), and is not a primary fuel. Therefore, other alcohols are being considered as alternative fuels [6]. Ethanol is an interesting and attractive fuel for electric vehicles, mobile telephone and laptops. Besides, ethanol can be produced from agricultural products and it is the major renewable biofuel obtained from the fermentation of biomass [7]. Ethanol is not toxic and less volatile. It is

¹ Reza Ojani: Electroanalytical Chemistry Research Laboratory, Department of Analytical Chemistry, Faculty of Chemistry, University of Mazandaran, Babolsar, Iran

² Jahan-Bakhsh Raoof, E-mail: J.Raoof@umz.ac.ir

³ Mona Goli, E-mail: Mona_g4485@yahoo.com



inexpensive and easily transported. It can be easily produced in great amounts by fermentation. So, proton exchange membrane fuel cells (PEMFC) using ethanol as a fuel have been studied [8,9].

In the present work, poly (m-toluidine) was prepared by electropolymerization of monomer solution in the presence of Triton X-100 at the surface of carbon paste electrode. Then, transition metal of nickel was incorporated at the surface of the polymer by electrodeposition of Ni (0) particles from NiSO₄ acidic solution using electrolysis at fixed potential. Therefore, poly (m-toluidine)/TX-100 modified CPE, which is a conductive organic matrix was prepared and allowed a better dispersion of nickel particles as a catalyst for ethanol electrooxidation which has a significant attraction in direct ethanol fuel cells.

2 Experimental

Graphite powder and paraffin were mixed by hand mixing with a mortar and pestle for preparation of carbon paste electrode. Then the resulting paste was inserted in the bottom of a glass tube (internal radius: 2.2 mm). The electrical connection was implemented by copper wire lead matched into the glass tube. Later modification of the mentioned electrode was performed as following: Electropolymerization of m-toluidine monomer aqueous solution by potential cycling (10 cycles at a scan rate of 50 mV s⁻¹) between 0.0 and 1.2 V versus Ag|AgCl|KCl (3 M) in aqueous solution containing 0.5 M H₂SO₄, 6 mM m-toluidine monomer and 6 mM Triton X-100. Deposition of nickel particles into PMT(TX-100) films by electroreduction of 1.5 M NiSO₄ in 1.0 M H₂SO₄ solution. Electroreduction step was carried out using chronoamperometry technique (-1.0 V versus Ag|AgCl|KCl (3 M) for 900 s). After this, the electrode was removed and rinsed with water and the sides were wiped with soft tissue paper.

3 Results and Discussions

3.1 Electrocatalytic oxidation of ethanol at Ni/PMT(TX-100)/MCPE

Figure 1 shows the cyclic voltammograms of the CPE, Ni/MCPE, Ni/PMT/MCPE and Ni/PMT(TX-100)/MCPE in the presence of 0.1 M ethanol and 0.1 M NaOH at the scan rate of 20 mV s⁻¹. Also, Inset Figure 1 shows the electrochemical behavior of Ni/PMT(TX-100)/MCPE in the absence and presence of ethanol. It is clear that there is a remarkable enhancement in the anodic peak current for ethanol oxidation at the surface of Ni/PMT(TX-100)/MCPE (Inset Figure 1 (curve b)). The difference in redox currents reflects the effective active surface areas that are accessible to the electrolytes. Apparently, the porous PMT(TX-100) has higher effective surface areas. These observations can explain clearly the role of the PMT(TX-100) on the enhancement of electrocatalytic oxidation currents of ethanol. Indeed the PMT(TX-100) is a good and proper bed for immobilization of nickel particles. It seems that the main and plausible reason for such an enhancement is the formation of a polymer film backbone at the surface of CPE that provides the facile arrival of ethanol on Ni catalytic centers. If we compare electrodes Ni/PMT(TX-100)/MCPE, Ni/PMT/MCPE and Ni/MCPE, we observe that Ni/PMT(TX-100)/MCPE is a more effective catalyst for the electrooxidation of ethanol.

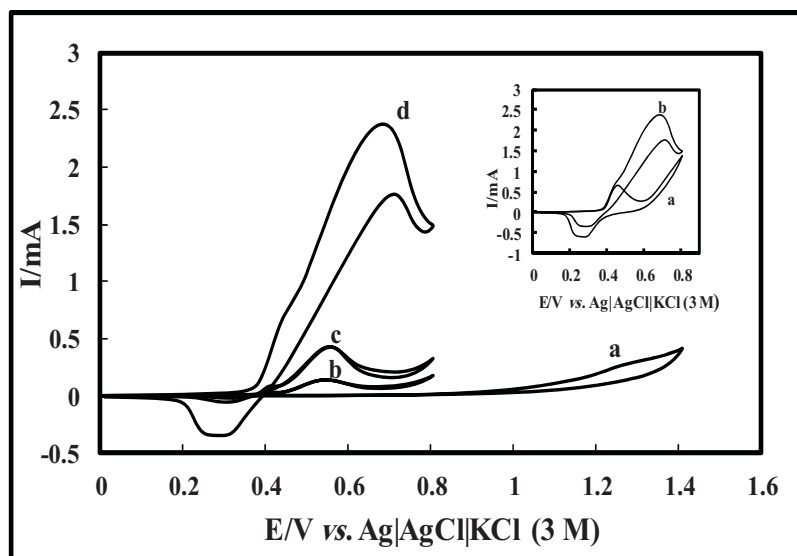


Figure 1: Cyclic voltammograms of (a) CPE, (b) Ni/MCPE, (c) Ni/PMT/MCPE and (d) Ni/PMT(TX-100)/MCPE in 0.1 M NaOH + 0.1 M ethanol at $\square = 20 \text{ mV s}^{-1}$. Inset: Electrochemical responses of Ni/PMT(TX-100)/MCPE in 0.1 M NaOH (a) in the absence and (b) the presence of 0.1 M ethanol, $\square = 20 \text{ mV s}^{-1}$.

3.2 Effect of ethanol concentration

Figure 2 shows cyclic voltammograms of Ni/PMT(TX-100)MCPE in the presence of various concentration of ethanol from 0.009 to 0.8 M. It is clearly observed that upon increasing ethanol concentration its oxidation develops in the region of the electrochemical formation of Ni(III). Thus, it is likely that the Ni(III) species are the active moiety which efficiently speeds up the oxidation of ethanol. In Inset Figure 2 is clearly observed that the anodic current increases with increasing ethanol concentration and levels off at concentrations higher than 0.4 M. We assume this effect to be due to the saturation of active sites at the surface the electrode. In accordance with this result, the optimum concentration of ethanol to obtain a higher current density may be considered as about 0.4 M. Also, there is a good linear relationship between oxidation peak current and ethanol concentration in the range of 0.009–0.09 M.

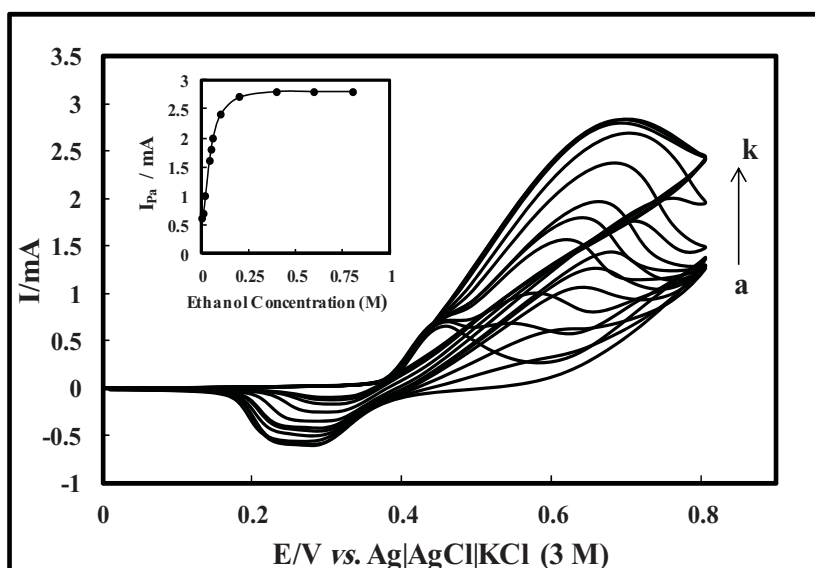


Figure 2: Current-potential curves of 0.1 M NaOH solution with different concentrations of ethanol (a) 0.0, (b) 0.009, (c) 0.02, (d) 0.04, (e) 0.05, (f) 0.06, (g) 0.09, (h) 0.2, (i) 0.4, (j) 0.6 and (k) 0.8 M at the Ni/PMT(TX-100)/MCPE at $\nu = 20 \text{ mV s}^{-1}$. Inset: Plot of the dependence of ethanol oxidation peak current on the ethanol concentration.

3.3 Effect of scan rate on the anodic peak height

In Figure 3 Cyclic voltammograms of Ni/PMT(TX-100)/MCPE in the presence of 0.1 M ethanol at the various scan rates were recorded. From this Figure it can be seen that, with increasing the potential scan rate, the peak potential for both catalytic oxidation of ethanol and oxidation of Ni(II) shifts to positive potentials, suggesting a kinetic limitation in the reaction between the redox sites of the Ni/PMT(TX-100)/MCPE and ethanol. This finding reveals that the heterogeneous oxidation of ethanol on Ni/PMT(TX-100)/MCPE is not a rapid reaction. The anodic current for ethanol oxidation (I_{paII}) decreases rapidly with increasing the potential scan rate. Indeed, the time window for ethanol oxidation process at higher scan rates becomes very narrow avoiding the facile electron transfer between substrate and catalytic sites. However, the peak currents of the oxidation of Ni(II) and the reduction of Ni(III) enhanced with increasing the scan rate. Therefore, it can be concluded that the Ni(II)/Ni(III) transformation process is much faster than the ethanol oxidation. Direct reaction between ethanol and Ni(III) (that formed on the electrode surface) produces Ni(II) leading to a little increase in the anodic peak current.

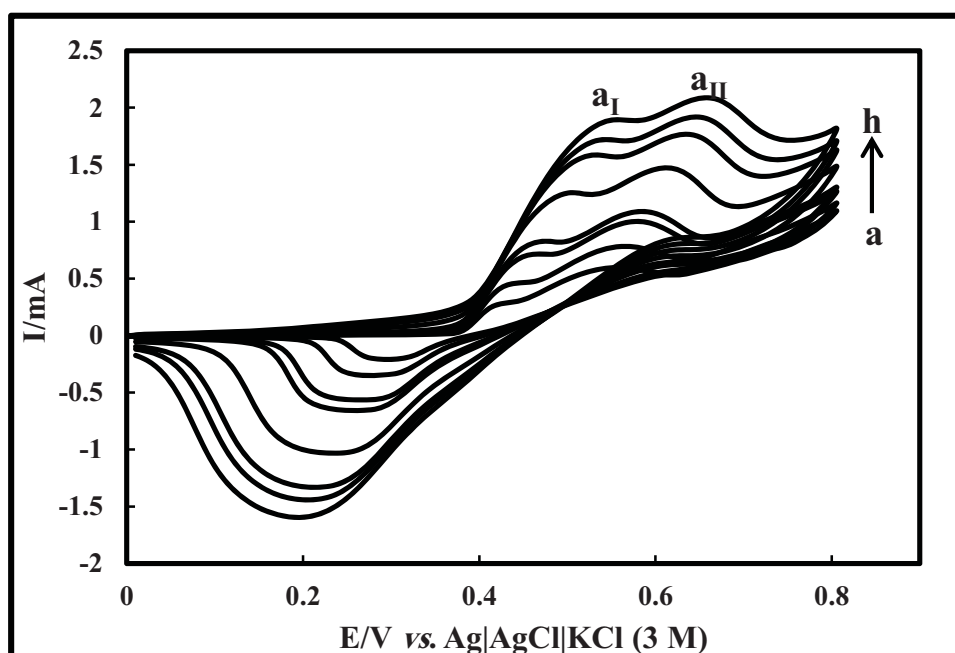


Figure 3: Cyclic voltammograms of the Ni/PMT(TX-100)/MCPE in the presence of 0.1 M ethanol in 0.1 M NaOH solution, scan rates: (a) 5 mV s^{-1} , (b) 10 mV s^{-1} , (c) 20 mV s^{-1} , (d) 50 mV s^{-1} , (e) 80 mV s^{-1} , (f) 100 mV s^{-1} , (g) 200 mV s^{-1} and (h) 400 mV s^{-1} respectively.

3.4 Chronoamperometric studies

Double potential step chronoamperometry, as well as other electrochemical methods, was employed for the investigation of electrochemical processes at Ni/PMT(TX-100)/MCPE. The main panel of Figure 4 represents the current – time profiles obtained by setting the working electrode potential at 0.56 V (first potential step) and 0.28 V (second potential step) for various concentrations of ethanol. The forward and backward potential step chronoamperometry of the modified electrode in the blank solution showed an almost symmetrical chronoamperogram with almost equal charges consumed for the oxidation and reduction of surface confined $\text{Ni(OH)}_2/\text{NiOOH}$ sites. However, in the presence of ethanol, the charge value associated with the forward chronoamperometry, Q is greater than that observed for the backward chronoamperometry (Figure 4, Inset A). The rate constant for the chemical reaction between the ethanol and redox sites of Ni/PMT(TX-100)/MCPE, can be evaluated by chronoamperometry. From the slope of the I_C/I_L vs. $t^{1/2}$ plot we can simply calculate the value of k for a given concentration of substrate. Inset B of Figure 4 shows one such plot, constructed from the chronoamperogram of the Ni/PMT(TX-100)/MCPE in the absence and presence of 0.05 M ethanol. The mean value for, k was found to be $3.87 \times 10^4 \text{ cm}^3 \text{ mol}^{-1} \text{ s}^{-1}$.

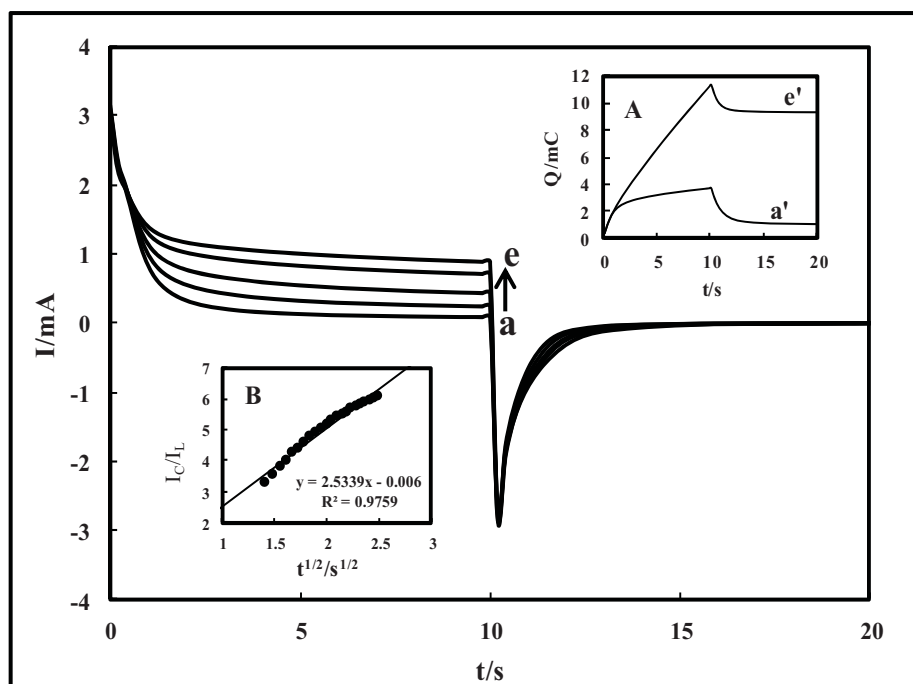


Figure 4: Double step chronoamperograms of Ni/PMT(TX-100)/MCPE in 0.1 M NaOH solution with different concentrations of: (a) 0.00, (b) 0.009, (c) 0.02, (d) 0.04 and (e) 0.05 M. Inset (A): Plot of Q vs. t derived from the data of chronoamperograms of a and e. Inset (B): Plot of I_C/I_L vs. $t^{1/2}$ derived from the data of chronoamperograms a and e.

4 Conclusion

The electrode has been described herein, consisting of nickel particles loaded into a poly(m-toluidine)/TX-100, by immersion of the polymeric modified electrode in a nickel acidic solution and electrodeposition of nickel ions. This modified electrode was found to be capable of catalyzing the electro-oxidation of ethanol very efficiently. The electro-oxidation of ethanol occurs through a mediated electron transfer mechanism by Ni(III) species. The anodic peak current for ethanol oxidation at Ni/PMT(TX-100)/MCPE are linearly proportional to the square root of scan rate. Double steps chronoamperograms for the modified electrode in the presence of ethanol show irreversible process. The values obtained for the rate constant, k, indicated that modified electrode can overcome the kinetic limitations for ethanol oxidation by a catalytic process.

References

- [1] B.C.H. Steele and A. Heinzl "Materials for fuel-cell technologies", J. of Nature, (2001). 414(1), 345-352
- [2] L. Su, W.Z. Jia, A. Schempf, Y. Ding and Y. Lei "Free-Standing Palladium/Polyamide 6 Nanofibers for Electrooxidation of Alcohols in Alkaline Medium", J. of Physical Chemistry C, (2009). 113(3), 16174-16180
- [3] X.N. Guo, R.J. Shang, D.H. Wang, G.Q. Jin, X.Y. Guo and K.N. Tu "Avoiding Loss of Catalytic Activity of Pd Nanoparticles Partially Embedded in Nanoditches in SiC Nanowires", J. of Nanoscale Research Letters, (2010). 5(2), 332-337



- [4] R.L. Orozco, M.D. Redwood, P. Yong, I. Caldelari, F. Sargent and L.E. Macaskie “Towards an integrated system for bio-energy: hydrogen production by Escherichia coli and use of palladium-coated waste cells for electricity generation in a fuel cell”, *J. of Biotechnology Letters*, (2010). 32(12), 1837-1845
- [5] V. Mazumder and S.H. Sun “Oleylamine-Mediated Synthesis of Pd Nanoparticles for Catalytic Formic Acid Oxidation”, *J. of American Chemical Society*, (2009). 131(13), 4588-4589
- [6] C. Lamy, E.M. Belgsirn and J.M. Leger “Electrocatalytic oxidation of aliphatic alcohols: Application to the direct alcohol fuel cell (DAFC)”, *J. of Applied Electrochemistry*, (2001). 31(7), 799-809
- [7] L.A. Rodríguez, M.E. Toro, F. Vazquez, M.L. Correa-Daneri, S.C. Gouiric and M.D. Vallejo “Bioethanol production from grape and sugar beet pomaces by solid-state fermentation”, *Int J. of Hydrogen Energy*, (2010). 35(11), 5914-5917
- [8] G.A. Camara, R.B. de Lima and T. Iwasita “Catalysis of ethanol electrooxidation by PtRu: the influence of catalyst composition”, *J. of Electrochemistry Communications*, (2004). 6(8), 812-815
- [9] C. Lamy, S. Rousseau, E.M. Belgsir, C. Coutanceau and J.M. Leger “Recent progress in the direct ethanol fuel cell: development of new platinum–tin electrocatalysts”, *J. of Electrochimica Acta*, (2004). 49(22), 3901-3908



Analysis of coolant flow and temperature distribution within PEM fuel cell stack

Amir Amirfazli^{*1}, Mehrdad bazazzadeh², Saeed Asghari³, Hooman Akhgar

^{*}Isfahan Malek-Ashtar University of Technology Shahin shahr, Isfahan, Iran

^{*}Isfahan Research Institute, Isfahan, Imam Khomeini Ave., Isfahan, Iran

^{*}Email: AmirAmirfazli@yahoo.com

Abstract:

In the present study, a mathematical model is developed for investigation of coolant flow and temperature distribution within PEMFC stack. The model consists of two main sub models: (1) a coolant flow distribution model, which is used to determine the coolant mass flow distribution between different cooling flow fields of the fuel cell stack; and (2) a thermal model, which computes the coolant temperature increase along the flow field and also the temperature distribution within each cell of the stack. A parametric analysis is also conducted on the effect of different parameters on stack temperature uniformity. The cross sectional area of manifolds, dimensions of coolant flow field channels and total coolant flow rate in U and Z stack configurations are selected as the design parameters and their optimum values are obtained by compromising between more temperature uniformity and less pressure drop.

Keywords: PEM fuel cell stack, coolant flow field, temperature distribution, Manifold

1. Introduction:

With the advantages of relatively high efficiencies, high power density, low temperature operation, quick start-up, system robustness, transient ability, and low emissions features, the polymer electrolyte membrane fuel cell (PEMFC) is considered to be more promising candidate for the next generation power source for transportation, stationary, auxiliary and portable applications. In spite of widespread researches and progressions on fuel cells, several technical barriers to their commercialization still exist, especially about their durability and cost. The heat generated due to electrochemical reactions in PEMFCs is comparable to electrical power output and must be removed efficiently to avoid overheating of the components and guarantee the favorable working temperature range of the current PEMFCs which is usually from 60 to 80°C. Improper thermal management and non-uniform temperature distribution within the fuel cell

¹ M.Sc. Student of Mechanical engineering

² Associate professor of Aerospace engineering

³ Assistant Professor of Mechanical engineering



6th Iranian Fuel Cell Seminar
March 12 & 13, 2013
Shahid Rajaee Teacher training University
Tehran - Iran



stack may cause electrolyte drying (global or local) or electrode flooding which both lower the fuel cell performance. On the other hand, the temperature difference between the PEMFC and the ambient is very small in comparison with the internal combustion engines. Thus, a proper thermal management for PEMFC stack is very challenging, particularly in automotive applications which require stacks with high power output and high power density[1-4].

Essentially, the issue of thermal management in fuel cell stack can be viewed at two levels; at the cell level to ensure proper membrane hydration and thereby ensure good conductivity of the membrane, and at the system level to ensure temperature uniformity along the stack and keep the stack from heating up of the fuel cell stack system[5]. In addition at system level we can investigate the effect of temperature distribution on fuel cell stack performance and also locate the failure cells and their effects on surrounding cells.

A number of studies have been conducted on the thermal management issue in the PEM fuel cells. In contrast with the extensive single cell models available in literature, quite limited number of studies is available for the modeling and simulation of cooling system of PEM fuel cell stacks. Most of the studies are devoted to modeling of cooling channel on bipolar plates, investigation of various cooling strategies and selection of an appropriate cooling method. Yu and Jung proposed a thermal management strategy of a PEMFC system with large active area for transportation application based on the investigation and the numerical experiments. They concluded that the fuel cell operating temperature can be effectively controlled by adjusting cooling fan operation. They stated that the reference operating temperature is system dependent and should be determined by considering membrane durability and system transient safety margins. In another study by Asghari et al., design of cooling flow field as well as thermal management subsystem of a 5kW PEM fuel cell system were investigated. The number of parallel channels in the parallel serpentine flow field was selected as the design parameter and its optimum value was obtained by compromising between the minimum pressure drop of coolant across the flow field and the maximum temperature uniformity within the bipolar plate[6]. Ana et al. used a theoretical 1D model, based on electrochemical and thermal equations, to estimate the performance of open-cathode PEM fuel cells, as well as to define an optimum cooling system and channel geometry for the cathode side[7]. Sasmito et al. carried out a computational study of PEMFC stacks with various cooling strategies. It was shown that liquid cooling yields best performance among the alternative designs examined[8]. Park and Li developed a non-isothermal stack model for PEM fuel cells consisted of flow network and heat transfer approaches. They analyzed the effect of reactant flows and temperature distribution on the stack performance[9].

As a rule of thumb, PEM fuel cell stacks above 5 kW should be water cooled, those below 2 kW air cooled, with a decision for stacks in between being a matter of judgment. One of the problems encountered when stacking fuel cells is a non-uniform coolant flow distribution to the cooling flow fields of cells, which causes an uneven temperature distribution within the stack. The geometrical design of the fuel cell coolant manifold is therefore an important issue to be considered. In this paper a theoretical model including two submodels is developed to study the coolant flow and temperature distribution within a water-cooled PEM fuel cell stack. Coolant flow distribution along the stack and each cell is obtained by a coolant flow distribution submodel. Considering heat generation in each cell with the assumption of non-uniform temperature distribution within the stack and using the result of flow distribution submodel, the



thermal submodel yields the temperature increase of coolant along the flow field and also the temperature distribution within the fuel cell stack. Finally an analytical study on effective parameters on fuel cell stack temperature distribution is conducted.

2. Mathematical model:

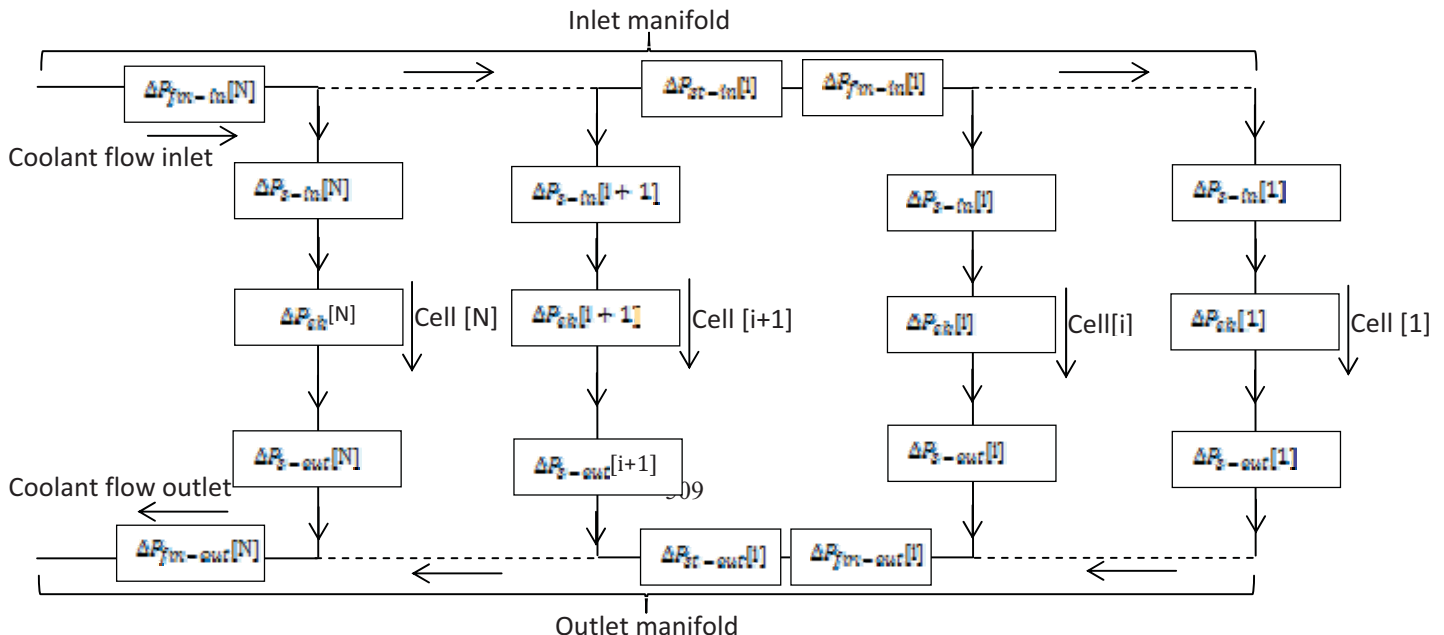
The theoretical model consists of two main submodels: (1) a coolant flow distribution model, which is used to determine the mass flow distribution of coolant between different cooling flow fields of the fuel cell stack; and (2) a thermal model, which computes the coolant temperature increase along the flow field and also the temperature distribution within the fuel cell stack.

By the coolant flow distribution model, the flow distribution is calculated using the Bernoullie equation and the fuel cell stack is modeled as a network of hydraulic resistances in parallel and in series; describing the resistances in the cooling flow fields and in the manifolds (Figure 1). As indicated in Figure 1, two flow patterns are considered in the current analysis: U-configuration and Z-configuration. The thermal model yields the temperature increase of coolant along the flow field and also the temperature distribution within the fuel cell stack by using the results of the flow distribution submodel.

2.1. Coolant flow distribution model:

The coolant flow and pressure distributions are determined using an iterative approach. A systematic algorithm is constructed based on the assumption, that the flow distribution in the fuel cell stack can be modeled by means of hydraulic resistances in the manifold and in the cooling flow fields. In other words, the stack is represented as a network of hydraulic resistances, in parallel and in series as shown in Figure 1. In the following, the pressure drops included in the model are described and the solution algorithm is explained in detail. The pressure drops included in the analytical model are divided into four classes:

1. The pressure drop due to splitting and combining of two streams in the inlet and outlet manifolds (ΔP_{st-in} , ΔP_{st-out})
2. The pressure drop due to friction of flow in the inlet and outlet manifolds (ΔP_{fm-in} , ΔP_{fm-out})
3. The losses caused by deflection of the main stream in the manifold into or out of the cells (ΔP_{s-in} , ΔP_{s-out})
4. The losses related to cooling flow fields of cells including friction and bending losses in the cooling flow field and also the expansion and contraction losses (ΔP_{ch})



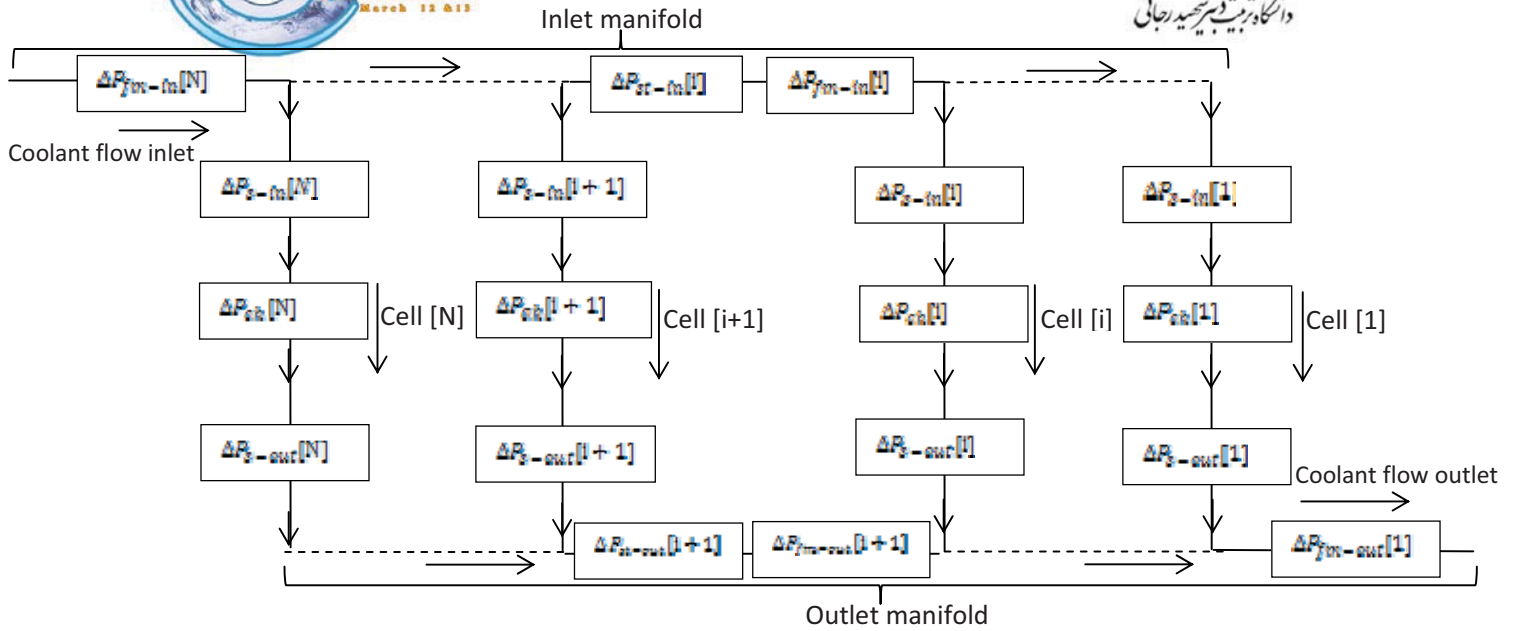


Figure [1]. Resistances in the cooling flow fields and in the manifolds

2.1.1. Pressure drop due to splitting and combining of two streams in the inlet and outlet manifolds

The shape of the junction between the manifold and the diffuser part in the cooling flow field of cells is approximated to a converging/diverging T shape for which the pressure drop relations are obtained from IDELCHICK's hydraulic resistances handbook [10].

These pressure drops are determined by using the below relations:

$$\Delta P_{st-in}[l] = 0.5 \cdot R_{st-in}[l] \cdot \rho \cdot U_{m-in}[l]^2 \quad (1)$$

$$\Delta P_{st-out}[l] = 0.5 \cdot R_{st-out}[l] \cdot \rho \cdot U_{m-out}[l]^2 \quad (2)$$

$$U_{m-in}[l] = \frac{Q_{m-in}[l]}{A_{m-in}} \quad (3)$$

$$U_{m-out}[l] = \frac{Q_{m-out}[l]}{A_{m-out}} \quad (4)$$

where $U_{m-in}[l]$ and $U_{m-out}[l]$ are coolant flow velocity in l th segment of the manifold, $R_{st-in}[l]$ and $R_{st-out}[l]$ are hydraulic resistances related to splitting and combining of coolant flow in the inlet and the outlet manifolds, A_{m-in} and A_{m-out} are the cross sectional areas of the manifolds, and $Q_{m-in}[l]$ and $Q_{m-out}[l]$ are the volumetric flow rate of the coolant.

The resistance coefficients due to splitting and combining of the fluid streams (R_{st-in} , R_{st-out}) are related to the flow ratios between the flow in the manifold and in the cells. These relations are shown in Table 1. In the cases where explicit relations for hydraulic resistances are not available, a correlation is obtained using curve fitting of data available in IDELCHICK's hydraulic resistances handbook [10].



2.1.2. Friction Losses in the manifolds

The flow in the manifolds is approximated to a flow in a conduit. With this assumption, the pressure drop can be determined by conventional internal fluid flow relations.

The amount of pressure drop due to friction in t_{in} segment of inlet manifold is determined based on the following correlations:

$$\Delta P_{f_{m-in}}[t] = 0.5 \cdot R_{f_{m-in}}[t] \cdot \rho \cdot U_{m-in}[t]^2 \quad (5-a)$$

$$R_{f_{m-in}}[t] = f_{m-in}[t] \times \frac{L}{D_{hm-in}} \quad (5-b)$$

$$f_{m-in}[t] = \begin{cases} 64/Re_{m-in}[t] & Re_m < 2100 \\ 0.316/Re_{m-in}[t]^{0.25} & Re_m > 2100 \end{cases} \quad (5-c)$$

$$Re_{m-in}[t] = \frac{\rho U_{m-in}[t] D_{hm-in}}{\mu} \quad (5-d)$$

Where $Re_{m-in}[t]$ is the Reynolds number, $f_{m-in}[t]$ the friction coefficient and D_{hm-in} and μ are hydraulic diameter and viscosity of the coolant, respectively.

The amount of pressure drop due to friction in t_{out} segment of the outlet manifold is determined based on the following correlations:

$$\Delta P_{f_{m-out}}[t] = 0.5 \cdot R_{f_{m-out}}[t] \cdot \rho \cdot U_{m-out}[t]^2 \quad (6-a)$$

$$R_{f_{m-out}}[t] = f_{m-out} \times \frac{L}{D_{hm-out}} \quad (6-b)$$

$$f_{m-out} = \begin{cases} 64/Re_{m-out}[t] & Re_m < 2100 \\ 0.316/Re_{m-out}[t]^{0.25} & Re_m > 2100 \end{cases} \quad (6-c)$$

$$Re_{m-out}[t] = \frac{\rho U_{m-out}[t] D_{hm-out}}{\mu} \quad (6-d)$$

2.1.3. The losses caused by deflection of the main stream in the manifold into or out of the cells:

The losses due to the deflection of the main stream into or out of cells are correlated to the flow ratio and the area ratio. This pressure loss can be determined from the following equations:



$$\Delta P_{s-in}[i] = 0.5 \cdot R_{s-in}[i] \cdot \rho \cdot U_{cell}[i]^2 \quad (7)$$

$$\Delta P_{s-out}[i] = 0.5 \cdot R_{s-out}[i] \cdot \rho \cdot U_{cell}[i]^2 \quad (8)$$

$$U_{cell}[i] = \frac{Q_{cell}[i]}{z \cdot A_{ch}} \quad (9)$$

Where $Q_{cell}[i]$ is the coolant flow rate per cell, $U_{cell}[i]$ is the coolant flow velocity in each channel of the cooling flow field, z is the number of channels of cooling flow field, A_{ch} is the cross sectional area of each channel and $R_{s-in}[i]$ and $R_{s-out}[i]$ are the hydraulic resistances. As shown in Table 1, these hydraulic resistances are functions of the flow ratio and the area ratio (area ratio between the cross sectional area of the manifold and cell).

2.1.4. Pressure losses related to cooling flow field

As shown in Eq. 10, the pressure drop related to cooling flow field is mainly caused by two factors:

$$\Delta P_{cell}[i] = \Delta P_{ch}[i] + \Delta P_{s-in}[i] + \Delta P_{s-out}[i] \quad (10)$$

- Pressure drop due to friction and rotation of coolant flow through bending sections of flow field channels (ΔP_{ch})
- Pressure drop due to contraction and expansion of coolant flow through T shape section between each cell and the corresponding manifold segment ($\Delta P_{en} + \Delta P_{ex}$)

To characterize the pressure drop due to friction and rotation of coolant flow through bending sections of the flow field channels (ΔP_{ch}), a numerical simulation is applied. A numerical model of the flow field is developed and run for various coolant flow rates. In this way, a set of data, including different coolant flow rates and their corresponding pressure drops of coolant across the flow field is extracted. The relationship between the pressure drop and the flow rate is defined by fitting of a second order polynomial to this data:

$$\Delta P_{ch}[i] = AU_{ch}[i]^2 + BU_{ch}[i] + \Delta P_{en}[i] + \Delta P_{ex}[i] \quad (11)$$

Where ΔP_{ch} is the pressure drop of the coolant across the flow field of i th cell, U_{ch} is the mean velocity of the coolant in the channels, A and B are constants which are determined by curve fitting. The first order and the second order terms come from the friction losses and channel bending, respectively. Finally, the pressure drops due to expansion and contraction of coolant flow at entrance and exit section of each cell are determined according to the following relations:

$$\Delta P_{en}[i] = 0.5 \cdot R_{en} \cdot \rho \cdot U_{cell}[i]^2 \quad (12)$$

$$\Delta P_{ex}[i] = 0.5 \cdot R_{ex} \cdot \rho \cdot U_{cell}[i]^2 \quad (13)$$

Where R_{en} and R_{ex} are hydraulic resistances due to expansion and contraction of coolant flow[11].



2.1.5. Solution algorithm:

The solution algorithm starts with an initial estimate of the coolant flow rate through the flow fields. A uniform flow distribution between different flow fields is assumed for the first iteration step. Then, the coolant flow rates in different sections of the manifolds are determined. Knowing the flow rate, the local velocities in the manifolds and in the channels of flow fields are computed. The different pressure drops are calculated using equations (1-13). The next step is to calculate the local pressures in the inlet and outlet manifolds. By assuming that the outlet pressure (the pressure at exit port of the stack) P_{exit} is zero, the local pressures in the inlet and outlet manifolds are calculated. The pressure drop in the cells can now be corrected by knowing the local pressures in the inlet and outlet manifolds (P_{in}, P_{out}). New cell flow rates are then calculated from the corrected pressure drops using following Equation.

$$Q_{new}[i] = U_{corr}[i] \times [z \times A_{ch}] \quad (14)$$

Where $Q_{new}[i]$ is the new flow rate of i_{th} cell, $U_{corr}[i]$ is corrected local velocity in the channels of flow fields, z is the number of channels of cooling flow field and A_{ch} is the cross sectional area of each channel. Under relaxation of the cell flow rates is also applied to ensure stable computation.

$$Q_{cell}[i] = Q_{cell}[i] + (Q_{new}[i] - Q_{cell}[i]) \times Fr \quad (15)$$

Where $Q_{cell}[i]$ is the new under relaxed flow rate of i_{th} cell and Fr is the under relaxation coefficient. Once the new flow rates are obtained, they are compared with the initial guess or the previously calculated cell flow rates. The calculations continue with the new obtained set of cell flow rates until the difference between the new and old values are within the convergence criteria. The final output of the coolant flow distribution model is the coolant flow distribution between different flow fields of the stack. A MATLAB code is developed using the above algorithm to determine the coolant flow distribution in the stack.

2.2. Thermal model:

The heat transfer model is used to determine the temperature distribution in the stack. Within the framework of the present study, each cooling flow field can be considered as a parallel flow heat exchanger in which several channels of rectangular cross-section extend in parallel to each other from the inlet manifold to the outlet manifold and heat is transferred from the cathode side of membrane electrode assembly (MEA) to the coolant streams. The analysis is based on the following assumptions:

1. Each cell in the stack has its own cooling flow field.
2. The heat generated by electrochemical reaction in the cathode side of each cell transfers to its adjacent cooling flow field stream through the bipolar plates by conductive heat transfer. The reaction rate over the active area of the MEA is assumed to be uniform. This yields an approximately uniform heat generation over the cell's active area and therefore a constant heat



6th Iranian Fuel Cell Seminar
 March 12 & 13, 2013
 Shahid Rajaee Teacher training University
 Tehran - Iran



flux at the walls of channels in the cooling flow field. By this assumption, the temperature distribution in each individual cell in the stack can be non-uniform. The rate of heat generation per each cell in the stack at any working voltage can be determined by using of the following equation[12]:

$$Q[i] = (1.23 - V[i])I, [36] \quad (16)$$

Where $Q[i]$, $V[i]$ and I are rate of heat generation per each cell, cell working voltage and output electrical current of the stack, respectively. Heat flux at the walls of cooling channels as a result of this heat generation can be determined by dividing the rate of heat generation by the surface areas of the cooling channels in the flow field.

3. The coolant flow and thermal conditions are fully developed, neglecting the entrance effects.
4. Thermal resistances at the surface of the cooling channels are negligible.
5. Viscous dissipation in coolant flow is negligible.
6. Only heat transfer by conduction in through-plane direction from the MEA to the cooling flow field is considered. Net conductive heat transfer in the in-plane directions in bipolar plate is neglected.
7. The convective heat transfer on the outside surface of the fuel cell stack is negligible.

Since the length of each manifold segment is very short in comparison with the length of cooling flow field channels therefore heat transferred between each cell and relevant manifold segments is negligible. However, in the present model the amount of temperature increasing at each manifold segment is calculated under an iterative procedure. At steady state, the heat generated in each cell is discharged completely so that the temperature distribution in cell will remain unchanged. Each individual channel in the cooling flow field is modeled as a tube of rectangular cross section extending from the inlet manifold to the outlet manifold in parallel with other channels of the same flow field. The temperature distribution in the bipolar plate along the flow channels is determined by using governing equations of internal flow in a tube with rectangular cross section and constant surface heat flux, as following[13]:

$$T_s(x) = \frac{q[i]}{hA_{ch,sa}} + T_m(x) = \frac{q[i]}{hA_{ch,sa}} + T_{m_i} + \frac{q_s''[i]p}{M_{ch}[i]c_p} x \quad (17)$$

Where h is the convection heat transfer coefficient, $T_m(x)$ is the local mean temperature, T_{m_i} is the mean temperature at channel inlet section, $q[i]$ is the contribution of each flow field channel from generated heat in related cell, x is the local distance of an assumed point from channel inlet section, M_{ch} is coolant mass flow rate in each channel, p is the perimeter of flow a channel and $A_{ch,sa}$ is the side area of each flow field channel that is equal to product of channel length to channel perimeter. The specific heat capacity of the coolant is assumed to be a function of temperature.



$$C_p [t] = a_1 \times \exp\left(-\frac{(T_{mean}[t]-b_1)^2}{c_1}\right) + a_2 * \exp\left(-\frac{(T_{mean}[t]-b_2)^2}{c_2}\right) + a_3 * \exp\left(-\frac{(T_{mean}[t]-b_3)^2}{c_3}\right) - a_4 * \exp\left(-\frac{(T_{mean}[t]-b_4)^2}{c_4}\right) + a_5 * \exp\left(-\frac{(T_{mean}[t]-b_5)^2}{c_5}\right) \quad (18)$$

Where $T_{mean}[t]$ is the mean temperature of inlet and outlet coolant temperature of each cooling flow field. The outlet coolant temperature and $C_p [t]$ in each cooling flow field is necessary to be determined to gather by an iterative procedure. The outlet temperature of coolant per each cell is determined by the following equation:

$$T_{c-out}[t] = \frac{q[t]}{M_c[t] \times C_p} + T_{c-in}[t] \quad (19)$$

Where $T_{c-in}[t]$ and $T_{c-out}[t]$ denoted inlet and outlet temperature of coolant water in each cell, respectively, $q[t]$ is generation heat per cell, $C_p [t]$ is heat capacity and $M_c [t]$ is coolant mass flow rate. Coolant mass flow rate is resulted from product of coolant density to coolant flow rate.

A concept of Index of Uniform Temperature (IUT) was proposed by Chen to evaluate the degree of uniform temperature profile across the cooling plates[14]. In the present study, a modified form of this index is introduced as following:

$$IUT = \frac{\sum_{i=1}^N \sum_{j=1}^M |T(i,j) - \bar{T}|}{N \times M}, \quad \bar{T} = \frac{\sum_{i=1}^N \sum_{j=1}^M T(i,j)}{N \times M} \quad (20)$$

Where N is the number of cells in the fuel cell stack, M the number of nodes taken along the cooling channel from the inlet manifold to the outlet manifold, \bar{T} the average temperature of the fuel cell stack and $T(i,j)$ is the local temperature in bipolar plate at i_{th} cell and j_{th} node each.

Regarding to the definition of this index in equation (20), its value decreases as the degree of temperature uniformity within the stack increases.

It should be noted about heat capacity that, according to the temperature gradient through each cell from inlet to outlet manifold, heat capacity is not constant. Thus it should be determined based on a mean temperature of cell coolant inlet and outlet temperature. On the other hand cell outlet temperature is not defined at first, so for determination of heat capacity in the mean temperature of inlet and outlet coolant temperature a try and error approach is employed. The procedure is that at first heat capacity is calculated at cell inlet coolant temperature. Then, outlet temperature of each cell is obtained. Now for next iteration using the mean temperature of cell inlet coolant temperature and obtained outlet coolant temperature. So, with iterations on mentioned method, cell outlet coolant temperature will be similar in two consecutive iterations for a specified cell. If we do this procedure for each cell, cell outlet temperature of coolant of each cell would be determined.



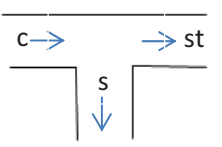
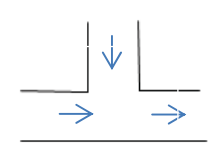
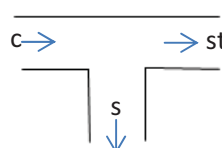
1.

R

result and discussion:

In this study, a theoretical modeling has been carried out for investigation of coolant flow and temperature distribution in two common PEM fuel cell stack designs (U & Z) which consist of 65 cells with 67.5 cm² active areas and generating about 8 KW as output power. The stack is supplied with coolant water with constant volumetric flow rate of 150 (Lit/Min) and the inlet temperature of the coolant stream is assumed to be at 333.15 (K). Figure 2 shows a three dimensional contour of stack temperature distribution in each cell. The surface plot represents a symmetric temperature distribution for Z configuration and an increasing temperature distribution for U configuration that is maximum near the stack inlet and decreases as the distance from the inlet increases. Regarding to the definition of index of uniform temperature (IUT), its value decreases as the degree of temperature uniformity within the stack increases. In Figure 3 the IUT is compared between the U and Z configuration for various cross sectional area of manifolds. According to this diagram, the Z configuration results in more uniform temperature than the U configuration in low values of cross sectional area. However, at the larger values, both configurations result in the same temperature uniformity. In this study a parametric analysis in three categories is conducted on effective parameters of coolant flow and temperature distribution along the stack and flow fields. These analyses include: the effects of inlet and outlet manifolds cross sectional area and the effect of total coolant flow rate. Each of mentioned categories is investigated in detail for U and Z stack arrangement.

Table 1. Hydraulic resistances relations and calculations process

	Shape of section	Derived or fitted equation	
Cell inlet		$+ 1267 \left(\frac{Q_s [i]}{Q_c [i]} \right)^4 - 497.7 \left(\frac{Q_{cell} [i]}{Q_{in-in} [i]} \right)^8 + 98.49 \left(\frac{Q_s [i]}{Q_c [i]} \right)^2$	$R_{c_s, in} [i] = \frac{R_{c_s, in} [i]}{\left(\frac{U_s [i]}{U_o [i]} \right)^2}$
Cell outlet		$R_{c_s, out} [i] = 1 + \left(\left(\frac{Q_s [i]}{Q_c [i]} \right) \left(\frac{A_s}{A_c} \right) \right)^2 - 2 \left(1 - \frac{Q_s [i]}{Q_c [i]} \right)^2$	$R_{s, out} [i] = \frac{R_{c_s, out} [i]}{\left(\frac{U_s [i]}{U_o [i]} \right)^2}$
Inlet manifold		$R_{c_{st}, in} [i] = -171.4 \left(\frac{Q_{st} [i]}{Q_c [i+1]} \right)^7 + 1266 \left(\frac{Q_{st} [i]}{Q_c [i+1]} \right)^8 - 369$ $- 5260 \left(\frac{Q_{st} [i]}{Q_c [i+1]} \right)^5 + 2966 \left(\frac{Q_{st} [i]}{Q_c [i+1]} \right)^4 -$ $- 22.98 \left(\frac{Q_{st} [i]}{Q_c [i+1]} \right) + 1.697$	$R_{st, in} [i] = \frac{R_{c_{st}, in} [i]}{\left(1 - \frac{Q_{out} [i+1]}{Q_{in} [i+1]} \right)^2} \times$

Outlet manifold		U type	$\left(\frac{Q_s[t+1]}{Q_c[t+1]}\right)^b - 2.9 \left(\frac{Q_s[t+1]}{Q_c[t+1]}\right)^a + 25.7 \left(\frac{Q_s[t+1]}{Q_c[t+1]}\right)^d - 5.6 \left(\frac{Q_s[t+1]}{Q_c[t+1]}\right)^e$ $0.4 \left(\frac{Q_s[t+1]}{Q_c[t+1]}\right) + 0.8$
		Z type	$\left(\frac{Q_s[t-1]}{Q_c[t-1]}\right)^b - 2.9 \left(\frac{Q_s[t-1]}{Q_c[t-1]}\right)^a + 25.7 \left(\frac{Q_s[t-1]}{Q_c[t-1]}\right)^d - 5.6 \left(\frac{Q_s[t-1]}{Q_c[t-1]}\right)^e$ $0.4 \left(\frac{Q_s[t-1]}{Q_c[t-1]}\right) + 0.8$

In this study a parametric analysis in three categories is conducted on effective parameters of coolant flow and temperature distribution along the stack and flow fields. These analyses include: the effects of inlet and outlet manifolds cross sectional area and the effect of total coolant flow rate. Each of mentioned categories is investigated in detail for U and Z stack arrangement.

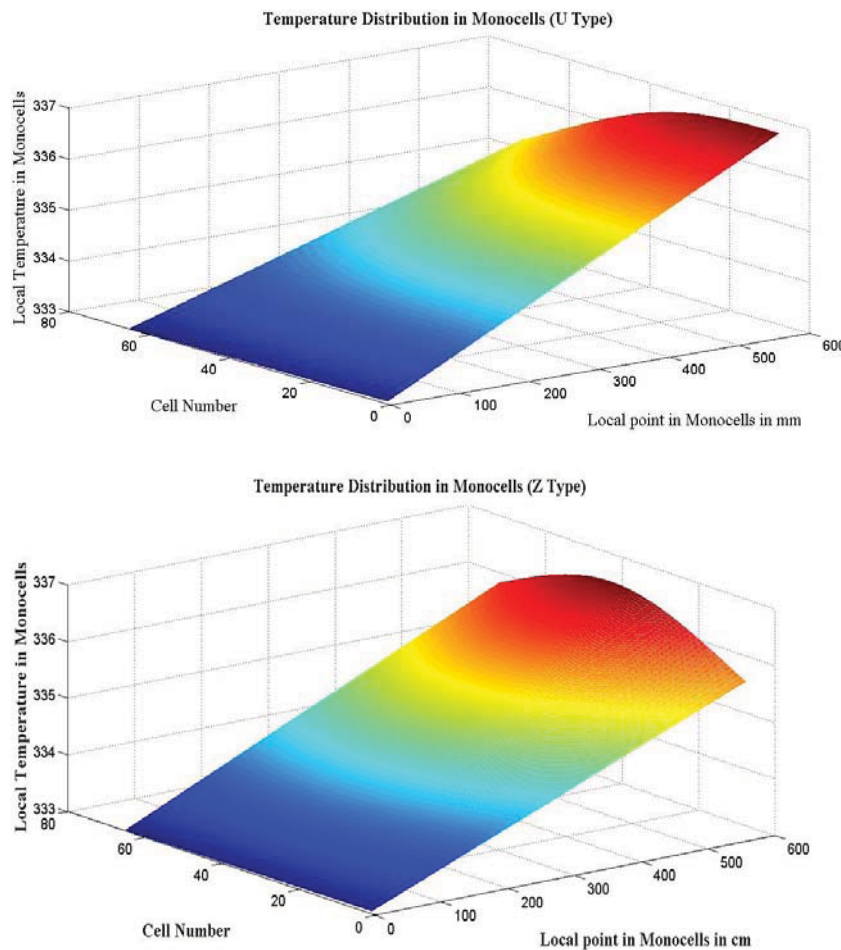


Figure 2.A three dimensional contour of stack temperature distribution

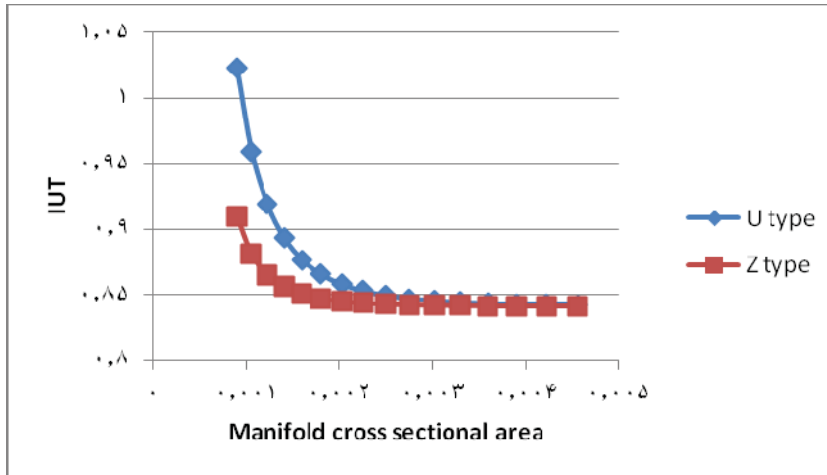


Figure3. IUT comparison between U and Z configuration of stack

1.1. Effect of inlet and outlet manifold cross sectional area:

As a matter of fact, non-uniformity of coolant flow distribution causes performance degradation of fuel cell stack. Sufficient temperature uniformity can be guaranteed by enlarging manifold cross sectional area; however it is limited by the size of bipolar plate[15, 16]. In this part stack inlet coolant flow rate and temperature are fixed to 28 (lit/min) and 60°C, respectively and flow field channels dimensions are 2 and 3 (mm). The stack inlet coolant flow rate is obtained with respect to total amount of heat generated in fuel cell stack that assumed to be 150 (watt) per cell. As Figure 4 (a), (b) shows, the degree of temperature uniformity within the U configuration stack increases as the cross sectional area of the inlet and outlet manifolds increase. This is due to the fact that as the inlet and outlet manifold cross sectional area increase the pressure drop in manifolds decrease in comparison with the pressure losses in flow field channels and thus more uniformity of coolant water distribution is obtained between cells. It is obvious from Figure 4(a); (b) that the effect of manifolds cross sectional area is more significant when they are in small ranges. The effect of inlet and outlet manifold cross sectional area on the degree of temperature uniformity (IUT) in the Z configuration stack is shown in Figure 4 (c), (d). As we know in Z configuration the most coolant flow uniformity in each manifold cross sectional area is obtained as the inlet and outlet manifold cross sectional areas are equal to each other. But in U configuration the coolant flow uniformity is always increase as the inlet or outlet manifold cross sectional area increases. Thus in Figure 4(c) inlet manifold cross sectional area increment increase coolant flow non-uniformity in small cross sectional area of outlet manifold. As the outlet manifold cross sectional area increase and comes close to the inlet manifold cross sectional area this trend gradually changes and a more uniform coolant flow and temperature distribution is obtained by increasing the inlet manifold cross sectional area. A similar trend is seen in Figure 4 (d). Then to satisfy sufficient temperature uniformity in Z configuration, a judicious selection of inlet and outlet cross sectional areas could balance their respective effect so that a uniform temperature distribution in the stack might be achieved.

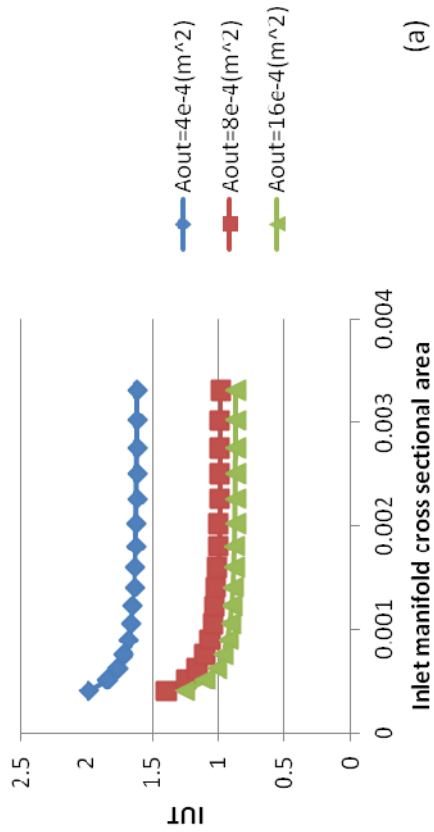
1.1. effect of total coolant flow:



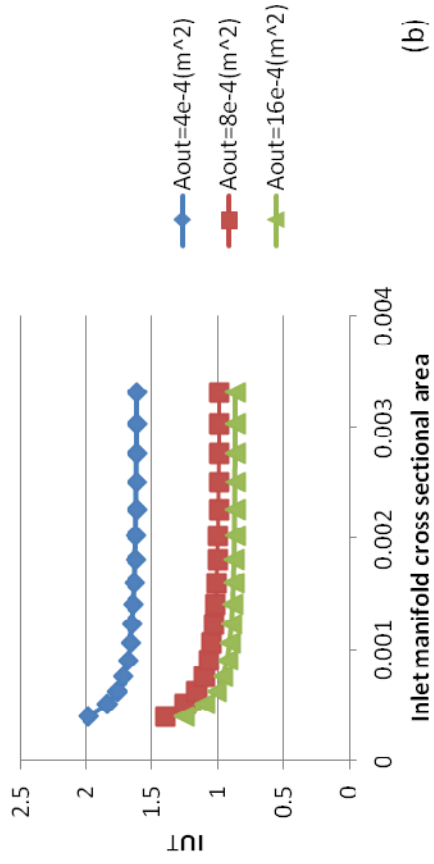
6th Iranian Fuel Cell Seminar
March 12 & 13 , 2013
Shahid Rajaee Teacher training University
Tehran - Iran



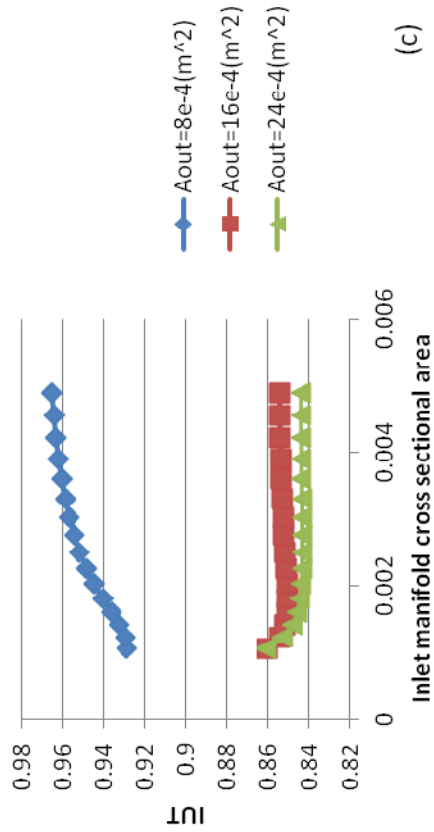
In the previous section it is shown that the coolant flow distribution between different flow fields is affected by the manifold cross sectional area and flow field channel dimensions. The effect of these two key factors can be minimized by ensuring sufficient flow uniformity through an enlarged manifold and reduced flow channel sizes. However excessively small flow channels can lead to excessive pumping power required to drive the reactant gas flow, in addition to other problems such as manufacturing difficulty and enlarging the manifolds is limited by the size of bipolar plates. Optimal performance of a PEM fuel cell stack can be achieved by optimizing the size of the manifold and flow channel as well as the coolant flow rate. Figure 5 (a) and (b) depicts the effect of coolant flow rate on the temperature uniformity under various manifold cross sectional area. According to these figures, coolant flow rate affected IUT more in Z configuration. However, for high value of coolant flow rate it seems to be less effective on temperature uniformity in both U and Z configuration. On the other hand, it should be consider that higher coolant flow rate leads to higher parasitic power due to coolant pumping. Thus a compromise between maximum temperature uniformity and minimum parasitic losses due to excessive coolant pumping determine optimized amount of total coolant flow rate.



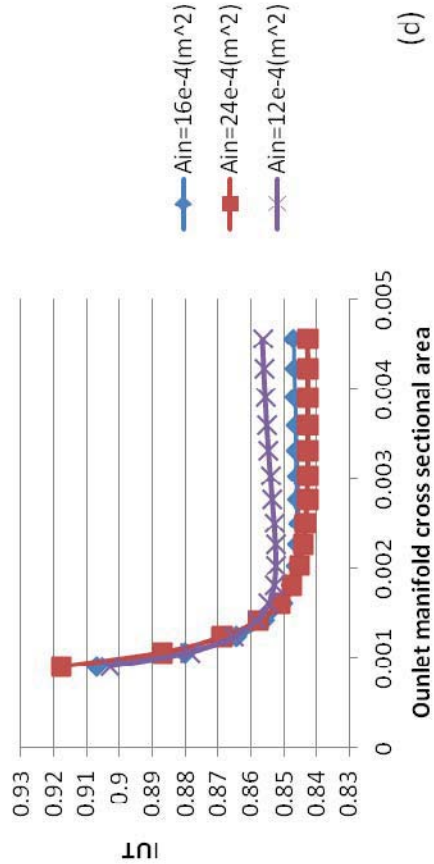
(a)



(b)



(c)



(d)



6th Iranian Fuel Cell Seminar

March 12 & 13 , 2013

Shahid Rajaee Teacher training University

Tehran - Iran



Fig.4. degree of temperature uniformity in U and Z configuration for various manifold cross sectional area, [a] U configuration temperature uniformity for various cross sectional area of outlet manifold, [b] U configuration temperature uniformity for various cross sectional area of inlet manifold, [c] Z configuration temperature uniformity for various cross sectional area of outlet manifold, [d] Z configuration temperature uniformity for various cross sectional area of inlet manifold

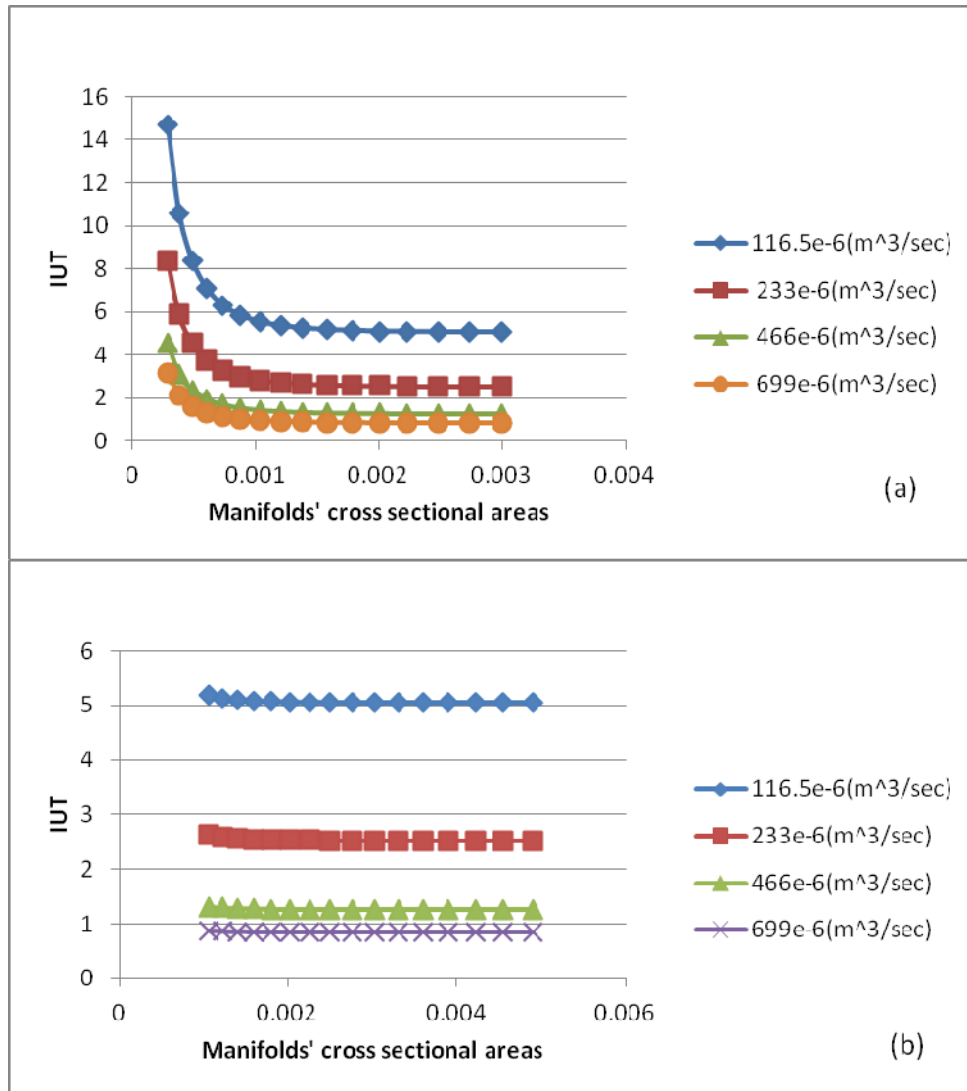


Figure 5. Effect of coolant flow rate on the temperature uniformity, [a] U configuration, [b] Z configuration

2. Conclusion:

In this study coolant flow and temperature distribution within a PEM fuel cell stack included 65 active cells, with various inlet–outlet configurations, was simulated under a theoretical model that consists of two submodels: a coolant flow distribution model and a thermal model. Furthermore, influence of effective parameters on stack temperature uniformity was investigated. Among various parameters, effect of manifolds cross sectional area, flow field channels dimension and stack intake coolant flow rate are selected as influential parameters and their optimum value was



6th Iranian Fuel Cell Seminar
March 12 & 13, 2013
Shahid Rajaee Teacher training University
Tehran - Iran



obtained by compromising between the minimum pressure drop and the maximum temperature uniformity within the stack criteria. The following results were obtained:

- 1- Z configuration results in more uniform temperature than the U configuration in low values of cross sectional area. However Z configuration is not proper for small manifold cross sectional area because of coolant back flow in some of middle cells.
- 2- The degree of temperature uniformity within the stack increases as the cross sectional area of the inlet and outlet manifolds increase.
- 3- Channel dimension increment forces the temperature uniformity to decrease in the stack. Moreover, temperature uniformity affected more in Z configuration by channel dimension. However in both configurations the IUT influenced less by channel dimension in smaller dimensions.
- 4- Larger coolant flow rate causes more uniform temperature distribution while lower flow rate leads to lower pressure drop and parasitic losses.

3. Acknowledgment:

The authors would like to acknowledge the financial support of Renewable Energy Organization of Iran (SUNA).

4. References:

1. Kang, S., et al., Configuration effects of air, fuel, and coolant inlets on the performance of a proton exchange membrane fuel cell for automotive applications. *International Journal of Hydrogen Energy*, 2009. 34(16): p. 6749-6764.
2. Duan, S. and S. Senkan, Catalytic conversion of ethanol to hydrogen using combinatorial methods. *Industrial & engineering chemistry research*, 2005. 44(16): p. 6381-6386.
3. Mehta, V. and J.S. Cooper, Review and analysis of PEM fuel cell design and manufacturing. *Journal of Power Sources*, 2003. 114(1): p. 32-53.
4. Costamagna, P. and S. Srinivasan, Quantum jumps in the PEMFC science and technology from the 1960s to the year 2000: Part I. Fundamental scientific aspects. *Journal of Power Sources*, 2001. 102(1-2): p. 242-252.
5. Zhang, Y., et al., A model predicting performance of proton exchange membrane fuel cell stack thermal systems. *Applied Thermal Engineering*, 2004. 24(4): p. 501-513.
6. Asghari, S., H. Akhgar, and B.F. Imani, Design of thermal management subsystem for a 5 kW polymer electrolyte membrane fuel cell system. *Journal of Power Sources*, 2011. 196(6): p. 3141-3148.
7. López-Sabirón, A.M., et al., Design and development of the cooling system of a 2 kW nominal power open-cathode polymer electrolyte fuel cell stack. *International Journal of Hydrogen Energy*, 2012. 37(8): p. 7289-7298.
8. Sasmito, A.P., E. Birgersson, and A.S. Mujumdar, Numerical evaluation of various thermal management strategies for polymer electrolyte fuel cell stacks. *International Journal of Hydrogen Energy*, 2011. 36(20): p. 12991-13007.



6th Iranian Fuel Cell Seminar
March 12 & 13 , 2013
Shahid Rajaee Teacher training University
Tehran - Iran



9. Park, J. and X. Li, Effect of flow and temperature distribution on the performance of a PEM fuel cell stack. *Journal of Power Sources*, 2006. 162(1): p. 444-459.
10. Idelchik, I., *Handbook of hydraulic resistance*, 1986. Hemisphere, New York: p. 640.
11. Fox, R.W., A.T. McDonald, and P.J. Pritchard, *Introduction to fluid mechanics*. Vol. 5. 1998: John Wiley & Sons New York.
12. Larminie, J., A. Dicks, and M.S. McDonald, *Fuel cell systems explained*. 2003.
13. Incropera, F. and D. DeWitt, *Introduction to heat transfer*. 1985.
14. Chen, F., et al., Analysis of optimal heat transfer in a PEM fuel cell cooling plate. *Fuel Cells*, 2003. 3(4): p. 181-188.
15. Nguyen, T.V. and R.E. White, A water and heat management model for Proton-Exchange-Membrane fuel cells. *Journal of the Electrochemical Society*, 1993. 140(8): p. 2178-2186.
16. Karimi, G., J. Baschuk, and X. Li, Performance analysis and optimization of PEM fuel cell stacks using flow network approach. *Journal of Power Sources*, 2005. 147(1): p. 162-177.



MODELING AND SIMULATION OF FUEL-CELL/BATTERY HYBRID VEHICLE AND POWER MANAGEMENT CONTROLLER DESIGN

Ali Farhadi¹, Homaiun Bakhtiari² and Peyman Naderi³
Shahid Rajaei Teacher Training University
A.farhadi@srctu.edu

Abstract

A hybrid vehicle structure used Fuel-Cell/Battery has been proposed, and an intelligent controller has been designed to power management. Elimination of the gasoline engine, an electrical machine can enforce requested power for driving and braking so, regenerative braking is possible in proposed structure. Fuel-cell is connected to battery as a DC bus via a DC/DC converter which can control the fuel-cell current by its switching control. A power demand feedback is considered, and the controller decision is based on this demand at the previous time step. Moreover, braking pedal displacement and the battery state of charge are considered as controller input signals and its relative decision to power split between two exist power sources. Finally, simulation results for some driving maneuvers, shows that the proposed structure has good performance for the vehicles as a civic automobile with zero emissions.

Keywords: Fuel-Cell, Regenerative braking, SoC.

1- Introduction

Regarding to recent solicitude about the fossil-fuel consumption and also environmental emission, the hybrid-electric vehicles are studying now, and many structure and relative controllers are designing. Using electrical machine as a mechanical power source is a usual technique in these vehicles. In a known structure, using electric machine instead to the gasoline engine, an electric-vehicle is produce, which is needed to an electrical source for supply. Battery, fuel-cell, ultra-capacitors and all the energy storage systems can be used as an input power supply in the mentioned structure. Considering a battery pack beside a fuel-cell is caused to produce a battery/fuel-cell hybrid vehicle (BFCHV). Power management controller is most important part of the mentioned vehicle which must compute the power shared among the battery and fuel-cell. Recently, development of control strategy for electric and hybrid vehicles are growing. In [1] by Guezennec et al., with solving the supervisory control problem for a FCHV, significant fuel economy has been shows by a quasi-static optimization technique. In [2], by Rodatz et al., power split has been done among of fuel cell and supercapacitor by a fuel minimization strategy and The concept of equivalent factors in hybrid-electric vehicles has been described by Sciarretta et al. [3]. Moreover, the comparison between their results and deterministic dynamic programming has been done. Fathy et al. [4] classified strategies for combined plant/controller optimization into sequential, iterative, bi-level, and simultaneous strategies. If a plant is optimized first and a controller is, then designed, it often leads to non-optimal overall system due to the coupling of plant/controller optimization. Developing scalable subsystem model is essential in this optimization problem. By Assanis et al. [5] a designed optimization algorithm has been proposed to find the best overall engine size, battery

1 - Shahid Rajaei Teacher Training University, Iran, Tehran

2 - Islamic Azad University, Iran, Dezgul Branche, bakhtiari348@yahoo.com

3 - Shahid Rajaei Teacher Training University, Iran, Tehran. P.naderi@srctu.edu

pack, and motor combination for maximizing the fuel economy. For the engine scaling, they replaced the linear scaling of experimental engine look-up tables with a high-fidelity simulation that predicts the nonlinear effects of scaling. In [6], using an optimization algorithm a good result to components sizing has been shown, but the control optimization was not addressed. Study on the size ratios for the FCHV, has been done by Ishikawa et al. of Toyota Motor Corporation [7], but they had not any illustration about their control strategy and algorithm. In [8], by Atwood et al, hybridization degree was studied using ADVISOR software. They fixed the power demand and studied on the fuel economy for various fuel cells. In [9], optimization problem has been formulated using the control variables for FCHVs, but the optimization was not warranty. A similar method has been proposed in [10], and designing method in terms of volume and type of the components has been proposed in [11] for FCHVs. In [12], a control strategy has been proposed to optimum performance of BFCHV. This controller, which is inspired by the Stochastic Dynamic Programming results, can be included as design variables in system optimization problems.

2- Proposed Structure

Using an electrical machine instead to gasoline engine, two power sources have been considered as power supplying, which are a battery pack and a fuel cell. A permanent magnet DC machine is a good choice for application due to its controllability. Some kinds of this machine have been proposed for using in hybrid-electric vehicles [13]. A DC/DC converter is used as an intermediate hardware between the fuel cell and batteries which is considered as a constant voltage bus. Now, the output current of fuel cell can be controlled by DC/DC converter switching. So, the power managing can be done via the converter switching. Moreover a motor controller is needed for Speed-Torque control of electrical machine, as shown in Fig. 1.

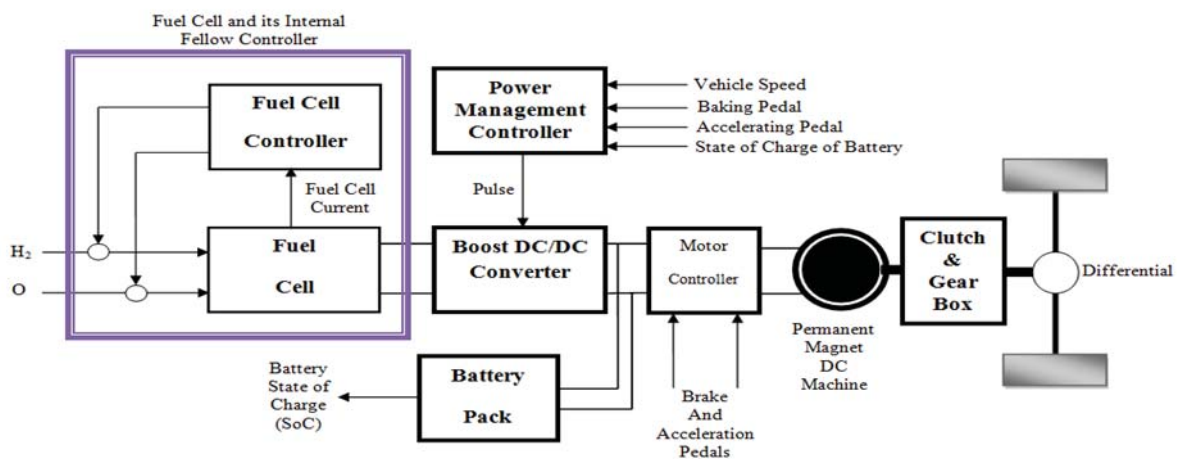


Fig1. Proposed structure for Fuel cell/Battery hybrid vehicle

3- System Modeling in matlab/simulink

Regarding to Fig.1, there are some separated systems to proposed structure modeling and design. It is important to mention that the models of fuel cell and its internal fellow controllers, batteries, and electrical machine, have been used from power system toolbox of MATLAB software so; the modeling of them has been not illustrated in this paper.

3-1- Vehicle and Tire Modeling

One quadrant model has been used for vehicle and tire simulation in this paper, which is proper for analysis of power management purpose. In this case, a simplified vehicle model can be used so, there are not to use of an ambiguous model. In fact, a model with only longitudinal dynamic is proper for driving energy usage, and the power management aim can be studied by this model. Regarding to above illustrations, all wheels can be modeled by once, and Braking/Driving torque will be applied to this. Regarding to nomenclature symbols, relative formulas can be written as following:

$$F_x - F_{ax} = M_T \cdot a_x \quad (1)$$

Where, aerodynamic force is defined as bellow [14-15].

$$F_{ax} = \frac{1}{2} A \cdot \rho \cdot C_d \cdot V_s^2 \quad (2)$$

F_x , is tire force in braking and driving conditions and is relative to some parameters such as the road gradient, vehicle speed, enforced torque and also vehicle mass. In this study, well-known Dugof's model has been used for tire modeling. When the mover torque (τ_w) is applied on the wheel, it will be rotated as follows [14-15].

$$I_{wv} \cdot \dot{\omega} = \tau_w - R_{wv} \cdot F_x - \tau_R - R_{wv} \cdot M_T \cdot g \cdot \sin(\beta) \quad (3)$$

Where, $\tau_R = C_0 \cdot F_z + C_1 \cdot V^2$. C_0 and C_1 are restricted as $0.04 < C_0 < 0.02$ and $C_1 \ll C_0$. τ_w , which is the tire enforced torque, is considered as the total braking or differential output torque. Regarding to this enforced torque, longitudinal slip of the wheel can be written as following.

$$\lambda = \begin{cases} 1 - \frac{R_{wv} \cdot \omega}{V_s} & \text{for } R_{wv} \omega_1 \leq V_s \\ -1 + \frac{R_{wv} \cdot \omega}{V_s} & \text{for } R_{wv} \omega_1 \geq V_s \end{cases} \quad (4)$$

Noticing to above equations, the vehicle model with longitudinal dynamic can be expressed by Fig2. Moreover, regarding to friction coefficient and road gradient, the tire force can be written as following equations.

$$H = \frac{C_x \cdot \lambda}{\mu \cdot M_T \cdot g \cdot \cos(\beta) (1 - \lambda)} \quad (5)$$

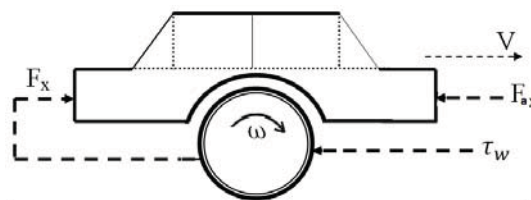


Fig2. One quadrant model of vehicle

3-2-Gear Box and Differential Modeling

Regarding to Fig1 and proposed structure, an electrical machine has been used instead to the gasoline engine. So, its output power will be enforced to driven wheels via the gear box and

differential subsystems. In fact, both the mentioned systems can be modeled by constant coefficient for Torque/Speed conversion and another constant can be considered for their efficiency. So, torque and speed of gear box can be written as following.

$$\omega_{gn} = k_d \cdot k_{gn} \cdot \omega \tag{8}$$

$$T_{gn} = \frac{\eta_d \cdot \eta_{gn}}{k_d \cdot k_{gn}} \cdot T_{EV} \tag{9}$$

The clutch can be modeled by two separate surfaces, which is connected between the gear box and engine shaft. For the gasoline engine, it may be some difference at the low speed (Less than 6 km/h approximately) between rotational speed of surfaces. It is a key note that using electric machine instead to the gasoline engine, it can be assumed that the clutch surfaces have equal speed even at low speeds. Regarding to these illustrations, the clutch modeling is not imperative. So, the bellow equations can be written

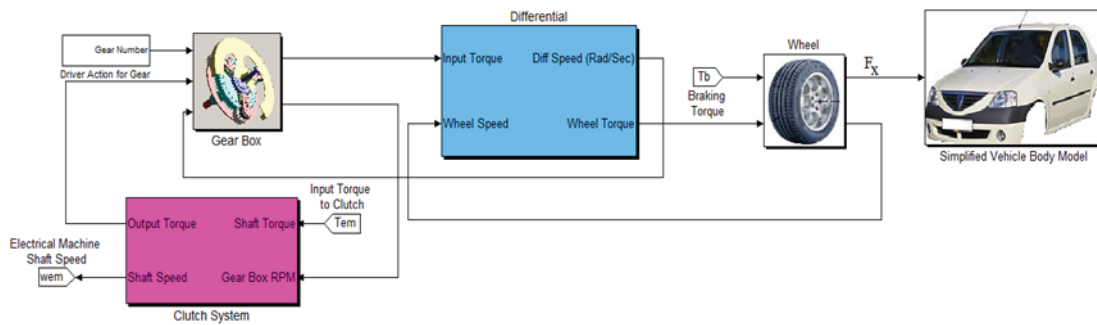


Fig3. Mechanical parts modeling in SIMULINK environment

$$\omega_{gn} = \omega_{EV} \tag{10}$$

$$T_{gn} = T_{EV} \tag{11}$$

Regarding to above illustrations, the modeling of relative subsystems can be done by MATLAB. Fig 3, shows the masked modeled.

3-3- Boost dc/dc converter

Noticing to Fig 1, a DC/DC converter has been used as an interface between the fuel cell and battery. Moreover, it can control the fuel-cell current by its switching duty cycle, which is output of the power management controller. Usually, the nominal voltage of fuel cell is less than battery voltage so, a boost converter is needed. Fig 4, show the mentioned converter and its internal switching controller.

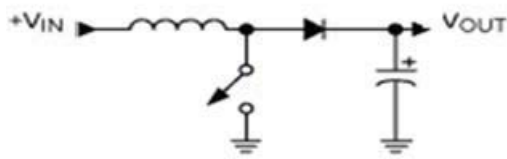


Fig4. Boost DC/DC converter schematic

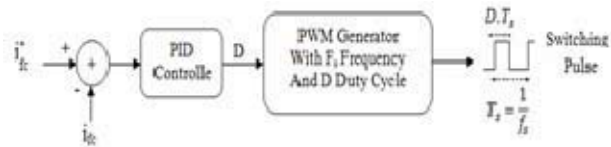


Fig5. Switching control of DC/DC converter

A simple PID controller has been used to computing of the pulse duty cycle of switching, which has a certain frequency, called f_s . Moreover, the switching pulse is generated by PWM generator as shown in Fig5 where i_{fc}^* is desired fuel cell is current.

3-4- Electrical Systems modeling

In addition to DC/DC converter, there are needed to fuel cell, battery and electrical machine modeling and their proper arranging according to proposed structure as shown in Fig1. The internal controller of fuel cell which can control of its fellow can see as some demo examples in MATLAB/SIMULINK environment. A permanent magnet DC machine (PMDC) proposed for electric vehicles [16], has been considered for using in the proposed vehicle. Fig 7 shows the DC machine which has been considered as a permanent magnet type and its driver. The torque demand is request by throttle pedal and also braking pedals which produced by PI current control. The produced torque is relative to machine current by bellow equation which k , is a constant value base on the machine properties. Fig 7 shows the mentioned model in SIMULINK software which is connected to another simulated parts.

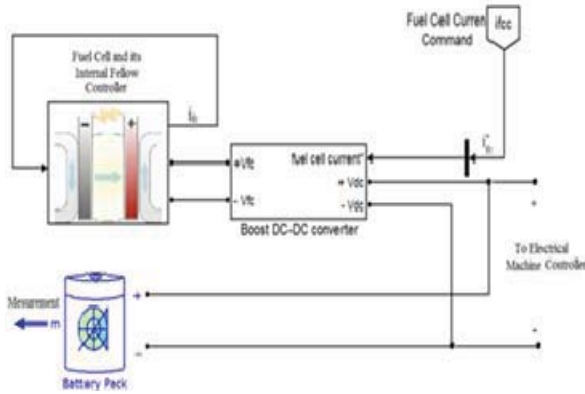


Fig6. Two power sources modeling in SIMULINK

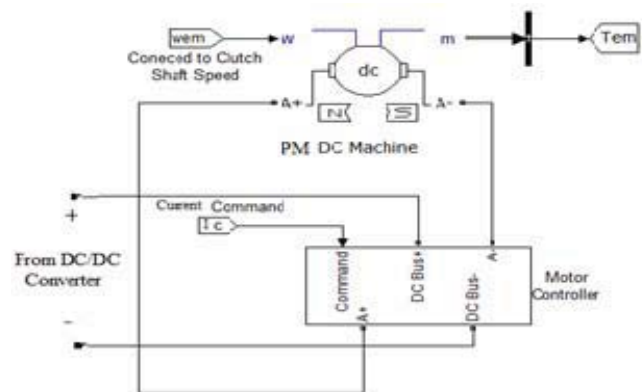


Fig7. Simulation of DC machine and its current-torque controller

$$T_{em} = k_p \cdot i_{em} \quad (12)$$

It is need for notation that the motor controller is bi-directional to regenerative ability. Fig7 shows a one directional controller but another similar controller is connected parallel for second direction which allows to power reversing from electrical machine according to pedals displacement.

3-5- Driving and braking pedals modeling

In final section of subsystems modeling, there is a need to simulation of pedals. In fact, the braking torque applied to wheel is depended to vehicle speed and braking pedal displacement. Moreover, it is assumed that the current of electrical machine is linearly depended to throttle pedal displacement. Regarding to these illustrations, two mentioned pedals can be modeled by two PID controller and also two lookup tables as shows in Fig.8. As shown in this figure, a certain part of braking pedal displacement ($K_t < 1$) has been considered for regenerative braking, which can be illustrated by bellow where X_{bp} , is devoted to braking pedal displacement.

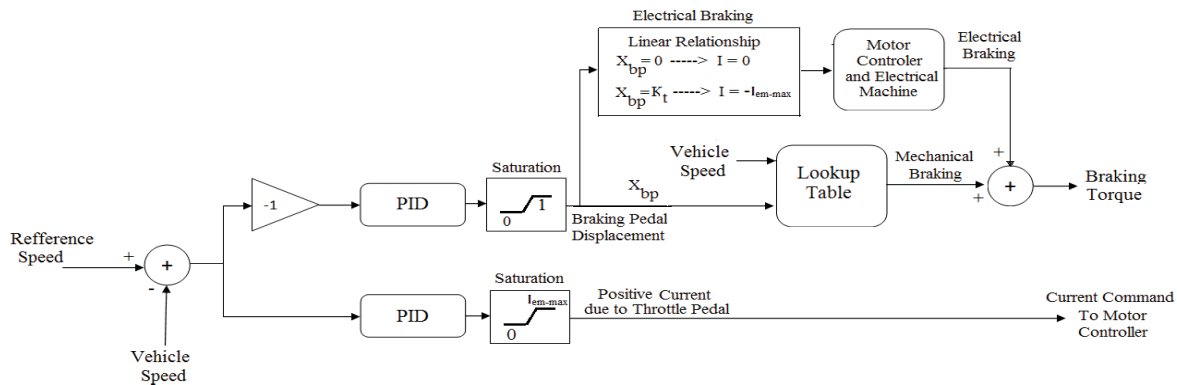


Fig8. Throttle and braking pedals modeling

$$\begin{cases} 0 < X_{bp} < K_t & \text{Not Exist Mechanical Braking} \\ K_t < X_{bp} < 1 & \text{Activation of Mechanical Braking} \end{cases}$$

Now, the fully model of the proposed hybrid vehicle is available. Clearly, there is a need a power management controller. Driver power demand will request by pedals and the controller so, this requested power should be divided between the fuel cell and battery. Operation of the controller is based on the various parameters such as battery stat of charge and driving condition.

4- Power Management Controller

4-1- Controller task

There are two main aims for the vehicle power management which can be summarized as following.

A - Power management in driving condition

This mode will be activated in driving via the throttle pedal pressuring. In this case, requested power by throttle pedal will be converted to current command and will be applied to motor controller. While the requested power is less than the fuel-cell nominal power, the electrical machine be supplied by only fuel cell, and it's reminded power is assigned for battery charging, but the full charging is assigned for lower SoC. So, the battery charging is not necessary when the battery is fully charged. It is a key note that the electrical machine may be operated in generator mode according to throttle pedal displacement and may be occur in some cases such as driving on downhill road.

B- Regeneration in braking condition

Regarding to section 3.5 and figure 8, a threshold (K_t), has been considered for braking pedal displacement to regenerative braking. While the mentioned displacement be less than K_t , only

negative current command be applied to the controller for speed reduction and there is not any mechanical braking torque in this case. This mode will be disabled in case of that the battery has good state of charge.

4-2- Design of Controller

Regarding to controller aims, input power of electrical machine which is power demand is computed at each time step by equation (13). So, it can normalize base on the fuel-cell nominal power by equation (14).

$$P_{em}(t) = i_{em}(t) \cdot V_{em}(t) \quad (13)$$

$$K_p = \frac{P_{em}(t)}{P_{fc-nom}} \quad (14)$$

Clearly, the battery charging will be possible by reminded power of fuel-cell for $K_p < 1$. Considering $P_b(t)$ as the specified power for battery charging, the fuel-cell power is clearly as following.

$$P_{fc}(t) = P_{em}(t) + P_b(t) \quad (15)$$

Considering the output voltage of the fuel-cell and its specified output power for each next time step, it's necessary current can be computed as bellow for each next time step.

$$i_{fc}^*(t + \Delta t) = \frac{P_{fc}(t + \Delta t)}{V_{fc}(t)} \quad (16)$$

The battery state of charge (SoC) and the K_p which is computed by (14), are considered as input signals and the controller output is the fuel-cell power for next time step. The "Sugeno" type of a fuzzy controller is base on Nero-Fuzzy controller and training data, which must present by an expert person. For this aim, noticing to battery state of charge, it has been considered that for the $K_p < 1$, the reminded power capacity of fuel-cell can be used for battery charging. However, the battery charging is not necessary in good SoC's which is considered 95% approximately. Moreover, in case of that the electrical machine power just is the driver request, be more than the fuel-cell nominal power, both the fuel cell and battery works for electrical machine supplying. In fact, the power management for next time step has been done by a fuzzy controller according to requested power demand, which is input power of electrical machine and also the battery state of charge. Regarding to above illustrations, the power management controller works only for $K_p < 1$ and its output is the percentage of nominal fuel-cell power which should be applied for battery charging. Five membership functions have been considered for each input as 'VL', 'L', 'M', 'H', and 'VH' which are corresponding to Very Low, Low, Medium, High, and Very High. The output surface is shows in Fig 9, which has been obtained base on training

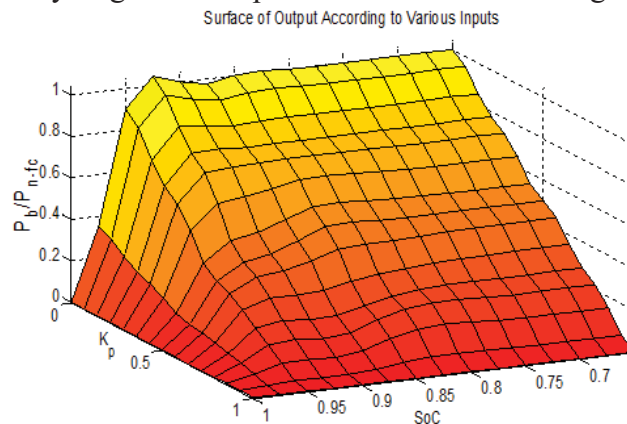


Fig 9. Output surface of controller



5- Simulation Results

In this section, some maneuvers have been simulated to show the effectiveness of proposed structure with relative control strategy. Typical parameters of subsystems have been considered for modeling, which are tabulated as following. Moreover, the relative curves of fuel-cell and battery are shown. The parameters shown in Figs 14 and 15 can be found in [17-18].

Table 1- Typical parameters of subsystem used for modeling

Parameter	Symbol	Value	Unit
Total vehicle mass	M_t	1150	kg
Drag coefficient of vehicle	C_d	0.35	$N.s^2/m^2$
Frontal area of vehicle	A	2	m^2
Longitudinal stiffness of wheel	C_x	17500	N
Radius of wheel	R_w	0.3	m
Inertia of wheel	I_w	0.9064	Kgm^2
Differential coefficient	K_d	8	--
Gear box coefficients	$K_{g1}, k_{g2}, k_{g3}, k_{g4}$	2.7, 2.1, 2.75, 0.861	--
Nominal continuous power of electrical machine	P_{n-em}	16	kw
Nominal continuous power of electrical machine for 30 sec	P_{n-em}	30	kw
Torque Constant of PMDC Electrical Machine	K_b	0.16	$N.m/A$
Maximum current of PMDC electrical machine	I_{em-max}	350	A
Nominal power of fuel-cell	P_{n-fc}	12	kw
Fuel-cell voltage at operation point	V_{fc}	45	v
Battery voltage	V_b	100	v
Battery capacity	Ah	160	A.h

Now, an acceleration maneuver has been simulated. The vehicle speed for this simulation has been shown in upper part of Fig10. The gear number is considered at 1 as shown in lower part of Fig10. The K_p value is shown in this figure and the power management has been confirmed by the controller according to initial SoC in case of $K_p < 1$. Regarding to figure 11, the fuel cell works in nominal power at all times for lower SoC which is 0.85. Also, it is clear that it works only for electrical machine supplying for full charged battery. The battery state of charge is shown in Fig12 and it is seen that more charging has been done in lower case of its initial state of charge and it is not charged in full charge case to avoid of not necessary charging.

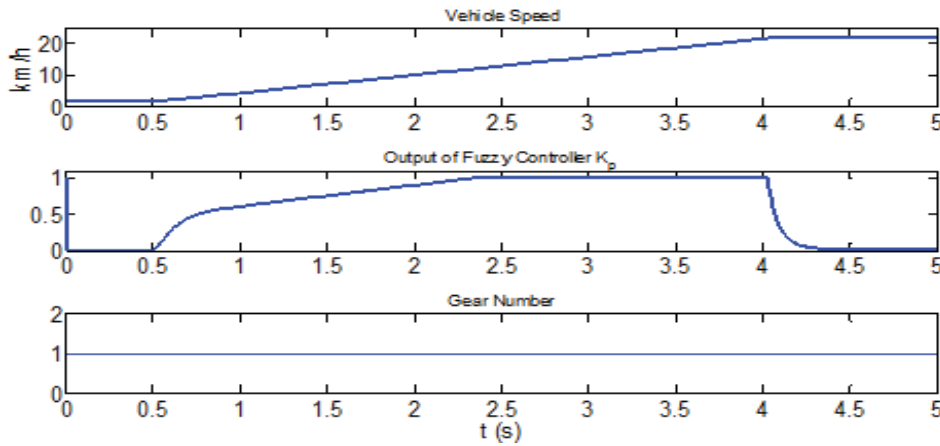


Fig10. Vehicle speed, K_p coefficient and gear number during acceleration maneuver

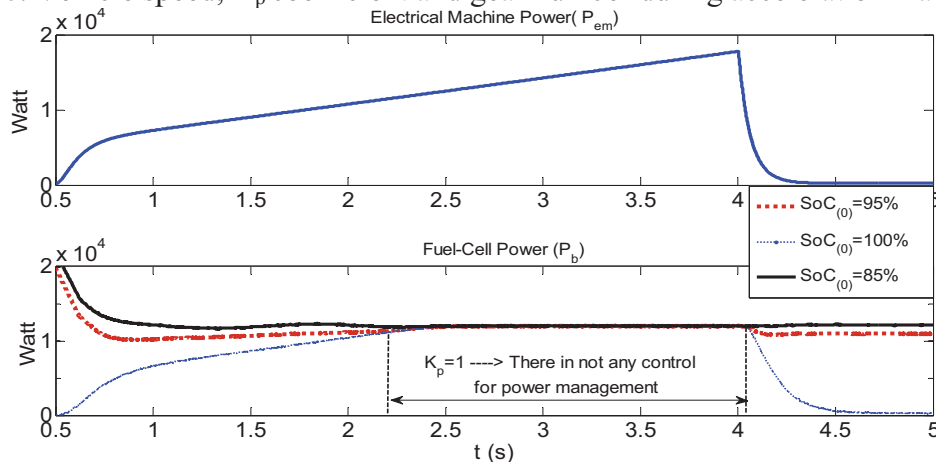


Fig11. Power demand and fuel-cell power during acceleration maneuver for various initial SoC's

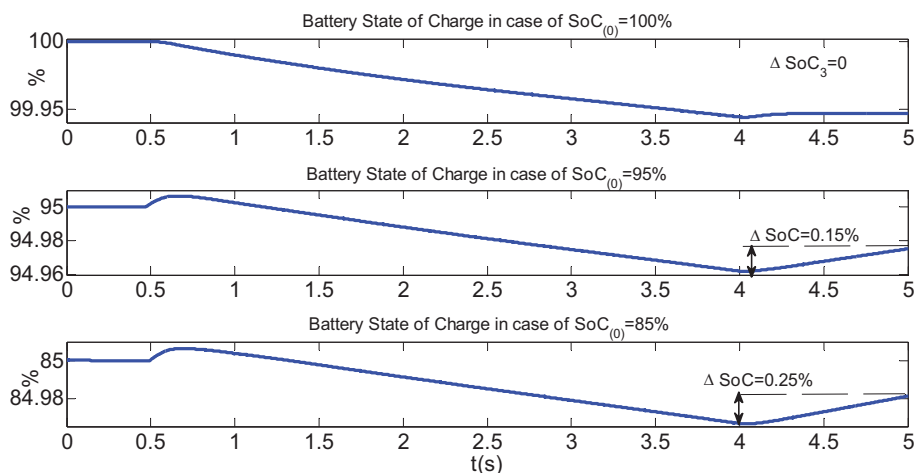


Fig12. Battery state of charge during the simulated maneuver



6- Conclusion

In this research, full modeling of a Fuel-Cell/Battery hybrid vehicle was introduced. Needed subsystems with proper modeling of components have been used and can be considered before experimental case study for the vehicle design with proposed structure. Objective to keeping of battery state of charge in a reliable area, a Regenerative braking and also power management controllers was designed using a Nero-Fuzzy controller. Considering a typical 100v, 16kw PMDC machine, a 12kw fuel-cell and a 100v battery pack was used as two parallel power suppliers. So, the power management with the regeneration ability was performed. Simulation results show the good performance to reaching of main considered aims. Cleary design, realism structure, fully modeling, and intelligent controller designed are advantages of this paper.

References

- [1] Y. Guezennec, T.-Y. Choi, G. Paganelli, G. Rizzoni , Supervisory Control of Fuel Cell Vehicles and its Link to Overall System Efficiency and Low-Level Control Requirements, Proceedings of the American Control Conference, Denver, CO, 2003.
- [2] P. Rodatz, G. Paganelli, A. Sciarretta, L. Guzzella, Optimal Power Management of an Experimental Fuel Cell/Supercapacitor-powered Hybrid Vehicle, Control Engineering Practice, Vol. 13, 2005, pp.41-53.
- [3] A. Sciarretta, L. Guzzella, C. H. Onder, On the Power Split Control of Parallel Hybrid Vehicles: from Global Optimization towards Real-time Control, Vol. 51,2003, pp.195-203.
- [4] H. Fathy, J. Reyer, P. Papalambros, A. Ulsoy, On the Coupling between the Plant and Controller Optimization Problems, Proceedings of the American Control Conference, Arlington, VA, 2001.
- [5] D. Assanis, G. Delagrammatikas, R. Fellini, Z. Filipi, J. Liedtke, N. Michelena, P. Papalambros, D. Reyes, D. Rosenbaum, A. Sales, and M. Sasena, An Optimization Approach to Hybrid Electric Propulsion System Design, Mechanics of Structures and Machines, Vol. 27, No. 4, 1999, pp. 393-421.
- [6] R. Fellini, N. Michelena, P. Papalambros, M. Sasena, Optimal Design of Automotive Hybrid Powertrain Systems, Proceedings of the First International Symposium on Environmentally Conscious Design and Inverse Manufacturing, Tokyo, Japan, February 1-3, 1999, IEEE Comput. Soc, Los Alamitos, CA, pp. 400-405.
- [7] T. Ishikawa, S. Hamaguchi, T. Shimizu, T. Yano, S. Sasaki, K. Kato, M. Ando, H. Yoshida, Development of Next Generation Fuel-Cell Hybrid System—Consideration of High Voltage System, SAE Paper No. 2004-01-1304.
- [8] P. Atwood, S. Gurski, D. Nelson, K. Wipke, T. Markel, Degree of Hybridization Modeling of a Hydrogen Fuel Cell PNGV-Class Vehicle, SAE Paper No. 2002-01-1945.
- [9] K. Wipke, T. Markel, D. Nelson, Optimizing Energy Management Strategy and Degree of Hybridization for a Hydrogen Fuel Cell SUV, Proceedings of the 18th Electric Vehicle Symposium, Berlin, Germany, 2003
- [10] A. Rousseau, P. Sharer, R. Ahluwalia, Energy Storage Requirements for Fuel Cell Vehicle, SAE Paper No. 2004-01-1302.
- [11] T. Markel, M. Zolot, K.B. Wipke, A.A. Pesaran, Energy Storage System Requirements for Hybrid Fuel Cell Vehicles, Proceeding of Advanced Automotive Battery Conference, Nice, France, June, 2003.
- [12] Min-Joong Kim and Huei Peng, Power Management and Design Optimization of Fuel Cell/Battery Hybrid Vehicles, Journal of Power Sources, Vol.165, issue 2, March 2007, pp.819-832.
- [13] *Manufacturers of high efficiency D.C machines. www.agnimotors.com.*
- [14]- P. Naderi, A.R. Naderipour, M. Mirsalim, and M.A. Fard, "Intelligent Braking System using Fuzzy Logic and Sliding Mode Controller", Control and Intelligent Systems, Vol. 38, No. 4, 2010.
- [15] P. Naderi, A.Farhadi, Non-Driven Wheels Application for Intelligent Multi Objective Control of Hybrid Vehicles, International Journal of Robotic and Control, Vol.27, No. 2,2012
- [16]- Agni motors production Co, Manufactures of high efficiency of DC machines, *www.agnimotors.com*
- [17]. Tremblay, O.; Dessaint, L.-A.; Dekkiche, A.-I., "A Generic Battery Model for the Dynamic Simulation of Hybrid Electric Vehicles," Vehicle Power and Propulsion Conference, 2007. VPPC 2007. IEEE 9-12 Sept. 2007, pp. 284-289.
- [18]- Matlab software guid,
- [19]- Advidor software Vehicle Simulator.



Oxygen reduction reaction on Pt/C at the presence of super paramagnetic of Fe₃O₄ nanoparticles in PEMFC

M. kheirmand*¹, F. Rastegary-Fard²

*Department of chemistry, faculty of sciences, Yasouj University, Yasouj, Iran
Corresponding Author E-mail: kheirmand@gmail.com*

Abstract

Ion-exchange polymer membrane fuel cell (PEMFC) is as power source that fed by hydrogen gas and produce water. Electrochemical oxygen reduction reaction (ORR) is one of the most important reactions in the fuel cell energy conversion. ORR in acidic condition is four electron reaction of oxygen to water. Oxygen is a powerful oxidizing agent and is actually responsible for the extraction of energy from the fuel. But sluggish kinetic of ORR in Fuel cell is a problem. In this paper the role of super paramagnetic iron oxide (SPMIO) nanoparticles with different loadings, at the presence of commercial Pt/C was evaluated via conventional three electrode system and electrochemical tests such as Cyclic Voltammetry, Rotating disk electrode (RDE), Chronoamperometry. The results show that ORR is improved with the same ratio of Pt/C and SPIO.

Keywords: PEMFC, Oxygen reduction reaction, Rotating disk electrode

Introduction

Low temperature fuel cell technology has being considered as popular technology. Ion-exchange polymer membrane fuel cell (PEMFC) is as power source that fed by hydrogen gas and produce water. Through, has attracted much attention due to friendly environmental, high energy conversion efficiency, high power density, good temperature performance, No need to recharging and application in automobile. However, commercialization is the way it challenges, including the high price of platinum and limited sources. Although platinum widely still use as catalyst. So researchers are looking for alternatives to reduce the price of fuel that can be produced by two routes: (a) reducing the platinum loading in the catalyst (b) replacing the platinum catalyst with non- platinum catalyst [1]. The electrochemical reduction of oxygen is one of the most important reactions in electrochemistry due to its central role in fuel cells, metal-air batteries. Depending on the electrode material and the solution composition, the oxygen reduction reactions (ORR) precede as a direct four-electron process

¹ Assistant prof. of physical chemistry

² M.Sc student of physical chemistry, Yasouj university, Yasouj, Iran



or a two-electron process. The production of water of four-electron reduction is favorite in PEMFC, while hydrogen peroxide is electrochemically generated by a two-electron reduction of oxygen. Carbon supported platinum catalyst shows a large surface area and increased catalytic activity for the ORR. Bimetallic catalysts were employed to increase the catalytic activity and to reduce the cost [2].

Some transition metal oxides, such as Oxides of Iron, Cobalt, Manganese and ruthenium can modify the electronic nature and is effective in reducing the platinum loading for instance Manganese Oxides have good activity for H₂O₂ decomposition. But the catalyst lifetime decreases by reducing Pt loading. Also Pt nanoparticles are placed onto carbon nanofibers such as carbon plate, graphene and carbon powder that is effective in oxygen reduction. Greater amount of Platinum used in fuel cell cathode to reduce oxygen because kinetic of oxygen reduction reaction (ORR) is slower than Hydrogen oxidation reaction (HOR). Overpotential of hydrogen oxidation and oxygen reduction is 25mv and 300mv respectively on pure platinum. Now the based platinum systems exhibit the best electrocatalytic activity. ORR reaction is reducing oxygen molecules to water molecules [3, 4]:



Compared to other metal oxides Fe₃O₄ has the advantage of low cost and compatibility with the environment. Recently, extensive work has been done in this context. Lai and et al [5] put platinum nanoparticles on the surface of three-dimensional Fe₃O₄/C. and used for Methanol oxidation reaction (MOR) catalyst. The new nano-composites made of carbon and separate advantage of Fe₃O₄. The groups on surface of nano-composite three-dimensional Fe₃O₄/C as –NH₂ and –OH can keep platinum on surface firmly cause to increasing electrocatalytic activity that showed threefold current density Pt/C for MOR In this paper used of platinum nano clusters at the presence of super Paramagnetic Iron oxide nanoparticles to improve kinetic of ORR in PEMFC.

Experimental:

For electrochemical test, 80 mg of Pt/C (10 wt.%) in 20 ml of a 1:1 ratio of water and 2-propanol was dispersed for 30 minutes using the ultrasonic probe. Electrochemical system include three electrodes system, Ag/AgCl reference electrode and plate platinum as the auxiliary electrode(counter) and glassy carbon (GC) electrode was as working electrode. 80 mg of Pt/C with different ratio of SPMIO (1:1, 1:2 and 1:3) was casted on GC electrode.

Cyclic Voltmetry:

Cyclic voltammetry tests were performed using a EG&G in conventional three-electrode system at room temperature. An Ag/AgCl used as reference electrode and platinum as counter electrode. The working electrode prepared by applying catalyst ink on glassy carbon surface then distilled a drop of nafion (5 wt. %) solution and dried. Voltamograms obtained in -0.3V to 1.2V in solution of sulfuric acid (0.5M) that was bubbled by inert gas (N₂). The electrochemical specific surface areas (EAS) of electrocatalysts were calculated by integrating

the areas under the peaks of hydrogen adsorption. To determine the EAS, the charge due to hydrogen adsorption (Q_H) was obtained by [6]:

$$EAS = \frac{Q_H}{[Pt] \times 0.21} \quad (1)$$

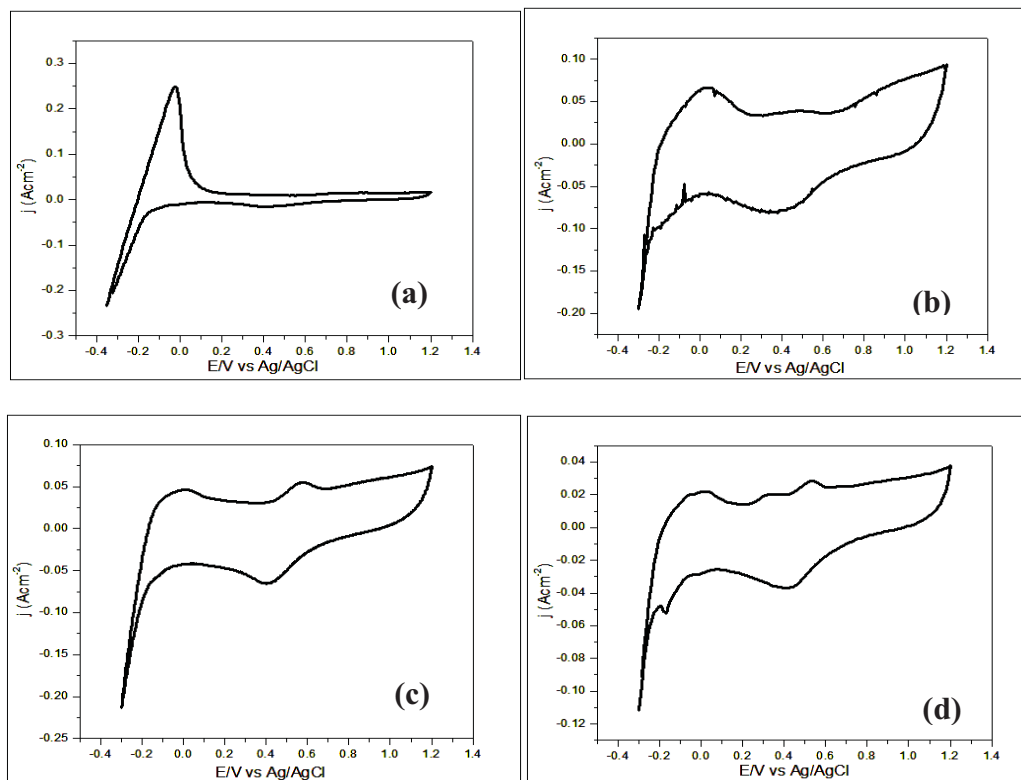


Figure 1: Cyclic Voltammetry of (a) Pt/C, (b) 1:1, (c) 1:2 and (d) for 1:3 ratio electrocatalysts of Pt/C: SPMIO in scan rate 50mvs⁻¹ and N₂ atmosphere and room temperature.

To investigate the effect of Iron oxide nanoparticles at the presence of Pt/C, cyclic voltammetry test was performed for methanol oxidation reaction. The results show that SPMIO particles increase the methanol oxidation resistance in cathode.

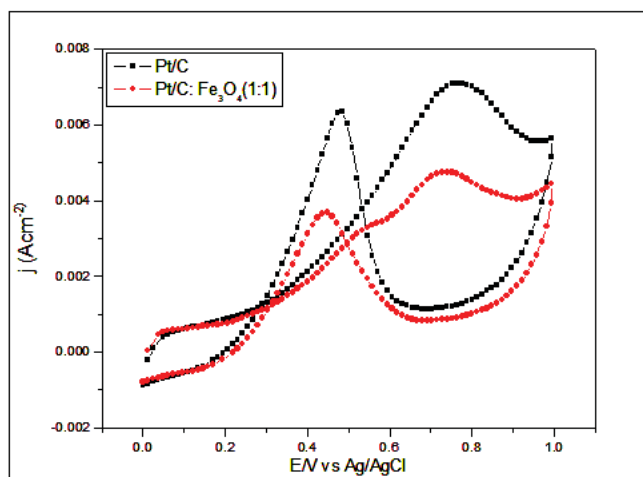


Figure 2. Comparison cyclic voltammograms of methanol oxidation reaction (MOR) in 0.5M of H₂SO₄ and 1M Methanol solution at the potential scan rate 50mvs⁻¹ at room temperature.

Table 1. Electrochemical active surface area calculated for electrocatalysts.

electrocatalyst	EAS(cm ² g ⁻¹)
Pt/C (10%wt)	124.90
Pt/C : Fe ₃ O ₄ (1:1)	106.11
Pt/C : Fe ₃ O ₄ (1:2)	61
Pt/C : Fe ₃ O ₄ (1:3)	33.36

Chronoamperometry:

Chronoamperometric technique is an effective method to evaluate the electrocatalytic stability of catalysts. Using this technique easily diffusivity, solubility and permeability, gas permeability of oxygen penetrating electrodes is obtained. These parameters depend on the extent of the time, according to the Cottrell equation is [7]:

$$i(t) = \frac{nFAD^{1/2}C_0}{(\pi t)^{1/2}} \quad (2)$$

Where, n, is the number of electrons exchanged for the overall electrode reaction. A, F, t and π are the area of electrode penetration and reagent concentration and Faraday's constant, the time, and the ratio of circumference to diameter, respectively.

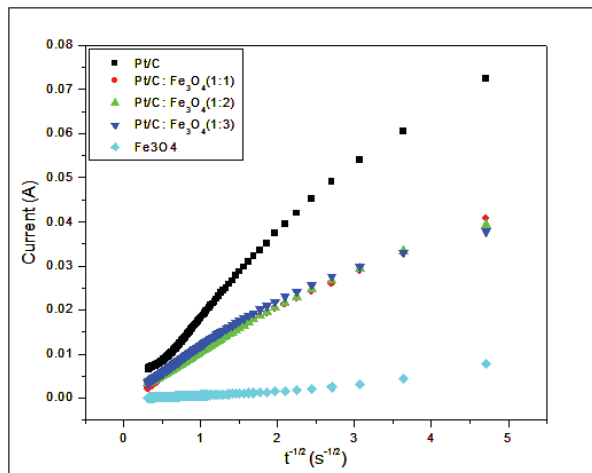


Figure 3: Chronoamperometry plots in O₂ saturated and room temperature.

Table 2. Diffusion Coefficient of Oxygen that calculated of Chronoamperometry slop.

electrocatalyst	D _{O₂} (cm ² /s)
Pt/C (10%wt)	1.13 × 10 ⁻⁵
Pt/C : Fe ₃ O ₄ (1:1)	3.93 × 10 ⁻⁶
Pt/C : Fe ₃ O ₄ (1:2)	3.18 × 10 ⁻⁶
Pt/C : Fe ₃ O ₄ (1:3)	3.18 × 10 ⁻⁶

Rotating disk electrode (RDE)

The ORR activities of electrodes were investigated in O₂ saturated 0.5 M H₂SO₄ solution. Fig 4 shows the linear scan voltammetry plots of electrodes measured with a scan rate of 1mvs⁻¹ at room temperature. To obtain kinetic parameters for the oxygen reduction reaction at fabricated electrodes followed [8]:

$$\frac{1}{j} = \frac{1}{j_k} + \frac{1}{j_d}$$

(3)

$$\frac{1}{j} = \frac{1}{nFk C_{O_2}^b} - \frac{1}{0.62nF D_{O_2}^{2/3} C_{O_2}^b \nu^{-1/6} \omega^{1/2}}$$

(4)

Spinning solution in electrochemical systems will facilitate diffusion coefficient of oxygen to the electrode surface and the diffusion limitation of oxygen recovery takes so kinetic starting potential change in response to the higher values and lower overpotential. The RDE results of electron exchange reaction in oxygen reduction were 3/6 in Pt/C electrocatalyst. So it can be

stated that the reaction mechanism of the four-electron pathway is gone. Electrocatalytic with the number of electrons in 1:1 ratio of Pt/C: Fe₃O₄ was $2.9 \approx 3$. Oxygen reduction reaction proceeds of both the electron and 2-electron 4 is gone in a direction that is parallel to both directions.

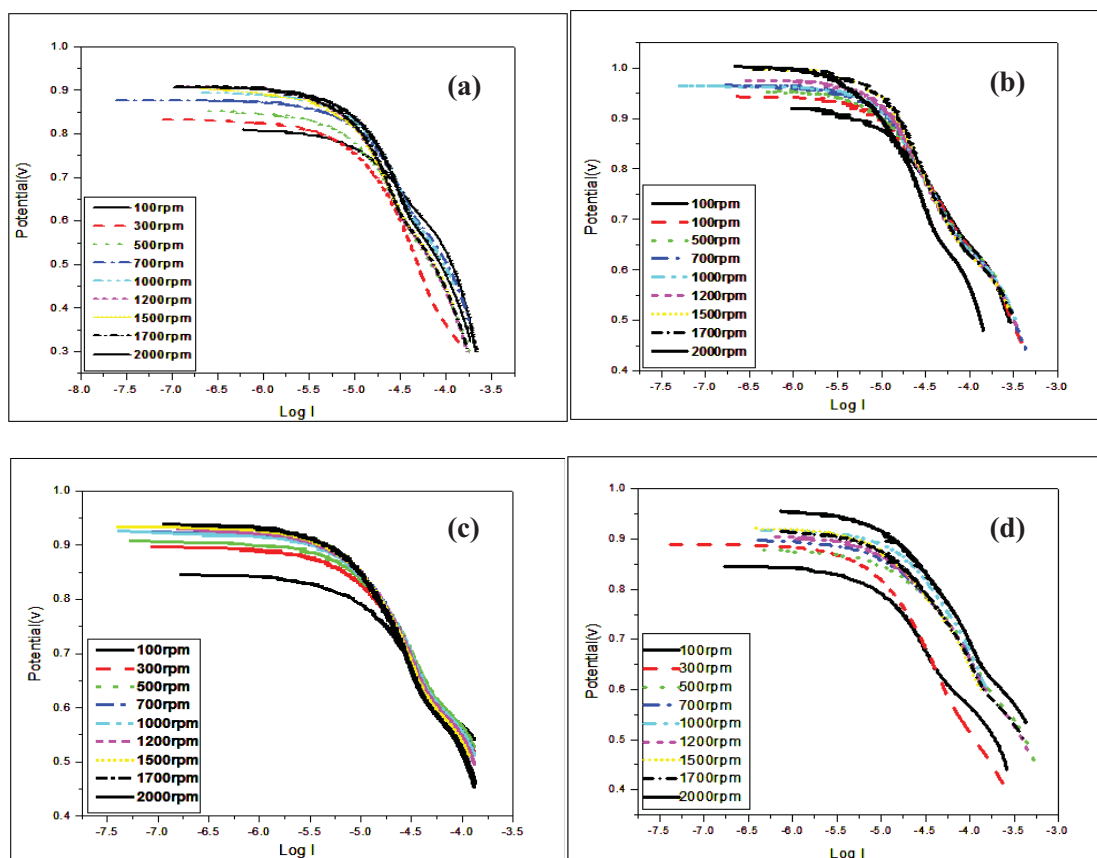


Figure 4. Linear sweep voltammetry on RDE for (a) Pt/C, (b) 1:1 ratio, (c) 1:2 ratio, (d) 1:3 ratio electrocatalyst in H₂SO₄ 0.5M and scan rate mvs^{-1} in 100rpm to 2000rpm.

With the assumption that the transition metals are more likely to produce H₂O₂, number of electrons exchange are reduced in the reaction of oxygen of these metals. On the other hand, H₂O₂ catalyst to attract more smaller particles are then absorbed by hydrogen peroxide in the presence of Iron oxide nanoparticles can also be involved. Can reduce the number of exchanged electrons to Iron oxide insulator and block attributes. Considering that the oxygen reduction reaction, 4 electron reduction Ideally, the electrocatalytic four-electron reduction of oxygen would figure more attention. In this test, a combination of the two and four-electron electrocatalytic ratio is 1:1. Therefore, more research on this than the Pt / C: Fe₃O₄ focus.

Reaction kinetic study and reaction to achieve the number of electrons exchanged the RDE results in charts $1/j$ by $\omega^{-1/2}$ were plotted [8]. The results are shown in the chart in Table 3.



Table 3. number of electron that calculated by Koutechy–Levich data.

electrocatalyst	Number of electron
Pt/C (10. wt%)	3.6
Pt/C : Fe ₃ O ₄ (1:1)	2.9
Pt/C : Fe ₃ O ₄ (1:2)	2.4
Pt/C : Fe ₃ O ₄ (1:3)	2.4

Conclusions

In this study the low loading of Pt (10%wt) was used as the cathode PEMFC for ORR with super paramagnetic of Fe₃O₄ nanoparticles. With regard to the different effects of the magnetic field on the molecule super paramagnetic particles of iron oxide can be used to increase the oxygen adsorption and increase its kinetic. These results were obtained from experiments conducted by the electrocatalytic Pt / C: Fe₃O₄ with a 1:1 ratio after Pt/C, for having more electrochemical active surface area for hydrogen adsorption and diffusion coefficient can be good electrocatalyst for Oxygen reduction reaction. However, due to the negative effects of iron oxide, including effects on carbon and platinum corrosion are waste reduction field and study of these effects is wide.

Reference

- [1] G. Liu, X. Li, P. Ganesan and B. Popov “Development of non-precious metal oxygen-reduction catalysts for PEM fuel cells based on N-doped ordered porous carbon”, *J. of Applied Catalysis B: Environmental*, (2009). 93, 156–165.
- [2] A. Ishihar, Y. Ohgi, K. Matsuzawa, S. Mitsushima and K. Ota Zhang “Progress in non-precious metal oxide-based cathode for polymer electrolyte fuel cells”, *J. of Electrochimica Acta*, (2010). 55, 8005–8012.
- [3] I. Kruusenberg, L. Matisen, Q. Shah, A.M. Kannan and K. Tammeveski “Non-platinum cathode catalysts for alkaline membrane fuel cell”, *J. of Hydrogen Energy*, (2012). 37, 4406-4412.
- [4] X. Cheng, Zh. Shi, N. Glass, L. Zhang and J. Zhang “A review of PEM hydrogen fuel cell contamination: Impacts, mechanisms, and mitigation”, *J. of Power Sources*, (2007). 156, 739-756.
- [5] L. Lai, G. Huang, X. Wang and J. Weng “Preparation of Pt nanoparticle-loaded three-dimensional Fe₃O₄/carbon with high electro-oxidation activity”, *J. of CARBON*, (2011). 49, 1581-1587.



[6] H. Sun, J. You, M. Yang and F. Qu “Synthesis of Pt/Fe₃O₄-CeO₂ catalyst with improved electrocatalytic activity for methanol oxidation”, J. of Power Sources, (2012). 205, 231-234.

[7] J. Zeng, S. Liao, J. Y. Lee and Zh. Liang “Oxygen reduction reaction operated on magnetically-modified PtFe/C electrocatalyst”, J. of Hydrogen Energy, (2010). 35, 942-948.

[8] A. Nozad Golikand , M. Asgari and E. Lohrasbi “Study of oxygen reduction reaction kinetics on multi-walled carbon nano-tubes supported Pt-Pd catalysts under various conditions”, J. of Hydrogen Energy, (2010). 1-8.



The study of synergism effect in physical mixture of Cobalt and platinum electro catalyst for oxygen reduction reaction in PEM fuel cell

Rasol Abdullah Mirzaei^{*1}, Mohammad safi Rahmanifar², Samane Sajedinia¹

1- Fuel cell Research Laboratory, Dep. Of chemistry, Faculty of science, Shahid Rajaei Teacher Training University, Tehran, IRAN
Corresponding Author E-mail: ra.mirzaei@srttu.edu

Abstract

Gas diffusion electrodes are one of the important parts in fuel cells. Optimizing electrocatalyst is one of the approaches for increasing the efficiency of the electrodes. The aim of the present research project is to increase the catalytic activity toward oxygen reduction reaction (ORR). Hence In this work, Platinum-Cobalt electrocatalyst on Graphite(Pt-Co/G) electrode was prepared by physical mixture of platinum and cobalt electro catalysts. For this purpose, Cobalt on Graphite(Co/G) and Platinum on graphite(Pt/G) mixtures at various percent (20:80, 40:60, 50:50, 60:40, and 80:20) were used for fabrication of gas diffusion electrode in cathode of PEM fuel cell. The amount of electrocatalyst in reaction layer was 0.3 mg/cm². the metal percentage in prepared electrocatalyst was 20 %. The electro catalytic performance of the electrode was investigated by electrochemical Impedance Spectroscopy (EIS) and Linear Sweep Voltammetry (LSV). according to the results, in the optimized condition the mixture of 80% Pt/G and 20% Co/G electrocatalyst in reaction layer provide excellent electrochemical condition for ORR and promote sluggish ORR compare to other electrodes results from other percent of physical mixture of Pt/G and Co/G electrocatalyst.

Keywords: fuel cell, synergism, Oxygen reduction reaction, physical mixture

Introduction

In the future, technology advances will require that mankind increase their electricity consumption. Fuel cells promise to be a clean power source for the energy requirement of the mankind in the near future. The advantage is an efficient and clean energy production because the waste product is water[1]. Fuel cells can produce electricity continuously as long as the fuel and oxidant flow are maintained. The fuel cells challenge is to find the suitable materials to

achieve this, due to efficiency losses occurring with time by degradation of their components (e.g. catalysts).The high cost of electrode is distributed to the presence of electrocatalyst usually Pt on electrode layer because Pt possesses a high exchange current density for oxygen reduction, a high resistance to chemical attack, excellent high-temperature

1. Fuel cell Research Laboratory, Dep. Of chemistry, Faculty of science, Shahid Rajaei Teacher Training University, Tehran, IRAN

2. Dep. Of chemistry, Faculty of basic science, Shahed University, Tehran, IRAN



characteristic, and has stable electrical properties, However, platinum is very expensive and much work has been focused on the reduction of platinum loading and the improvement of electro catalytic activity of platinum [2,3]. possibly, the most significant barrier that proton exchange membrane fuel cell (PEMFC) had to overcome was the costly amount of platinum required as a catalyst[4]. Many studies have reported synergistic properties for mixed systems such as mixed surfactants, physical mixture of catalyst, etc.[5]. In this work, the combined processes of impregnation and seeding was used to prepared Pt–Co/G electro catalysts. The prepared electro catalysts were in physical mixture of Pt and Co electro catalysts for the oxygen reduction reaction in PEM fuel cells.

Experimental

Electro catalyst preparation

Initially, the Pt solution was obtained from metal precursors, H_2PtCl_6 (Merck), in order to reach metal loading of 20%(w/w). The Graphite slurry was prepared by dispersing required amount of graphite in de-ionized water, sonicating for 10 min. For the seeded electrocatalyst was prepared by mixing approximately 10% (v/v) of the Pt solution with the graphite slurry and sonicated for 30 min. The seeded powder was obtained by the reduction of the previous solution with 0.1 M $NaBH_4$, sedimented by centrifugation and the pellet was harvested and dried at 110° C. Thereafter, the obtained graphite powder, covered by the seeded Pt, was dispersed in de-ionized water, sonicated for 30 min and then added to the remaining Pt solution (90%) to the required metal loading on graphite substrate (20% (w/w)). The mixture was again reduced with 0.1 M $NaBH_4$ under sonication to obtain the catalyst powder, which settled from the solution. The electrocatalyst solution was filtered, washed thoroughly with de-ionized water and dried overnight at 110° C. the Co catalyst was prepared in a same process like Pt catalyst, in this case the metal precursor was $CoCl_2$ (Merck)[2].

treatment of carbon support

a Carbon paper was used as a gas diffusion layer for fabricating gas diffusion electrode which was a circle with the diameter of 11 mm. in order to remove fat and redundant, carbon paper was rinsed in de ionized water and acetic acid with equal ratio and the dried at 200C.

Preparation of electrode

Pt/G and Co/G electrocatalysts were used for fabricating GDE with the loading of 0.3 mg/cm^2 at various percentage of them (20:80, 40:60, 50:50, 60:40, and 80:20(%w/w)) were used. (in a table 1. Different percent of fabricated electrodes with short names were taken). They mixed to distilled H_2O and C_3H_7OH with equal volumic ratio, then certain amount of polytetrafluoro ethylene (60%wt PTFE, Aldrich) with the loading of 30%, was added and sonicating at room temperature for 30 min, After evaporating the solvents, an uniform paste obtained which uniformly spread over the carbon paper and next sintered at 200 °C for 1 h.



No	percent of fabricated electrode	short name
1	Pt 20%-Co 80% /G	PtCo(28)
2	Pt 40%-Co 60% /G	PtCo(46)
3	Pt 50%-Co 50% /G	PtCo(55)
4	Pt 60%-Co 40% /G	PtCo(64)
5	Pt 80%-Co 20% /G	PtCo(82)

Electrochemical analysis

The oxygen reduction reaction (ORR) was evaluated in the cathode via an approach, in which the current density measured with respect to potential using a half-cell measurement apparatus which comprised a three-electrode system. An Ag/AgCl electrode was employed as the reference electrode, a Pt electrode constructed from Pt plate was utilized as the counter electrode and the GDE described above was used as the working electrode. The GDE was set in a holder and then placed in sulfuric acid (0.5 M). oxygen was introduced into the holder under a pressure of 1 atm. The room temperature was (300 K). The scanning rate, used in the experiments were as 1 mV.s⁻¹. The voltage scanned from -0.2 to 0.8 V vs. an Ag/AgCl electrode. by the means of LSV and EIS analysis, synergism effect was studied and the electrode with the highest performance to ORR determined.

Results and discussion

in fig.1 The polarization curves for different percentage of physical mixture of platinum and cobalt electrocatalyst were shown. As it was seen, the ORR current was increase with decreasing the potential. the PtCo(82) electrode has highest performance toward ORR compare to others and Platinum electrode either, it means cobalt improve the catalytic activity of platinum electrode. So it could be said that synergism effect was seen in PtCo(82). in Fig. 2 the Nyquist plots of the electrodes were shown. all of them indicate two incomplete semi-circle that overlap each other, by the means of z-view software, equivalent circuit elements were drawn. Since, the diameter of the semi-circle is equal to the polarization resistance, so with decreasing the polarization resistance ORR activity was improved. In the PtCo(82) fabricated GDE, the best performance for ORR was seen. In this electrode, the charge transfer resistance was minimum. It intends to fast electron transfer in the GDE for leading to highest performance for ORR. Also the amount of cobalt in the reaction layer affected on electrochemical activity of electrode for ORR. Except in optimized percent, With increasing of Cobalt amount in reaction layer, the performance of electrode was decreased.

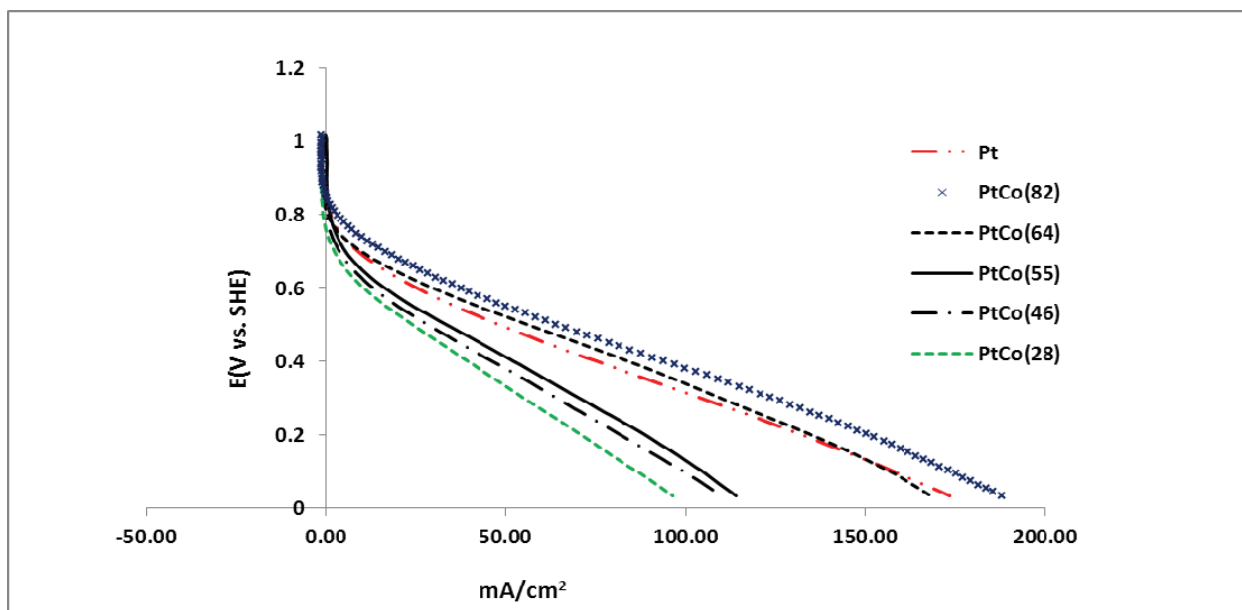


Fig.1. Polarization curves of a single PEM fuel cell for oxygen reduction at potential range of -0.02 to 1 vs. an Ag/AgCl with an electrocatalyst loading on GDL of 0.5 mg/cm² when using Pt-Co/G electrocatalyst prepared at metal loading on Graphite substrate of 20% at 300K.

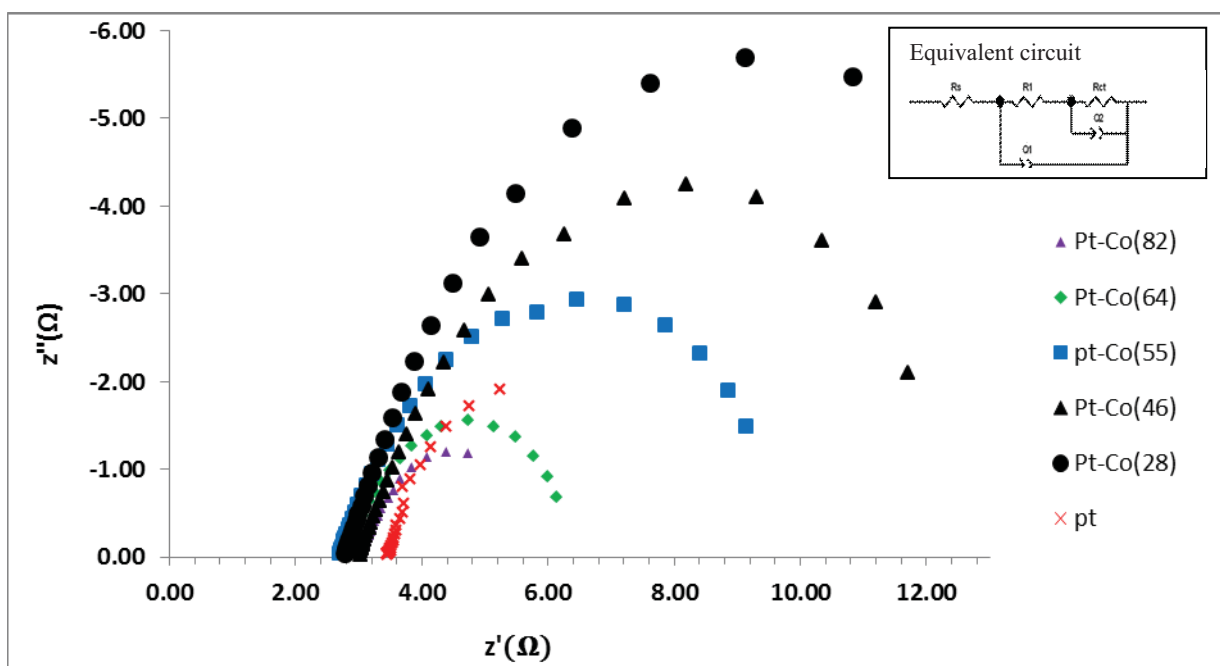


Fig.2. Nyquist plots obtain from synthesized electrocatalyst at the potential of 300 mv in frequency range of 15kHz to 10Hz

Conclusion:

In this work, synergism effect in physical mixture of GDEs electrode were studied. According to linear sweep voltammetry and impedance spectroscopy, PtCo(82)/G electrode showed synergism effect and had high catalytic activity toward ORR. In other word the presence of Cobalt with percent of 20 % (w/w) in the mixture of Platinum and Cobalt electro catalysts, provide special condition for synergism effect. However in other percent, With



increasing the Cobalt amount in the reaction layer, the performance of electrode was diminished.

References

1. Zhao Fu, Weishan Li, Weiguang Zhang, Fengqiang Sun, Zhihui Zhou, Xingde Xiang.” Preparation and activity of carbon-supported porous platinum as electrocatalyst for methanol oxidation “, international journal of hydrogen energy (2010), 35: 8101 – 8105
2. Juan Ma, Yawen Tang, Gaixiu Yang, Yu Chen, Qun Zhou, Tianhong Lu, Junwei Zheng .”Preparation of carbon supported Pt–P catalysts and its electrocatalytic performance for oxygen reduction”, Applied Surface Science (2011) 257: 6494–6497
3. Wiruyn Trongchuan kij , Kejvalee Pruksathorn, Mali Hunsom. ” Preparation of a high performance Pt–Co/C electrocatalyst for oxygen reduction in PEM fuel cell via a combined process of impregnation and seeding”. Applied Energy (2011) 88: 974–980
4. S. Litster, G. McLean.” PEM fuel cell electrodes Review”. Journal of Power Sources (2004),130: 61–76
5. Hussien Gharibi, Rasol Abdullah Mirzaie” Fabrication of gas-diffusion electrodes at various pressures and investigation of synergetic effects of mixed electrocatalysts on oxygen reduction reaction”. Journal of Power Sources (2003), 115: 194–202



Novel organic-inorganic nanocomposite membranes for PEM fuel cells

Khadijeh Hooshyari¹, Mehran Javanbakht^{2,*}, Morteza Enhessari³

Department of Chemistry, Amirkabir University of Technology, Tehran, Iran

khadijeh_hooshyari@yahoo.com

Abstract

PVA (poly vinyl alcohol)-Fe₂TiO₅ (PF) and PVA-PVP (poly vinyl pyrrolidone)-Fe₂TiO₅ (PPF) nanocomposite membranes have been prepared with solutions casting method. Glutaraldehyde (GA) was used as cross linking agent. The nanocomposite membranes were characterized by using AC impedance spectroscopy (IS), Fourier transform infrared spectroscopy (FT-IR), scanning electron microscopy (SEM) coupled with energy dispersive x-ray (EDX), tensile strength (TS) and thermogravimetric analysis (TGA). The results showed that the good water uptake and proton conductivity of the PF and PPF nanocomposite membranes respect to the PVA based membrane. PPF nanocomposite membranes containing 3 wt % of Fe₂TiO₅ nanoparticles and mass ratio of (PVA: PVP 76:23) demonstrated higher water uptake (310%) and proton conductivity (0.26 S/cm) than that of PF and other PPF nanocomposite membranes.

Keywords: PEMFC; Poly vinyl alcohol; Poly vinyl pyrrolidone; Nanocomposite; Proton exchange membrane; Proton conductivity.

1. Introduction

Proton exchange membrane fuel cells (PEMFCs) are generally accepted as an attractive conventional power sources, due to their high efficiency and lack of pollution [1, 2]. Perfluorosulfonated ionomers, such as Nafion, are one of the most advanced commercially available membranes for PEMFCs because of their excellent chemical and thermal stability, good mechanical strength and high proton conductivity [3]. However, Nafion membrane applications in PEMFCs are still limited by operation at temperatures below 80°C, high cost and methanol crossover [4]. Therefore, preparation of composite membranes with low-priced and high proton conductivity to replace commercial Nafion membrane has been the challenge of continuous researches. Poly vinyl alcohol, PVA, is highly hydrophilic, nontoxic and low cost polymer with an excellent film forming property. PVA films have good chemical and mechanical stability and high potential for chemical cross-linking [5, 6]. These properties of PVA must be considered by researchers. But low proton conductivity and high swelling (even dissoluble in water at higher temperature) of PVA membrane limit its application in PEMFCs [7]. According to a new research report, addition of hygroscopic metal oxide nanoparticles such

¹ - Department of Chemistry, Amirkabir University of Technology, Tehran, Iran.

² - Renewable Energy Research Center, Amirkabir University of Technology, Tehran, Iran, mehranjavanbakht@Gmail.com.

³ - Department of Chemistry, Naragh Branch, Islamic Azad University, Naragh, Iran, Enhessari@gmail.com



as titanium oxide, zirconium oxide and zeolite in a PVA polymer matrix improves its water uptake and proton conductivity [8]. One of the effective approaches is to blend PVA with hydrophilic polymer such as Nafion, SPEEK, poly (styrene sulfonic acid-co-maleic acid) (PSSA-MA), which resulting enhance of the proton conductivity [9]. Several researches have used an aldehyde and dialdehyde to cross link of PVA and control its mechanical stability [10]. Previous researches have used sulfonation agents, such as sulfoacetic acid, and sulfosuccinic acid (SSA) as cross linking agents to prepare PVA based membranes

Recently, we introduced new proton conducting hybrid membranes for PEM fuel cells based on poly (vinyl alcohol) and nanoporous silica containing phenyl sulfonic acid.

In the previous work [11], we synthesized Nafion/Fe₂TiO₅ nanocomposite membranes by dispersion of Fe₂TiO₅ nanoparticles within the commercial Nafion membranes and the results showed 0.23 S/cm proton conductivity for Nafion/Fe₂TiO₅ nanocomposite membranes (2% wt) at room temperature. However, the high cost of commercial Nafion membrane is still considered as a fundamental problem. In this study, for the first time PVA/PVP/ Fe₂TiO₅ nanocomposite membranes were prepared at various operational conditions. In previous project [12], different parameters were investigated to optimize the preparation of PVA/PVP/Fe₂TiO₅ nanocomposite membranes in this work. Thermal and tensile properties of new membranes in this study were investigated and the results obtained are compared with Nafion/Fe₂TiO₅ nanocomposite membranes. In the present work, poly vinyl alcohol /poly vinyl pyrrolidone /Fe₂TiO₅ nanocomposite membranes were prepared by solution casting method. The structure, water uptake, proton conductivity, morphology, thermal stability and mechanical properties of nanocomposite membranes were investigated. The Fe₂TiO₅ nanoparticles content and PVP effects on the water uptake and proton conductivity, as two important parameters, were evaluated in this study.

2. Experimental

2.1. Materials

Poly (vinyl alcohol), PVA, 99+% hydrolyzed, with an average molecular weight of 145,000 was used as supplied by Merck. The cross-linking agent was a 25 wt % solution of glutaraldehyde (GA) in water (Merck). Poly vinyl pyrrolidone (average MW=40,000) was purchased from the Sigma-Aldrich and used as blend polymer with PVA membrane. Fe₂TiO₅ nanoparticles with a particle size range of 20 to 25 nm were used as modifier.

2.2. Preparation of membranes

The PVA based membranes were obtained by dissolving appropriate amounts of PVA and Fe₂TiO₅ nanoparticle, in de-ionized (DI) water under stirring at 80 °C. Water solutions of PVP were separately prepared and mixed with PVA solution. Then GA was gradually added. The resulting solution was stirred at 80 °C until becoming homogeneous and viscous. The well-mixed solution was cast into petri-glass dishes and allowed to dry and solidify for 24 h at room temperature. When visually dried, the membrane was dislodged from the petri-glass dishes easily. The prepared nanocomposite membranes were then stored in DI water to be kept hydrated for other process.

2.3. Water uptake measurements

Water uptake was determined as reported before. The membrane was equilibrated in de-ionized water at room temperature for 24 h. The saturated membrane was removed and the remaining water on the surface was dried by tissue papers, finally weighted instantly. For dried weight, the



membrane was dried in oven at 80 °C for 24 h, and then weighted immediately. This process reiterated for several times until reaching a stable result. The water uptake was calculated by the following equation:

$$\text{water uptake\%} = \frac{W_{\text{wet}} - W_{\text{dry}}}{W_{\text{dry}}} \times 100$$

Where, W_{wet} and W_{dry} are weights of wet and dry membrane, respectively.

2.4. Proton conductivity measurements

The proton conductivity of membranes was calculated by the AC impedance spectroscopy with PGSTAT303N potentiostat/Galvanostat (Ecochemie). The sample membrane was immersed in de-ionized water for 24 h at room temperature and then sealed between two platinum plates electrodes. The measurements were carried out on the potentiostatic mode. The spectra were recorded with Signal amplitude of 50 mV in the frequency range of 100 Hz – 1 MHz with 100 points .The resistance of the membrane was obtained from the high-frequency intercept of the impedance. The conductivity values were calculated by using the equation ($\sigma = L/RS$), where, σ , L, R, S respectively refer to, proton conductivity (S cm^{-1}), thickness (cm), resistance from the impedance data (Ω) and cross-sectional area (cm^2) of the membranes.

2.5. FT-IR ATR spectra

The FT-IR ATR spectra ($600\text{-}4000 \text{ cm}^{-1}$, resolution 4 cm^{-1}) were recorded with a Bruker Equinox 55 using an attenuated total reflectance (ATR, single reflection) accessory purged with ultra dry compressed air.

2.6. SEM and EDX measurements

The morphology of nanocomposite membranes were investigated by using a Scanning electron microscopy (SEM), (JSM-5600, Jeol Co.), coupled with energy dispersive x-ray (EDX) spectroscopy. The samples were freeze-fractured in liquid N_2 and coated with gold plate before SEM observations were carried out.

2.7. Thermal and mechanical stability

Thermogravimetry analysis (TGA) of the nanocomposite membranes were carried out by using a TGA TA Instruments 2050 system ,at the heating rate of $20 \text{ }^\circ\text{C}/\text{min}$ in nitrogen atmosphere from 25 to $600 \text{ }^\circ\text{C}$. For determining mechanical properties at first membranes were dried and then mechanical properties of the prepared membranes were measured by using Zwick/Roell Z030 tensile test machine. All the membranes were cut to the standard shape and all tests were performed at a crosshead speed of $10 \text{ mm}/\text{min}$ and room temperature (25°C).

3. Results and Discussion

3.1. Water uptake and proton conductivity measurements

Water uptake is a very important parameter in the membrane because the proton conductivity powerfully depends on water content. The nanocomposite membranes based PVA were prepared with Fe_2TiO_5 nanoparticles. PF and PPF (PVA: PVP 84:16) nanocomposite membranes respectively with 4 wt % and 3 wt % of Fe_2TiO_5 nanoparticles displayed a higher water uptake and proton conductivity than that of PVA based membranes (Table 1). This

improvement was attributed to the hydrophilic nature of Fe_2TiO_5 nanoparticles and PVP within the PVA matrix.

PVA nanocomposite membranes displayed high proton conductivity compared with Nafion/ Fe_2TiO_5 nanocomposite membranes [11] due to high water uptake which attributed to hydrophilic nature of PVA and PVP.

According to the high surface energy of Fe_2TiO_5 nanoparticles, they have chemical interactions with the environment; therefore they are extremely unstable. Hence, their self-aggregation leads to a decrease in their specific surface and consequently in their water uptake and proton conductivity. So Fe_2TiO_5 nanoparticles content, as a key parameter in manufacturing of nanocomposite membranes, was investigated in this study. Figure 1 shows that addition of higher than 4 wt % and 3 wt % of Fe_2TiO_5 nanoparticles respectively decreased the proton conductivity of PF and PPF nanocomposite membranes, this results can be attributed to the self-aggregation of the nanoparticles inside the membranes.

PPF (PVA: PVP 84:16) nanocomposite membranes with 3 wt % of Fe_2TiO_5 nanoparticles demonstrated a higher water uptake and proton conductivity than PM nanocomposite membranes. Table 1 and Figure 1 confirm these results. PVP owing to high polarity of $-\text{N}-\text{C}=\text{O}$ group has good hydrophilic nature and makes strong hydrogen-bonding with water result an increase in the water uptake and proton conductivity of PPF nanocomposite membranes.

The Nyquist plot for PPF (PVA: PVP 84:16) membranes were shown in Figure 2, at fully hydrated condition. PPF (PVA: PVP 84:16) nanocomposite membranes with 3%.wt. of nanoparticles displayed a lower resistance (higher proton conductivity) than that of the other PPF nanocomposite membranes.

The results showed that, the water uptake of the synthesized nanocomposite membranes was higher than commercial Nafion 117 membrane and their proton conductivity was successfully comparable to that.

3.2. FT-IR ATR spectra

Figure 3 shows the typical ATR spectra measured for PVA and PPF (containing 3 wt % of Fe_2TiO_5 nanoparticles and PVA: PVP 84:16) membranes. The broad bands at around $3200-3600\text{ cm}^{-1}$ are observed due to hydrogen bonding and $-\text{OH}$ single vibration. The high intensity of the $-\text{OH}$ peak in the PPF nanocomposite membranes compared with PVA membranes, because of hydrogen bonding of PVP, was also clearly observed. The bands at 2907 cm^{-1} and $1324-1422\text{ cm}^{-1}$ were attributed to the C-H stretching and bending vibrations of methylene groups respectively. The peak around 2850 cm^{-1} suggests the presence of such free aldehyde groups. The peak at $1720-1730\text{ cm}^{-1}$ suggests the presence of such free $\text{C}=\text{O}$ groups, but was apparently covered by vicinity band in this region. The presence of PVP in the PPF nanocomposite membrane was confirmed by the bands assigned to the $\text{C}=\text{O}$ and $\text{N}-\text{C}$ stretching vibrations at $1657-1674\text{ cm}^{-1}$. The peak at 1000 cm^{-1} was assigned to the C-O groups of PVA based membrane. The presence of $-\text{OH}$ groups in the PVA chain allows the reaction with $-\text{CHO}$ groups in GA and formation of ether bonds (C-O-C). The bands at $1200-1250\text{ cm}^{-1}$ were attributed to the ether bonds (C-O-C).

3.3. SEM and EDX measurements

The SEM morphologic examination of PVA, PF (4 wt % of nanoparticles) and PPF (containing 3 wt % of nanoparticles and PVA: PVP 84:16) membranes are shown in Figures 4(a), (b) and (c) respectively.

The SEM image showed in Figure 4(a), demonstrated that the PVA based membrane has a homogenous structure. From SEM images in Figures 4(b) and (c), the Fe_2TiO_5 nanoparticles in



the PF and PPF nanocomposite can be clearly seen. Dispersion of the Fe and Ti nanoparticles in the cross-section of PPF nanocomposite membrane, with 3 wt % of Fe_2TiO_5 nanoparticles and PVA: PVP 84: 16 was investigated by the EDX mapping images and displayed in Figure 5. EDX distribution demonstrated homogenous distribution of Fe and Ti nanoparticles in the PPF nanocomposite membranes.

3.4. Thermal properties

From the Figure 6, PF (4 wt %) and PPF (3 wt %, PVA: PVP 84:16) nanocomposite membranes demonstrated a higher thermal stability than PVA based membrane. Incorporation of Fe_2TiO_5 nanoparticles in PVA polymer matrix leads to increase the decomposition temperature of nanocomposite membranes compared with PVA based membrane. GA as cross linking agent causes PVA structure to become more compacted and rigid and resulting a decrease in the free volume capable of containing water molecules and an increase in the thermal stability of nanocomposite membranes compared with PVA based membrane. PVP and Fe_2TiO_5 nanoparticles are strongly hydrophilic components and in appropriate amount can produce membranes with good thermal and water uptake properties.

PPF nanocomposite membranes due to high polarity of $-\text{N}-\text{C}=\text{O}$ group of PVP, which make strong hydrogen-bonding with PVA and intense intra-molecular interaction, displayed a higher thermal stability than PF nanocomposite membranes. The high thermal stability of PPF (PVA: PVP 84:16) nanocomposite membranes with 3 wt % of Fe_2TiO_5 nanoparticles, confirmed their capabilities at high temperatures PEMFCs.

It should be noted that the thermal stability of the PVA nanocomposite membranes (350 °C) in amounts less than the Nafion/ Fe_2TiO_5 nanocomposite membranes (500 °C).

3.5. Mechanical properties

Table 2 shows mechanical properties of the PVA, PF (4 % wt of nanoparticles) and PPF (PVA: PVP 84:16, 3% wt of nanoparticles) membranes. It was found that the nanocomposite membranes due to strong interactions of Fe_2TiO_5 nanoparticles with PVA based membrane, displayed a higher mechanical stability than PVA based membrane. The PPF nanocomposite membranes because of the strong interfacial interactions of PVP show the best mechanical properties. Uniform dispersion of nanoparticles in the PPF nanocomposite membranes, which increases the PVA-nanoparticles interactions, plays also a key role in improvement of its mechanical stability. PPF nanocomposite membranes are adequate to be fabricated into membrane electrode assemblies.

Conclusion

In this work, we synthesized nanocomposite membranes using high hydrophilic, nontoxic and low cost PVA which displayed high proton conductivity compared with Nafion/ Fe_2TiO_5 nanocomposite membranes.

Advanced nanocomposite membranes based of PVA/PVP/ Fe_2TiO_5 were prepared by solution casting method. PVA, PVP and Fe_2TiO_5 were used as based polymer, blend polymer with PVA and inorganic modifier respectively. Glutaraldehyde (GA) was used as cross-linking agent. The nanocomposite membranes with 3 wt % of Fe_2TiO_5 nanoparticle in the presence of PVP due to the strongly hydrophilic character of PVP and Fe_2TiO_5 nanoparticles, showed a higher water



uptake and proton conductivity compared to those of the PVA based membrane. The strong surface interactions of Fe_2TiO_5 nanoparticles and great interfacial interactions of PVP increase the mechanical properties of nanocomposite membranes. The results of SEM-EDX analysis have provided detailed information about the homogenous distribution of nanoparticles in the nanocomposite membranes. FT-IR ATR spectra confirmed characteristic peaks of -OH, C-H, C=O, C-O and C-O-C groups at nanocomposite membranes.

References

- [1] J.M. Andujar, F. Segura "Fuel cells History and updating, A walk along two centuries", *Renewable & Sustainable Energy Reviews*, (2009). 13, 2309-2322.
- [2] Appleby AJ, Foulkes FR "Fuel cell handbook", New York: Van Nostrand Reinhold, (1989).
- [3] C.Y. Chen, J.I. Garnica, M.C. Duke, D.F. Dalla, A.L. Dicks, J.C. Diniz "Nafion/polyaniline/silica composite membranes for direct methanol fuel cell application", *J Power Sources*, (2007). 166, 324-330.
- [4] Z. Wu, G. Sun, W. Jin, H. Hou, S. Wang, Q. Xin "Nafion and nano-size $\text{TiO}_2\text{-SO}_4^{2-}$ solid superacid composite membrane for direct methanol fuel cell", *J Membr Sci*, (2008). 313, 336-343.
- [5] R.K. Nagarale, W. Shin, P.K. Singh "Progress in ionic organic-inorganic composite membranes for fuel cell applications", *J Polym Chem*, (2010). 1, 388-408.
- [6] A. Martinelli, M.A. Navarra, A. Matic, S. Panero, P. Jacobsson, L. rjesson "Structure and functionality of PVDF/PAN based, composite proton conducting membranes", *Electrochim Acta*, (2005). 50, 3992-3997.
- [7] C.C. Yang, W.C. Chien, T.J. Li "Direct methanol fuel cell based on poly (vinyl alcohol)/titanium oxide nanotubes/poly (styrene sulfonic acid) (PVA/nt- TiO_2 /PSSA) composite polymer membrane", *J Power Sources*, (2010). 195, 3407-3415.
- [8] D.S. Kim, H.B. Park, J. Rhim, Y.M. Lee "Preparation and characterization of crosslinked PVA/ SiO_2 hybrid membranes containing sulfonic acid groups for direct methanol fuel cell applications", *J Membr Sci*, (2004). 240, 37-48.
- [9] C.E. Tsai, C.W. Lin, J. Rick, B.J. Hwang "Poly (styrene sulfonic acid)/poly (vinyl alcohol) copolymers with semi-interpenetrating networks as highly sulfonated proton-conducting membranes", *J Power Sources*, (2011). 196, 5470-5477.
- [10] D.S. Kim, H. Cho, D.H. Kim, B. Lee, S. Yoon, Y. Kim, G. Moon, H. Byun, J. Rhim "Surface fluorinated poly(vinyl alcohol)/poly(styrene sulfonic acid-co-maleic acid) membrane for polymer electrolyte membrane fuel cells", *J Membr Sci*, (2009). 342, 138-144.
- [11] K. Houshyari, M. Javanbakht, L. Naji, M. Enhessari "Physical and Electrochemical Study of Nafion/ Fe_2TiO_5 Nanocomposite Membranes for High Temperature PEM Fuel Cells", 4th International Conference on Nanostructures (ICNS4).
- [12] K. Houshyari, M. Javanbakht, L. Naji, M. Enhessari "Nanocomposite proton exchange membranes based on PVA (Poly vinyl alcohol) - PVP (Poly vinyl pyrrolidone) containing Fe_2TiO_5 nanoparticles for PEMFC", 4th International Conference on Nanostructures (ICNS4).

Table 1- Specification of synthesized PVA nanocomposite membranes.

Membranes	Nanoparticles wt %	Water uptake %	Proton conductivity (S cm ⁻¹)
PPF (PVA:PVP 84:16)	3	430	0.26
PF	4	250	0.35
PVA	-	180	0.0005
Nafion/Fe ₂ TiO ₅	4	15	0.015
Nafion/Fe ₂ TiO ₅	3	20	0.04
Nafion/Fe ₂ TiO ₅	2	35	0.23

Table 2- Mechanical properties of PVA nanocomposite membranes.

Membranes	Nanoparticles wt %	Elongation at break (%)	Tensile strength (MPa)
PPF (PVA: PVP 84:16)	3	20.34	105.5
PF	4	5.83	270.13
PVA	-	5.23	22.19

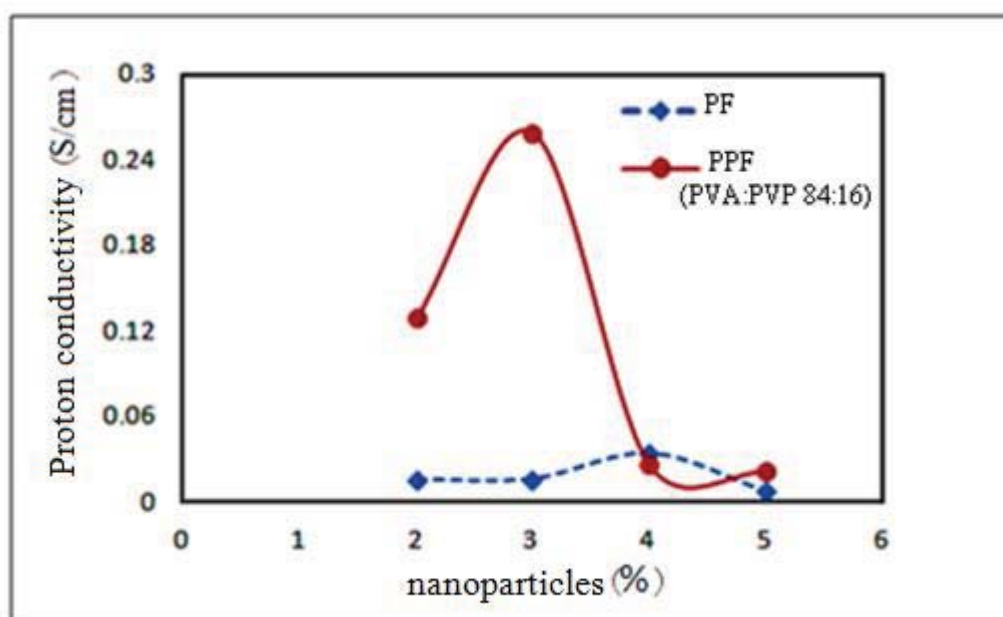


Figure 1. Proton conductivity of PF and PPF nanocomposite membranes.

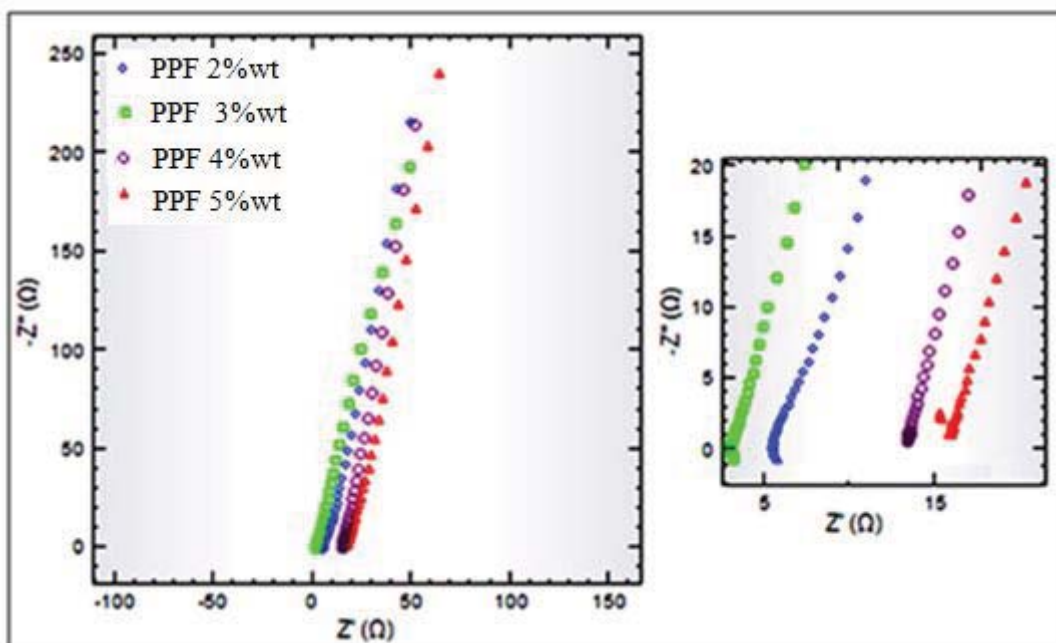


Figure 2. Nyquist plot of PPF (PVA:PVP 84:16) nanocomposite membranes.

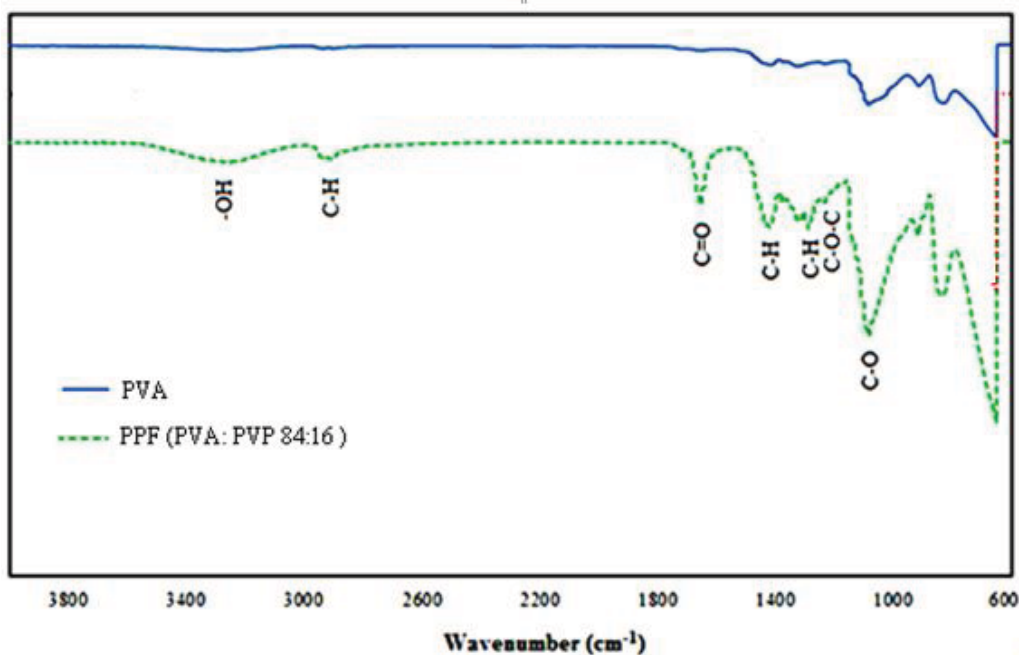


Figure 3. ATR spectra measured for PVA and PPF (3 wt %, PVA: PVP 84:16) membranes.

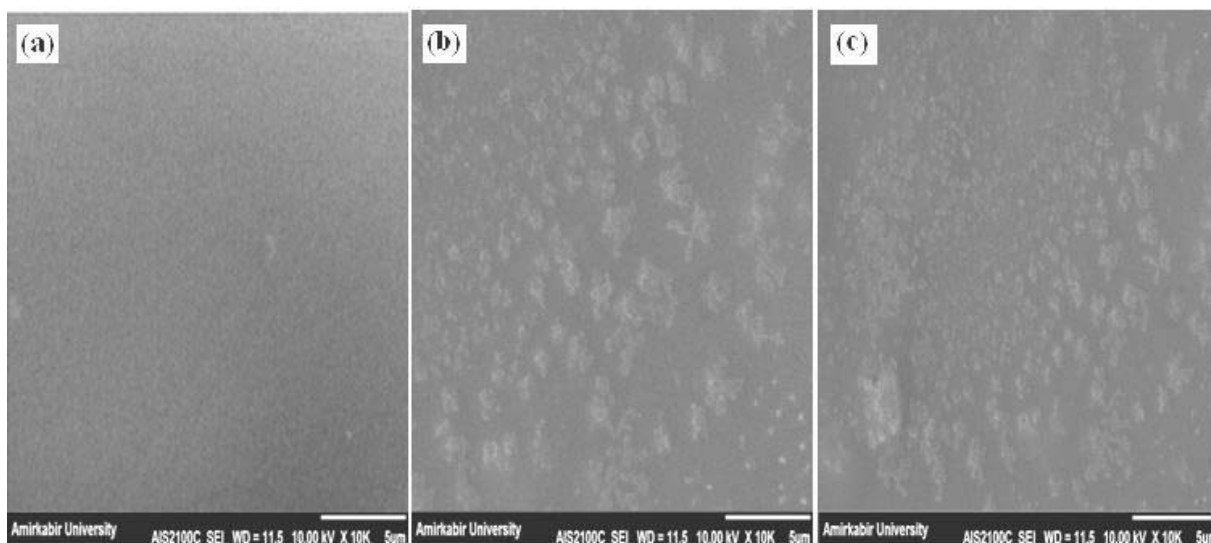


Figure 4. SEM images of the (a) PVA, (b) PF (4 wt %) and (c) PPF (3 wt %, PVA: PVP 84:16)

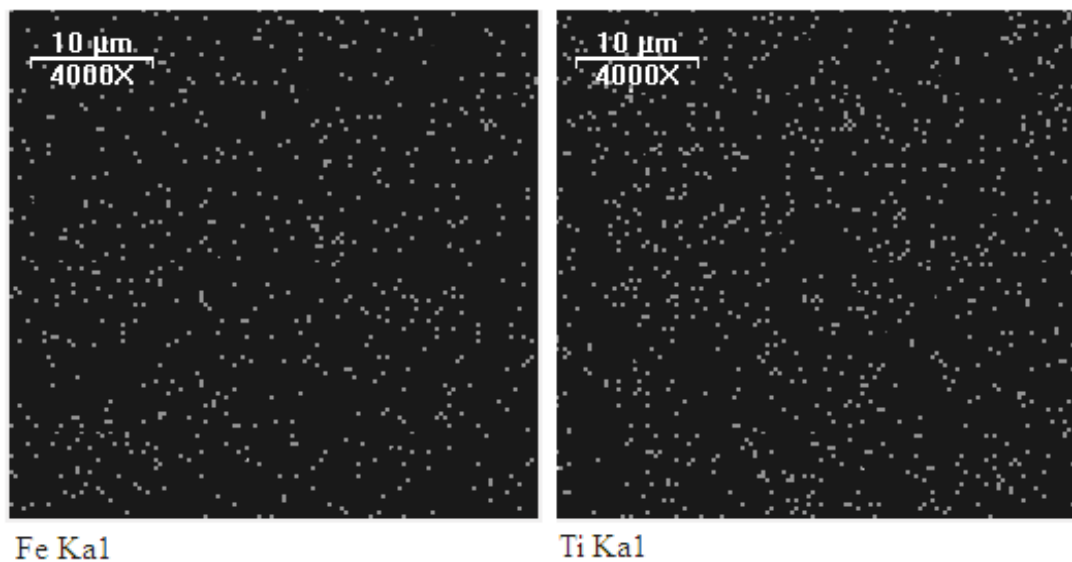


Figure 5. Nyquist plot of PPF (3 wt %, PVA: PVP 84:16) nanocomposite membranes.

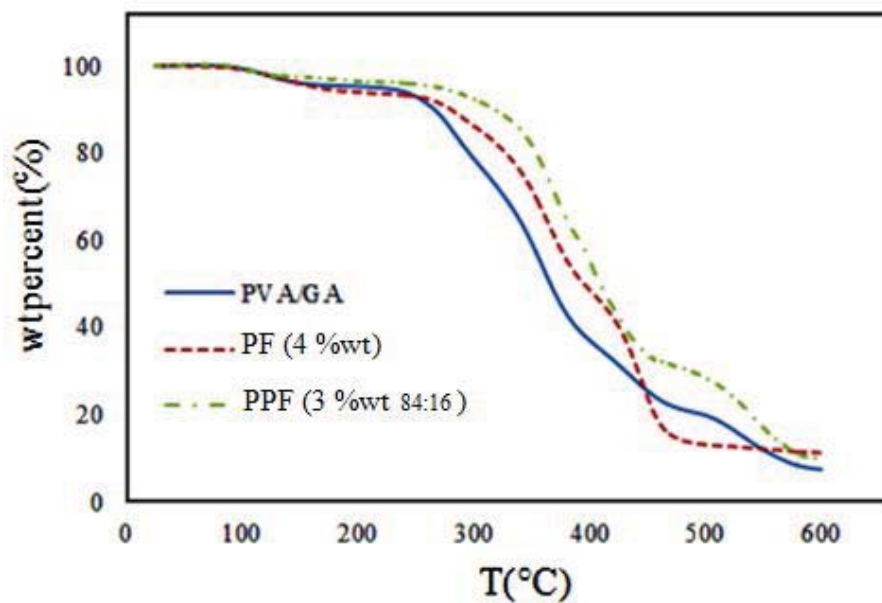


Figure 6. TGA data of PVA membranes.